Design Guide for FRP Composite Connections

ASCE Manuals and Reports on
Engineering Practice No. 102

Ayman S. Mosallam, Ph.D., P.E.

ASCE

CI ASCE | CONSTRUCTION INSTITUTE

Design Guide for FRP Composite Connections

By Ayman S. Mosallam, Ph.D., P.E.

Sponsored by
the Structural Composites and Plastics Committee of
the Construction Institute of
the American Society of Civil Engineers

ASCE AMERICAN SOCIETY
OF CIVIL ENGINEERS

CI
CONSTRUCTION
INSTITUTE
ASCE

Any statements expressed in these materials are those of the individual authors and do not necessarily represent the views of ASCE, which takes no responsibility for any statement made herein. No reference made in this publication to any specific method, product, process, or service constitutes or implies an endorsement, recommendation, or warranty thereof by ASCE. The materials are for general information only and do not represent a standard of ASCE, nor are they intended as a reference in purchase specifications, contracts, regulations, statutes, or any other legal document.

ASCE makes no representation or warranty of any kind, whether express or implied, concerning the accuracy, completeness, suitability, or utility of any information, apparatus, product, or process discussed in this publication, and assumes no liability therefor. This information should not be used without first securing competent advice with respect to its suitability for any general or specific application. Anyone utilizing this information assumes all liability arising from such use, including but not limited to infringement of any patent or patents.

ASCE and American Society of Civil Engineers—Registered in U.S. Patent and Trademark Office.

Photocopies and permissions. Permission to photocopy or reproduce material from ASCE publications can be obtained by sending an e-mail to permissions@asce.org or by locating a title in ASCE's online database (http://cedb.asce.org) and using the "Permission to Reuse" link. *Bulk reprints.* Information regarding reprints of 100 or more copies is available at http://www.asce.org/reprints.

MANUALS AND REPORTS
ON ENGINEERING PRACTICE

(As developed by the ASCE Technical Procedures Committee, July 1930, and revised March 1935, February 1962, and April 1982)

A manual or report in this series consists of an orderly presentation of facts on a particular subject, supplemented by an analysis of limitations and applications of these facts. It contains information useful to the average engineer in his or her everyday work, rather than findings that may be useful only occasionally or rarely. It is not in any sense a "standard," however; nor is it so elementary or so conclusive as to provide a "rule of thumb" for nonengineers.

Furthermore, material in this series, in distinction from a paper (which expresses only one person's observations or opinions), is the work of a committee or group selected to assemble and express information on a specific topic. As often as practicable, the committee is under the direction of one or more of the Technical Divisions and Councils, and the product evolved has been subjected to review by the Executive Committee of the Division or Council. As a step in the process of this review, proposed manuscripts are often brought before the members of the Technical Divisions and Councils for comment, which may serve as the basis for improvement. When published, each work shows the names of the committees by which it was compiled and indicates clearly the several processes through which it has passed in review, in order that its merit may be definitely understood.

In February 1962 (and revised in April 1982) the Board of Direction voted to establish a series entitled "Manuals and Reports on Engineering Practice," to include the Manuals published and authorized to date, future Manuals of Professional Practice, and Reports on Engineering Practice. All such Manual or Report material of the Society would have been refereed in a manner approved by the Board Committee on Publications and would be bound, with applicable discussion, in books similar to past Manuals. Numbering would be consecutive and would be a continuation of present Manual numbers. In some cases of reports of joint committees, bypassing of Journal publications may be authorized.

MANUALS AND REPORTS ON ENGINEERING PRACTICE CURRENTLY AVAILABLE

PREFACE

In recent years, the construction industry has realized the potential of using fiber-reinforced polymer (FRP) composites in construction applications. As with any emerging technology, the construction industry and civil engineering community struggled with the design and application of these systems. Frequently, engineers experienced tremendous difficulties when they attempted to utilize FRP materials in a manner similar to practice with conventional materials such as steel, concrete, and wood. One obstacle was a lack of design standards and authoritative codes for the use of FRP materials in construction applications. Despite the fact that there was a great deal of research and applications information available from the aerospace industry, which spanned more than a half-century, civil engineers are still searching for ways to convince themselves as to the reliability, applicability, and structural efficiency of FRP materials. The Construction Institute's Structural Composites and Plastics Committee (SCAP) of the American Society of Civil Engineers (ASCE) recognized the need for developing reliable design specifications for FRP composites and has been working with the composite industry and the civil engineering community to achieve this goal.

One FRP composite product that is getting attention from the construction industry is pultruded FRP (PFRP) composites. PFRP composites have been available for the past 40 years or so, and they are popular in specific industries for their noncorrosiveness, electromagnetic transparency, and high strength-to-weight characteristics. For this reason, they have been used mainly by structural engineers—with some exceptions—as secondary, nonstructural applications. SCAP has been taking the lead in providing reliable information on PFRP composite materials. In the late 1980s, two pioneering publications were developed by SCAP,

namely, the *Structural Plastic Design Manual* in 1984, and the *Structural Plastics Selection Manual* in 1985. In 1995, ASCE jointly with the Pultrusion Industry Council (PIC) of the Society of the Plastics Industry (SPI) launched a multiphase project with a long-range goal of developing accepted standards for structural design, fabrication, and erection of PFRP composite structural systems. The first phase of the project was completed in 1996 with a prestandard document that was co-developed by the author. Currently, the second phase of the PFRP standard development project is underway and is expected to be available to the public in the near future. As a continuing effort by ASCE-SCAP, this publication is aimed at providing analytical and design information on critical aspects that are essential in designing PFRP composite structures, that is, PFRP plate joints and frame shear and moment connections.

This technical design manual, comprising nine chapters, covers major issues related to the analysis and design of composite joints and frame connections that are lacking in other national and international standards, design manuals, and technical publications. In this manual, the term "joint" refers to plate shear joints such as single- and double-lap joints that are commonly used in aerospace applications, and some civil engineering structural elements such as gusset plates for PFRP trusses and bracing members. The term "connection" in this manual refers to civil engineering-type construction framing joints between structural members such as beams, girders, columns, bases and foundations, and truss members. Examples of these typical connection details are presented and discussed in Chapters 7 and 8 of this manual.

Topics covered herein are: (1) design philosophy and design considerations for structural composite members and connections; (2) basic information and research and development work on the mechanics of fasteners and bolted composite joints; (3) analysis and design methods for bolted composite joints; (4) basic physical and mechanical information on structural adhesives and bonded composite joints; (5) analysis and design methods for bonded composite joints; (6) structural performance combined (bolted/bonded) joints; (7) basic information and research and development related to PFRP framing connections; (8) analysis and design methods for PFRP framing connections; and (9) numerical analysis review of available finite element codes suitable for modeling and designing composite frame structures. Throughout this manual, step-by-step practical numerical design examples and connection details are presented to make this manual unique, more effective for designers, and suitable as an undergraduate and graduate textbook. In addition, and in order to facilitate the analysis and design procedures, FORTRAN computer codes were developed to analyze both single- and multi-bolted pultruded composite joints as well as adhesively bonded joints. The bolted joints program is based on experimental studies conducted on a large number of typical

off-the-shelf pultruded composite joint specimens. User instructions are provided, in addition to several graphs generated from these programs to assist design engineers, at the Construction Institute Web site, http://www.constructioninst.org. A second computer code for analyzing adhesively bonded composite joints is available at the same site, along with user instructions. This program is based on a simplified approach developed by NASA. The Web site provides information on using these FORTRAN programs and finite element animation for selected FE models described in Chapter 9.

This manual is intended for structural engineers (civil, aerospace, mechanical, naval, etc.) designing with FRP composites in general and pultruded composites in particular. It is also a useful source of information for composite manufacturers, especially pultruders, FRP fabricators, contractors, code and national standards developers, buildings officials, and academics and researchers as well as undergraduate and graduate students and others who have interest in composite frame connections.

I gratefully acknowledge the support of the ASCE Construction Institute led by Dr. Marvin Oey, the SCAP committee chaired by Dr. Albert Doris, and the contributions of all members of SCAP. Special thanks to Professor Hota GangaRao, West Virginia University, for his valuable technical contributions and for his careful technical review of the manuscript, and to Professor Robert Yuan, Lamar University, for his assistance in providing the Phase I ASCE/SCAP Connections Report. Thanks also go to the two technical review panels of this manual.

The technical contributions of the following individuals are highly acknowledged:

- Dr. L. J. Hart-Smith, Boeing Company, Long Beach, California, for his constructive advice and support, and for providing valuable technical information that was used throughout this manual,
- Dr. Chris Chamis of NASA-Glenn for providing valuable information on bolted and adhesively bonded composite joints,
- Mr. Xiantan Liu, Air Cargo Co., Los Angeles, California, and Professor Jesa Kreiner of California State University at Fullerton, for their valuable contributions in Chapter 9 related to finite element modeling of PFRP frames,
- Dr. Hussein Elsanadedy of the Helwan University, Egypt, for his efforts in the development of the FORTRAN computer codes for bolted and bonded joints,
- Professor Nahla Hassan of Ain Shams University, Egypt, and Mr. C. Rosner, independent consulting engineer, for providing valuable experimental information that was used as the foundation of the design approach I developed in Chapter 3,

- Dr. Rashid Miraj of the University of California for his tremendous effort and technical contributions in all chapters of this manual, and
- Dr. Frank Abdi of AlphaSTAR Corporation, Long Beach, California, for providing information on GENOA progressive failure analysis of composite T-joints.

The careful editorial review of Ms. Shayla Markham and the technical reviews and input of Professor Selim Pul of Karadeniz Technical University of Turkey are highly appreciated, as are the contributions toward figure and table production by Dr. Ahmed Nasr and Mr. Ahmed El Sadek of the University of California, Irvine.

I would like to thank two pultrusion companies for providing photographs that were used in this manual, Fiberline Company A/S of Denmark, Strongwell Company of the United States, and ApATeCh of Russia.

I would like to give special and sincere thanks to my wife, Hanaa, for her patience and tremendous support and encouragement, in addition to her voluntary contributions in typing a large portion of Chapter 2, and to my two sons, Tamer and Dean, hoping that they will forgive me for being away from them while preparing this manual.

Finally, I would like to state that I have endeavored to bring all of my experience, knowledge, and wisdom into the pages of this design manual. It is my hope and desire that practicing engineers will use this tool to develop safe and innovative systems. It is also my wish that the next generation of engineers will use this manual as a roadmap to avoid the errors of the past. In that regard, best practices save lives and ASCE continues to lead the way.

Ayman S. Mosallam, Ph.D., P.E.
Professor, Civil & Environmental Engineering Department
Professor, Materials & Chemical Engineering Department
Director, Structural Engineering Testing Hall
University of California, Irvine
Irvine, California 92697-2175
e-mail: mosallam@uci.edu
Web Page: http://www.eng.uci.edu/users/ayman-mosallam

BLUE RIBBON REVIEW PANEL

Frank Abdi, AlphaSTAR
Alan Lau, Hong Kong Polytechnic University Department of Mechanical Engineering
Mahmoud Taha, University of New Mexico Department of Civil Engineering

To my wife Hanaa, and my sons Tamer and Dean. . . .

CONTENTS

CHAPTER 1

DESIGN PHILOSOPHY AND DESIGN CONSIDERATIONS FOR STRUCTURAL COMPOSITE MEMBERS AND CONNECTIONS

1.1 INTRODUCTION

One of the major obstacles preventing the wide use of fiber-reinforced polymer (FRP) composites in structural applications is the absence of relevant unified design standards. An FRP composite-related design standard, supported by national consensus, is essential to encourage the acceptance and use of such composites by practicing engineers in construction. In the United States, the Construction Institute of the American Society of Civil Engineers (ASCE) has recognized the urgent need to establish unified design standards for the emerging FRP construction materials. Therefore, in 1995, ASCE and the Pultrusion Industry Council (PIC) initiated a joint multiphased project to produce the standard document for the design of pultruded fiber-reinforced polymer (PFRP) composite structures. The first phase of this project was completed in 1996. Similar efforts have been initiated in Japan, Canada, and Europe. This document represents the most current effort to support the design and fabrication community. As an historical note, the "old" PIC existed for many years as part of the Composites Institute of the Society of Plastics Industry (SPI). In 1998, the Composites Institute left the SPI and merged with the Composite Fabricators Association (CFA). Under the tutelage of the CFA, the PIC was reestablished in 1999 with new bylaws and a new focus on initiatives. In October 2003, the CFA reorganized and changed its name to the American Composite Manufacturers Association (ACMA).

1.2 BACKGROUND

Over the past five decades or so, ASCE has played an important role in the development of several standard documents for different materials and systems. Since the 1960s, ASCE has developed or co-developed several engineering publications dealing with both unreinforced and FRP materials and systems. For example, in 1984 the ASCE *Structural Plastics Design Manual* (ASCE 1984) was published by the Plastics Research Council of the Materials Division of ASCE (currently known as the Structural Composites and Plastics Committee, SCAP). As the acceptance of and demand for FRP materials increased in the late 1980s, ASCE recognized the need for the development of defined standards for working with FRP composites in construction. Consequently, ASCE, together with the Society of the Plastics Industry (SPI), established a long-range, multiphase standards development program in the early 1990s. The ultimate goal of this joint program is to develop accepted standards for structural design, fabrication, and erection of FRP composite systems. In 1995, the Pultrusion Industry Council (PIC) of the Society of Plastics Industry (SPI) sponsored the first phase of the program to develop a design draft standard, or prestandard, with a view toward approval of the completed prestandard as an ASCE national consensus standard in accordance with the rules of the American National Standard Institute (ANSI). In Phase I of the FRP standards development project, the author was a co-developer of the prestandard document. Thescope of Phase I was to:

1. Survey and evaluate existing design and materials information. This task included researching both published and unpublished technical literature, including government and university reports, performance data, standards and specification documents [e.g., ASTM International, American Concrete Institute (ACI), ASCE, Japan Society of Civil Engineers (JSCE), the Eurocodes], manufacturer's materials data, and current practices relative to the use of FRP composites.
2. Develop a computerized database containing the relevant and evaluated useful technical information.
3. Identify gaps in knowledge that might impede promulgation of the standard using the database.
4. Develop the prestandard outline by defining the approach, including the recommended design philosophy and relationship of the ASCE design standard to other material or industry standards such as American Association of State Highway and Transportation Officials (AASHTO), ASTM International (ASTM), International Organization for Standardization (ISO), International Conference of Building Officials (ICBO), and other test standards.

The ASCE prestandard documents database now contains some 350 documents published since 1980. These documents were screened for relevance from more than 1,000 initial selections. The database is annotated with a capsule summary system that generates a brief abstract of the content of each document. This summary system is a valuable aid to the development of prestandard documents and, ultimately, to the development of the ASCE FRP standards. The database sorts material into seven categories representing key subjects in pultruded fiber-reinforced polymer (PFRP) composites structural design:

1. Material properties
2. Environmental durability
3. Time effects, including creep, creep rupture, and cyclic fatigue
4. Member performance, including analysis, design, and performance tests
5. Buckling, including local and overall instability and interactions thereof
6. Joints, including adhesives, mechanical fasteners, and combinations thereof
7. General category, dealing with textbooks, handbooks, design manuals, and standards and specifications.

Table 1-1 presents the summary of the chapters outlined in the Phase I ASCE prestandard document.

Currently, the second phase of this project is being developed, based on the outlines of this prestandard document, by the ASCE Structural Institute with funding from the Pultrusion Industry Council of the American Composites Manufacturers Association (ACMA).

1.3 DESIGN APPROACHES

The ASCE *Structural Plastics Design Manual* (ASCE 1984) summarizes the contemporary philosophy of structural design of civil engineering structures as indicated in the following excerpt.

> The purpose of design is the achievement of acceptable probabilities that the structure being designed will not become unfit for the use for which it is required, i.e., it will not reach a limit state during its designed service life. (ASCE 1984)

There are two commonly used design approaches: (1) the allowable stress design approach (ASD), and (2) the load and resistance factor design (LRFD) approach. The following sections describe these two design approaches.

Table 1-1. Summary of Chapters Outlined in Phase I, ASCE Prestandard Document

Chapter No.	Title	Contents
1	General Provisions	Describes the objective of the standard and gives general provisions applied to the standard as a whole.
2	Design Requirements	Includes general serviceability criteria; refers to future applications and specific design appendices and codes for serviceability criteria.
3	Tension Members	Deals with concentric loaded axial members in tension. Refers to Chapter 5 for combined bending and axial tension loaded members, and to Chapter 7 for tension in connection zones.
4	Compression Members and Bearing	Discusses concentric axial compression loaded members and localized compression at the bearing area. Refers to Chapter 5 for combined bending and axial compression loaded members, and to Chapter 7 for tension in connection zone.
5	Members in Bending and Shear	Covers both compact and noncompact prismatic FRP structural members subjected to a combination of bending, shear, and torsion loading conditions. Refers to Chapter 6 for members loaded in biaxial bending and/or combined bending and axial tension or compression. Refers to Chapter 2 for serviceability criteria and to Chapter 8 for single angles.
6	Members under Combined Forces and Torsion	Discusses prismatic members subjected to both axial and bending loads about one or both principal axes, with or without torsion, and/or torsion only.
7	Connections, Joints, and Fasteners	Covers the design of mechanical, bonded, and combined joints for connecting FRP members, including beam-column, column-base, beam-girder, and beam-beam connections. Bonded joints include wet lay-up and adhesive-bonded single- and double-lapped, as well as field-fabricated butt and strap joints. Fasteners include both metallic and nonmetallic threaded rods and nuts.
8	Special Considerations	Discusses special design considerations, including strength design of thin-walled flanges and unidirectional angles.

1.3.1 Allowable Stress Design

This approach, referred to ASD and also known as working stress design (WSD), was utilized for decades by civil engineers because of its simplicity. However, over the past 30 years, the ASD/WSD method has gradually been replaced with the newer LRFD approach (further described in Section 1.3.2), which is based upon limit states, except for deflection limit state design.

In the ASD design approach, a single safety factor (*SF*) is used to account for variability of materials, load effects, and member strength as well as long-term strength degradation of the structural member. Hence, the design is based on an allowable stress rather than on the ultimate strength of a material. In other words, this approach lumps together the combined effects of load variation and member characteristics without distinguishing these two effects or weighting the contribution of each effect to the overall reliability of the structural member (e.g., joints and frame connections).

The ASD approach requires the following:

Calculated Stress ≤ Allowable Stress Sum of Loads ≤ Resistance (Member Strength ÷ Safety Factor), or

$$\sum Q_i = \frac{R}{SF} \tag{1-1}$$

where:
Q_i = sum of the expected load
R = member resistance or strength
SF = factor of safety.

1.3.2 Load and Resistance Factor Design Approach

The LRFD design approach was developed to better estimate separately the contributions of load effects (stresses) applied to a structure, and the member resistance (strength). Therefore, the goal of developing the LRFD design protocol was to refine the existing design strategy (ASD or WSD) to better estimate both the effects of loads applied to a structure and the expected strength (resistance or capacity) of that particular member or structural system. The approach is to maintain the following inequality:

The Sum of the Load Effects ≤ The Factored Load Resistance, or

$$\sum \gamma_i \, Q_i \leq \varphi \, R^*$$

and   (1-2)

$$R^* = R \times C_1 \times C_2 \times C_3 \times \text{......} \times C_n$$

where

γ_i = load factor to account for deviations, load-related uncertainties, and variability specified in ASCE 7 (ASCE 1996) or in codes having jurisdiction over the project. For a given applied load, the load factor ranges from 0.2 to 1.6, depending on the load combination.

Q = nominal load, which is also specified in ASCE 7 or in codes having jurisdiction over the project.

φ = resistance (or strength) factor, which reflects the variabilities of material properties, mode and consequences of failures, and uncertainties.

R = reference resistance (or strength), which refers to the material or joint stiffness, under standard reference service conditions, including specific values for load duration and surrounding environmental conditions such as moisture and temperature.

$C_1, ... , C_n$ = adjustment factors to account for conditions outside the standard reference conditions, such as surrounding environmental exposures (e.g., extreme temperatures, moisture, freeze–thaw cycles), load duration, and other factors that may affect the strength and the stiffness of the member during the service life.

R^* = adjusted resistance (or strength), which is a reduced value of the member resistance due to conditions outside the standard reference conditions, such as surrounding environmental exposures (e.g., extreme temperatures, moisture, freeze–thaw cycles), load duration, and other factors that may affect the strength and the stiffness of the member during the service life.

For new materials such as composites, the emphasis is on determining appropriate methods for calculating R and specifying values of φ, which represent the confidence level in reaching these resistance levels in each application type. In addition, methods for calculating Q_i as needed (e.g., stress in PFRP or deflections) are essential.

1.4 DESIGN LOADS

The most accepted standard document for design loads for civil engineering applications in the United States is *Minimum Design Loads for*

Buildings and Other Structures, ASCE/SEI 7-10 (ASCE 2010). This document presents procedures for determining the minimum loads and load combinations for buildings and other types of structures. Another industry recognized document for load and resistance design related to steel structures is the AISC Steel Construction Manual, 13th Edition (AISC 2006). For composites, additional procedures may be required to account for such inherent physical and mechanical properties as time-dependent factors, glass transition temperature, and so forth. This approach was adopted in developing the 1995 ANSI/AF&PA *National Design Specification for Wood Construction* LRFD specifications for engineered wood construction, which was updated in 2005 (AWD 2006). It was also the primary concern of the committee for Fiberglass Reinforced Plastics Stacks Standards, whose goal was to create a standard for the design, fabrication, erection and maintenance of free-standing, self-supporting, wind-exposed FRP stacks.

1.5 SAFETY FACTORS

As for other construction materials, a factor of safety should be used when designing composite joints. The factor of safety (*FS*) is defined as "the ratio of the ultimate allowable stress divided by the maximum service stress":

$$FS = \frac{\sigma_u}{\sigma_a} \qquad (1\text{-}3)$$

where
FS = safety factor
σ_u = ultimate stress, psi (MPa)
σ_a = allowable stress, psi (MPa).

A factor of safety between 3 and 4 is recommended for unidirectional pultruded composites. However, it should be noted that these recommended factors of safety do not include the effect of the environment and are mainly for normal environmental and loading conditions. The results of a field survey performed by Mosallam (1998) not only served as a foundation for the ASCE Pre-standard Document for FRP Composite Structures, but also illustrated that premature failure of pultruded unidirectional joints occurred in harsh environments when environmental safety factors were not considered. The reader is referred to the calculations presented in Chapters 2 and 5 of the ASCE *Structural Plastics Selection Manual* (ASCE 1985): Chapter 2, Example 2-2 discusses bolt prestress losses with temperature change in service, and Example 2-3 discusses the
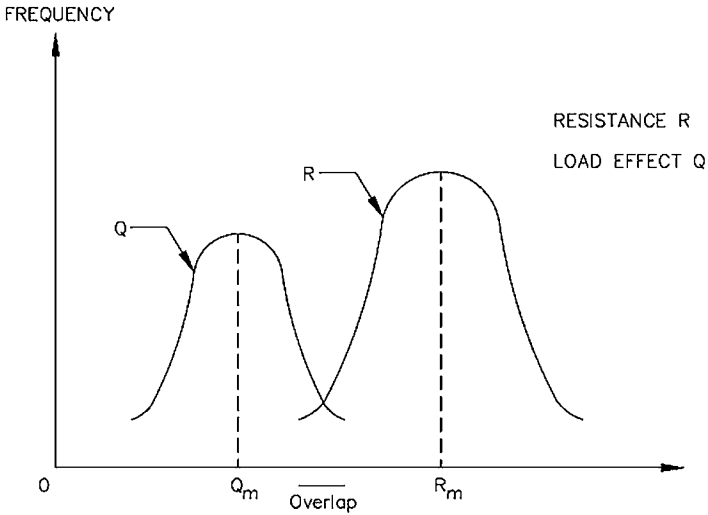
Figure 1-1. Probability density functions for load and resistance.

bolt prestress loss for joints at high service temperature and in a corrosive environment. Chapter 5 presents the selection criteria for structures exposed to fire hazard.

1.6 GUARANTEED MECHANICAL PROPERTIES

The mechanical properties of PFRP composite profiles should be provided by the pultruder. Pultruders should report what are called "guaranteed" values. For example, a guaranteed ultimate shear strength is defined as "the mean strength of a specimen (tested according to (ASTM D5379, ASTM D5379M -05 protocols) minus three times the standard deviation, that is:

$$\tau_u^{gr} = \tau_u^{mean} - 3S \qquad (1\text{-}4)$$

where
τ_u^{gr} = guaranteed ultimate shear strength
τ_u^{mean} = mean ultimate shear strength
S = the standard deviation.

These guaranteed properties provide a 99.87% probability that the indicated values are exceeded (Mutsuyoshi et al. 1990). A description of the method(s) used to obtain the guaranteed properties should be provided by the pultruder. The reader is referred to Chapters 2 and 6 of *MIL 17: The Composite Materials Handbook* (ASTM 2002) for more information on test

methods and sampling techniques. More discussion on this subject is presented in Section 1.7.

1.7 PROPOSED PHILOSOPHY

Currently, no unified approach exists for the design of pultruded composite members and joints. Approach unification has been impossible because of limited experimental information on the mechanical behavior of pultruded composite members and joints. Instead, a variety of approaches have been developed. For example, the *EUROCOMP Design Code and Handbook* published in 1996 (Clarke 1996) adopted the LRFD approach. In the United States, several researchers have adopted the same approach using *assumed* load factors in designing pultruded members and joints, such as Parbhakaran et al. (1996a & 1996b).

The proposed philosophy described herein is intended for the analysis, design, and evaluation of structures made of continuous fiber-reinforced polymer (FRP) composites. In addition to mechanical, thermal, and stress wave properties of FRP composites, physical and chemical aging and viscoelastic responses play a major role in designing composite structural systems. Many safety and resistance factors have to be incorporated in the design to account for long-term performance, load combinations, interlaminar shear and edge effects, local impact and damage, galvanic corrosion, flammability, and many other conditions.

The structure shall be designed to avoid catastrophic failure under impact or fire. Furthermore, for PFRP structural shapes or systems, potential failure should be limited by appropriate choice of (1) reducing the hazard (e.g., designing a curb to redirect a vehicle that has collided with a guard rail); (2) designing for a high degree of indeterminacy; (3) selecting or designing a cross section to absorb large shocks; and (4) incorporating suitable materials, active and/or passive controls, etc. Therefore, the WSD approach as well as the LRFD approach have been proposed as two alternative methods of the design of structures made of FRP composites.

1.7.1 Working (Allowable) Stress Design Philosophy

As discussed earlier, in the WSD approach, safety is covered in design loads obtained in a conventional manner from the current building or bridge design code. In addition, safety factors for working stresses or strains of structural shapes are obtained by making sure that the strain in any fiber direction shall not exceed 20% of the minimum guaranteed long-term laminate strain. Stress level in a laminate shall also be limited based on an appropriate failure criterion incorporating a safety margin. For

example, the well established Hoffman-Hill or Tsai-Wu criterion should be used to establish limiting failure stresses. Alternative criteria must be shown to be appropriate prior to applications of limiting stress level as a design criterion. It might also be necessary to consider something other than first-ply failure in the design.

1.7.2 Load Resistance Factor Design Philosophy

With acceptable probabilities, a structure shall be designed to sustain all actions (bending, shear, axial, or combinations) likely to occur during service and to have adequate durability (i.e., the structure should remain functional through its intended service life; the maximum factored load of 1.3 [1.67 (LL + IM) +DL] shall be less than 20% of the ultimate long-term strain of laminate. The effect(s) of the randomness of load intensities, uncertainties in analytical procedures, nonlinear structural responses, computational inaccuracies, and approximations that neglect local effects should be considered while developing probability coefficients.

The design should account for ductile failure by ensuring that the serviceability limit state (deformation, vibration, cracking, etc.) is reached prior to its ultimate limit state (collapse, instability, etc.). In addition, the design should consider service, transient, and accidental conditions. For structures not fully covered herein, particularly in terms of structural resistance issues in the design philosophy, the proposed provisions may be applied by augmenting additional design criteria as needed from military research programs, aerospace research programs, and/ or from ongoing FRP research work in the United States and foreign countries.

1.7.3 Analysis

The proposed design philosophy is based on the following:

1. Analysis of different FRP materials, shapes, and systems
2. Development of design specifications
3. Establishment of various strength and serviceability limit states.

1.7.4 Fiber-Reinforced Polymer Material Behavior, Shape, and System Analysis

Constituent material properties in composites determine the composite characteristics. Physical and mechanical properties of laminate shall be measured at 75 ÷ 4 °F and 50 ± 5% relative humidity (RH). Mechanical properties should be measured at severe operational temperature of 120 ± 4 °F and 85 ± 5% RH. Coupon preconditioning is required as per ASTM

D 618 before testing. The production process should be specified in terms of cure time, temperature, and pressure. The void content should be stated along with equilibrium moisture content and dimensional changes (swelling) for severe hygrothermal conditions. A property data sheet should be provided for individual lamina and laminated composite for minimum, average, and maximum operating temperatures and humidity. Interlaminar shear strength should be specified, including the method of measurement. Longitudinal, transverse, and shear moduli and Poisson's ratio should be specified for individual lamina. Longitudinal tensile, compressive, and flexural strengths and Poisson's ratios should be measured on laminated composite coupons.

Fatigue properties should be determined by testing on appropriate specimens (ASTM D 3039). Impact-induced interlaminar damage should be established by drop-weight tests. Similarly, creep and stress rupture behavior should be quantified at the maximum service temperature (ASTM D 3039). Guaranteed minimum strength properties and the glass transition temperature must be established for adhesives by testing representative joints. Mechanical, thermal, and fatigue properties of adhesives, along with environmental degradation and creep behavior, must be established or provided by the material supplier in the form of property data sheets.

At the coupon level, the mechanical behavior of FRP material shall be considered to be linear up to failure. However, regarding special fiber and fabric lay-up, coupon or structural shapes may behave nonlinearly, and structural systems may also behave in a nonlinear manner due to different joining methods beyond certain load levels. These nonlinear behaviors must be properly understood by the analyst and the FRP structure must be designed accordingly (i.e., beyond a certain linear threshold level). The established micro- and macro-mechanics models shall be used for strength and stiffness computation for FRP composite coupons and components. Elastic (FRP) material properties do change with time, environmental effects, and load (sustained, dynamic, etc.) conditions. These conditions should be included in the analysis (i.e., analysis shall be conducted for different service ages and environmental exposures).

1.7.5 Material Nonlinearity

Where inelastic (material nonlinearity) analysis is used, re-analysis must be carried out for post-first-ply failure response of an FRP structural system after establishing anticipated failure mechanisms and failure modes. The analysis shall ascertain whether the mode of failure is bending, shear, buckling, etc. in the FRP structural components. If the designer so chooses, he or she shall proceed with the formulation of a predetermined inelastic failure mechanism to control failure. Such an approach may be

highly complicated and require in-depth understanding of the mechanics of FRP composite materials and laminates.

1.7.6 Geometric Nonlinearity

Geometric nonlinearities shall be taken into account in the analysis if deformations lead to changes in structural configuration (e.g., angular changes between beam and column joints). The geometric nonlinearity models shall be based on test data on FRP structural members and joints, and should include initial crookedness of components, which may be very important in the stability analysis. For slender components, viscoelastic characteristics must be considered in the analysis, in addition to interaction of various forces in a member. Only factored loads shall be used in the nonlinear analysis and no superposition of force effects shall be applied in the nonlinear range.

1.7.7 Analytical Procedures Requirements

The following are the proposed analytical procedures:

1. Idealize the geometry and the behavior (e.g., elastic, dynamic, nonlinear) of the structure.
2. Conduct laminate stress analysis, under mechanical and/or hygrothermal loads, by accounting for interlaminar stresses and edge effects utilizing "classical laminations theory" ("thin plate idealization"), and do so only after establishing the stress–strain relation of the lamina. Netting theory may be employed, where appropriate, by neglecting resin effects on laminates. It should be noted that laminate membrane, bending, or combined stresses may be computed. Temperature changes produce thermal strains, while moisture absorption leads to swelling strains. Therefore, thermal expansion and swelling coefficients must be used in the analysis to account for thermal conduction and moisture diffusion. Nonlinear viscoelastic properties of composites for varying temperatures shall be determined only when they are *essential*.
3. Incorporate (in the analysis) thickness effects, residual stresses, and strains while scaling up from lamina to laminate. It should be note that failure may occur at edges as a result of delamination at locations of high interlaminar stresses due to low interlaminar strength. Classical lamination theory, assuming plane stress, cannot predict edge stresses. Therefore, edge failure may be avoided by (1) careful selection of laminate stacking order, (2) minimizing any mismatch between Poisson's ratio, (3) identification of coefficients of thermal expansion, and (4) being aware of swelling coefficients of adjacent

lamina. For example, central lamina may be made of low-shear-modulus material to minimize shear effects.

4. Establish the internal force and displacement distribution over the entire structure, including local effects. Put another way, this requirement involves a complete global and local response analysis of a structure after idealization of Step 1.

5. Ignore shear and axial effects on deformations if they are to be less than 10% to 15% of those effects under bending. Axial effects may be considered for stability.

6. Adopt the load cases and combinations accepted in international building codes, such as the International Code Council's 2009 International Building Code and the 2009 International Residential Code for One- and Two-Family Dwellings, as well as the ASCE's Minimum Design Loads for Buildings and Other Structures, ASCE/SEI 7-10.

7. Account for geometric imperfections in manufacturing and second-order effects in the overall analysis in a manner similar to current structural analysis methods.

8. All analytical methods shall satisfy force equilibrium, compatibility checks, force–deformation (stress–strain) relations, and stability checks (buckling and crippling). In addition, deformation or rotation capacity of joints should be included in the analysis. Where possible, joints should be located away from critical locations.

9. Effects of material anisotropy shall be incorporated, maintaining laminate symmetry during production. Lamina properties are computed as functions of type, volume fraction, and orientation of fibers, whereas upgraded-to-laminate properties are computed as a function of the number of plies. This upgrade is done using well-accepted techniques.

1.7.8 Development of Design Specifications

In developing design specifications for PFRP design, the structural engineer will:

1. Establish material properties, including their characteristic value and design values. These two values are related by the material property safety factor. Since failures in composites are likely to be local, the dependence upon local characteristics of high variability makes the analysis of failure mechanism more complex than the physical property analysis (e.g., the relationship between the strength of the composite and the properties of the constituents is less developed than the analysis for stiffness).

2. Develop geometric properties, including imperfections and dimensional tolerances (e.g., nominal vs. actual span length).

3. Include all load arrangements, load cases, and load combinations. All loads (dead load, live load, wind load, friction, temperature, earthquake, dynamic fatigue, etc.*)* as well as their corresponding variations in time under permanent, variable, and accidental conditions shall be included.

1.7.9 Design Requirements

The following are the design requirements for PFRP structural systems:

- All load cases and combinations, including possible deviations, shall be considered in design computations.
- All relevant serviceability and ultimate limit states shall be satisfied.
- Durability shall be ensured by considering the required performance criteria, environmental conditions, physical and chemical aging processes of constituent materials in FRP composites, structural detailing, and product quality and protective measures, including maintenance, during the service life.

1.7.9.1 Member Design.   In any design, the basic conditions to be satisfied are ultimate limit states and serviceability limit states. In terms of ultimate limit state checks, the internal forces and stresses, and deformations and rotations, developed in a structure must be analyzed, as stated earlier. For a successful design, these ultimate forces and stresses, and the deformations and rotations, must be less than the design resistance values. For example, a design resistance (bending stress) value in bending is the product of the characteristic value of a member in bending and a partial safety factor, which is less than 1.0. The characteristic value of the material property may be determined from either of the following procedures:

- Theoretical derivations of laminate properties using constituent material properties, and/or
- FRP composite coupon or component testing.

The basic conditions to be satisfied under serviceability limit states are:

- Deformation and rotation affecting the appearance or effective use of the structure
- Deformation and rotation leading to damage of finish materials, including nonstructural elements, leading to aesthetic concerns
- Excessive vibrations causing discomfort to users.

Serviceability limit states are well established in different bridge and building codes that are in practice, and these values shall be adopted wherever needed. Specific limit-state values for deformation, rotation, etc. will be presented in the following section. As a minimum, members must be designed depending on their function (i.e., in tension, compression, bending, shear or torsion, stability, or a combination of these five straining actions). In addition, depending on member size, portions of a member (e.g., a web or flange) must be designed as two-dimensional orthotropic plates with in-plane or out-of-plane forces, or a combination of in-plane and out-of-plane forces. Since FRP structural composites are made of unidirectional or multidirectional reinforcements of several layers, the stresses and strains in FRP composites must be determined using an appropriate means of analysis and design of individual lamina, combined effects of individual lamina leading to stress, and strain properties of FRP laminates. Established procedures are available to determine the stresses and strains in the laminate. The analysis shall be carried out using stiffnesses of the individual lamina appropriate to the limit state under consideration. Depending upon the function of a structure, the FRP composite member design shall include effects under creep, fatigue, impact, blast, fire, and chemical attack. These effects must include factors affecting, for example, creep, fatigue, and impact magnitude, quantification of stresses or strains and deformations of members, and design methodologies.

Nominal strength (resistance) and stiffness values for design are obtained by multiplying the base values (obtained from micro-mechanics and first-ply failure theories for a coupon [e.g., 1 in. × 1/4 in. × 18 in. (or 25.4 mm × 6.35 mm × 457.2 mm) with 50% fiber volume] for actual conditions of use as:

$$F = F_o \, C_f C_m C_c C_a C_{st} \qquad (1\text{-}5)$$

$$E = E_o C_m \qquad (1\text{-}6)$$

where

F = nominal resistance in bending (b), or torsion (t), or compression (c), or shear (v) and should be specified parallel and perpendicular to unidirectional rovings

F_o = base resistance of b, t, c, or v parallel and perpendicular to unidirectional rovings

E = nominal modulus of elasticity for b, t, c, or v parallel and perpendicular to unidirectional rovings

E_o = base modulus of elasticity

C_f = size effect factor varies with width, depth, and length of a component when compared to a coupon [1 in. × 1/4 in. × 18 in. (or 25.4 mm × 6.35 mm × 457.2 mm)] mechanical properties

C_m = moisture content factor varies from 1.0 to 0.5 depending on the percent moisture absorbed by a coupon [1 in. × 1/4 in. × 18 in. (or 25.4 mm × 6.35 mm × 457.2 mm)] that is coated on all six sides, and it will be 1.0 for components under cover

C_c = environmental factor varies with the FRP material's exposure to chemicals, temperature levels, and sustained stress levels.

C_a = physical aging factor varies with number of years of service of FRP component, type of resin and fiber, and the manufacturing method, including curing type

C_{st} = sustained factor.

It should be noted that the use of fire-retardant resins may lead to reduction in mechanical properties and durability reductions. The manufacturer shall provide the reduction factors of FRP components made of resins with fire-retardant additives.

1.7.10 Limit States

To prevent ductile failure, the design should account for serviceability, strength, stability, and extreme event limit states of a component and/or a system. These limit states are as follows:

- *Serviceability Limit State:* deflection limits, rotational limits, cracking limits, vibration limits, instability limits, and human response limits must be established in a manner similar to span-to-depth ratios, thickness of flange, web-to-width or -depth ratios, and so on.
- *Strength Limit State:* factored resistance shall be the product of nominal resistance determined as stated above; the resistance factors vary for flexure, shear, compression parallel and perpendicular to units, and tension parallel to units. As in structural member design of conventional materials, for certain load combinations, resistance factors shall be multiplied by 0.75.
- *Stability Limit State:* the structural component shall be checked for resistance to sliding, overturning, uplift, and local and global buckling.
- *Extreme Event Limit State:* for the extreme event limit state, resistance factors shall be taken as 1.0.

REFERENCES

American Institute of Steel Construction (AISC). (2006). *Steel Construction Manual, 13th Edition* American Institute of Steel Construction, Chicago, Ill.

ASCE. (2010). Minimum design loads for buildings and other structures, ASCE/SEI 7-10, ASCE, Reston, Va.

ASCE. (1984). *Structural plastics design manual*. ASCE, Reston, Va.

American Wood Council (AWD). (2006). *ANSI/AF&PA NDS-2005 National design specification (NDS) for wood construction and NDS supplement—Design values for wood construction*, American Wood Council, Washington, D.C.

ASTM. (2002). *MIL 17 handbook: The composite materials handbook*, ASTM International, West Conshohocken, Pa.

ASTM. (2009). ASTM D 3647-09: *Standard Practice for Classifying Reinforced Plastic Pultruded Shapes According to Composition,* ASTM International, West Conshohocken, Pa.

Clarke, J. L., ed. (1996). "Structural design of polymer composites." *EUROCOMP design code and handbook*. E & FN Spon/Chapman & Hall, London.

Mosallam, A. S. (1998). "ASCE prestandard document for FRP composite structures." A. Mosallam, ed., *Proc., SRRS1*, November 9, Fullerton, Calif., pp. 1–8.

Mutsuyoshi, H., Uehara, K., and Machida, A. (1990). "Mechanical properties and design method of concrete beams reinforced with carbon fiber-reinforced plastics." *Trans., Japan Concrete Inst.*, Vol. 12, Japan Concrete Institute, Tokyo, pp. 231–238.

Prabhakaran, R., Razzaq, Z., and Devara, S. (1996a). "Load and resistance factor design (LRFD) approach for bolted joints in pultruded composites." *Composites: Part B*, Vol. 27B, 351–360.

Prabhakaran, R., Razzaq, Z., and Sirjani, M. M. (1996b). "Load and resistance factor design (LRFD) approach for reinforced-plastic channel beam buckling." *Composites: Part B*, Vol. 27B, 361–369.

This page intentionally left blank

CHAPTER 2

CHARACTERIZATION AND BEHAVIOR
OF BOLTED COMPOSITE JOINTS

2.1 BACKGROUND

In the past two decades or so, a number of research studies were con-
ducted on characterizing the structural behavior of pultruded composite
connections. In general, there are three schemes for pultruded fiber-rein-
forced polymer (PFRP) joints: (1) bolted, (2) adhesively bonded, and (3)
combined (bolted and bonded). The bolted joint is one of the most common
forms of joints in civil engineering applications. Adhesively bonded joints
generally result in a catastrophic "no-warning" failure. If a higher degree
of end restraint is required, the combined bolted/bonded joint will be
efficient. Combined joints will minimize the stress concentration at the
bolt/hole zone by producing better stress distribution between the con-
nected elements. The advantage of combined joints is the extra benefit of
using the clamping force exerted by the bolt/nut/washer system, which
is required for the curing process of the adhesives during erection. Test
results obtained by Mosallam et al. (1993) indicated that an increase in
joint ductility could be achieved using combined joints. However, the
efficiency of any joint will depend on several factors, including type of
adhesive(s), surface preparation, curing process, surrounding environ-
ment, applied torque, edge distance, and other geometrical ratios for the
connecting elements and connection geometry and lay-up.

Matthews (1988) discussed the mechanical behavior and design
methods for single-bolt joints in double shear. Strength characteristics of
FRP adhesively bonded joints were discussed by Matthews et al. (1982).
Fatigue behavior of composite bolted joints was investigated by Little and
Mallick (1990). They found that washer size and thickness have a strong
influence on the fatigue life of composite bolted joints. A study on the

influence of material and geometry variations on the behavior of bonded FRP tee connections was conducted by Shenoi and Hawkins (1992). In this study, experimental load–deflection graphs were presented and physical characteristics of the joint under load were noted. The joint modeling was performed using finite element analysis techniques. A comprehensive review of the behavior of composited bolted joints was reported by Thoppul et al. (2009). The review included relevant mechanical test methods and standards; a discussion of the mechanics aspects of design, including joint design methodologies; considerations of the influence of geometric effects; fastener preload selection; failure prediction for both statically and dynamically loaded joints; time-dependent joint preload relaxation; the effects of temperature and moisture on joint strength and failure; and nondestructive evaluation techniques for monitoring joints.

In 1991, Doyle conducted a study of both mechanical and adhesive joint behavior of FRP materials using both steel and FRP blots (J. R. Doyle, "Behavior of Bolt and Adhesive Connections in Glass Fiber-Reinforced Plastic Members." Master's thesis, Department of Civil Engineering, West Virginia University, Morgantown, WV, 1991). The prediction of the normal force within the joint was performed using the screw friction equation. Based on his work, the following conclusions were reported:

1. The optimum edge distance of four times the diameter of steel bolts ($4 \phi^s$) is recommended.
2. By increasing bolt torque while maintaining a constant edge distance, the joint strength can be improved up to 30%.

Doyle provided details of this study and presented an overall summary of the research program on connectors for FRP members. In this report, simplified design equations for bolted and adhesively bonded FRP joints were presented.

Rosner (1992) reported the results of an experimental and theoretical research program on bolted connections for PFRP. The experimental program involved testing a total of 102 single-bolt double-shear lap joints to study the effects of several design variables, including member thickness, t; member width, w; to-hole diameter (d), w/d; edge distance (e), to-hole diameter ratio, e/d; and fiber orientation. Figure 2-1 shows the test setup for the single-bolt double-shear specimens. A total of 215 pultruded composite bolted joint specimens were tested to determine compression, tensile, and shear properties of the material. Three unidirectional fiber orientations were tested, namely, 0 degrees, 45 degrees, and 90 degrees. The different joint failure modes are described by a finite element model (FEM) based on the Tsai-Wu failure criterion, which was used to predict the behavior of each joint. The FEM model accounts for through-the-thickness effects and fastener plate contact action. The results of this study
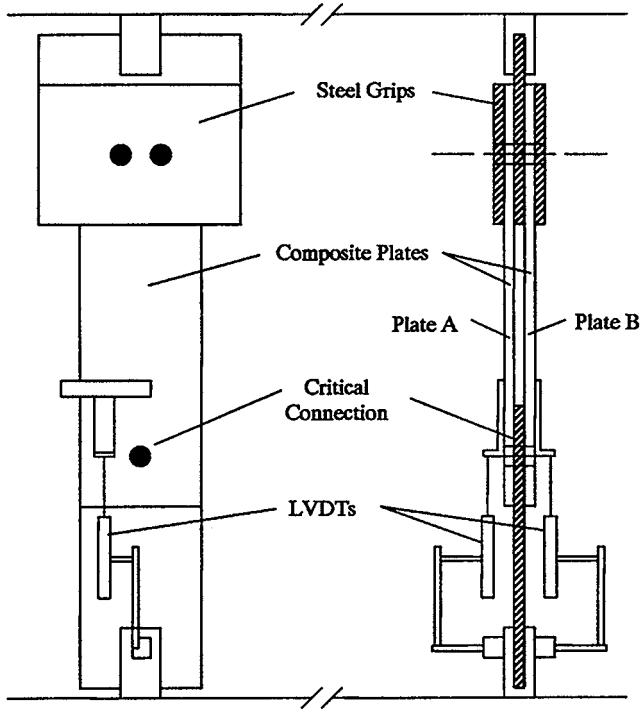
Figure 2-1. Pultruded composite bolted joint test setup.
Source: Rosner (1992), courtesy of Charles Rosner.

indicated that connection strength could be improved by increasing one
or more of the following variables: (1) member thickness, (2) ratio w/d,
(3) ratio e/d, and (4) the member width. A detailed description of the
research program is presented by Rosner.

Cooper and Turvey (1995) reported the results of a comprehensive
investigation of 81 bolted pultruded joint specimens. In that study, both
joint geometry and the effect of bolt clamping torque on the joint ultimate
strength were investigated. The study covered both double-lap and sin-
gle-bolt joints. Based on their results, the authors provided recommenda-
tions for e/d and w/d values for pultruded composite joints, which are
summarized in Table 2-1. Turvey (1998) presented a literature review and
results of a series of tests on single-bolt tension tests for pultruded com-
posites. Test results showed that a small amount of bolt slip occurs even
when the holes are nominally a tight fit, and that the bolt displacement
at failure varies from 5 to 10 times the initial slip value. It was also
reported that the initial stiffness of PFRP bolted joints does not vary much
with the ratio of edge distance to bolt diameter (e/d), but increases as the
width-to-diameter ratio (w/d) increases and as the off-axis angle decreases.

Table 2-1. Comparison between Steel and PFRP Recommended Geometries, Design Loads,
and Bearing Strengths for Single-Bolt Joints in Tension

Material	Edge Distance-to-Hole Diameter Ratio, e/d	Member Width-to-Hole Diameter, w/d	Design Load[a] (kN)	Bearing Strength (N/mm^2)
Steel (Grade 43)	1.2–3	>3	14.6	230
6.35-mm-thick PFRP flat plate[b]	2–4.5 (typically 3)	3–7 (typically 4)	14.0	220
6.35-mm-thick PFRP flat plate[c]	3	4	15.1	238

[a] Calculated by taking the bearing strength of the material and multiplying by area of bolt in contact with specimen (6.35×10).
[b] Strongwell (2004).
[c] Cooper and Turvey (2005).

More details on this study will be described in Section 2.3. Wong (2002) reported results of experimental and analytical study that focused on characterizing the influence of geometry and loading schemes on PFRP bolted joint strength and the associated failure modes. In this study, a large number of compressive and tensile bearing tests on bolted PFRP joints were performed.

Love and Bisarnsin (1992) conducted an experimental investigation on fasteners used for industrial building applications. The experimental investigation consisted of a series of static pullout tests, a series of cyclic tests, and a combination of the two that were performed to determine the amount of retained pullout capacity after cyclic loading. Figure 2-2A shows the test setup for the pullout apparatus. The results of this study indicated that self-tapping fasteners are applicable for connecting FRP panels to PFRP structural members.

In 1993, Morsi and Larralde conducted a study on three types of fasteners: standard stainless steel (S.S.) bolts and nuts, self-tapping screws, and flat-head screws. The tests were performed on PFRP H-beam and PFRP plate specimens. Figure 2-2B shows the test setup for testing PFRP plates with self-tapping screws. Experimental results indicated that self-tapping screws, despite their relatively limited load-carrying capacity, are the simplest and most economical solution to minor load situations, especially where connectors are in inaccessible locations. However, these fasteners can only be used in locations exposed to *minor* loads. Furthermore, additional stiffening details are required to increase the efficiency of these fasteners.
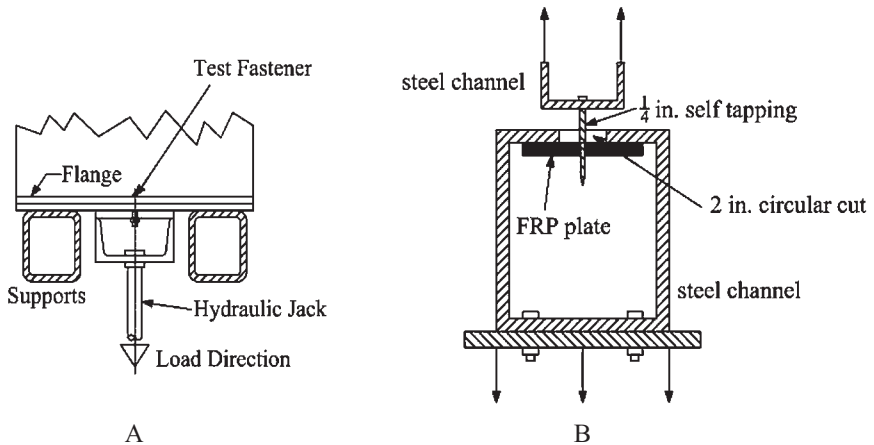

Figure 2-2. Pullout test apparatus: (a) Love and Bisarnsin (1992); (b) Morsi and Larralde (1993).

Johansen et al. (1993) conducted a full-scale experimental study on the ultimate strength characteristics of PFRP/Kevlar cable structural systems. The majority of local failures were at the connections. The connection details described in that study mimic the form, shape, and function of connections commonly used with steel. For example, the design of the end plate connections employed unidirectional PFRP plates with minimal or no resistance in the transverse directions.

Chapter 4 of ASCE's *Structural Plastics Design Manual* (ASCE 1984) contains valuable information about mechanical joints, fasteners, and adhesives for different types of structural plastics. In addition, the chapter includes several joint selection criteria. A comparison between different joining techniques is also presented in tabulated form. ASCE's *Structural Plastics Selection Manual* (ASCE 1985) contains scattered information on bolted joints. Specifically, examples in Chapter 2 discuss the prestress losses caused by temperature and harsh environments.

The European Cooperation in the Field of Scientific and Technical Research (COST C1; now called the European Cooperation in Science and Technology, COST) published a special publication on pultruded joints, *State-of-the-Art Review on Design, Testing, Analysis and Applications of Polymeric Composite Connections* (COST 1998). Information on bolted composite joints is presented in Chapters 1 and 2 as follows:

- *Chapter 1, Plate-to-Plate Mechanical—Part I, Analysis and Design:* In this chapter, sections on determination of load distribution in multi-row bolted composite joints, stress analysis, and failure of bolted composite joints are presented. Though design philosophy is not covered, the information presented is essential to understanding the basic characteristics and performance of plate-to-plate mechanical composite joints.
- *Chapter 2, Plate-to-Plate Mechanical—Part II, Testing and Applications:* This continuation of Chapter 1 covers plate-to-plate bolted connections. A review of the latest research work (at that time) on bolted plate-to-plate joints is presented. This includes identification of the common failure modes and a description of the different tension test methods for both single-bolt and multi-bolt connections. Again, neither design formulae nor numerical examples are presented. However, the chapter refers to design methods suggested by both Prabhakaran et al. (1996a) and Hassan et al. (1997).

The majority of published pultruders' design guides contain limited information on bolted composite joints design and details. The following are a sample of pultruders' design guides chapters related to bonded joints:

- Chapter 4, *Fiberline Design Manual* (Fiberline Composites A/S 2004)
- Chapters 12 and 13, *EXTREN Design Manual* (Strongwell 2004)
- Chapter 7, *Creative Pultrusions Design Guide* (Creative Pultrusions, Inc., 2004).
- Chapter 6, *BRP Design Guide*, (Bedford Reinforced Plastics, Inc., 1995)

2.2 MECHANICAL BEHAVIOR OF BOLTED JOINTS

2.2.1 Background

Work on investigating the use of bolted joints for composite structures was begun by the aerospace industry in the United States in the mid-1960s; refer to the *MIL 17 Handbook* (ASTM 2002). Based on numerous studies conducted by the industry and universities, including studies on the anisotropic and brittle nature of polymer composites, a new braid of metal and composite was designed specifically for composite structures. (Unfortunately, this is not the case for pultruded composites, where standard metallic bolts designed mainly for metallic structures are currently being used to connect PFRP composites.) These special mechanical fasteners feature larger tail footprint areas to improve the composite joint efficiency. In addition, durability and material compatibility studies resulted in eliminating the use of aluminum fasteners because of their sensitivity to galvanic corrosion. Galvanic corrosion occurs when metals are in direct contact with carbon composites, which leads to matrix corrosion of composites.

2.2.2 Common Modes of Failure of Pultruded Composite Bolted Joints Subjected to Tensile Loads

The emphasis in this manual is on "tensile" rather than "compression" loaded composite joints. The reason for this emphasis on tensile joints is that composite joints subjected to compression are less sensitive to joint geometry (e.g., edge distance, width, and thickness) and are generally stronger than joints subjected to tensile forces.

In general, there are seven modes of failure for pultruded composite bolted joints subjected to tensile forces:

1. Bearing failure
2. Shear-out failure
3. Net tension failure
4. Cleavage-tension failure (tension and shear-out failure)

5. Bolt failure
6. Punching failure (bolt pulling through laminate)
7. Any combination of these modes.

Figure 2-3 describes the general failure modes of single-bolt composite bolted joints (Hart-Smith 1994a). The first four failure modes are considered the fundamental (common) modes of failure for pultruded composites, as observed and reported in the research (e.g., Hassan et al. 1997; Rosner and Rizkalla 1995; Turvey 1998).

2.2.2.1 Bearing Strength.   For composite bolted joints, the bearing failure mode is much less catastrophic than other modes of failure, such as tension, shear out, bolt pulling through the laminate, cleavage-tension, bearing or bolt failure (Fig. 2-3). To ensure an efficient bolted joint design, the bearing stress should be kept as low as possible on the most critical fastener in the composite structure. The use of stronger fasteners will require a higher bearing strength, which is not typically available for the majority of off-the-shelf unidirectional pultruded composites. In fact, weaker bolts that are compatible with the limited bearing strength of pultruded composites are preferred. The bearing failure stress is
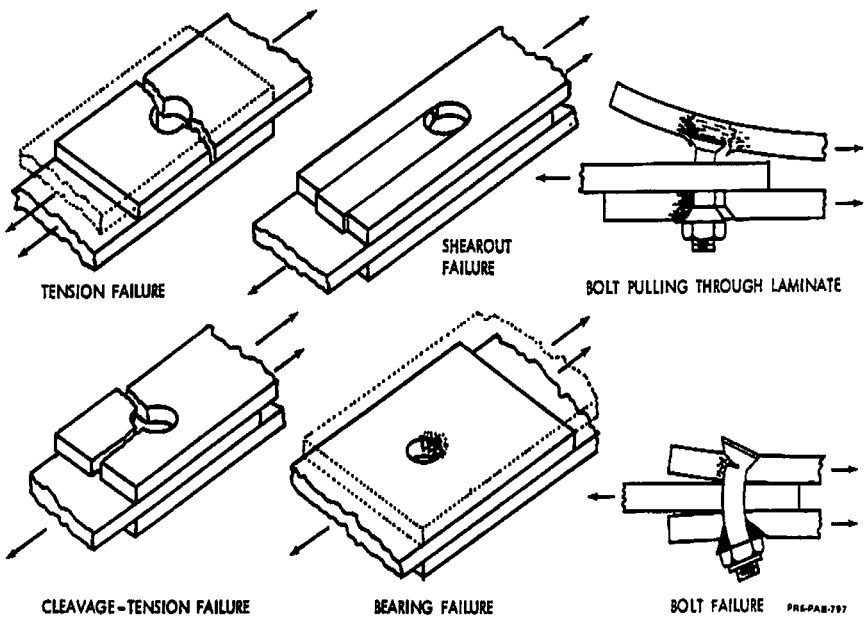

Figure 2-3. Failure modes of composite bolted joints.
Source: Hart-Smith (1994), courtesy of Dr. John Hart-Smith and the Boeing Company.

dependent on the compressive strength of the composites. Thus, for a given bolt shear force (i.e., a given total cross-sectional area of bolts), the most effective strategy is to use several small-diameter bolts, rather than fewer large-diameter bolts, to generate a greater bearing area.

Bearing failure occurs at the immediate adjacent contact zone between the bolt and the composite member, and, as mentioned earlier, is caused primarily by excessive compressive stresses that develop at the hole boundary surface (Eriksson et al. 1995). Bearing failure for constrained bolted joints occurs through buckling or "brooming," that is, end-crushing delamination failure of the composite material (Eriksson 1990). According to ASCE's *Structural Plastics Design Manual* (ASCE 1984), bearing strength is defined as the average bearing stress at a deformation of 4% of the bolt diameter. Several factors affect the joint bearing strength. For example, increasing the clamping torque and using an adequate washer diameter will increase the joint bearing strength.

Little and Mallick (1990) describe one method of improving the pin-bearing strength of a composite laminate, which is to apply a lateral clamp-up pressure distributed around the hole by means of a washer or a collar. Their results indicated the application of a slight clamping pressure (e.g., by finger-tightening) can significantly increase the static pin-bearing strength capacity. This capacity increase is attributed to the effect of the lateral restraint provided by the washer and the frictional resistance against joint slip. Crews (1981, pp. 131–144) studied this effect by subjecting composite joints to fatigue loads. He reported the same effect of increasing cyclic bearing capacity. However, he also found that the increase in the pin-bearing strength tends to level off at high clamping pressure. For pultruded unidirectional composites, Cooper and Turvey (1995) reported that lightly clamped and fully clamped joints exhibit a 30% and 96% increase, respectively, in the mean damage loads.

The bearing strength of a bolted composite joint is also affected by the fiber architecture of the composite member (Collings 1982), as well as by the stacking sequence of the laminate (Quinn and Matthews 1977). Reid et al. (1994) reported on the effect of the hole pattern on bearing strength. They found that adding another bolt in series had no effect on the bearing strength of the joint, while the introduction of an additional hole in tandem reduced the joint bearing strength to less than half when compared to the single-hole joint. Bearing failure initiates as cracks at the edges of the bolt hole and propagates to the edge of the constrained zone, where failure tends to revert to a mode of local instability and delamination (Collings 1977).

Some joint geometrical parameters have great impact on the joint bearing strength, while others have minimal or no effect. For example, an increase in the hole-diameter-to-thickness ratio (d/t) will result in an appreciable decrease of the bearing strength of composite bolted

joints. While other geometrical parameters, such as edge-distance-to-hole-diameter ratio (e/d) and joint-width-to-diameter ratio (w/d), control the ultimate failure mode of the joint, they have little influence on joint bearing strength as reported in the research (e.g., Collings 1982; Rosner and Rizkalla 1995).

2.2.2.2 Net-Section Tensile Strength.   The net-section tension strength is a function of both joint geometry and composite material strength (refer to Fig. 2-3A). The associated failure mechanism is assumed to be caused by tangential or compression stresses at the hole edge and is likely to occur when the hole-diameter-to-width ratio (d/w) is large and the bypass-to-bearing-load ratio is high. In this case, the cracks will propagate in a transverse direction to load direction. Figure 2-4 shows the different failure plans for a composite bolted joint.

2.2.2.3 Shear-Out Failure.   Shear-out failures should be regarded as a special case of bearing failures. In most cases, the shear-out failure is a consequence of a bearing failure with a short edge distance, e (refer to Fig. 2-3B). However, for highly orthotropic composites, shear-out failures occur at very large edge distances. Shear-out failure is a combination of in-plane and interlaminar shear failures. The shear-out failure can also be characterized by a single-plane "cleavage" failure, where the apparent laminate transverse tensile strength is less than the corresponding in-plane shear strength. Bolted composite joints are usually designed to avoid this brittle mode of failure.

Commonly, pure bearing joint specimens are used to determine the shear-out strength of composite joints. This has led to misinterpretation of the experimental results which usually indicate that smaller e/d ratios reduce the bolted composite joint bearing strength (ASTM 2002). In fact, the premature failure of shear lap specimens with small e/d ratios, at lower joint bearing stresses as compared to the laminate ultimate stress, is caused by the occurrence of shear-out failure in the shearing surfaces that prevents the occurrence of the bearing failure mode.

In a 1999 personal communication to me, L. J. Hart-Smith said, "There is *no* such thing as a material shear-out 'strength' for composite materials
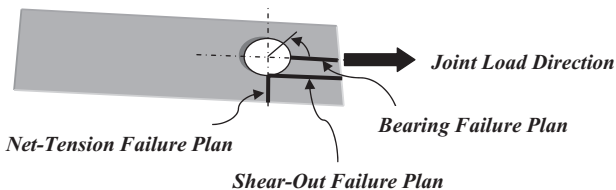

Figure 2-4. Failure plans for a composite bolted joint.

in the manner customarily assumed for ductile metals." Shear-out failures are the secondary propagation of a local failure adjacent to the bolt. To avoid or decrease the probability of catastrophic shear-out failure in FRP composites, an optimized fiber pattern should be selected, at least for those parts present at the connection zone. Shear-out failures are prevalent for fiber patterns that are both rich in 0-degree plies and deficient in 90-degree plies (refer to Fig. 2-5). Tests on boron/epoxy laminates for a fiber pattern of 50% 0-degree plies and 50% ±45-degree plies have exhibited the same joint strength and failure mode when $e/d = 2$ as well as when $e/d = 22$, as shown in Fig. 2-6. Figure 2-7 shows the shear stress contours for bolted graphite/epoxy joints.

The preferred fiber patterns for polymer composite laminates are shown in Fig. 2-8. As shown in this figure, shear-out failure does not occur within the shaded area of laminate pattern. Outside that area, the widespread splitting accompanies shear-out, and the low load level at which it occurs discourages the installation of fasteners in such highly orthotropic laminates. Therefore, to avoid catastrophic shear-out failures, the following guidelines are recommended for optimized fiber architecture for pultruded members:

1. Decrease the maximum percentage of 0-degree plies. Unfortunately, the majority of commercially produced pultruded composites are unidirectional, except for some specialty pultruded profiles for bridge applications recently being produced by some pultruders (e.g., ApATeCh, Fiberline, Creative Pultrusions, Strongwell, Bedford

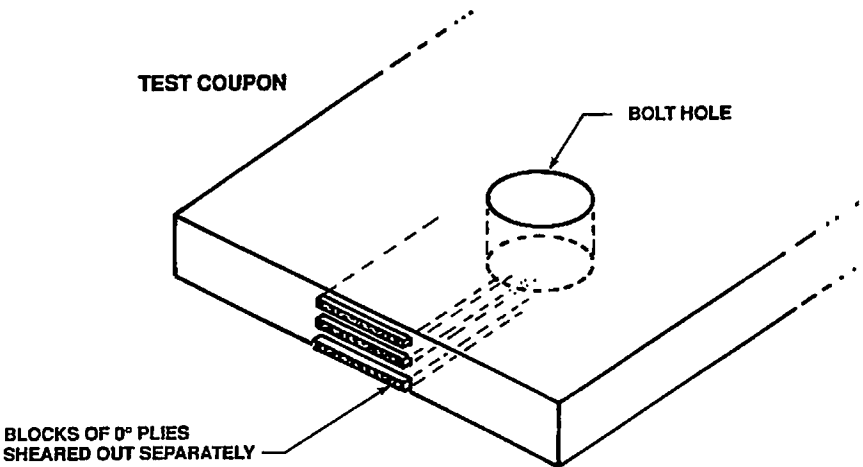*Figure 2-5. Shear-out failures at bolt holes in composite laminates with clustered parallel plies.*
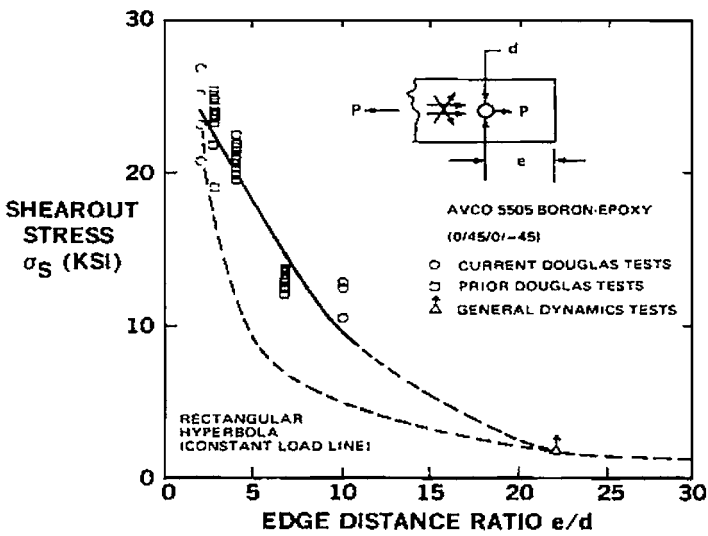
Figure 2-6. Insensitivity of shear-out resistance to edge distance for polymer composites.
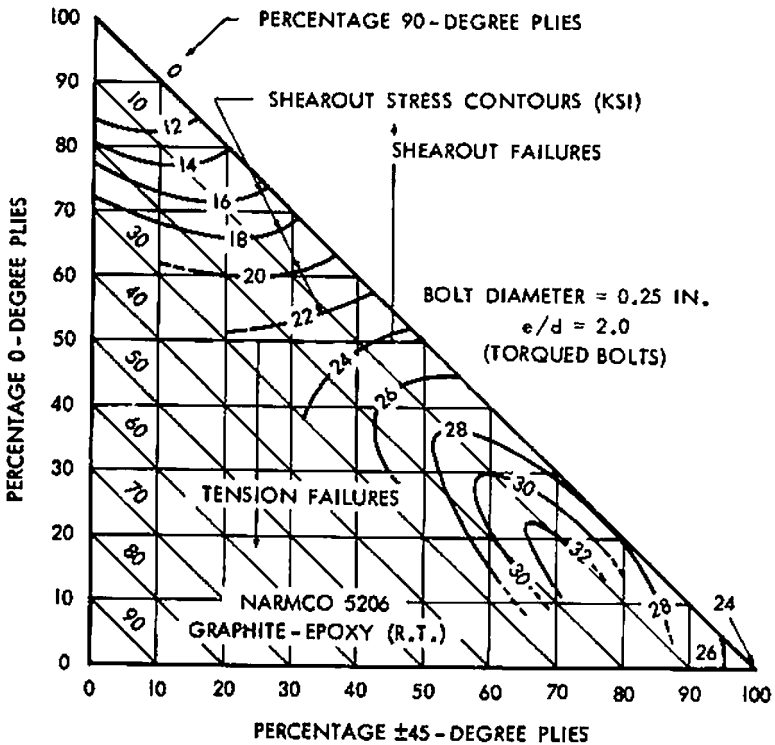*Source: Hart-Smith (1978), courtesy of Dr. John Hart-Smith and the Boeing Company.*

Figure 2-7. Shear-out stress contours for bolted composite joints.
Source: Hart-Smith (1986), courtesy of Dr. John Hart-Smith and the Boeing Company.
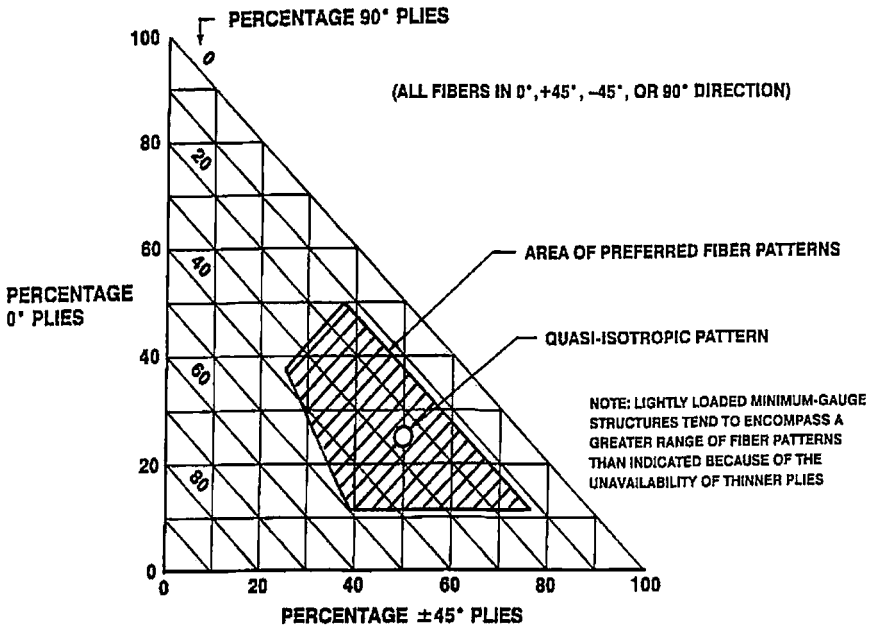
Figure 2-8. Preferred fiber patterns for polymer composite laminates. Source: Hart-Smith (1986), courtesy of Dr. John Hart-Smith and the Boeing Company.

Reinforced Plastics, Inc., and others) where quasi-isotropic lay-up is being used.

2. Increase the minimum percentage of 90-degree or ±45-degree plies.
3. Allow for better interspersion of the layers.

2.2.2.4 Cleavage Tension Failure.   Cleavage failures are another form of low-strength joint failure resulting from the too-close proximity of the end of the specimen (refer to Fig. 2-3D). In many cases, the cleavage failure is triggered by an incomplete net-section tension failure. This type of failure is usually initiated at the joint end rather than adjacent to the bolt hole. This mode of failure is a combination of both tension and shear failure. The higher stresses initiating this mode of failure are the result of three-point bending of the *short beam* beyond the bolt. The failure of this short beam is aggravated, for a given bolt load, by an increase in the *beam length* due to tensile failure of the net-section through the bolt. In summary, cleavage failures can be avoided by selecting an appropriate edge distance and by optimizing the joined member laminate's architecture, which should contain an adequate percentage of transverse 90-degree plies.

2.2.2.5 Bolt Pulling through Laminate Failure Mode.   This mode of failure is frequently associated with countersunk fasteners that are not common for pultruded shapes; it is likely to occur for joints with a sufficiently large thickness-to-bolt-hole diameter (t/d). In this case, the bolt head is pulled through the laminate after bolt bending (refer to Fig. 2-3C). This mode of failure may also vary, for any given geometry, as a function of the joined pultruded member laminate fiber architecture.

2.3 FACTORS INFLUENCING BOLTED JOINT STRENGTH

Despite the anisotropic nature and lack of ductility of pultruded composites, bolted composite joints fail in a fashion similar to metallic joints. However, because no *yielding* occurs in composites, the failure mechanisms of composites and metallics are completely different from each other (Kretsis and Matthews 1985; ASTM 2002).

Several factors influence the modes of failure of pultruded composites:

- *Geometrical factors:* width, edge distance, thickness, hole diameter, etc.
- *Materials factors:* matrix and fiber type, fillers content and volume fraction, fiber surface treatment, etc.
- *Fasteners factors:* type of fasteners, fastener size, hole size and tolerance, and applied torque
- *Design factors:* joint type, load directions, loading rate, static versus dynamic loading, etc.
- *Long-term and environmental exposure factors:* creep and creep rupture, humidity, temperature cycling, chemical attacks and stress corrosion, etc.

2.3.1 Effect of Thickness

The effect of joined member thickness, t, is usually expressed as a ratio of the hole-diameter-to-thickness (d/t). In general, the d/t ratio should be greater than unity to minimize the possibility of bolt failure. For high-modulus composites such as carbon/epoxy, the effects of d/t almost disappear for high lateral pressure values (Collings 1977). However, d/t ratio values greater than 3 will have a pronounced effect on the strength of bolted joints made of low-modulus composites (e.g., commercially produced pultruded E-glass/polyester or E-glass/vinylester materials) (Kretsis and Matthews 1985). The joint's ultimate bearing strength increases with a decreasing the d/t ratio. Based on this fact, the designer should try to use small d/t values, noting that a lower limit exists below which fasteners would fail in shear (i.e., by considerably decreasing the

diameter of the bolt as compared to the thickness, the failure is driven to the fastener). This lower limit depends naturally on the quality and type of bolt, but in general it is recommended *not* to use values of d/t below 1.2.

2.3.2 Effect of Width

Bearing failure occurs in composite joints with small hole-diameter-to-joint-width (d/w) ratios. As the joined member width decreases, there is a point where the mode of failure changes from bearing to net-tension (i.e., the composites fail across the width at the net-section, with cracks originated from the bolt hole), as shown in Fig. 2-9. Changing the mode of failure from bearing to net-tension, as w/d decreases, results in a considerable drop in joint strength. Experimental results reported by Kretsis and Matthews (1985) indicated that there are no well-defined transition points for one mode to another. For this reason, it is more appropriate to describe transition "regions" instead of transition points. The transition region can roughly be identified by extending half a unit of w/d on either side of the transition points.

2.3.3 Effect of Edge Distance

The edge distance, e, is defined as the distance from the hole centerline to the free edge of the joined pultruded member. This distance has a major impact on the bolted composite joint strength. Its effect is usually expressed
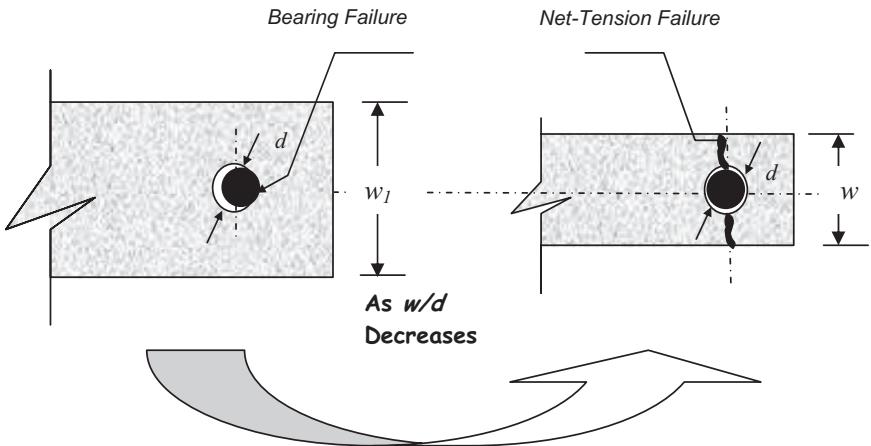

Figure 2-9. Influence of w/d ratio on the failure mode of bolted composite joints.

as a ratio of the edge-distance-to-hole diameter (e/d). As the e/d decreases, the bearing failure mode is likely to change to one of shear-out mode, depending on the laminate fiber architecture. However, the structural engineer should note that the shear-out failure results from unsatisfactory fiber patterns and not because of shorter edge distance selections, as thought by many engineers. However, selecting a shorter edge dimension will decrease both the bearing and tensile joint strengths, as mentioned earlier. If the edge distance is increased until it is equal to the bolt pitch, an appreciable increase in both bearing and tensile strengths is expected, but *not the resistance to shear-out failures.* Thus, in designing bolted pultruded joints, the engineer should not rely only on increasing the e/d ratio to enhance shear-out resistance.

2.3.4 Pitch or Bolt Spacing

Minimum spacing between adjacent fasteners, or pitch distances (i.e., pitch or back pitch), is specified to preclude premature failures due to tensile stresses and to enable each bolt to develop its full strength. As with minimum edge distance criteria, minimum pitch distances are expressed as a function of bolt diameters and are best determined by testing. Like w/d ratios, typical pitch distance (p/d) ratios for structural composites range up to 5. Minimum back pitch ratios (pb/d) are dictated by fiber orientations.

Multiple row fasteners are usually less effective in polymer composites than in metals (Godwin and Matthews 1980; Kretsis and Matthews 1985; Wong and Matthews 1981). This is particularly true for unidirectional laminates. Reduced efficiencies can be attributed to the severing of reinforcing fibers at the bolt holes and inability to reestablish unnotched capacities between the rows. Pyner and Matthews (1979) warn that strength data from single-hole test specimens be used with caution when applied to multi-hole bolted joints. Close fits between fasteners and holes are desirable with nonductile (brittle) plastics and reinforced plastics to obtain well-distributed bearing stresses around the hole and to develop the full bearing capacity of the composite member (ASCE 1984).

The single-row joint geometry for tension and bearing failures is shown in Fig. 2-10A and B, respectively. Figure 2-10C shows the two-row joint geometry for bearing failures. As shown in this figure, the bolt spacing (center-to-center) of a single-row joint tension failure is $3d$. Similarly, the distance to the edge of the plate from the center of the row is also $3d$. For bearing failure of a single-row joint, the larger spacing of $5d$ is required with an edge distance of $3d$. To avoid bearing failure in a two-row joint, spacing between individual bolts of $8d$, and spacing between rows of $4d$, are suggested by Hart-Smith (1987). In addition, the same edge distance of $3d$ is required.
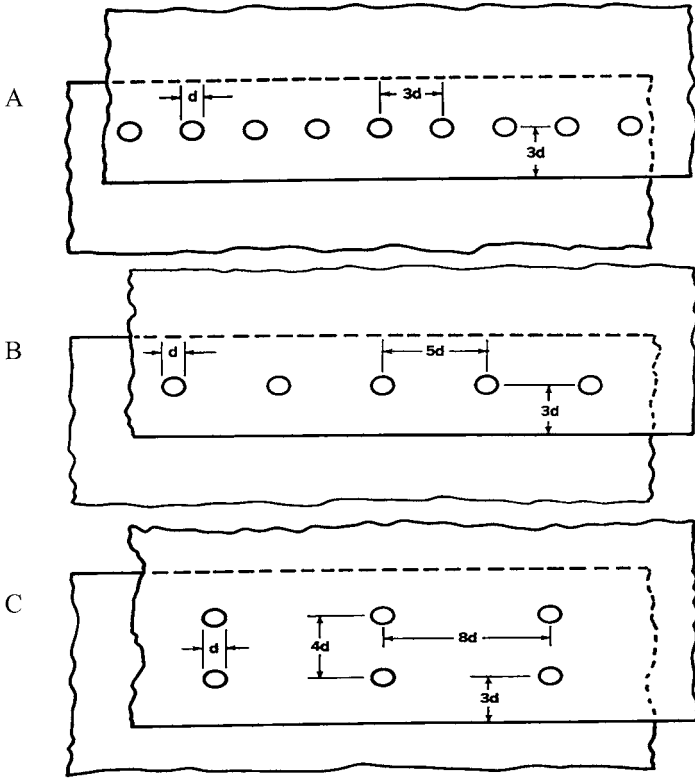
Figure 2-10. (a) Single-row joint geometry for tension failures; (b) single-row joint geometry for bearing failures; (c) two-row joint geometry for bearing failures.
Source: Hart-Smith (1989), courtesy of Dr. John Hart-Smith and the Boeing Company.

2.3.5 Effect of Lay-Up (Fiber Orientations)

The laminate lay-up or fiber architecture has a great impact on the bolted composite joint strength and failure mechanisms. The most efficient lay-ups for mechanical fasteners are those that are nearly quasi-isotropic, as opposed to those that are highly orthotropic. A quasi-isotropic laminate is a laminate with a stacking sequence such that it behaves in a nearly isotropic fashion (e.g., 0-degree/90-degree/±45-degree). However, designers often strive to select highly orthotropic fiber patterns in an attempt to optimize their designs. The highest bearing strengths are attained with lay-ups containing about 50% of 0-degree plies. When ±45-degree plies are added to this fiber architecture, an improvement in the compressive strength of the concentrated 0-degree plies is expected. As

stated earlier, shear-out joint failure can be avoided by using a minimum percentage of 90-degree or ±45-degree plies, and by allowing for better interspersion of the layers. As a general rule, an excess of 40% of the fibers oriented in any one direction can adversely affect the joint bearing strength and should be avoided. To minimize splintering when drilling bolt holes and to protect basic load-carrying plies, at least one pair of ±45-degree plies should be placed at the surface of each laminate. A single ply of fabric will suffice.

2.3.6 Effect of Loading Direction with Respect to a Member's Pultrusion Axis

Due to the anisotropic nature of pultruded composites, bolted joint strengths will vary with load direction. A maximum joint strength will be achieved if the direction of the applied load coincides with the direction of maximum strength (e.g., the pultrusion direction for unidirectional pultruded composites). Practically, this coincidence is difficult to achieve. In addition, it is common practice to use unidirectional flat plates for joining frame and truss structures, which usually have different angles with respect to the pultruded gusset plate (refer to Fig. 2-11). Johansen et al. (1993) reported shear-out failure at unidirectional pultruded plate connections where the load direction was non-coincident with the strong pultrusion direction of pultruded truss members.
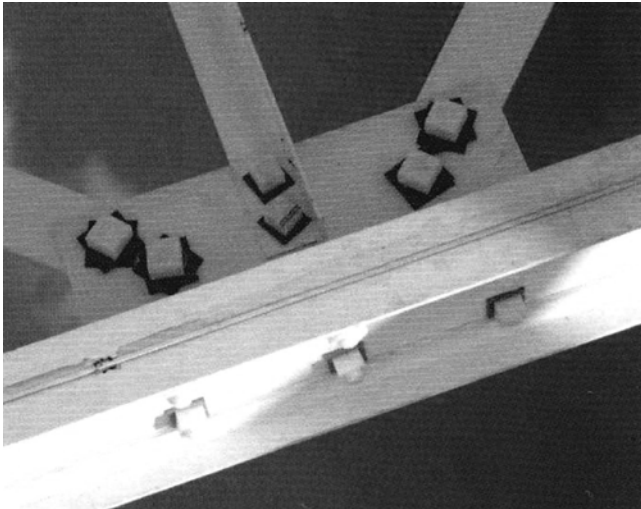

Figure 2-11. An example for non-coincidence of the load direction with the major fiber direction of a typical unidirectional pultruded composite truss joint. Source: Fiberline Composites A/S (2004), courtesy of Fiberline Composites A/S.

The effect of loading direction with respect to a member's pultrusion axis on PFRP bolted joint behavior was examined by Prabhakaran et al. (1996b). In their study, 105 specimens were tested to investigate the influence of the angle between the loading direction and the pultrusion direction. The bolted joint test specimens were fabricated from E-glass/polyester pultruded flat plates (Series 1500, manufactured by Creative Pultrusions, Inc.). Tests were performed on unnotched, pin-loaded specimens. Three pin-loaded joints were tested for each orientation angle, θ, for 0 degrees to 90 degrees in steps of 15 degrees.

The following conclusions were drawn from the results of this study:

- The unnotched tensile strength and modulus falls sharply as angle θ values increase from 0 degrees to 45 degrees, and then is less sensitive to the angle orientation, and then is insensitive to the angle orientation.
- For off-axis unnotched specimens, dual fracture modes were observed due to the dual laminate structure (roving and continuous strand mat).
- As compared to θ = 0 degrees, the joint bearing strength decreases as the value of θ increases, with a maximum strength degradation of about 30% θ at θ = 60 degrees. In addition, the bearing strength starts to increase slightly for values of θ greater than 60 degrees. These results conform with the previous observations reported by Mallick and Little (1985).
- The variation of shear-out strength with joint orientation angle θ has been evaluated, and test results indicated that a sharp drop in the joint shear-out strength occurs as the value of θ increases, with a maximum degradation of 28% at θ = 75 degrees.
- A sharp drop in the joint net-tension strength occurs as the value of θ increases, with a maximum degradation of 60% at θ = 30 degrees, and then is less sensitive to the angle orientation up to 90 degrees. Net-tension failure was observed for all angles for both notched and pin-loaded specimens.

A similar study on pultruded composites was conducted by Turvey (1998). In this study, test specimens were fabricated from a 1/4-in. (6.4-mm) thick E-glass/polyester pultruded flat plate (EXTREN 500 Series). [This flat plate was twice the thickness used by Prabhakaran et al. (1996a) manufactured by the Strongwell Company.] The reported data and conclusions clearly indicate that Turvey was not aware of Prabhakaran et al.'s (1996a) work. The two investigations used different parameters, such as thickness, material manufacturers, and test setup. Nevertheless, Turvey's 1998 study confirmed the conclusions of the earlier Prabhakaran et al. study. It is interesting that both studies, regardless of some differences in

experimental parameters, obtained remarkably similar results and conclusions. For example, both researchers concluded that there is little evidence of any bearing failure once the off-axis angle, θ, exceeds 30 degrees. In addition, it was concluded that cracks, which initiated at the hole and propagated along the rovings, were the main precipitators for ultimate failure of the joint. This failure pattern may be viewed by some engineers as negative (i.e., weak zones) and at the same time as a positive characteristic as crack guides and/or inhibitors. For all off-axis loaded specimens, the strength is derived mainly from the continuous strand mat (CSM) and the matrix, since the off-axis roving strength is negligible. Therefore, the engineer should realize that when the load is applied at any angle relative to the pultrusion axis, the effective strength and stiffness will be different from those listed in manufacturer tables (on-axis strength and stiffness values) and will decrease as the phase angle, θ, increases.

Yuan et al. (1996) investigated the effect of several parameters on the behavior of composite bolted joints, including the alignment of fibers with respect to the loading direction. Based on the experimental results of that study, it was concluded that the joint ultimate strength decreases as the fiber-to-load direction increases in a linear fashion. It was also observed that a fiber-to-load direction of less than 45 degrees resulted in a ductile mode of failure, while a brittle failure mode was observed for joints with a fiber-to-load direction greater than 45 degrees.

It is recommended that the following points be considered when designing off-axis loaded pultruded members regarding the effects of width-to-diameter and edge-distance-to-diameter ratios:

- For on-axis loaded joints, increasing the value of the e/d ratio will greatly improve the joint strength. However, this increase will level off as the value of e/d approaches a limiting value of 5 because the failure mode changes to bearing failure mode.
- For off-axis loaded joints, it appears that, unlike on-axis loaded joints, no e/d limit exists. In other words, increasing the e/d values beyond 5 will still contribute to increasing the joint strength. It should be noted that this conclusion is based on specific values of $w/d = 10$. For this reason, the designer may select larger values of e/d, different from those used for on-axis loaded members for the same joint. This may influence the selection of the dimensions of pultruded members. For example, for the truss joint shown in Fig. 2-12, an e/d value of 5 for the diagonal members may be selected, while an e/d ratio of 8 for the bottom chord member may be selected. For the same hole diameter and same range of loading, the dimensions of the bottom chord may be forced to be larger than what is originally calculated to carry a member's axial load, in order to provide the required joint strength.
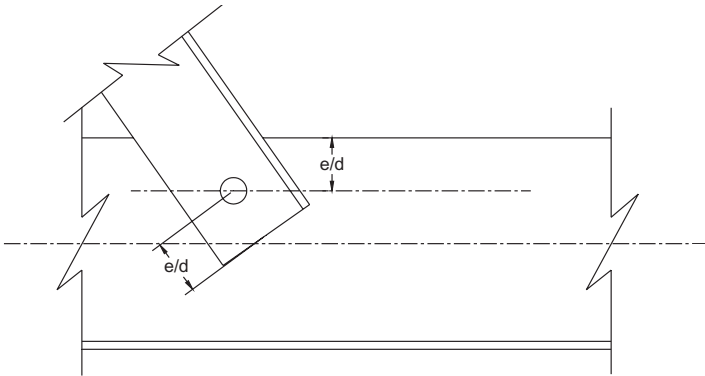
Figure 2-12. Edge distance for on-axis and off-axis loaded members.

- For on-axis loaded joints, increasing the value of the w/d ratio will greatly improve the joint strength. However, this increase will level off as the value of w/d approaches the limiting value of 8 because the failure mode changes to bearing failure mode.
- For off-axis loaded joints, and unlike on-axis loaded joints, no limit of w/d seems to exist. In other words, increasing the w/d values contributes in increasing the joint strength. It should be noted that this conclusion is based on specific values of $e/d = 6$ for $\theta = 90$ degrees, 45 degrees, and 30 degrees, and $e/d = 5$ for $\theta = 0$ degrees. For e/d, the designer may select larger values of w/d that differ from those used for on-axis loaded members for designing the same joint.
- According to Turvey's (1998) study, for $\theta = 90$ degrees, the bolt slip decreases as e/d and w/d increase, while the bolt slip increases as e/d and w/d increase for $\theta = 30$ degrees and for $\theta = 45$ degrees. Again, this conclusion is solely based on this study for a specific pultruded product and joint geometry.
- The bolt displacement at failure increases rapidly as the e/d and w/d ratios increase for 30 degrees and 45 degrees off-axis loadings, while only a slight displacement increase occurs as these ratios increase for off-axis transverse loading ($\theta = 90$ degrees).
- The bearing strength of 4% of the bolt hole diameter deformation, defined by ASTM and ASCE in the *Structural Plastics Design Manual* (ASCE 1984), compares favorably with the incipient failure load observed in joint tests (Yuan et al. 1996).
- In general, increasing the value of the w/d ratio will result in increasing the joint stiffness.
- For a given w/d ratio, increasing the value of the e/d ratio has a slight impact on increasing the joint stiffness.

2.3.7 Effect of Type and Rate of Loading

Within the normal range of loading rate corresponding to static testing, the strength of composite bolted joints is insensitive to loading rate.

2.3.7.1 Sustained Loading Conditions.   Due to the viscoelastic behavior of composites, it is expected that when sustained loading conditions are present, a lower joint strength is expected. Viscoelastic relaxation in bolted composite joints was evaluated for 1,000 hours by Schmitt and Horn (1990). In this program, a total of 78 bolted single-shear joints were tested. For thermoset pultruded composite joints, limited information on creep behavior is available, with the exception of a pilot study conducted by Mosallam and Schmitz (1996) and Mosallam (1999) on creep behavior of pultruded exterior moment frame connection. In this study, stiffness degradation up to 46% was observed after 420 hours of loading at ambient conditions. Details of this study are presented in Chapter 5 of this manual. Mosallam (2009) describes a recent work on the creep behavior of pultruded composites under different conditions.

2.3.7.2 Impact Loading Conditions.   Limited information is available on the effect of impact loading on the behavior of bolted composite joints. However, similar to creep, it is expected that impact loading will contribute to a reduction of the bolted composite joint strength. Traditionally, the residual static strength after impact damage has set the upper limit on design operating strain levels under compression, even for bolted structures (Hart-Smith 1996b).

2.3.7.3 Tension–Tension Fatigue Loading Conditions.   With few exceptions, bolted composite joints have excellent performance under tension–tension fatigue loading conditions (Hart-Smith 1996a). The major exception to this is in the case of joints with loose bolt holes, particularly under reversed cyclic loading conditions. It should be noted that, unlike ductile metal joints, there are far higher "static" stress concentrations at bolt holes in bolted composite joints. However, the subsequent strength loss under fatigue loading is far less with composite bolted joints as compared to bolted joints for metals. Well-designed bolted composite joints are not sensitive to cumulative damage under fatigue loads. Experimental results indicate that gentle tensile–tensile fatigue of composites tends to *increase* the residual strengths of composite structures due to the progressive relief of the stress concentration (see Fig. 2-13).

Little and Mallick (1990) conducted a study to evaluate the tension–tension fatigue behavior of sheet molding compound (SMC-R18) composite bolted joints. In this investigation, the effects of e/d and w/d ratios as well as the washer geometry on the fatigue strength of bolted composite
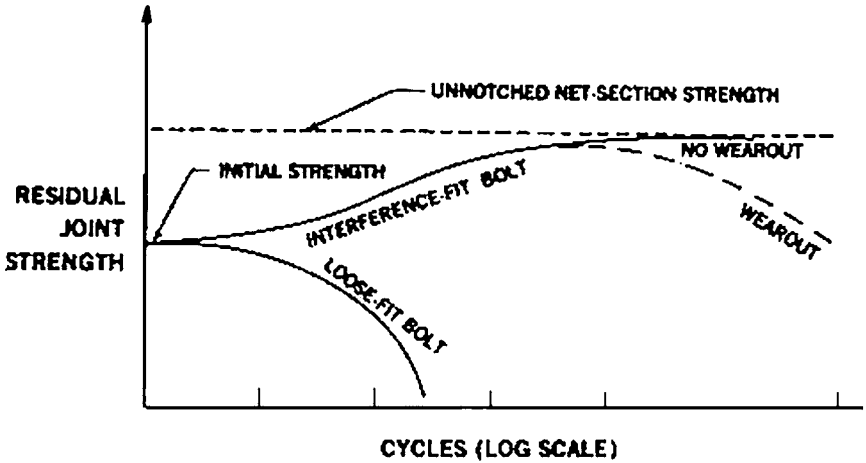
Figure 2-13. Fatigue of notched composites or bolted composite joints. Source: Hart-Smith (1986), courtesy of Dr. John Hart-Smith and the Boeing Company.

joints were studied. Based on their results, Little and Mallick drew the following conclusions:

1. For highly tightened joints with relatively lower values of w/d (e.g., $w/d \leq 4$), the fatigue failure is likely to occur away from the bolted joint.
2. For highly tightened joints with relatively higher values of w/d (e.g., $w/d \geq 6$), the likelihood of fatigue failure at the bolted joint increases rapidly.

The washer size and thickness have a great impact on the fatigue life of bolted joints. The clamping pressure distribution that gradually diminishes from a high value directly under the bolt head to the outside edge of the washer appears to be advantageous. It should be noted that the above conclusions are based on investigating a specific type of composite, and it is expected that these conclusions may be changed for pultruded composite bolted joints. However, due to the limited nature of reliable information on pultruded composites, it is more prudent to recommend conservative values—8 and 5—for both w/d and e/d for pultruded joints subjected to tension–tension cyclic loads. More work in this area is required to establish more reliable and precise values for pultruded composite bolted joints.

Sarkani et al. (1999) reported the experimental and analytical results of a study on fatigue behavior of composite bolted joints. In the experimental

program, three types of composite joints were evaluated under fully reversed loading, including bolted, bonded, and combined bolted/ bonded configurations. Figure 2-14 shows the geometry of the specimens tested in this program. The composite materials used in this study were cross ply (0 degrees/90 degrees) and angle ply (±45 degrees) E-glass/ epoxy laminates that were fabricated using the Seemann composite resin infusion molding process (SCRIMP). Figure 2-15 shows the S-N curve for
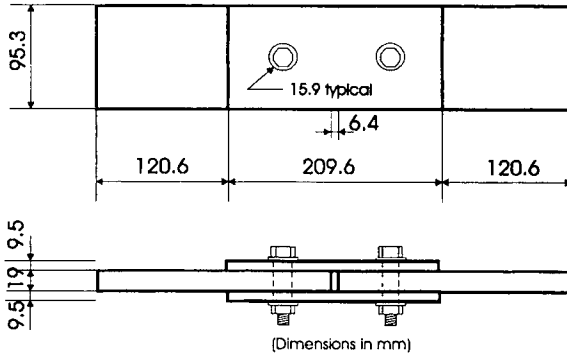

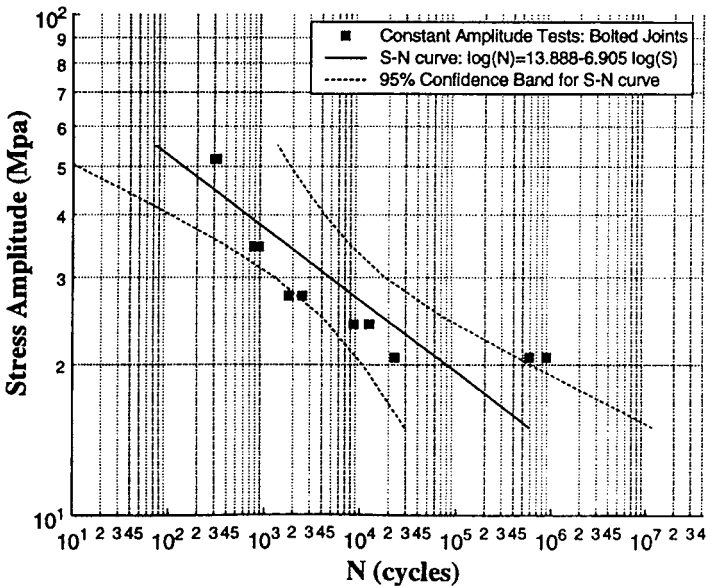*Figure 2-14. Specimen geometries for tested joint configurations (Sarkani et al. 1999).*

Figure 2-15. S-N curve for bolted composite joints (Sarkani et al. 1999).

the bolted joints tested in this program. Recently, a study on fatigue characteristics of bolted joints of unidirectional composite laminates was reported by Lim et al. (2006). Test results indicated that laminates whose major plies are stacked in the axial direction can be used for the bolted joint structures under fatigue load when an appropriate clamping pressure is applied to the bolted joint.

Very limited quality work on fatigue behavior of bolted joints for pultruded composites is available. One of the earlier published studies that focused on fatigue performance of pultruded composite box and H-beams with and without flexural connections was investigated by Nagaraj and GangaRao (1998). In this study, 35 tests were conducted on sections with connections to compare the performance and efficiency of sections with splice connections to sections with no connections. Van Wingerde et al. (2003) performed a number of static and fatigue tests of normal bolted connections and resin injected bolted connections using so-called injection bolts. Since the amplitude of the cyclic loading has a major effect on the fatigue performance, the maximum stress-maximum cycle relationship (S-N) is determined for one specific loading amplitude. The amplitude is expressed as the R ratio value, which is the minimum peak stress divided by the maximum peak stress ($R = \sigma_{min}/\sigma_{max}$). It is most common to test at an R ratio of 0.1, but families of curves, with each curve at a different R ratio, are often developed. In this program, fatigue tests for $R = 0.1$, $R = -1$, and $R = 10$ were performed on connections with web plates between H-beams at different stress levels. Experimental results indicated that the connection evaluated in the study performed well under fatigue loading, with a slope of $m = -5$ or better of a line that reaches the static strength for $N = 1$, a single cycle. The study showed also that there was no improvement on bolted joint's static strength when injected with resin, while some gain in joint stiffness was observed for the injected bolted joints. Furthermore, experimental results showed that the fatigue performance for both types of connections showed only modest improvements for $R = 0.1$, but major enhancements for $R = -1$, suggesting that injection bolts could be an attractive option. For truck chassis pultruded applications, Klett et al. (2004) and Sun et al. (2004) discussed the use of the Palmgren-Miner linear relationship in conjunction with the results of constant amplitude fatigue tests to estimate the cumulative damage caused by low-frequency cycles.

2.3.7.4 Fatigue of Pultruded Threaded Rods and Molded Composite Nuts. The basic principle in designing mechanically fastened joints is that the material being joined should fail before the fastener (ASTM 2002). However, Mosallam and Schmitz (1996) and Mosallam (1999) reported that the major mode of failure of pultruded composite connections under cyclic loading is the failure of the pultruded composite threaded rods far

earlier than noticeable damage to either the connecting element of the joined member (refer to Fig. 2-16).

2.3.7.5 Compression–Compression Fatigue Loading. Under compression–compression cyclic loading, unnotched composite laminates can experience delamination, particularly after lateral impact damage. For compressive in-plane loads, the design operating strain level of typical composites has been limited by the interlaminar spread of impact damage. When composite bolted joints are subjected to compression–compression cyclic loading conditions, the same kind of micro-damage that alleviates tensile stress concentration around the bolt hole mentioned earlier "destabilizes" the fibers under compression. Unlike tension–tension loading conditions, where this damage grows at an ever-diminishing rate under tensile loads, once initiated it grows at an exponentially increasing rate under compression loading conditions. It should be noted that "double-shear" bolted joints are more resistant to fatigue loading than are "single-shear" bolted joints. The limited available information on fatigue behavior of composite bolted joints suggests that lifetimes of several million cycles can be expected for loads as high as 70% of the joint static strength of
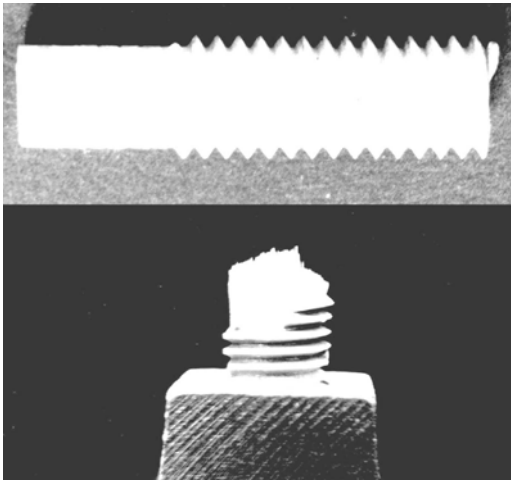

Figure 2-16. Failure of composite threaded rods under fully reversed cyclic loading. Mallick (1988) conducted a similar study to investigate the effects of hole stress concentration and its mitigation on the tensile strength of sheet molding compound composites. In this study, it was observed that most fatigue cracks initiated at the fraying surfaces of the SMC-C30R20 composites, whereas fatigue cracks for SMC-R18 composite joints originated around the washer edge on the outside surface.

double-shear bolted joints. For single-shear bolted joints, a drastic reduction in joint fatigue strength is expected (Matthews 1988).

2.3.8 Effect of Bolt Fit (Hole Clearance)

Ideally, the maximum joint strength is achieved when the bolt hole is reamed to size. Similarly, the ideal joint performance is achieved if the washer hole is reamed to fit the bolt. Allowing clearance (i.e., "normal fit") for the hole and washer can reduce the joint bearing strength by up to 25% over that for a "complete fit."

Yuan et al. (1996) conducted an experimental investigation on the effect of bolt fit on the structural performance of bolted pultruded composite joints. In this study, five different bolt hole clearances were tested, while the edge distance and specimen width and thickness were kept invariant. The material used in this study was EXTREN Series 500 E-glass/polyester flat sheet (manufactured by Strongwell). The thickness, width-to-hole-diameter ratio (w/d), and edge-distance-to-hole-diameter (e/d) ratio of the jointed pultruded plates were 3/8 in. (9.525 mm), 4 in. (101.60 mm), and 4 in., respectively. Stainless steel bolts, 1/2 in. (12.7 mm) in diameter, were used for all tests. The hole diameters were 1/2 in. (12.70 mm), 9/16 in. (14.28 mm), 5/8 in. (15.87 mm), 11/16 in. (17.46 mm), and 3/4 in. (19.05 mm). A total of five joint specimens for each hole clearance were tested. For all tests, the stainless steel bolts were loosely tightened (finger-tight) to eliminate the torque effect on the joint performance. Test results indicated that all joint specimens failed in bearing mode, as was intended. The bearing failure was characterized by the development of a progressive deformation with a continuous crippling of the glass fibers and crushing of the polyester matrix. From this study, the following points can be used as a guideline for the selection of bolt clearance for unidirectional pultruded composite bolted joints:

- Selecting larger hole clearances for bolted pultruded joints will result in a reduction in the toughness of the joint.
- Both ultimate load and load at the incipient failure decrease with an increase of hole clearance. However, the test results indicated that hole clearance less than 9/16 in. (14.288 mm) has little effect on joint ultimate strength. Thus, the current practice of using the hole diameter equal to the bolt diameter, d_b, plus 5/8 in. (15.875 mm) is acceptable; that is,

$$d = [d_b + 15.875 \text{ mm}] \qquad (2\text{-}1)$$

For close-fit conditions and adequate e/d and w/d ratios, the bearing strength at 4% of hole diameter deformation, as defined by ASTM and

ASCE in the *Structural Plastics Design Manual* (ASCE 1984), has a safety factor of 3 and 4 in bearing strength at incipient failure and ultimate load, respectively.

2.3.9 Effect Bolt Torque (Applied Clamping Load)

The applied clamping force and the distribution of such forces affect the performance of PFRP bolted joints.

2.3.9.1 Applied Clamping Force.   Bolt bearing failure modes in composite materials are a mixture of compressive and delamination failure at the bolt hole. The applied clamping force prevents the expected delamination with a consequent increase in failure load (Stockdale and Matthews 1976). Similar to bolted steel joints, increasing the through-the-thickness clamping force provided by tightening the bolt improves the joint strength of PFRP bolted joints. It is possible that a grossly overtightened bolt could result in damage to the composite laminate by forcing the washer into the surface (Matthews 1988). However, for normal volume fractions this local damage is less likely to develop. Instead, for a reasonable hole-diameter-to-thickness ratio (d/t), it is more likely that damage by stripping of the bolt threads will occur before laminate damage occurs. This process was observed for PFRP threaded rods in several full-scale studies (Mosallam et al. 1993; Mosallam and Schmitz 1996). The bearing strength of a fully tightened bolt is up to four times that for a pin-joint. On the other hand, the finger-tight bolted joint has twice the strength of the corresponding pin-bearing strength (Matthews 1988).

Nassar et al. (2007) conducted an experimental and analytical investigation of the behavior of a double-bolted single-lap shear composite joint. Several bolt tightness scenarios were considered for composite-to-composite and composite-to-aluminum bolted joints. Based on both analytical and experimental results, it was concluded that increasing the bolt tightness without exceeding the joint strength would significantly reduce the potential for delamination around the bolt hole when a tensile load is applied. It has been also concluded that tightening of at least one bolt in a two-bolt composite joint has increases the joint bearing strength. Also, joint stiffness is increased only when both bolts are sufficiently tightened.

The study by Doyle referenced earlier (J. R. Doyle, "Behavior of Bolt and Adhesive Connections in Glass Fiber-Reinforced Plastic Members." Master's thesis, Department of Civil Engineering, West Virginia University, Morgantown, WV, 1991) indicates that an increase of up to 31% in PFRP bolted joint strength is achieved by tightening the steel bolts by the maximum permissible tension, as compared to similar "finger-tightening" the bolted joints. The applied axial force can be calculated from the following expression, from Doyle:

$$W = \frac{12T_s}{r\tan(\alpha + \theta_s)}$$

(2-2)

where
W = applied axial force, lb (N)
T_s = applied torque, ft-lb (N·m)
r = radius of bolt bet area, in. (mm)
α = angle of inclination of bolt threads
θ_s = angle of static friction.

Matthews et al. (1982) observed losses in the bolt tension when the bolt was fully tightened and the joint was not loaded. However, under the same condition but with the joint loaded, the bolt tension increased as the applied tensile force on the joint increased. Cooper and Turvey (1995) reported the results of their study on the effect of bolt torque and joint geometry. The material used in that study was 1/4-in. (6.35-mm)-thick E-glass/polyester EXTREN 500 Series (manufactured by Strongwell). Tables 2-2, 2-3, and 2-4 summarize the experimental pin-joint, lightly clamped joint, and fully clamped joint, respectively. Based on this study, the following conclusions were drawn:

- The joint strength increased by 45% and 80% for lightly-clamped (3 N-m) and fully clamped (30 N-m) joints [2.21 ft-lb (3 N·m)], respectively, as compared to pin-joint strength.
- Increasing bolt torque significantly increases the critical values of e/d and w/d ratios.
- Bolt torque does not affect the initial bolt displacement.
- Bolt-clamping torque and e/d ratio have a small effect on the joint initial stiffness.

Klett et al. (2004) and Sun et al. (2004) reported results of several tests on both steel-to-steel and several bolted pultruded composite joints with different thicknesses. The applied torque of all bolted joints was 50 ft-lb (67.8 N-m). Test results showed that the loss of preload with time was relatively low for steel-to-steel bolted joints and as compared to pultruded bolted joints with different thicknesses. The test results further indicated that major preload loss occurred for bolted pultruded joints with largest thickness [t = 1/4 in. (6.35 mm)]. It was also reported that a significant portion of preload loss occurred during the first 5 min after the bolt has been tightened, and a very rapid decrease in preload occurred within the first 30 sec after application of the torque. Based on the results of the initial tests, it was suggested that retightening the bolts within a few minutes of the initial assembly may assist in reducing the bolt's preload loss rate with time, as well as the overall loss of preload.

Table 2-2. Hole Clearance Tests Summary Results

Test Group	Hole Clearance [in. (mm)]	Load at Incipient Failure [kips (kN)]	Ultimate Joint Load [kips (kN)]	Failure Mode
D8/16	0 (0)	6.65 (29.60)	9.24 (41.12)	Bearing
D9/16	0.03125 (0.794)	6.1 (27.15)	9.1 (40.50)	Bearing
D10/16	0.0625 (1.5875)	6.0 (26.70)	8.86 (39.43)	Bearing
D11/16	0.09375 (2.38125)	4.75 (21.14)	8.74 (38.94)	Bearing
D12/16	0.125 (3.175)	4.20 (18.69)	8.43 (37.51)	Bearing

Source: Cooper and Turvey (1995).

Table 2-3. Average Failure Loads and Joint Stiffnesses of Pin-Bearing Single-Bolt Joints
in EXTREN 500 Series 6.35-mm-Thick Flat Plates[a]

Member Width-to-Hole Diameter, w/d	Edge Distance-to-Hole Diameter Ratio, e/d	Average Failure Load (kN)	Average Damage Load (kN)	Typical Failure Mode	Average Initial Joint Stiffness (kN/mm)
5.0	1.5	11.2	—	Shear	20.3
5.0	2.0	15.2	12.9	Cleavage	28.6
5.0	3.0	19.7	16.8	Bearing	29.9
5.0	4.0	19.3	16.2	Bearing	28.5
5.0	5.0	17.2	13.8	Bearing	29.6
2.0	4.0	8.7	—	Tension	15.6
3.0	4.0	16.8	14.8	Tension	23.2
4.0	4.0	18.6	17.7	Bearing	27.9
7.0	4.0	17.5	15.2	Bearing	30.2

[a] d = 10 mm.
Source: Cooper and Turvey (1995).

Table 2-4. Average Failure Loads and Joint Stiffness of Lightly Clamped (3 N·m)
Single-Bolt Joints in EXTREN 500 Series 6.35-mm-Thick Flat Plates[a]

Member Width-to-Hole Diameter, w/d	Edge Distance-to-Hole Diameter Ratio, e/d	Average Failure Load (kN)	Average Damage Load (kN)	Typical Failure Mode	Average Initial Joint Stiffness (kN/mm)
10.0	2.0	16.8	—	Shear	34.1
10.0	3.0	23.6	21.4	Shear	37.6
10.0	4.0	27.5	21.0	Cleavage	37.8
10.0	5.0	28.9	21.5	Bearing	41.8
10.0	6.0	27.5	18.2	Bearing	36.9
2.0	5.0	10.1	—	Tension	17.2
4.0	5.0	21.4	19.5	Tension	29.4
6.0	5.0	25.5	17.7	Bearing	32.0
8.0	5.0	29.3	19.4	Bearing	35.7

[a] d = 10 mm.
Source: Cooper and Turvey (1995).

2.3.9.2 Effect of Using Washers. The torque is transferred to the specimen in the form of lateral pressure (σ_z) exerted by the washer onto the area around the bolt. The use of washers is important to prevent the composite from splitting through the thickness on the hole's loaded side. Assuming that the width, w, and the edge distance, e, are large compared to the hole diameter, d (i.e., $w > 6d$, and $e > 6d$), the failure area is confined to within one or two diameters of distance from the loaded half of the bolt hole, i.e., a bearing failure (Kretsis and Matthews 1985). If the laminate is restrained laterally, the part of the laminate under the washers develops shear cracks but is not allowed to expand under compression, thus the lateral expansion; hence, the delamination is spread into a wider area outside the washer boundary. The ultimate load is therefore expected to increase since the easiest failure modes are suppressed.

The bearing stress increases asymptotically; however, the bearing stresses are expected to decrease when the magnitude of σ_z becomes high enough to cause the washer to punch through the laminate. Matthews et al. (1982) reported that increasing the contact area by replacing a washer with a composite plate resulted in a slight increase in failure load. W. S. Arnold, in his Ph.D. dissertation (Dept. of Mechanical Engineering, Paisley College of Technology, Paisley, UK, 1989) titled "The Behavior of Mechanically Fastened Joints in Composite Structures," reported that the use of recessed washers results in significant damage compared to the use of plain and beveled washers. Khashabaa et al. (2006) studied the effect of washer size and tightening torque on the performance of bolted composite joints. The experimental results showed that (in the range of the investigated tightening torques) the slope of the load–displacement curve (stiffness) increased with increasing the tightening torque as a result of increasing the contact pressure. Also, bolt bearing strength increased as the tightening torque increased and, under the same tightening torque, joint stiffness increased with the decreasing washer size. The results also indicated that the load–displacement curve of bolted joint specimens finger-tightened, $T = 0$ Nm, had the lowest stiffness, with several knees (inflection points in the load-displacemet curve), which indicated unstable development of internal damage.

For bolted pultruded composite joints, Abd-El-Naby (unpublished Ph.D. dissertation, "Experimental and Theoretical Investigations of Bolted Joints for Pultruded Composite Materials," Dept. of Civil Engineering, University of Surrey, Surrey, UK, 1992) and Abd-El-Naby and Hollaway (1992) conducted a study to investigate the effect of clamping area and the materials used for clamping on the bearing strength and extensibility of the single-bolt pultruded composite joint. The pultruded material used in this study was E-glass/polyester manufactured by the Strongwell Company. The bolt diameter, d_b, was 3/8 in. (9.5 mm), and the washers were tight-fitting with an outer diameter, d_w, equal to 2.2 times the bolt

diameter [i.e., 0.825 in. (20.90 mm)]. The *small* clamping torque used for all specimens was equivalent to the finger-tight condition. The test was conducted on three specimen groups, each being subjected to a different clamping condition. It was also reported that parts of the joint specimens with steel washers were separated from the rest of the PFRP plate by two cracks that extended from the hole parallel to the specimen axis. The material between these two cracks was not damaged because of the presence of the steel washer suppressing the bearing failure mechanism.

It should be noted that in most of the current reported works on frame connections (e.g., Mosallam 1999; Mosallam and Schmitz 1996), the use of washers did not affect the mode of failure of the pultruded connections. This can be attributed to the relatively large area of the FRP molded square nuts as compared to the bolt diameters that were used in these investigations. However, and due to the sharp corners of the molded FRP nuts, a high stress concentration is likely to develop, which was observed to result in localized punching shear damage. In these cases, the sharp corners of the FRP molded nuts should be rounded, and an FRP thin composite plate is recommended. It should be noted that other FRP bolt-and-nut systems are manufactured by the Strongwell Company, are available commercially, and not only help to avoid stress concentration at the square nut sharp edges but also have built-in washers, as shown in Fig. 2-17.

Klett et al. (2004) and Sun et al. (2004) performed an experimental study to evaluate the effect of washer size on the strength of pultruded bolted

Figure 2-17. Fibrebolt threaded rods and molded nut system.
Courtesy of Strongwell Company, Bristol, Va.

joints made of EXTREN profiles. Several pultruded composite lap shear joint specimens with a nominal size washer (15.9 mm diameter), an oversize washer [1 in. (25.4 mm) diameter], and a steel plate washer (50 mm × 35 mm × 6 mm) were evaluated. Test results indicated that the static strength increased approximately 10% with an oversize washer and approximately 20% with a plate, compared with the nominal washer. It was further observed that joint specimens with nominal and large washers showed the typical characteristics of a bearing type of failure. However, bolted joints with a constraining plate did not show clear strength degradation prior to reaching the peak joint strength. In all three washer types, a common cleavage tension failure mode was observed and the damage was initiated in all cases at the border of the bolt hole.

2.3.10 Environmental Effects

Numerous studies have been published regarding enviromental effects on composite materials, including pultruded structures. However, very few publications are found related to the behavior of composite bolted joints subjected to harsh enviroments. Kim and Whitney (1976) conducted a study on the effect of both temperature and moisture content on the structural performance of the pin-bearing strength of composite laminates. Their results indicated a reduction of up to 40% of the ultimate joint load under certain combined temperature and moisture environmental conditions. The environmental effects on the cyclic performance of composite bolted joints are discussed in detail by Ramkumar and Tossavainen (1984) and by Jeans et al. (1980). These studies indicated that the fatigue threshold may be lower under hot/wet [218 °F/wet (103 °C/wet)] conditions. The thermal effects on the bearing behavior of composite joints was studied and reported by S. P. Walker in his 2001 Ph.D. dissertation "Thermal Effects on the Bearing Behavior of Composite Joints" (Mechanical and Aerospace Engineering, University of Virginia, Charlottesville, Va.). In this study, pin-bearing tests of several lay-ups were conducted to develop an understanding of the effect of temperature changes on the pin-bearing behavior of the material. Test results showed that for all lay-ups that failed in the bearing mode, pin-bearing strength decreased with an increase in temperature. Ahmed et al. (2003) evaluated the bolt bearing behavior of highly stressed composite joints subjected to high-temperature environments.

For pultruded composite joints, a limited number of durability studies are available. The effect of moisture and temperature was studied by Hurd and Yuan (1996, pp. 243–249). All pultruded single-bolt joint specimens were constructed from Pultex Series 1525 E-glass/polyester pultruded flat plates manufactured by Creative Pultrusions, Inc. The joint geometry was designed to ensure bearing failure by providing sufficient

width-to-diameter (*w/d*) and edge-distance-to-hole-diameter (*e/d*) ratios of 7 and 5, respectively. The specimens were immersed in four different water baths: 73 °F (23 °C), 100 °F (38 °C), 125 °F (52 °C), and 150 °F (66 °C). For room-temperature–immersed specimens [73 °F (23 °C)], tests were conducted at exposure time intervals from 0 to 60 days. The other specimens were exposed to elevated wet environments and were tested after 1-day and 30-day exposures. The maximum moisture contents ranged from 0.5% at room temperature [73 °F (23 °C)] to 1.7% at 150 °F (66 °C). For room-temperature specimens, the maximum moisture content was 0.5% by weight. At higher temperatures, the maximum moisture content was 0.7%, 1.3%, and 1.7% by weight at 100 °F (38 °C), 125 °F (52 °C), and 150 °F (66 °C), respectively. Thus, joint specimens immersed in water under temperatures higher than 100 °F (38 °C) demonstrated a dramatic increase in the moisture content.

Experimental results indicated that degradation in the joint bearing capacity as the temperature and the immersion time increased ranged from 27% to 50%. In addition, test results showed that the combined moisture and elevated temperature exposure condition resulted in a greater reduction in the bearing capacity of the bolted pultruded joint than did the moisture-alone exposure condition. The following are some of the important conclusion drawn from the Hurd and Yuan (1996) study:

- Appropriate safety factors (or knock-down factors) should be considered by the structural engineer when designing pultruded frame structures with continuous exposure to wet and/or elevated temperature conditions. For example, the result of this experiment concluded that exposure to moisture alone could reduce the bolted joint bearing capacity by nearly 30% as compared to the joint dry bearing strength. This reduction can be further increased up to 50% when bolted pultruded composite joints are exposed to both moisture and higher temperatures. This reduction was observed in a failure case reported by Mosallam (1998).
- Care should be taken in applying compatible sealant to the drilled holes when fabricating and installing pultruded structures. Sealant penetration through unsealed holes provides surrounding moisture more direct access to the composite laminate. For this reason, the pultruded members are more susceptible to the effect of moisture and temperature at the location of an unsealed bolt hole. This effect is amplified when the surrounding environment includes other corrosive agents, such as acids and alkaline (Mosallam 1998).

A similar study was conducted by Prabhakaran et al. (1997a) on PFRP joints exposed to seawater environment. The results of the study confirmed some of the results of the Yuan and Weyant (1997) research. In this

study, both single-bolt and multi-bolt pultruded joints were evaluated under the following four different conditions:

- Dry, finger-tightened joints
- Dry, torqued joints with 196 ft-lb (1.36 N·m)
- Saltwater-soaked, finger-tightened joints
- Saltwater-soaked, torqued joints with 196 ft-lb (1.36 N·m)

All joint specimens were fabricated from Pultex Series 1500 E-glass/epoxy pultruded flat plates manufactured by Creative Pultrusions, Inc. The specimen dimensions and bolt hole configurations were selected to promote block shear and net-tension failure modes. The joints were made up of 5/8-in. (15.875-mm) high-strength steel bolts and washers. The hole clearance was about 0.005 in. (0.127 mm). To accelerate the effect of saltwater on the composite laminates, the seawater was heated to 125 °F (52 °C), and specimens were soaked for 4.5 months. At the end of the exposure time, the specimens were either finger-tightened or torqued to 196 ft-lb (1.36 N·m). Test results indicated that application of torque to tighten bolts improved the strength of the dry joints as well as those specimens exposed to the heated seawater environment. This improvement was significant because bolted pultruded joints failed in a net-tension failure mode. The joint strength degradation of finger-tightened specimens increased for all observed failure modes. However, the application of a bolt-tightening torque did not fully compensate for the damages resulting from exposure to heated seawater. The modes of failure were cleavage for single-bolt joints, block shear for two bolts in a raw joint, and net-shear for two bolts in series and for all the four-bolt joints. A summary of the experimental failure loads and modes of failures for dry and saltwater-soaked with finger-tightened and torqued joints, respectively, is presented in Tables 2-5 and 2-6. These tables show that a strength degradation up to 29% for finger-tightened joints and up to 20% for torqued joints occur when joints are exposed to heated seawater environments. For this reason, the structural engineer should consider an appropriate knock-down factor for bolted joint strength when a pultruded structure is exposed to similar environments.

Dutta et al. (2003, pp. 825–835) presented the results of an experimental study aimed at evaluating the structural behavior and residual strength of bolted, bonded, and combined pultruded composite joints subjected to dry, cold, hot, and wet environments. In this study, 20 two-row bolted pultruded E-glass/epoxy joints were evaluated under the aforementioned hygrothermal conditions. In this study, both high- and low-temperature tests were performed with wet specimens, whereas room-temperature tests were done only on dry specimens. Therefore, the separate contributions of temperature and moisture to strength reduction were not clear.

Table 2-5a. Failure Loads and Modes for Dry Finger Tight Specimens

Specimen	Failure Mode	Failure Modes (lb)	Dry Finger Tight Average Load (lb)
A-1	Cleavage	12,770	
A-2	Cleavage	12,820	12,547
A-3	Cleavage	12,050	
B-1	Net-Tension	21,530	
B-2	Net-Tension	23,280	22,760
B-3	Block Shear	23,470	
C-1	Block Shear	27,000	
C-2	Block Shear	24,260	24,923
C-3	Block Shear	23,510	
D-1	Net-Tension	45,600	
D-2	Net-Tension	46,100	45,100
D-3	Net-Tension	43,600	
E-1	Net-Tension	43,200	
E-2	Net-Tension	45,500	44,100
E-3	Block Shear	43,600	

Source: Prabhakaran et al. (1997a).

Pure adhesive bonding at high temperature has shown a drastic reduction in strength. Examination of the failed surfaces revealed that the adhesive, being applied manually, was not spread over the whole of the bonding surface and that the surface preparation was inadequate. Thus, without imposing strict quality control measures, the reliability of adhesively bonded joints would be low, especially in high-temperature environments. The difference in performance of bolted joints as opposed to bolted and adhesive-bonded joints was not drastic. In fact, the results indicated that the pure bolted joint was marginally better than the combined bolted and adhesive joints. Apparently moisture plays a key role in the strength reduction. In this effort, the effects of moisture alone could not be determined because few specimens were available. It was also observed that moisture absorption by composites increased with time of exposure. It was recommended that future research work is needed to examine the effect of moisture alone on the strength of different types of FRP composite joints, separately without the temperature effects.

   Turvey and Wang (2007) reported the results of an experimental study to assess the impact of hot/wet environments on the strength of pultruded E-glass/polyester (EXTREN 500 series) single-bolt tension joints. In this study, two joint geometries, with different e/d ratios were evaluated. Experimental results indicated that bolted joints failed in tension after being immersed in water at three temperatures for two periods of

Specimen	Failure Mode	Dry Torqued Failure Load (lb)	Average Load (lb)	Dry Finger Tight; Average Load (lb)	Percentage Increase
A-1	Cleavage	19,170			
A-2	Cleavage	16,770	16,277	23,547	46%
A-3	Cleavage	18,890			
B-1	Net Tension	25,120			
B-2	Net Tension	24,920	24,770,	22,760	9%
B-3	Net Tension	24,270			
C-1	Block Shear	32,170			
C-2	Block Shear	.2,330	33,100	24,923	33%
C-3	Block Shear	34,800			
D-1	Net Tension	50,200			
D-2	Net Tension	49,200	49,833	45,100	11%
D-3	Net Tension	50,100			
E-1	Net Tension	47,000			
E-2	Net Tension	45,400	46,822	44,100	6%
E-3	Net Tension	48,000			

Source: Prabhakaran et al. (1997a).

Table 2-6a. Failure Loads and Modes for Seawater-Soaked
and Finger-Tight Specimens

Specimen	Failure Mode	Failure Modes (lb)	Average Loads (lb)	Percentage Decrease[a]
A-1	Cleavage	10,460		
A-2	Cleavage	10,150	10,487	16%
A-3	Cleavage	10,850		
B-1	Net-Tension	19,320		
B-2	Net-Tension	19,480	18,220	20%
B-3	Net-Tension	15,860		
C-1	Block Shear	19,780		
C-2	Block Shear	20,220	19,693	21%
C-3	Block Shear	19,080		
D-1	Net-Tension	31,600		
D-2	Net-Tension	29,390	32,073	29%
D-3	Net-Tension	35,230		
E-1	Net-Tension	34,470		
E-2	Net-Tension	31,380	34,650	21%
E-3	Net-Tension	38,100		

[a] Compared to dry finger-tight case.
Source: Prabhakaran et al. (1997a).

time. The general conclusion was that exposing pultruded composite bolted joints to hot/wet environment had a major adverse influence on the load-bearing capacity of such joints. For example, it was found that more than 60% of the load-carrying capacity of a single-bolt tension joint was lost after being immersed in water for 6.5 weeks at 140 °F (60 °C). The serious issue was that this temperature at which major strength degradation was observed was lower than the manufacturer's recommended maximum service temperature for this type of pultruded composites. It was also reported that for bearing design joints, about 63% of the load capacity was lost when the joint material was immersed in water for 6.5 weeks at 140 °F (60 °C), as compared to that tested under dry ambient conditions. The loss in load capacity increased to 86% when the temperature was 176 °F (80 °C). Based on the range of temperature levels and water immersion periods used in this study, it was concluded that exposure to high temperature had a greater adverse effect on single-bolt tension E-glass/polyester pultruded joint strength, as compared to the period of exposure to a wet environment.

In the last few years, several investigations were conducted to use hybrid pultruded composites/concrete members for bridge and building

Table 2-6b. Failure Loads and Modes for Seawater-Soaked and Torqued Specimens

	Seawater-Soaked and Torqued			Percent Change, Compared to		
Specimen	Failure Mode	Failure Loads (lbs)	Average Loads (lbs)	Finger-Tight Dry	Torque Applied Dry	Seawater-Soaked, Finger-Tight
D-1	Net-Tension	39,350				
D-2	Net-Tension	38,300	38,583	−14%	−23%	+20%
D-3	Net-Tension	38,100				
E-1	Net-Tension	41,300				
E-2	Net-Tension	39,900	40,567	−8%	−13%	+17%
E-3	Net-Tension	40,500				

Source: Prabhakaran et al. (1997a).

applications, including Alagusundaramoorthy et al. (2006), Yu et al. (2006), and H. N. Honickman's 2008 MS (Engineering) thesis "Pultruded GFRP sections as stay-in-place structural open formwork for concrete slabs and girders." (Dept. of Civil Engineering, Queen's University, Kingston, Ontario, Canada).

This is due the superiority and economy of concrete materials, especially when exposed to compression. However, alkaline and moisture exposures of portions of E-glass pultruded members that are filled with concrete, especially at early stages, has been a major concern. It is well documented that exposing E-glass composites to high pH levels can cause severe problems due to the sensitivity of glass fibers to moisture and alkalinity, both of which are constituents of concrete pore-water solution. This concern has inhibited wide utilization of such hybrid systems except for applications subjected to very low stresses.

Keller and Riebel (2007) presented the results of a study that focused on the long-term compression performance of three-cell pultruded E-glass/polyester members of a hybrid PFRP/steel joint for concrete structures exposed to concrete pore-water solution. The effect of moisture and alkalinity on the mechanical properties of the structural element over the estimated service life of 70 years was evaluated. The PFRP elements (both uncapped and capped) were immersed in simulated concrete pore-water solutions of pH 13.4 and different temperature levels for 18 months. The Arrhenius rate law was used to predict the residual strength. The results of this study revealed the following facts: (1) moisture uptake occurred very quickly within a few days, mainly through the wicking effect along the fiber/matrix interfaces and matrix cracks up to full element saturation; (2) the loss of matrix stiffness due to swelling and plasticization led to an initial rapid and significant strength drop; and (3) the application of the Arrhenius rate law was found to be applicable to predict the element strength decrease.

2.3.11 Effect Relaxation and Creep

The inherent low through-the-thickness properties of typical off-the-shelf pultruded composites suggest that bolted composite assemblies will experience a loss of preload over time due to the relaxation or creep of the softer composite material.

2.3.11.1 Thread Relaxation of Metal and Fiber-Reinforced Polymer Composite Fasteners.   For both metal and FRP threaded rods, relaxation will occur that could affect the bolt or threaded rod performance. This is caused by the introduction of a high stress level in the threaded part (Kulak et al. 1987). For steel bolts (A325 and A354 grade/bolt), test results (Chesson and Munse 1965) indicated that immediately upon completion

of the torquing, a drop of 2% to 11% of the load had occurred. This drop in bolt tension can be attributed to the elastic recovery. The bolt tension force relaxation will increase as the grip length is decreased. It is recommended that a special type of epoxy be applied to both the bolt and nut threads to maintain the clamping force and to decrease the level of bolt tension losses (several off-the-shelf products are available for steel bolts). This is especially important when dynamic loads exist, such as wind, traffic, motors, and other vibration sources.

Galvanized stainless steel bolts or PFRP threaded rods are usually recommended when PFRP composite structures are constructed in a corrosive environment. However, in a survey (Mosallam 1994) the majority of survey respondents, both in the United States and worldwide, preferred to use stainless steel over the FRP threaded rods and nuts because of their strength limitation. If galvanized steel bolts are used, the designer should be aware that the relaxation of galvanized steel bolts is about twice as great as that for plain steel bolts. This can be attributed to the thickness of the galvanized coating. In this case, the increase in the galvanized bolt relaxation is caused by the creep, or flow, up the zinc coating under sustained high clamping pressures. The engineer should be aware of the mechanical (including viscoelastic properties) and thermal properties mismatch of metallic bolts and pultruded composites that may result in a complicated failure mode.

Prabhakaran et al. (1997b) conducted an experimental study on steel bolt-preload relaxation in pultruded composite joints. Their study included tests on pultruded composite specimens subjected to compressive loads in the thickness direction as well as pultruded composite specimens subjected to bolt-preloads. Tables 2-7 through 2-9 summarize the details and the results of this study.

The following expressions were used to predict the bolt relaxation:

$$P = P_o t^{-B} \tag{2-3}$$

Table 2-7. Statistical Variations of Stabilized Bolt Preloads

Condition	Torque (ft-lb)	Preload (lb)	
		Mean	Standard Deviation
Dry	75	4,143	704
	215	15,740	3,201
Lubricated	75	5,506	997
	215 (fresh)	16,530	2,808

Source: Prabhakaran et al. (1997b).

where
P = load at time t, kip (kN)
P_o = initial load, kip (kN)
B = relaxation exponent constant.

The tightening torque and the resulting bolt preload are related by the following expression:

$$T = KFd \qquad\qquad (2\text{-}4)$$

where
T = applied torque, ft-lb (N·m)
F = bolt preload
d = nominal bolt diameter, in. (mm)
K = torque coefficient.

Table 2-8. Failure Loads of Open Hole and Pin-Loaded Specimens, With and Without Prior Torque

Condition	Mean Failure Load (lb)
Open hole (no torque)[a]	13,800
Open hole (prior torque)[b]	14,600
Pin-loaded (no torque)[a]	13,300
Pin-loaded (prior torque)[b]	13,900
Under torque	15,500

[a] No previous torque applied on the specimen.
[b] A 215 ft-lb torque was applied 10 times prior to testing.
Source: Prabhakaran et al. (1997b).

Table 2-9. Initial and Steady Torque Coefficients under Dry and Lubricated Conditions

Condition	Torque (ft-lb)	Mean Torque Coefficient	
		Initial	Steady
Dry	75	0.35	0.46
	215	0.27	0.34
Lubricated	75	0.27	0.32
	215	0.26	0.29

Source: Prabhakaran et al. (1997b).

The torque coefficient, *K*, depends on the friction of the bolt assembly and other parameters, including lubrication (Shigley and Mischke 1989). It should be noted that the torque equation (Eq. 2-4) was developed for steel bolted joints and, hence, more experimental and analytical work needs to be conducted to establish specific numerical values for pultruded composites.

Several points were concluded from this study (Prabhakaran et al. 1997a):

- The presence of voids in the pultruded composite laminates contributes an additional influence on the time-dependent behavior of pultruded composites.
- The performance of pultruded composites under preload can be correlated with their behavior when subjected to direct compressive loads in the thickness direction.
- Dismantling and repeated bolt tightening, which corresponds to reuse of the structural member in a joint, will introduce compressive stresses that will compress the pultruded member internal voids, which will result in strength improvement. However, original clamping loads applied to a pultruded bolted joint may induce some damage, which needs to be considered.

2.3.11.2 Creep of PFRP Threaded Rods. Due to the viscoelastic nature of composites, FRP threaded rods and nuts are more sensitive to creep than are steel or other metal bolts. In addition to the relaxation of the threads, another limitation is the creep rupture phenomenon of FRP composites, which does not represent a problem for metals in ambient temperature. If the FRP joints are subjected to a sustained loading, depending on the FRP member and rod/nut materials type, stress level, temperature, and other environmental effects, creep rupture (static fatigue) can occur, especially for glass-based composites. Test results (Mosallam 2009) indicated that creep rupture failure of pultruded E-glass composites can be prevented when the sustained stress level is below 25% to 30% of ultimate tensile strength of pultruded composites. Although no experimental data are available specifically on creep and creep rupture of pultruded threaded rods, it is recommended to maintain the stress level in the rods to less than 30% of the unidirectional ultimate stress of the composite rods.

REFERENCES

Abd-El-Naby, S. F. M., and Hollaway, L. (1992). "The experimental behavior of bolted joints in pultruded glass/polyester material. Part 1: Single-bolt joints." *Composites*, 24(7), 531–538.

Ahmed, H., Johnson, W. S. and Counts, W. A. (2003). "Evaluation of bolt bearing behavior of highly loaded composite joints at elevated temperature." *J. Composite Mat.,* 37(6), 559–571.

Alagusundaramoorthy, P., Harik, I. E. and Choo, C. C. (2006). "Structural behavior of FRP composite bridge deck panels." *ASCE J. Bridge Eng.,* 11(4), 384–393.

American Society of Civil Engineers (ASCE). (1985). *Structural plastics selection manual*. ASCE, New York.

ASCE. (1984). *Structural plastics design manual*. ASCE, New York.

ASTM International (ASTM). (2002). *MIL 17 handbook: The composite materials handbook*, ASTM International, West Conshohocken, Pa.

Bedford Reinforced Plastics, Inc. (1995). *BRP design guide*, Bedford Reinforced Plastics, Inc., Bedford, Pa.

Chesson, E., Jr., and Munse, W. H. (1965). "Studies of the behavior of high-strength bolts and bolted joints." *Eng. Exper. Bull. 469*, University of Illinois, Urbana. Ill.

Collings, T. A. (1982). "On the bearing strengths of CFRP laminates." *Composites*, 13, 241–252.

Collings, T. A. (1977). "The strength of bolted joints in multidirectional CFRP laminates." *Current Paper No. 1380*, Aeronautical Research Council, London.

Cooper, C., and Turvey, G. J. (1995). "Effects of joint geometry and bolt torque on the structural performance of single bolt tension joints in pultruded GRP sheet materials." *Composite Struct.*, 32, 217–226.

Creative Pultrusions, Inc. (2004). *Creative Pultrusions design guide*, Creative Pultrusions, Inc., Alum Bank, Pa.

Crews, J. H., Jr. (1981). "Joining of composite materials." I. M. Daniel, ed., *ASTM Special Technical Publication 787: Proc., Composite Materials: Testing and Design (6th Conf.)*, Phoenix, Ariz., May 12–13, ASTM International, West Conshohocken, Pa.

Dutta, P. K., Mosallam, A. S., and Lampo, R. (2003). "Response of FRP composite joints in hygrothermal environments." *Proc., International Conference on Performance of Construction Materials (ICPCM) Conf.,* Cairo, Egypt, February 18–20.

Eriksson, I. (1990). "On the bearing strength of bolted graphite/epoxy laminate." *J. Composite Mat.* 24, 1246–1269.

Eriksson, I., Bäcklund, J., and Möller, P. (1995). "Design of multiple-row bolted composite joints under general in-plane loading." *Composites Eng.*, 5(8), 1051–1068.

European Cooperation in Science and Technology (COST). (1998). *State-of-the-art review on design, testing, analysis and applications of polymeric composite connections*, T. Mottram and J. Turvey, eds., European Cooperation in the Field of Scientific and Technical Research, now European Cooperation in Science and Technology (COST), Brussels.

Fiberline Composites A/S. (2004). *Fiberline design manual*, Kolding, Denmark.

Godwin, E. W., and Matthews, F. L. (1980). "A review of the strength of joints in fiber-reinforced plastics." *Composites*, 11, 155–160.

Hart-Smith, L. J. (1987). "Mechanically fastened joints for advanced composites: Phenomenological considerations and simple analyses," *Proc., Fourth Conference on Fibrous Composites in Structural Design,* Plenum, N.Y., 543–574.

Hart-Smith, L. J. (1996a). "Analysis methods for bolted composite joints subjected to in-plane shear loads," *Proc., AGARD 83rd Structures and Materials Panel: Bolted/Bonded Joints in Polymeric Composites, Specialist Meeting*, Florence, Italy, September 2–3. McDonnell Douglas Corp. Paper MDC 96K-0086.

Hart-Smith, L. J. (1996b). "Design and analysis of bolted and riveted joints in fibrous composite structures." *Paper 121*, McDonnell Douglas Corp., St. Louis, Mo.

Hart-Smith, L. J (1994a). "Designer's corner: The key to designing efficient bolted composite joints." *Composites*, 25(8), 835–898.

Hassan, N. K., Mohamedien, M. A., and Rizkalla, S. H. (1997). "Rational model for multibolted connections for GFRP members." *J. Composites for Constr.* 1(2), 71–78.

Hurd, S. and Yuan, R. (1996). "Hydrothermal effects on the bearing strength of GFRP composite joints." *Proc., 4th ASCE Mat. Engineering Conf.*, ASCE, New York.

Jeans, L. L., Grimes, G. C., and Kan, H. P. (1980). "Fatigue spectrum sensitivity study for advanced composite materials." *AFWAL-TR-80–3130*, Vol. I, Technical summary, Wright Aeronautical Laboratories, Wright Patterson Air Force Base, Ohio.

Johansen, G. E., Wilson, R., Roll, F., and Ritchie, P. (1993). "Ultimate strength characteristics of an FRP/Kevlar cable structural system," *Proc., 48th Annual Conference, Composites Institute*, Society of the Plastics Industry, Inc., February 8–11, Cincinnati, Ohio.

Keller, T., and Riebel, F. (2007). "Multifunctional hybrid GFRP/steel joint for concrete slab structures," *Proc., 8th International Symposium on Fiber Reinforced Polymer Reinforcement for Concrete Structures* (FRPRCS-8), Patras, Greece.

Khashabaa, U. A., Sallamb, H. E. M., Al-Shorbagya, A. E., and Seif, M. A. (2006). "Effect of washer size and tightening torque on the performance of bolted joints in composite structures." *Composite Struct.*, 73, 310–317.

Kim, R. Y., and Whitney, J. M. (1976). "Effect of temperature and moisture on pin bearing strength of composite laminate." *J. Composite Mat.*, 10, 149–155.

Klett, L. B., Herling, D. R., Diamond, S., and Sklad, P. S. (2004). "Attachment techniques for heavy truck composite chassis members." *High*

strength weight reduction materials. FY 2004 annual progress report, *contractors,* Oak Ridge National Laboratory, Pacific Northwest National Laboratory, Contract Nos. DE-AC05-00OR22725, DE-AC06-76RL01830.

Kretsis, G., and Matthews, F. L. (1985)*.* "The strength of bolted joints in glass fiber/epoxy laminates." *Composites*, 16(2), 92–102.

Kulak, G. L., Fisher, J. W., and Struik, J. H. (1987). *A guide to design criteria for bolted and riveted joints*, 2nd ed. John Wiley & Sons, Inc., New York.

Lim, T. S., Kim, B. C., and Lee, D. G. (2006). "Fatigue characteristics of the bolted joints for unidirectional composite laminates." *J. Composite Struct.*, 72(1), 58–68.

Little, R. E., and Mallick, P. K. (1990)*.* "Fatigue of bolted joints in SMC-R18 sheet molding compound composites." *J. Composites Tech. and Res.*, 12(3), 155–163.

Love, E. A., and Bisarnsin, T. (1992). "Experimental investigation of self-tapping fasteners for attachment of corrugated cladding panels to pultruded fiber-reinforced plastic beams in industrial building construction." *Proc., Materials Engineering Congress, Atlanta, Ga.,* August 10–12, pp. 577–584.

Mallick, P. K., and Little, R. E. (1985)*.* "Pin bearing strength of fiber-reinforced composite laminates." *Proc., Advanced Composites Conf.*, ASTM International, West Conshohocken, Pa, pp. 39–47.

Mallick, P. K. (1988). "Effects of hole stress concentration and its mitigation on the tensile strength of R-50 sheet molding compound composites." *Composites*, 8, 504–517.

Matthews, F. L. (1988). "Chapter 18: Bolted joints." S. W. Tsai, ed., *Composites design*, Think Composites, Dayton, Ohio.

Matthews, F. L., Kilty, P. E., and Godwin, E. (1982). "Load-carrying joints in fiber-reinforced plastics." *Plastics and Rubber Proc. and Appl.*, 2(1), 19–25.

Morsi, E., and Larralde, J. (1993). "Test results of fasteners for structural fiberglass composites," *Proc., 48th SPI Annual Conf., Composites Institute, Society of the Plastics Industry*, p. 11B-1–11B-4.

Mosallam, A. (2009). "Mechanical behavior of pultruded composites under elevated temperatures." *Proc., 2nd Global Pultrusion Conf.*, Baltimore, Md., May 21–22 [CD ROM].

Mosallam, A. S. (1999). "Cyclic behavior of FRP interior frame connections for pultruded structures." *Proc., 5th Materials Congress*, ASCE, Reston, Va., pp. 84–91.

Mosallam, A. S. (1998). "Durability of pultruded fiber-reinforced polymer (PFRP) composites in mining environments." *Proc., 1st Int. Conf. on Durability of Fiber-reinforced Polymer (FRP) Composites for Construction*, July18–20, Sherbrooke, Canada, pp. 649–659.

Mosallam, A. S., and Schmitz, H. G. (1996). "Experimental investigation on the behavior of UC beam-to-column composite connections under

cyclic and sustained loads." *Proc., 1st Int. Conf. on Composites in Infra-structures (ICCI '96)*, University of Arizona, Tucson, Ariz., Jan. 15–17, pp. 638–650.

Mosallam, A. S. (1994). "Connections for pultruded composites: A review and evaluation." *Proc., 3rd ASCE Materials Eng. Conf.*, San Diego, Calif., ASCE, New York.

Mosallam, A. S., Abdel Hamid, M. K., and Conway, J. (1993). "Performance of pultruded FRP connections under static and dynamic loads." *J. Reinf. Plastics and Composites*, 13, 386–407.

Nagaraj, V. and GangaRao, H. V. S. (1998). "Fatigue behavior and connection efficiency of pultruded GFRP beams." *J. Composites for Const.*, 2(1), 57–65.

Nassar, S.A., Virupaksha, V. L. and S. Ganeshmurthy (2007). "Effect of bolt tightness on the behavior of composite joints." *J. Pressure Vessel Tech.*, 129, 43–51.

Prabhakaran, R., Devara, S., and Razzaq, Z. (1997a). "An investigation of the influence of tightening torque and seawater on bolted pultruded composite joints." *Proc., Int. Composites Expo '97*, Composites Institute, Society of the Plastics Industry, Washington, D.C.

Prabhakaran, R., Srinivas, R., and Razzaq, Z. (1997b). "An experimental investigation of bolt-preload relaxation in pultruded composite joints." *Proc., Int. Composites Expo '97*, Composites Institute, Society of the Plastics Industry, Washington, D.C.

Prabhakaran, R., Razzaq, Z., and Devara, S. (1996a). "Load and resistance factor design (LRFD) approach for bolted joints in pultruded composites." A. Mosallam et al., eds., *Composites part B: Engineering*, 27B(3–4), Infrastructure Special Issue, 351–360.

Prabhakaran, R., Devara, S., and Razzaq, Z. (1996b). "The effect of fiber orientation angle on the unnotched, open hole, and pin-loaded strength of a pultruded composite." *Proc., 51st Annual Conf. of the Composites Inst.*, Society of the Plastics Industry, Washington, D.C., 1–15.

Pyner, G. R., and Matthews, F. L. (1979). "Comparison of single and multi-hole bolted joints in glass fibre reinforced plastic." *J. Composite Mat.*, 13, 232–239.

Quinn, W. J., and Matthews, F. L. (1977). "The effect of stacking sequence on the pin-bearing strength in glass fibre reinforced plastic." *J. Composite Mat.*, 11, 139–145.

Ramkumar, R. L., and Tossavainen, E. W. (1984). "Bolted joints in composite structures: Design, analysis and verification, task I test results–single fastener joints." *AFWAL-TR-84–3047*, Wright Aeronautical Laboratories, Wright Patterson Air Force Base, Ohio.

Reid, R. L., Chen, P., Black, K., and El-Shiekh, A. (1994). "Bearing behavior of 3-D braided carbon/epoxy composite joints." *Proc., 39th Int. SAMPE*

Symp., Society for the Advancement of Material and Process Engineering, Long Beach, Calif., pp. 2013–2022.

Rosner, C. (1992). "Single-bolted connections for orthotropic fiber-reinforced composite structural members." Master's thesis, University of Manitoba, Winnipeg, Canada.

Rosner, C. N., and Rizkalla, S. H. (1995). "Bolted connections for fiber-reinforced composite structural members: Analytical and design recommendations." *J. Mat. Civil Eng.*, 7(4), 232–238.

Sarkani, S., Michaelov, G., Kihl, D. P., and Beach, J. E. (1999). "Stochastic fatigue damage accumulation of FRP laminates and joints." *J. Struct. Eng.*, 125(12), 1423–1431.

Schmitt, R. R., and Horn, W. J. (1990). "Viscoelastic relaxation in bolted thermoplastic composite joints." *Proc., 35th Int. SAMPE Symp.*, Society for the Advancement of Material and Process Engineering, Long Beach, Calif., pp. 1336–1347.

Shenoi, R. A., and Hawkins, G. L. (1992). "Impact of material and geometry variations on the behavior of bonded tee connections in FRP ships." *Composites*, 23(5), 335–345.

Shigley, J. E., and Mischke, C. R. (1989). *Mechanical engineering design*. McGraw-Hill, New York.

Strongwell Company. (2004). *EXTREN design manual*, Strongwell Company (formerly MMFG), Bristol, Va.

Strongwell Company (1989). *Fiberglass Structural Shape—Design Manual*, Strongwell Company (formerly MMFG), Bristol, VA.

Strongwell Company (1983). *EXTREN Design Manual*, Strongwell Company (formerly MMFG), Bristol, VA.

Stockdale, J. H., and Matthews, F. L. (1976). "The effect of clamping pressure on bolt bearing loads in glass fiber-reinforced plastics." *Composites*, 2, 34–38.

Sun, X., Herling, D., and Stephens, E. (2004). "Static and fatigue strength evaluations for bolted composite/steel joints for heavy vehicle chassis components." *Proc., 2004 SPE Automotive Composites Conference & Exposition, Detroit, Mich., September 14–15* [CD ROM].

Thoppul, S. D., Finegan, J., and Gibson, R. F. (2009). "Mechanics of mechanically fastened joints in polymer–matrix composite structures: A review." *Composites Sci. & Tech.*, 69, 301–329.

Turvey, G. J. (1998). "Single-bolt tension joint tests on pultruded GRP plate: Effects of tension direction relative to pultrusion direction." *Composite Struct.*, 42(4), 341–351.

Turvey, G. J., and Wang, P. (2007). "Failure of pultruded GRP single-bolt tension joints under hot–wet conditions." *Composite Struct.*, 77, 514–520.

Van Wingerde, A. M., Van Delft, D. R. V., and Knudsen, E. S. (2003). "Fatigue behaviour of bolted connections in pultruded FRP profiles." *J. Plastics, Rubber and Composites*, 32(2), 71–76.

Wong, C. M. S., and Matthews, F. L. (1981). "A finite element analysis of single and two-hole bolted joints in fibre reinforced plastic." *J. Composite Mat.*, 15, 481–491.

Wong, Y. (2002). "Bearing behavior of joints in pultruded composites." *J. Composite Mat.*, 36, 2199–2216.

Yu, T., Wong, Y. L., Teng, J. G., Dong, S. L., and Lam, E. S. S. (2006). "Flexural behavior of hybrid FRP-concrete-steel double-skin tubular members." *ASCE J. Composites for Const.*, 10(5), 443–452.

Yuan, R. L., and Weyant, S. E. (1997). "The effect of environmental exposure on the behavior of pultruded mechanical connections." *Proc., Int. Composites Expo '97,* Composites Institute, Society of the Plastics Industry, Washington, D.C.

Yuan, R. L, Liu, C. J., and Daly, T. (1996). "Study of mechanical connection for GFRP laminated structures." *Proc., 2nd Int. Conf. on Advanced Composites Materials and Structures*, Montreal, Canada, August 11–14, pp. 951–958.

This page intentionally left blank

CHAPTER 3

ANALYSIS AND DESIGN OF BOLTED COMPOSITE JOINTS

3.1 BACKGROUND

3.1.1 Efficient Bolted Composite Joint Design

To achieve an efficient bolted joint design, the structural engineer must consider two limitations. First, composites are too brittle to be analyzed using the conventional, fully plastic method of designing metallic bolted joints because composite fibers fail in a brittle mode at a typical strain level of 2%, whereas ductile metals, such as aluminum, yield by as much as 13% before failure, enabling drastic load redistribution between the fasteners. Second, the use of linear elastic analysis is equally inappropriate due to the great strength increase resulting from benign micro-failures in the immediate vicinity of small bolt holes (Hart-Smith 1989). Typically, the use of linear elastic analysis underestimates the actual bolted joint strength by a factor of 2. Figure 3-1 illustrates this situation.

In an infinite elastic homogenous plate loaded by a central bolt (or for finite-width strips), the peak tension stress along the bolt hole side is roughly equal to the average bearing stress. Thus, to prevent tension-through-the-hole failures, it is necessary to restrict the bearing stresses. This phenomenon does not apply for metallic joints with fully plastic behavior. The plasticity of metallic joints eliminates the stress concentration prior to the occurrence of static joint failure.

3.1.2 Similarities and Differences between Composites and Metallic Joints

Metallic bolted joints are usually more critical in fatigue as compared to ultimate strength. The reason is that yielding redistributes the loads
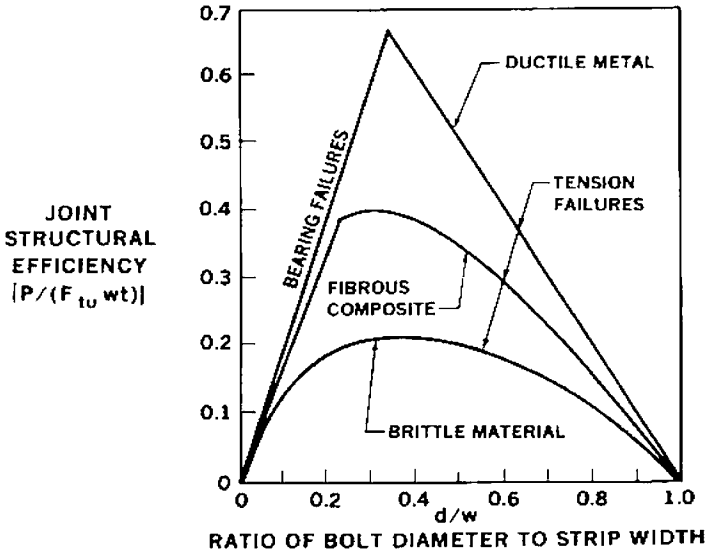
Figure 3-1. Relationship between strengths of bolted joints in ductile metal, FRP composites, and brittle materials.
Source: Hart-Smith (1989), courtesy of John Hart-Smith and the Boeing Company.

and hence alleviates local stresses. In contrast, bolted composite joints are more critical in static strength, with little degradation due to fatigue loads (residual strength can increase with increasing number of cycles). However, Mosallam et al. (1993) and Mosallam (1999) observed that fatigue loading becomes critical when commercially produced pultruded threaded rods and molded nuts are used in bolted composite frame connections subjected to cyclic loads. Mosallam (1999) also reported that sensitivity to fatigue loading decreases when steel bolts are used.

While the fibers and the matrix of the connected pultruded members are essentially linear until failure, the micro-cracks and delamination around the bolt holes cause substantial internal load redistribution that is not considered in conventional mathematical models (Hart-Smith 1985, pp. 479–495). For that reason, there appears to be substantial nonlinear behavior associated with the normal bolt sizes used in composite structures. It should be noted that the development of softened zones at the micro-level, as shown in Fig. 3-2, is different from the yielding process developed in ductile metal joints in similar circumstances.

There are striking similarities between metallic and composite joint behaviors at the micro-level (Hart-Smith 1985, pp. 479–495). For example, in metal, the residual stress zone around cold-worked holes leads to a substantial increase in the fatigue life. In composites, any increase in the
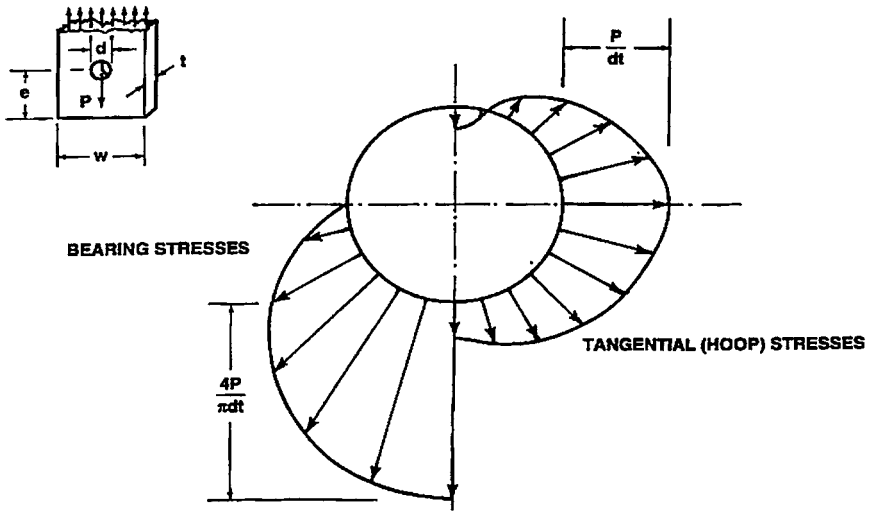
Figure 3-2. Bearing and hoop stresses at loaded bolt hole.
Source: Hart-Smith (1994), courtesy of Dr. John Hart-Smith and the Boeing Company.

(much smaller softened) zone around fasteners results in an increase in the joint static strength.

3.2 EFFICIENCY OF THE BOLTED JOINT

The efficiency of a composite bolted joint is different from metallic joints in that the former is based on net strength whereas the latter is based on load-carrying ability (Dastin 1986). Joint efficiency (η) of a pultruded composite joint is defined as the ratio of the strength of the joined member (notched) to the strength of an unjoined (unnotched) continuous member of the same size, or:

$$\eta = \frac{S_j}{S_m} = \frac{P_{ult}}{t \cdot w \cdot F_{tu}}$$ (3-1)

where
η = joint efficiency, %
S_j = ultimate joint strength, lb (N)
S_m = ultimate load capacity of unnotched member with the same size and properties = gross cross-sectional area × allowable tensile strength of the pultruded member
P_{ult} = ultimate joint load, lb (N)
t = member thickness, in. (mm)
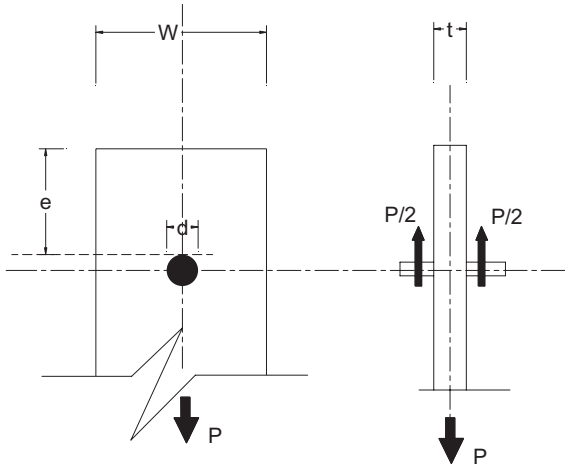
Figure 3-3. Geometry of a double-lap bolted joint.

w = member width, in. (mm)
F_{tu} = allowable tensile strength of the pultruded member
d = hole diameter.

Figure 3-3 illustrates different joint geometric parameters.

3.3 DESIGN OF THE SINGLE-BOLTED JOINT

3.3.1 A Simplified Approach

The following analytical procedure to predict strength and failure modes of mechanically fastened composite bolted joints is based on a model developed by Hart-Smith (1978) with some modifications proposed for pultruded composites by Rosner (1992). This model is semiempirical and consists of two basic failure criteria accounting for the different possible failure modes of the pultruded double-shear singlebolted joint.

3.3.1.1 Background   In 1978, Hart-Smith presented a simple theory to predict the strength and mode of failure of bolted composite joints. The bases of this model are the stress concentration factors for elastic isotropic materials with the same geometry as the composite joint under consideration. The stress concentration factors (derived from experimental joint tests) are modified by an empirically determined factor that simultaneously accounts for the specific composite material of the joint, including its orthotropy, nonhomogeneity, and nonlinearly.

3.3.1.2 Net-Tension Criterion   The maximum stress in the joint shown in Fig. 3-3, adjacent to the bolt hole on the diameter perpendicular to the load direction, can be expressed as follows:

$$\sigma = k_{te} \frac{P}{t(w-d)} \tag{3-2}$$

where k_{te} is the elastic concentration factor that corresponds to the maximum stress adjacent to the hole. Note that t, w, and d are defined in Section 3.2, Eq. 3-1. The following are the procedures for calculating the elastic concentration factor (k_{te}) for both single- and multi-bolted composite joints.

1. *Single-Bolted Joint:* Expressions for the stress concentration factor on the net-section for both loaded and unloaded bolt holes were proposed by Hart-Smith (1994) to produce a monotonic function in terms of both the hole-diameter-to-width ratio (d/w), and the edge-distance-to-width ratio (d/w):
   a. Loaded hole:

$$k_{te} = \frac{w}{d} + \frac{d}{w} + 0.5\left(1 - \frac{d}{w}\right)\theta \approx \frac{w}{d} + \frac{d}{w} \tag{3-3}$$

$$\theta = \left(\frac{w}{e} - 1\right) \quad \text{for } e/w \leq 1, \theta = 0 \quad \text{for } e/w \geq 1 \tag{3-4}$$

   b. Unloaded hole:

$$k_{te} = 2 + \frac{d}{w} + \left(1 - \frac{d}{w}\right)^3 \tag{3-5}$$

2. *Multiple Bolted Joints with Identical Holes:* Similar expressions have been also proposed by Hart-Smith (1994) for the composite joints with multiple holes:
   a. Loaded hole:

$$k_{te} = \frac{p}{d} + 0.5\left(1 - \frac{d}{p}\right)\theta \approx \frac{p}{d} \tag{3-6}$$

$$\theta = \left(\frac{p}{e} - 1\right) \quad \text{for } e/p \leq 1, \theta = 0 \quad \text{for } e/p \geq 1 \tag{3-7}$$

   b. Unloaded hole:

$$k_{te} = 1 + 2\left(1 - \frac{d}{w}\right)^{\frac{3}{2}} \tag{3-8}$$

where

θ = a nondimensional factor that is a function of e/w for a single-bolted joint, and a function of p/e for a multi-bolted joint

p = hole pitch (the distance between the bolt holes centerlines), as shown in Fig. 3-4.

In the modified procedure proposed by Rosner (1992), an older expression for the stress concentration factor, which was proposed by Hart-Smith in 1978, was modified. The basis of this modification was the experimental observation that, for pultruded composite bolted joints, the ultimate net stress of the joint increased by increasing the e/w ratio even past the value of e/w as shown in Fig. 3-5. However, in this chapter, this modification was not adopted, since in the new expression presented by
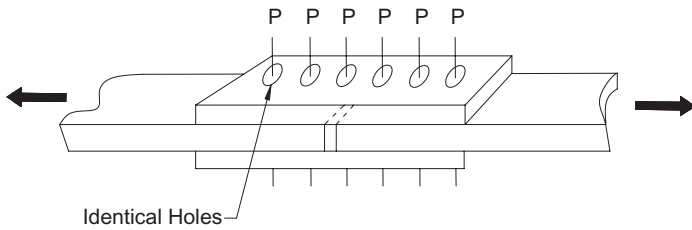
Figure 3-4. Multiple-hole joint.
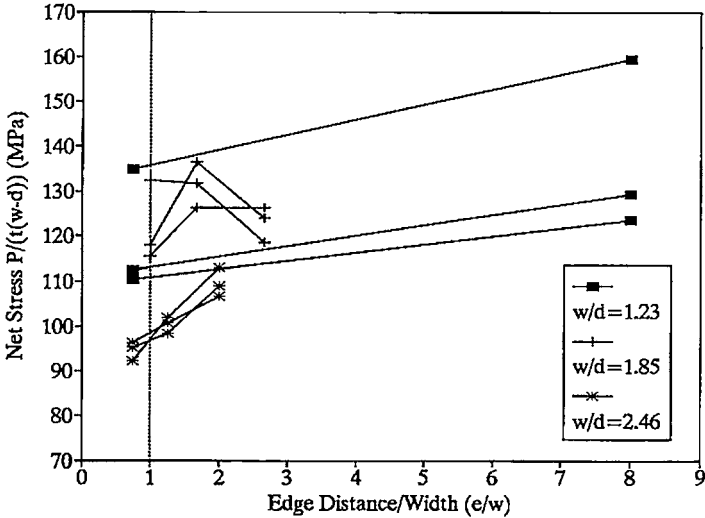
Figure 3-5. Effect of e/w on net stress for single-bolted pultruded joint.
Source: Rosner (1992), courtesy of Charles Rosner.

Eq. 3-3, the effect of the θ-*term* is negligible and can be ignored. Consequently, the stress concentration factor can be reduced to the following expression:

$$k_{te} = \frac{w^2 + d^2}{dw} \tag{3-9}$$

The net-tension failure occurs when $\sigma_{max} \geq F_{tu}$. This mode of failure is usually sudden and brittle in nature. An expression for the net-tension failure load can be obtained by rearranging Eq. 3-2 and by using $\sigma_{max} = F_{tu}$ as follows:

$$P = \frac{F_{tu}}{k_{te}} t(w - d) \tag{3-10}$$

Thus, efficiency of a bolted composite joint will be:

$$\eta = \frac{S_j}{S_m} = \frac{\dfrac{F_{tu}}{k_{te}} t(w - d)}{t \cdot w \cdot F_{tu}} = \frac{(w - d)}{w k_{te}} = \left(1 - \frac{d}{w}\right) k_{te}^{-1} \tag{3-11}$$

For perfectly plastic materials, the material can undergo extensive yield before failure (e.g., steel), and the stress concentration factor, k_{te}, can reach unity (refer to Fig. 3-6). In this case, the joint efficiency expression of Eq. 3-11 can be reduced to:

$$\eta = \left(1 - \frac{d}{w}\right) \tag{3-12}$$
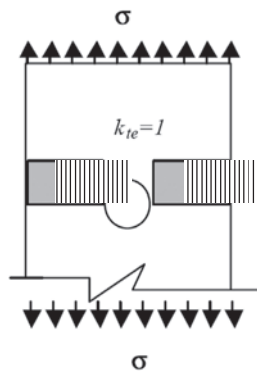
Figure 3-6. *Stress concentration for perfectly plastic materials.*

A graphical representation of Eq. 3-11 (for perfectly elastic materials) and Eq. 3-12 (for perfectly plastic materials) as compared to the behavior of composite materials is shown in Fig. 3-1.

3.3.1.3 Stress Concentration Reduction Factors for Composite Materials   As stated previously, composite joints behave differently than joints made up of both ductile and brittle materials. Composites exhibit some nonlinearity due to their heterogeneity, but not enough to completely alleviate stress concentrations. Although both fibers and the resin matrix are essentially linear up to failure, the development of micro-cracks and delaminations around the bolt hole result in a substantial internal load redistribution that is not usually considered in mathematical modeling of composite bolted joints. Figure 3-7 shows the development of softened zones at the micro-level. However, this softening effect is different from the yielding that occurs in ductile metallic materials. For this reason, it is not recommended to use the stress concentration factor corresponding to perfectly isotropic elastic materials (k_{te}) because it will overestimate the stresses in the case of composite materials.

To correlate the behavior of the two materials, Hart-Smith (1978) suggested that a linear relationship can be reasonably postulated between two sets of stress concentrations in the following form:
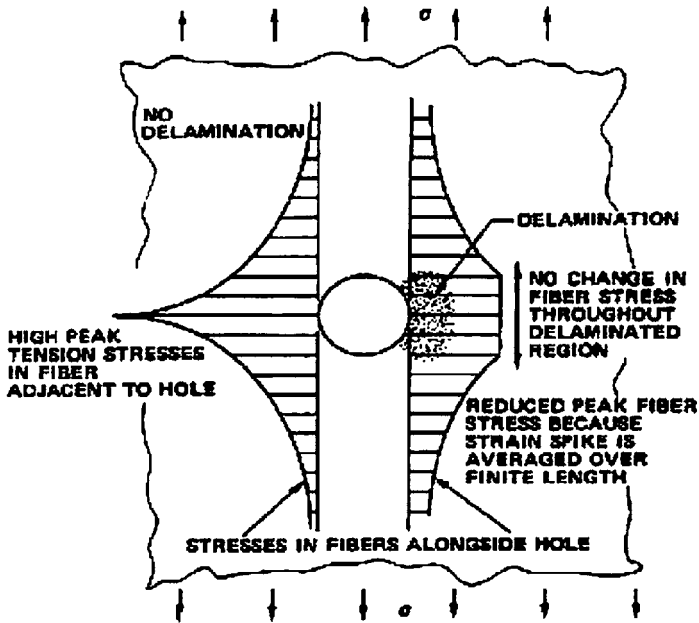
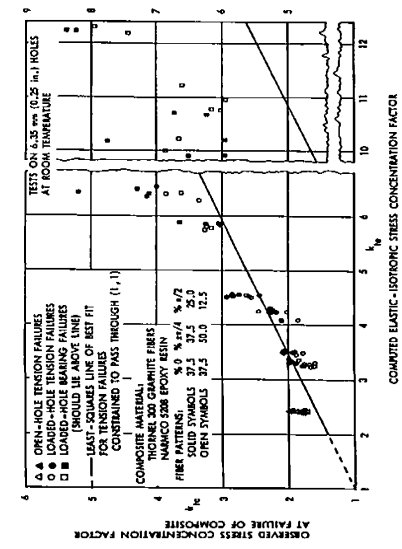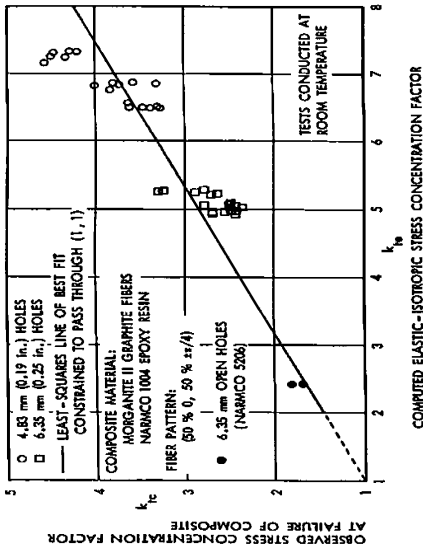*Figure 3-7. Stress concentration relief in polymer composite joints.*
*Source: Hart-Smith (1986), courtesy of Dr. John Hart-Smith and the Boeing Company.*

$$k_{tc} - 1 = C(k_{te} - 1) \tag{3-13}$$

where

k_{tc} = stress concentration factor observed at the ultimate failure of the composite joint

k_{te} = corresponding elastic isotropic stress concentration factor for the same geometry.

The stress concentration factor, k_{tc}, can be determined using the following expression:

$$k_{tc} = \frac{F_{tu}t(w-d)}{P} \tag{3-14}$$

It should be noted that the linear relationship shown in Eq. 3-13 is only valid as long as the failure mode of the composite joint is net-section tension.

The values of the coefficient, C, can be determined by constructing plots between k_{te} for each test geometry, as calculated by Eqs. 3-3, 3-5, 3-6, 3-8, or 3-9, as appropriate, and the experimentally observed value of k_{tc} (refer to Eq. 3-14). The relationship between experimentally determined stress concentration factors, k_{tc}, for composites at failure and predicted stress concentration factor, k_{te}, for elastic isotropic materials is shown in Fig. 3-8. The variation in the value of the coefficient is a direct function of the fiber architecture of the laminate. This effect is shown in Fig. 3-9. Research (Hart-Smith 1978) indicates that the value of the coefficient, C, is a function of several factors, including:

- The absolute bolt size
- The fiber stacking sequence
- Laminate thickness (for very thin laminates)
- The environment and any preconditioning

For pultruded composites, Rosner (1992) conducted several tests on bolted joints made of EXTREN Pultruded Flat Sheet/Series 500 manufactured by the Strongwell Company. The tests were conducted on joint specimens with 0-degree, 45-degree, and 90-degree fiber orientations. The k_{tc} versus k_{te} graphs reported by Rosner (1992) are shown in Figs. 3-10, 3-11A, 3-11B and 3-12.

For these graphs, the C-coefficients were determined by calculating the slope of the best-fit straight line with an origin at coordinate (1,1). As anticipated, these plots indicate that pultruded bolted joints tested with principal fiber reinforcement at 45 degrees and 90 degrees to the applied load (off-axis strengths) had lower ultimate strength as compared to the
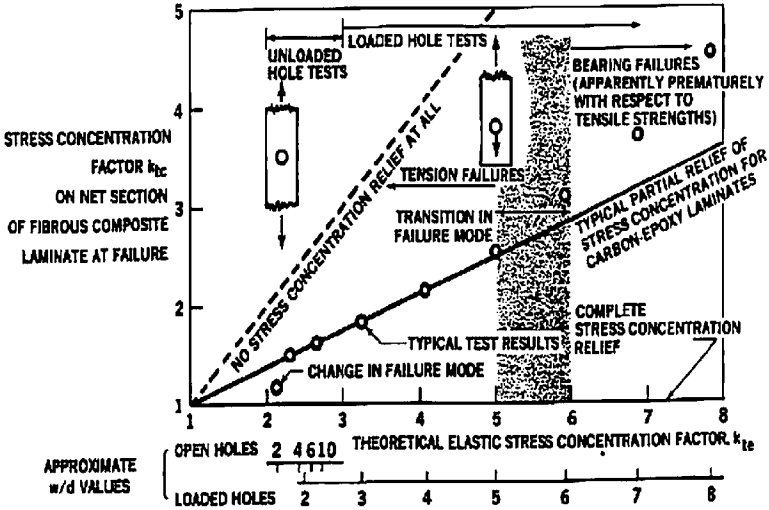
Figure 3-8. Relation between experimentally determined stress concentration factors k_{tc} for composites at failure and predicted stress concentration factor k_{te} for elastic isotropic materials.
Source: Hart-Smith (1996), courtesy of Dr. John Hart-Smith and the Boeing Company.

corresponding joints with principal fiber reinforcement coinciding with the loading direction (on-axis strength). Due to the lower off-axis F_{tu} values, the corresponding efficiencies are higher than the on-axis values. Based on this observation, Rosner (1992) suggested that failure envelopes for the 0-degree case could be used to predict conservative values for the off-axis cases. In this case, only one set of failure envelopes can be used to predict the bolted joint behavior in all directions. Different values of factor *C* for different composites are presented in Table 3-1.

The joint efficiency for composite bolted joints can now be calculated knowing the appropriate values of k_{tc} and the *C*-factor and by using Eq. 3-11:

$$\eta = \frac{S_j}{S_m} = \left(1 - \frac{d}{w}\right)k_{tc}^{-1} \tag{3-15}$$

Equation 3-15 can be expressed in terms of the *C*-coefficient by rearranging Eq. 3-13 as follows:

$$k_{tc} = c(k_{te}-1)+1 \tag{3-16}$$

$$\eta = \frac{1}{C(k_{te}-1)+1}\left(1 - \frac{d}{w}\right) \tag{3-17}$$
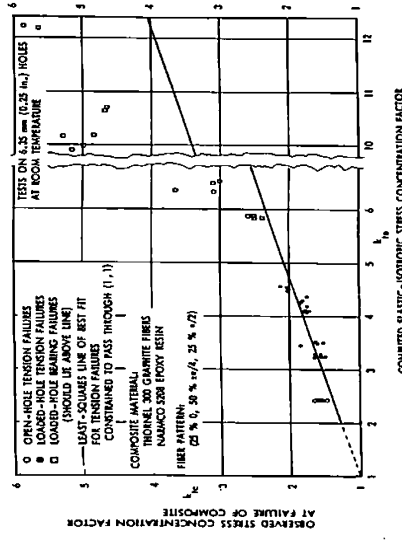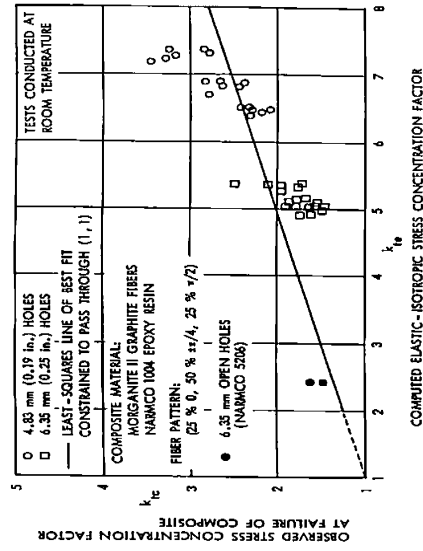
Figure 3-9. Stress concentration factors at failure for composite bolted joints.
Source: Hart-Smith (1996), courtesy of Dr. John Hart-Smith and the Boeing Company.
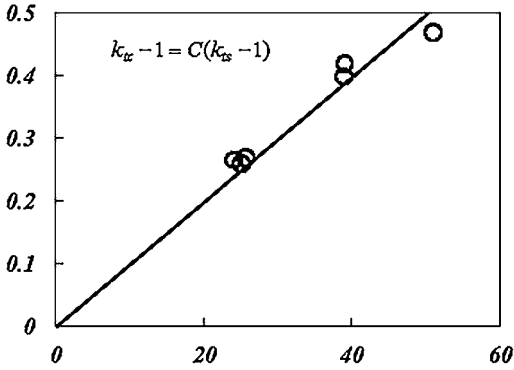
Figure 3-10. The effect of percentage of 0-degree plies on the value of coefficient C.
Source: Rosner (1992), courtesy of Charles Rosner.

Table 3-1. Different Values of Factor C for Different Composites

Material	C-Factor	Source
Thornel 300/Narmco 5208	0.27	Hart-Smith (1978)
Morganite II/Narmco 1004 Graphite Epoxies	0.25	Hart-Smith (1978)
Aluminum alloys	0.00	Hart-Smith (1978)
Quasi-isotropic laminates (e.g., window glass)	1.00	Hart-Smith (1978)
Pultruded composites (EXTREN Flat Sheet/ Series 500):		
• 0° fiber orientation	0.33	Rosner (1992)
• 45° fiber orientation	0.21	Rosner (1992)
• 90° fiber orientation	0.25	Rosner (1992)

For perfectly brittle materials, $C = 1$, and $k_{tc} = k_{te}$. In this case, the joint efficiency can be expressed as:

$$\eta = \left(1 - \frac{d}{w}\right) k_{tc}^{-1} = \left(1 - \frac{d}{w}\right) k_{te}^{-1} \tag{3-18}$$

For perfectly plastic materials, $C = 0$, or $k_{tc} = 1$. In this case, the efficiency is expressed as:

$$\eta = \left(1 - \frac{d}{w}\right) \tag{3-19}$$
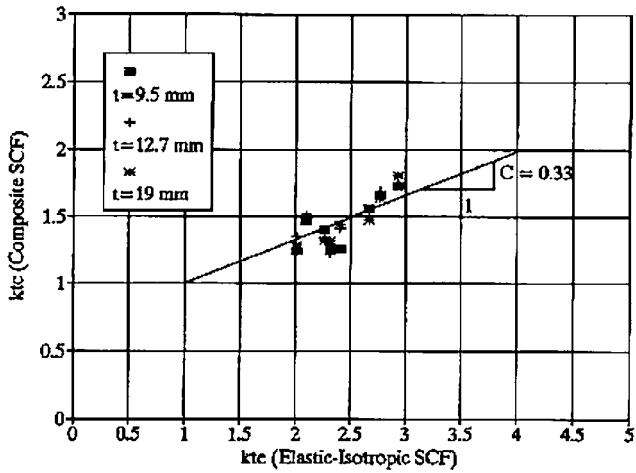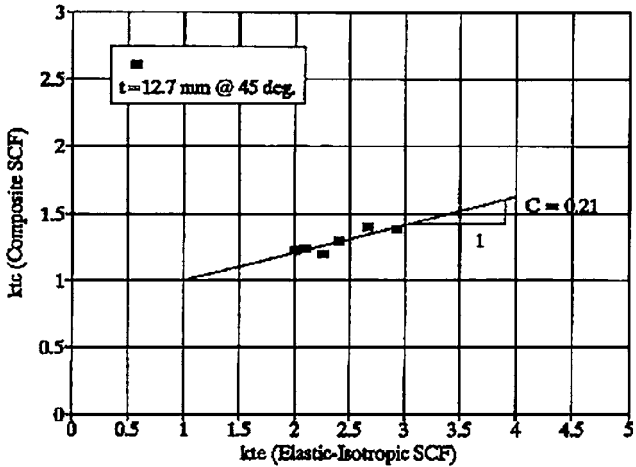
Figure 3-11. A. Correlation coefficients for 0-degree fiber pattern pultruded bolted joints; B. correlation coefficients for 45-degree fiber pattern pultruded bolted joints.
Source: Rosner (1992), courtesy of Charles Rosner.
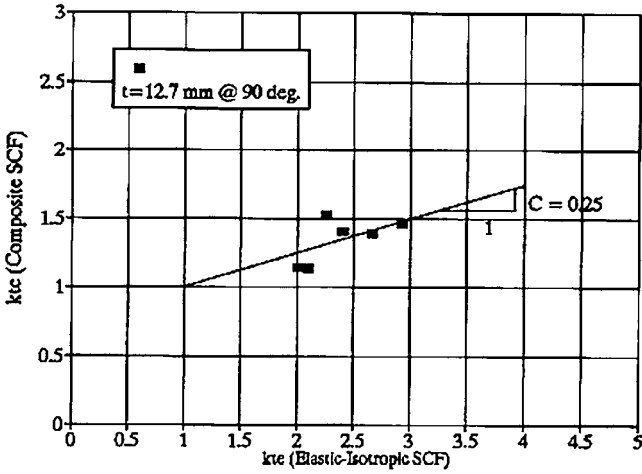
Figure 3-12. Correlation coefficients for 90-degree fiber pattern pultruded bolted joints.
Source: Rosner (1992), courtesy of Charles Rosner.

Using Eqs. 3-1 and 3-17, an expression for the ultimate load capacity of a single-bolted composite joint can be obtained as:

$$P_u = \frac{F_{tu}t(w-d)}{C(k_{te}-1)+1} \tag{3-20}$$

Equation 3-20 will reduce to Eq. 3-10 for perfectly elastic materials ($C = 1$); for perfectly plastic materials, $C = 0$ or $k_{tc} = 1$, the ultimate load will reduce to the original net-section formula:

$$P_u = F_{tu}t(w - d) \tag{3-21}$$

To investigate the sensitivity of Eq. 3-17 to the joint geometry, a family of failure envelopes was generated (Figs. 3-13 through 3-15) by plotting the joint efficiency versus the d/w ratio for different e/d ratios and for different loading directions.

As shown in these figures from the Rosner (1992) study, as the e/d ratio increases the joint strength increases up to a maximum value of $e/d = 5$. For this reason, Rosner suggested that the failure envelope corresponding to an e/d limiting value of 5 is the outermost failure envelope.

Hart-Smith (1978) showed that for small d/w or d/p values, failure by bolt bearing precedes and prevents the occurrence of joint tension failure. The ratio of joint bearing strength to tension strength affects both the peak maximum joint strength as well as the optimum d/w or d/p ratio at which
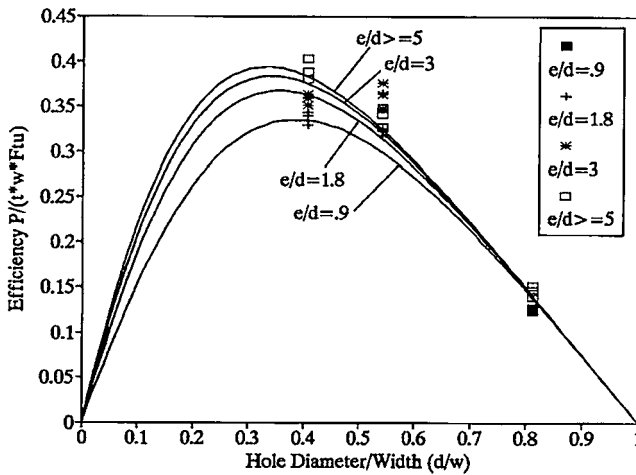
Figure 3-13. Net-tension failure envelopes for 0-degree joints.
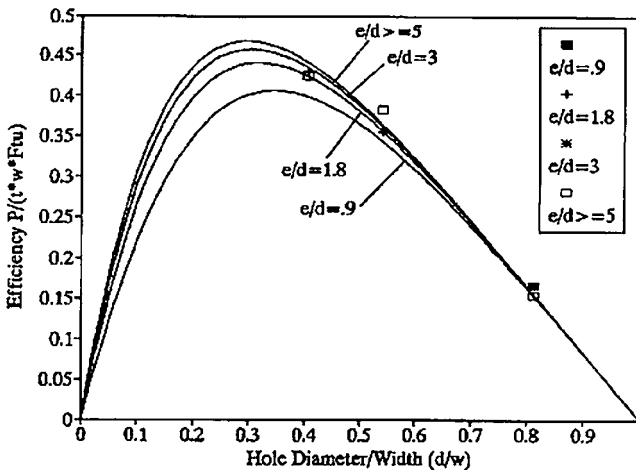
Figure 3-14. Net-tension failure envelopes for 45-degree joints.

that peak strength is obtained. According to Hart-Smith (1994), the optimum bolt pitch for highly orthotropic laminate is about 2.5*d* and for near-isotropic patterns about 3*d*. Avoiding the catastrophic tension failure of near-isotropic laminate will require increasing the bolt pitch to about 5*d* and decreasing joint strength.

3.3.1.4 Bearing/Cleavage Failure Criterion   Bolt bearing failure will precede the undesirable catastrophic joint tension failure if bolt holes are
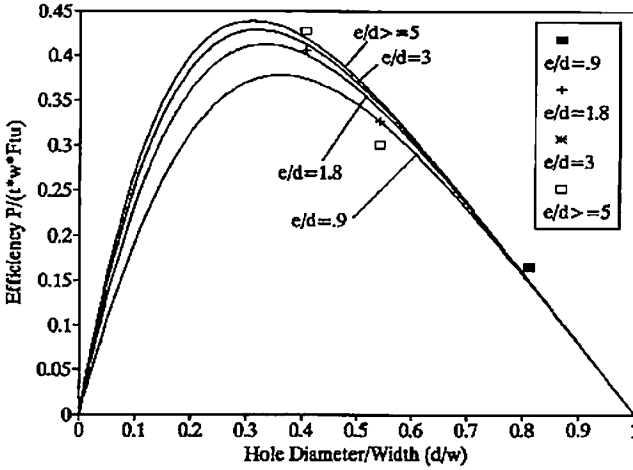
Figure 3-15. Net-tension failure envelopes for 90-degree joints.

widely spaced. The bearing failure will likely occur for large strip widths and large edge distances (i.e., larger *w/d* or, in a more general case, for larger *w/p*).

Since shear-out joint failure is frequently a consequence of a bearing failure with a short edge distance, it should be regarded as a special case of bearing failure (refer to Fig. 2-3B). It should be noted that, for highly orthotropic composite laminates, shear-out failure occurs at a very large edge distance. For single-hole bolted joints, the main interest in studying both the shear-out and cleavage failures is to understand how to prevent them rather than to precisely characterize them. The bearing strength of composite joints can be determined from the following equation:

$$F_{br} = \frac{P_{ult}}{t d_{bolt}} \qquad (3\text{-}22)$$

where d_{bolt} is the bolt diameter. The joint efficiency that fails in bearing can be expressed as a function of the *d/w* ratio, as follows:

$$\eta = \frac{F_{br}}{F_{tu}} \frac{d_{bolt}}{d} \frac{d}{w} \qquad (3\text{-}23)$$

Figure 3-16 presents various F_{br}/F_{tu} ratios with d/d_{bolt} for both isotropic and pultruded composite joints, respectively. Figure 3-16 indicates that maximum strength is achieved for both isotropic and pultruded joints typically at about 67% of the gross strength at a bolt pitch of 3*d* for the case of $F_{br} = 2F_{tu}$.
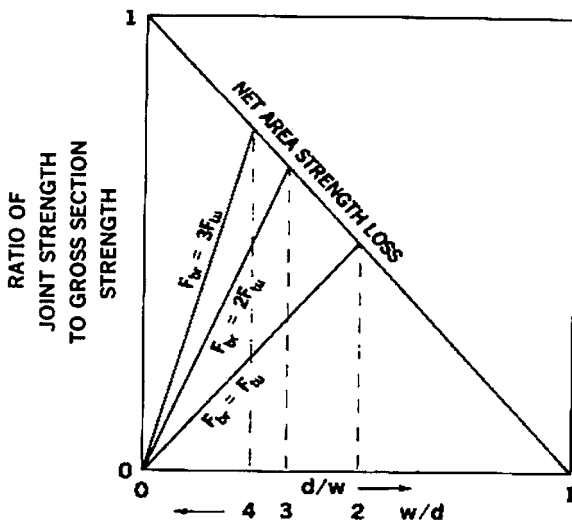
Figure 3-16. Influence of joint geometry on plastic strength of bolted in isotropic joints.

Rosner (1992) also reported, based on a study on bolted joints made of off-the-shelf pultruded flat sheets, that when e/d ratio exceeded 5, no appreciable gain in the joint bearing strength was observed. Based on this observation, Rosner suggested that all bolted pultruded composite joints with $e/d \geq 5$ be used to calculate the bearing strength of composite bolted joints.

The strength ratio F_{br}/F_{tu} for single-bolt pultruded composite joints was evaluated experimentally by Rosner (1992). Figure 3-17 illustrates the best-fit lines using a least-squares regression analysis for joints with applied load at 0 degrees, 45 degrees, and 90 degrees with respect to the pultrusion direction. Table 3-2 summarizes the experimental results for bolted pultruded composite joints conducted by Rosner (1992).

As the e/d ratio decreases, the mode of failure of a single-bolt pultruded composite joint tends to change from bearing to cleavage failure. Rosner and Rizkalla (1995) observed that the cleavage failure is related to bearing failure of single-bolt pultruded composite joints by a simple quadratic relation. The relation can be expressed in terms of radius-to-edge-distance ratio ($d/2e$). The proposed quadratic expression represents a reduction factor, ψ, which relates the efficiency, η, of a joint that is likely to fail in bearing, to the efficiency of a similar joint (with similar edge distance) that would tend to fail in a cleavage mode of failure. The proposed cleavage reduction factor, ψ, is expressed by the following relation:

$$\varphi = \left(1 - \frac{d}{2e}\right)^2 \tag{3-24}$$
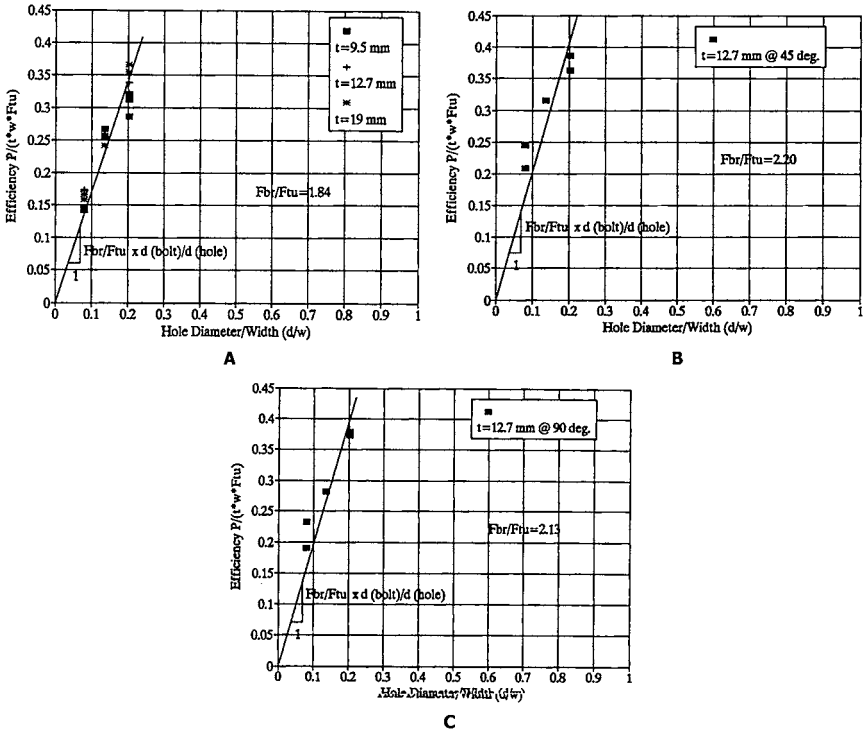
Figure 3-17. Bearing strength of pultruded bolted joints for A, 0 degrees; B, 45 degrees; C, 90 degrees.

Table 3-2. Different Values of Strength Ratio Fbr/Ftu for Single-Bolt Pultruded Composite Joint

Load Direction Relative to the Pultrusion Direction		Fbr/Ftu	Fbr ksi (MPa)
	0°	1.84	44.4 (306)
	45°	2.2	37.4 (258)
	90°	2.13	34.1 (235)

Source: Rosner (1992).

Experimental results indicated that this reduction factor fit well with the measured test data conducted on unidirectional pultruded composite joints.

Using Eqs. 3-23 and 3-24, an expression that characterizes both bearing and cleavage failure is obtained by multiplying the numerator term of Eq. 3-23 by the cleavage reduction factor, ψ:

$$\eta = \frac{F_{br}}{F_{tu}} \frac{d_{bolt}}{d} \left(1 - \frac{d}{2e}\right)^2 \frac{d}{w} \qquad (3\text{-}25)$$

Assuming a finger-tight fit, i.e., $d = d_{bolt}$, then,

$$\eta = \frac{F_{br}}{F_{tu}} \left(1 - \frac{d}{2e}\right)^2 \frac{d}{w} \qquad (3\text{-}26)$$

Equation 3-24 satisfies the two limiting cases for e/d. For example,

$$\eta = \frac{F_{br}}{F_{tu}} \frac{d}{w} \quad \text{for } e/d \Rightarrow \infty \qquad (3\text{-}27)$$

$$\eta = 0 \text{ for } e/d \Rightarrow 1/2 \text{ (or } e = d/2) \qquad (3\text{-}28)$$

Equation 3-27 is identical to Eq. 3-23 for bearing failure. The second limiting value appearing in Eq. 3-28 indicates the fact that the edge distance, e, measured from the bolt hole center must be larger than the bolt hole diameter; otherwise, the joint will have no strength, as shown in Fig. 3-18.

As mentioned earlier, experimental results indicated that for pultruded bolted joints with $e/d \geq 5$ (Fig. 3-19), the likely mode of failure is bearing. Based on this fact, the reduction factor, ψ, should reduce to unity when $e/d = 5$. To enforce this condition, the constants in the ψ-factor expression must be computed based on the observed limiting conditions. Rewriting Eq. 3-26 in terms of two constant coefficents, a and b, gives:

$$\eta = \frac{F_{br}}{F_{tu}} \left(a - b\frac{d}{e}\right)^2 \frac{d}{w} \qquad (3\text{-}29)$$
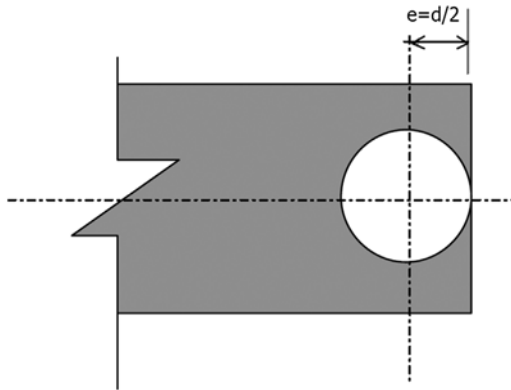
Figure 3-18. A joint with zero efficiency when $e = d/2$ (ref. Eq. 3-28).
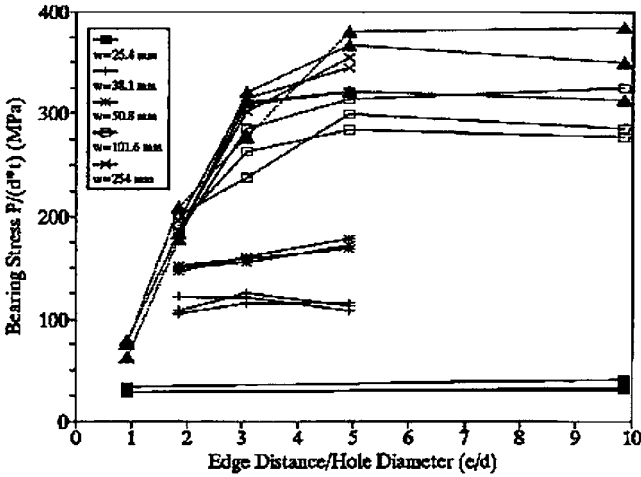
Figure 3-19. Effect of e/d ratio on joint bearing stresses.

where a and b are constants to be determined from the limiting observed upper and lower limits of joint efficiency.

To satisfy the observed upper limit of $e/d = 5$, or $d/e = 1/5$, then:

$$\left(a - b\frac{1}{5}\right) = 1 \tag{3-30}$$

and to satisfy the lower limit for $e/d = 1/2$ or $d/e = 2$ (refer to Fig. 3-21), then:

$$(a - 2b) = 0 \quad \text{or} \quad a = 2b \tag{3-31}$$

Now, solving Eqs. 3-30 and 3-31 for a and b, we get:

$$a = 2b = 10/9 \quad \text{or} \quad b = 5/9 \tag{3-32}$$

Using these coefficients, an expression for the joint efficiency can be written:

1. Cleavage failure for $e/d \leq 5$:

$$\eta = \frac{F_{br}}{F_{tu}} \frac{d}{d_{bolt}} \left(\frac{10}{9} - \frac{5}{9}\frac{d}{e}\right)^2 \frac{d}{w} \tag{3-33}$$

2. Bearing failure for $e/d \geq 5$:

$$\eta = \frac{F_{br}}{F_{tu}} \frac{d_{bolt}}{d} \frac{d}{w} \tag{3-34}$$
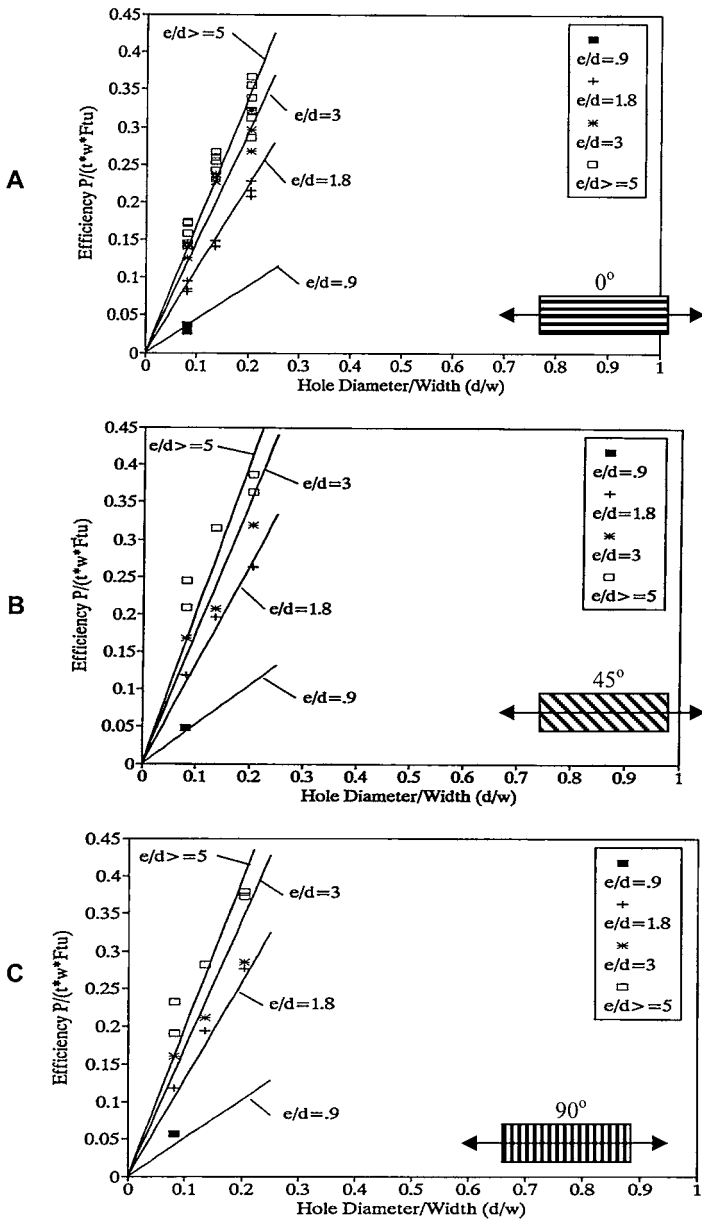
Figure 3-20. Bearing failure envelopes for bolted joints loaded at with respect to the pultrusion direction and for constant e/d ratios.

Note that Eq. 3-34 is identical to Eq. 3-23.

Figure 3-20 presents a family of failure envelopes as a function of η and d/w for joints loaded at 0 degrees, 45 degrees, and 90 degrees with respect to the pultrusion direction and for constant e/d ratios (0.9 to 5).

Using both Eqs. 3-33 and 3-34, the ultimate load of the pultruded bolted joint can be expressed as follows:

$$P_{u/t} = \eta(twF_{tu}) \qquad (3\text{-}35)$$

where η is described in Eqs. 3-33 and 3-34 for cleavage and bearing failure modes, respectively. Using appropriate η, the ultimate load capacity expressions for both cleavage and bearings for bolted pultruded joints are as follows:

1. Cleavage failure:

$$P_{ult}^{clavage} = F_{br}t\,\frac{d^2}{d_{bolt}}\left(\frac{10}{9} - \frac{5}{9}\frac{d}{e}\right)^2 \qquad (3\text{-}36)$$

2. Bearing failure:

$$P_{ult}^{bearing} = F_{br}t\,\frac{d^2}{d_{bolt}} \qquad (3\text{-}37)$$

3.3.1.5 Design Envelopes Rosner (1992) developed a family of design failure envelopes for each load direction (Fig. 3-21) by superimposing the failure envelopes for both cleavage and bearing failure criteria. These curves can be used for design proposes to predict the failure load as well as the bolted joint efficiency when particular joint geometry, such as t, w, e, d, and d_{bolt} is known. The same results can be predicted using Eq. 3-20 for net-section failure and Eqs. 3-36 and 3-37 for cleavage and bearing failures, respectively. The lowest value obtained from the two failure criteria will govern the joint capacity and the expected failure mode. Figure 3-22 shows a comparison between the experimental and predicted results for pultruded bolted joints loaded at 0 degrees, 45 degrees, and 90 degrees, with respect to the pultrusion direction, and for constant e/d ratios (Rosner 1992). As shown in this figure, an excellent agreement between the experimental and predicted results is achieved, and the majority of data points fall close to the 1:1 correspondence line or are on the conservative side.

3.3.1.6 Important Design Conclusions for Pultruded Bolted Joints Based on the discussion presented in this section, several important observations can be made:
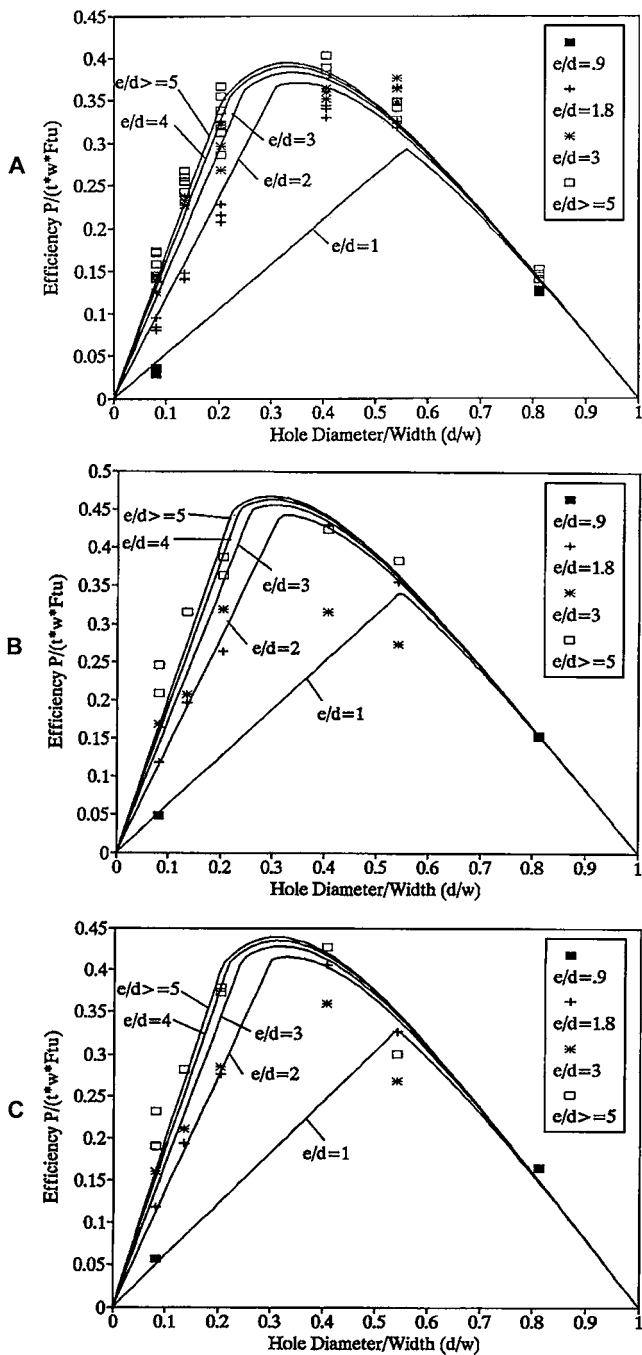
Figure 3-21. Design envelopes for bolted joints loaded at A, 0 degrees; B, 45 degrees; and C, 90 degrees with respect to the pultrusion direction and for constant e/d ratios.
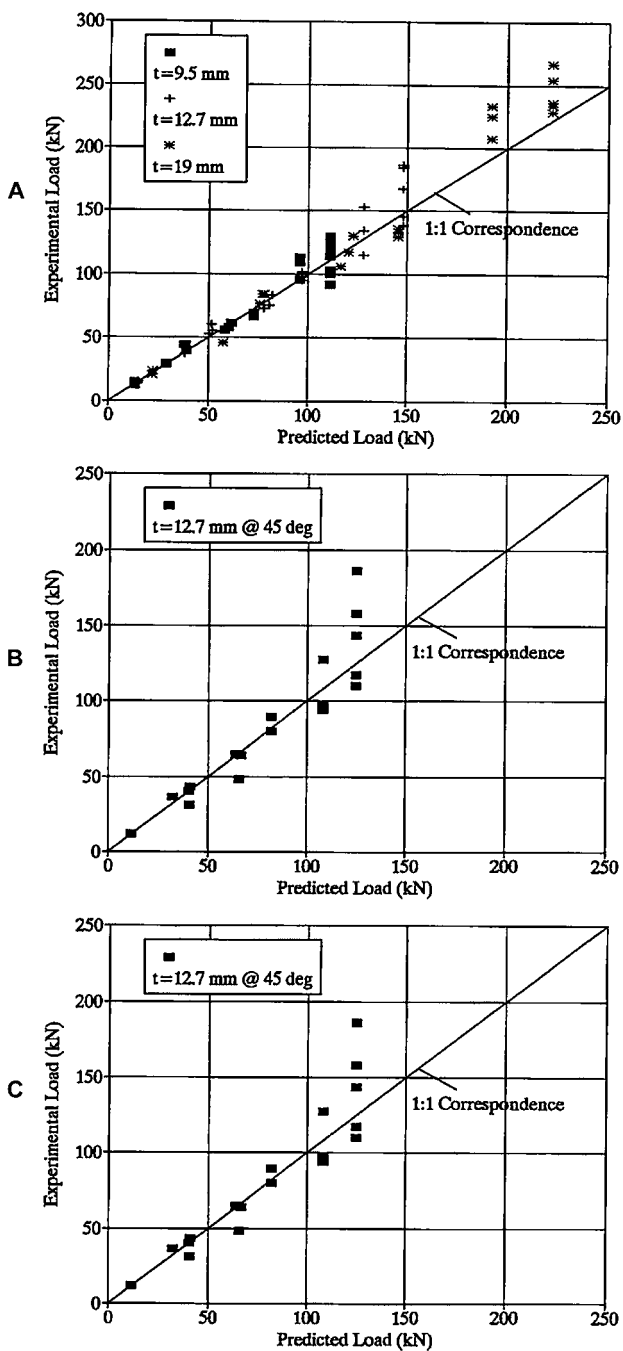
Figure 3-22. Experimental vs. model results for bolted joints loaded at A, 0 degrees; B, 45 degrees; and C, 90 degrees with respect to the pultrusion direction and for constant e/d ratios.

1. The simplified semi-empirical approach proved to be a satisfactory design tool for bolted pultruded composite joints.
2. Based on the experimental results, it has been concluded that the failure envelopes for bolted joints loaded in the pultruded direction (0 degrees with respect to primary unidirectional reinforcement) can be used in predicting the joint capacity loaded in all directions, and that procedure will result in a conservative predictions due to lower values of F_{tu} of all off-axis loading directions.
3. The optimum value for d/w, based on Rosner's work, is about 0.3, with an optimum e/d of 5. These optimum ratios will result in a joint efficiency of approximately 40%. Table 3-3 presents the optimum values obtained by Rosner and those recommended by the author, along with the expected bolted joint efficiencies.
4. As shown in Table 3-3, the recommended value of the d/w is selected to be 0.2 ($w = 5d$) to ensure bearing failure of the joint. In this case, a lower joint efficiency is expected. However, the trade-off for a safer mode of failure will require a 5% drop in the efficiency from 40% to 35%.
5. It should be clear to the reader that the design values for pultruded composite bolted joints are based on a specific type of unidirectional pultruded composites, specifically EXTREN Flat Sheet/Series 500 (E-glass/polyester) with average mechanical properties listed in Table 3-4.

Table 3-3. Experimental and Recommended Values for Geometry and Efficiency of Bolted Pultruded Joints

	e/d Ratio	d/w Ratio	Maximum Efficiency (η)
Rosner (1992)	5	0.3	0.40
Recommended	5	0.2	0.35

Table 3-4. Average Values of Mechanical Properties of EXTREN Flat Sheet/Series 500

Thickness in. (mm)	On-Axis Tensile Strength ksi (MPa)	On-Axis Tensile Strain At Failure (%)	On-Axis Tensile Modulus Msi (GPa)
3/8 (9.525)	28.7 (198)	1.6	2.2 (15.2)
1/2 (12.70)	24.1 (166)	1.6	1.84 (12.7)
3/4 (19.05)	24.1 (166)	1.6	1.9 (13.1)

Source: Strongwell Company.

Although the simplified semi-empirical approach is general, some coefficients, such as *C*, must be verified experimentally for every type of composite, including other pultruded products produced by other pultruders. Also, the optimum values and the corresponding joint efficiency may change from one material to another. However, for most commercially produced unidirectional pultruded profiles in the United States, with volume fractions of 45% to 50%, minimum variation is expected.

3.4 DESIGN AND ANALYTICAL PROCEDURE

Prior to analysis or design, the following basic information should be known and/or assumed:

- Bolt diameter
- Clearance
- Thickness of the joined pultruded parts
- Expected load, and loading direction
- Edge distance, or e/d ratio
- Width of the joined pultruded member, or w/d ratio
- Ultimate tensile strength of the joined pultruded materials
- Ultimate bearing strength of the pultruded materials

Given the above design information, the structural engineer can determine both the joint capacity and the corresponding mode of failure either by using the *graphical method,* which utilizes the failure envelopes described in Fig. 3-21, or by using the step-by-step *analytical method*; both are described below.

3.4.1 Graphical Method

The following are the steps to be followed in this method:

1. Assuming e/d and w/d ratios (refer to Table 3-3), the joint efficiency, η, can be determined from Fig. 3-21A. [This assumes that the failure envelope for a 0-degree applied load orientation is valid for all other orientations (*conservative approach*)].
2. Using the approximate η-value, an ultimate loading capacity for the joint can be determined using Eq. 3-35.
3. From Fig. 3-21A, check for the following:
   - If d/w and e/d ratios fall on the curved part of the envelopes (up to η = 0.35 for values of e/d of 2, 3, 4, and 5 or larger, and η = 0.28 for e/d = 1). In these cases, the expected governing mode of failure is net-tension.

- If d/w and e/d ratios fall on the straight-line portion of the failure envelopes of Fig. 3-21A, and if $e/d \geq 5$, the expected joint mode of failure is bearing (preferred). However, if the $e/d < 5$, the expected mode of failure is cleavage.

3.4.2 Analytical Method

The following are the steps to be followed in this method:

1. Using the pultruded joint basic information, Eq. 3-17 for net-section tension failure, and Eqs. 3-36 and 3-37 for cleavage and bearing failures, respectively, three values for η can be calculated.
2. Select the lowest η-value calculated in Step 1 as the governing joint efficiency.
3. Use Eq. 3-35 to calculate the ultimate loading capacity of the joint.
4. The expected load of failure of the joint corresponds to the failure mode associated with the lowest η-value calculated in Step 2.

For convenience, a FORTRAN computer code (BOLT.EXE) was developed to facilitate the analytical approach described in this chapter. The program is user-friendly and it requires the engineer to input known and assumed basic joint information described earlier. The code calculates the joint efficiency and joint capacity and determines the expected mode of failure. The code is provided on the ASCE Construction Institute Web site, http://www.constructioninst.org, along with user instructions. It should be noted that the program can also analyze multi-bolted composite joints. However, the joint configurations that can be handled by this code are limited to those described in Table 3-6.

3.5 NUMERICAL EXAMPLES

The following examples illustrate use of the graphical method and analytical methods.

Example 3-1: Using the Simplified Approach defined in Section 3.3.1, analyze a bolted joint made from unidirectional pultruded composites with the following geometrical parameters:

- Thickness = t = 1/2 in. (12.70 mm)
- Width = w = 5 in. (127 mm)
- Assumed edge distance = e = 1½ in. (38.1 mm)
- Hole diameter = d = 7/8 in. (22.23 mm)

- Clearance = 1/8 in. (3.175 mm)
- Bolt diameter = 3/4 in. (19.05 mm)
- Unnotched tensile strength of the joined parts = F_{tu} = 24 ksi (166 MPa)
- Bearing strength of the joined parts = F_{br} = 1.84 F_{tu} = 44.30 ksi (305.44 MPa)

Solution:

Step 1. Calculate design ratios:

$$d/w = 0.175, \; e/d = 1.71, \; e/w = 0.3, \text{ and } d/d_{bolt} = 1.17$$

- *Graphical Method:* Knowing the values of both d/w and e/d, and using a linear interpolation of Fig. 3-21A, the joint efficiency is about 0.24.

Step 2. Calculate load capacity, P_{ult}, as

$$P_{uit} = \eta t w F_{tu} = (0.24)(1/2 \text{ in.})(5 \text{ in.})(24 \text{ ksi}) = 14.4 \text{ kips (63.7 kN)}$$

Step 3. Identify failure mode:

The values of d/w and e/d ratios fall on the straight-line portion of the failure envelope, and since $e/d = 1.71 < 5$, the expected mode of failure of this joint is *cleavage* (it also could be *shear-out* failure).

- *Analytical Method:* Knowing the value of P_{ult} (from Step 2), the joint efficiency can be calculated using Eq. 3-17 and using $C = 0.33$ for on-axis loading (Table 3-1). Knowing that $e/w = 0.3 \le 1$ ($w/e = 3.33$), then:

$$\theta = (3.33 - 1) = 2.33, \text{ then:}$$

$$k_{te} = 5.714 + 0.175 + 0.5(1 - 0.175)2.33 = 6.85 \approx \left(\frac{w}{d} + \frac{d}{w} = 5.88 \right)$$

$$\eta = \frac{1}{0.33(6.85 - 1) + 1}(1 - 0.175) = 0.28(0.31)$$

Step 4. Calculate ultimate load capacity for net-tension:

$$P_{ult} = \eta t w F_{tu} = (0.28)(1/2 \text{ in.})(5 \text{ in.})(24 \text{ ksi}) = 16.8 \text{ kips (74.3 kN)}$$

Step 5. _Identify failure mode:_ Since e/d = 1.17 < 5, use Eq. 3-36 for cleavage failure:

$$\eta^{cleavage} = (1.84)(1.17)\left(\frac{10}{9} - \frac{5}{9}(0.584)\right)^2 0.175 = 0.23$$

Based on the analysis, it was found that:

$$P_{ult}{}^{cleavage} < P_{ult}{}^{net-tension}$$

That is, the governing mode of failure is _cleavage mode_ (same conclusion obtained using the graphical method).

Example 3-2: To demonstrate the influence of the e/d ratio on the failure mode of bolted pultruded joints, Eq. 3-1 is resolved using different e/d ratios. All other design information is the same, except a larger value of e/d is used. In this example, the edge distance is assumed to be 5 in. (127 mm).

Solution:
This exercise is solved using both the graphical method and the computer code BOLT.EXE.

- _Graphical Method:_ Knowing the values of both d/w and e/d, d/w = 0.175, e/d = 5.71, and d/d_{bolt} = 1.17.

Step 1. _Calculate joint parameters:_ Using Fig. 3-21A, the joint efficiency is about 0.29.

Step 2. _Calculate load capacity, P_{ult}, as:_

$$P_{ult} = \eta twF_{tu} = (0.29)(1/2 \text{ in.})(5 \text{ in.})(24 \text{ ksi}) = 17.4 \text{ kips (76.9 kN)}$$

Step 3. _Identify failure mode:_

The values of d/w and e/d ratios fall on the straight-line portion of the failure envelope, and since e/d = 5.71 > 5, the expected mode of failure of this joint is _bearing_.

- _BOLT.EXE Program:_ P_{ult} (net-tension) = 19.5 kips, P_{ult} (cleavage) = 17.1 kips, and P_{ult} (bearing) = 16.6 kips. Since the lowest P_{ult} value

determines the joint capacity and the corresponding mode of failure, the ultimate capacity of this joint is 16.6 kips, and the expected mode of failure is bearing. (This is the same conclusion as was obtained from the graphical solution. It should be noted that the graphical solution is approximate, and hence the exact values must be determined analytically or using the computer code.)

3.6 DESIGN OF MULTI-BOLTED JOINTS

3.6.1 Background

In practical design details, several bolts are usually used in pultruded bolted joints. Unlike single-bolt pultruded joints with limited structural efficiency, the use of more than one row of fasteners can improve the efficiency of the pultruded joints. It is strongly recommended that the minimum number of bolts should be two. In a multi-bolt composite joint, the first row of bolts will usually transfer more load. However, any insignificant local bearing failure will redistribute the load to the next bolt row, and so on (Chamis 1990). Studies by Pyner and Matthews (1979) and Agarwal (1980a) indicate that as multi-bolted composite joints become more complicated, use of the analytical procedure based on data from single-bolted joints leads to inaccurate conclusions. Also, experimental results reported by Haruna and Hamada (1996) indicate that designing multi-bolted composite joints based on data obtained from single-bolt joints is risky. This is because joints that are wide enough to exhibit bearing failure in a single-bolt joint exhibit a net-tension failure in the case of a multi-bolted composite joint. McCarthy et al. (2005) showed the importance of clearance in multi-bolted composite joints that can cause major changes in the load distribution and damage mechanisms, leading to a significant reduction in the load at which initial failure (due to bearing at one of the holes) occurs.

Limited investigations have been reported on the behavior of multi-bolted pultruded composite joints. One of the pioneering studies was conducted by Abd-El-Naby and Hollaway (1992). In this study, a comprehensive experimental test program was performed on two-bolt pultruded composite joints loaded in axial tension. The pultruded materials used in this study were commercially produced pultruded glass/polyester materials manufactured by Fiberforce Ltd., UK. The results of this work are as follows:

- The load distribution between the bolts tends to approach uniformity near failure unless obstructed by premature tensile and shear

failures. For joints that fail in bearing, the load distribution is uniform and, accordingly, the load per bolt is equal to the strength of a single-bolted joint.

- The achievement of full-load redistribution has been found to depend on the amount of local deformation that can be developed before the failure of the pultruded composite joint.
- The use of two-bolt joints increases the efficiency of the pultruded joints. However, the designer should dimension such joints such that they fail in bearing. This can be achieved by selecting the bolt diameters such that the tensile strength of the cross section passing through the inner bolt is, according to the authors, "stronger than twice the bearing strength of the single-bolt joints."
- A reduction in the strength per bolt will result for joints failing in shear through the bolts. In this case, arranging the bolts in parallel could be more efficient due to the increase in the area resisting failure.

A similar study conducted on multi-bolted pultruded composite joints was reported by Prabhakaran et al. (1996). The most recent, and perhaps most comprehensive, study was conducted by Hassan et al. (1997). In this study, a total of 115 multi-bolted, double-lap pultruded composite joints with five different configurations were tested. The composite materials for the joints were Strongwell EXTREN 500 Series pultruded composites. In addition, this study included both analytical and numerical investigations. The following are some of the important conclusions drawn from this study:

1. The load-displacement behavior is linear regardless of the failure mode of the joint.
2. The e/d has a significant influence on the mode of failure of unidirectional pultruded joints with a single-row or a single-column configuration. For a relatively small e/d ratio (<3), the failure mode was cleavage, while intermediate values of e/d (>3), resulted in a net-tension failure of the joints.
3. For joints with 0-degree, 45-degree, and 90-degree fiber orientation (with respect to the applied load), the bearing strength and the efficiency (net-tension) increase as the e/d ratio increases, up to $e/d = 5$. Based on this observation, a limiting value for the e/d ratio of 5 is recommended for the design of pultruded multi-bolted joints.
4. Variation in bolt pattern has a minor effect on the overall efficiency of the joints.
5. Arranging bolts in a column results in a higher bearing strength as compared to arranging the bolts in a row, especially when $e/d < 3$.

6. Increasing the number of bolts in a column or in a row results in increasing the joint efficiency for joints with the same width (w). This effect is more significant for lower values of e/d ratio ($e/d < 3$) due to the cleavage failure mode mechanism.

7. The increase in the ultimate strength of pultruded multi-bolted joints is not directly proportional to the increase in the number of bolts.

8. Joints with fiber orientation perpendicular to the applied load (90 degrees) are more susceptible to net-tension failure mode.

9. Increasing the thickness (t) of the joined pultruded members slightly increases the joint ultimate capacity with a minor effect on the failure mode of the joint. Based on the test results of the program, it is suggested that the use of high-strength (or stainless steel) bolts with a torque of 24 ft-lb (32.5 N·m) is adequate to lessen the effect of material thickness (t).

10. Increasing the vertical pitch-hole-diameter ratio (p/d) beyond 4 results in a slight increase in joint ultimate capacity. However, this increase in the p/d ratio has a minor effect in the resulting mode of failure of the joint. Based on this observation, it is suggested that a limiting value of 4 for the p/d ratio be used. Values of p/d ratio beyond 4 will result in no redistribution of stress fields between the bolts.

11. The joint width (w) has a major effect on the magnitude of the strain concentrations along the net-section perpendicular to the applied load. As the width increases, the strain concentration increases. This is because the stresses at a section away from the bolt are resisted by the material within the vicinity of the bolt.

12. Increasing the edge distance (e) lowers the strain concentration factors, since larger edge distance allows the material at the net-section to be efficiently utilized by allowing free flow of the stresses away from the bolt holes. (As would be expected, small edge distances lead to higher stress concentration factors, which in turn result in steeply varying stress fields that flow very close to the bolt holes.)

13. Joints with fiber orientation perpendicular to the applied load (90 degrees) have higher strain concentration factors as compared to joints loaded in parallel to the pultrusion axis (0 degrees). This can be attributed to the lower values of both the transverse tensile strength (σ_{22}), and the transverse tensile modulus (E_{22}) for commercially produced unidirectional pultruded composites.

Mottram and Turvey (2003) have compiled a comprehensive database for most of the available tests performed on both single- and multi-bolted PFRP plate joints.

3.6.2 Analysis of Multi-Bolted Composite Joints

3.6.2.1 Background   The analysis of multi-bolted composite joints is more complicated as compared to single-bolted composite joints. For example, when analyzing multi-bolted joints, several factors need to be considered, including the following:

1. Load distribution between individual bolts
2. Effect of bolt pattern
3. Effect of number of bolts in a row or in a line
4. Effect of numbers of rows and column
5. Interaction stress fields associated with each individual bolt hole

The major factor is the load distribution between individual bolts, which is greatly affected by misalignment of bolt holes and variation of hole size (Hassan et al. 1997).

According to Hart-Smith (1994), the key to the analysis of multi-row bolted composite joints is a formula for the bearing-bypass interaction (refer to Fig. 3-23).

The bearing load is the load resisted by the bolts, and for joints subjected to tension load is equal to P_{br}^+:

$$P_{br}^+ = \sigma_{br}^+ dt \tag{3-38}$$

For joints subjected to compression loads, the bearing load $P^-{}_{br}$ is given by:

$$P_{br}^- = \sigma_{br}^- dt \tag{3-39}$$

The bypass load, P_{bypass}^-, interrupted by the bolt hole, is the remainder of the total applied load not carried by the bolt, as shown in Figs. 3-23 and 3-24.

For joints subjected to *tensile* loading, the bypass load is given by:

$$P_{bypass} = \sigma_{tu}(w - d)t \tag{3-40}$$

and for joints subjected to *compression* is given by:

$$P_{bypass} = \sigma_c (w - d)t \tag{3-41}$$

and for an open hole with no bolt, or in the case of a loose bolt, is given by:

$$P_{bypass} = \sigma_c wt \tag{3-42}$$
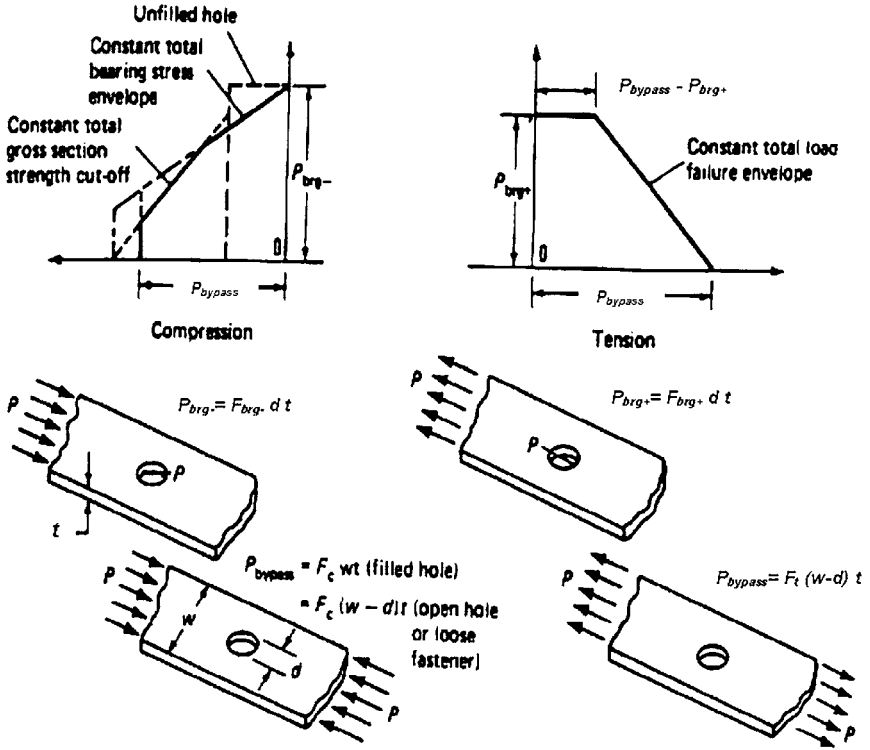
Figure 3-23. Outer envelope of bearing-bypass interactions.
Source: Hart-Smith (1998), courtesy of Dr. John Hart-Smith and the Boeing Company.

From equilibrium, the total load, P_{Total}, equal to the sum of bearing load, P_{br}, and the bypass load, P_{bypass}, is:

$$P_{Total} = P_{br} + P_{bypass} \tag{3-43}$$

When the bearing load is high enough, there is a bearing stress cutoff for sufficiently wide bolt spacing. For closer bolt spacing, the expected failure mode is net-tension, whether the load is all resisted by the bolt (pure bearing) or all reached at other fasteners in the joint (pure bypass).

The extremities of the interactions (refer to Fig. 3-24) can be established by tests if a theory is not available.

As shown in Fig. 3-24, there is a linear interaction between bearing and bypass loads whenever the composite bolted joint fails in tension through the hole; that is,

$$(\sigma_{net}k_{tc})_{bearing} + (\sigma_{net}k_{tc})_{bypass} \le F_{tu}, \; (and \; \sigma_{brg} \le F_{brg}) \tag{3-44}$$
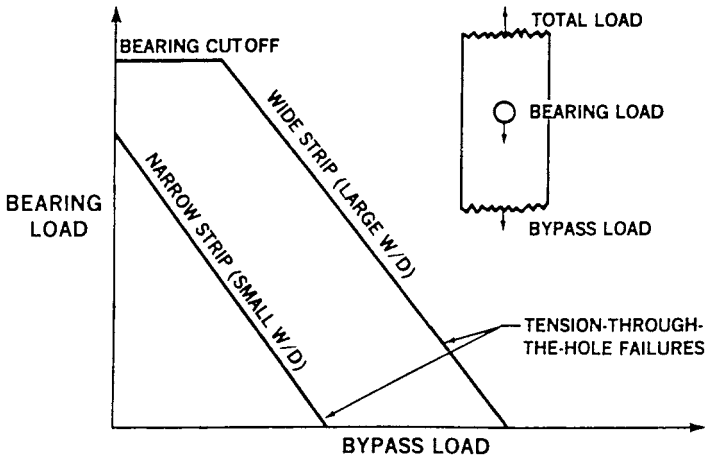
Figure 3-24. Bearing-bypass load interaction for loaded bolts in composites.

The influence of the bypass-to-bearing-load ratio on the structural performance of multi-bolted composite joints was also reported by Ramkumar and Tossavainen (1984) and Tang (1981). Based on experimental results, Ramkumar and Tossavainen reported there is a linear reduction in composite joint strength with increasing bearing/bypass load ratio.

According to the *MIL-17 Handbook* (ASTM 2002), tests may be required for composite bolted joints in which the load transfer is greater than 20% of the total load at an individual bolt. Several test methods have been developed by the aerospace industry to evaluate the bearing/bypass strength of bolted composite joints. These methods can be classified into three general catogries:

1. Passive
2. Independent bolt load
3. Coupled bolt load–bypass load

The *MIL-17 Handbook* recommends that, in evaluating the bearing/bypass characteristics, the load should be loaded independently and the load resisted by the bolt should be measured directly. In this scenario, the bearing stress can be calculated without resorting to backing out a value from the strain gage readings on the jointed parts. This method is recommended and was developed by the NASA-Langley Research Center; details of the test procedure and test matrix are reported by Crews and Naik (1986). Figure 3-25 shows a sketch of the suggested improvement to standard bearing/bypass test specimen proposed by Hart-Smith (1996).
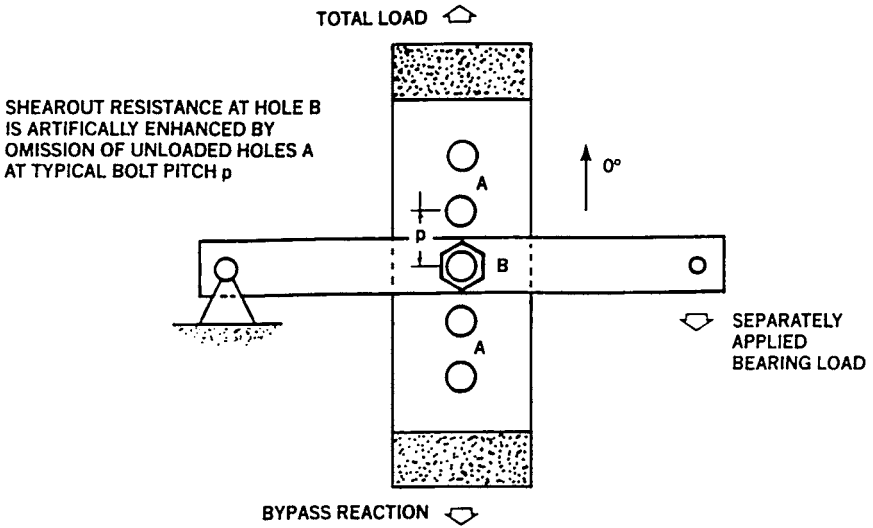
Figure 3-25. Suggested improvement to standard bearing-bypass test specimen proposed by Hart-Smith (1996).

3.6.2.2 Analytical and Design Procedure   An approach similar to the approach described in Section 3.2.1 is adopted for multi-bolted composite joints. As mentioned earlier, this approach is based on the analytical procedure that was developed by Hart-Smith (1978) to predict the strength and failure mode of mechanically fastened composite bolted joints. The recommended analytical procedure includes some modifications proposed for pultruded composites by Rosner (1992) and by Hassan (1994). This model is semi-empirical and consists of two basic failure criteria accounting for the different possible failure modes of the pultruded double-shear multi-bolted joints.

3.6.2.2.1 Stress Concentration Factors.   Hart-Smith (1996) proposed similar expressions for the composite joints with multiple holes:

1. Loaded hole:

$$k_{te} = \frac{p}{d} + 0.5\left(1 - \frac{d}{p}\right)\theta \approx \frac{p}{d} \qquad (3\text{-}45)$$

$$\theta = \left(\frac{p}{e} - 1\right) \quad \text{for } e/p \leq 1, \theta = 0 \quad \text{for } e/p \geq$$
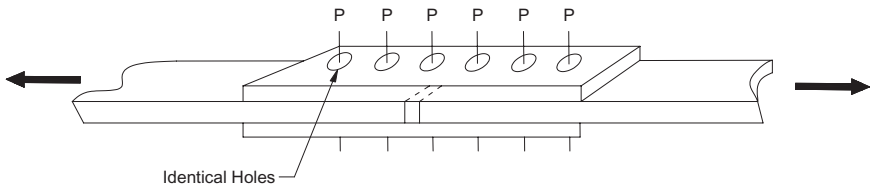
Figure 3-26. Multi-bolted composite joint.

2. Unloaded hole:

$$k_{te} = 1 + 2\left(1 - \frac{d}{w}\right)^{\frac{3}{2}}$$ (3-46)

where θ is a nondimensional factor that is a function of e/w for single-bolted joints, and a function of p/e for multi-bolted joints (p is the hole pitch as shown in Fig. 3-26).

Now, by expressing pitch, *p-cap*, as the ratio of the width, w, to the number of bolts in the raw, n, that is,

$$\hat{p} = \frac{w}{n}$$ (3-47)

then k_{te} can be written as:

$$k_{te} = \frac{w}{nd} + 0.5\left(1 - \frac{nd}{w}\right)\theta \approx \frac{w}{nd}$$ (3-48a)

where

$$\theta = \left(\frac{w}{ne} - 1\right) \text{ for } e/\hat{p} \le 1 \quad \text{and} \quad \theta = 0 \text{ for } e/\hat{p} \ge 1$$ (3-48b)

3.6.2.2.2 Stress Concentration Reduction Factor.   As mentioned in Section 3.1.1.3, composite joints behave differently as compared to both ductile and brittle materials. For that reason, a stress concentration reduction factor exists as described in Eq. 3-13. The correlation factor, C, is expressed as:

$$C = \frac{k_{tc} - 1}{k_{te} - 1}$$ (3-49)

Table 3-5 presents different values for the correlation factor, C, which were obtained experimentally for five different pultruded composite joint configurations (Hassan 1994). Figures 3-27 through 3-31 show the graphs used for obtaining these correlation factors for joints loaded in the pultrusion direction (0 degrees). Similar curves for calculating these factors for other directions (90 degrees and 45 degrees) are shown in Figs. 3-32 through 3-38.

As shown in the preceding graphs and tables, the correlation factor, C, is highly sensitive to the number of bolt columns and rows. For example, by increasing the number of bolts in a column, the value of C decreases. This can be demonstrated by comparing the values of C for joint detail A and joint detail C, where the value of C dropped from 0.22 (for detail A) to 0.16 (for detail C). This can be attributed to the increase in the joint load capacity, and, consequently, a decrease of the composite stress concentration factor, k_{tc}, that lowers the value of C. Thus, the number of bolts in a column is inversely proportional to the value of C. The results also indicate that increasing the number of bolts in a given row (i.e., number of bolt columns) will result in an increase of the value of C. This can be attributed to the decrease in the net stress of the joint due to the disproportional increase of the load with respect to the cross-sectional area of the joined member (Hassan 1994). Consequently, the value of the composite stress concentration factor, k_{tc}, will increase, resulting in an increase of the value of C.

3.6.2.3 Efficiency of Multi-Bolted Composite Joints   Using Eq. 3-10, the expression for the net area, A_{net}, becomes:

$$A_{net} = t\,(w - nd) \tag{3-50}$$

then

$$P_{ult} = \frac{F_{tu}}{k_{te}} t(w - nd) \tag{3-51}$$
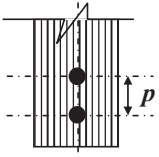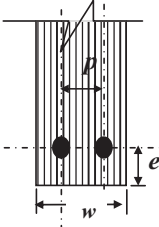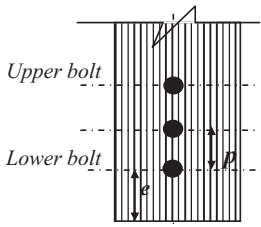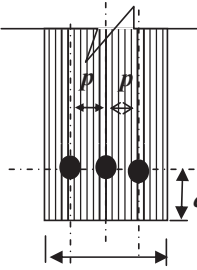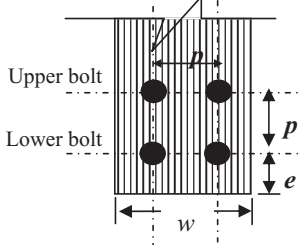
or

$$\eta = \frac{S_j}{S_m} = \frac{\dfrac{F_{tu}}{k_{te}} t(w - nd)}{t \cdot w \cdot F_{tu}} = \frac{(w - nd)}{wk_{te}} = \left(1 - \frac{nd}{w}\right) k_{te}^{-1} \tag{3-52}$$

For isotropic materials at full plastic deformation, k_{te} approaches 1, and

$$\eta = \left(1 - \frac{nd}{w}\right) \tag{3-53}$$

Table 3-5. Values of the Correlation Factor, C,
for 0-Degree Fiber Orientation

Joint Identifier	Joint Detail	C
A		0.22
B		0.40
C		0.16
D		0.50
E		0.30

Source: Hassan (1994), courtesy of Dr. Nahla Hassan.
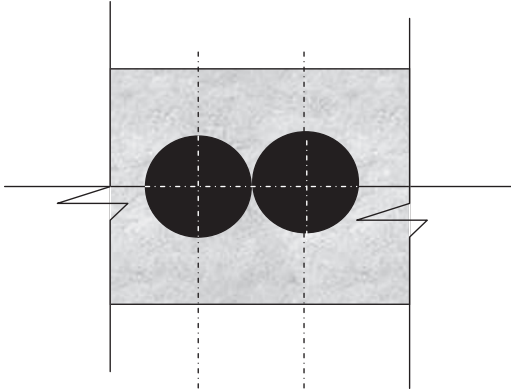
Figure 3-27. As $\dfrac{d}{p}$ approaches unity, the joint efficiency approaches zero for both elastic and plastic materials.
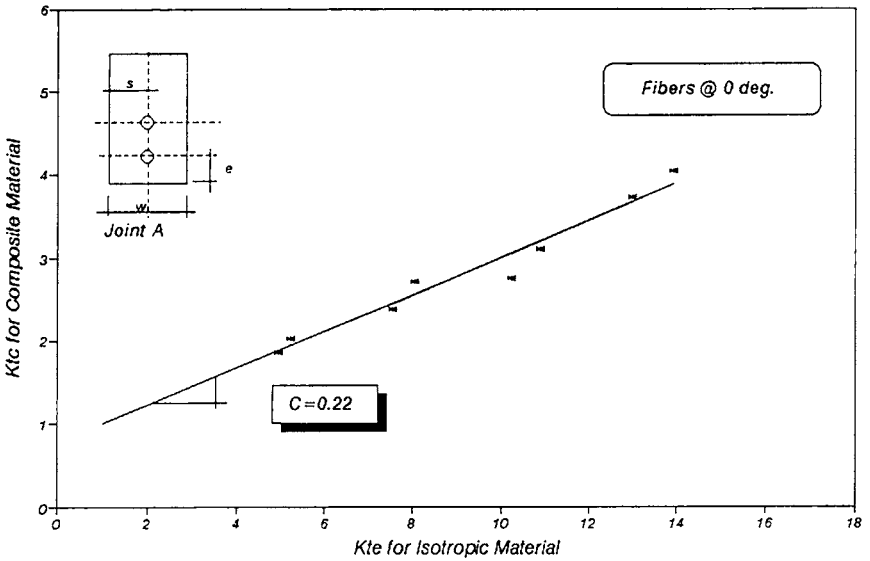
Figure 3-28. Correlation factor, C, for joint type A at 0-degree fiber orientation.
Source: Hassan (1994), courtesy of Dr. Nahla Hassan.
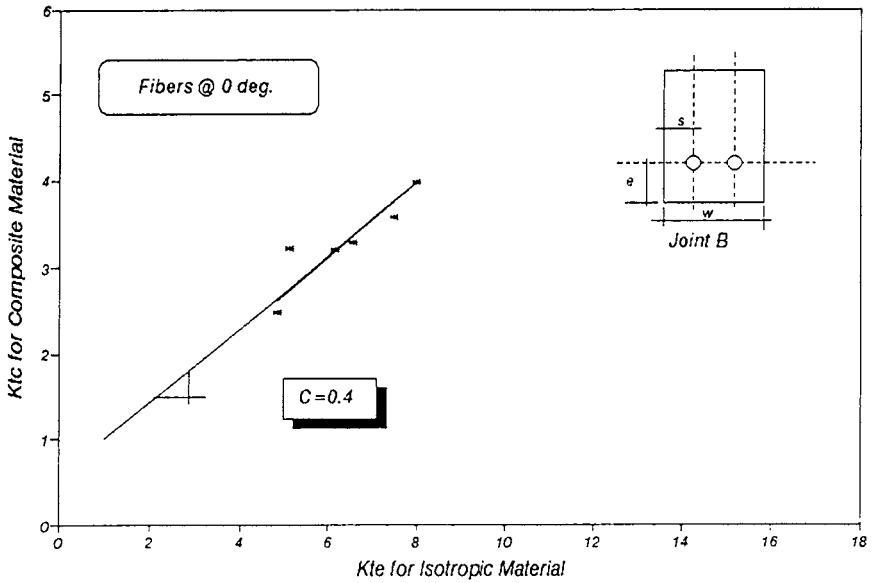
Figure 3-29. Correlation factor, C, for joint type B at 0-degree fiber orientation.
Source: Hassan (1994), courtesy of Dr. Nahla Hassan.
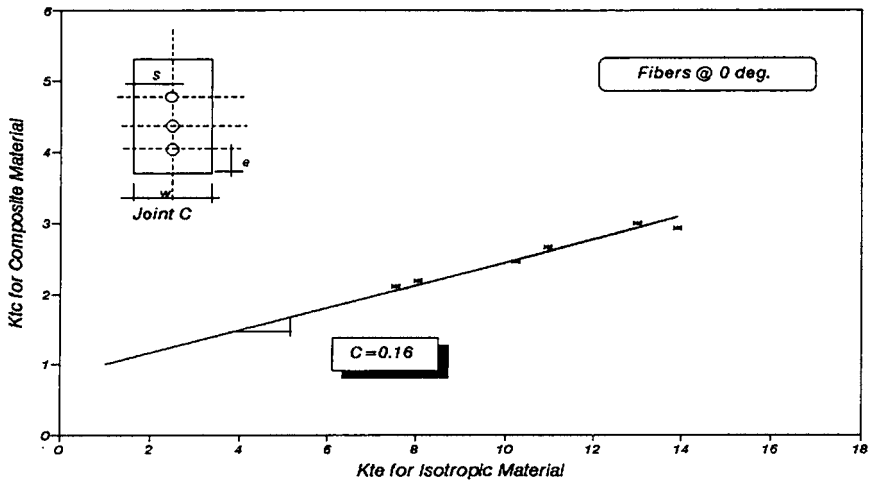
Figure 3-30. Correlation factor, C, for joint type C at 0-degree fiber orientation.
Source: Hassan (1994), courtesy of Dr. Nahla Hassan.
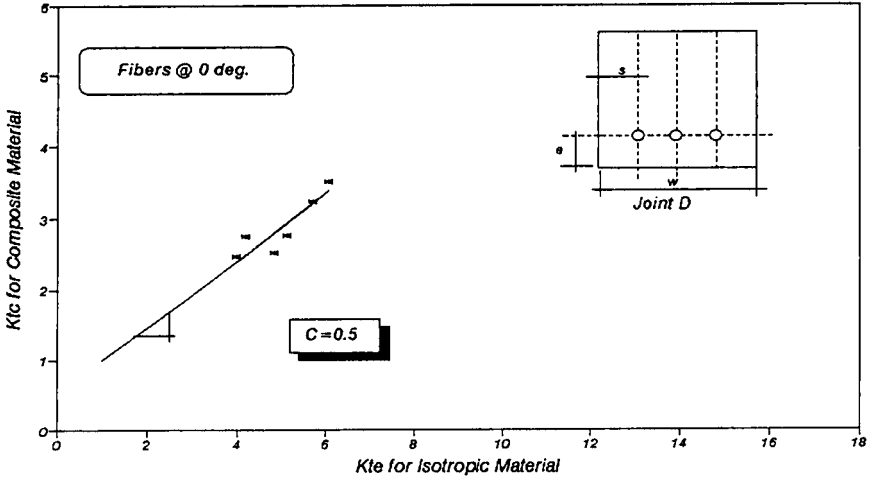
Figure 3-31. Correlation factor, C, for joint type D at 0-degree fiber
orientation.
Source: Hassan (1994), courtesy of Dr. Nahla Hassan.
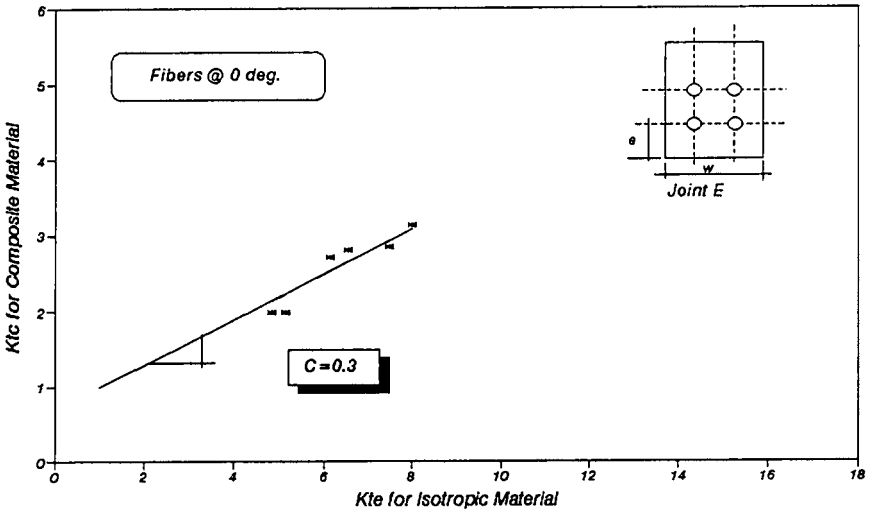
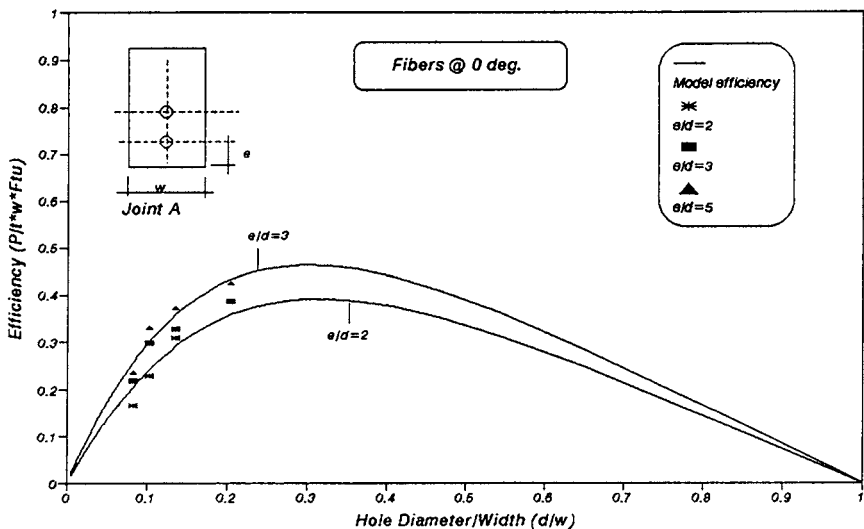
Figure 3-32. Correlation factor, C, for joint type E at 0-degree fiber
orientation.
Source: Hassan (1994), courtesy of Dr. Nahla Hassan.
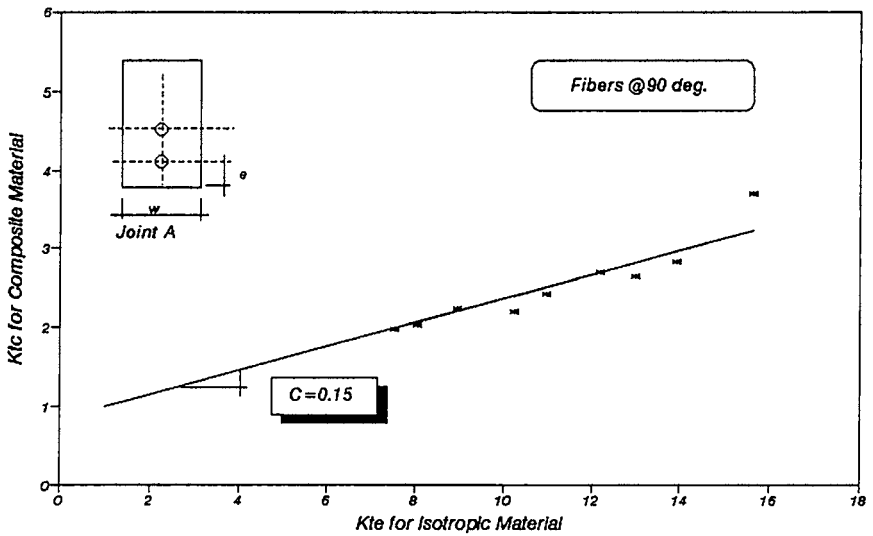
Figure 3-33. Correlation factor, C, for joint type A at 90-degree fiber orientation.
Source: Hassan (1994), courtesy of Dr. Nahla Hassan.
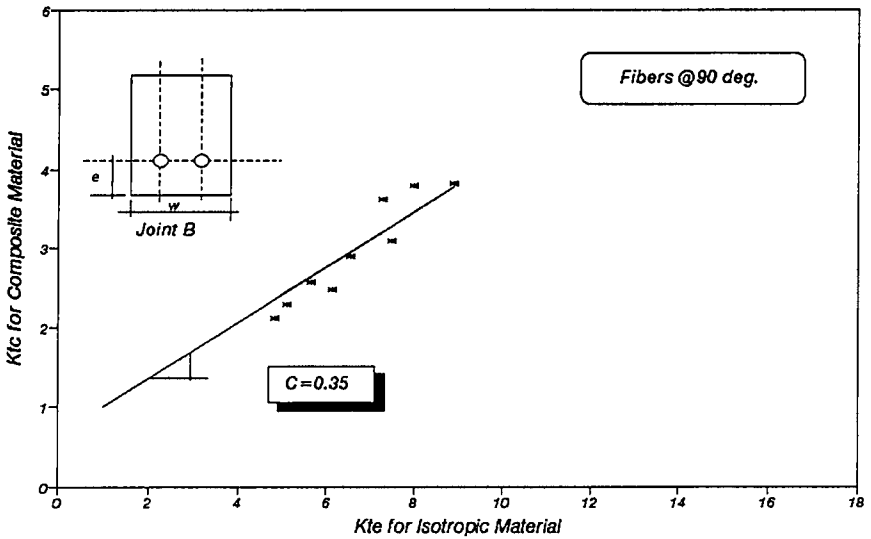
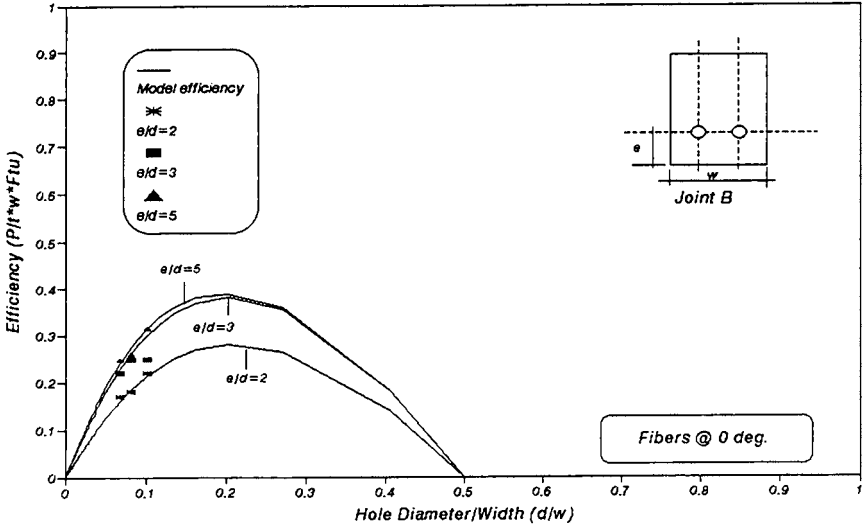

Figure 3-34. Correlation factor, C, for joint type B at 90-degree fiber orientation.
Source: Hassan (1994), courtesy of Dr. Nahla Hassan.
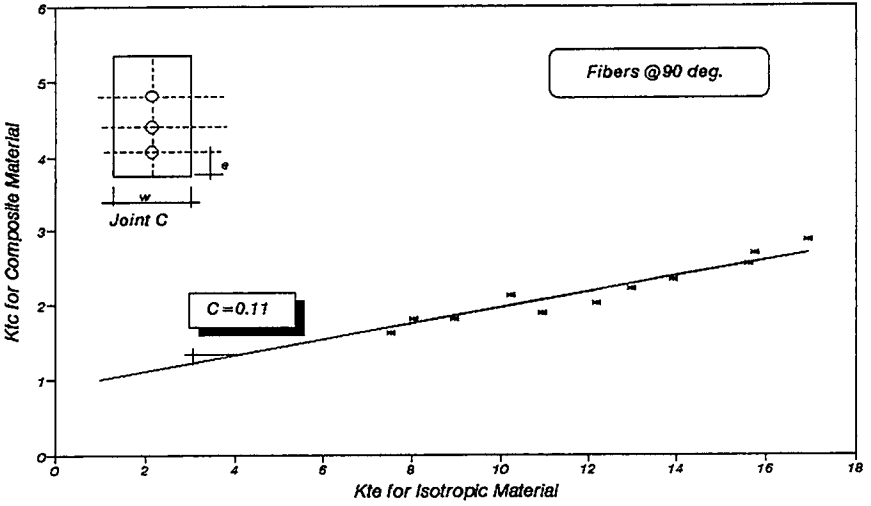
Figure 3-35. Correlation factor, C, for joint type C at 90-degree fiber orientation.
Source: Hassan (1994), courtesy of Dr. Nahla Hassan.
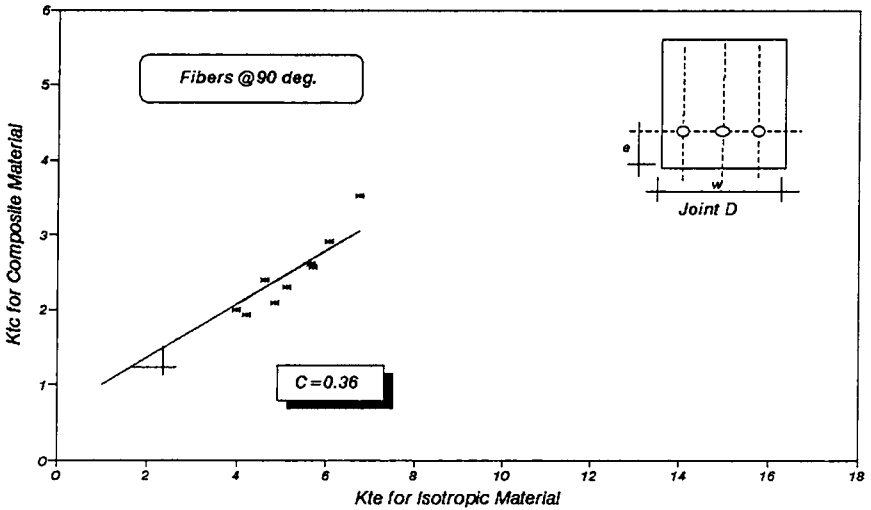
Figure 3-36. Correlation factor, C, for joint type D at 90-degree fiber orientation.
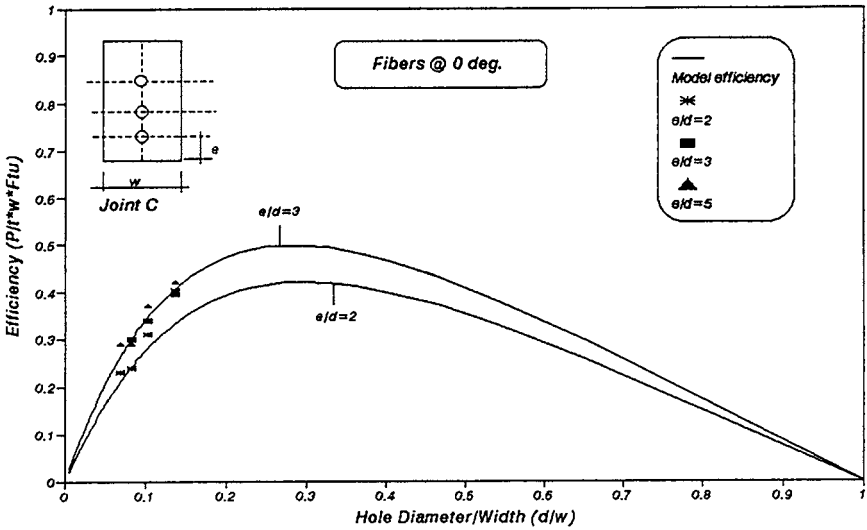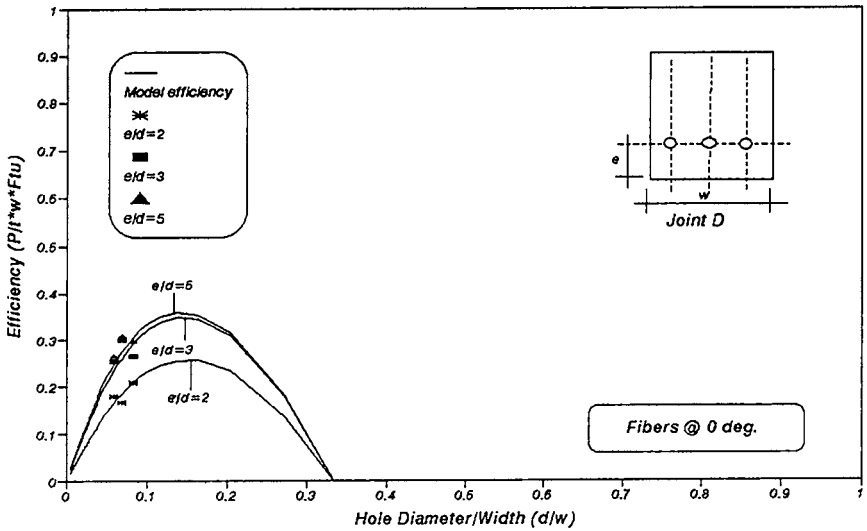Source: Hassan (1994), courtesy of Dr. Nahla Hassan.
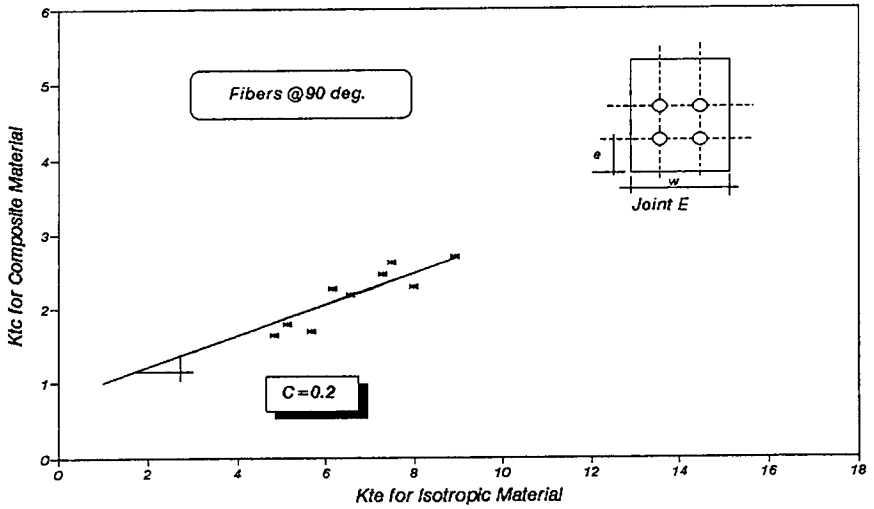
Figure 3-37. Correlation factor, C, for joint type E at 90-degree fiber orientation.
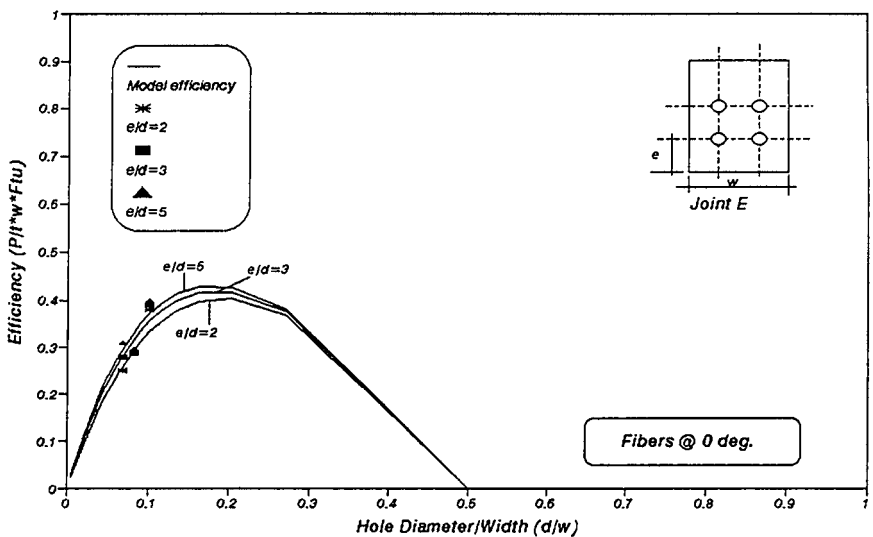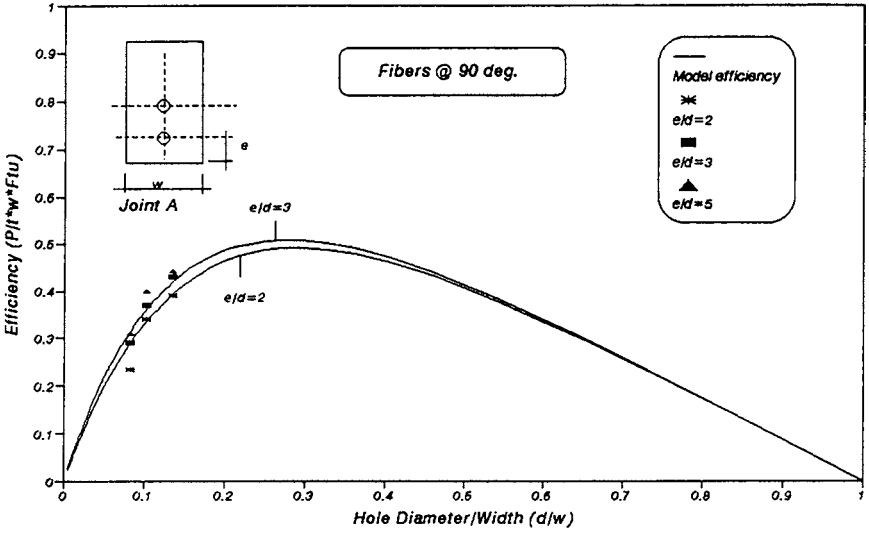*Source: Hassan (1994), courtesy of Dr. Nahla Hassan.*
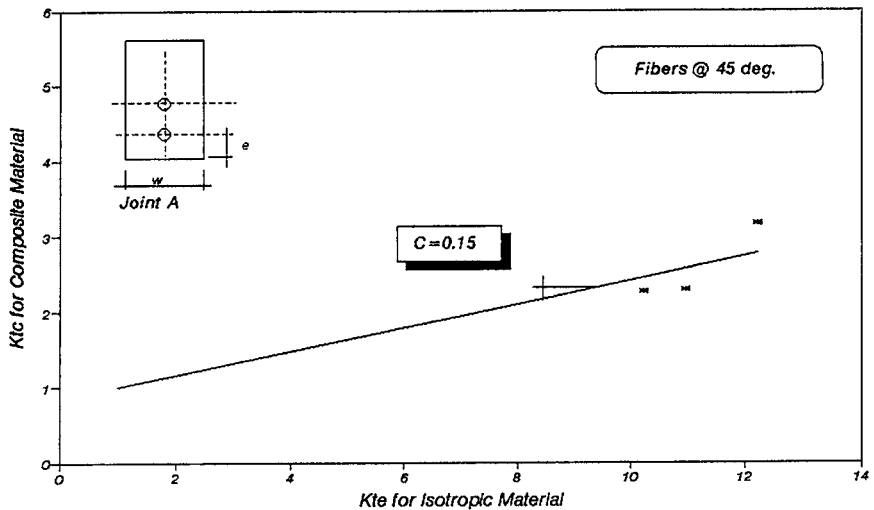
Figure 3-38. Correlation factor, C, for joint type A at 45-degree fiber orientation.
Source: Hassan (1994), courtesy of Dr. Nahla Hassan.

or

$$\eta = \left(1 - \frac{d}{p}\right)$$
(3-54)

When $\dfrac{d}{p}$ approaches unity, the joint efficiency approaches zero for both elastic and plastic materials (refer to Fig. 3-39). Also, when the spacing between fasteners, p, is very large as compared to the hole diameter, i.e., $\dfrac{d}{p}$ approaches zero, then joint efficiency reaches its maximum.

Using the stress concentration factor, k_{tc}, and the correlation factor, C, described in Eq. 3-13, the efficiency of a multi-bolted composite joint can be expressed as:

$$\eta = \left(1 - \frac{nd}{w}\right) k_{tc}^{-1}$$
(3-55)

or

$$\eta = \frac{1}{[1 + C(k_{te} - 1)]}\left(1 - \frac{nd}{w}\right)$$
(3-56)
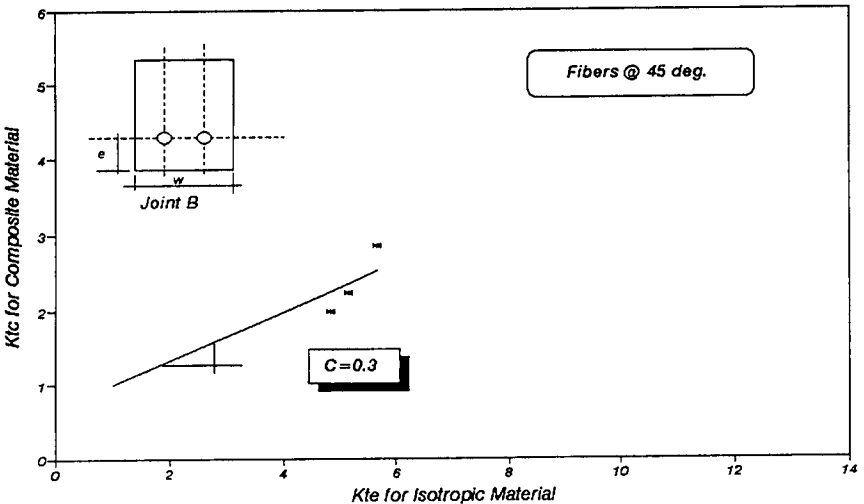
Figure 3-39. Correlation factor, C, for joint type B at 45-degree fiber orientation.
Source: Hassan (1994), courtesy of Dr. Nahla Hassan.

and the ultimate net-tension load can now be expressed as:

$$P_{u/t} = \eta(F_{tu}tw) \tag{3-57}$$

Using Eq. 3-57, a family of failure envelope curves, as a function of the joint efficiency, η, and the d/w ratio was generated (Hassan 1994). The failure envelope curves for five different details of multi-bolted pultruded joints, loaded in the pultrusion direction, are shown in Figs. 3-40 through 3-44. The failure envelope curves for different joint details loaded at 90-degree and 45-degree angles with respect to the pultrusion axis are shown in Figs. 3-45 through 3-49 and Figs. 3-50 and 3-51, respectively. It should be noted that each envelope is developed for a constant e/d ratio. As shown in these figures, the efficiency of all joint details approaches zero as the nd/w (or d/p) ratio approaches unity.

3.6.2.4 Reduction Factor (ψ) for Cleavage Failure of Multi-Bolted Composite Joints   Similar to the approach presented in Section 3.2.1.3, Hassan (1994), based on the experimental results, reported that the joint failure mode was in net-tension for all multi-bolted joint details with e/d
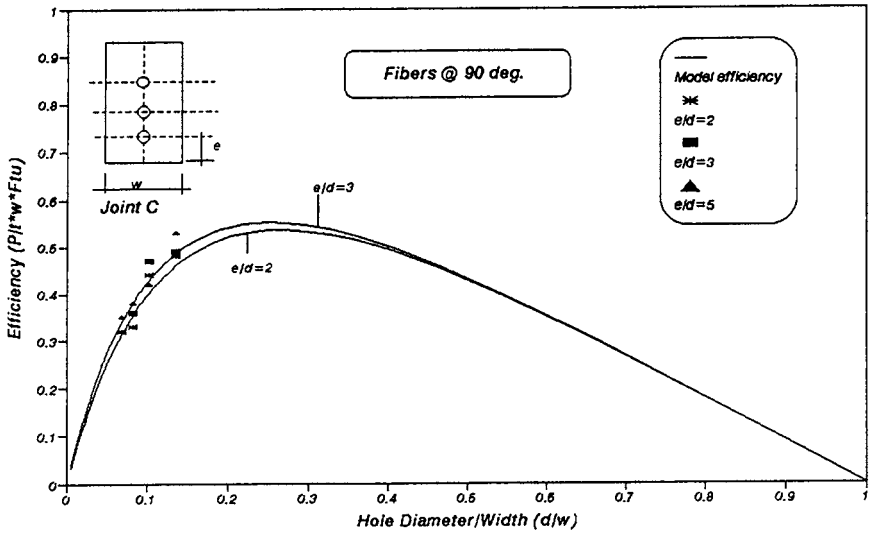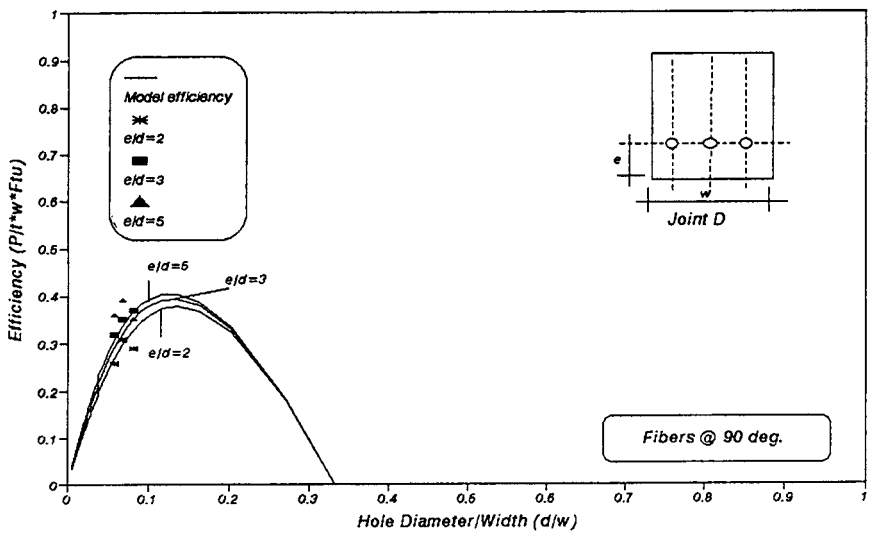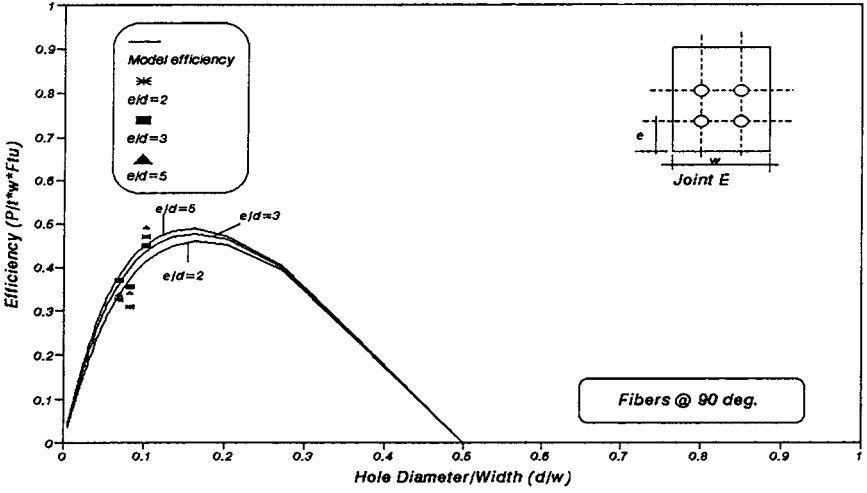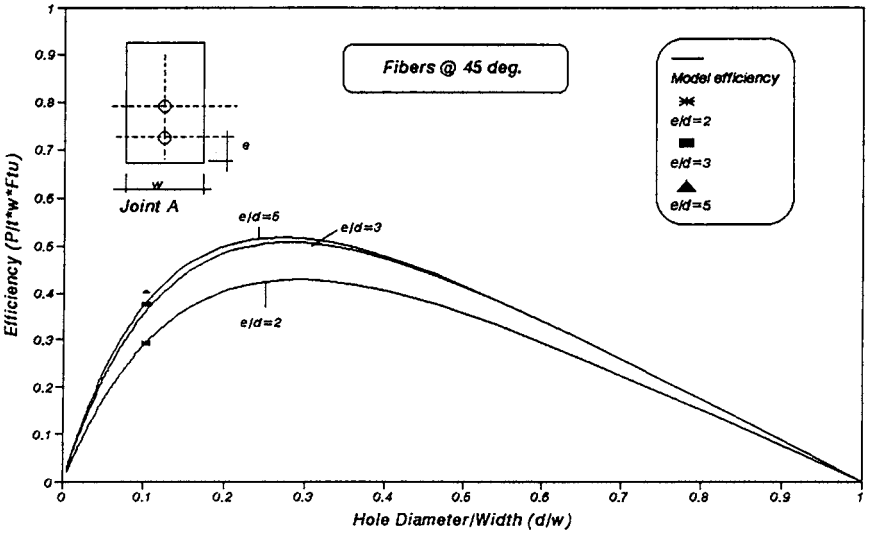

Figure 3-40. Failure envelope for pultruded joint type A at 0-degree fiber orientation.
Source: Hassan (1994), courtesy of Dr. Nahla Hassan.

Figure 3-41. Failure envelope for pultruded joint type B at 0-degree fiber orientation.
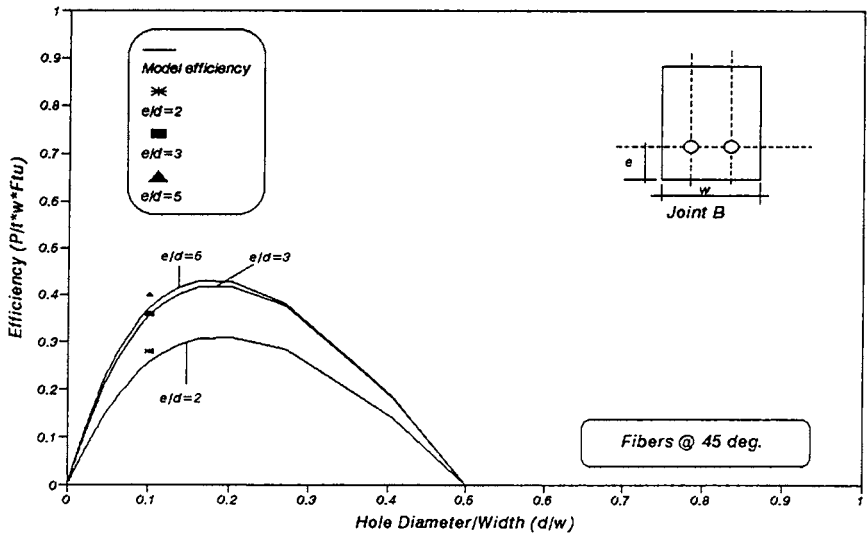*Source: Hassan (1994), courtesy of Dr. Nahla Hassan.*

Figure 3-42. Failure envelope for pultruded joint type C at 0-degree fiber orientation.
Source: Hassan (1994), courtesy of Dr. Nahla Hassan.

Figure 3-43. Failure envelope for pultruded joint type D at 0-degree fiber orientation.
Source: Hassan (1994), courtesy of Dr. Nahla Hassan.

Figure 3-44. Failure envelope for pultruded joint type E at 0-degree fiber orientation.
Source: Hassan (1994), courtesy of Dr. Nahla Hassan.

Figure 3-45. Failure envelope for pultruded joint type A at 90-degree fiber orientation.
Source: Hassan (1994), courtesy of Dr. Nahla Hassan.
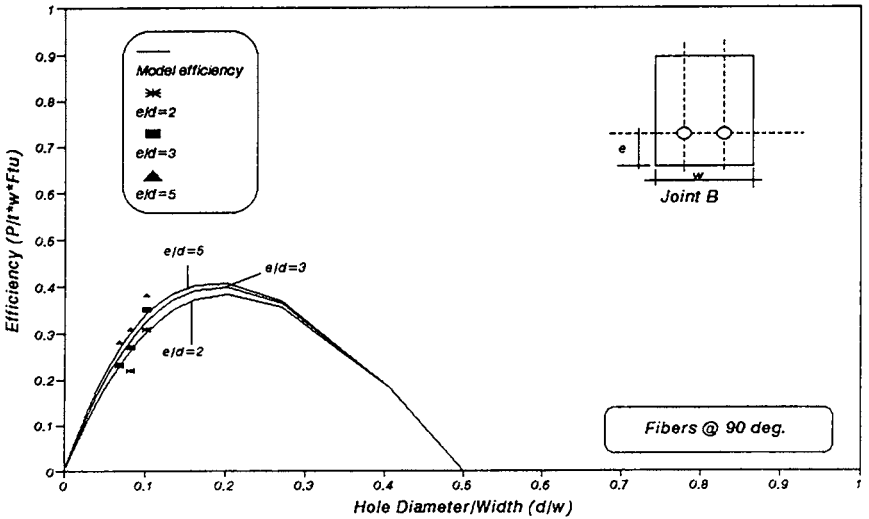
Figure 3-46. Failure envelope for pultruded joint type B at 90-degree fiber orientation.
Source: Hassan (1994), courtesy of Dr. Nahla Hassan.

Figure 3-47. Failure envelope for pultruded joint type C at 90-degree fiber orientation.
Source: Hassan (1994), courtesy of Dr. Nahla Hassan.

Figure 3-48. Failure envelope for pultruded joint type D at 90-degree fiber orientation.
Source: Hassan (1994), courtesy of Dr. Nahla Hassan.

Figure 3-49. Failure envelope for pultruded joint type E at 90-degree fiber orientation.
Source: Hassan (1994), courtesy of Dr. Nahla Hassan.

Figure 3-50. Failure envelope for pultruded joint type A at 45-degree fiber orientation.
Source: Hassan (1994), courtesy of Dr. Nahla Hassan.

Figure 3-51. Failure envelope for pultruded joint type B at 45-degree fiber orientation.
Source: Hassan (1994), courtesy of Dr. Nahla Hassan.

ratio greater than 3 ($e/d > 3$). Based on this fact, the reduction factor, ψ, should reduce to unity when $e/d = 3$. To enforce this condition, the constants in the ψ-factor expression must be computed based on the observed limiting conditions.

Following the same approach described in Section 3.2.1.3 for single-bolted pultruded joints, the following expression for ψ is developed:

$$\psi = \left(\frac{6}{5} - \frac{3}{5}\frac{d}{e}\right)^2 \tag{3-58}$$

A general expression that characterizes cleavage failure is the cleavage reduction factor (ψ):

$$\eta = \frac{1}{[1 + C(k_{te} - 1)]}\left(1 - \frac{nd}{w}\right)\left(\frac{6}{5} - \frac{3}{5}\frac{d}{e}\right)^v \tag{3-59}$$

where
$v = 2$ for joints with single row of bolts column [e.g., joint details B and D (Hassan 1994)]. (In this case, e/d ratio has a great effect on their ultimate load capacity.)

v = 1 for joints with multiple bolt row in a single column [e.g., joint details A and C (Hassan 1994)]. (In this case, e/d ratio has a small effect on their ultimate load capacity.)

v = 0 for joints with two rows and two columns of bolts [e.g., joint details A and C (Hassan 1994)]. (In this case, the e/d ratio has *no* effect on their ultimate load capacity, and the failure mode is net-tension regardless of the value of the e/d ratio.)

3.6.2.5 Effect of Fiber Architecture on the Strength of Multi-Bolted Composite Joints   Hassan (1994) reported that all joint specimens loaded at 90 degrees to the pultrusion direction failed in net-tension mode along the most stressed bolt row regardless of the value of e/d ratio. It was also found that changing the load direction from 0 degrees to 90 degrees with respect to the pultrusion direction results in a lower value of C and more ductile behavior. This ductile behavior may be attributed to the fact that in the 90-degree direction the majority of the bypass load is resisted by the continuous strand mat (CSM), which has multidirectional strength that behaves similarly to isotropic materials. However, these joints exhibit a lower ultimate capacity as compared to those loaded parallel to the pultrusion direction. Due to the lower value of the F_{tu} in the 90-degree direction, the efficiency in this case is higher than that loaded parallel to the pultrusion direction. Based on this fact, the failure envelopes predicted for joints loaded in the pultrusion direction can be used conservatively to predict the strength of multi-bolted pultruded joints loaded in any other direction.
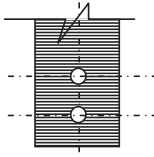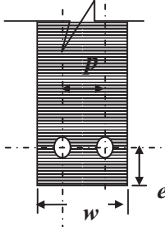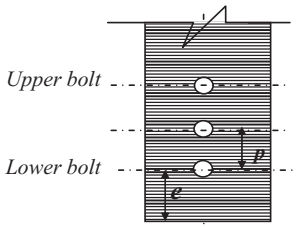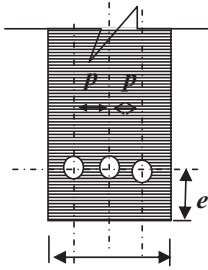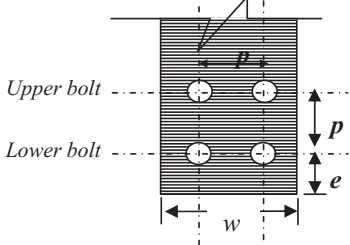
When joints are loaded at a 45-degree angle with respect to the pultrusion axis, the failure mode is shown to be dependent on the e/d ratio. For example, when e/d ratio is greater than 3 ($e/d > 3$), the failure mode is net-tension, while the cleavage mode of failure occurs when the e/d ratio is smaller than 3 ($e/d < 3$).

3.6.2.6 Design and Analytical Procedure Summary   The design and analytical procedure is as follows:

1. Using the pultruded joint basic information and Eq. 3-17 for net-section tension failure, and Eqs. 3-36 and 3-37 for cleavage and bearing failures, respectively, three values for η can be calculated.
2. Select the lowest η value calculated in Step 1 as the governing joint efficiency.
3. Use Eq. 3-35 to calculate the ultimate loading capacity of the joint.
4. The expected load of failure of the joint corresponds to the failure mode associated with the lowest η value calculated in Step 2.

The analysis also can be performed using the computer code BOLT.EXE described earlier (the source code of the program and user's instructions

Table 3-6. Values of the Correlation Factor, C,
for 90-Degree Fiber Orientation

Joint Identifier	Joint Detail	C
A		0.15
B		0.35
C		0.11
D		0.36
E		0.20

Source: Hassan (1994), courtesy of Dr. Nahla Hassan.

are provided on the ASCE Construction Institute Web site, http://www.
constructioninst.org). The code calculates the joint efficiency and joint
capacity, and determines the expected mode of failure. However, the joint
configurations that can be handled by this code are limited to those
described in Table 3-6.

3.7 GENERAL DESIGN CONSIDERATIONS

In designing any composite joint, the structural engineer should con-
sider the following issues as prerequisites to the composite joint design:

1. Establish the desired maximum service load and the required factor
   of safety.
2. Determine the controlling design variables, including expected
   service life, loading type (static versus fatigue), creep, thermal envi-
   ronments, and other expected environmental exposures; and estab-
   lish the appropriate safety margins (knock-down factors).
3. Consider the thermo-mechanical mismatch when joining compos-
   ites with other materials (e.g., when joining FRP composite deck
   with a steel stringer) or when the two joined members are made of
   different thicknesses, different fiber architecture, or different materi-
   als types of composites (e.g. E-glass/polyester with carbon/epoxy).
4. Determine the joint mode of failure and loading conditions.
5. Determine the effect of combined loading conditions on bolted joint
   allowable, where the allowable is a statistical expression of strength
   where 90% of the scattered experimental data exceeds a given value
   with an accuracy of 95%.

The design should be modified if the joint analysis shows the joint
failing load to be less than or equal to the joint design load (design load
is defined as the product of the maximum anticipated load multiplied by
the established factor of safety).

3.8 RULES OF THUMB FOR DESIGNING BOLTED COMPOSITE JOINTS

Hart-Smith (1996) recommends that these rules of thumb be followed
in designing bolted composite joints:

1. Design the joint first and fill the gaps afterward. Optimizing the
   "basic" structure first compromises the joint design and could
   result in low overall structural efficiencies.

2. The best bolted joint can barely exceed half the strength of unnotched laminates.
3. Optimum single-row joints have approximately 75% of the strength of optimum four-row joints.
4. Joints designed to fail in tension are stronger than those designed to fail in bearing.
5. Many bolted composite joints contain too few bolts, spaced too far apart, with a too-small diameter to permit maximizing the load carried by the laminate.
6. Rated shear strength of mechanical fasteners should not be a factor in design. Bolts need to be sized to restrict bearing stresses in the laminates.
7. Peak hoop tension stress around bolt holes is roughly equal to the average bearing stress.
8. Bolt bearing strength is sensitive to through-the-thickness clamp-up.
9. Bolt bending is much more significant for composites as compared to metals because, for a given load, composite members are thicker and are more sensitive to non-uniform bearing stresses due to the brittle failure mode.
10. Bolted joint strength varies far less with the percentage of 0-degree plies in the fiber pattern than does the unnotched laminate strength.
11. The best fiber patterns are fully interspersed (parallel plies not bunched together) and have at least 12.5% of the plies in each of the four directions of 0 degrees, +45 degrees, −45 degrees, and 90 degrees.

REFERENCES

Abd-El-Naby, S. F. M., and Hollaway, L. (1992). "The experimental behavior of bolted joints in pultruded glass/polyester material. Part 1: Single-bolt joints." *Composites*, 24(7), 531–538.

Agarwal, B. L. (1980a). "Behavior of multi-fastener bolted joints in composite material." *Proc., AIAA 18th Aerospace Science Meeting*, Paper No. 80-0307, Reston, Va.

ASTM International (ASTM). (2002). *MIL 17 handbook: The composite materials handbook*, ASTM International, West Conshohocken, Pa.

Chamis, C. C. (1990). "Simplified procedures for designing composite bolted joints." *J. Reinf. Plastics and Composites*, 9, 614–626.

Crews, J. H., and Naik, R. A. (1986). "Combined bearing and bypass loading on a graphite/epoxy laminate." *Composite Struct.*, 6, 21–40.

Dastin, S. J. (1986). "Repairing Advanced Composite Materials," *Machine Design*, vol. 58, No. 4, pp. 86–90, Penton Media, Cleveland, Ohio.

Hart-Smith, L. J. (1978). "Mechanically fastened joints for advanced composites—Phenomenological considerations and simple analysis." *Proc., 4th Int. Conf. on Fibrous Composites in Structural Design*, Plenum Press, New York, pp. 543–574.

Hart-Smith, L. J. (1985). "Joints." *Engineering materials handbook*, *Vol. 1, Composites*, ASTM International, West Conshohocken, Pa,.

Hart-Smith, L. J. (1989). "The design of efficient bolted and riveted fibrous composite structures," *Paper 8335,* Douglas Aircraft Company, Long Beach, Calif.

Hart-Smith, L. J. (1994). "The key to designing efficient bolted composite joints." *Composites*, 25(8), 835–837.

Hart-Smith, L. J. (1996). "Design and analysis of bolted and riveted joints in fibrous composite structures." *Paper 121*, McDonnell Douglas Corp., St. Louis, Mo.

Haruna, K., and Hamada, H. (1996). "Designing of mechanically fastened joints in composite structures." *Proc., 51st Annual Conf. of the Composites Institute*, Society of the Plastics Industry, Washington, D.C.

Hassan, N. K. (1994). "Evaluation of multibolted connections for GFRP members." Ph.D. dissertation, Dept. of Civil Engineering, University of Manitoba, Winnipeg, Canada.

Hassan, N. K., Mohamedien, M. A, and Rizkalla, S. H. (1997). "Rational model for multibolted connections for GFRP members." *ASCE J. Composites for Const.*, 1(2), 71–78.

McCarthy, C. T., McCarthy, M. A., and Lawlor, V. P. (2005). "Progressive damage analysis of multi-bolt composite joints with variable bolt-hole clearances." *Composites Part B: Eng.*, 36(4), 290–305.

Mosallam, A. S. (1999). "Cyclic behavior of FRP interior frame connections for pultruded structures." *Proc., 5th Materials Congress*, ASCE, Reston, Va., pp. 84–91.

Mosallam, A. S., Abdel Hamid, M. K., and Conway, J. (1993). "Performance of pultruded FRP connections under static and dynamic loads." *J. Reinf. Plastics and Composites*, 13, 386–407.

Mottram, J. T., and Turvey, G. J. (2003). "Physical test data for the appraisal of design procedures for bolted joints in pultruded FRP structural shapes and systems." *Prog. Struct. Eng. Mat.*, 5(4), 195–222.

Prabhakaran, R., Razzaq, Z., and Devara, S. (1996). "Load and resistance factor design (LRFD) approach for bolted joints in pultruded composites." *Composites Part B: Eng.*, A. Mosallam et al., eds. 27B(3–4), Infrastructure Special Issue, pp. 351–360.

Pyner, G. R., and Matthews, F. L. (1979). "Comparison of single and multi-holed bolted joints in glass fiber-reinforced plastics." *J. Composite Mat.*, 13(7), 232–239.

Ramkumar, R. L., and Tossavainen, E. W. (1984). "Bolted joints in composite structures: Design, analysis and verification, task I test results—

single fastener joints," *AFWAL-TR-84–3047*, Wright Aeronautical Laboratories, Wright Patterson Air Force Base, Ohio.

Rosner, C. N. (1992). "Single-bolted connections for orthotropic fiber-reinforced composite structural members." M.S. thesis, University of Manitoba, Winnipeg, Canada.

Rosner, C. N., and Rizkalla, S. H. (1995). "Bolted connections for fiber-reinforced composite structural members: Experimental program." *J. Mat. Civil Eng.*, 7(4), 223–231.

Tang, S. (1981). "Failure of composite joints under combined tension and bolt loads." *J. Composite Mat.*, 15(7), 329–335.

This page intentionally left blank

CHAPTER 4

STRUCTURAL ADHESIVES

4.1 INTRODUCTION

"Adhesive" is a general term used for substances (e.g., cement, glue, and paste) capable of holding materials together by surface attachment (Mays and Hutchinson 1992). Adhesion is associated with intermolecular forces acting across an interface and involves a consideration of surface energies and interfacial tensions. The materials being joined are referred to as the "adherends" or "substrates."

Adhesives offer several advantages for joining pultruded composite members:

1. More uniform distribution of joint stresses
2. Larger stress-bearing areas
3. Superior fatigue and impact resistance
4. High strength-to-weight ratios
5. Comparatively rigid connections
6. The ability to join dissimilar materials (with appropriate surface treatment)

There also are some limitations for the use of structural adhesives in joints:

1. Difficulties in ensuring a good standard of surface pretreatment
2. Difficulties in verifying the integrity of bonded joints (inspection procedures)
3. Long curing times and a need to provide temporary support during curing

4. Special storage requirements
5. Potentially short pot life (working life)

Table 4-1 lists the advantages and limitations of adhesive bonding. Continued development of improved formulations aimed at facilitating their use strongly suggests that adhesives will increasingly be considered a preferred method of connecting structural composites. This chapter introduces several considerations for the selection and design of adhesives used with pultruded composites.

4.2 MECHANICS OF ADHESION

Once the interfacial contact between the adhesive and the adherend is developed under favorable thermodynamic conditions, adhesive curing enables the stress transfer. Currently, there are four main theories of adhesion:

1. Mechanical interlocking
2. Absorption

Table 4-1. Advantages and Disadvantages of Adhesively Bonded Joints

Advantages	Limitations
• Can join dissimilar adherends • Can efficiently join thin adherends • Can produce uniform shear stress distribution at the interface that indirectly enhances the composite bonded joint fatigue resistance • Can produce a smooth, unaltered finished surface • Bond line acts as a sealant • Eliminates need for field equipment for hole drilling, sealing, and torque application • Produces lighter structure as compared to bolted joints	• Requires proper surface pretreatment • Cannot be used with all polymers (e.g., polyethylene is practically impossible to connect by adhesives) • Requires proper design and testing • Requires long cure time and special curing conditions of pressure, temperature, and humidity control to promote cure and strength development of the adhesives • Sensitivity to moisture, elevated temperature, fire, and subzero temperature exposure • Sensitivity to sustained loads, especially at higher temperatures • Flammability and smoke toxicity during fire of some adhesives, such as epoxies

3. Diffusion
4. Electrostatic

Among these four theories, the absorption mechanism is generally favored. Detailed discussions of these theories can be found in the literature (e.g., Brewis 1985; Wake 1989).

4.3 FACTORS AFFECTING THE CAPACITY AND INTEGRITY OF ADHESIVELY BONDED JOINTS

Several factors may affect the capacity and integrity of an adhesively bonded joint:

1. Surface preparation
2. Mechanical properties of the adhesive and adherends
3. Thickness of the adhesive and adherends
4. Joint geometries
5. Service conditions

4.4 IMPORTANT ADHESIVE PROPERTIES

The majority of civil engineers have little experience in selecting appropriate adhesives. This section describes properties of adhesives—in their unmixed, mixed, curing, and hardened states—that should be considered when specifying an adhesive system.

1. *Unmixed State (Shelf Life):* As with any chemical materials, there is a period during which the unmixed adhesive components may be stored without undergoing significant deterioration. This period is often called "shelf life." Most commercially produced structural adhesives have an average shelf life ranging from 6 months to several years. The specified shelf life may be prolonged by storing the adhesives at low temperature (e.g., in refrigerators). Depending on the application schedule and the expected construction delays, the engineer and/or the contractor should estimate the ordering time of adhesives and ensure that no material is used at or after the specified expiration date provided by the manufacturer or supplier.
2. *Freshly Mixed State:* The engineer should evaluate the following properties of mixed adhesives:
   a. *Viscosity:* For ease of spreading, a viscosity range of between 20 and 150 Pa at a shear rate of 10^{-1} is recommended. When

adhesives are applied on a vertical surface, a yield stress of at least 20 Pa is required. It should be noted that the viscosity of the adhesives is altered by changing the ambient temperature and by the addition of fillers. Figure 4-1 illustrates the influence of temperature and filler content on adhesive flow curves (Mays and Hutchinson 1992).

b. *Usable Life (Pot Life):* The cross-linking process starts as soon as the resin and the hardener of a room-temperature-cure adhesive are mixed. The rate of cross-linking, and consequently hardening, depends on both the reactivity of the adhesive formulation and the mobility of the molecules. The pot life of an adhesive defines the workability limit, while the "gel time" defines the point at which solidification commences. In many cases, the pot life and the gel time are very similar. However, the engineer is more interested in the pot life.

c. *Wetting Ability:* The ability of an adhesive to wet a substrate surface is essential to develop the adhesion process. Adhesives applied toward the end of their pot life tend to lack wetting ability.

d. *Joint Open Time:* The joint open time starts as soon as the adhesive is applied to the composite parts. It represents the time limit during which the joint should be closed; otherwise, an appreciable reduction in the adhesive bond strength may result. Joint open time may be reduced at higher temperature and higher relative humidity.

3. *Curing State:* The impact of surrounding temperature on the curing process varies from one adhesive to another. In general, the curing time is inversely proportionate to the surrounding temperature. The curing time is reduced at higher temperatures, while a colder environment will result in a prolonged curing time. In fact, many epoxies stop curing below 41 °F (5 °C) unless a special formulation designed for the colder environment is used. Figure 4-2 illustrates the effect of formulation and cure temperature on the flexural strength development of two-part epoxy adhesives. Figure 4-3 shows a typical cure temperature–time relationship for one-part toughened epoxy. The civil engineer should provide adequate environmental information to the manufacturer in order to specify the appropriate adhesive system. It should be noted that manufacturers can custom-design adhesives for different environments (Fig. 4-2).

4. *Hardened State*: The mechanical properties of a structural adhesive in the hardened state are related to its internal structure, including the molecular interactions of the adhesive system. It should be noted that, if the internal structure of the adhesive is modified to change certain mechanical properties (e.g., strength, stiffness, and
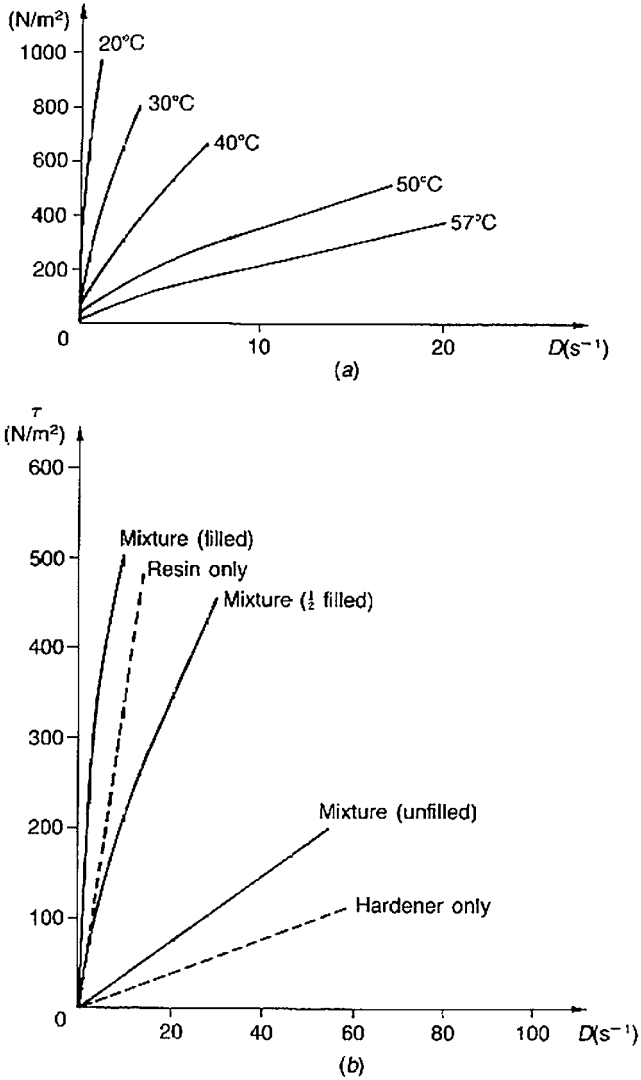
Figure 4-1. Influence of temperature and filler content on adhesives flow curves. A, Temperature effect on one-part hot-cure toughened epoxy; B, filler content effect on three-part flexibilized epoxy polyamine.
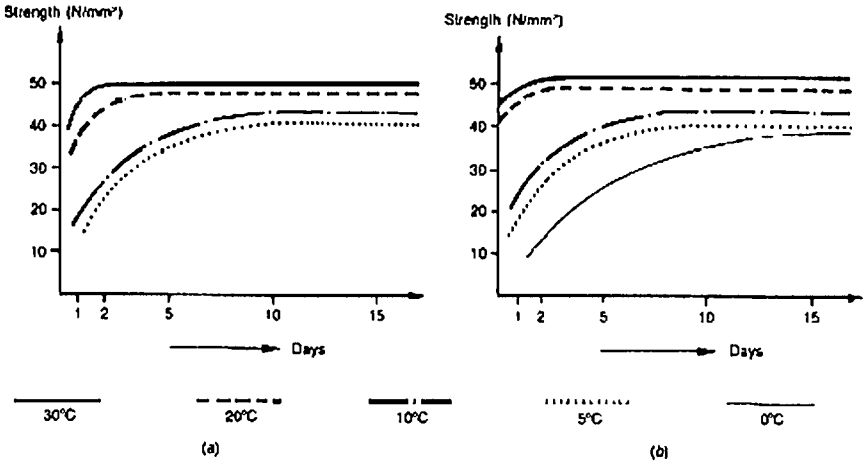*Source: Mays and Hutchinson (1992), reprinted with the permission of Cambridge University Press.*

Figure 4-2. *Effect of formulation and cure temperature on flexural strength development of two-part epoxy adhesives. A, Normal type; B, rapid-cure type. Source: Mays and Hutchinson (1992), reprinted with the permission of Cambridge University Press.*
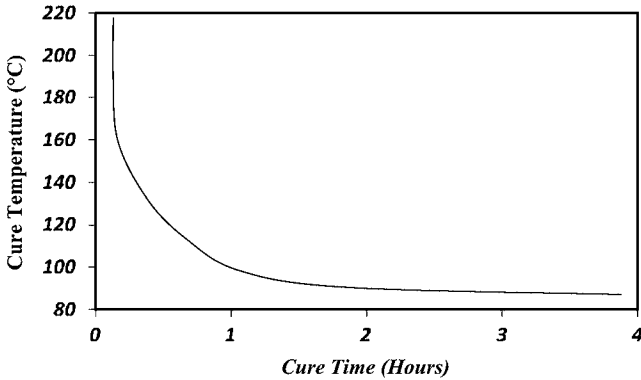
Figure 4-3. *Cure temperature vs. time relationship for one-part epoxy.*

toughness), this will be at the expense of reducing other properties. For example, if the desired property is higher toughness, the trade-off will be lower stiffness. For this reason, the engineer should set the required criteria for the application before specifying the adhesive system. In other words, be aware of the impact of requiring a higher value for one property on the other structural properties of the adhesive system under consideration. The mechanical properties of adhesives at the hardened state are usually provided by the

manufacturer. However, the engineer may require verification tests for some critical properties for both short- and/or long-term behavior of the specified adhesive system.

Figure 4-4 shows a typical test specimen used to evaluate the tensile, shear, and flexural strength of hardened adhesives (Mays and Hutchinson
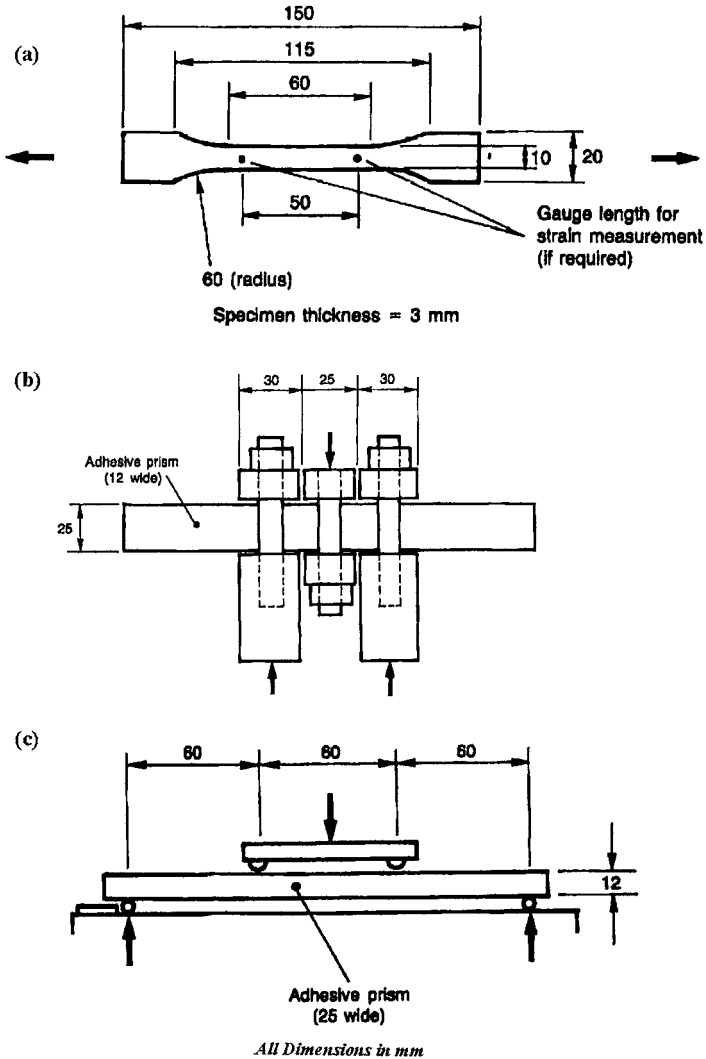
Figure 4-4. Typical adhesives tests. A, Tensile specimen; B, shear box test on adhesive prism; and C, flexural test on adhesive prism.
Source: Mays and Hutchinson (1992), reprinted with the permission of Cambridge University Press.

1992). A typical tensile stress-strain curve for a range of epoxy adhesives is shown in Fig. 4-5. Chapter 7 of the *MIL-17 Handbook* (ASTM 2002) contains detailed information on mechanical testing of adhesively bonded joints.

Fracture toughness is another property that the engineer should evaluate when using adhesives, especially in seismic zones and for structures subjected to vibration and dynamic loading. For the hardened state, the engineer should also determine the state of the surrounding service environment and the expected temperature variation. One of the physical properties that should be evaluated is the glass-transition temperature (T_g), which, for any polymer, is defined as the specific temperature at which the polymers change from a relatively rigid, "glass-like" substance to a relatively viscous, "rubbery" material. This transition temperature varies from one adhesive to another and depends on several factors, including the polymer molecular weight, adhesive curing temperature, and rate of loading if the measurement process involves mechanical deformation.

One of the most convenient methods of measuring T_g is using a differential scanning calorimeter (DSC), as shown in Fig. 4-6. For engineers, quasi-static mechanical methods using a flexural test on a hardened
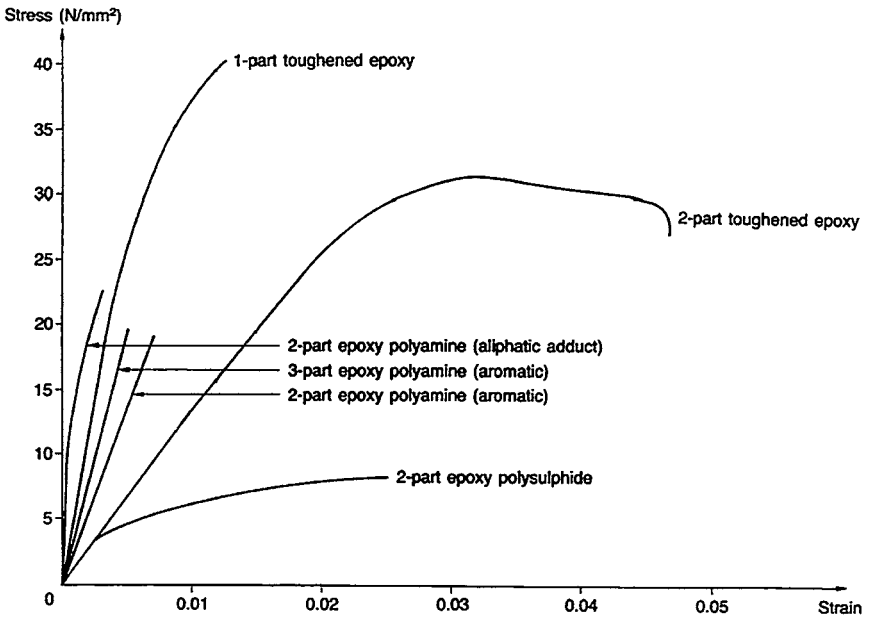
Figure 4-5. Typical tensile stress–strain curves for a range of epoxy adhesives. Source: Mays and Hutchinson (1992), reprinted with the permission of Cambridge University Press.
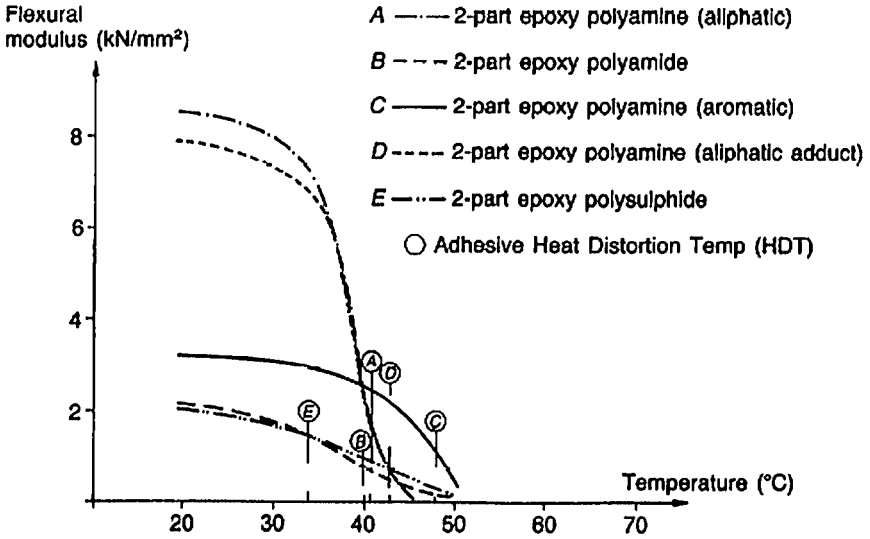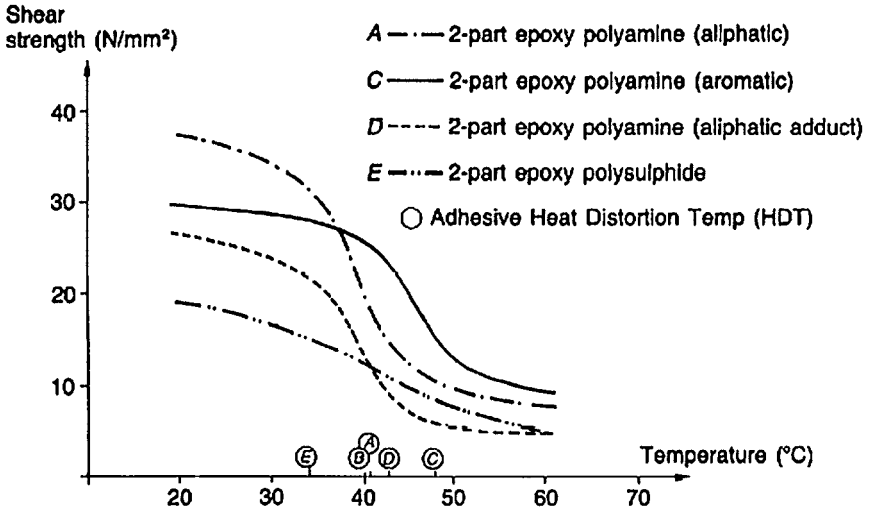
*Figure 4-6. Temperature dependence of bulk adhesive flexural modulus.
Source: Mays and Hutchinson (1992), reprinted with the permission of
Cambridge University Press.*

Table 4-2. Heat Distortion Temperatures of Cold-Cure Epoxies

Adhesive Type	HDT (°C/°F)
Two-part cold-cure polyamide	40/104
Two-part cold-cure polyamine (aliphatic)	41/105.8
Two-part cold-cure polyamine (aliphatic adduct)	43/109.4
Two-part cold-cure polyamine (aromatic)	48/118.4
Two-part cold-cure polysulphide	34/93.2

HDT, heat distortion temperature.

adhesive prism are more convenient for determining the heat distortion
temperature (HDT). It should be noted that the results of such quasi-static
methods are good only for comparative purposes since the results of these
tests depend on the specimen configuration and the selected rate of
loading. Table 4-2 presents typical values for HDT for cold-cure epoxies.
As shown in Table 4-2, the HDT values range from 93.2 °F to 118.4 °F (34
°C to 48 °C), which, in many cases, will be exceeded, especially when the
composite joints or composite/metallic bonded joints are directly exposed
to high temperatures. In these cases, the engineer may evaluate the use
of a one-part hot cure epoxy product with a T_g value of 212 °F (100 °C).
Figures 4-7 and 4-8 illustrate the temperature effect on the bulk adhesive
flexural modulus and bulk adhesive shear strength, respectively.

Figure 4-7. Temperature dependence of bulk adhesive shear strength.
Source: Mays and Hutchinson (1992), reprinted with the permission of
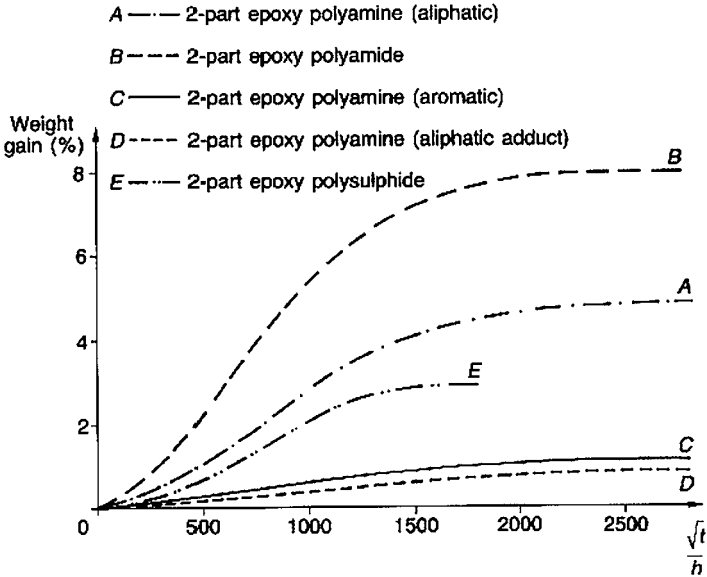*Cambridge University Press.*

Figure 4-8. Water uptake plots for a range of epoxy adhesives.
Source: Mays and Hutchinson (1992), reprinted with the permission of
Cambridge University Press.

Another important factor that needs to be considered by the structural engineer when specifying a structural adhesive is the possibility of water or water vapor attacks. All adhesives are sensitive to exposure to water or water vapors (except those specifically formulated for underwater applications). The water uptake is accommodated to a large extent by swelling.

To measure the water uptake properties of a structural adhesive, a thin-film adhesive specimen may be immersed in water at a known temperature or stored in an environmental humidity chamber where the humidity and temperature are controlled for a specified time. The water uptake is then measured after a specified exposure time and the fractional uptake is plotted against the square root of time per unit thickness, as shown in Fig. 4-9. The strength loss of composite bonded joints due to water exposure may be dictated by adhesive plasticization or by displacement of the adhesive from the substrate due to water "wicking" along the interface, or by both indications (Mays and Hutchinson 1992).

Like other polymers, adhesives are viscoelastic materials and are susceptible to "creep." The engineer should be aware of this property when estimating the long-term stiffness of composite bonded joints. Creep is a phenomenon of movement, strain, or deformation in excess of the normal movement that results from the elastic qualities of the bonded joint. There are three creep stages, as shown in Fig. 4-10: (1) primary creep (1st stage); (2) secondary creep (2nd stage); and (3) tertiary (3rd stage) or creep rupture. It should be noted that creep curves obtained from bulk hardened adhesive specimens do not necessarily compare with those obtained from bonded composite joints under similar stress and environmental conditions due to the nature of adherend restraint.
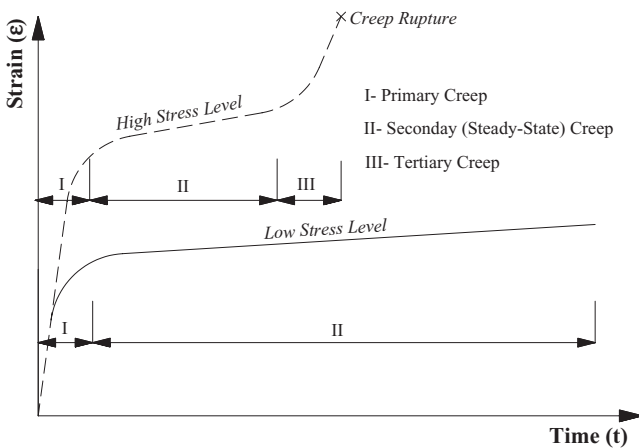

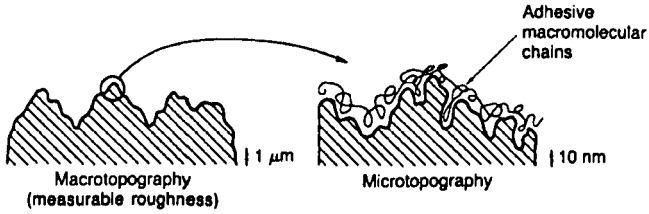*Figure 4-9. Typical creep and creep rupture time curves.*

Figure 4-10. Schematic topography of solid surfaces.
Source: Mays and Hutchinson (1992), reprinted with the permission of
Cambridge University Press.

Creep rates of adhesives follow exponential laws similar to those of stress-rupture analysis (Lubin 1982). Generally, the creep rate, $\dot{v}$, of an adhesive can be expressed by the following equation:

$$\dot{v} = Ae^{\frac{-Q}{RT}} \tag{4-1}$$

where
A, Q = constants dependent on stress level and material properties
R = gas constant
T = temperature in the joint.
Brittle (e.g., high shear modulus) adhesives are less sensitive to creep as compared to ductile adhesives. In general, the more highly cross-linked the hardened adhesive structure and the higher the curing temperature, and hence the higher the T_g, the better the creep resistance (Mays and Hutchinson 1992).

In addition to moisture, three major factors that affect the creep of adhesives are stress, time, and temperature. Generally, high levels of stress are accompanied by high rates of creep; thus, the higher the level of stress, the greater the rate of creep. As the temperature increases (above ambient temperature), the creep rate increases with a greater rate when T_g is reached. As mentioned earlier, the T_g is sensitive to the rate of loading. For this reason, a "time/temperature superposition technique" was developed to characterize the long-term response of polymers. This technique, initially articulated by Leaderman (1943) and further developed by Findley and Onaran (1976), allows for predicting the long-term creep behavior of a specific adhesive system at different temperatures and loading conditions from relatively short-term test data.

Another important consideration in specifying the structural adhesive system is the fatigue characteristic of the adhesives. This is especially critical when the composite structure is subjected to cyclic or dynamic loading, such as bridges, machinery-supporting floors, and structures subjected to high wind loads.

The fatigue performance of an adhesive is affected by the viscoelastic nature of the material and its resistance to crack propagation, or fracture toughness. When adhesives are subjected to dynamic loads with low frequencies in a high-temperature environment, their viscoelastic effects will predominate their performance in a manner similar to that experienced with creep. Adhesives fracture when subjected to high-frequency dynamic loads coupled with low-temperature environment, due to crack propagation either within the adhesive layer or at the adhesive/substrate interface. In this case, the crack propagation tends to control the number of load cycles that can be resisted by the adhesive prior to failure. In general, the fatigue performance of a structural adhesive in a composite bonded joint is linked to the joint configuration and the stress distribution within the joint. For this reason, this issue is discussed further in Chapter 5.

4.5 GENERAL PROPERTIES OF ADHESIVES AND ADHERENDS

Generally, adhesives used with polymer composites display characteristics similar to the composites they join. Stress–strain characteristics of adhesives are nonlinear, and their mechanical properties are significantly affected by elevated service temperatures and humidity as well as sustained loadings.

Surface preparation plays a dominant role in the reliability of an adhesive bond. Surface properties, such as a composite's wettability and roughness, affect the ability of structural composites to be reliably bonded. Wetting is a measure of an adhesive's ability to spread across a solid surface. Liquids tend to bead on surfaces that have poor wetting characteristics. Materials such as polyethylenes and polypropylenes display poor wettability characteristics and are very difficult to bond. In contrast, plastics such as epoxies and polyesters are readily wetted and bonded. Roughened adherend surfaces usually enhance the performance of an adhesive bond by developing greater mechanical interlock.

Most adhesives display higher compressive and shear capacities than tensile and peel strengths. In addition, most display significantly greater shear than tensile deformations prior to fracture.

As a rule, thinner bond lines are preferred for maximum bond strengths and rigidities. Thinner bond lines are more resistant to cracking when flexed, and they display less creep. They also display lower residual thermal stresses and have a lower probability of adverse inclusions.

Although adhesive joints provide a more uniform stress distribution within the joint as compared to mechanically fastened connections, stress concentrations are still present. The stress concentrations experienced in a simple lap joint are a significant concern in polymer composites. These stresses can induce peeling along the ends of the joints, causing an

interlaminar failure in a laminate. For this reason, it is preferred that adhesively bonded composite parts be designed such that they are stressed parallel to their reinforcement. Maintaining small angles between layers of laminates can also minimize the potential for delaminations.

Adverse peeling loads can be avoided by either providing tapered laps or eliminating eccentricities within the connection by employing a double-lap, scarf, or similar configuration. They can also be avoided by employing mechanical fasteners together with an adhesive.

Another factor in the selection of a joint configuration is the need to choose a joint design in which the component parts are pressed down upon the adhesive rather than slid into position during assembly. With this method there is less likelihood that the adhesive will be pushed out of place.

4.6 SURFACE PRETREATMENT

Surface pretreatment is considered the single most important aspect of the bonding process. Careful attention to surface preparations or pretreatments is critical to the performance of an adhesive connection. To ensure reliable bond strength and durability, production of a roughened surface, cleaned of contaminants (particularly any chemicals, wax, or grease resulting from exposure or after the composite fabrication process), is essential (Taib et al. 2006). Inadequate surface pretreatment is usually the main cause of bonded joint failure. Surface pretreatment is recommended to remove contaminants and weak surface layers. In addition, proper surface pretreatment provides surface conditions that can be more readily bonded. It also can introduce new chemical groups to provide, at least in the case of bonding composites to metal, an oxide layer that is more receptive to the adhesive. Surface preparations and cleaning procedures primarily depend on the materials to be joined (i.e., the nature of the adherends) and the service environment. Most structural composites require comparatively simple surface preparations. A visual appreciation of the effects of pretreatment has been facilitated in particular by electron microscopy in its various forms, examples of which are shown in Fig. 4-11.

In evaluating structural adhesives for use in a specific project, the engineer should understand that the high initial bond strength is generally not as important as the bond long-term durability dictated by the environmental stability of the adherend/adhesive interface. In addition, it should be clear that the surface pretreatment, while largely affecting bond line durability, generally has less effect on the initial strength of the adhesive. Technical publications that address this requirement include Hutchinson (1987), Kinloch (1982; 1983; 1987), and Vinson (1989).

Composite matrix materials that are readily wetted (i.e., most thermosets, epoxies, and polyesters), typically require the removal of

× 20

× 200

× 2000

× 20000
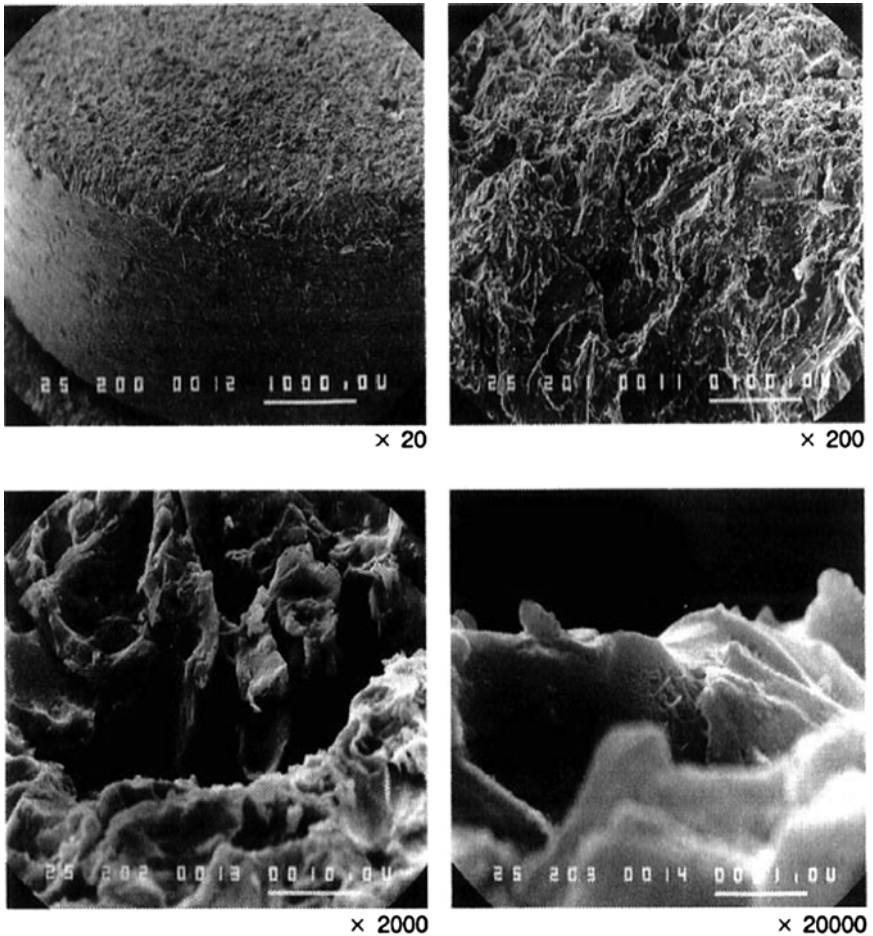
Micron scale shown in bottom r.h. corners

Figure 4-11. Scanning electron micrographs (SEM) of a grit-blasted bright steel bar (surface inclined at 45 degrees).
Source: Mays and Hutchinson (1992), reprinted with the permission of Cambridge University Press.

contaminants (such as mold release agents, oils, and dirt) prior to bonding. The surface preparation for thermoset composites is commonly achieved by minor abrasion or solvent cleaning. In contrast, thermoplastics such as polyethylene and polypropylene cannot be reliably joined by adhesives unless extensive surface treatments are employed.

For composites that can be readily wetted, surface abrasion generally enhances the bond strength. However, for composites that are not readily wetted, surface abrading may have a negligible or possibly adverse

effect on their ability to be bonded. For these composites, surface abrasion may hold an adhesive at the top of roughened areas and inhibit full contact.

Surface preparations are mandatory for most composites. Aside from abrasion to improve mechanical adhesion, surface treatments for composites are basically concerned with the removal of release agents and the formation of higher energy surfaces which are more readily wetted.

Pretreatments for composites are typically more complicated than those employed for the bonding of materials such as wood, metal, or concrete. For example, the use of sandpaper alone to roughen the adherend surface is discouraged. Adhesive used to bond the sand to the sandpaper tends to dislodge and contaminate the surface, thereby negating the benefits of the abrasion. Any abrasion with sandpaper should be followed by a solvent wash (e.g., acetone, methanol, or isopropyl alcohol) of the surface. Caution must be exercised in the selection of a solvent. Some solvents can cause surface crazing or other adverse reactions on particular composites.

Proper surface preparations have a great effect on the performance of adhesively bonded joints. Results of numerous studies have indicated multifold improvements in adhesion when adequate surface preparations have been performed (Brewis 1985). The benefits of surface preparations are most evident when bonding is completed in a timely fashion.

4.7 SELECTION PROCESS

Both the physical and chemical properties of an adhesive and an adherend influence the quality of a bonded joint. To select an adhesive for a particular application from the variety of epoxies and urethanes available, the following criteria must be considered by the engineer:

1. *Substrates:* Select an adhesive that is designed for application to the specific substrates. The following properties should be evaluated:
   a. Thickness
   b. Stiffness
   c. Surface characteristics
   d. Solubility
   e. Thermal properties
2. *Service Environment:* The engineer should evaluate the expected service environment to which the selected adhesive will be exposed, including humidity, temperature, and chemical attacks. In addition, if appropriate for the application, consider whether bonded parts are capable of withstanding immersion in water or other fluids.

3. *Anticipated Stresses*: Select an adhesive that demonstrates the desired peel, tensile, lap shear, and compressive strengths, as well as toughness, needed for the specific application.

4. *Handling/Processing Requirements:* Review the type of surface treatment required for preparing substrates for bonding and decide whether the adhesive will be manually or automatically mixed and dispensed. Also, evaluate the required viscosity of the adhesive system and whether it is appropriate for the mixing and dispensing methods.

5. *Pot Life and Curing*: Consider the size of the bonding project and the desired pot life that will be required for the adhesive system. In addition, evaluate the required cure process for the selected adhesive. A room-temperature-cure system might be preferable to an adhesive that requires application of heat. Conversely, production time may dictate accelerated heat cure.

As a general rule, adhesives are selected that are less rigid than their adherends so that stress concentrations within the joint can be minimized.

The use of standardized questionnaires to guide the designer in the selection of the proper adhesives is recommended. The engineer should work closely with the adhesives manufacturers and seek technical assistance from their engineering departments. Numerous resources for adhesives manufacturers are available on the World Wide Web, where many companies provide detail product information on their specific Web sites.

4.8 TYPES OF ADHESIVES

Principal adhesives used to join structural composites include epoxies, polyurethanes, cyanoacrylates, methacrylates, and solvent cements. These are described in the following sections.

4.8.1 Epoxies

Epoxies are the most commonly employed adhesive for joining rigid structural composites. They display good strength, versatility, and adhesive properties. Epoxies can be formulated or modified through additives and fillers to display a considerable range of properties. The addition of relatively small quantities of elastomeric polymers can produce a substantial increase in their peel and impact strengths. Generally, epoxies display good resistance to adverse environmental conditions and have low shrinkage and creep characteristics.

4.8.2 Polyurethanes

Polyurethane adhesives were first developed in Germany during World War II. Early researchers claimed they could stick "anything to anything." Polyurethanes display high resistance to impact loads, strong resistance to swelling in wet or humid environments, and an ability to remain flexible in low-temperature environments. Undesirable features of polyurethanes include limited capacities at elevated temperatures, poor creep characteristics, and poor aging properties. At temperatures of 150 °F (66 °C), polyurethanes may lose up to 50% of their room-temperature capacities. The use of polyurethanes is not recommended in service temperatures in excess of 248 °F (120 °C). The strength of polyurethane adhesives is sensitive to the thickness of their bond lines. In general, most polyurethane bonds are 0.002 to 0.006 in. (2 to 6 mil) thick.

4.8.3 Cyanoacrylates

Cyanoacrylates are fast-setting adhesives that display high bond strengths between wide varieties of adherends. Cyanoacrylates may be more commonly known as "super glues." Uncured cyanoacrylates are typically clear, watery liquids. Cyanoacrylates exhibit very low viscosities and have very thin bond lines. This may result in inadequate coverage and low bond strengths when used between rough or poorly matched surfaces. Cyanoacrylates also are expensive. Connections using cyanoacrylates are brittle and they display poor heat and moisture resistance. They also are subject to deterioration from exposure to ultraviolet light. As with epoxies, cyanoacrylates can be modified. Fillers and additives can be employed to improve their viscosities and impact, aging, and thermal characteristics. Currently, cyanoacrylates have limited specialty applications within civil engineering.

4.8.4 Methacrylates

Methacrylates are toughened acrylates that have recently evolved as viable structural adhesives. Proprietary blends of methacrylates, polymers, and impact modifiers have been developed that provide adhesives that are competitive with the more commonly used polyurethanes and epoxies (Briggs et al. 1991). These methacrylates offer some distinct advantages over other types of adhesives, including significant improvements in strength and toughness, fast cure rates, and ability to bond to a wide variety of adherends. As compared to other adhesives, methacrylates offer excellent penetration through dirt, oil, and grease, thus reducing surface preparation problems.

4.8.5 Solvent Cements

Solvent cements are composed of a polymerized component that is dissolved or dispersed in an organic solvent or water. The liquid solvent or water lowers the viscosity of the polymerized component in order to promote the adhesive's wetting characteristics. Once wetting has been achieved, the liquid dispersing agent must be removed by evaporation, sometimes referred to as "flash-off." Removal of the liquid dispersing agent during the curing process results in long curing times and the possibility of adverse effects, such as crazing a composite adherend.

Solvent cements used with thermoplastics dissolve an adherend's surface and, in effect, weld the elements together. Solvent cements are used extensively to bond polyvinyl chloride (PVC) piping and liners, a process often referred to as "solvent welding." Many thermoplastics are easier to join by solvent cementing than by conventional bonding. The successful use of solvent cements is based on providing the proper amount of solvent for a given application. Too much solvent can weaken the adherend near the joint, whereas too little solvent will result in a weakened, undeveloped joint.

Solvent cements are most effectively employed on thermoplastics. Several types of solvents can be employed, so selection of an appropriate solvent for a given thermoplastic is dictated by the solubility of both the solvent and the thermoplastic.

4.9 STANDARD TEST METHODS FOR STRUCTURAL ADHESIVES

As with other methods of connection, testing is an integral part of both the design and fabrication of adhesive bonds. Because of the wide diversity of potential physical and chemical interactions between an adhesive and a structural composite, successful designs are largely empirically based (Vinson 1989). Likewise, the importance of surface preparations, application techniques, and curing of adhesive bonds encourages the use of in-process inspections. Structural composite and adhesive manufacturers have undertaken extensive testing programs to advance the reliability of their products. These testing programs usually investigate variables such as surface preparations, application methods, joint configurations, and curing conditions under a wide range of potential service conditions. Consequently, it is important that users adhere to the manufacturers' recommendations.

ASTM International (ASTM) tests for adhesives can provide pertinent comparisons of different adhesives. In addition, these tests can serve as guides for subsequent tests for applications that may require more extensive testing programs. Some primary ASTM tests are listed in Table 4-3.

Table 4-3. Applicable ASTM Adhesive Test Procedures

Test Parameter	ASTM Standard Test	Description and Comments
Adhesion	D-3808	Spot adhesion test
Adhesive-plastic compatibility	D-3929	Evaluates the stress cracking of plastics by adhesives using the bent beam method
Cleavage	D-3807	For engineering plastic substrates
	D-3433	Flat and contoured cantilever-beam specimens for determining the adhesive fracture energy
Creep resistance	D-1780	Single-lap joint loaded in tension employed
	D-2294	Single-lap joint, having a long overlap and between "rails," loaded in compression
	D-2296	Single-lap joint loaded in tension employed
Environmental resistance	D-896	General method for assessing resistance of joints to chemicals; may use any ASTM standard test geometry
	D-904	General method for assessing resistance of joints to artificial and natural light; may use any ASTM standard test geometry
	D-1151	General method for assessing resistance of joints to moisture and temperature; may use any ASTM standard test geometry
	D-1828	General method for assessing resistance of joints to natural outdoor aging; may use any ASTM standard test geometry
	D-2918	Method for assessing the effect of stress and moisture and temperature; uses a peel joint test
	D-2919	As above but uses single-lap joints loaded in tension
	D-3762	As above but uses a wedge

Compression	D-4027	For measuring shear modulus and strength of adhesive; uses "rails" to maintain only shear load
Tension	D-3983	Thick substrates used in a single-lap joint; shear modulus and strength of adhesive determined
Peel	D-1876	"T" Peel test
	D-3167	Floating roller test
	D-903	180° peel test
Shear	D-4501	Block shear
	D-3163	Lap shear
	D-3983	Thick adherend
Torsional shear	D-229	Uses a "napkin ring" test for determining shear modulus and shear strength of structural adhesives
Wetting characteristics	D-2578	Wetting tension of plastic films
Surface treatments	D-2093	Preparation of surfaces of plastics prior to adhesive bonding

As with any testing, it is important that the testing of adhesive bonds be designed to simulate as nearly as possible the expected service conditions.

4.10 ESSENTIAL INFORMATION

4.10.1 Quality Control Data

The adhesive manufacturer should keep on file the normal quality control test data for each batch of adhesive, and a copy of this report should be provided to the engineer-of-record when requested. The manufacturer should certify the conformance of the adhesive products with the supplied specifications. The average test results provided by the manufacturer to the adhesive supplier should meet the project specifications requirements, and no single result may be more than 15% below the engineering specifications.

4.10.2 Packaging Information

The adhesive manufacturer or supplier should pack the structural adhesives in appropriate containers of suitable sizes so that weighing or measurements are not required. In this case, the correct proportions of each part (e.g., parts A, B, and C) can be achieved by mixing the entire contents of each container.

It is also highly recommended, especially for adhesives to be mixed at construction sites, that a color code be used to label each part of the adhesive system to avoid any error in mixing by construction workers. It is also recommended that "per volume" mixing proportions be provided in lieu of "per weight" mixing proportions to avoid any error resulting from an uncalibrated weighing scale at the construction site.

Each container should be clearly labeled with the following information:

1. Manufacture's name, address, and contact phone number
2. Date of manufacturing and batch number
3. Expiration date or shelf life
4. Requirements for storage to achieve the listed shelf life
5. Mixing ratio and conditions
6. Pot life and mixing environment to achieve the listed pot life
7. Safety precautions and details of any possible health hazards resulting from improper use or exposure

Recent practice and stricter legislative guidelines have resulted in the introduction of a material safety data sheet (MSDS) with all

commercial adhesive products. MSDSs are standardized forms that contain data associated with the properties of a particular substance, which makes them important components of product stewardship and workplace safety. Additional information on MSDSs is provided in Section 4.12.

4.10.3 Manufacturer's Instruction Information

With each delivery of adhesives, the manufacturer should provide dated, coded, and titled instructions. The instruction sheet should contain the following information:

1. Chemical type of each component of the adhesive system
2. Recommended storage conditions and associated shelf life
3. Instructions for the use of primer that includes optimum thickness and suggested range of permissible thickness
4. Mixing instructions, including any temperature requirements and the allowable variations in the mix ratio
5. Application instructions, including the required clamping pressure allowable, temperature range, joint open time, acceptable relative humidity at the project site, and information on whether the adhesives should be applied to one or both adherends
6. Curing conditions (e.g., temperature, pressure, and relative humidity) and curing time required before applying loads on the joint
7. Safety precautions for all components of the adhesive system and primer

4.11 COMMON CAUSES OF ADHESIVE FAILURE

In general, composite bonded joints may fail in one of two ways: (1) *Adhesive* (or interfacial or bondline) failure, and (2) *cohesive* failure where the separation is within the adhesive itself. In the latter case, adhesive remains on both substrate surfaces but the two items separate.

When an adhesive fails, the root cause will generally fall into one of four categories: (1) not enough adhesive, (2) incomplete cure, (3) inappropriate adhesive, or (4) poor adhesive quality. Visual inspection is generally sufficient to determine whether the amount of adhesive is acceptable. Evaluating joint performance versus the amount of adhesive dispensed can determine whether more adhesive is needed. Adhesive that is completely uncured is easy to detect; however, in some cases, examination of the adhesive may not indicate an incomplete cure. Comparing present cure conditions with those employed when the process was initially set up can help identify changes that may be contributing to

poor performance. For example, a drop in relative humidity may be the factor that causes a moisture-cure product to fail an in-line test it had previously passed. A malfunctioning oven or light source might deliver insufficient energy to complete an adhesive cure.

In some cases, the adhesive initially selected turns out to be inappropriate for the application. New performance requirements sometimes develop, or the definition of an acceptable joint might change. Sometimes, the rigors of production prove to be too much for an adhesive that worked well in the prototype stage. A particular lot of the adhesive also can turn out to be bad; thus, checking adhesive shelf life and testing the joint using a fresh lot will help determine the quality of a suspect batch.

Valuable information can be obtained by testing the performance of a failing adhesive and checking the adhesive manufacturer's retained stock of that lot against the adhesive's original manufacturing specifications. If the failing material shows significantly poorer results than the adhesive manufacturer's remaining stock, then the adhesive was probably stored improperly. If both samples meet the adhesive maker's manufacturing specifications, those specifications may be too broad for the given process, or the process may depend on a characteristic that was not evaluated as part of the adhesive specifications. If both samples fail to meet specification, the adhesive supplier might need to correct the adhesive manufacturing process to adequately address the customer's needs.

4.12 MATERIAL SAFETY DATA SHEETS

The MSDS is a detailed informational document prepared by the manufacturer of any hazardous chemical. This document describes the physical and chemical properties of the product. It contains useful information such as toxicity, flash point (the minimum temperature at which the liquid produces a sufficient concentration of vapor above it that it forms an ignitable mixture with air), procedures for spills and leaks, and storage guidelines. It is very critical that the engineer and contractor familiarize themselves with MSDS information to assist them in the selection of safe products, and to understand the potential health and physical hazards of a chemical and proper response to exposure situations. An MSDS may be useful but it cannot substitute for prudent practices and comprehensive risk management.

Safety information on polymer matrix composites, including resins, is detailed in the Occupational Safety & Health Administration (OSHA) *Technical Manual* (*OTM*), *Section III: Chapter 1: Polymer Matrix Materials: Advanced Composites* (OSHA 1999), which is accessible to the public on the OSHA Web site.

REFERENCES

ASTM International (ASTM). (2002). *MIL 17 handbook: The composite materials handbook*, ASTM International, West Conshohocken, Pa.

Brewis, D. M. (1985). "Adhesion problems at polymer surfaces." *Prog. Rubber and Plastic Tech.*, 1(4), 1–21.

Briggs, P., Rose, G., Roeteeny, K., and Sivy, G. T. (1991). "Structural methacrylates yield process, performance benefits." *Adhesives Age*, June, 17–22.

Findley, W. N., and Onaran, K. (2976). *Creep and relaxation of nonlinear viscoelastic materials*, North-Holland Publishing Company, Toronto.

Hutchinson, A. R. (1987). *Proceedings of the International Conference on Structural Faults and Repair-87*, M. Forde, ed., University of London, London, UK, p. 235.

Kinloch, A. J. (1987). *Adhesion and adhesives*, Chapman & Hall, New York.

Kinloch, A. J. (1983). *Durability of structural adhesives*, Applied Science Publishers, London.

Kinloch, A. J. (1982). "Review of science of adhesion. Part 2: Mechanics and mechanisms of failure." *J. Mat.l Sci.*, 17, 617–651.

Leaderman, H. (1943). *Elastic and creep properties of filamentous materials and other high polymers*, Textile Foundation, Washington, D.C.

Lubin, G., ed. (1982). *Handbook of composites*, Van Nostrand Reinhold, New York.

Mays, G. C., and Hutchinson, A. R. (1992). *Adhesives in civil engineering*, Cambridge University Press, New York.

Occupational Safety & Health Administration (OSHA). (1999). "Technical manual (OTM), Section III: Chapter 1: Polymer matrix materials: Advanced composites." *U.S. Dept. of Labor, OSHA,* <http://www.osha.gov/dts/osta/otm/otm_iii/otm_iii_1.html> [April 7, 2010].

Taib, A., Boukhili, R., Achiou, S., Gordon, S., and Boukehili, H. (2006). "Bonded joints with composite adherends. Part I. Effect of specimen configuration, adhesive thickness, spew fillet and adherend stiffness on fracture." *Int. J. Adhesion & Adhesives*, 26, 226–236.

Vinson, J. R. (1989). "Adhesive bonding of polymer composites." *Polymer Eng. Sci.,* Oct., 1325–1331.

Wake W. C. (1989). *Synthetic adhesives and sealants*, John Wiley & Sons, Inc., New York.

This page intentionally left blank

CHAPTER 5

ANALYSIS AND DESIGN OF ADHESIVELY BONDED COMPOSITE JOINTS

5.1 INTRODUCTION

Adhesive bonding represents the most natural method for joining members of fiber-reinforced polymer (FRP) material. This is because the matrix in a composite is itself a polymer and acts as an adhesive to transfer interlaminar shear forces while holding the geometry of the shape intact. Adhesive joints are capable of high structural efficiency and constitute a resource for structural weight saving. In addition, the potential to eliminate stress concentrations cannot be achieved with mechanically fastened joints. However, there are limitations to the practical use of adhesively bonded joints. For example, catastrophic failures are caused when brittle adhesives are used. In cases where ductile adhesives are used, the joint may run into creep-related problems. The stiffness of the adherend can affect the intensity of the peel stresses in the joint.

Usually the adhesive is the weak link in the joint. However, efforts have been made to ensure that failure in the adherend precedes failure in the adhesive. This is because failure in the adherend may be controlled, while failure in the adhesive is resin-dominated. The adhesive strength is a function of percentage of voids, thickness variations, environmental effects, processing variations, deficiencies in surface preparation, and other factors that are not always properly controlled. The practical use of adhesively bonded joints has been limited due to the lack of accurate analysis methods, reliable and relevant material properties, and knowledge of long-term joint behavior.

As discussed in Chapter 4, successful adhesively bonded joints require a carefully developed fabrication process that provides the following:

- Proper selection of adhesive
- Proper surface pretreatment
- Proper strength and ductility properties of the selected adhesive
- Adequate thickness
- Proper conditions of clamping pressure, temperature, and humidity control to promote cure and strength development of adhesives (ASCE 1984)
- Chemical and physical compatibility of adhesive with adherends and with the service environment. Adhesives must be suitable for the service temperature range, chemical and ultraviolet (UV) exposure, and loading duration. For example, a rigid epoxy provides high strength at room temperature, but essentially no strength at $-10\ °F\ (-23\ °C)$ or $350\ °F\ (177\ °C)$.

5.2 TYPES OF STRESS CONDITIONS DEVELOPED IN COMPOSITE BONDED JOINTS

Adhesively bonded composite joints should be designed such that the adhesive layers are primarily stressed in shear or compression. The designer should avoid, or carefully evaluate, bonded joints that are exposed to high direct tension, cleavage, and peel forces. Figure 5-1 illustrates the different stress conditions in a bonded joint (ASCE 1984).

5.3 BONDED JOINT CONFIGURATIONS

Tables 5-1 and 5-2 present a summary of common bonded joint configurations for composite structures. The following are the most common configurations:

1. Single-lap bonded joint
2. Single-strap joint
3. Double-lap bonded joint
4. Double-strap joint
5. Stepped-lap joint
6. Scarf joint

Figure 5-2 shows the details of these joints.

The strength of different bonded joint configurations as a function of the adherend thickness, which is proportional to intensity of the joint design load, is illustrated in Fig. 5-3. In this figure, each curve represents the best strength for each joint configuration. The diagonal line through the origin represents the adherend strength outside the joint zone.
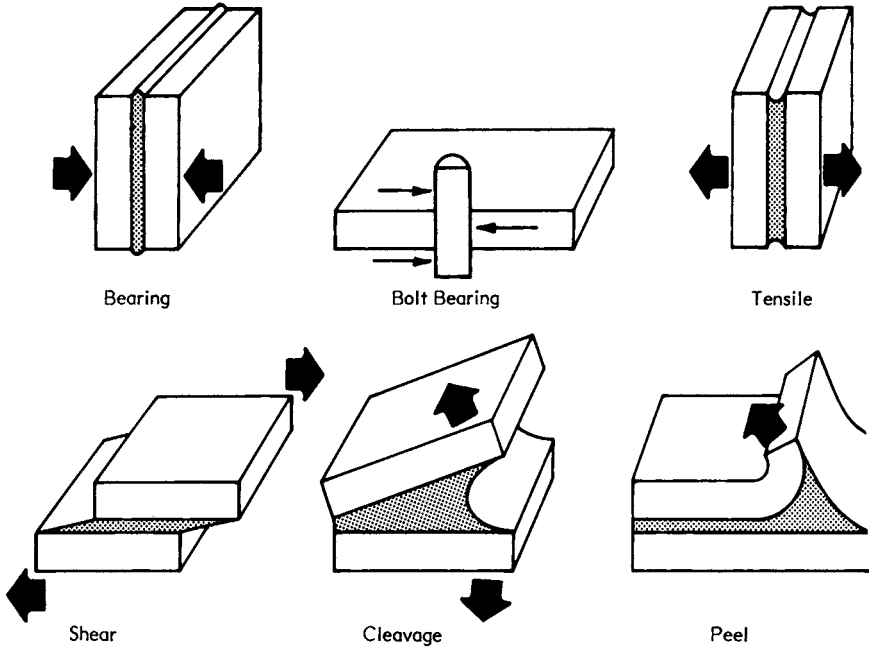
Figure 5-1. Structural behavior of composite bonded joints.
Source: ASCE (1984).

5.3.1 Single-Lap Bonded Joints

The unsupported single-lap joint (Fig. 5-2B) is a nonstructural joint that has low efficiency because of the eccentricity in the load path. This configuration is suitable for quality control testing because it tests simultaneously for a large number of effects (Hart-Smith 1974). However, adhesive shear stresses play only a minor role in the failure of unsupported single-lap bonded joints. It is difficult to predict the reliability of the joint strength experimental results due to the complex influence of joint geometry on the measured strength values.

Typical structural efficiencies for unsupported single-lap joints are 25% to 35% (Hart-Smith 1974). As shown in Fig. 5-3, the unsupported single-lap bonded joint is the weakest joint as compared to four joint configurations illustrated in this figure. Beyond small thickness, the critical failure for unsupported single-lap bonded joints is governed by the peel stresses developed at the adhesive layer at the end of the overlap. In the case of thick adherends, the joint efficiency drops rapidly. Figure 5-4 illustrates the effect of eccentricity on the structural behavior and failure of unsupported single-lap joints.

Table 5-1. Bonded Joint Concepts (Part I)

Joint	Comments
1. **Single-Lap (Unsupported) Joint**	Nonstructural joint having low efficiency because of bending of the adherend due to the eccentricity in the load path. Thick adherends are associated with failures by the peel rather than by shear.
2. **Supported Single-Lap Joint**	Practical joint for the thin adherends. Needs to be mounted on moment-resistant support to avoid the above limitations. Joint load capacity does not increase indefinitely with overlap. Load capacity is limited by the single bond surface.
3. **Supported Single-Strap Joint**	Same as for No. 2. Suitable for flush exterior applications but limited to thin adherends, and needs either good moment-resistant supports or very large l/t ratios.
4. **Balanced Double-Lap Joint** **Balanced Double-Strap Joint**	Efficient practical joint for thin and moderately thick adherends. Simple joint with tolerant fit requirements. Joint strength is limited by adherend thickness and independent of overlap beyond very short (uniformly stressed) lengths of bond. Maximum strength limit is set by peel stresses for moderately thick adherends rather than by adhesive shear stresses. For thin adherends, peel stresses are negligible and shear strength usually exceeds adherend strength.
5. **Unbalanced Double-Lap Joint**	Weaker than No. 4 due to the unbalanced nature of the design. In this construction the thin adherend is used or extends to its capacity, while the thicker adherend has an unusable reserve.
6. **Tapered-Lap Joint**	Efficient practical joints for moderately thick adherends, but shares similar overpeel-stress limitations of No. 2. Strength limited by adhesive shear strength for thick adherends. Best strengths are obtained with optimum stiffness imbalance between adherends to compensate for shear strength loss due to taper. Only moderate precision requirements

Source: Hart-Smith (1974), courtesy of Dr. John Hart-Smith and the Boeing Company.

Table 5-2. Bonded Joint Concepts (Part II)

Joint	Comments
7. **Flush Joints**	Nonstructural joints suffering from net-section loss just outside the joint regions.
8. **Stepped-Lap Joint**	Used extensively in advanced composite-to-titanium bonded joints. Detail design can be critical. Need to avoid composite net-section reduction at the end of the titanium. End titanium step needs to have lower l/t ratio than other steps.
9. **Stiffness-Balanced Stepped-Lap Joint**	Improvement on No. 8 because both ends of the joint are then loaded equally instead of concentrating the load transfer through the thin end of the titanium (or stiffer) adherend in No. 8.
10. **Double-Stepped-Lap Joint**	Needed for thick sections beyond the practical capabilities of No. 9.
11. **Scarf Joints**	Most efficient of all bonded joints. Necessary for thick adherends, unnecessary for thin adherends. Strength is maximized by balancing adherend stiffness at each end of the joint. Precise fit requirements for efficient joints can be reduced in some situations by co-curing and bonding of composite laminates.
12. **Joggled Lap Joint**	Nonstructural joint used (because of aerodynamic smoothness requirements) on exterior skins subjected to normal rather than in-plane loads. See also comments on No. 1.

Source: Hart-Smith (1974), courtesy of Dr. John Hart-Smith and the Boeing Company.
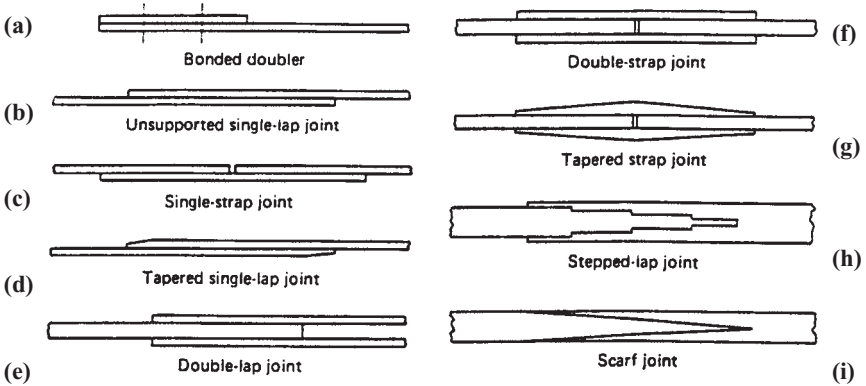
Figure 5-2. Bonded joint configurations.
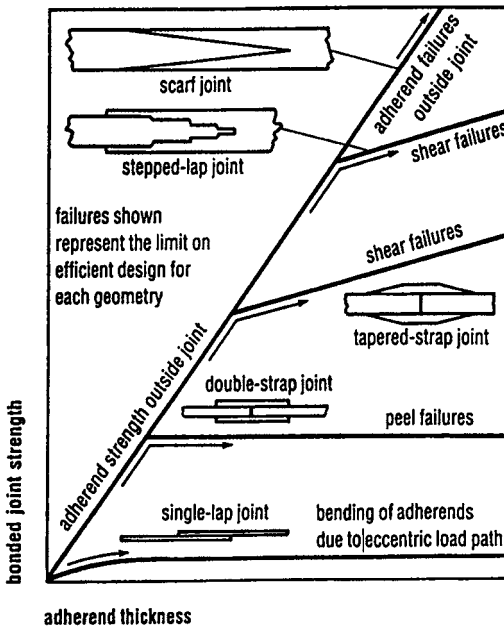
Figure 5-3. Influence of member size on selection of optimum joint configuration.
Source: Hart-Smith (1974), courtesy of Dr. John Hart-Smith and the Boeing Company.

In designing unsupported single-lap bonded joints, adherend bending must be taken into account due to the eccentricity of the load path, as shown in Fig. 5-4. The analysis should involve both adhesive shear stresses and peel stresses that are coupled, rather than independent, for all except joints between identical adherends (Hart-Smith 1981). The in-plane shear
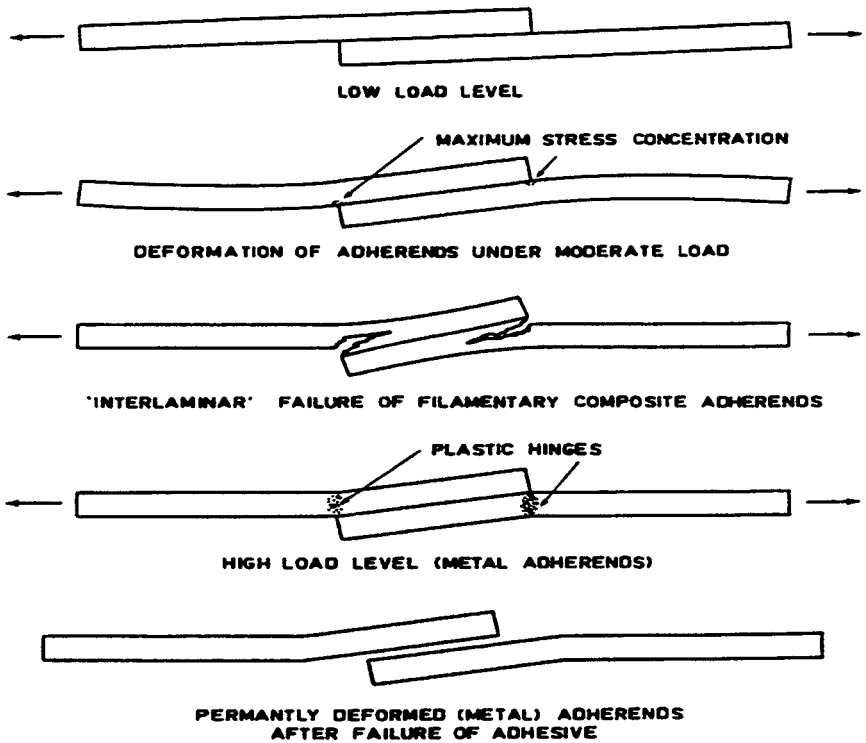
Figure 5-4. Failure of unsupported single-lap bonded joints with brittle and yielding adherends.
Source: Hart-Smith (1974), courtesy of Dr. John Hart-Smith and the Boeing Company.

loading of a single-lap bonded joint does not involve out-of-plane deformations of the adherends, and the appropriate analysis is to treat the unsupported single-lap bonded joint as one-half of a double-lap joint. This also applies to supported single-lap bonded joints, which are restrained against out-of-plane deflection. One way to rectify the problems associated with unsupported single-lap bonded joints is to firmly support these joints to nullify the effects of the load path eccentricity. This can be done by providing a kick-load at each end of the overlap to balance the applied bending moment (refer to row 2 of Table 5-1). For single-lap bonded joints, the peel stresses can be reduced by tapering the ends of the adherends and by increasing the overlap length. The latter approach also improves the efficiency of the joint by alleviating the induced bending moment.

5.3.2 Single-Strap Bonded Joints

This type of joint configuration is similar to the supported single-lap joint configuration. The load capacity of this joint is limited by a single

bond surface. The use of this configuration is limited to thin adherends (refer to row 3 of Table 5-1).

5.3.3 Double-Lap and Double-Strap Bonded Joints

These configurations are the simplest structural bonded joints. They are efficient in joining thin and moderately thick adherends. The strength of these joints is limited by the adherend thickness and is independent of the overlap beyond very short (uniformly stressed) lengths of bond. The maximum strength limit of these joints is set by the peel stresses for moderately thick adherends, rather than by the adhesive shear stresses. For thin adherends, peel stresses are negligible and the adhesive shear strength usually exceeds adherend strength.

The shear transfer characteristics of double-lap bonded joints are illustrated in Fig. 5-5 in a normalized form. This figure shows that the joint strength is independent of the overlap beyond some transitional value, and only for a very short overlap (uniformly fully plastic adhesive) is there a proportionality between the joint strength and the bond area.

In designing double-lap bonded joints, engineers often neglect the effect of out-of-plane bending, which is essential in designing single-lap bonded joints as mentioned earlier. However, neglecting the effects of bending is an acceptable approximation for double-lap joints with thin noncomposite adherends (refer to Fig. 5-6).

For composite adherends, the bending effect is critical due to the fact that peel stresses are induced by the bending of the outer adherends (outside the joining zone). These peel stresses are proportional to the fourth power of the adherend thickness, while the shear stresses are proportional to the second power. In addition, FRP composite adherends have lower interlaminar tensile strengths as compared to stresses that can be developed under peel loads for the adhesives. For double-lap with either composite or noncomposite, thicker adherends, the presence of significant peel stresses detracts from shear stress of the adhesive due to the combined loading. For this reason, an engineer must either account for this interaction or redesign the joint by tapering the splice plates (refer to Fig. 5-7) or thickening the adhesive at the end of the overlap in order to suppress the generation of induced peel stresses that can cause premature failures (Hart-Smith 1981).

The idea of tapering is to make the tips of the adherends thin and flexible, resulting in a significant reduction of peel stresses. If the overlap is long enough, it is impossible to overdo the peel stress relief (refer to Fig. 5-8). This figure shows that the joint strength remains constant with varying amounts of tapering because the other end of the joint, where no peel stresses are developed, is unchanged. For long-overlap bonded joints,
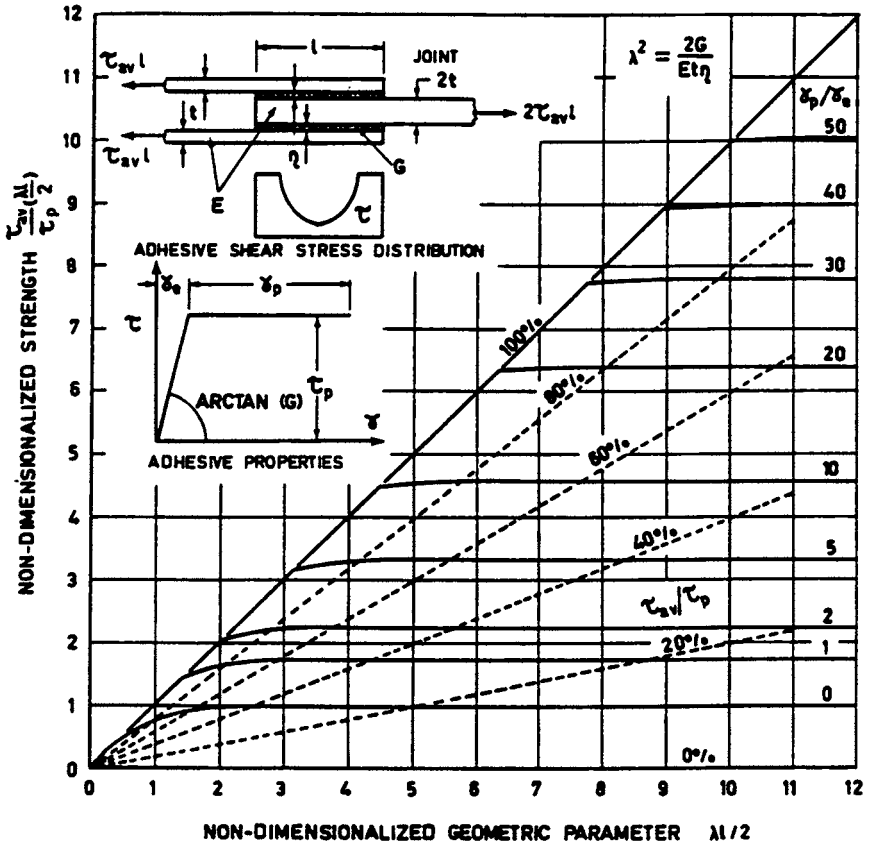
Figure 5-5. Shear strengths of balanced double-lap bonded joints.
Source: Hart-Smith (1981), courtesy of Dr. John Hart-Smith and the Boeing
Company.

the adhesive stresses around the edges of bonded splices are the same as
those around the periphery of wide-area doublers (refer to Fig. 5-9).

5.3.4 Scarf-Bonded Joints

Scarf-bonded joints (Fig. 5-2I) have the greatest possible structural effi-
ciency among other bonded joint configurations (refer to Fig. 5-3).
Although this joint configuration works for all adherend thicknesses, it is
strongly recommended for thick adherends beyond the capacity of dou-
ble-lap joints. As compared to other bonded joint configurations, manu-
facturing and position tolerance aspects of scarf-bonded joints are more
stringent. For this reason, this joint configuration is used only where it is
structurally necessary. One important distinction between scarf and
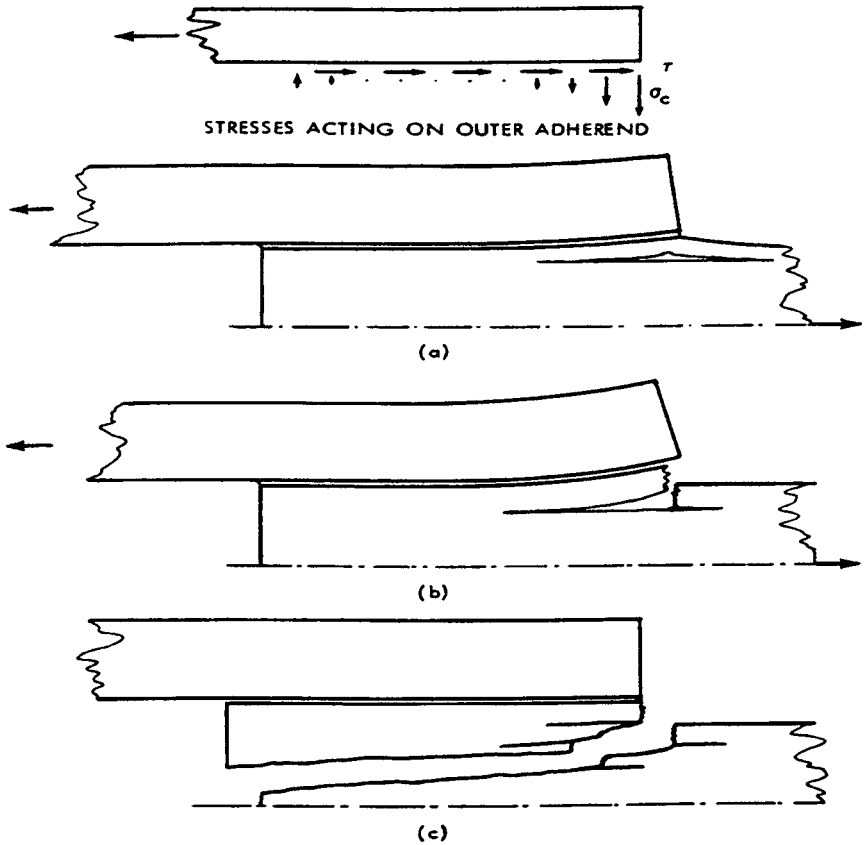
Figure 5-6. Peel stress failure of thick composite bonded joints. Failure sequence indicated by A, B, and C. Failure is normally in the central adherend rather than the outer adherend(s), due to the presence of higher in-plane stresses.
Source: Hart-Smith (1981), courtesy of Dr. John Hart-Smith and the Boeing Company.

double-lap bonded joints is that scarf-bonded joints are essentially free from all peel-stress effects for practical proportions for realistic materials, whereas peel stresses become more critical than shear stresses for thick uniform double-lap bonded joints (Hart-Smith 1974). A summary description of scarf joints is presented in row 11 of Table 5-2.

5.4 FAILURE MODES

The typical modes of failure of composite bonded joints are:

1. *Mode I*:
   - Cohesive failure within the adhesive layer
   - Adherend matrix surface resin layer failure
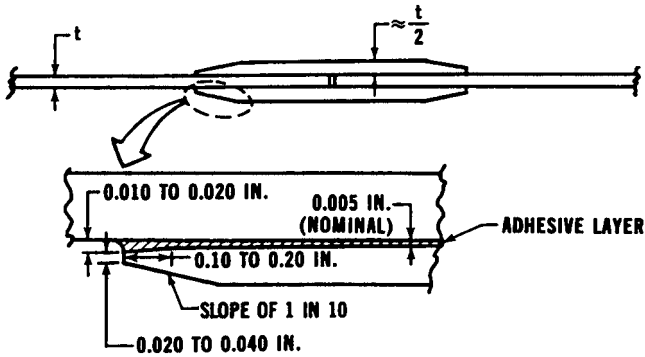
Figure 5-7. Tapering of splice plate edges to relieve adhesive peel stresses. Source: Hart-Smith (1994), courtesy of Dr. John Hart-Smith and the Boeing Company.
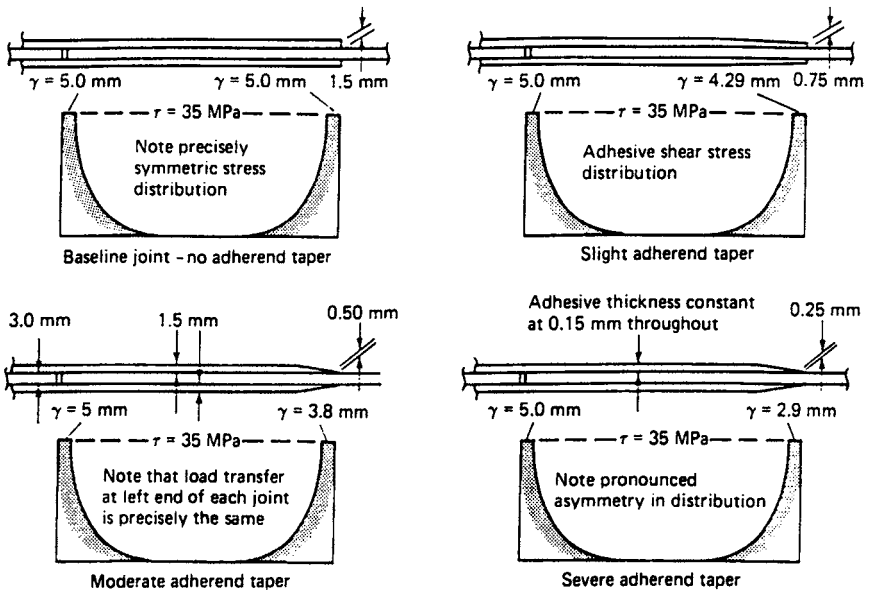
Figure 5-8. Insensitivity of adhesively bonded joint strength to modifications at one end only (long overlap).

2 *Mode II:*
   • Adhesive–adherend interface failure on the resin surface
3 *Mode III:*
   • Interlaminar resin layer failure
4 *Mode IV:*
   • Transverse (parallel to the fibers) lamina failure (resin only)
   • Transverse (parallel to the fibers) lamina failure (fiber–resin interface)
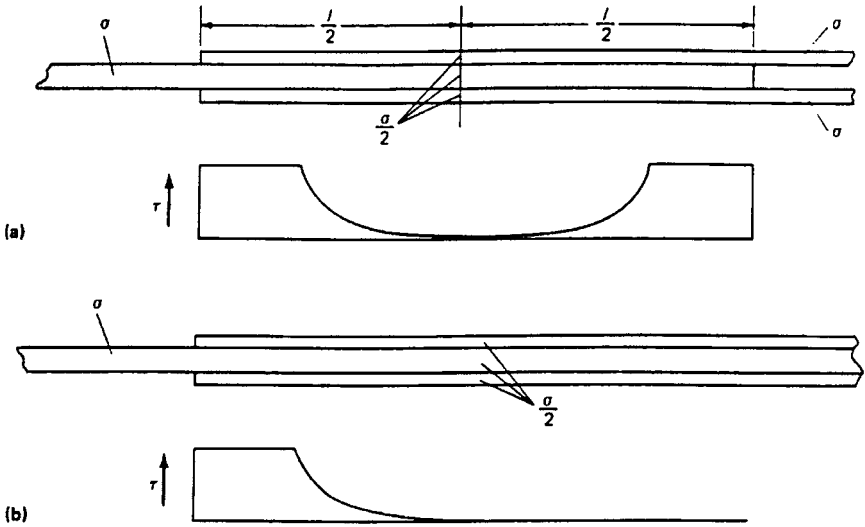
Figure 5-9. Similarity of bonded stress joints and doublers.
Source: Hart-Smith (1989; 1994), courtesy of Dr. John Hart-Smith and the
Boeing Company.

- Longitudinal (perpendicular to the fibers) lamina failure (fiber plus resin)
5 *Mode V:*
- Adherend tension failure

The typical modes of failure of adhesively bonded composite joints can be divided into five micro- and macro-fracture characteristic types: (1) cohesive, (2) interface, (3) interlaminar, (4) lamina, and (5) laminate. An adherend–adhesive interface failure occurs on a macro-scale when processing or material quality is poor. Poor processing or material quality lead to a lower failure load below the elastic limit of both the adhesive and the adherends. Cohesive (within the adhesive) failure occurs by brittle fracture or by a rubbery tearing, depending on the type of adhesive used (Grimes and Greimann 1975). Interlaminar failure (not related to edge effects) may be caused by poor processing, voids, delaminations, or thermal stresses. These possible causes of interlaminar failure should be considered on a gross scale in their effect on the resin layer tension-shear failures. The three types of lamina failures, on a micro-scale, can usually be considered as one type of layer failure on a macro-scale.

The following are some recommendations to prevent catastrophic failure of adhesively bonded composite joints:

- The surface should be properly pretreated.
- The joint should be properly proportioned such that the bond is never the weak link in the structure.
- The integrated strength of the adhesive bond across the bonded area must be greater than the strength of the adherends outside the joint. This will ensure that local flaws and damage can be tolerated without any possibility of causing the bond to unzip instantaneously throughout the remaining bond area (Hart-Smith 1989).
- Some part of the bond area must be lightly stressed so as to avoid adhesive creep that can lead to adhesive failure due to creep rupture. To ensure this, the joint should be designed such that the adhesive shear stress distribution is nonuniform. This issue is discussed further in Section 5.6.

5.5 ADHESIVE STRESS–STRAIN CHARACTERIZATION

To precisely predict the failure of adhesively bonded joints, the nonlinear adhesive behavior should be considered in the design. Hart-Smith (1981) employed a two-straight-line (bilinear) adhesive characterization for different bonded joint geometries. The adhesive failure criterion in shear is uniquely defined by the adhesive shear strain energy per unit bond area, regardless of the individual characteristics that contribute to that strain energy. The nonlinear strain energy is frequently 100 times greater than the linear value that would represent a ten-fold increase in the predicted strength of the bonded joint.

Figure 5-10 shows a typical adhesive stress–strain characterization in shear. The linear elastic model can be used whenever the applied loads are relatively low. The advantage of using the bilinear elastic-plastic adhesive model is that it is closer to the actual characteristic of the adhesive throughout its entire deformations range. In this case, a simple model can be used to determine the internal stresses associated with a specified joint load for which the adhesive strain is not known.

Adhesive characteristics change with both temperature (refer to Fig. 5-11) and moisture content. However, the strain energy to failure does not vary with environmental changes, as do individual properties. Normally, ductile epoxy adhesives are used in the majority of bonded joint applications (refer to Figs. 5-11 and 5-12). In some cases where operating temperatures are high, much more brittle adhesives may be specified. Figure 5-12 illustrates the difference of behavior of ductile and brittle adhesives. As shown in this figure, even brittle adhesives exhibit proportionally significant nonlinear behavior near the upper limit of their operating environments. For this reason, a linear model does not suffice for brittle adhesives.
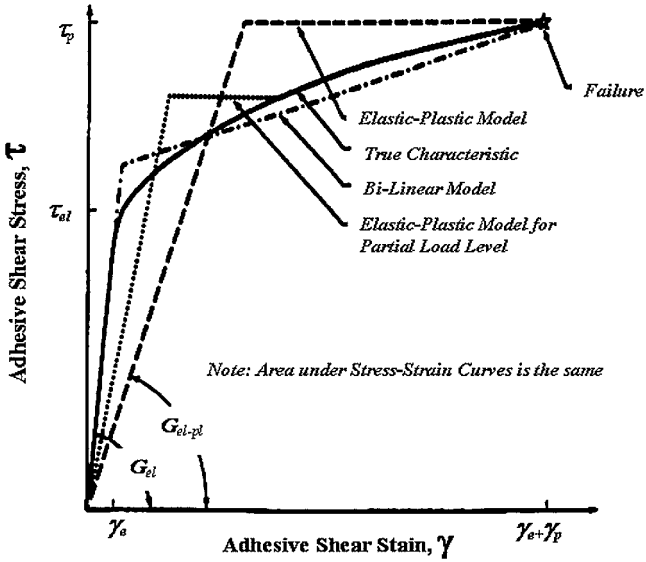
Figure 5-10. Adhesive shear stress–strain curves and mathematical models.
Source: Hart-Smith (1981), courtesy of Dr. John Hart-Smith and the Boeing Company.
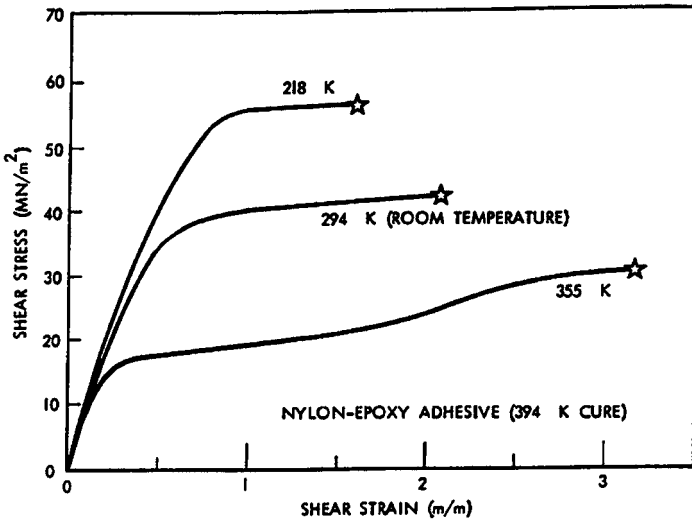

Figure 5-11. Effect of temperature on the shear stress–strain behavior of structural adhesives.
Source: Hart-Smith (1981), courtesy of Dr. John Hart-Smith and the Boeing Company.
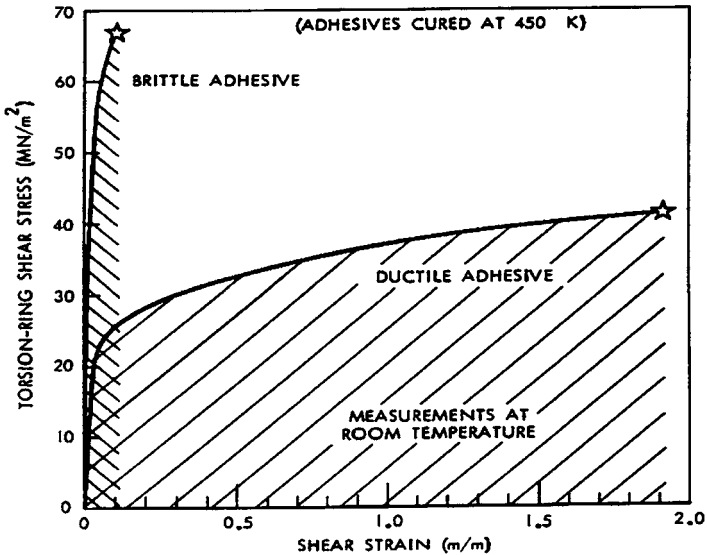
Figure 5-12. Stress–strain behavior of brittle and ductile adhesives. Source: Hart-Smith (1981), courtesy of Dr. John Hart-Smith and the Boeing Company.

5.6 LOAD TRANSFER IN ADHESIVELY BONDED COMPOSITE JOINTS

5.6.1 Basic Sources of Nonuniform Adhesive Shear Load Transfer in Bonded Composite Joints

Differential movement of the bonded adherends creates the shear stresses and strain in a bonded composite joint. There are three basic sources of nonuniform adhesive shear load transfer in bonded composite joints:

1. *The effect of adherend extensibility in a balanced joint:* "Balanced" means the two adherends are identical (e.g., same material and same thickness). This effect is as illustrated in Fig. 5-13. This figure shows that stiffer adherends promote a more uniformly loaded joint, while flexible adherends have little bond load transfer at the middle of the overlap.

2. *The effect of adherend stiffness imbalance*: This effect is illustrated in Fig. 5-14. The adhesive shear strains are intensified at the ends of the joint from which the less stiff adherend(s) extend(s). The same end of the joint is critical, whether the applied load is tensile, compression, or in-plane shear (Hart-Smith 1978). As compared to the behavior of stiffness-balanced bonded joints, this imbalance reduces the joint strength by unloading the less-critical end and developing a smaller plastic adhesive zone at that
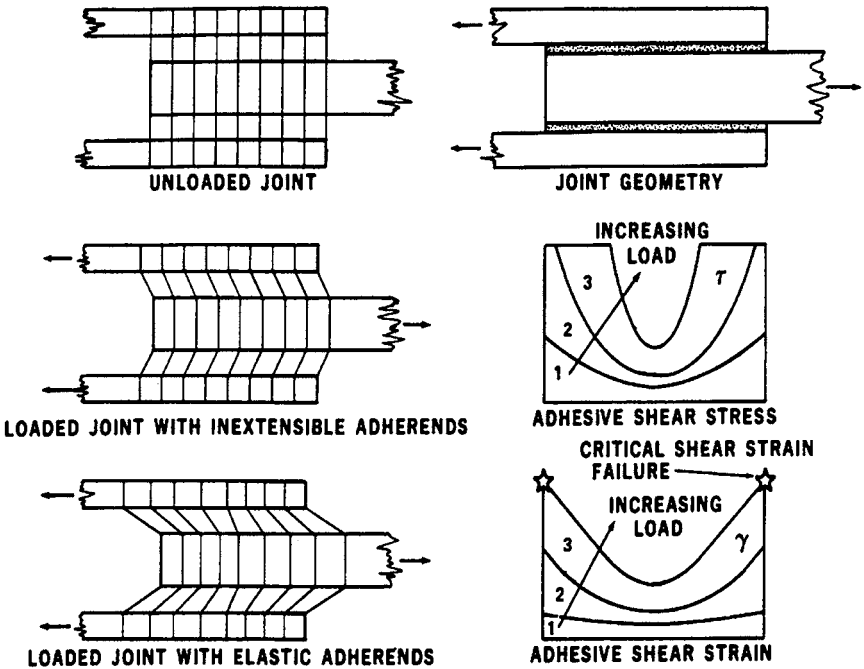
Figure 5-13. Shearing of adhesive in balanced bonded joints.
Source: Hart-Smith (1978), courtesy of Dr. John Hart-Smith and the Boeing Company.

end. As shown in Fig. 5-13, there is an equally effective end zone at each end of the bonded joint.

3. *The effect of adherend thermal mismatch:* When joining dissimilar adherends (e.g., E-glass or carbon composites to galvanized steel, E-glass composites to carbon composites, or carbon composites to concrete), a reduction in the joint strength is expected due to the difference in the coefficient of thermal expansion of the two adherends. Figure 5-15 illustrates the mechanics of this imbalance in thermal properties. This effect is particularly important when high-temperature-cure adhesives are used. In this case, the noncomposite adherend (e.g., steel) tends to shrink more than the composite adherend during cooldown to operating temperature. This shrinkage is partially resisted by the outer composite adherends, thereby introducing residual bond stresses that detract from the bonded joint capability to resist the applied mechanical loads.

In the case of bonding metallic to polymeric adherends, the two adherends will have both thermal and stiffness mismatched properties. The consequence of these simultaneous adherend mismatches is that the joint strength, and the more critical end, can change between tensile and compression loading (Hart-Smith 1978). When this type of joint is loaded in
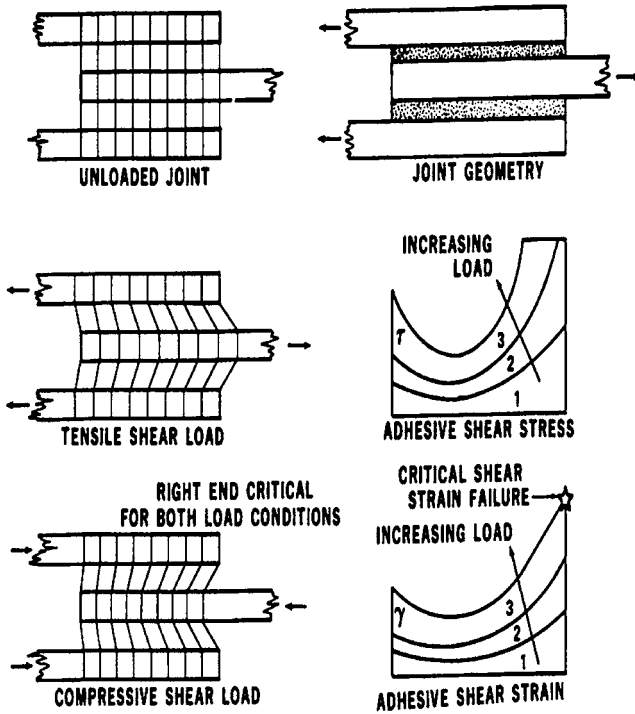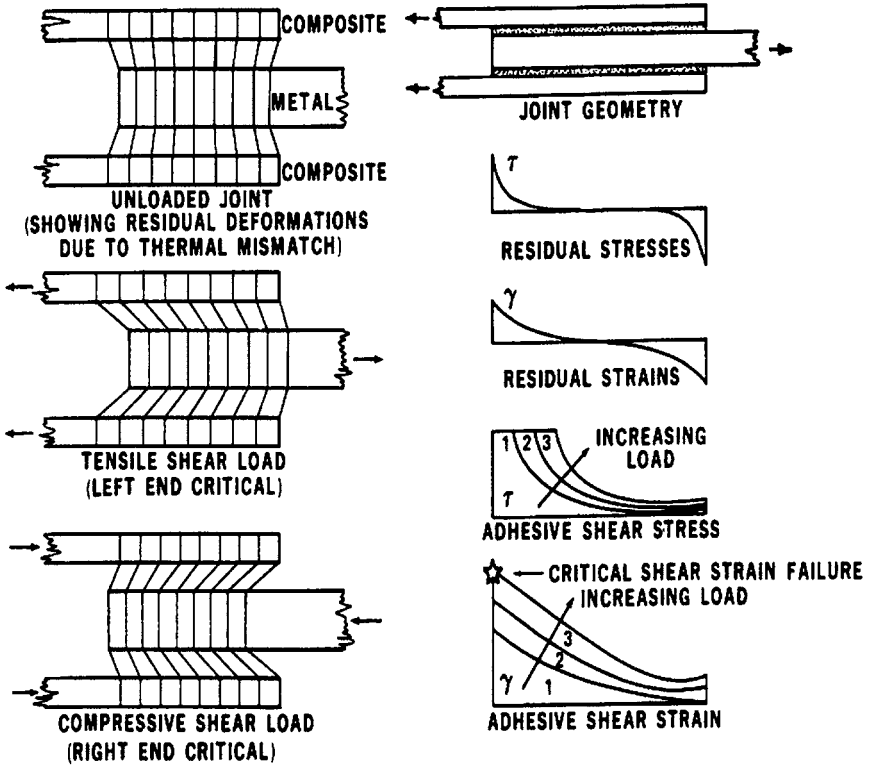
Figure 5-14. Effect of adherend stiffness imbalance on shear transfer behavior of bonded joints.
*Source: Hart-Smith (1978), courtesy of Dr. John Hart-Smith and the Boeing Company.*

shear, the thermal mismatch effect becomes most severe at the corners of the bonded area instead of along one or more edges. In this case, it is necessary to consider orthogonal strains in the adhesive layer instead of just those along a single axis. Also, the engineer should be aware that galvanic corrosion could possibly develop when carbon-based composites are bonded to metallic parts. These issues are very critical in composite bridge deck applications, where FRP composites are bonded to existing steel girders of a bridge (refer to Fig. 5-16).

5.6.2 Significance of the Nonuniform Load Transfer Distribution in Bonded Joints

The significance of the nonuniform load transfer distribution is illustrated in Figs. 5-17 and 5-18. As shown in Fig. 5-17B, the minimum shear stress at the middle of the short overlap test coupon configuration is almost as high as the maximum stresses at the ends of the overlap. The use of short lap length is suitable for test coupons to promote adhesive

Figure 5-15. Effect of adherend thermal mismatch on shear transfer behavior of bonded joints.
Source: Hart-Smith (1978), courtesy of Dr. John Hart-Smith and the Boeing Company.
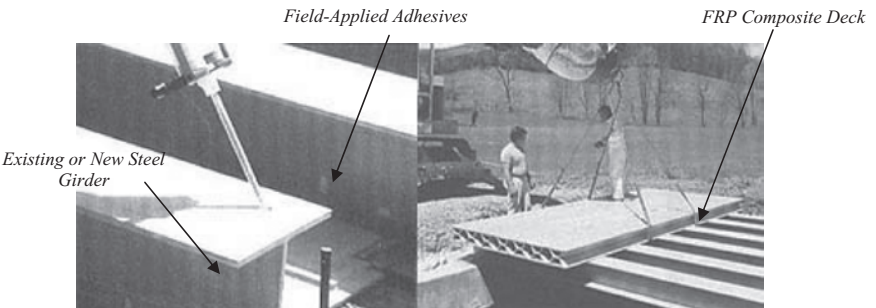
Figure 5-16. Effect of adherend thermal mismatch on shear transfer behavior of bonded joints in bridge deck replacement applications.
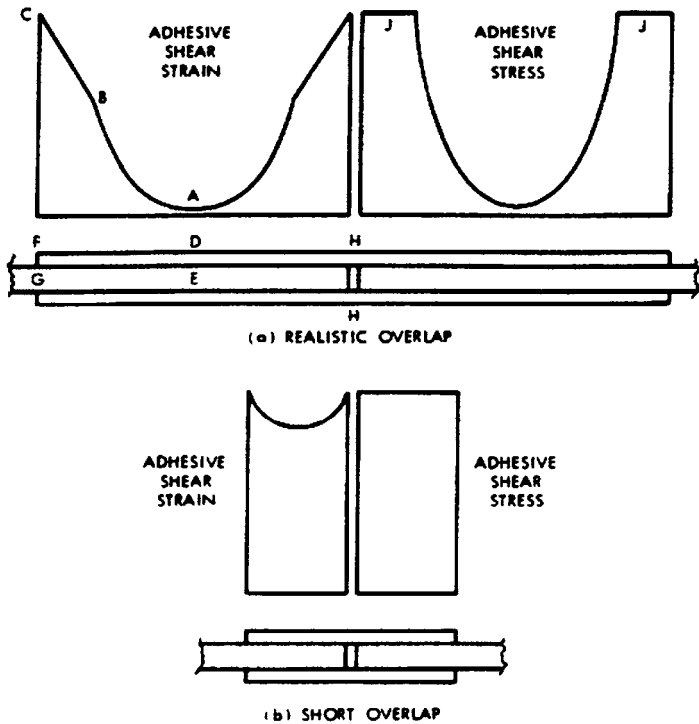*Source: Federal Highway Administration.*

Figure 5-17. Nonuniform stress and strain distributions in adhesively bonded joints.
Source: Hart-Smith (1978), courtesy of Dr. John Hart-Smith and the Boeing Company.

failure rather than adherend failure so that the state of stress in the adhesive can be properly characterized. However, in an actual joint design, the uniformity resulting from the use of short overlap is not desirable. This stress uniformity significantly lowers the joint creep resistance. The total overlap must be sufficient to ensure that the adhesive shear stress at the middle of the overlap (point A in Fig. 5-17A) is essentially zero or at least low enough so that creep cannot occur at this region, regardless of environmental exposures or the duration of loading.

Point A in Fig. 5-17A, or points D and E in the adherends (Fig. 5-18A), serves as the "joint memory" because there can be essentially no relative motion at these points prior to failure elsewhere, regardless of the load duration (Hart-Smith 1978). To avoid creep rupture, it is recommended that the minimum operating stress not exceed 10% of the maximum adhesive stress at the edges, as shown in Fig. 5-19.
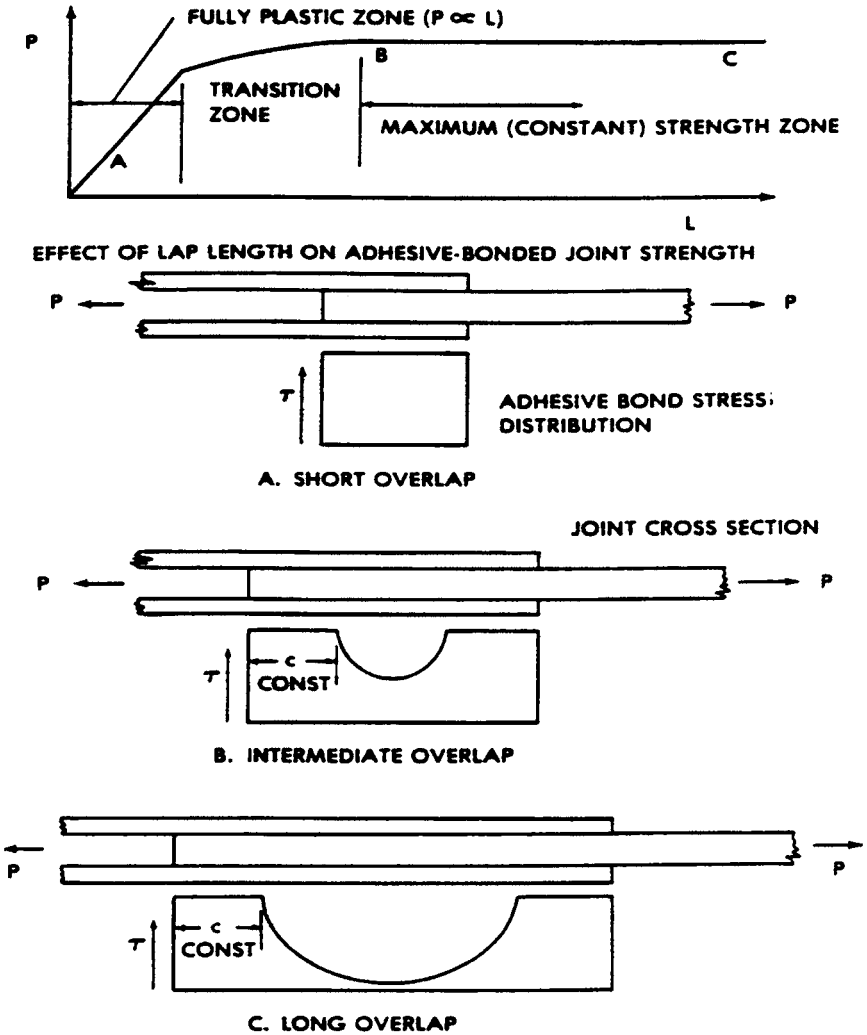
Figure 5-18. Influence of lap length on bond stress distribution. In a long-overlapped bonded joint (refer to C above, and Fig. 5-17A), the adhesive stresses are nonuniform and the average shear stress is insignificant due to the large stress variations at the ends and middle of the overlap. In this case, where creep has an insignificant effect at the middle, the maximum adhesive shear strain at the ends of the overlap is limited by the strain needed to fail the adherends outside the joint. If the load is sustained for a sufficiently long duration, creep occurs in the adhesive at the ends of a bonded joint with long overlap. However, experimental results indicate that creep would recover during the unloading part of the cycle.
Source: Hart-Smith (1974), courtesy of Dr. John Hart-Smith and the Boeing Company.

$2t$ t_a G E

t

$\dfrac{t \, \sigma_{ult}}{2 \tau_p}$

For balanced joint (E= E_1=E_2 and t=t_1=t_2)

τ_p

ADHESIVE SHEAR
STRESS DISTRIBUTION

$\tau_{min} = \tau_p/10$

$\dfrac{3}{\lambda}$ $(\lambda^2 = \dfrac{2G}{Et\eta})$
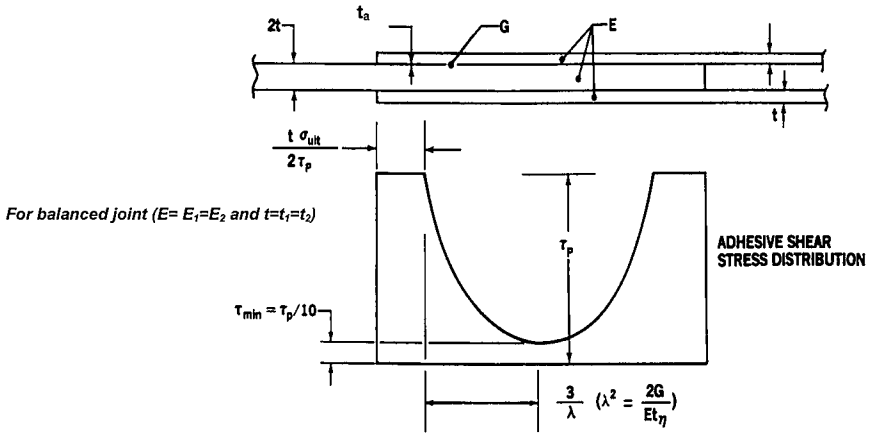
Figure 5-19. Geometrical and mechanical parameters for a "balanced" composite bonded joint.

5.7 ANALYSES AND DESIGN OF COMPOSITE BONDED JOINTS

This section presents several analytical and design approaches for composite bonded joints. The first approach is the original approach proposed by Hart-Smith (1972). Based on this approach, the *EUROCOMP Design Code and Handbook* (Clarke 1996) procedure was developed. In addition, a simplified approach was proposed by Chamis and Murthy (1989).

Like bolted joints, the efficiency of a bonded joint is defined as the ratio of actual (or potential) joint strength to the strength of the adherend(s); that is:

$$\eta_b = \frac{S_j}{S_a} \tag{5-1}$$

where
η_b = bonded joint efficiency
S_j = bonded joint strength
S_a = adherend(s) strength

A value of $\eta_b < 1$ implies that the structure outside the joint is inefficiently loaded. As mentioned earlier, the maximum reported efficiency of unsupported single-lap bonded joints is about 30% to 40%, due to the inherent load path eccentricity (refer to Fig. 5-4).

5.7.1 Hart-Smith Design Approach

Hart-Smith (1973a) used an elastic-plastic adhesive model to account for the nonlinear behavior of the adhesives in shear. In addition, the

influences of the adherend stiffness imbalance and thermal mismatch were included in this approach. This approach was based on the earlier work by Volkersen (1938) and Goland and Reissner (1944), which was based on an elastic model instead of the Hart-Smith elastic-plastic model discussed in Section 5.5 and illustrated in Fig. 5-10.

In this approach, several assumptions are made:

- Shear stress is constant through the thickness of the adhesive layer.
- Adherend stresses are constant across their thickness.
- There is no interaction between shear and peel effects in the analytical solution. If this interaction effect occurs at potential bond strength far in excess of the adherend strengths, the problem may by justifiably ignored. However, if such an interaction is predicted to occur at a load level close to or below the adherend strength, the joint configuration should be redesigned to eliminate this problem.
- One-dimensional analysis is required along the length of the joint. In this manner, nonuniformities across the joint width and bond stresses along the thickness coordinate direction may be ignored.

These approximations seem to have minor effects in the case of balanced bonded joints. This was confirmed by the good correlation between results obtained from Hart-Smith's closed-form solution and finite element analysis results reported by Teodosiadis (1968).

Five nondimensionalized governing equations describe the behavior of composite bonded joints. These five equations are defined as follows.

Adhesive shear stress distribution along the bonded joint:

$$\lambda l = l \sqrt{\frac{G_a}{t_a} \left(\frac{1}{E_1 t_1} + \frac{1}{E_2 t_2} \right)} \tag{5-2}$$

Adhesive peel stress distribution and the associated interlaminar tensile stresses for composite adherends:

$$\chi t = t \left(\frac{E_c}{4 D t_a} \right)^{0.25} = \left(\frac{3 E_a'(1 - \upsilon^2) t}{E t_a} \right)^{0.25} \tag{5-3}$$

Influence of adherend stiffness imbalance from one end of the joint to the other:

$$n = \frac{E_1 t_1}{E_2 t_2} \tag{5-4}$$

Characterization of the effect of adherend thermal mismatch (e.g., adherends with different materials):

$$I = \frac{((\alpha_2 - \alpha_1)\Delta T \lambda)}{\tau_p \left(\dfrac{1}{E_1 t_1} + \dfrac{1}{E_2 t_2} \right)} \tag{5-5}$$

Extent of adhesive plastic deformation with respect to that obtained elastically:

$$R = \frac{\gamma_p}{\gamma_e} \tag{5-6}$$

where

$D \quad = \dfrac{Et^3}{12(1-\upsilon^2)} = $ adherend flexural stiffness (lb/in. or N/mm)

$E \quad = $ Young's modulus for adherend

$E_a' \quad = $ effective adhesive peel modulus (transverse tension of a constrained film)

$G_a \quad = $ adhesive film shear modulus

$l \quad = $ overlap length

$t \quad = $ adherend thickness (subscripts 1, 2, etc., identify adherend segment)

$I \quad = $ parameter defining the effect of adherend thermal mismatch

$R \quad = $ ratio of plastic to elastic adhesive strain

$\Delta T \quad = $ temperature difference $= T_{operating} - T_{stress\text{-}free}$ (°F/°C)

$\alpha \quad = $ coefficient of thermal expansion (subscripts 1, 2, etc., identify adherend segment)

$\gamma_e \quad = $ elastic adhesive strain

$\gamma_p \quad = $ plastic adhesive strain

$t_a \quad = $ thickness of adhesive layer

$\lambda \quad = $ exponent of shear stress distribution in adhesive (in.$^{-1}$ or mm^{-1})

$\upsilon \quad = $ Poisson's ratio for adherends

$\chi \quad = $ exponent of adhesive peel stress distribution (in.$^{-1}$ or mm^{-1})

$\tau_p \quad = $ plastic adhesive shear stress (same as maximum elastic value as shown in Fig. 5-10).

Figure 5-20 illustrates the different parameters used in Eqs. 5-2 through 5-6.

The complete mathematical details of Hart-Smith's elastic-plastic model are presented elsewhere (Hart-Smith 1973b). The Hart-Smith solution is performed in terms of the adhesive shear strain rather than adhesive shear stress because of the non-uniqueness of the shear stress distribution in the plastic zone. The solution starts with the development of force–equilibrium equations for differential elements of adherends
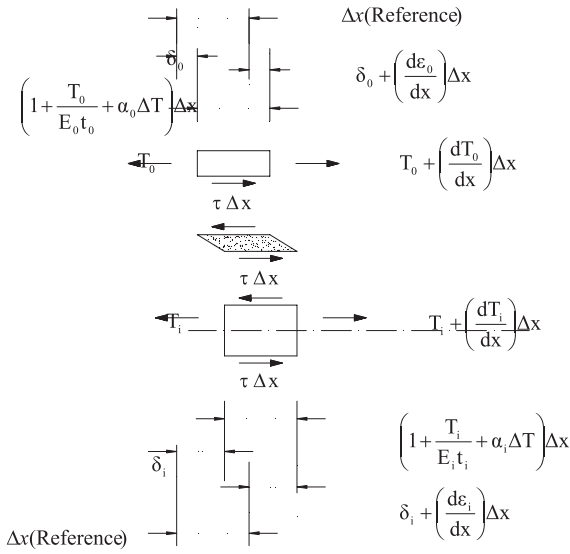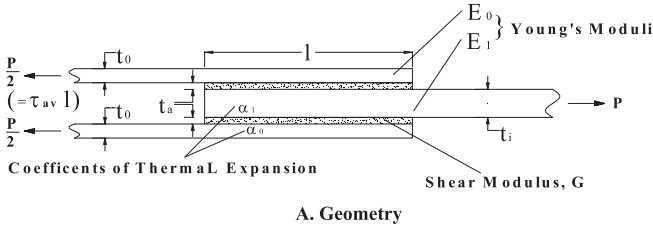
A. Geometry

B. Forces and Displacements

Figure 5-20. Coordinate system and deformations in a composite bonded joint with dissimilar adherends.
Source: Hart-Smith (1972), courtesy of Dr. John Hart-Smith and the Boeing Company.

(refer to Fig. 5-20), and of stress–strain relations for both adherends and adhesive, using compatibility conditions, which ensures bond continuity. Two governing equations—one for the elastic adhesive zone and the other for the plastic adhesive zone(s)—are then developed and solved using boundary conditions both at the elastic-to-plastic transition(s) and at the joint extremities. Figure 5-21 shows typical stress and strain distributions for balanced adherends. The complete nondimensionalized solution for balanced double-lap bonded joints is illustrated in Figure 5-5.

5.7.1.1 Shear Strength of Bonded Joints.   As mentioned earlier, the joint load is proportional to the overlap for short (fully plastic) overlaps. For balanced double-lap bonded joints, the plateau strengths are defined by the following relation:

τ

γ_e γ_p

τ_p

ARCTAN (G)

γ

Adhesive Properties

d

Plastic   Elastic   Plastic

1

Adhesive Behaviour

τ_p

Adhesive Shear Stresses

$\gamma_e + \gamma_p$ γ_e

Adhesive Shear Strain

σ_0

Adrerend Stresses

σ_i
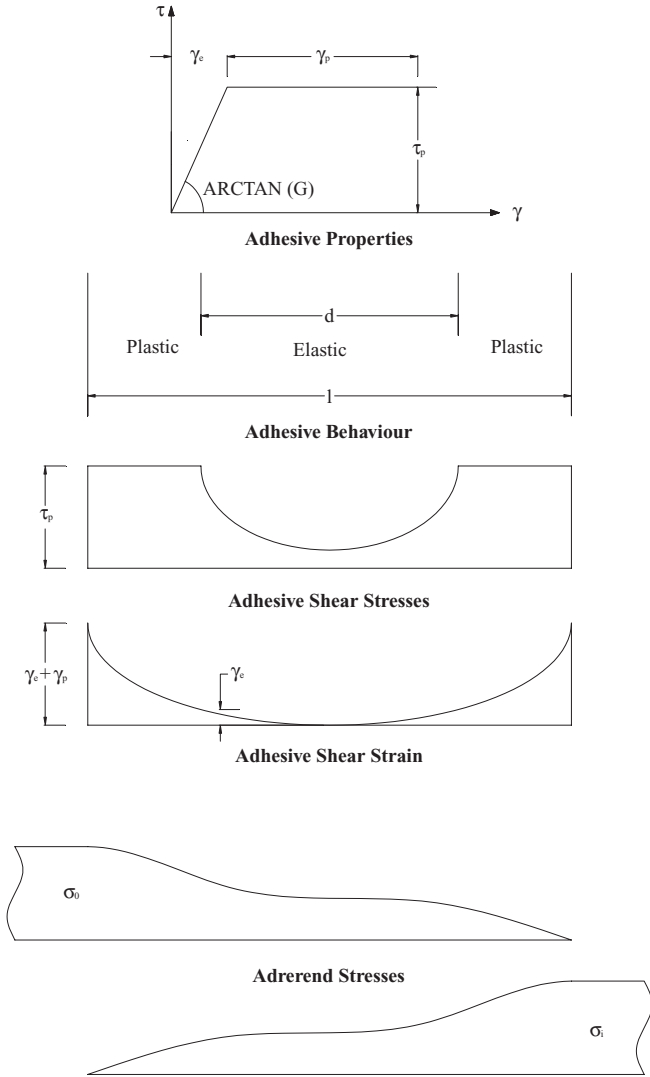
Figure 5-21. Stresses and strains in double-lap bonded joints.
Source: Hart-Smith (1972), courtesy of Dr. John Hart-Smith and the Boeing
Company.

$$\frac{\tau_{av}}{\tau_p}\left(\frac{\lambda l}{2}\right) \rightarrow \sqrt{1 + 2\frac{\gamma_p}{\gamma_e}} \qquad (5\text{-}7)$$

It should be recalled that τ_{av} refers to average shear stress, identified in
Fig. 5-20a, while τ_p represents the plastic adhesive shear stress, which is
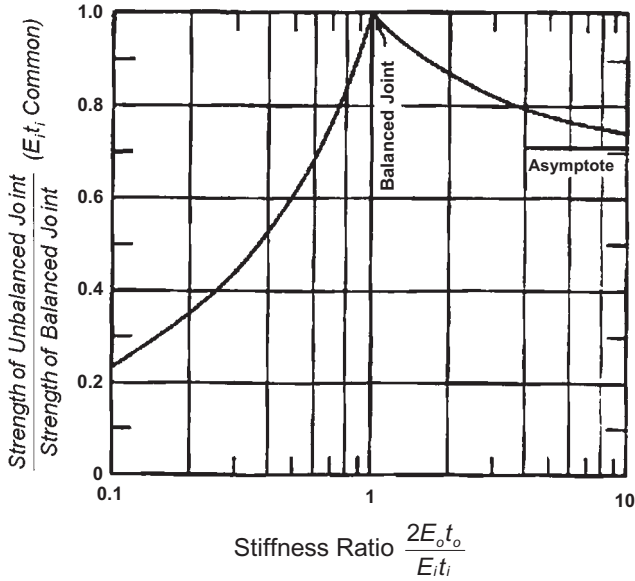equivalent to the maximum elastic value. Rearranging Eq. 5-7 leads to the
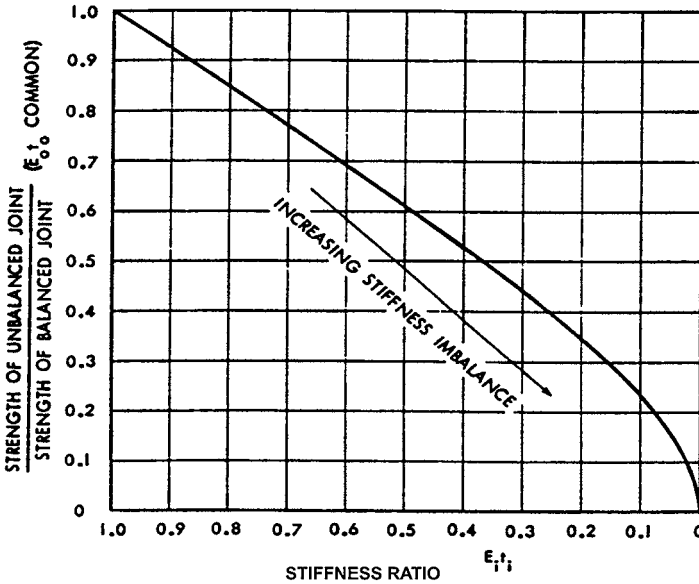
Figure 5-22. Strength reduction factor in unbalanced double-lap bonded joints due to adherend stiffness imbalance.
Source: Hart-Smith (1972), courtesy of Dr. John Hart-Smith and the Boeing Company.

following explicit expression for maximum shear load transferable in a balanced joint:

$$P = 2\tau_{av}l = \sqrt{4t_a\tau_p\left(\frac{\gamma_e}{2} + \gamma_p\right) \cdot 4E_o t_o} \tag{5-8}$$

The quantity $\tau_p\left(\frac{\gamma_e}{2} + \gamma_p\right)$ represents the area under the stress–strain curve per unit volume of adhesive. Multiplying this quantity by the adhesive thickness, t_a, converts it to the shear strain energy per unit area of bond. Equation 5-8 is restricted to balanced bonded joints. Here, E_o and t_o respectively refer to the stiffness and thickness of the balanced adherends. For unbalanced bonded joints (i.e., bonded joints with dissimilar adherends), the predictions have the form of Eq. 5-9; however, the plateau strengths are reduced. Figures 5-22 and 5-23 provide a correction factor to be applied to the plateau strength predictions for a balanced bonded joint. It should be noted that, in Fig. 5-22, the outer adherends are the common reference between the balanced and unbalanced sets of adherends, while in Fig. 5-23, the reference is the inner adherend. Figure 5-24

The figure's y-axis is labeled "$\dfrac{\text{Strength of Unbalanced Joint}}{\text{Strength of Balanced Joint}}$ ($E_i t_i$ Common)" with values 0, 0.2, 0.4, 0.6, 0.8, 1.0. The x-axis is labeled "Stiffness Ratio $\dfrac{2E_o t_o}{E_i t_i}$" ranging from 0.1 to 10. Labels "Balanced Joint" and "Asymptote" appear on the plot.

Figure 5-23. Strength reduction factor in unbalanced bonded joints due to adherend stiffness imbalance.
Source: Hart-Smith (1972), courtesy of Dr. John Hart-Smith and the Boeing Company.

provides a correction factor to be applied to the plateau strength predictions due to adherends thermal mismatch.

For double-lap bonded joints with unbalanced adherends, the theory predicts that the most critical end of a bonded joint may not be identifiable by inspection. For that reason, the maximum possible bond shear strength for a given set of adherends is determined by the lesser of the following pair of equations (refer to Fig. 5-20):

$$P = 2\tau_{av}l = (\alpha_o - \alpha_i)\Delta T E_i t_i + \sqrt{\left[2kt_a\tau_p(\gamma_e + \gamma_p)\cdot 2E_i t_i\left(1 + \frac{E_i t_i}{2E_o t_o}\right)\right]} \qquad (5\text{-}9)$$

$$P = 2\tau_{av}l = (\alpha_i - \alpha_o)\Delta T E_o t_o + \sqrt{\left[2kt_a\tau_p(\gamma_e + \gamma_p)\cdot 4E_o t_o\left(1 + \frac{2E_o t_o}{E_i t_i}\right)\right]} \qquad (5\text{-}10)$$

where E_i and t_i respectively refer to the stiffness and thickness of the unbalanced adherends and k is a strain ratio determined from the adhesive stress–strain characteristics, which is expressed as follows:
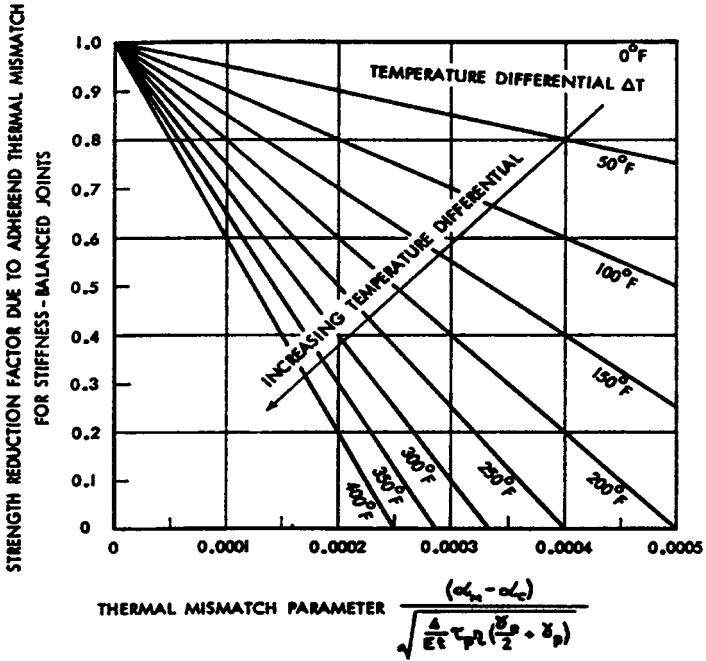
Figure 5-24. Strength reduction factor in unbalanced bonded joints due to adherend thermal mismatch.
Source: Hart-Smith (1972), courtesy of Dr. John Hart-Smith and the Boeing Company.

$$k = \frac{\left(\dfrac{\gamma_e}{2} + \gamma_p\right)}{(\gamma_e + \gamma_p)} \tag{5-11}$$

For mechanically unbalanced, thermally balanced bonded joints, Eqs. 5-9 and 5-10 are reduced to the following forms using Eq. 5-11:

$$P = 2\tau_{av}l = \sqrt{\left[2t_a\tau_p\left(\frac{\gamma_e}{2} + \gamma_p\right)\cdot 2E_it_i\left(1 + \frac{E_it_i}{2E_ot_o}\right)\right]} \tag{5-12}$$

$$P = 2\tau_{av}l = \sqrt{\left[2t_a\tau_p\left(\frac{\gamma_e}{2} + \gamma_p\right)\cdot 4E_ot_o\left(1 + \frac{2E_ot_o}{E_it_i}\right)\right]} \tag{5-13}$$

It should be noted that Eqs. 5-12 and 5-13 correspond to Eqs. 5-72 and 5-73, page 546, of the *EUROCOMP Design Code and Handbook* (Clarke 1996). However, there are some differences between the original Eqs. 5-12 and 5-13 derived from Hart-Smith (1973b) and the equations presented in the *EUROCOMP Design Code and Handbook*. The differences are described below.

- The term $\left(1+\dfrac{E_i t_i}{2E_o t_o}\right)$ in the original Eq. 5-12 is shown as $\left(1+\dfrac{E_i t_i}{E_o t_o}\right)$
  in Eq. 5-72 of the *EUROCOMP Design Code and Handbook.*

- The term $4E_o t_o \left(1+\dfrac{2E_o t_o}{E_i t_i}\right)$ in the original Eq. 5-13 is shown as
  $2E_o t_o \left(1+\dfrac{E_o t_o}{E_i t_i}\right)$ in Eq. 5-73 of the *EUROCOMP Design Code and Handbook.*

5.7.1.2 Peel Strength of Bonded Joints.

5.7.1.2.1 Single-Lap Bonded Joints with Identical Adherends.   The peak adhesive peel stress at the ends of the overlap due to the application of tensile lap shear loads is:

$$\sigma_{c\max} = M_e \sqrt{\frac{E_c}{2t_a D}} \tag{5-14}$$

where
$\sigma_{c\max}$ = peak adhesive peel stress
E_c = transverse adhesive peel modulus
t_a = adhesive thickness
D = bending stiffness of the adherends
M_e = bending moment in the adherends at the ends of the overlap,
and is expressed by the following relation:

$$M_e = \frac{\dfrac{P(t+t_a)}{2}}{1+\xi c+\dfrac{1}{6}\xi^2 c^2} = \frac{kP(t+t_a)}{2} \tag{5-15}$$

where
t = adherend thickness
P = applied tensile load per unit width
c = half the bonded overlap length in the direction of the applied load
ζ = an exponent described by the following equation:

$$\xi = \sqrt{\frac{P}{D}} \tag{5-16}$$

Equation 5-14 shows that the peak peel stress is proportional to the adherend bending moment, M_e, which decreases as the overlap increases, as illustrated in Fig. 5-25.
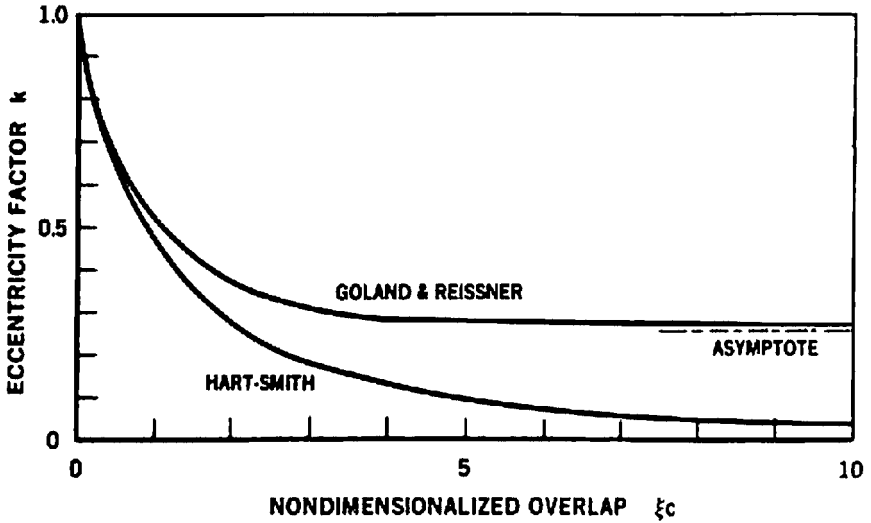
Figure 5-25. Comparison between solutions for adherend bending stresses in balanced single-lap bonded joints.
Source: Hart-Smith (1981), courtesy of Dr. John Hart-Smith and the Boeing Company.

5.7.1.2.2 Single-Lap Bonded Joints with Dissimilar Adherends. At the ends of a single-lap joint with adherends with different thicknesses, both the adherend bending moment and the peak adhesive peel stress are intensified at the end from which the thinner adherend extends. Figure 5-26 illustrates the effect of stiffness imbalance on reducing the adherend bending strength of single-lap bonded joints with dissimilar adherends. The associated increase in the adhesive peel stresses for one particular value of the nondimensionalized peel stress coefficient (CPEEL = 0.5) is shown in Fig. 5-27.

5.7.1.2.3 Double-Lap and Double-Strap Bonded Joints. For double-lap and double-strap bonded joints, the load path has no eccentricity; however, peel stresses are still generated at the outer adherend. Figure 5-28 illustrates the source of peel stresses induced in these bonded joints. The peak adhesive peel stress for double-lap and double-strap bonded joints is given by

$$\frac{\sigma_{c_{\max}}}{\tau_p} = \left[3(1-\upsilon^2)\frac{E_c}{E} \right]^{\frac{1}{4}} \left(\frac{t_o}{t_a} \right)^{\frac{1}{4}} \tag{5-17}$$
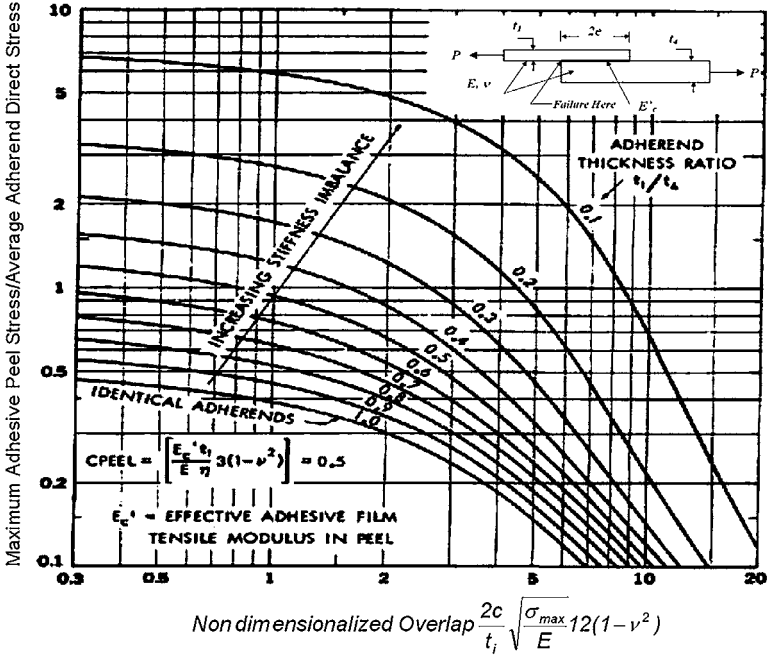
where
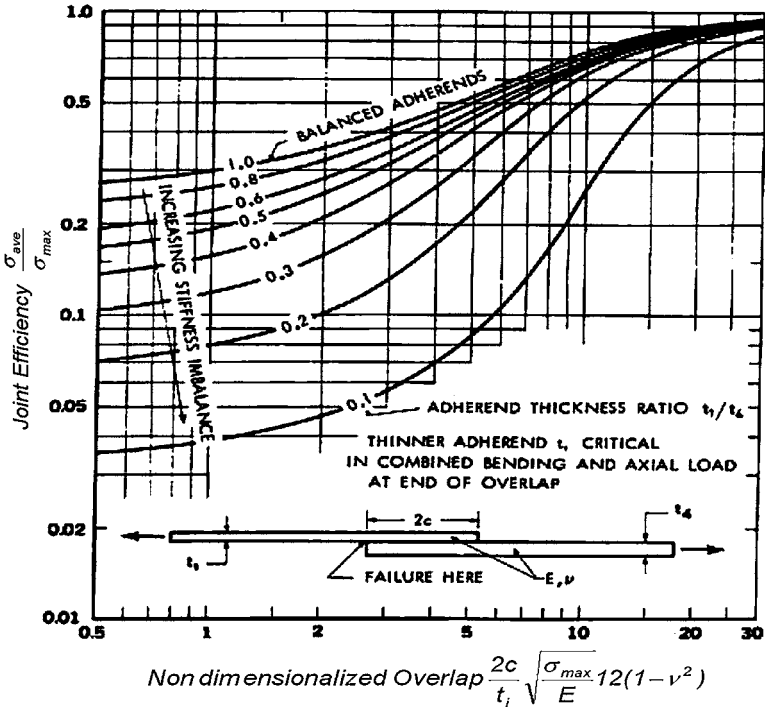
Figure 5-26. Effect of adherend stiffness imbalance on adherend bending strength of single-bonded joints.
Source: Hart-Smith (1981), courtesy of Dr. John Hart-Smith and the Boeing Company.

τ_p = peak adhesive shear stress (assumed to be constant throughout the area at the very end of the overlap)

E = modulus of elasticity of adherend

E_c = adhesive film tensile modulus in peel

t_o = adherent thickness (constant)

t_a = adhesive thickness

υ = Poisson's ratio of adherend.

Equation 5-17 indicates that, as the adherend/adhesive thickness ratio decreases, the peel stress decreases, with maximum reduction when this ratio equals unity. This concept was illustrated previously in Fig. 5-7.

The failure mode of double-lap bonded joints is a strong function of the adherend thickness (refer to Fig. 5-29). As shown, in bonded joints with sufficiently thin adherends, the weak link will always be in the adherends outside the joint. On the other hand, if the adherends are sufficiently thick, peeling is likely the predominant mode of failure (except

Figure 5-27. Effect of adherend stiffness imbalance on peel stresses in single bonded joints.
Source: Hart-Smith (1986), courtesy of Dr. John Hart-Smith and the Boeing Company.
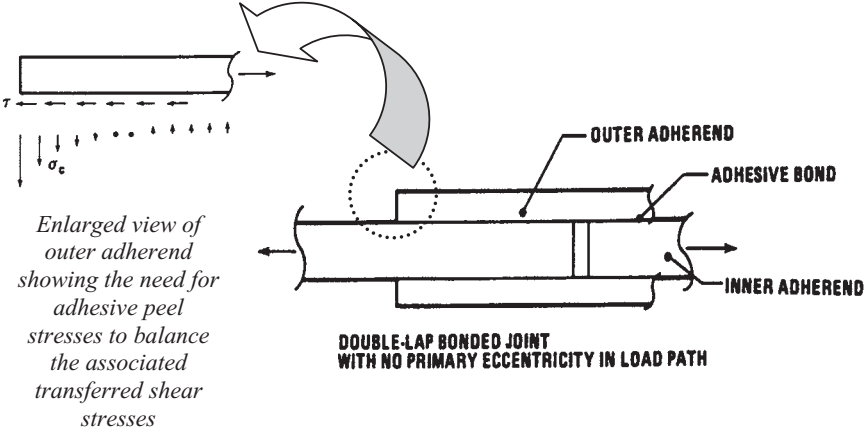
Figure 5-28. Induced peel stresses in double-lap bonded joints.
Source: Hart-Smith (1986), courtesy of Dr. John Hart-Smith and the Boeing Company.
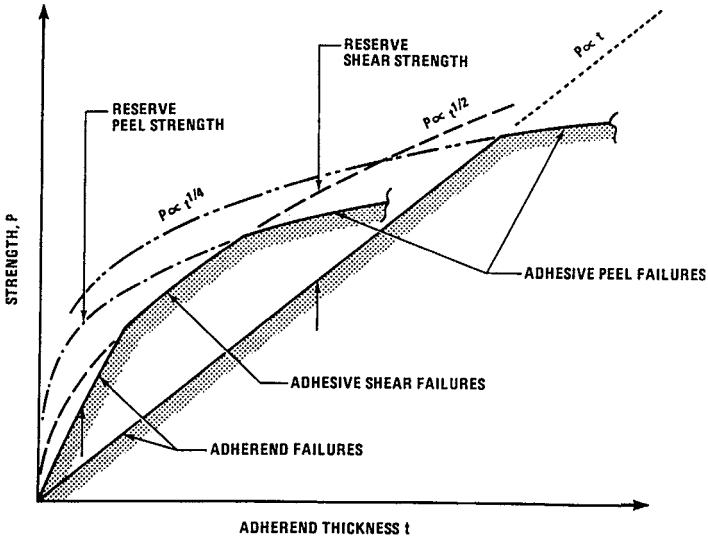
Figure 5-29. Relative severity of adhesive shear and peel stresses on ultimate strength of bonded joints.
Source: Hart-Smith (1986), courtesy of Dr. John Hart-Smith and the Boeing Company.

if tapered ends are used as shown in Fig. 5-7). Figure 5-29 also shows that the adhesive shear failure would occur according to a $t^{1/2}$ power low (refer to Eqs. 5-12 and 5-13), while peel failure will occur according to a $t^{1/4}$ relation for a peel failure (refer to Eq. 5-17).

5.7.2 EUROCOMP Design Code and Handbook Approach

Chapter 5 of the *EUROCOMP Design Code and Handbook* (Clarke 1996) presents two design methods for bonded joints:

- *Simplified Design Procedure:* This procedure is based on experimental test data obtained from standard tests, such as ASTM D 3163-01, "Standard Test Method for Determining Strength of Adhesively Bonded Rigid Plastic Lap-Shear Joints in Shear by Tension Loading"; ISO 4587-1979; or corresponding test protocols. According to the simplified design procedure, the lap length is taken as twice the total lap length of the test specimen and should not be less than 2 in. (50 mm). The simplified procedure is only recommended for preliminary design of primary structural joints or for final design of nonstructural joints. Section 5.3.5.4 of the *EUROCOMP Design Code and Handbook* provides a detailed description of this method.

• *Rigorous Design Procedure:* According to this method, the following limit-state conditions should be met:

$$\tau_{o_{max}} \leq \tau_{o_{allowable}} \tag{5-18}$$

$$\sigma_{o_{max}} \leq \sigma_{o_{allowable}} \tag{5-19}$$

$$\sigma_{o_{max}} \leq \sigma_{z_{allowable}} \tag{5-20}$$

where
$\tau_{o_{max}}$ = maximum adhesive shear stress
$\tau_{o_{allowable}}$ = allowable adhesive shear stress
$\sigma_{o_{max}}$ = maximum adhesive peel (tensile) stress
$\sigma_{o_{allowable}}$ = allowable adhesive peel (tensile) stress
$\sigma_{z_{allowable}}$ = allowable adherend through-the-thickness tensile stress.

For single-lap and single-strap bonded joints, the *EUROCOMP Design Code and Handbook* adopted the analysis performed by Goland and Reissner (1944) that was adopted earlier by Hart-Smith (1973b). The Hart-Smith (1973b) approach was adopted by the *EUROCOMP Design Code and Handbook* for the analysis of double-lap and double-strap bonded joints (see Section 5.7 of this chapter). For the scarf-bonded joints analysis, the *EUROCOMP Design Code and Handbook* adopted the methodology of the European Space Agency (ESA 1988). Section 5.3.5.5 of the *EUROCOMP Design Code and Handbook* provides a detailed description of this method.

5.7.3 Chamis and Murthy Modified Approach

This approach was developed at the NASA Lewis Research Center (currently called the NASA Glenn Research Center) by Chamis and Murthy in 1989. This modified procedure is intended for preliminary design of adhesively bonded composite joints. In this procedure, equations to check the critical conditions of the bonded joint—such as minimum length, maximum adhesive shear stress, and peel-off stresses—are used in the preliminary design of bonded joints. This analytical approach includes the environmental effects on the behavior of composite bonded joints. In addition, a FORTRAN program (BOND.EXE) was developed—based on the modified approach of Chamis and Murthy (1989)—to facilitate the analysis. The program is user-friendly and requires the engineer to input known and assumed basic joint information (described later in this section). Additional information related to this program may be found on the ASCE Construction Institute Web site, http://www. constructioninst.org.
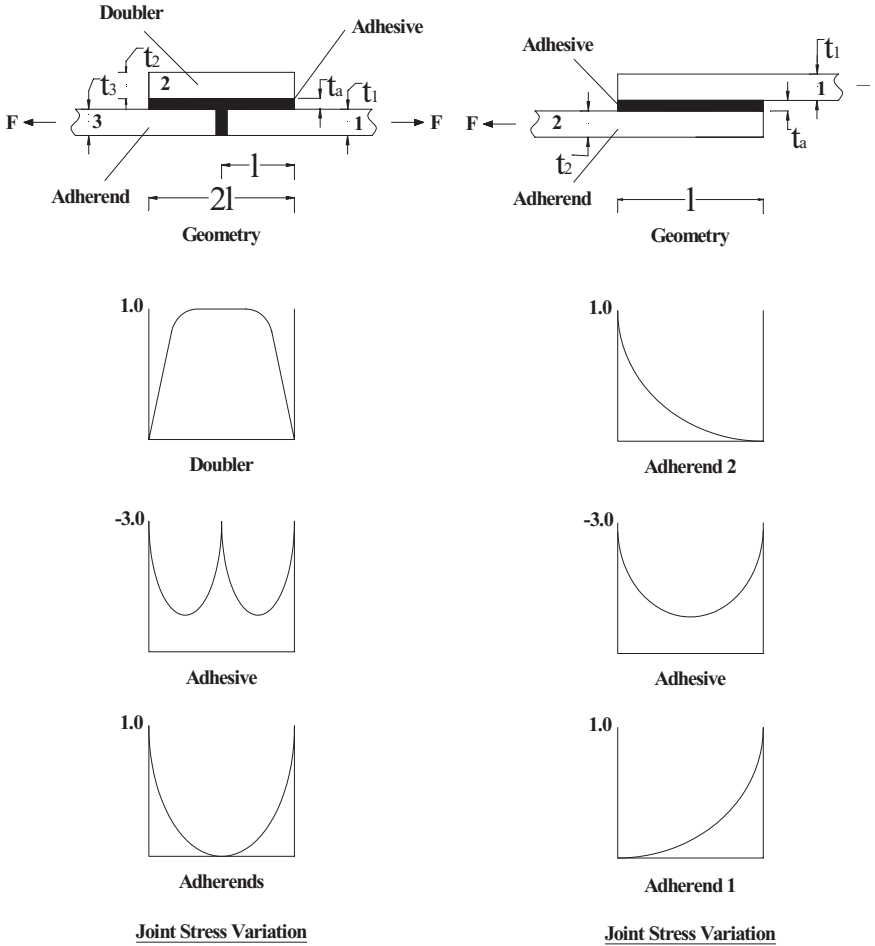
Figure 5-30. Adhesively bonded joint definitions and fundamentals.
Source: Courtesy of Dr. Chris Chamis, NASA Glenn.

The fundamentals and terminology associated with adhesively bonded joints used in this method are illustrated in Fig. 5-30. In this figure, only two joint configurations are shown: strap, or "single-doubler," and single-lap joints. However, the notation and geometrical dimensions are similar for all different joints, including double-lap, scarf, step, and double-doubler joints, as shown in Fig. 5-31. It should be noted that, in these figures, single-strap joints are called butt/single-doubler, and double-strap joints
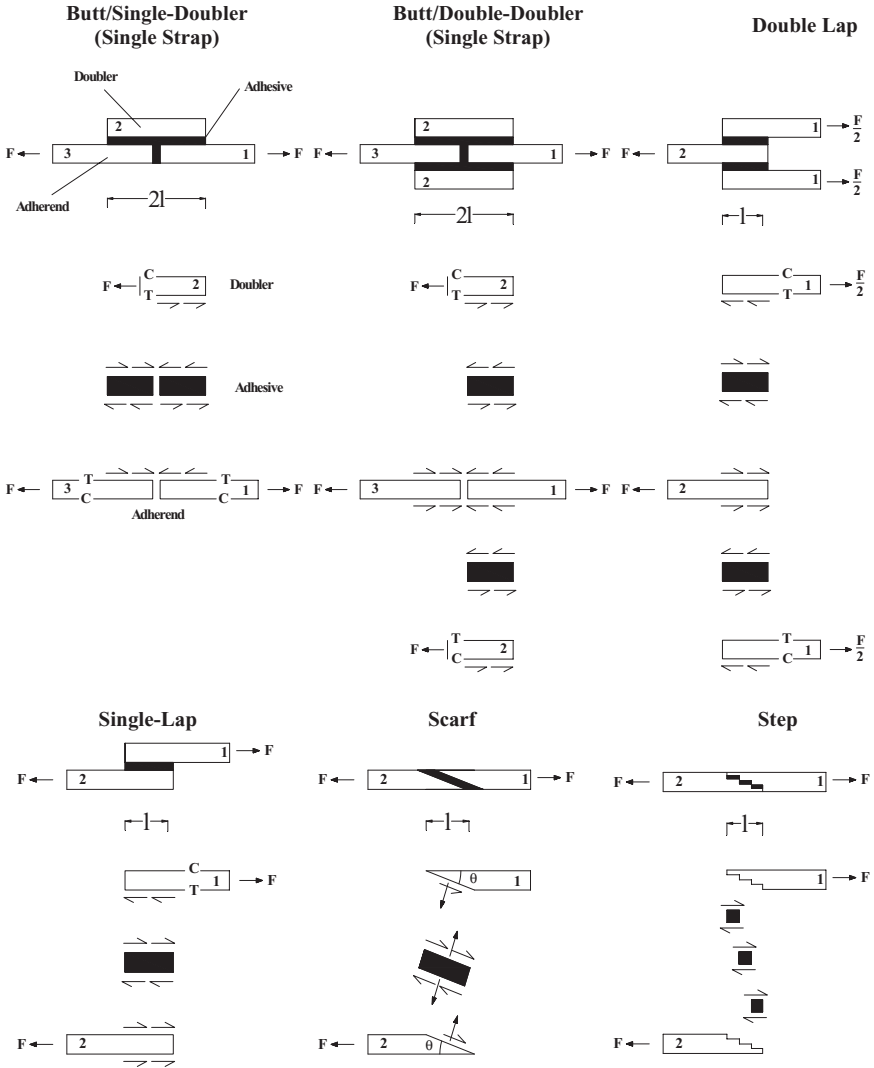
Figure 5-31. Schematics of commonly used adhesive joints (free-body diagram and governing equations).
Source: Courtesy of Dr. Chris Chamis, NASA Glenn.

are called butt/double-doubler. Also, adherends and/or doublers are identified by numerical subscripts, while the adhesive is identified by the subscript letter "a." The term "doubler" is equivalent to the "splice plate(s)" in civil engineering terminology. The in-plane stress in the adherend is denoted by σ_{ixx}, for example, where the subscript "xx" refers to the x-axis which is taken along the joint length.

In Fig. 5-30, the following points should be noted:

- The stresses transfer from one adherend to the adhesive and then to the other adherend.
- These stresses increase very rapidly from the end and are highly nonlinear.
- The estimates are obtained from simple shear-lag theory for minimum length (l^{min}), maximum adhesive shear stress (σ_{as}^{max}), and maximum adhesive peel stress (σ_{an}^{max}).

Few modifications to the Chamis and Murthy (1989) solution strategy have been made. This includes the method of calculating the joint length and the thickness of the doubler(s) or splice plate(s). Details of these modifications are presented in Section 5.7.4.1.

5.7.3.1 General Steps for Designing Adhesively Bonded Composite Joints.   According to the Chamis and Murthy (1989) method, the following steps are to be performed in designing bonded composite joints:

Table 5-3. Predicted Laminate Properties of T300/E at 0.6 FVR Laminates Using ICAN Code

Property	$(0/\pm45/0/90)_s$	$(0_3/\pm80)_s$	$(0/+30/0^{s^a}/-30/0)_s$
E_{cxx} (mpsi)	10.0	12.5	12.8
E_{cyy} (mpsi)	6.5	8.3	1.7
E_{czz} (mpsi)	1.4	1.4	1.5
G_{cxy} (mpsi)	2.4	7.9	2.0
G_{cyz} (mpsi)	0.43	0.43	0.39
G_{cxz} (mpsi)	0.48	0.48	0.59
v_{cxy}	0.31	0.06	0.91
v_{cyz}	0.32	0.38	0.36
v_{cxz}	0.26	0.36	~0
α_{cxx} (μ–in./in./°F)	0.41	0.53	−0.53
α_{cyy} (μ–/in./°F)	1.5	1.3	10.1
α_{czz} (μ–/in./°F)	20.1	20.1	16.3

FVR, fiber volume ratio; ICAN, International Code of Area Nomenclature.
[a]0^s denotes S-G/E ply.

Table 5-4. Predicted Fracture Stress (Strength) for T300/E (@ 0.6 FVR Laminates Using ICAN Code

Property	$(0/\pm45/0/90)_s$	$(03/\pm80)_s$	$(0/+30/0^{s^a}/-30/0)_s$
S_{cxxT} (ksi)	79.2	94.8	129.3
S_{cxxC} (ksi)	79.7	99.1	70.5
S_{cyyT} (ksi)	49.8	61.0	6.3
S_{cyyC} (ksi)	51.5	67.8	14.7
S_{cxyS} (ksi)	38.7	13.1	20.0
S_{czyS} (ksi)	21.8	21.8	21.8

$^a0^s$ denotes S-G/E ply.
FVR, fiber volume ratio; ICAN, International Code of Area Nomenclature; S_c, laminate strength; x, y, z: directions (x, y = laminate plane, z = thickness); T, C, S: tension, compression, and shear.

1. Establish joint design requirements, including loads, laminates, adhesive, safety factors, and other special considerations.
2. Obtain laminate dimensions and properties for the adherends using composite mechanics. (Typical properties needed for this procedure are summarized in Tables 5-3 and 5-4 for three different laminates.)
3. Obtain the following adhesive properties: (1) shear strength, and (2) peel strength.
4. Depending on the expected service conditions, degrade the adhesive properties to account for moisture, temperature, and cyclic loads using the following equations:

$$\frac{S_a}{S_{ao}} = \left[\sqrt{\frac{T_{gw} - T}{T_{gd} - T_o}} \right] - 0.1 \quad \log(N) \tag{5-21}$$

where
S_a = expected adhesive strength being calculated for a particular loading environment
S_{ao} = corresponding strength at reference conditions (usually taken as room temperature dry)
N = number of cycles the bonded joint must endure under the design stress
T_{gw} = wet adhesive glass-transition temperature given by:

$$T_{gw} = (0.005M^2 - 0.1M + 1.0)T_{gd} \tag{5-22}$$

where
M = adhesive moisture content in percent by weight
T_{gd} = adhesive dry glass transition temperature at service conditions
T_o = reference temperature at which S_{ao} was determined (usually taken as room temperature).

5. Select design allowables that are either set by the design criteria or chosen as follows:
   a. A load factor on the force, F, usually 1.5 or 2.0, or
   b. A safety factor of one-half (0.5) of the degraded adhesive strength, S_a, described earlier in Step 4, above. This alternative is preferable since the force, F, may already contain a load factor.
6. Select the length, l, of the joint. This procedure is different from the one adopted by Chamis and Murthy (1989). Instead of using the average shear stress in calculating the length, the following modification in calculating the joint length is proposed, based on the shear lag equations shown in Fig. 5-30:

$$\because \sigma_{ns}^{max} \leq \overline{S_{as}} \tag{5-23}$$

and

$$\overline{S_{as}} = (S_{as}) \cdot (SF)_a \tag{5-24}$$

where
σ_{as}^{max} = maximum adhesive shear stress
$\overline{S_{as}}$ = allowable adhesive shear strength
$(SF)_a$ = adhesive safety factor.

According to the shear lag equations, we have:

$$\sigma_{as}^{max} \approx 3\sigma_{as} \tag{5-25}$$

where σ_{as} can be calculated for different joint configurations using the following expressions:

For butt/single-doubler, single-lap, and stepped joints:

$$\sigma_{as} = \frac{F}{l} \tag{5-26}$$

For butt/double-doubler and double-lap joints:

$$\sigma_{as} = \frac{F}{2l} \tag{5-27}$$

For scarf joints:

$$\sigma_{as} = \frac{F}{2t_1}\sin 2\theta \qquad (5\text{-}28)$$

Now, substituting by the appropriate adhesive shear stress expressions (Eqs. 5-26 through 5-28) for each joint configuration into Eq. 5-25, $\sigma_{as}^{\max}$ expressions for each joint configuration can be developed. Finally, substituting by the different $\sigma_{as}^{\max}$ expressions into Eq. 5-23 and rearranging terms, the following expressions for the joint length, l, are obtained:

$$
\begin{aligned}
l &= \frac{3\overline{F}}{\overline{S}_{as}} &\text{(Butt/Single-Doubler Joints)} &\quad\text{(a)}\\[6pt]
&= \frac{3\overline{F}}{2\overline{S}_{as}} &\text{(Butt/Double-Doubler Joints)} &\quad\text{(b)}\\[6pt]
&= \frac{3\overline{F}}{\overline{S}_{as}} &\text{(Single-Lap Joints)} &\quad\text{(c)}\\[6pt]
&= \frac{3\overline{F}}{2\overline{S}_{as}} &\text{(Double-Lap Joints)} &\quad\text{(d)}\\[6pt]
&= \frac{3\overline{F}}{\overline{S}_{as}} &\text{(Stepped Joints)} &\quad\text{(e)}\\[6pt]
&= \frac{t_1}{\tan \theta} &\text{(Scarf Joints)} &\quad\text{(f)}
\end{aligned}
\qquad (5\text{-}29)
$$

where
$\overline{F}$ = load (tensile/compression/shear) in the adherends per unit width
$\overline{S}_{as}$ = design allowable shear stress in the adhesive
t_1 = adherend thickness as shown in Fig. 5-31
θ = bond-line angle, given by:

$$\theta = \tan^{-1}\left(\frac{t_1}{l}\right) \qquad (5\text{-}30)$$

7. Check the minimum length from the following equation:

$$l^{\min} = 0.7 t_a \sqrt{\frac{E_{cxx}}{G_a}} \geq 1.0 \text{ in.} \ (\geq 25.4 \text{ mm}) \qquad (5\text{-}31)$$

where
$l^{\min}$ = minimum joint length (for *half* of the total lap length of butt/single-doubler and butt/double-doubler joints, and for the *total* lap length of double-lap, scarf and step bonded joints)
t_a = adhesive thickness

E_{cxx} = adherend modulus of elasticity along the joint length
G_a = adhesive shear modulus.

8. Compare the calculated length (Step 6) with the minimum length (l^{min}) calculated in Step 7. Adjust the length to satisfy the shear lag equation and/or to make it practical to fabricate. This length will now be designated as the modified or selected length (l^{sel}). If the selected length is different from the calculated length, check the modified average adhesive shear stresses σ_{as}' using the selected corresponding length (l^{sel}) for the particular joint configuration under consideration (Eqs. 5-26 through 5-28).

9. Calculate the margin of safety (MOS) for average adhesive shear stress as:

$$MOS(\sigma_{as}') = \frac{\overline{S_{as}}}{\sigma_{as}'} - 1 \qquad (5\text{-}32)$$

10. Check the maximum adhesive shear stresses ($\sigma_{as}^{max'}$) using the modified values of the average adhesive shear stress obtained from Step 8 and using the following equation:

$$\sigma_{as}^{max'} \cong 3\sigma_{as}' \qquad (5\text{-}33)$$

11. Calculate the MOS for maximum adhesive shear stress $MOS(\sigma_{as}^{max'})$ using the following equation:

$$MOS(\sigma_{as}^{max'}) = \frac{\overline{S_{as}}}{\sigma_{as}^{max'}} - 1 \qquad (5\text{-}34)$$

12. Calculate the adhesive peel-off stress (σ_{an}) using the following equations:

$$\sigma_{an} = \begin{cases} \dfrac{3F}{l^{sel} + t_{adhr}} & \text{(Butt/Single-Doubler Joints)} & \text{(a)} \\[3mm] \dfrac{3F}{l^{sel} + t_{dbl}} & \text{(Butt/Double-Doubler Joints)} & \text{(b)} \\[3mm] \dfrac{3F}{l^{sel} + t_{adhr}} & \text{(Double-Lap Joints)} & \text{(c)} \\[3mm] \dfrac{3F}{l^{sel} + t_{min}} & \text{(Single-Lap Joints)} & \text{(d)} \\[3mm] \approx 0 & \text{(Stepped Joints)} & \text{(e)} \\[3mm] \dfrac{F}{t_1}\sin^2\theta & \text{(Scarf Joints)} & \text{(f)} \end{cases} \qquad (5\text{-}35)$$

where

σ_{an} = adhesive peal-off stress
t_{adhr} = adherend thickness
t_{dbl} = doubler or splice plate thickness
t_{min} = thickness of the thinner adherend of the single-lap joint
θ = bonding angle (refer to Eq. 5-28 and Fig. 5-31).

13. Calculate the MOS for adhesive peel-off stress (σ_{an}) as:

$$MOS(\sigma_{an}^{max}) = \frac{\overline{S_{an}}}{\sigma_{an}} - 1 \qquad (5\text{-}36)$$

where $\overline{S_{an}}$ is the design allowable shear stress in the adhesive, calculated as:

$$\overline{S_{an}} = (S_{an}) \cdot (SF)_a \qquad (5\text{-}37)$$

14. Calculate the bending stresses in the doublers (splice plates) and adherends using the following equations:
   a. *Doublers (Splice Plates):*
      ▪ Butt/single-doubler

$$\sigma_t^{dbl} = \frac{4F}{t_{dbl}} \quad \& \quad \sigma_c^{dbl} = \frac{-2F}{t_{dbl}} \qquad (5\text{-}38)$$

      ▪ Butt/double-doubler

$$\sigma_t^{dbl} = \frac{2F}{t_{dbl}} \quad \& \quad \sigma_c^{dbl} = \frac{-F}{t_{dbl}} \qquad (5\text{-}39)$$

      ▪ Double-lap

$$\sigma_t^{dbl} = \frac{4F}{t_1} \quad \& \quad \sigma_c^{dbl} = \frac{-2F}{t_1} \qquad (5\text{-}40)$$

   b. *Adherends:*
      ▪ Butt/single-doubler

$$\sigma_t^{adhr} = \frac{4F}{t_{adhr}} \quad \& \quad \sigma_c^{adhr} = \frac{-2F}{t_{adhr}} \qquad (5\text{-}41)$$

      ▪ Butt/double-doubler

$$\sigma_t^{adhr} = \frac{F}{t_{adhr}} \qquad (5\text{-}42)$$

- Double-lap

$$\sigma_t^{adhr} = \frac{F}{t_{adhr}} \tag{5-43}$$

- Scarf and stepped

$$\sigma_{t1}^{adhr} = \frac{F}{t_1} \quad \& \quad \sigma_{t1} = \frac{F}{t_2} \tag{5-44}$$

- Single-lap

$$\sigma_{t1}^{adhr} = \frac{4F}{t_1}, \qquad \sigma_{c1}^{adhr} = \frac{-2F}{t_1}$$
$$\sigma_{t2}^{adhr} = \frac{4F}{t_2}, \qquad \sigma_{c2}^{adhr} = \frac{-2F}{t_2} \tag{5-45}$$

where
$\sigma_{t1}^{adhr} = \sigma_{1xxT}$ = longitudinal tensile stress in the top adherend, as shown in Fig. 5-32
$\sigma_{c1}^{adhr} = \sigma_{1xxC}$ = longitudinal compressive stress in the bottom adherend, as shown in Fig. 5-32
$\sigma_{t2}^{adhr} = \sigma_{2xxT}$ = longitudinal tensile stress in the bottom adherend, as shown in Fig. 5-32
$\sigma_{c2}^{adhr} = \sigma_{2xxC}$ = longitudinal compressive stress in the bottom adherend
t_1 = thickness of the top adherend, as shown in Fig. 5-32
t_2 = thickness of the bottom adherend, as shown in Fig. 5-32.

15. Calculate the bonded joint efficiency, η_b, as follows:

$$\eta_b = \frac{\text{Joint Force Transferred}}{\text{Adherend Fracture Load}} \times 100 \quad \text{or}$$
$$\eta_b = \frac{F}{S_{cxx}\, t_1} \times 100 \tag{5-46}$$

where
η_b = bonded joint efficiency (%)
F = load transferred through the joint
S_{cxx} = adherend longitudinal strength
t_1 = adherend thickness.

16. Summarize the joint design.
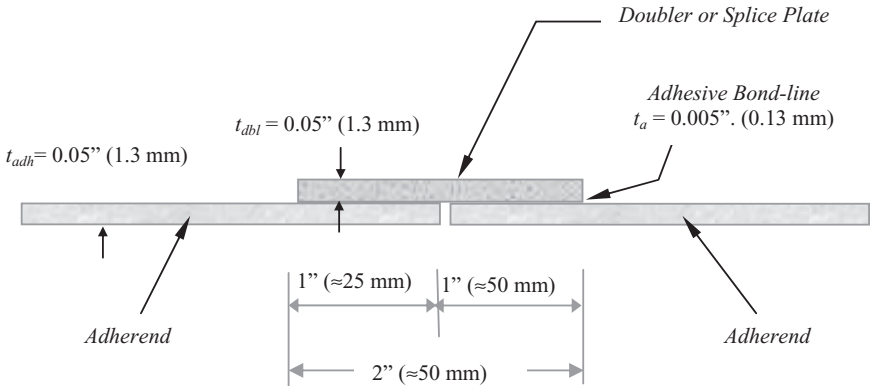
Figure 5-32. Geometrical details of the bonded single-doubler (single-strap) butt joint of Example 5-1.

5.7.3.2 Numerical Examples.   This section presents two numerical examples that follow the modified Chamis and Murthy (1989) approach. It should be noted that the information adopted in these examples is identical to the information used by Chamis and Murthy except for the larger number of loading cycles used in Example 5-2. However, and due to the modifications introduced to their approach, different conservative results were obtained.

The first example deals with the preliminary design of a bonded joint with a butt/single-doubler (single-strap bonded joint) with no environmental effects. The second example deals with the design of a butt joint with a single-doubler (single-strap joint) in a hygrothermal environment and under cyclic loading conditions.

Example 5-1. Design a Bonded Composite Joint with the Following Specifications

Joint design requirements:

Loads: 800 lb/in. static
Service environment: Room temperature, dry conditions
Laminates (adherends): Both adherends have the following properties:
   Lay-up: $(0/\pm45/0/90)_s$ T300/E @ 0.6 fiber volume ratio (FVR) (refer to Tables 5-3 and 5-4)
   Thickness: 0.05 in. (1.27 mm)
Adhesive:
   Epoxy matrix (same as in the laminate)
   Adhesive thickness = 0.005 in. (0.127 mm)
Safety factors (SF): 1.0 on joint load, 0.5 on adhesive strengths

Laminate properties: Refer to Tables 5-3 and 5-4.

Adhesive properties: t_a = 0.005 in. (0.127 mm), E_a = 0.5 × 10⁶ psi, G_a = 0.18 × 10⁶ psi, v_a = 0.35, α_a = 30 ppm/°F, S_{an} = 15 ksi, and S_{as} = 13 ksi.

Environmental effects: None

SOLUTION

Design allowables: Calculate the design allowable load and adhesive strength values using the corresponding safety factors, listed above, as follows:

- Joint load (SF = 1): 1 × 800 lb/in. = 800 lb/in.
- Allowable adhesive normal or peel strength [(SF)$_a$ = 0.5]:

$$\bar{S}_{an}=0.5\times15\,\text{ksi}=7.5\,\text{ksi or } 7{,}500\,\text{psi}$$

- Adhesive shear strength [(SF)$_a$ = 0.5]:

$$\bar{S}_{as}=0.5\times13\,\text{ksi}=6.5\,\text{ksi or } 6{,}500\,\text{psi}$$

Joint length: Using Eq. 5-29a, the half lap length is calculated as:

$$l=\frac{3F}{\bar{S}_{as}}=\frac{3\times800\,(\text{lb}/\text{in.})}{6{,}500\,(\text{psi})}=0.37 \text{ in. (9.4 mm)}$$

and the total lap length = $2l$ = 0.74 in. (18.8 mm).

1. Check joint critical conditions. In this step, the following three conditions must be checked:
   - Check minimum half length (l_{min}),
   - Check maximum adhesive shear stress σ_{as}^{max}, and
   - Check maximum adhesive peel stress σ_{an}^{max}.
     First, calculate the minimum length (l_{min}) using Eq. 5-31, where t_a = 0.005 in. (0.127 mm), E_{cxx} = 10 × 10⁶ psi, and G_a = 0.18 × 10⁶ psi.

$$\therefore l_{min}=0.7\times0.005 \text{ in.}\sqrt{\frac{10\times10^6 \text{ psi}}{0.18\times10^6 \text{ psi}}}=0.026 \text{ in.} < l < 1.0$$

   Thus, l_{min} = 1 in. (25.4 mm), and $2l_{min}$ = 2 in. (50.80 mm). Note that the value of the adhesive shear modulus, G_a, was not degraded by the 50% safety factor. However, degrading the shear modulus by 50% (0.5 × 0.18 mpsi = 0.09 mpsi) would result in a negligible

difference of 0.01 in. when calculating the minimum joint length (0.037 in. versus 0.026 in.).

Using this selected length, calculate corresponding value of the adhesive shear stress:

$$\sigma'_{as} = \frac{F}{l^{sel}} = \frac{800 \ (\text{lb/in.})}{1 \ \text{in.}} = 800 \ \text{psi}$$

2. Calculate MOS for actual average adhesive shear stress as:

$$MOS(\sigma'_{as}) = \frac{\overline{S_{as}}}{\sigma'_{as}} - 1 = \frac{6,500 \ (\text{psi})}{800 \ (\text{psi})} - 1 = 7.12$$

3. Check maximum adhesive shear stresses ($\sigma_{as}^{max'}$) using the modified (actual) value of the average adhesive shear stress (Eq. 5-33):

$$\sigma_{as}^{max'} \cong 3\sigma'_{as} = 3 \times (\text{psi}) = 2,400 \ \text{psi}$$

4. Calculate MOS for maximum adhesive shear stress ($\sigma_{as}^{max'}$) from Eq. 5-34:

$$MOS(\sigma_{as}^{max'}) = \frac{\overline{S_{as}}}{\sigma_{as}^{max'}} - 1 = \frac{6,500 \ (\text{psi})}{2,400 \ (\text{psi})} - 1 = 1.71$$

5. Calculate actual adhesive peel-off stress $MOS(\sigma_{as}^{max'})$ using Eq. 5-35a:

$$\sigma'_{an} = \frac{3F}{l^{sel} + t_{adhr}} = \frac{3 \times 800 \ (\text{lb/in.})}{1 \ (\text{in.}) + \ 0.05 \ (\text{in.})} = 2,286 \ \text{psi} < 7,500 \ \text{psi} \ \text{okay}$$

6. Calculate MOS for adhesive peel-off stress (σ'_{as}) from Eq. 5-36:

$$MOS(\sigma_{an}^{max}) = \frac{\overline{S_{an}}}{\sigma_{an}} - 1 = \frac{7,500 \ (\text{psi})}{2,286 \ (\text{psi})} - 1 = 2.28$$

7. Calculate the bending stresses developed in both the adherends and the doubler (splice plate):

Adherends: Using Eq. 5-41, both tensile and compressive stresses are calculated as follows:

$$\sigma_t^{adhr} = \frac{4F}{t_{adhr}} = \frac{4 \times 800 \ (\text{lb/in.})}{0.05 \ (\text{in.})} = 64,000 \ \text{psi} < 79,200 \ \text{psi} \ \text{okay}$$

$$\sigma_c^{adhr} = \frac{-2F}{t_{adhr}} = -\sigma_t^{adhr} = 32,000 \text{ psi} < 79,200 \text{ psi} \text{ okay}$$

Doublers (Splice Plates): In this example, the doubler thickness and laminate properties were not specified. Assuming the same laminate as for the adherends, and for ease of fabrication, assume the same adherend thickness of 0.05 in. Accordingly, the tensile and the compression stresses developed in the splice plate can be determined from Eq. 5-38, which is identical to Eq. 5-41 (i.e., the same stress values are developed in both adherends and doubler, and they are below the longitudinal tensile and compressive strengths of the laminate). Hence, the laminate design is acceptable.

Instead of arbitrarily assuming the thickness of the doubler, Eq. 5-37 can be used to determine the minimum required thickness. This can be accomplished by setting

$$\sigma_t^{dbl} = S_{cxxT} \text{ (from Table 5-4), and}$$
$$\sigma_c^{dbl} = S_{cxxC} \text{ (from Table 5-4).}$$

(5-47)

Rearranging the two expressions of Eq. 5-47, and using Eq. 5-38, two values of the doubler thickness are generated, and the larger thickness is selected:

$$t_{dbl}^{\min T} = \frac{4F}{S_{cxxT}}$$
$$= \frac{4 \times 800 \text{ (lb/in.)}}{79,000 \text{ (psi)}} = 0.04 \text{ in. } (\cong 1 \text{ mm}), \text{ and}$$

(5-48)

$$t_{dbl}^{\min C} = \frac{2F}{S_{cxxC}}$$
$$= \frac{2 \times 800 \text{ (lb/in.)}}{79,000 \text{ (psi)}} = 0.02 \text{ in. } (\cong 0.5 \text{ mm})$$

(5-49)

In this example, the laminate has identical values for both tensile and compressive strength properties. For this reason, the minimum thickness calculated from Eq. 5-48 will govern the design. However, this is only a special case; in general, both values must be calculated and the larger thickness value will govern the design thickness of the doubler. For a practical fabrication, a thickness of 0.05 in. (1.27 mm) may be selected.

8. Calculate MOS for the adherends and doubler bending stresses (in this example, both margins of safety are the same for adherends and doubler):

$$MOS(\text{Bending} - \text{Tensile}) = \frac{S_{cxxT}}{\sigma_t} - 1$$
$$= \frac{79,000\,(\text{psi})}{64,000\,(\text{psi})} - 1 = 0.24$$

(5-50)

$$MOS(\text{Bending} - \text{Compressive}) = \frac{S_{cxxC}}{\sigma_c} - 1$$
$$= \frac{79,000\,(\text{psi})}{32,000\,(\text{psi})} - 1 = 1.49$$

(5-51)

9. Calculate the joint efficiency using Eq. 5-46:

$$\eta^b = \frac{F}{S_{cxx}t_1} \times 100 = \frac{800\,(\text{lb}/\text{in.})}{79,200\,(\text{psi}) \times 0.05\,(\text{in.})} \times 100 = 20.2\%$$

Joint design summary: The design summary is presented in Tables 5-5 and 5-6. Figure 5-32 shows the geometrical details of the joint of Example 5-1.

Design evaluation and observations: The following observations are made based on the calculated results presented in this example:

- The critical conditions of the adhesives were satisfied with substantial margins (the MOS values were high), indicating that single-doubler butt joints are generally not efficient joints.
- For both the adherends and the doubler, the margins of safety were relatively small as compared to those of the adhesives.

Table 5-5. Design Results Summary of Example 5–1: Physical

	Doubler	Adherends	Adhesives
Material	T300/E	T300/E	*Structural Epoxy*
Lay-up	$(0/\pm 45/0/90)_s^a$	$(0/\pm 45/0/90)_s^a$	—
Length	2 in. (≈ 50 mm)	—	2 in. (≈ 50 mm)

[a] Subscript s denotes symmetric layup.

Table 5-6. Design Results Summary of Example 5–1: Mechanical[a]

Material	Calculated Stresses, σ (ksi)	Allowable Strengths, S (ksi)	Margin of Safety, MOS
Adhesive			
• Shear (average)	0.8	6.5	7.12
• Shear (maximum)	2.4	6.5	1.71
• Peel-off	2.3	7.5	2.28
Doubler/adherend			
• Combined tension	64	79.2	0.24
• Combined compression	32	79.7	1.49

[a] Joint efficiency = 20.2%

- The joint length calculated by the load transfer was very small, and the minimum joint length predicted using the shear lag equation was negligible, indicating that the load transfer occurs in a very short distance.
- The laminate fracture stresses used for in-plane loads were approximate and were appropriate for preliminary design. An improved estimate of these stresses would be obtained by using laminate analysis to calculate the ply stresses.
- The joint efficiency of about 20% is considered to be very poor. This poor efficacy is typical for all bonded joints that induce bending stresses in both the doubler and the adherends. The efficiency of this joint can be improved by selecting other joint configurations without bending (refer to Fig. 5-31) if the structure geometry permits. Another alternative to increase the joint efficiency is to use thicker laminates for both the adherends and the doubler, which will increase the fabrication complexity and consequently the cost of the joint. This same example was also solved using the BOND.EXE program, which was identified earlier in the chapter. Figure 5-33 presents the BOND.EXE program output file for Example 5-1.

```
    ************************************************************
    *             Program [Adh-Joint] for Analysis of          *
    *              Adhesively Bonded Composite Joints           *
    *            This Program is based on the work presented    *
    *   by C.C. Chamis and P.L.N. Murthy, Lewis Research Center *
    *       However, some modifications have been applied       *
    *        Note: No experimental verification was available   *
    ************************************************************

 Input Data
 **********

 JOB TITLE : ASCE Manual Example 5.1
 ** English Units (lb-inch)**
 ** Butt/Single Doubler joint **

  •   Load per unit length =    800.000
  •   Thickness of adherends =    .050
  •   Thickness of doubler =    .050
  •   Thickness of adhesive =    .00500
  •   Safety factor for joint load = 1.000
  •   Knock down factor for adhesive strength =  .500
  •   Tensile modulus of laminate in the x direction =  10000000.0000
      •      Tensile strength of laminate in the x direction =     79200.0000
  •   Compressive strength of laminate in the x direction =    79200.0000
  •   Tensile modulus of adhesive =    500000.0000
  •   Shear modulus of adhesive =    180000.0000
  •   Adhesive normal or peel-off strength =    15000.0000
  •   Adhesive shear strength =    13000.0000

 Program Results
 ***************
 Joint length =          1.000
 Doubler length =        2.000
 Doubler Thickness =      .05000

 Stresses             Calculated    Allowable      MOS

 Adhesive
 Shear average          800.00      6500.00       7.13
 Shear maximum         2400.00      6500.00       1.71
 Peel-off              2285.71      7500.00       2.28

 Doubler
 Combined-tension     64000.00     79200.00        .24
 Combined-compression 32000.00     79200.00       1.48
```

Figure 5-33. Output file (Example1.out) summarizing the design results of Example 5-1 obtained from the BOND.EXE computer program.

Example 5-2. Redesign the same joint described in Example 5-1, assuming that the joint will be exposed to a hygrothermal environment of 150 °F (65.6 °C) and 1% moisture by weight, and must endure 1 million cycles of design load. The room temperature is assumed to be 70 °F (21.1 °C).

This example follows the same procedure of Example 5-1. The only difference is that the adhesive properties are reduced to reflect the effects

of the environment and cyclic loading requirements. However, additional information on the adhesives is needed, such as the adhesive dry glass-transition temperature at service conditions, T_{gd}, which is taken as 420 °F (215.6 °C). The wet adhesive glass-transition temperature, T_{gw}, can be calculated using Eq. 5-22.

The joint design requirements, laminate properties, and adhesive properties are identical to those used in Example 5-1. The environmental effects are calculated as follows:

- Degrade adhesive properties for environmental and cyclic loading effects using Eq. 5-21. First, calculate the wet adhesive glass-transition temperature (T_{gw}) using Eq. 5-22:

$$T_{gw} = (0.005M^2 - 0.1M + 1.0)T_{gd}$$
$$= [0.005(1)^2 - 0.1(1) + 1.0] \times 420°\text{F} = 378\,°\text{F}$$

- Knowing the adhesive dry and wet glass-transition temperatures, and the number of loading cycles, the corresponding degrading factor is calculated using Eq. 5-21:

$$\frac{S_a}{S_{ao}} = \left[\sqrt{\frac{T_{gw} - T}{T_{gd} - T_o}} \right] - 0.1 \quad \log(N)$$
$$= \left[\sqrt{\frac{378°\text{F} - 150°\text{F}}{420°\text{F} - 70°\text{F}}} \right] - 0.1 \quad \log(1{,}000{,}000) = 0.207$$

- The reduced values of adhesive mechanical properties are calculated as follows:

$$S_{an}^{Reduced} = 0.207 \times 15{,}000\ (\text{psi}) = 3{,}150\ \text{psi},$$
$$S_{as}^{Reduced} = 0.207 \times 13{,}000\ (\text{psi}) = 2{,}691\ \text{psi, and}$$
$$G_a^{Reduced} = 0.207 \times 180{,}000\ (\text{psi}) = 37{,}260\ \text{psi}.$$

SOLUTION

Design allowables: Calculate design allowable load and adhesive strength values using the corresponding safety factors (see Example 5-1) as follows:

- Joint load ($SF = 1$): 1×800 lb/in. = 800 lb/in.
- Allowable adhesive normal or peel strength [$(SF)_a = 0.5$)]:

$$\overline{S_{an}} = 0.5 \times 3{,}150\ (\text{psi}) = 1{,}575\ \text{psi}$$

- Adhesive shear strength $[(SF)_a = 0.5)]$:

$$\bar{S}_{as} = 0.5 \times 2{,}691 (\text{psi}) = 1{,}345.5\,\text{psi}$$

Joint length: Using Eq. 5-29a, the half lap length is calculated as:

$$l = \frac{3F}{\bar{S}_{as}} = \frac{3 \times 800\,(\text{lb}/\text{in.})}{1{,}345.5\,(\text{psi})} = 1.78\ \text{in.}\ (\cong 45\ \text{mm})$$

and the total lap length = $2l$ = 3.56 in. (90.4 mm).

1. *Check joint critical conditions:* In this step, the following three conditions must be checked:
   - Check minimum half length (l_{min}),
   - Check maximum adhesive shear stress (σ_{as}^{max}), and
   - Check maximum adhesive peel stress (σ_{an}^{max}).

   First, calculate the minimum length (l_{min}) using Eq. 5-31, where t_a = 0.005 in. (0.127 mm), E_{cxx} = 10 × 10^6 psi, and G_a = 37,260 psi.

$$\therefore l_{min} = 0.7 \times 0.005\ \text{in.}\ \sqrt{\frac{10 \times 10^6\ (\text{psi})}{37{,}260\ (\text{psi})}} = 0.05\ \text{in.} < l < 1.78\ \text{in.}$$

   For practical fabrication, use l^{sel} = 2 in. ($\cong$ 50 mm), and 2 l^{sel} = 4 in. ($\cong$ 100 mm). Using this selected length, calculate corresponding value of the adhesive shear stress:

$$\sigma'_{as} = \frac{F}{l^{sel}} = \frac{800\,(\text{lb}/\text{in.})}{2\ \text{in.}} = 400\ \text{psi}$$

2. Calculate MOS for actual average adhesive shear stress as:

$$MOS(\sigma'_{as}) = \frac{\bar{S}_{as}}{\sigma'_{as}} - 1 = \frac{1{,}345.5\,(\text{psi})}{400\,(\text{psi})} - 1 = 2.36$$

   Check maximum adhesive shear stresses $(\sigma_{as}^{max'})$ using the modified (actual) value of the average adhesive shear stress (Eq. 5-33):

$$\sigma_{as}^{max'} \cong 3\sigma'_{as} = 3 \times 400\ (\text{psi}) = 1{,}200\,\text{psi}$$

3. Calculate MOS for maximum adhesive shear stress $MOS(\sigma_{as}^{max'})$ from Eq. 5-34:

$$MOS(\sigma_{as}^{max'}) = \frac{\bar{S}_{as}}{\sigma_{as}^{max'}} - 1 = \frac{1{,}345.5\,(\text{psi})}{1{,}200\,(\text{psi})} - 1 = 0.12$$

4. Calculate actual adhesive peel-off stress (σ'_{an}) using Eq. 5-35a:

$$\sigma'_{an} = \frac{3F}{l^{sel} + t_{adhr}} = \frac{3 \times 800 \,(\text{lb}/\text{in.})}{2\,(\text{in.}) + 0.05\,(\text{in.})} = 1{,}170.73 \text{ psi} < 1{,}575 \text{ psi okay}$$

5. Calculate MOS for adhesive peel-off stress (σ'_{an}) from Eq. 5-36:

$$MOS(\sigma_{an}^{\max}) = \frac{\bar{S}_{an}}{\sigma_{an}} - 1 = \frac{1{,}575 \,(\text{psi})}{1{,}170.73 \,(\text{psi})} - 1 = 0.35$$

Bending stresses: The bending stresses developed in both the adherends and the doubler (splice plate) are the same as in Example 5-1 since neither the laminate allowables nor the thickness were changed. However, an improved estimate based on ply properties must be calculated by degrading the resin-dominated ply properties (Murthy and Chamis 1986). Also, the joint efficiency is still the same as in Example 5-1 since neither the laminate allowables nor the thickness were changed.

Joint design summary: The design summary is presented in Tables 5-7 and 5-8. Figure 5-34 shows the geometrical details of the joint of Example 5-2.

Table 5-7. Design Results Summary of Example 5–2: Physical

	Doubler	Adherends	Adhesives
Material	T300/E	T300/E	Structural epoxy
Lay-up	(0/±45/0/90)ₛ[a]	(0/±45/0/90)ₐ[s]	—
Length	4 in. (≈ 100 mm)	—	4 in. (≈ 100 mm)

[a] Subscript s denotes symmetric layup.

Table 5-8. Design Results Summary of Example 5–2: Mechanical[a]

Material	Calculated Stresses, σ (ksi)	Reduced Allowable Strengths, S (ksi)	Margin of Safety, MOS
Adhesive			
• Shear (average)	0.4	1.35	2.36
• Shear (maximum)	1.2	1.35	0.12
• Peel-off	1.17	1.58	0.35
Doubler/adherend			
• Combined tension	64	79.2	0.24
• Combined compression	32	79.7	1.49

[a] Joint efficiency = 20.2%.
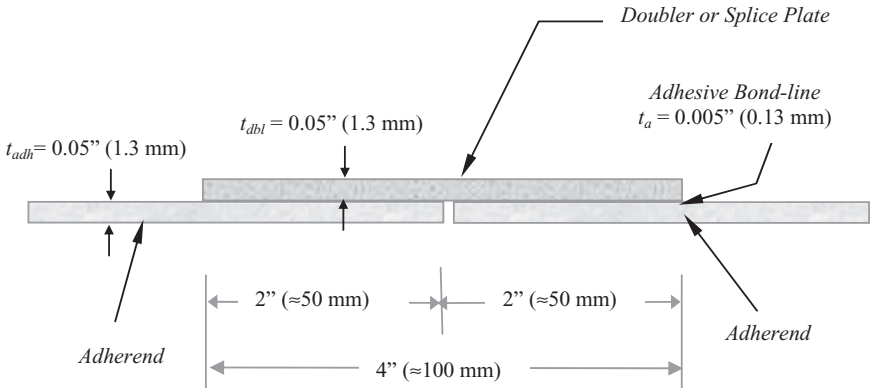
Figure 5-34. Geometrical details of the bonded single-doubler (single-strap) butt joint of Example 5-2.

Design evaluation and observations: The following observations are based on the calculated results presented in this example:

- Environmental and cyclic loading effects degraded the bonded joint integrity, as illustrated by the substantial reduction in the MOS values (refer to Table 5-8).
- Due to the environmental and cyclic loading effects, the joint length was doubled [2 in. (50 mm) versus 4 in. (100 mm)]. In fact, the length selection was a lucky guess. Had the actual calculated length of 1.784 in. been used, the design would have been unsatisfactory, as shown in the output file of BOND.EXE program that calculated the MOS values based on the exact value of the calculated length (refer to Fig. 5-35). Also, if the calculation of the length had been based on the original approach of Chamis and Murthy (1989) and not on the modified approach proposed in this chapter, the length would be too small (one-third of the value calculated), which would require more design iterations.
- The bending stresses are generally not affected if no environmental degradation factors are imposed on the laminate properties. This is true if 0-degree plies are placed adjacent to the adhesive bond-line in both the doubler and the adherends since fiber-dominated properties are not sensitive to moisture and temperature changes (Chamis and Murthy 1989).

```
    ************************************************************
    *              Program [Adh-Joint] for Analysis of         *
    *               Adhesively Bonded Composite Joints         *
    *           This Program is based on the work presented    *
    *   by C.C. Chamis and P.L.N. Murthy, Lewis Research Center *
    *          However, minor modifications have been applied   *
    *        Note: No experimental verification was available   *
    ************************************************************


 Input Data
 **********
  JOB TITLE : ASCE Manual Example 5-2)
 ** English Units (lb-inch)**
 ** Butt/Single Doubler joint **
 •   Load per unit length =    800.000
 •   Thickness of adherends =     .050
 •   Thickness of doubler =    .050
 •   Thickness of adhesive =    .00500
 •   Safety factor for joint load = 1.000
 •   Knock down factor for adhesive strength =  .500
 •   Tensile modulus of laminate in the x direction = 10000000.0000
 •   Tensile strength of laminate in the x direction =    79200.0000
 •   Compressive strength of laminate in the x direction =   79200.0000
 •   Tensile modulus of adhesive =    103500.0000
 •   Shear modulus of adhesive =    37260.0000
 •   Adhesive normal or peel-off strength =    3150.0000
 •   Adhesive shear strength =    2691.0000

 Program Results
 ***************
 Joint length =          1.784
 Doubler length =        3.567
 Doubler Thickness =     .05000

 Stresses              Calculated    Allowable      MOS

 Adhesive
 Shear average           448.50      1345.50       2.00
 Shear maximum          1345.50      1345.50        .00
 Peel-off               1308.81      1575.00        .20


 Doubler
 Combined-tension      64000.00     79200.00        .24
 Combined-compression  32000.00     79200.00       1.48
```

Figure 5-35. Output file (Example2.out) summarizing the design results of Example 5-2 obtained from the BOND.EXE computer program.
NOTE: The adhesive stresses and the corresponding MOS values are different from those presented in Example 5-2 because the above values were calculated based on the calculated length (l = 1.784 in.) rather than the selected length (l = 2 in.) adopted in Example 5-2.

5.8 DESIGN RECOMMENDATIONS

The following are design recommendations for adhesively bonded composite joints:

- From the standpoint of joint reliability, it is vital to avoid the condition where the adhesive layer is the weak link in the joint (i.e., the joint should be designed to ensure that the adherends fail before the bond layer whenever possible) (Hart-Smith 1986).
- Due to processing considerations and defect sensitivity of the bond material, bond layer thickness is generally limited to a range of 0.005 in. to 0.015 in. (0.125 mm to 0.39 mm) (Hart-Smith 1986).
- All types of joints are adversely affected by unequal adherend stiffnesses. Therefore, wherever possible, the stiffnesses should be kept approximately equal.
- Adhesive layers of bonded joints should primarily be stressed in shear or compression. Tensile, cleavage, and peel loads should be avoided, or their effect should be evaluated with great care (Clarke 1996).
- Shear stress and peel stress concentrations are common in adhesively bonded joints. Tapering the ends of the adherends is an effective way of reducing peel stresses. Use of ductile adhesive can help in reducing the value of maximum shear stress in the adhesive.
- Use of symmetric joint configurations, such as double-lap or double-strap, is recommended over single-lap or single-strap joints. This will greatly reduce the effects of eccentricity in loading.
- The use of adhesive fillets and tapering the adherend ends may significantly increase the load-bearing capacity of the joint by reducing stress concentrations at the ends of the overlap. The effect of these methods is based on the increased flexibility of the joint ends, resulting in more favorable stress distribution within the overlap. Full utilization of these methods requires the use of a ductile adhesive (Clarke 1996).
- The use of a peel ply on the bond surface during component manufacture is recommended to prevent surface contamination (Clarke 1996).

REFERENCES

American Society of Civil Engineers (ASCE). (1984). *Structural plastics design manual*. ASCE, New York.

ASTM International (ASTM). (2002). *MIL 17 handbook: The composite materials handbook*, ASTM International, West Conshohocken, Pa.

Chamis, C. C., and Murthy, P. L. N. (1989). "Simplified procedures for designing adhesively bonded composite joints." *Proc., 44th Annual Conf. of the Composites Institute*, Society of the Plastics Industry, Washington, D.C.

Clarke, J. L., ed. (1996). "Structural design of polymer composites." *EUROCOMP design code and handbook*. E & FN Spon/Chapman & Hall, London.

European Space Agency (ESA). (1988). "Composites design handbook for space structure applications." *ESA PSS-03-1101*, 2(1), European Space Agency, Nordwijk, The Netherlands.

Goland, M., and Reissner, E. (1944). "The stress in cemented joints." *J. Appl. Mech.*, 11, A17–A27.

Grimes, G. C., and Greimann, L. F. (1975). "Composite materials." C. C. Chamis, ed., *Structural design and analysis*, Part II, Vol. 8, Chapter 10, Academic Press, New York.

Hart-Smith, L. J. (1989). "Joints." C. A. Dostal, ed., *Engineered materials handbook*, Vol. 1: Composites, ASTM International, West Conshohocken, Pa., 479–495.

Hart-Smith, L. J. (1986). "Adhesively bonded joints for fibrous composite structures." *Proc., Int. Symp. on Joining and Repair of Fiber-Reinforced Plastics*, Imperial College, London.

Hart-Smith, L. J. (1981). "Stress analysis of adhesively bonded joints: A continuum mechanics approach." A. J. Kinloch, ed., *Development in adhesives*, 2nd ed., Applied Science Publishers, London.

Hart-Smith, L. J. (1978). "Adhesive-bonded joints for composites: Phenomenological considerations." *Douglas Aircraft Paper 6707*, Douglas Aircraft Company, Long Beach, Calif.

Hart-Smith, L. J. (1974). "Advances in the analysis and design of adhesive-bonded joints in composite aerospace structures." *Proc., 19th Int. SAMPE Symp. and Tech. Conf.*, Society for the Advancement of Material and Process Engineering, El Segundo, Calif.

Hart-Smith, L .J. (1973a). "Adhesive bonded single lap joints." *NASA Langley Research Center Contract Number NASA-CR-112236*, NASA Langley Research Center, Langley, Va.

Hart-Smith, L. J. (1973b). "Development of design criteria for advanced composite bonded joints." *NASA Langley Research Center Contract Number NASA-CR-112234*, NASA Langley Research Center, Langley, Va.

Hart-Smith, L. J. (1972). "Design and analysis of adhesive-bonded joints." *Douglas Aircraft Paper 6059A*, Douglas Aircraft Company, Long Beach, Calif.

Murthy, P. L. N., and Chamis, C. C. (1986). "ICAN: Integrated Composite Analyzer." *J. Composite Tech. Res.*, 8(1), 8–17.

Teodosiadis, R. (1968). "Plastic analysis of bonded composite lap joints." *Douglas Aircraft Company IRAD Report No. DAC-67836*, Douglas Aircraft Company, Long Beach, Calif.

Volkersen, O. (1938). "Die nietkraftverteilung in zugbeanspruchten niet-verbindungen mit konstanten laschenquerschnitten." *Luftfahrtforsc-hung*, 15, 4–47.

CHAPTER 6
COMBINED JOINTS

6.1 INTRODUCTION

In combination joints, both adhesives and mechanical fasteners are used. This method of joining composites can provide the joint with greater capacity and reliability. In combined joints, the inherent strengths of the component elements are enhanced to produce a joint that displays significantly improved performance. However, it must be clear to the structural engineer that the combined joint strength is not the algebraic sum of the individual bonded and bolted strengths. Bolted/bonded joints have greater strength, stiffness, and fatigue life in comparison to adhesively bonded joints. However, this is particularly true in joints with lower-modulus adhesives which allow for load sharing between the adhesive and the bolt (Kelly 2006). The analysis and design of combined joints are very complex and require the use of nonlinear techniques. The load transfer in bolted/bonded composite joints is complicated due to the difference in stiffness of the alternative load paths (Kelly 2005).

Some joint details are superior to others, particularly those for composites. In some cases, such as prolonged loadings on low-modulus thermoplastic composites, mechanical fastening alone is impractical. Stress concentrations displayed by a mechanical fastener can contribute to pronounced deformations in materials that are sensitive to creep.

Improved joint performance is achievable through a variety of mechanisms, once the general behavior of the various connections and, to a lesser extent, their effectiveness in different types of composite structures are understood.

Mechanically fastened, welded (for thermoplastic composites), and adhesively bonded connections each display unique benefits and

characteristics. On the one hand, mechanical fasteners are comparatively easy to install but they induce significant stress concentration factors. On the other hand, welding and adhesive bonds for thermoplastic composite joints provide a greater load distribution within a connection but also require more skillful labor. Table 6-1 compares different joining techniques.

Although combination-type connections, particularly mechanical-adhesive, are commonly employed in structural applications, there is limited published information on the subject. This chapter provides an overview of the behavior of simple connections and discusses the potential benefits of employing combination-type joints. A brief summary of known applications is included.

6.2 REVIEW OF RELATED WORK

Hart-Smith (1982; 1984) discussed the structural behavior of bonded/bolted composite joints. In these works, various aspects of the combination

Table 6-1. Comparison of Mechanical, Adhesive, and Welded Connections

Characteristic	Mechanical	Adhesive	Welded
Stress concentration at joint	High	Medium	Medium
Strength-to-weight ratio	Low	Medium	Medium
Use with nonrigid polymers	Inserts required	Yes	Yes
Seals assembly (watertightness)	No	Yes	Yes
Thermal or electrical insulation	No	Yes	Yes
Attractiveness (smooth joints)	Bad	Good	Good
Fatigue endurance	Bad	Good	Good
Sensitive to peel loading	No	Yes	No
Disassembly	Possible	Impossible	Impossible
Inspection	Easy	Difficult	Difficult
Skill required of fabricator	Low	High	High
Heat or pressure required	No	Yes	Yes
Tooling costs	Low	High	High
Time to attain ultimate strength	Instantaneous	Long	Short

Source: ASCE (1984).

of adhesive bonding and mechanical fastening for fibrous composite structures were presented. It was shown that the combination of bonding and bolting is particularly beneficial for the repair and prevention of damage from spreading in composite structures. Early research by Vinson (1989) showed that combined bolted and adhesively bonded composite joints were 50% stronger than similar bolted-only joints. Experimental strength values for combined bolted/bonded joints were also markedly greater than for adhesively bonded-only joints. Fu and Mallick (2001) evaluated, both experimentally and numerically, the fatigue behavior of combined joints for sheet molding compound (SMC) composites and structural reaction injection molded (SRIM) composites. In this study, static and fatigue experiments were conducted with hard round washers and both thin and thick square washers. The main purpose of this investigation was to evaluate the impact of washer type and geometry on the performance of bolted/bonded joints. Test results indicated that the presence of high peel stresses at the lap ends of adhesive and bonded joints is the principal failure initiator.

It was concluded that square washers are more effective in either preventing or delaying the failure by fiber tear as compared to a round washer, which does not provide lateral clamping in the outside corners of the lap ends. Kelly (2006) investigated the quasi-static strength and fatigue life of hybrid (bonded/bolted) composite single-lap joints. The results of this study indicated the presence of three distinct stages in the fatigue life of hybrid joints where the adhesive, the bolt, and their combination were all contributing to the load transfer. It was also reported that fatigue crack initiation was found to occur later in the hybrid joints where the bolt transferred a significant portion of the load. Results of this study also showed that the failure mode of the joints was dependent upon the relation between the hybrid joint strength and the bearing strength of the laminate.

For pultruded (PFRP) frame connections, full-scale quasi-static and cyclic test results (Mosallam et al. 1994; Mosallam 1996) indicated that an appreciable increase in both rotational stiffness and strength is achieved when both adhesive and mechanical fasteners are employed. This is apparent from the experimental moment–rotation curves reported by Mosallam et al. (1994) and shown in Fig. 6-1. In the same study, the dynamic effect of using a combination of both adhesives and mechanical fasteners also was evaluated. Based on the experimental frequency response analysis (refer to Fig. 6-2), the bolted PFRP beam-to-column connections are relatively flexible as compared to the combined connection detail. Consequently, the damping capabilities of bolted connections—which utilize friction PFRP, threaded rods, and nuts—are higher than the combined connection details, which utilize both mechanical fasteners and adhesives.
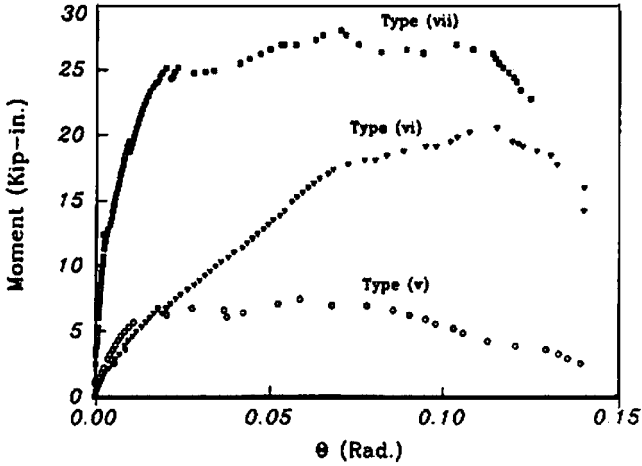
Figure 6-1. Moment–rotation curves for different PFRP frame connections. Type v, bolted-only (steel-like); type vi, bolted-only (universal connector; UC); and type vii, bolted/bonded (combined) UC connection.
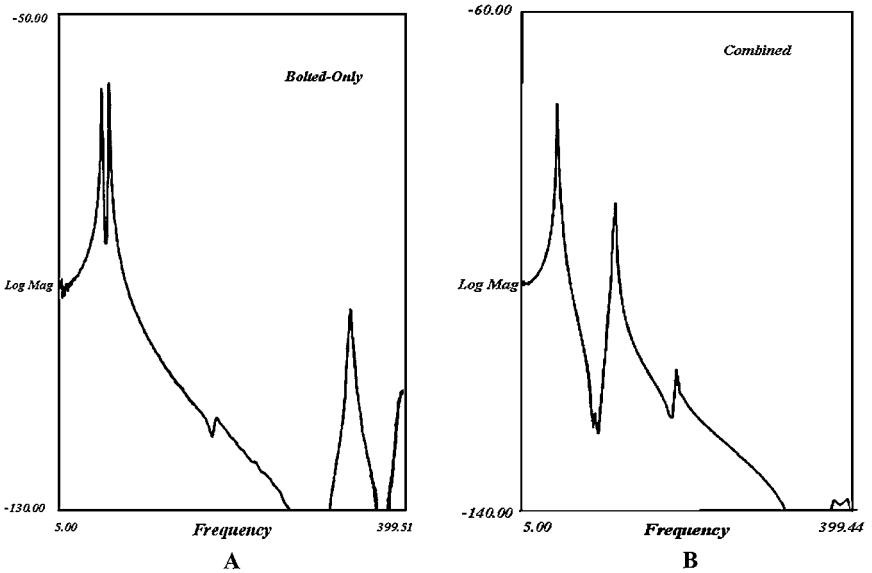
Figure 6-2. Frequency response plots for bolted (A) and combined (B) PFRP beam-to-column frame connections.

Mosallam (1996) reported that the low-fatigue behavior of combined bolted/bonded composite connections was more satisfactory than bolted-only connection details. Under a quasi-static loading regime, experimental results in this study showed that the ultimate moment capacity of the combined connection detail was about 33% higher (closing mode) and 43% higher (opening mode) than the ultimate moment capacity values obtained for bolted-only connection details. In addition, a gain in the connection rotational stiffness of about 81% was achieved when both adhesives and mechanical fasteners were employed (refer to Fig. 6-3). A detailed description of this study is presented in Chapter 7 of this manual.

6.3 ADVANTAGES AND APPLICATIONS OF COMBINED JOINTS

Combined mechanical-adhesive connections exhibit the following advantages over connections that use mechanical fasteners or adhesives alone:

1. Higher overall capacities
2. Greater resistance to environmental and thermal deterioration
3. Less subject to peel or cleavage failures
4. Improved joint stress distribution
5. Improved fatigue and impact characteristics
6. Increased rigidity
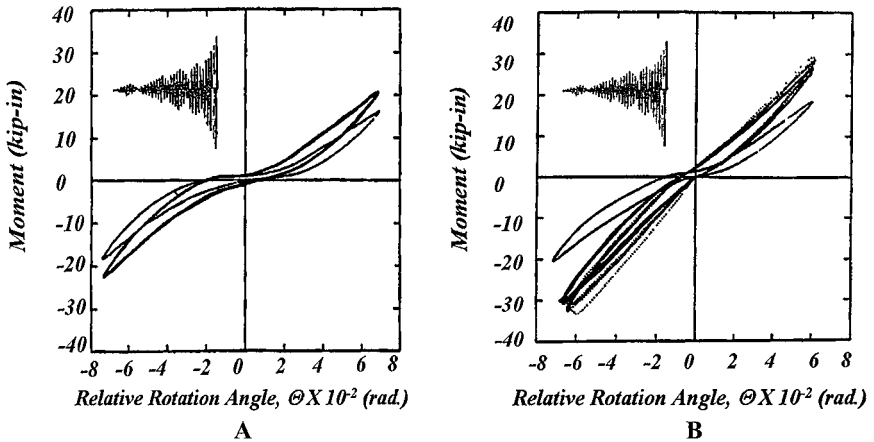
Figure 6-3. Hysteresis curves for bolted (A) and bolted/bonded (B) exterior PFRP beam-to-column connection details.

7. Reduced peel and cleavage effects in eccentric joints due to the presence of mechanical fasteners in combination with structural adhesives (USAFDL 1977)
8. Higher factors of safety

Bonded/bolted joints are especially useful for joining composite laminates. It is generally accepted that the integrity of mechanical fastener joints depends on the local laminate bearing strength. In the same manner, the integrity of adhesively bonded joints mainly depends on local interlaminar shear strength. Bonded/bolted composite joints also offer some advantage during erection. Mechanical fasteners can contribute the contact pressure required for curing an adhesive. Likewise, adhesives can serve as a means of maintaining alignments for mechanical fasteners.

The following are some practical applications for bonded/bolted joints:

1. The use of adhesives in combination with mechanical fasteners can provide additional rigidity to a connection. The use of a combined adhesive-bolted connection can provide a more rigid, less complex connection, thereby producing increased capacity and a more efficient overall design.
2. Adhesively bonded reinforcements for an existing bolted joint at fastener holes can increase the capacity of a mechanically fastened joint by up to 55% (Hart-Smith 1985).
3. In flexible membranes, such as single-ply roofing, mechanical fasteners provide a secondary means of attachment, in addition to adhesives, that is less subject to environmental deterioration. Mechanical fasteners also serve as battens or reinforcing strips.
4. In certain cases of repair, bolts are substituted for locally defective or damaged bonds. In these cases, bolts inserted through the damaged or defective bond areas in adhesively bonded joints not only successfully carry existing loads but also help to alleviate any adjacent critical locations in the adhesive bond, which may arise as a result of the damage, by redirecting stresses away from the those areas to the bolt (refer to Fig. 6-4).
5. Consequently, the remaining adhesive can be stressed more highly before ultimate failure occurs. The mechanical fasteners serve primarily to reduce the criticality of the peak strain developed in the adhesive adjacent to the flaw or local damaged area. As a result, the remaining adhesive will pick up more stress than it would without the presence of these bolts. Thus, a greater load level can be resisted by the adhesive until critical stresses in the adhesives are reached. More details of this application are reported in Hart-Smith (1981).
6. The combined use of both adhesives and mechanical fasteners provides an effective tool in preventing damage from spreading. One
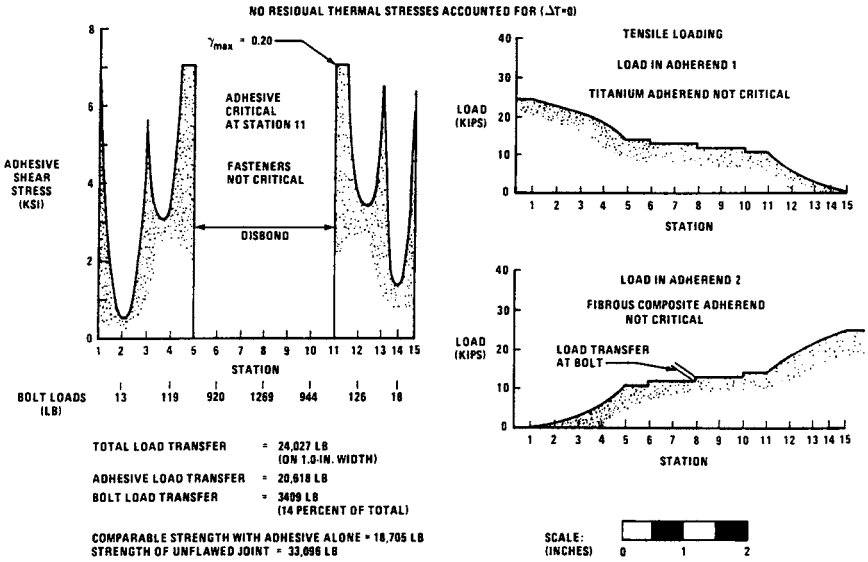
Figure 6-4. Load transfer through damaged (flawed) bonded joint reinforced by bolts.
Source: Hart-Smith (1984), courtesy of Dr. John Hart-Smith and the Boeing Company.

example is the case of the adhesive bonding of different stiff materials where one is broken or abruptly terminated, as shown in Fig. 6-5. It could also occur at a stiffener run-out or in adhesively bonded metallic structures where one member has developed a crack initiated at the bolt hole. The use of bolts in conjunction with the existing adhesive will assist in picking up significant load, which will result in a drop in the intensity of the peak developed in the adhesive shear stress distribution (at the tip of the adhesive disbond). As a result, any further damage propagation will be eliminated.

7. The addition of bolts results in creating fail-safe load paths in bonded joints. For example, the residual strength of the joint shown in Fig. 6-6 is limited by the composite laminate strength through the reduced section at a bolt hole. As shown in the figure, any fracture would be projected to occur in the resin adjacent to the adhesive bondline rather than in the adhesive itself. The use of mechanical fasteners in this case would be very effective in arresting further damage that otherwise would propagate throughout the composite structure. Hence, the bolts provide fail-safe load paths in bonded joints (refer to Figs. 6-6 and 6-7). For thinner composite members, and contrary to the previous case for thicker members, adhesive bonding actually provides the fail-safe mechanism for bolts. In this case, the bond is
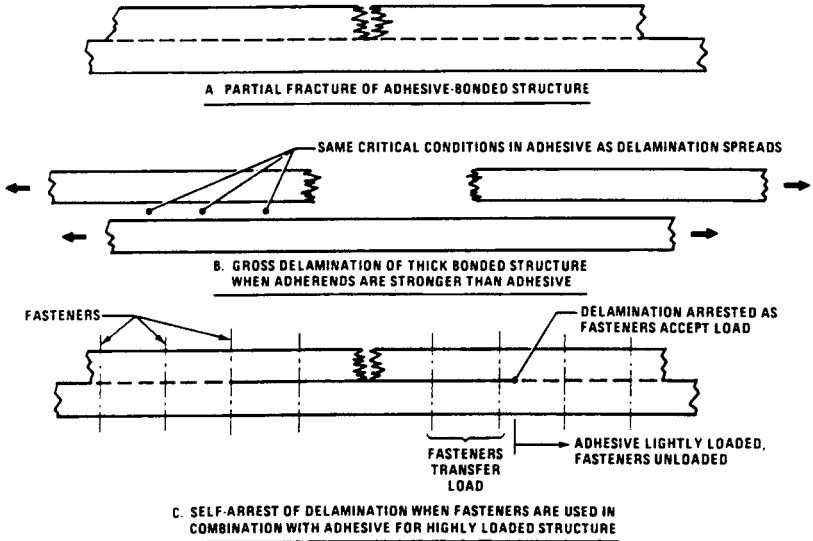
Figure 6-5. The need for fail-safe fasteners in thick bonded joints.
Source: Hart-Smith (1984), courtesy of Dr. John Hart-Smith and the Boeing Company.
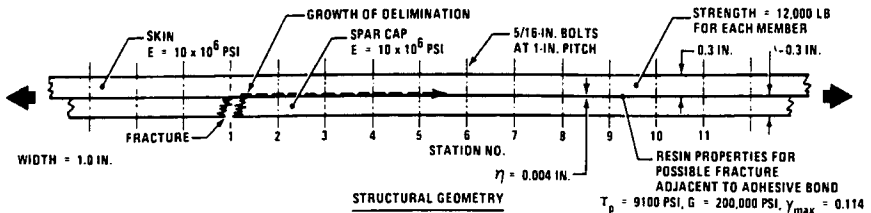
STATION NUMBER	1	2	3	4	5	6	7	8	9	10	11
1. ZERO DELIMITATION: FAILURE AT 6,313 lbs											
ADHESIVE SHAER STRESS (ksi)	9100	74	0	0	0	0	0	0	0	0	0
FASTENER LOAD (lb)	0	0	0	0	0	0	0	0	0	0	0
2. 1.0"DELIMITATION: FAILURE AT 6,903 lbs											
ADHESIVE SHAER STRESS (ksi)	0	9100	74	0	0	0	0	0	0	0	0
FASTENER LOAD (lb)	0	0	1	0	0	0	0	0	0	0	0
3. 2.0" DELIMITATION: FAILURE AT 10468 lbs											
ADHESIVE SHAER STRESS (ksi)	0	0	9100	74	0	0	0	0	0	0	0
FASTENER LOAD (lb)	0	1783	295	1	0	0	0	0	0	0	0
4. 3.0" DELIMITATION: FAILURE AT 12,000 lbs*											
ADHESIVE SHAER STRESS (ksi)	0	0	0	9100	38	0	0	0	0	0	0
FASTENER LOAD (lb)	0	2602	1137	163	0	0	0	0	0	0	0
5. 4.0" DELIMITATION: FAILURE AT 12000 lbs*											
ADHESIVE SHAER STRESS (ksi)	0	0	0	0	6530	20	0	0	0	0	0
FASTENER LOAD (lb)	0	2782	1394	608	0	0	0	0	0	0	0
6. 2.0"DELIMITATION : FAILURE AT 12000 lbs*											
FASTENER LOAD (lb)	0	2853	1496	785	412	216	113	58	29	12	0

* Limited by Adhesion Strength

Figure 6-6. The use of bolts as fail-safe load paths in bonded joints.
Source: Hart-Smith (1984), courtesy of Dr. John Hart-Smith and the Boeing Company.
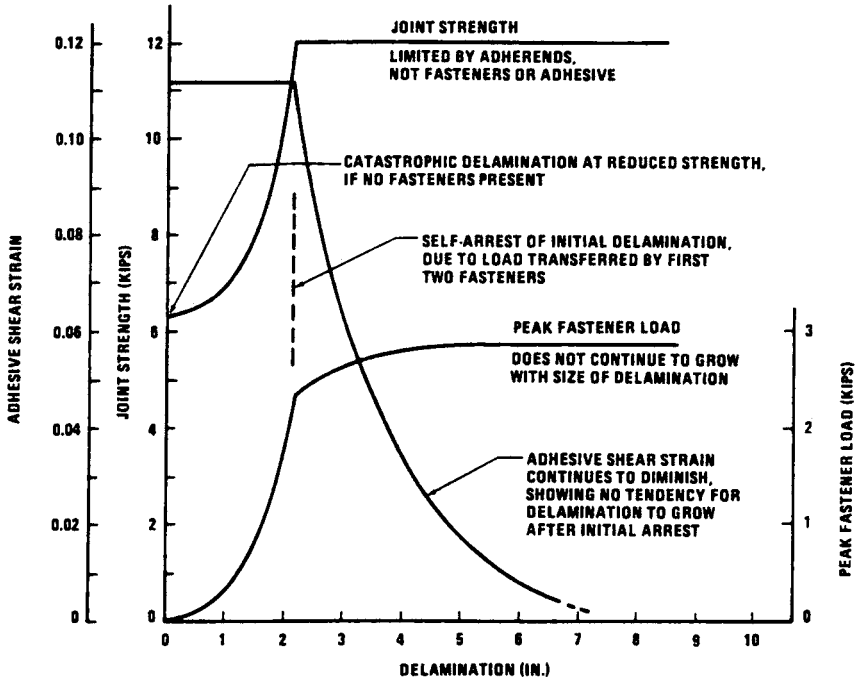
Figure 6-7. Damage confinement by combination of bonding and bolting. Source: Hart-Smith (1984), courtesy of Dr. John Hart-Smith and the Boeing Company.

the least likely source of failure, as illustrated in Fig. 6-8. Therefore, adding adhesives to the mechanically fastened joint will provide a fail-safe load path that will protect the composite laminate from tearing along the bolt line.

6.4 BEHAVIOR OF COMBINED BONDED/BOLTED COMPOSITE JOINTS

In combined (bonded/bolted) joints, the adhesives are usually stronger than the adherends. The most critical location in this joint is at the first bolt hole in the composite laminate. As long as the adhesive layer is intact, it is likely that the mechanical fasteners will not be subjected to sufficient motion relative to the adherends. Consequently, no significant loads are expected to develop in the bolts until the failure of the bondline.

In an investigation of combined composite joints reported by Hart-Smith (1985), it was shown that, in a combined joint, the load transferred by bolts was about 1% of the total load transferred (refer to Fig. 6-9). This is because bolts represent a load path that is much less stiff than that
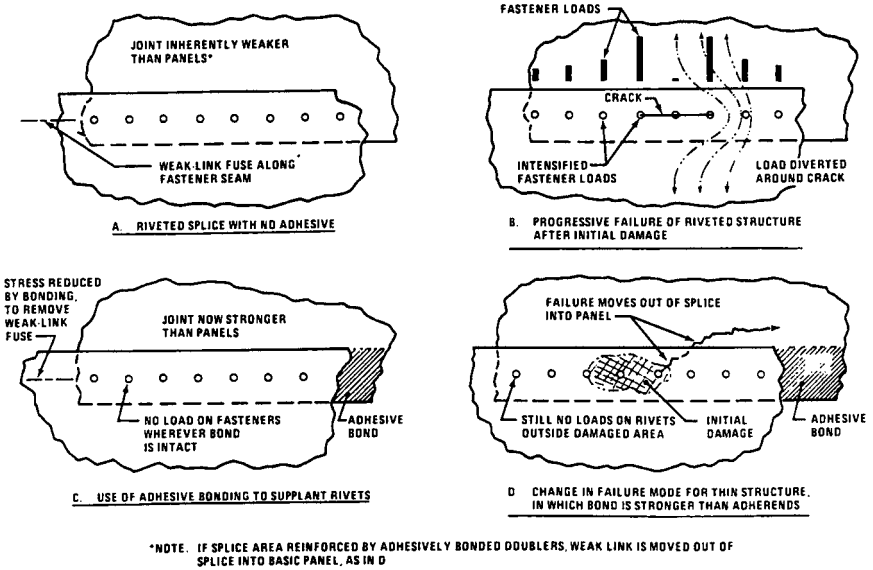
Figure 6-8. Use of adhesive bonding to provide fail-safety for mechanically fastened joints in thin composite structures.
Source: Hart-Smith (1984), courtesy of Dr. John Hart-Smith and the Boeing Company.
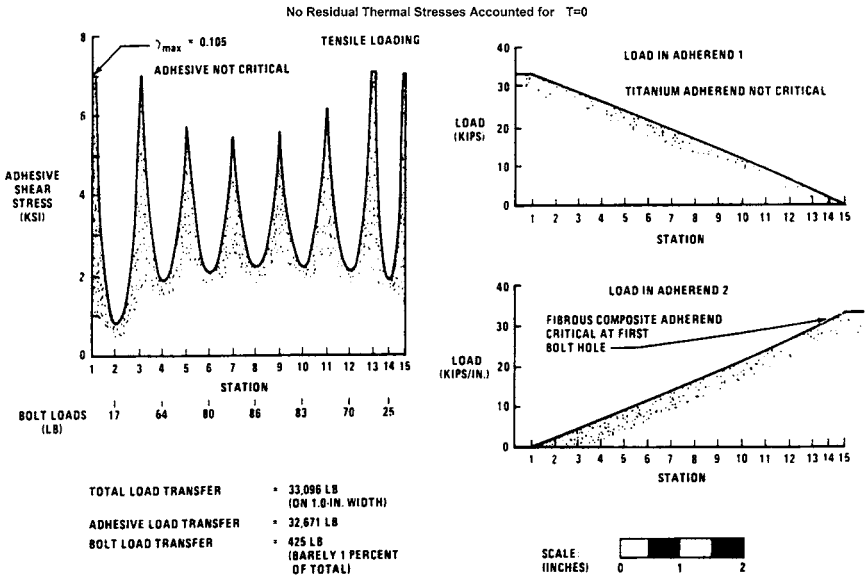
Figure 6-9. Load transfer through a bonded/bolted joint.
Source: Hart-Smith (1984), courtesy of Dr. John Hart-Smith and the Boeing Company.
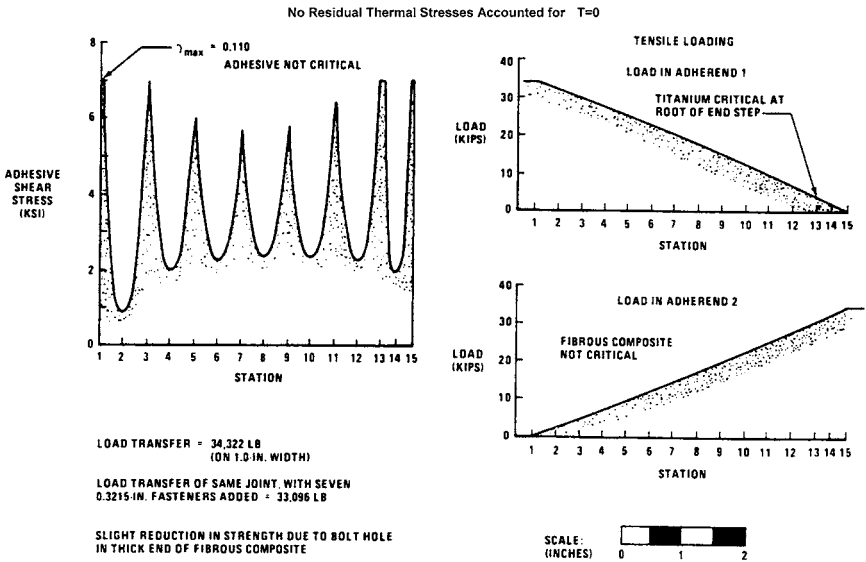
Figure 6-10. Load transfer through a bonded joint.
Source: Hart-Smith (1984), courtesy of Dr. John Hart-Smith and the Boeing Company.

provided by the adhesive. Figure 6-10 shows the predicted strength of a similar joint where only adhesive was used. This figure shows that a slight drop in joint strength occurred. This can be attributed to the elimination of holes in the bonded joint detail which contributed to moving the critical location of the composite laminate. Again, the adhesive is not critical, although it is strained beyond the desired minimum with regard to creep resistance.

The effect of omitting the adhesive and relying on bolts to transfer the load is illustrated in Fig. 6-11. The figure shows that the use of bolts alone enabled the joint to transfer slightly less load as compared to the bonded joint. However, a greater relative motion between the jointed members was observed. In this case, the critical location in the composite laminate was at the second row of bolts.

6.5 MECHANICALLY FASTENED/WELDED JOINTS FOR THERMOPLASTIC COMPOSITES

Mechanical/welded connections may display benefits similar to those of mechanical/adhesive connections. However, while mechanical/adhesive connections are commonly used during final erection, mechanical/welded connections are more likely to be used with thermoplastics.
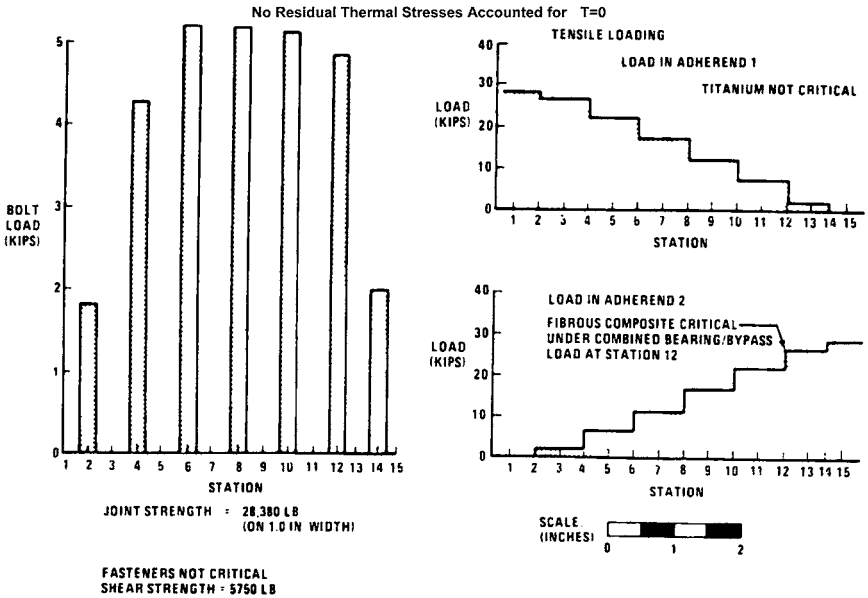
Figure 6-11. Load transfer through a bolted joint (without adhesives).
Source: Hart-Smith (1984), courtesy of Dr. John Hart-Smith and the Boeing
Company.

The use of metallic inserts in thermoplastic elements can provide improved performance for a given mechanical connection. In addition to providing greater bearing capacities and improved assembly/disassembly cycles, ultrasonically welded inserts can reduce potentially adverse stress concentration.

6.6 CONCLUDING REMARKS

Based on the information presented in this chapter, it is clear that the use of a combination of mechanical fasteners and adhesives is one of the optimum methods of joining composites. Unfortunately, the analysis and the design of such details are cumbersome and involve a great deal of nonlinear analysis. In addition, insufficient experimental information is available, especially for pultruded composites. As discussed in this chapter, the engineer should be well aware of the fundamental fact that bonded/bolted combined joint strength is not the algebraic sum of the individual bonded and bolted strengths. It is recommended that joints or frame connections be designed as bolted-only, with the adhesive included as an additional benefit to the joint to ensure uniform stress distribution.

This recommendation may seem to be a conservative approach; however, it is easily justified based on the following:

1. Lack of experimental information characterizing both the service and ultimate behavior of such combined detail
2. Lack of and complexity of reliable design and analytical procedures for combined joints

It also should be noted that this approach seems contradictory to the aerospace industry's approach, in which bonded joints are preferred and the use of bolts will add the benefit of providing clamping force during the curing process of the adhesives. However, this conclusion is based on the author's multi-year experimental program results, which deal specifically with pultruded composite frame connections. Experimental and field survey observations indicate that it is always a difficult task for construction crews to properly apply room-temperature adhesives at the site. Hence, based on the inherent brittle failure behavior of bondlines, it is in the best interests of the civil engineer, at least at the present time, to design the composite joint or connection as bolted-only, even if adhesives are used in combination with mechanical fasteners. In this scenario, the adhesive will act as a second line of defense for durability and superior long-term performance of the composite structure.

REFERENCES

American Society of Civil Engineers (ASCE). (1984). *Structural plastics design manual*. ASCE, New York.

Fu, M., and Mallick, P. K. (2001). "Fatigue of hybrid (adhesive/bolted) joints in SRIM composites." *Int. J. Adhesion & Adhesives*, 21, 145–159.

Hart-Smith, L. J. (1984). "Bonded-bolted composite joints." *Proc., AIAA/ASME/AHS 25th Structures, Structural Dynamics and Materials Conf.*, Long Beach, Calif.

Hart-Smith, L. J. (1982). "Design methodology for bonded-bolted composite joints." *U.S. Air Force Flight Dynamics Laboratory Contract No. AFWAL-TR-81-3154*, Wright Aeronautical Laboratories, Wright Patterson Air Force Base, Ohio.

Hart-Smith, L. J. (1981). "Design and analysis of bonded repairs of fibrous composite aircraft structures." *Douglas Aircraft Paper No. 7133*, Long Beach, Calif.

Kelly, G. (2006). "Quasi-static strength and fatigue life of hybrid (bonded/bolted) composite single-lap joints." *Composite Struct.*, 72, 119–129.

Kelly, G. (2005). "Load transfer in hybrid (bonded/bolted) composite single-lap joints." *Composite Struct.*, 69, 35–43.

Mosallam, A. S. (1996). "Performance of composite framing connections for pultruded structures." *Proc., 1st Middle East Workshop on Structural Composites*, Egyptian Society of Engineers, Sharm El-Sheikh, Egypt, pp. 457–469.

Mosallam, A. S., Abdelhamid, M. K., and Conway, J. H. (1994*). "Perfor- mance of pultruded FRP connections under static and dynamic loads." *J. Reinf. Plastics and Composites*, 13, 386–407.

U.S. Air Force Flight Dynamics Laboratory (USAFDL). (1977). *Advanced composites design guide*, Vol. I: Design; Vol. II: Analysis. U.S. Air Force Flight Dynamics Laboratory, Wright Patterson Air Force Base, Ohio.

Vinson, J. R. (1989). "Mechanical fastening of polymer composites." *Polymer Eng. Sci.*, 29(19), 1332–1339.

CHAPTER 7

BEHAVIOR OF PULTRUDED COMPOSITE FRAME CONNECTIONS

7.1 INTRODUCTION

Understanding the behavior of frame connections for pultruded fiber-reinforced polymer (PFRP) structures is an essential key to satisfying both the safety and efficiency requirements of such structures. This issue is particularly important when designing load-bearing pultruded composite structures such as bridges and building skeletons (refer to Figs. 7-1 through 7-4).

Despite their critical structural role, little attention has been given to PFRP frame connections. Regardless of the type of material used in any structural system, connections are needed to attach member ends to other structural members *sufficiently* to allow the loads to continue in an orderly flow to the foundation. The efficient connection design must produce a joint that is safe, economical, and practical (i.e., easily built at both shop and site). For other construction materials such as steel, varieties of structurally sound connection details are available (e.g., AISC 2005). Until recently, most available connection details were duplications of steel details (Mosallam 1993b). For this reason, and due to the absence of an authoritative unified design code (Chambers 1993), structural designers of most PFRP structures built in the last decade or so have utilized and continue to utilize *inadequate* and in most cases *unsafe* "steel-like" connection details (Fig. 7-5). In general, it is difficult to introduce a new structural material with no technical and scientific backup. For this reason, structural composites will have great difficulty in penetrating the construction industry without the development of strong design specifications.

Some of the major obstacles limiting the use of pultruded structural composites in the construction industry are:

229

Figure 7-1. The Fiberline all-pultruded composites cable-stayed bridge in Kolding, Denmark.
Source: Courtesy of Fiberline Composites A/S, Denmark.

Figure 7-2. Pedestrian bridge in recreation zone of Dubna City.
Source: Courtesy of ApATeCh Applied Advanced Technology Company Ltd., Russia.

Figure 7-3. Pultruded composites frame structure.
Source: Courtesy of Strongwell Company, USA.

A   B
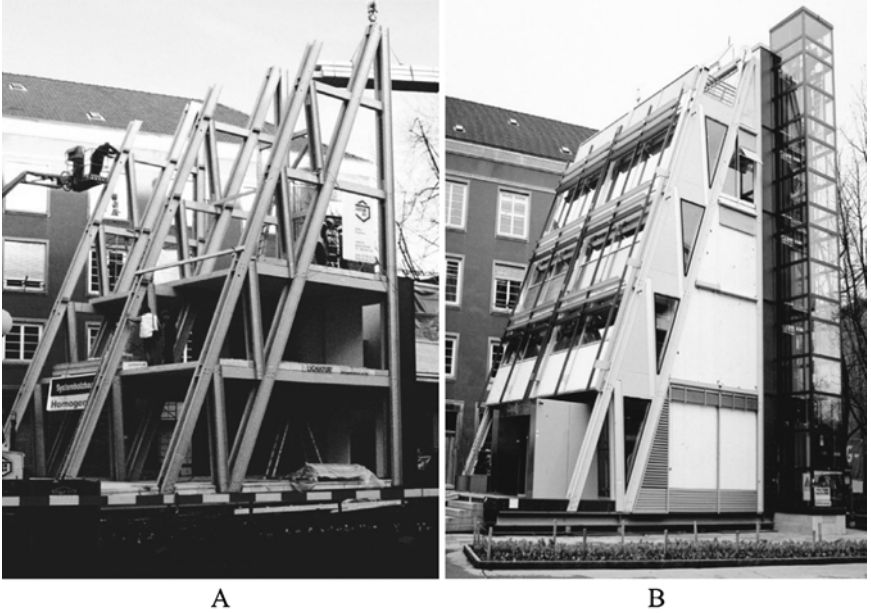
Figure 7-4. The all-composite "Eyecatcher" building in Switzerland. A,
Pultruded frame skeletons; B, the completed structure.
Source: Courtesy of Fiberline Composites A/S, Denmark.

Figure 7-5. An example of "steel-like" frame connections.

- Lack of mechanical information on both short- and long-term performance
- Lack of design standards and acceptance by building codes
- Structural deficiency of some structural shapes amplified by a lack of communication and coordination between pultruders and the researchers
- Limited sponsored-research programs
- Lack of quality control of commercial products

In this chapter, several recommendations for repair and rehabilitation of steel-like PFRP connections are presented.

7.2 IMPACT OF CONNECTION DETAIL DESIGN ON THE OVERALL BEHAVIOR OF PULTRUDED COMPOSITES FRAME STRUCTURES

Previous full-scale studies [e.g., Mosallam (1990) and Mosallam and Bank (1992)] on the performance of PFRP portal frames illustrated the major impact of connection behavior on the overall performance of these structures. This includes buckling and post-buckling capacity (Fig. 7-6), premature localized failure of open-web members, and the ultimate strength as well as the overall creep behavior of thin-walled FRP structures.

For pultruded composites to be considered as structural materials for civil engineering applications, these materials must be proven to have structural reliability and higher efficiency under different loading conditions (e.g., dead, live, wind, earthquake) during the expected useful life of the structure. The efficiency of a composite connection can be expressed as:
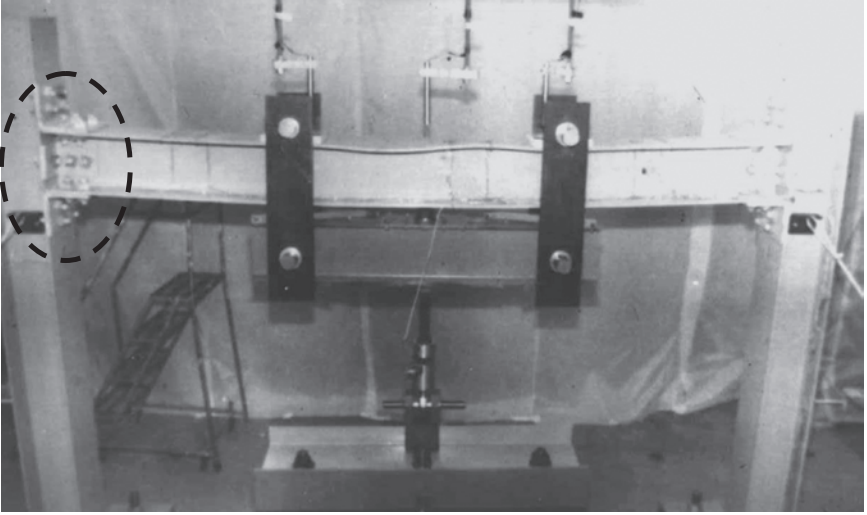
Figure 7-6. Effect of joint flexibility on buckling and post-buckling behavior of pultruded frame structures.
Source: Mosallam (1990).

$$\eta = \frac{P_j}{P_m} \qquad\qquad (7\text{-}1)$$

where
η = connection efficiency (%)
P_j = load producing failure to connection
P_m = load producing failure to member.

For this reason, reliable information on the behavior of pultruded composites under these loading regimes must be available to structural engineers. The majority of previous PFRP composite connection studies have focused mainly on the static behavior of these FRP connections, with little work on the dynamic and seismic behavior of these joints. Furthermore, due to the fact that composites are viscoelastic materials, structural engineers must include the long-term (creep) effects under ambient and other varying environmental conditions.

7.3 CODES AND STANDARDS ACTIVITIES

7.3.1 United States

Both the American Society of Civil Engineers (ASCE) and the Pultrusion Industry Council (PIC) of the Society of the Plastics Industry (SPI) have realized the importance and the urgent need for authoritative codes

and standards for structural pultruded composites. As discussed earlier, the availability of such documents is important to encourage and increase the acceptance and use of polymer composites by structural engineers dealing with polymer composites.

In 1996, the first phase of an ASCE/PIC multi-phase project on developing design standards for pultruded composite structures was completed (Mosallam 1999). In this project, the author acted as a subcontractor and technical advisor. A state-of-the-art "live" database was developed. More than 500 technical papers and reports in this area were reviewed and evaluated, but only 300 documents were found to be useful in establishing the initial standard document. Building on the foundation of phase I, the second phase was begun as a joint project between ASCE and the American Composites Manufacturers Association (ACMA) in 2007. This standards document is expected to be completed in the near future.

7.3.2 European Effort

In 1996, the first *Structural Design of Polymer Composites: EUROCOMP Design Code and Handbook* was published (Clarke 1996). This document was written based on the technical information available 1994 in the field of composites. The design code presented connection design approaches based on design equations of plate-to-plate (lap, butt, and strap) bolted, and adhesively bonded joints. Unconventional composite connecting systems are presented in Chapter 9 of this manual. No formal coverage of frame connections was included in the EUROCOMP code document.

In 1997, the European Commission of the European Communities published a state-of-the-art review on design, testing, analysis and applications of polymeric composite connections (Mottram and Turvey 1998). The report was prepared by the members of Working Group 7 of the COST C1 [formerly the European Cooperation in the field of Scientific and Technical Research; now the European Cooperation in Science and Technology (COST)]. This eight-chapter document covers the following related topics: plate-to-plate mechanical joints, frame connections, anchorage systems, bolted connections, and FRP connections with other materials. Content descriptions of the COST chapters are given below:

- *Glossary:* A short glossary defining special related terminologies in connection analysis and design.
- *Chapter 1. Plate-to-Plate Mechanical: Part I: Analysis & Design*: Sections on determination of load distribution in multi-row bolted joints, stress analysis, and failure of bolted connections are presented. It should be noted that the chapter does not provide design philosophy. However, the summary information presented is essential to understanding the basic characteristics and performance of plate-to-plate mechanical composite joints.

- *Chapter 2. Plate-to-Plate Mechanical: Part II: Testing & Applications:* This chapter is a continuation of Chapter 1, dealing with plate-to-plate bolted connections. A summary review of the latest research work on bolted plate-to-plate joints is presented. Topics include identification of the common failure modes and descriptions of the different tension test methods for both single-bolt and multi-bolt connections. Again, neither design formulas nor numerical examples are presented. However, the chapter does refer to design methods suggested by both Prabhakaran et al. (1996) and Hassan et al. (1997a and 1997b).
- *Chapter 3. Frame Connections:* Includes a comprehensive summary of the current research work (at that time) on composite frame connections for pultruded composites. A classification for common types of frame connections is presented. The semi-rigid connection concept is discussed, including the effect of rotational stiffness of the beam-ends on the deflection calculations. Research on testing semi-rigid connections is also presented.
- *Chapter 4. Anchorage Systems:* This chapter discusses the different anchoring systems for composite tendons commonly used for prestressed concrete members.
- *Chapter 5. Bonded Connections:* Provides an overview of adhesively bonded joints with a focus on lap joint applications. Discussion on possible modes of failures and parameters affecting failure of bonded adhesives is presented. This chapter also discusses the two design approaches presented in the EUROCOMP code documents: the simplified design approach and the rigorous design procedure. The former approach uses mechanical information obtained from single-lap joint tests performed according to ISO 4587-1997, ASTM D 3163-73c, or other approved test methods. The rigorous procedure is based on closed-form models (Goland and Reissner 1944) and the modified model developed by Hart-Smith (1973a, b, and c). Again, no numerical example or detailed design procedure is provided except for reference to the EUROCOMP code document. This chapter also presents "steel-like" bonded connections.
- *Chapter 6. FRP Connections with Other Materials*: This chapter focuses on the applications of bonded composite plates to masonry, concrete, wood, and metal members. Again, the information is limited and not specifically related to pultruded composite bonded joints.
- *Chapter 7. FRP Bond to Concrete*: Focuses on the use of general composites for concrete repair applications.
- *Chapter 8. Design Guides*: This short chapter briefly discusses the impact of design standards and codes. A table summarizing the joint categories, joining techniques, and joint configuration is also presented.

In conclusion, the COST document provides a general overview and opinions on various related composite joints research works. This report is a valuable research document that identifies areas for future research. It also provides a source summary for a variety of major research and code publications.

7.4 PULTRUDERS' DESIGN GUIDES

Generally, with few exceptions, limited technical information and design formulas are available in design guides or selection manuals published by the industry. The following is an evaluation summary of selected pultruders' design guides with emphasis on composite joint design:

EXTREN Design Manual (Strongwell 2004): The Strongwell *EXTREN Design Manual* contains a section on fabrication (Section 13). This section offers an introduction to basic information on PFRP joints. Parameters affecting the selection of type of connection are discussed, including joint capacity, joint reliability, available space, types of member profiles, service environment, suitability of joint fabrication, need of future disassembly, and aesthetic requirements. Benefits of combined connections are also presented. Common types of mechanical fasteners are presented, including bolts with washers and nuts made from different materials, pultruded threaded rod and nuts, self-tapping and thread-cutting screws, rivets of different materials, spring clips, nails, staples, threaded inserts with bolts, and threaded holes with bolts. The *EXTREN Design Manual* recommends the use of stainless steel fasteners to avoid corrosion problems. The design guide uses the minimum edge distance and pitch values, as recommended by the *Structural Plastics Design Manual* (ASCE 1984). It should be noted that the values appear in the table on p. 439 of the *Structural Plastics Design Manual* are based on experimental results that were conducted on different types of composites for marine applications. For this reason, they are different from the values recommended for pultruded composites described in Table 3-3 of this manual.

Several steel-like connection details are also presented in the *EXTREN Design Manual* as well as the *EXTREN Fabrication & Repair Manual* and the *Strongwell Fiberglass Structures & Systems for Industrial Product Line* document. This includes beam-shear connections where unidirectional angles are attached to the two sides of a unidirectional web. Also, recommendations for adhesively bonded joints are provided. This includes surface preparation procedures, epoxy mixing instructions, repair procedures, as well as application and curing instructions. Another Strongwell document focusing on pultruded railing is also available; it provides information on recommended joints and field fabrication of SAFRAIL products.

Creative Pultrusions (CP) *Design Guide* (Creative Pultrusions, Inc. 2004): The original 1973 edition of the CP design manual has been updated and

now contains 10 chapters covering different structural design aspects of pultruded composites. Chapter 9 of this manual focuses on fabrication techniques that include bolted and bonded joints for pultruded composites. The chapter provides detailed recommended guidelines for surface preparation for bonded joints. Some basic information on adhesives similar to those described in detail in the *Structural Plastics Design Manual* (ASCE 1984) is discussed. No specific design procedure or tables are provided, but useful information on types of adhesives, and advantages and disadvantages of adhesives is provided. It also includes tables for different types of recommended mechanical fasteners. The only information dealing with pultruded composites framing joints is discussed at the end of the manual, where a few "steel-like" connections details are presented, similar to those presented in the Strongwell EXTREN manual. Procedures for testing web clip shear connection are also presented in Appendix A of the Creative Pultrusions manual.

Enduro Tuff Span Technical Data and Design Guide (Enduro Systems, Inc. 2009): In comparison to the Strongwell EXTREN document, little technical information on connection design is included in the Tuff Span guide. All of the provided information is for fasteners and sealants primarily used for the Tuff Span corrugated composite roof system. On the other hand, unlike other pultruders' details, the connection details presented in this document are acceptable for composite structures. Figure 7-7 shows a sample of connection details described in this manual.

Bedford Reinforced Plastics (BRP) *Design Guide* (Bedford Reinforced Plastics, Inc. 2007): The 2007 edition of the *BRP Design Guide* included proper guidelines for joining PFRP frame structures. Older editions adopted the anisotropic joining details and elements developed by Mosallam (1994b). However, in the new edition, all proper details were removed and replaced with the common steel-like connection details similar to those presented in both the EXTREN and CP manuals. Neither of the BRP editions include any specific connection design procedure.

Fiberline Design Manual (Fiberline Composites A/S 2004): Compared to all available pultruders' design guide documents, the *Fiberline Design Manual* discusses in depth both bonded and bolted joints design and details. Section 4 of this document presents the analysis and design of bolted joints. Unlike other manuals, the *Fiberline Design Manual* includes design procedures and numerical design examples for bolted joints. It also includes discussions on load-bearing capacity of bolts, static conditions, stress-related conditions, and values for characteristic strengths for both the longitudinal and transversal directions of connecting members. In addition, the *Fiberline Design Manual* describes the design limit-state and load-bearing capacity of bolts subjected to tension and shearing. Three ultimate limit-state design tables for the longitudinal bearing capacity of bolts in longitudinal and transversal directions, as well as the load-bearing capacity of bolts subjected to traction, are provided. Several numerical

Figure 7-7. A portal frame fabricated according to Enduro Tuff Span connection details.
Source: Green (1985).

examples of typical steel-like bolted connections using the aforementioned design tables are presented, including:

- Design of column-base connections for both I- and C-profiles (the manual refers to this profile as U-profile) and box pultruded profiles
- Interior beam-to-column bolted connections for different pultruded profiles (C-beams to an I-column, and C-beams to a square column) and similar profiles (both beams and column are I-profiles)

- Bolted connections between two horizontal similar-profile beams (two I-beams and two C-beams)

Section 5 of the manual contains very little technical information on bonded and combined joints.

Delta Design Manual (Delta Composites, Inc. 2009): Section 14 of the *Delta Design Manual* contains some design examples for bolted pultruded joints. However, the information does not highlight the anisotropic nature of composites, and, instead, it follows steel-like design procedures.

7.5 PFRP CONNECTIONS: RELATED WORK

In the past few decades, several research studies have been conducted in the area of characterizing the structural behavior of pultruded composite frame connections. In 1984, Morsi et al. conducted an experimental study on a PFRP column-to-base connection using both composite and metal connecting elements (Morsi et al. 1984). In this study, PFRP angles and bolts were used to connect a "steel" column to the base plate. There was no explanation about why PFRP composite columns were not used instead of steel columns.

7.5.1 Examination of Steel versus PFRP Connectors

Three connection details were tested by Morsi et al. (1984), including (1) PFRP bolts with steel angles; (2) steel bolts with PFRP angles; and (3) PFRP pultruded angles and threaded rods. Four different angle sizes with 1/2 in. (12.7 mm) bolts and nuts were evaluated. In all tests, bending was induced about the weak axis of the pultruded column. Figure 7-8 shows the typical test setup used for all tests. All pultruded profiles were off-the-shelf E-glass/isophthalic polyester materials. Near the failure load of all tests, the connecting PFRP angles developed large longitudinal cracks, particularly at the inside corner of the pultruded angles. This common mode of failure is due to the development of the radial tension–stress component of the curved corner. The subject is discussed by Mosallam (1990; 1994b) and is shown in Fig. 7-14.

As expected, at moderately high shear stresses FRP threaded rods failed due to failure of the molded threads, and the FRP molded nuts could not be removed from the failed threaded rods. This mode of failure was reported in several papers by Mosallam (1990, 1994a, 1994b, 1997a). Load versus angle of rotation (P/θ), and load versus deflection (P/δ) curves are shown in Figs. 7-9 and 7-10, respectively. A summary of Morsi et al.'s (1984) test results is listed in Tables 7-1 and 7-2. Between 1984 and 1990, no significant research work was reported on PFRP frame
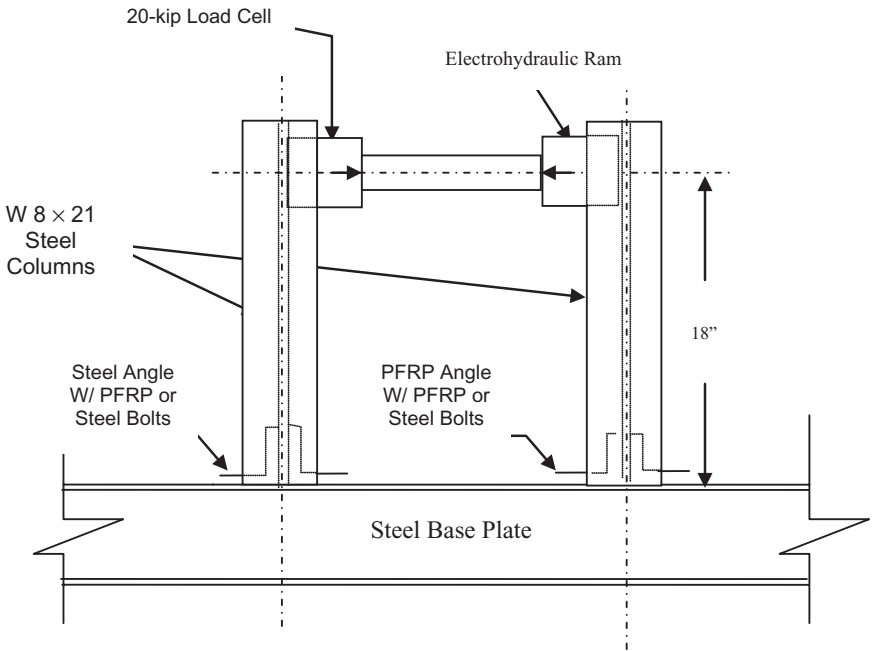
Figure 7-8. Steel column-base connection test setup using PFRP angles and FRP bolts.
Source: Morsi et al. (1984).

connections. The first comprehensive, full-scale study was conducted by and reported in Mosallam (1990). In this study, detailed theoretical and experimental investigations on the short- and long-term behavior of PFRP frame structures were conducted. In this investigation, two portal frame structures were constructed from off-the-shelf, commercially produced pultruded sections (refer to Fig. 7-7). In addition, an analytical investigation was performed to predict the nonlinear response of the frame. The numerical model includes the effects of axial, shear, and flexural deformation of the pultruded numbers; flexibility of the beam-to-column connections; and the post-buckling of the frame girder. An expression for the nonlinear rotational stiffness of the pultruded beam-to-column connection is presented. The experimental data obtained from the full-size test correlated very well with the analytical model. A brief description on this work is presented in the following section.

7.5.2 Interaction between Pultruded Sections and PFRP Connectors

In 1992, Mosallam and Bank (1992) presented results of an experimental and analytical investigation on the behavior of a pultruded composite portal frame subjected to short-term static loads that had been initiated
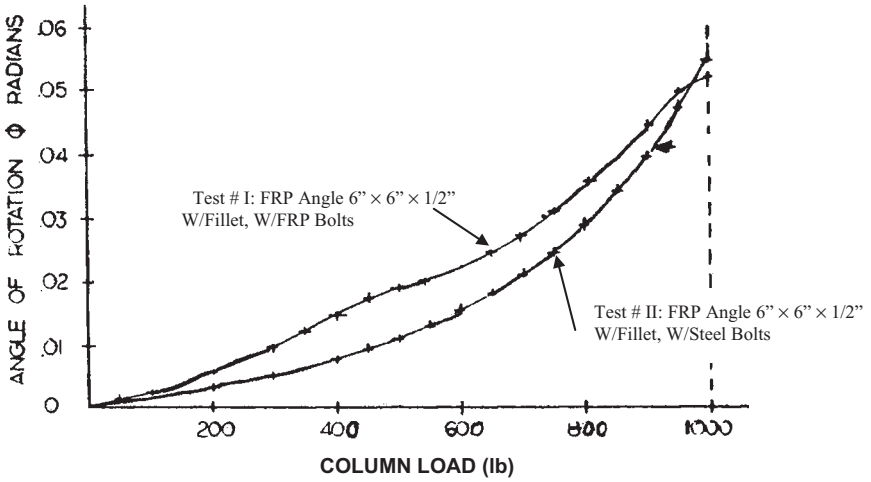
Figure 7-9. Load vs. angle of rotation.
Source: Morsi et al. (1984).
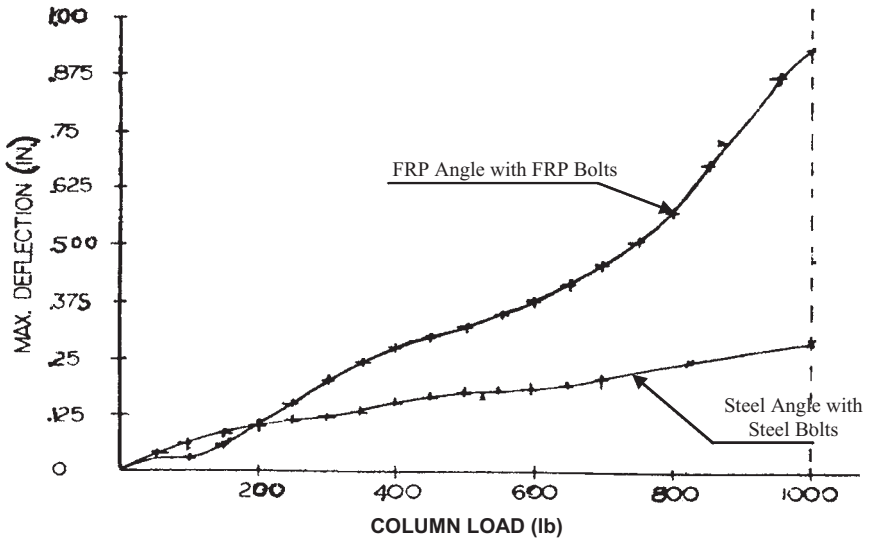
Figure 7-10. Load vs. deflection.
Source: Morsi et al. (1984).

earlier by Mosallam (1990). (Following the specifications of Mosallam (1990), the frame was 6 ft (1.83 m) tall, 9 ft wide (2.74 m), and was designed and constructed entirely from E-glass/vinylester PFRP thin-walled sections (refer to Fig. 7-11). The composite profiles used in this study were standard off-the-shelf H-profiles 8 in. × 8 in. × 3/8 in. (20.32 cm × 20.32 cm × 0.95 cm) (depth × flange width × wall thickness) glass/vinylester Pultex

Table 7-1. PFRP Angles with Steel Bolts vs.
Steel Angles with PFRP Threaded Rods

Test No.	Angle Size and Type (in.)	Maximum Load (lb)	Maximum Moment (ft-lb)	Maximum Deflection (in.)
A	$4 \times 4 \times 3/8$ W/O Fillet	450	844	0.876
B	$4 \times 4 \times 1/2$ W/ Fillet	750	1,406	0.904
C	$4 \times 4 \times 1/2$ W/ Fillet	850	1,594	0.464
D	$4 \times 4 \times 3/8$ W/O Fillet	400	740	0.969
E	$6 \times 6 \times 1/2$ W/ Fillet	1,000	1,875	0.952
F	$6 \times 6 \times 1/2$ W/ Fillet	950	1,781	0.923
G	$6 \times 6 \times 1/2$ W/O Fillet	900	1,688	0.927

Source: Morsi et al. (1984).

Table 7-2. PFRP Angles with PFRP Threaded Rods vs.
Steel Angles with Steel Bolts

Test No.	Angle Size and Type (in.)	Maximum Load (lb)	Maximum Moment (ft-lb)	Maximum Deflection (in.)
H	$6 \times 6 \times 1/2$ W/O Fillet	1,300	2,438	1.289
I	$6 \times 6 \times 1/2$ W/ Fillet	1,000	1,875	0.939
J	$4 \times 4 \times 3/8$ W/O Fillet	650	1,219	1.413
K	$4 \times 4 \times 1/2$ W/ Fillet	1,450	2,719	0.967

Source: Morsi et al. (1984).

1625 pultruded profiles. These commercially produced pultruded composite sections consisted of E-glass roving and continuous strand mat (occupying approximately 45% by volume) in a vinylester resin. The beam-to-column and base-plate connections were detailed according to general recommendations of the majority of pultruders' design manuals (e.g., Creative Pultrusions; Strongwell).

In all connection details, Pultex 1625 pultruded equal-leg angles (6 in. × 6 in. × 1/2 in.) (152.4 mm × 152.4 mm × 12.7 mm) together with pultruded 3/4 in. (19.05 mm) and 1 in. (25.4 mm)-diameter threaded rods and compression-molded FRP nuts were used to join the H-profiles. The details of the frame connections used in this study are shown in Fig. 7-12. Figure 7-13 shows the dimensions and the location of strain gages and linear variable differential transducers (LVDTs) used in this test.

The first indication of local failure occurred at a load of 15,700 lb (69.83 kN) [the ultimate load was 25,000 lb (111.2 kN)] when the left-hand
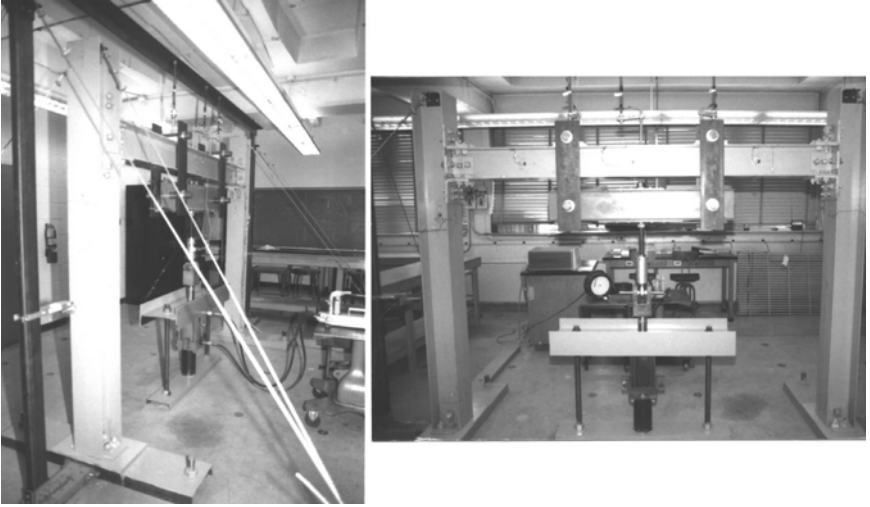
Figure 7-11. Study on PFRP portal frame with steel-like connection details.
Source: Mosallam (1990).
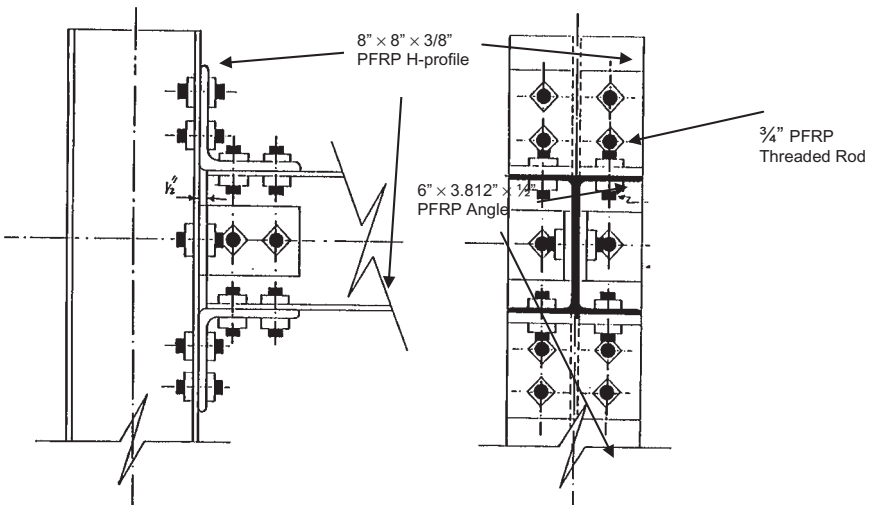
Figure 7-12. Beam-to-column connection details.
Source: Mosallam (1990).

beam-to-column connection began to "yield" (i.e., exhibited excessive rotation). This load was referred to as the "initial failure load" of the frame. The failure was not in the connection elements (angles, threaded rods, or nuts) but, rather, in the column section itself. The flange of the column separated from the web, behind the top row of bolts of the top angle, creating a hollow internal cavity in the pultruded section at the
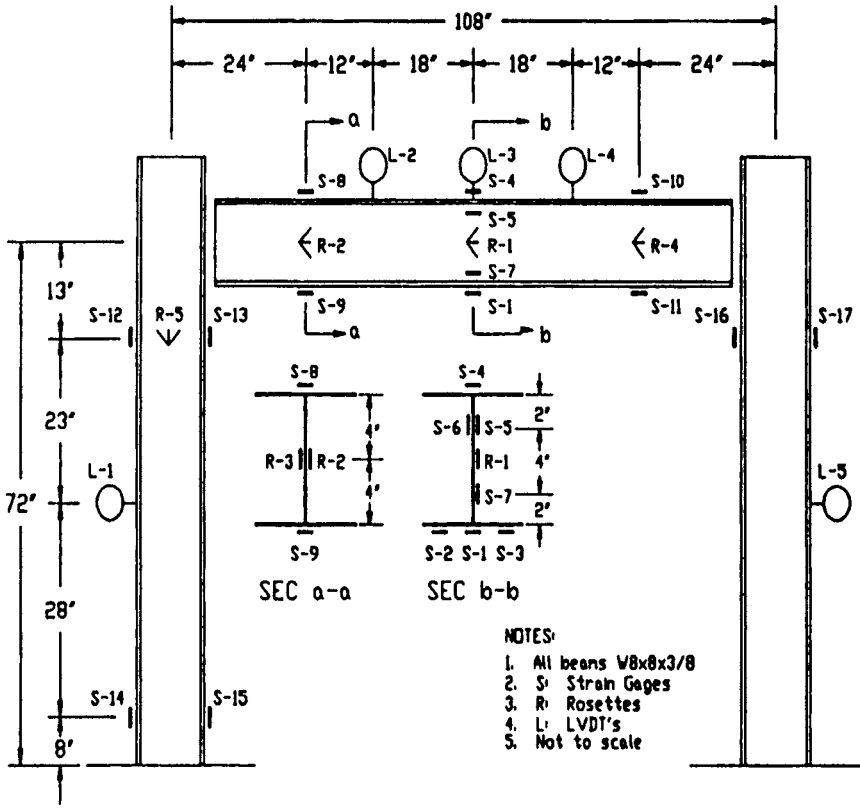
Figure 7-13. Dimensions and locations of strain gages and LVDTs for the PFRP portal tested by Mosallam and Bank (1992).

flange-web intersection (refer to Figs. 7-14, 7-15 and 7-16). This transverse tension failure occurred perpendicular to the direction of longitudinal fiber-reinforced in the pultruded section. (Unidirectional pultruded sections are weak in the transverse direction, especially at the intersection of the web and flange, due to negligible transverse reinforcement. The major roving reinforcement is aligned along the beam axis in the longitudinal direction.) The unidirectional pultruded equal-leg angles used in this program had the major fiber reinforcements running in the *wrong* directions relative to the load path and applied stresses. For this reason, a premature failure initiated by hair cracks at the corners was unavoidable (refer to Fig. 7-15). These cracks were due to the resulting radial stress component (in the top angle in the connection closing mode) and, eventually, would cause delamination due to the inherent poor interlaminar shear and through-the-thickness properties of all 2-D fiber-reinforced
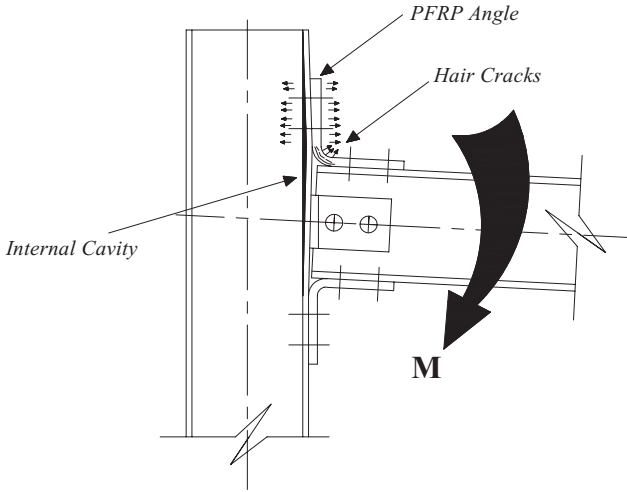
*Figure 7-14. Premature failure of open-web unidirectional pultruded profiles
and delamination of unidirectional PFRP angles.*
Source: Mosallam (1990).
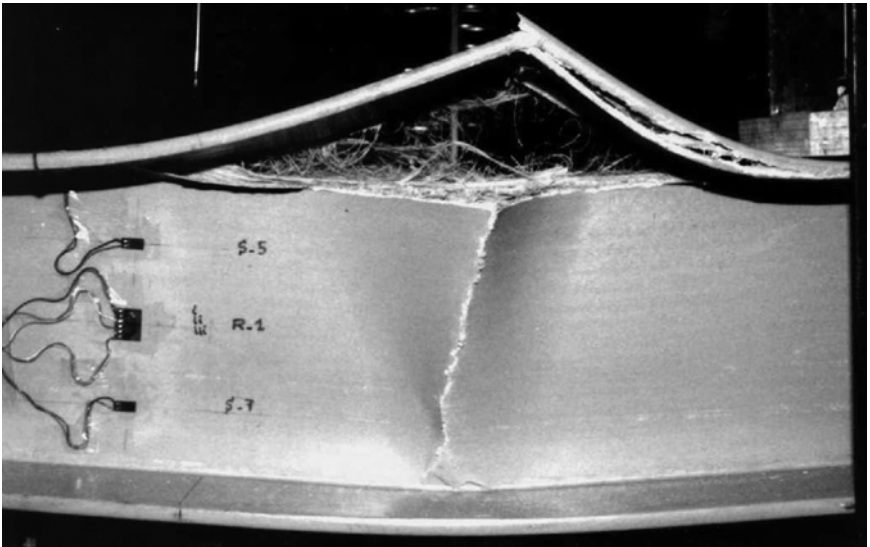
Figure 7-15. Premature failure of open-web unidirectional pultruded profiles.
Source: Mosallam (1990).

composites (refer to Fig. 7-16). A sample of the experimental results gener-
ated from this work is presented in Fig. 7-17.

A computer code was developed by Mosallam (1990) to describe the
behavior of semi-rigid connected PFRP frame structures. The
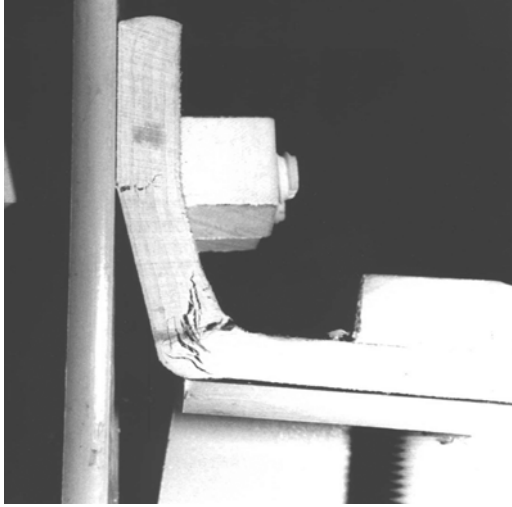
Figure 7-16. Dramatic loss of connection stiffness initiated by the development of hair cracks at the corners of the PFRP unidirectional angles.
Source: Mosallam and Bank (1992).

experimental moment–rotation behavior was included in the program using the following equation:

$$\theta = C_1 M + C_2 M^2 + C_3 M^3 \quad \text{for} \quad 0 < M \le 28 \qquad (\text{k} \cdot \text{in})$$
$$\theta = C_4 + C_5 M \qquad\qquad \text{for} \quad 28 < M \le 52 \qquad (\text{k} \cdot \text{in}) \qquad (7\text{-}2)$$
$$\theta = C_6 M + C_7 M \qquad\quad \text{for} \quad 52 < M \le M_{\max} \quad (\text{k} \cdot \text{in})$$

Equation 7-2 was developed using the experimental M/θ curve shown in Fig. 7-18. Figure 7-19 verifies the validity of the analytical approach in modeling the flexibility of the PFRP frame connections.

7.5.3 Connector Design and Overall Systems Performance

Based on the findings of the experimental study conducted by Mosallam (1990), the effect of connection details made of pultruded FRP composites, and their semi-rigid behavior, have been investigated by Bank et al. (1990). Figure 7-20 presents the four connection details evaluated in this study. For conservative preliminary design purposes, it is acceptable to use a single initial (linear) value for the connection's rotational stiffness (refer to Fig. 7-21). This argument was adopted and evaluated by Mosallam (1990), and approximate theoretical results using initial rotational stiffness values were compared to the full-scale experimental results. Figure 7-21 presents the initial rotational stiffness curves tested in this study. Values for the initial stiffness coefficients, k_o, are presented in Table 7-3.
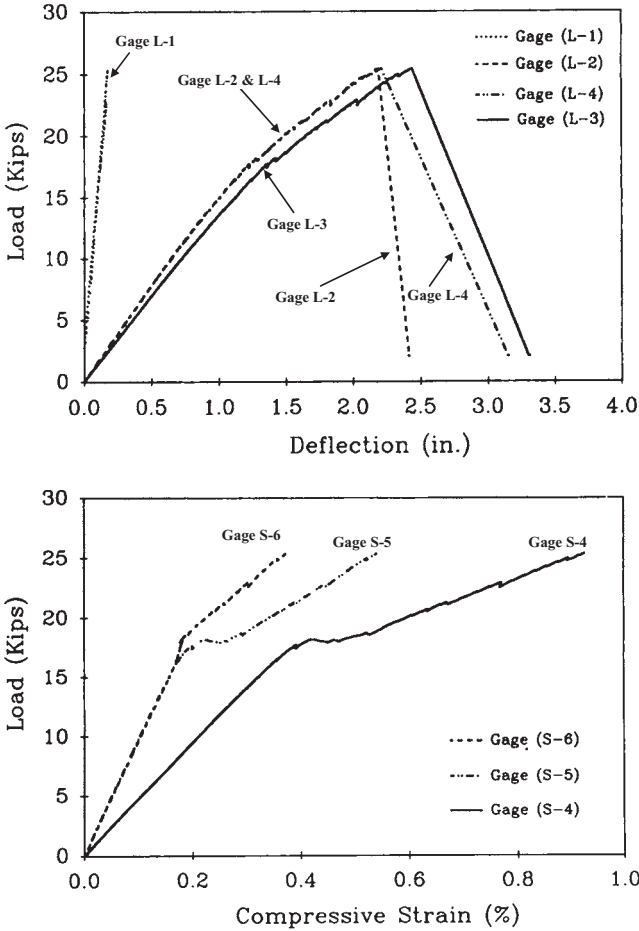
Figure 7-17. Sample of the experimental results presented by Mosallam (1990) and Mosallam and Bank (1992).

As will be seen later, the results from this preliminary study prepared the foundation for more extensive examinations of PFRP connections that included analytical, computational, and experimental investigations to optimize the load transfer process. Initial test specimens were based on Mosallam (1990) and Bank et al. (1990). Accordingly, Type i, the first iteration, corresponded to the connection assembly identified as (D) in Fig. 7-20. Subsequent designs and modifications, such as Types ii and iii, would represent attempts to improve the performance of the overall system. As with the initial connections, experimental efforts would be employed to develop displacement curves and extract polynomial expressions of rotational-stiffness.
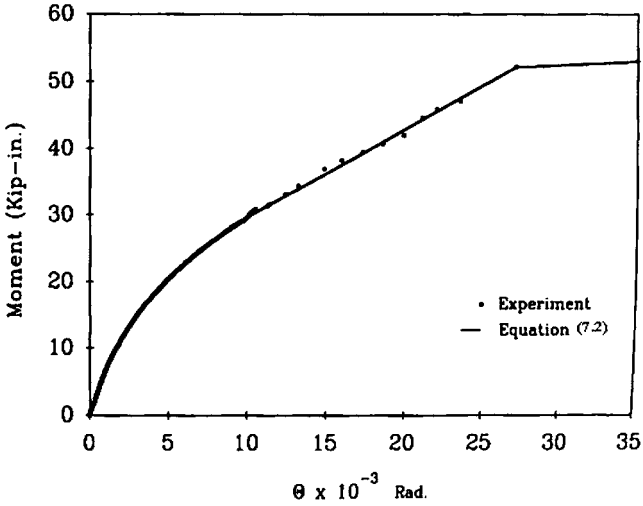
Figure 7-18. Experimental moment–rotational curve used to generate Eq. 7-2 for linear modeling of the PFRP frame.
Source: Mosallam (1990) and Mosallam and Bank (1992).
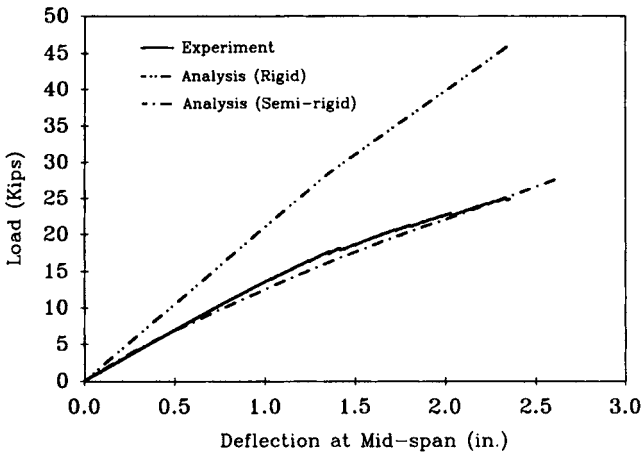
Figure 7-19. Comparison between the experimental and analytical results presented by Mosallam (1990) and Mosallam and Bank (1992).

For comparison purposes, the k_o value for a 1/2 in. (12.7 mm) steel angle in a top and seated connection detail (Stelmack et al. 1986) is included in Table 7-3. This pilot investigation involved both experimental and analytical evaluation of several connection details for pultruded frame structures. All of the connections tested focused on exterior beam-to-column connections with a flange attachment configuration.
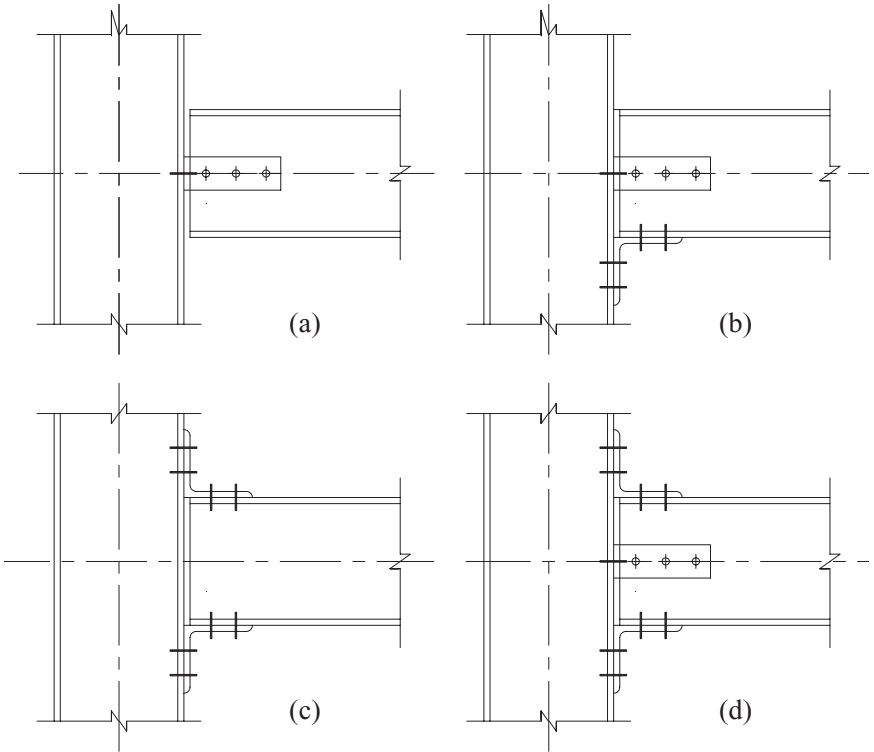
Figure 7-20. PFRP connection details evaluated by Bank et al. (1990).
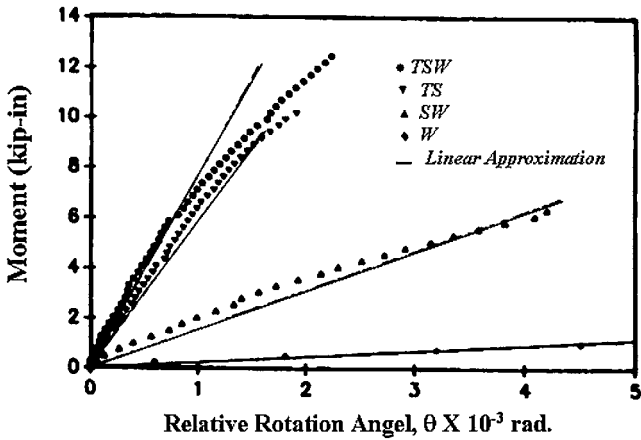
Figure 7-21. Initial rotational stiffness experimental curves of four PFRP connection details evaluated by Bank et al. (1990).

Table 7-3. Initial Rotational Stiffness Coefficients

Connection Detail	Initial Stiffness Coefficient, k_o (kip-in./rad)
TSW[a]	7,000
TS[a]	6,000
SW[a]	1,500
W	250
TS (Steel)[b]	17,500

[a] Bank et al. (1990).
[b] Stelmack et al. (1986).
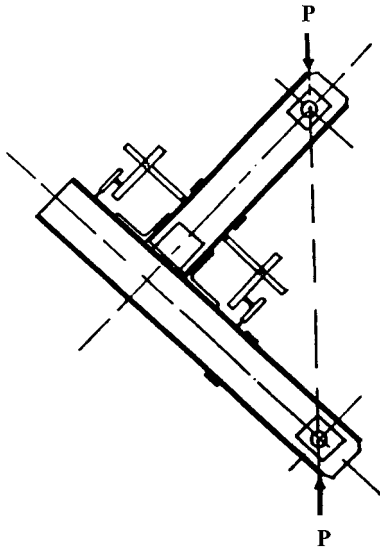
Figure 7-22. Exterior PFRP beam-to-column connection setup.
Source: Bank et al. (1990).

Experimental results of three different PFRP connection details were pre-sented. The test setup used in this study is shown in Fig. 7-22.

Figure 7-23 shows the M/Θ curve for detail (D) shown in Fig. 7-20, which was the same detail used in the PFRP portal frame investigated by Mosallam (1990) and Mosallam and Bank (1992). Regression analysis of the M/Θ experimental data was performed and the following polynomial equations describing the nonlinear rotational stiffness of the connection detail was developed (note that a tri-linear expression for the same con-nection was reported in Eq. 7-2:

For $0 < M$ (kip-in.) ≤ 28:

$$\theta = 1.33 \times 10^{-4} M + 2.08 \times 10^{-6} M^2 + 1.69 \times 10^{-7} M^3, \text{ and}$$

For 28 < M (kip-in.) ≤ *M$_{max}$*

$$\theta = -1.24 \times 10^{-2} + 7.56 \times 10^{-4} M \qquad (7\text{-}3)$$

The regression curve based on these equations is shown as a solid line in Fig. 7-23.

As reported by Mosallam (1990) and illustrated in Fig. 7-14, a premature failure in the form of a local separation of the column flange from the web was the major cause of the limited strength of this detail. For this reason, Bank et al. (1990) suggested a simple detail to avoid this premature failure by introducing a transfer member in the form of a unidirectional pultruded angle placed at the web-flange junction of the column at the connection zone, as shown in Fig. 7-24. As expected, the addition of this
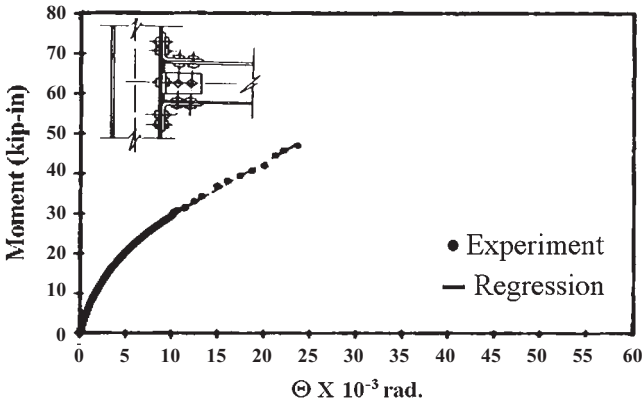
Figure 7-23. Moment–rotation curve for exterior PFRP beam-to-column connection detail D described in Fig. 7-20 as Type i.
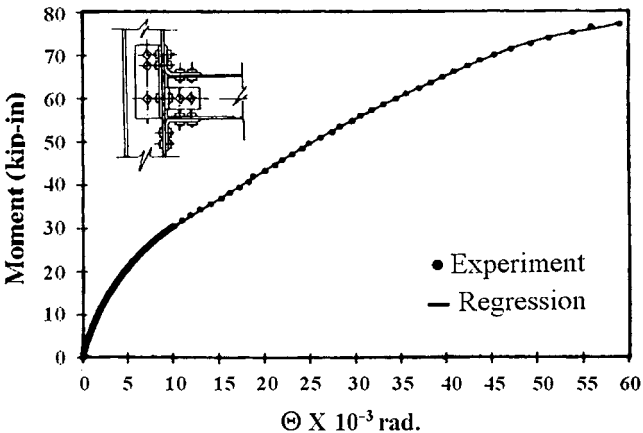
Figure 7-24. Moment–rotation curve for exterior PFRP beam-to-column connection (detail D) with transfer angle (Type ii).

transfer member prevented, to a large extent, the formation of the cavity behind the connection and resulted in an increase in the strength up to 50% [52.3 kip-in. (5.9 kN-m) vs. 77.5 kip-in. (8.64 kN-m)]. In addition, the plastic relative rotation increased from 0.025 rad to about 0.059 rad, with an increase of about 136% of the ultimate plastic deformation of the connection. However, no gain in stiffness was achieved up to the ultimate moment of the unstiffened detail (refer to Figs. 7-23 and 7-24). As for the unstiffened connection detail, a full regression analysis was performed. A single polynomial equation was developed to describe the full range of the rotational stiffness of this stiffened connection detail as follows:

$$\Theta = 1.32 \times 10^{-4}\, M + 5.32 \times 10^{-6}\, M^2 - 3.93 \times 10^{-7}\, M^3 + 3.04 \times 10^{-8}\, M^4$$
$$- 7.13 \times 10^{-10}\, M^5 + 6.66 \times 10^{-12}\, M^6 - 2.05 \times 10^{-14}\, M^7 \qquad (7\text{-}4)$$

A more complete list of piecewise polynomial expressions for rotational-stiffness of the various connection assemblies is presented in Table 7-4. These piecewise expressions are defined in terms of moment and used to describe the behavior of Types i, ii, iii, and iv connections.

Figures 7-25 and 7-26 show the ultimate failure load of connection details Types i and ii, respectively.

7.5.4 Design Innovation and Moment Resistance

As a continual effort in improving the structural behavior of steel-like connection details, Bank and Mosallam (1991b) proposed another PFRP

Table 7-4. Multilinear Rotational Stiffness Expressions for Four PFRP Beam-to-Column Exterior Connection Details (Flange Attachment/ Closing Mode)

Connection	$\Theta = f(M)$	
Type i	$\Theta = 1.43 \times 10^{-4}\, M$	$(0 < M < 12)$
	$\Theta = -3.25 \times 10^{-3} + 4.14 \times 10^{-4}\, M$	$(12 \leq M < 32)$
	$\Theta = -1.95 \times 10^{-2} + 9.23 \times 10^{-4}\, M$	$(32 \leq M < 52)$
	$\Theta = -1.27 \times 10^{-1} + 3.00 \times 10^{-3}\, M$	$(52 \leq M < 55)$
Type ii	$\Theta = 1.43 \times 10^{-4}\, M$	$(0 < M < 12)$
	$\Theta = -3.25 \times 10^{-3} + 4.14 \times 10^{-4}\, M$	$(12 \leq M < 32)$
	$\Theta = -1.95 \times 10^{-2} + 9.23 \times 10^{-4}\, M$	$(32 \leq M < 72)$
	$\Theta = -10.9 \times 10^{-4} + 2.20 \times 10^{-3}\, M$	$(72 \leq M < 76.5)$
Type iii	$\Theta = 1.10 \times 10^{-4}\, M$	$(0 < M < 20)$
	$\Theta = -8.00 \times 10^{-3} + 5.00 \times 10^{-4}\, M$	$(20 \leq M < 80)$
	$\Theta = -9.74 \times 10^{-2} + 1.62 \times 10^{-3}\, M$	$(80 \leq M < 114.6)$
Type iv	$\Theta = 3.84 \times 10^{-5}\, M$	$(0 < M < 26)$
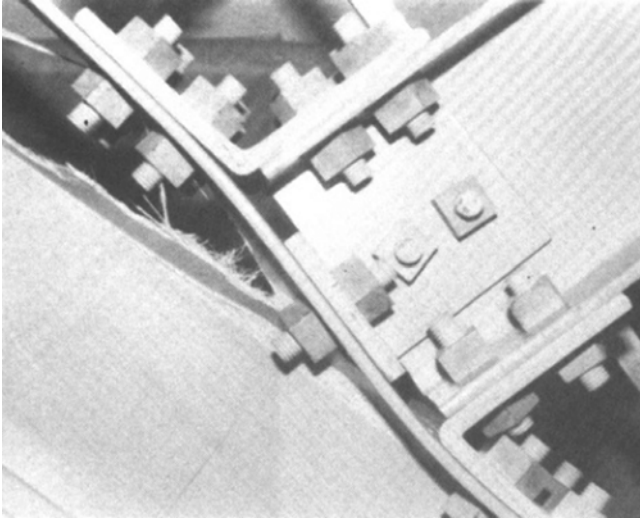
Figure 7-25. Ultimate failure mode of connection details Type i.
Source: Bank et al. (1990).
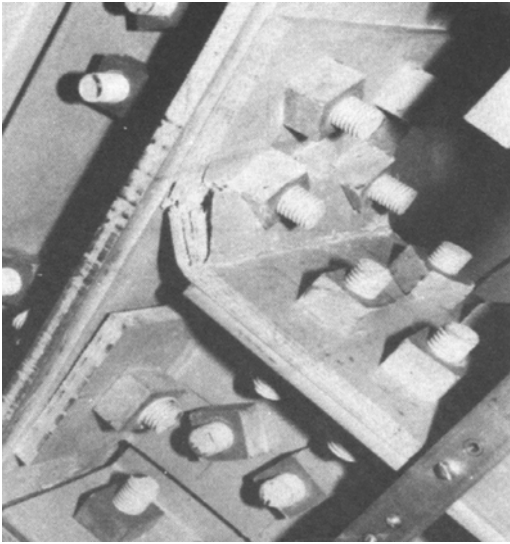
Figure 7-26. Ultimate failure mode of connection details Type ii.
Source: Bank et al. (1990).

beam-to-column connection detail using several off-the-shelf pultruded elements. This connection detail was referred to as Type iii. The Type iii detail was similar to the Type ii detail, except for replacing the top pultruded angle by a miter connector consisting of two 9 in. (228.6 mm) long,

PFRP Slotted T-Flange
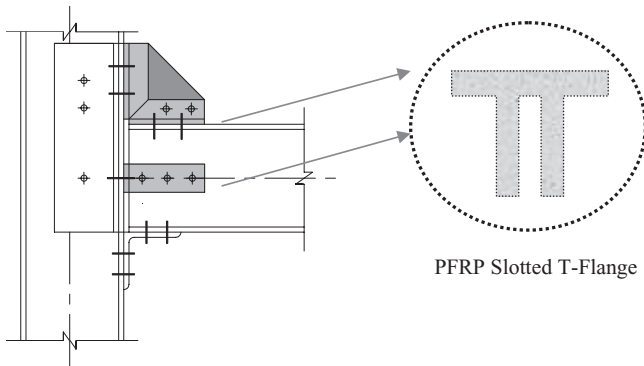
Figure 7-27. PFRP connection details Type iii evaluated by Bank and Mosallam (1991b).

6 in. (152.4 mm) wide T-flange elements bolted to the flanges of both the column and beam using 1/2 in. (12.7 mm) pultruded plates. The fiber orientation of the pultruded plate was aligned at a 45 degreeswith respect to the beam and column flanges, as shown in Figure 7-27.

The PFRP plate was attached to the slotted section using PFRP threaded rods and FRP molded nuts. The reason for stiffening only the top connecting element was that the connection specimen was tested in a closing mode (refer to Figure 7-22). In this closing mode, excessive tensile stresses at the top portion of the connection (behind the top angle) will develop, resulting in a premature separation of the column inner flange of the column from the web, as discussed earlier. However, if this connection were required to resist full reversed cyclic loading, the same stiffening details would have been required at both the top and the bottom of the connection.

The failure mode of the Type iii connection specimen was initiated by a local transverse tension failure of the unidirectional pultruded elements. The *initial* failure occurred due to the development of high transverse tensile stresses at the unstiffened beam portion beneath the top T-flange miter joint (note that the transfer angle was not extended to cover the whole connection area, as shown in Figure 7-27). The second local damage was also caused by the high transverse tension stresses at the slotted section of the flange. This local failure was initiated first through the bolt holes connecting the T-flange and propagated to about half of the pultruded plate. The ultimate global failure was a combination of sudden splitting of the T-flange, shaving of the PFRP threads of the threaded rod connecting the shear PFRP angle, and separation of the pultruded beam from the column (refer to Figure 7-28).

Figure 7-29 shows a comparison between the three types of connection details Type i, ii, and iii. As shown by this graph, it is hard to distinguish
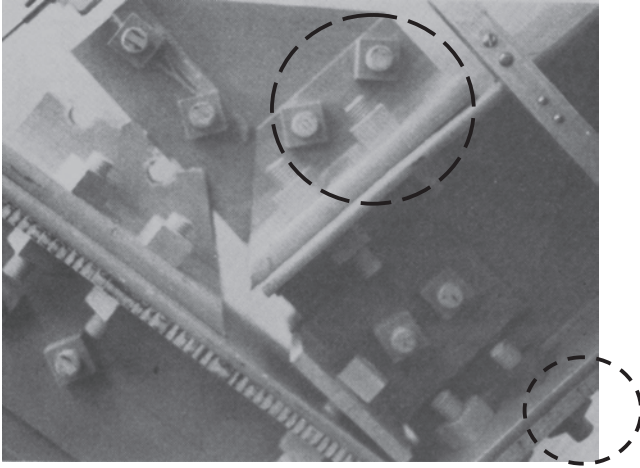
Figure 7-28. Ultimate failure mode of connection details Type iii. Source: Bank and Mosallam (1991b).
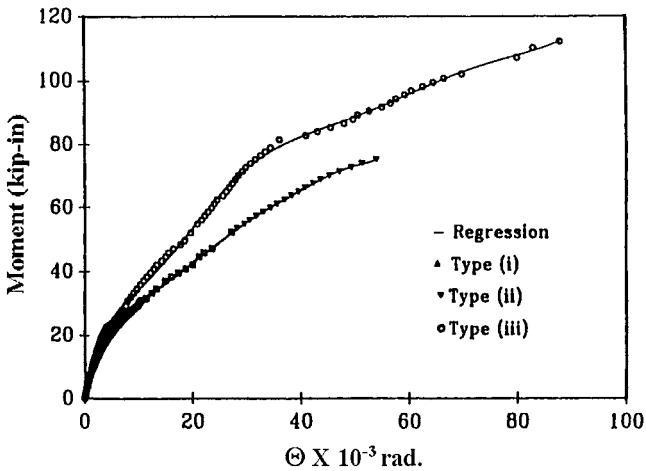
Figure 7-29. Moment–rotation curves of connection details tested by Bank and Mosallam (1991b).

between the curves for Type i and Type ii, up to the failure moment of the Type i connection detail. However, this graph shows an appreciable increase in both the stiffness and the strength of the Type iii connection detail. The gain in the rotational stiffness of this detail was about 48% as compared to the rotational stiffness of connections Type i and Type ii. In addition, appreciable strength gains of about 119%, and 50% were achived, as compared to ultimate moment capacity of connections Type i and Type ii, respectively.
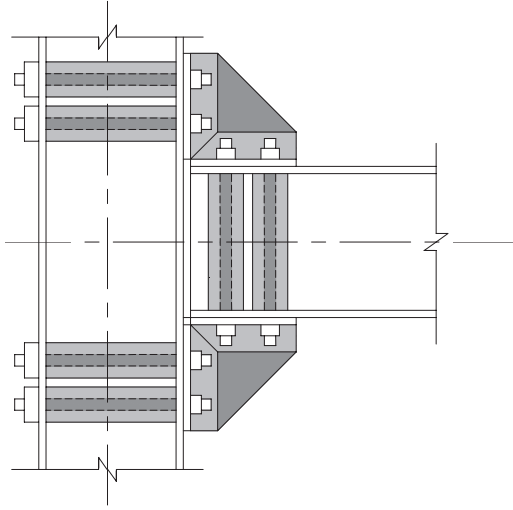
Figure 7-30. PFRP connection details Type iv.

In 1992, Bank, Mosallam, and McCoy (Bank et al. 1992) presented a summary of different PFRP frame connections tested in previous studies (Mosallam 1990; Bank et al. 1990; Bank and Mosallam 1992). In addition, a new connection detail was proposed and was referred to as Type iv. Figure 7-30 shows the details connection Type iv. In evaluating this detail, the same test setup was used as shown in Figure 7-31.

As seen in Figs. 7-30 and 7-31, this connection detail was an improved version of the connection detail Type iii. However, in this detail, both the top and bottom PFRP seated angles were replaced with the T-flange/plate system described earlier for detail Type iii. The PFRP plate was attached to the slotted section using epoxy adhesives, and no bolts were used. All PFRP threaded rods connecting the flanges of the T-sections were extended to the opposite flanges of the beam and column sections, and PFRP 2 in. ×2 in. 1/4 in. box sleeves where used to house the threaded rods between the flanges [this approach was later proven unnecessary by Mosallam et al. (1993a) and by Mosallam (1994b), as will be discussed later in this chapter.] The ultimate failure of this connection was catastrophic due to failure of the adhesives (Figure 7-32). The adhesive failure can be attributed to lack of sufficient surface pretreatment of the adherends, especially in preparing the interior surfaces of the slot (or groove) of the T-flange sections.

Figure 7-33 shows the experimental moment–rotation curves for the four connection details (Types i, ii, iii, and iv). As shown in this figure, a substantial improvement in both the strength and rotational stiffness was
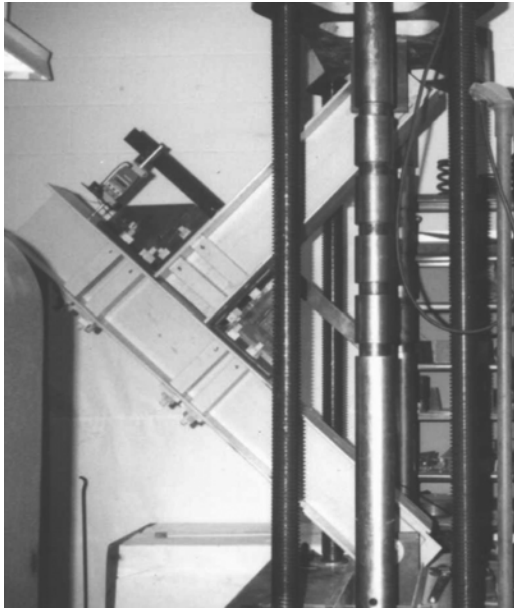
Figure 7-31. PFRP exterior connection test setup.
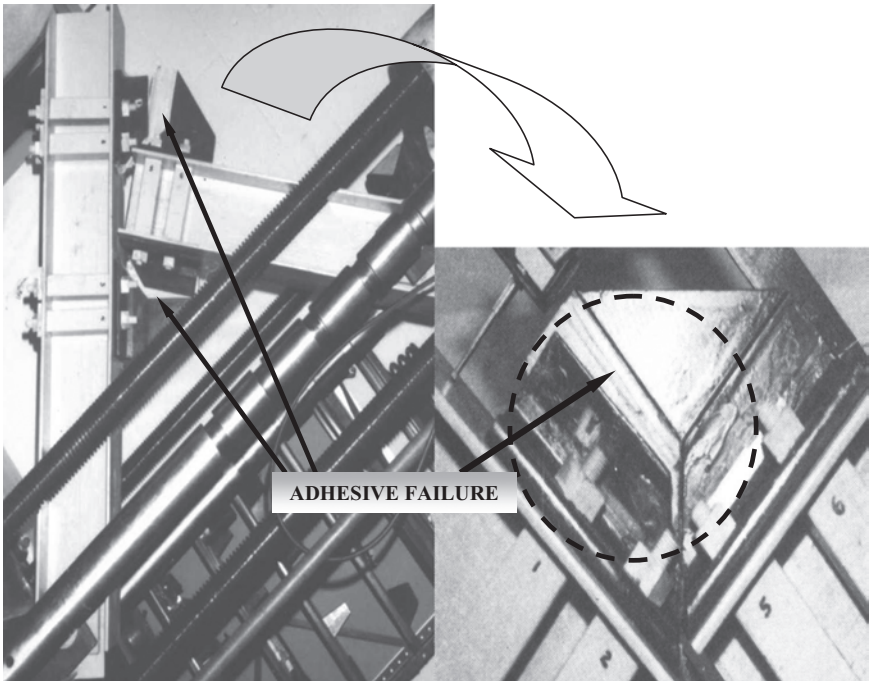
ADHESIVE FAILURE

Figure 7-32. Adhesive failure of connection detail Type iv.

achieved using this connection detail. For example, the gains in the strength and rotational stiffness for Types iii and iv were about 196%, and 272%, respectively, as compared to the strength and stiffness of connection detail Type i used in the portal frame study by Mosallam (1990). However, and as shown in Figs. 7-33 and 7-34, a tremendous loss in plastic rotational deformation (of connection Type iv) was observed (ultimate relative rotation of Type iv is 0.02 rad vs. ultimate relative rotation of Type iii of 0.09 rad). This reflects the lack of ductility of connection detail Type iv.

To incorporate the nonlinear semi-rigid behavior of these connections in any structural analysis, expressions based on experimental results must be obtained. Instead of using a complex nonlinear equation, it was decided to use multilinear expressions (refer to Figure 7-34). Table 7-4 presents
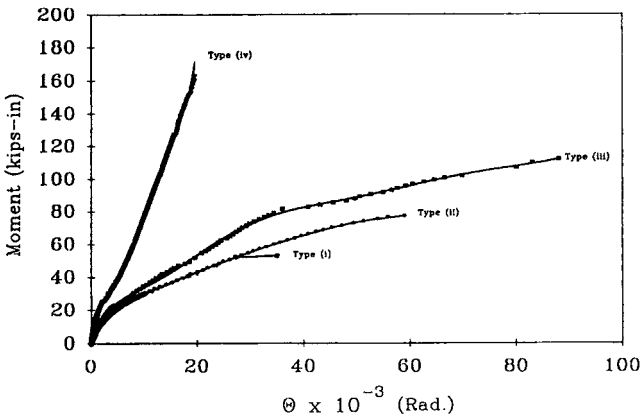
Figure 7-33. Moment–rotation curves for Type i, Type ii, Type iii, and Type iv PFRP connection details.
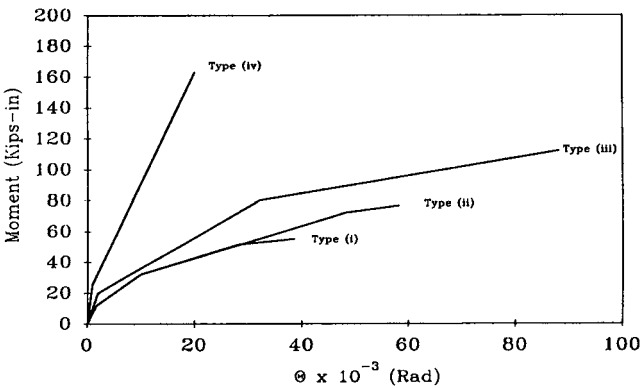
Figure 7-34. Multilinear moment–rotation curves for Type i, Type ii, Type iii, and Type iv PFRP connection details.

expressions for the different connection details evaluated in this program. These multilinear expressions are very useful in conducting detail analysis for any structural frame structure built with one of these connection details. The validity of these expressions in predicting the behavior of PFRP portal frames has been verified by Mosallam (1990) (refer to Figure 7-35).

For design purposes, a simple approach can be used to include the flexibility of such connections in the analysis. This can be done by using a single linear expression. The linear rotational stiffness coefficients can be obtained by a piecewise linear fit to the experimental M/Θ curves. Table 7-5 presents the calculated values of the initial rotational stiffness coefficients, K_e, final rotational stiffness coefficients, K_f, the ultimate moment capacity, M_{ult}, and the relative rotation at failure, Θ_{ult}. In designing these
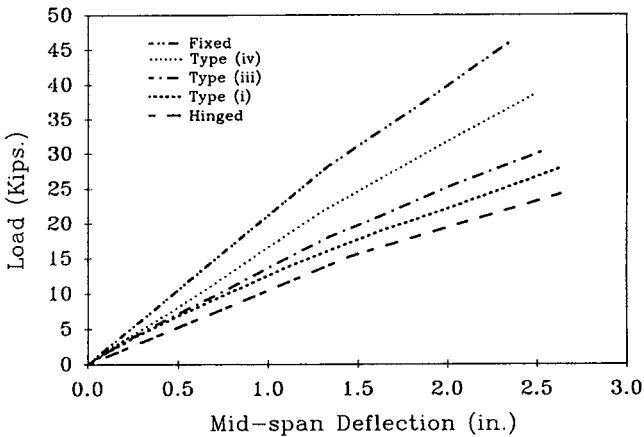
Figure 7-35. Modeling of PFRP portal frame behavior using multilinear expressions (Type i) presented in Table 7-4.

Table 7-5. Linear Rotational Stiffness Coefficients for Design of PFRP Beam-to-Column Exterior Connection Details (Service Load/Flange Attachment/Closing Mode)[a]

Connection	K_e (kip-in./ rad)	K_f (kip-in./ rad)	M_{ult} (kip-in.)	Θ_{ult} (rad)
Type i	6,993	333	55.0	0.0380
Type ii	6,993	455	76.5	0.0590
Type iii	9,091	617	114.6	0.0883
Type iv	26,091	7,194	162.9	0.0200

[a]1 kN-m/rad = 0.112 kip-in./rad.

connections for the service load [within the linear range of the connection; for example, for connection Type ii up to 12 kip-in. (1.36 kN-m)], the initial rotational stiffness coefficient may be used. Another alternative is to use the first equation for each connection detail presented in Table 7-4.

Based on the past unsuccessful experience of utilizing "un-engineered" off-the-shelf pultruded products as connecting elements [e.g., Mosallam 1990); Bank and Mosallam (1991)], a different approach was adopted Mosallam (1993b) to develop customized connection details.

7.5.5 Universal Connector

In 1993, Mosallam presented a novel approach to connecting PFRP framing elements using appropriate composite connectors (Mosallam 1993d). The development of these connectors was the result of a combination of past experience, available research and design data, and knowledge of the anisotropic behavior of the composite materials. The design criteria for what is called the "universal connector" (UC) included (1) proper fiber orientation; (2) ease of erection and duplication; (3) geometrical flexibility and suitability for use in connecting a large variety of commercially available pultruded shapes; and (4) maximizing both the overall connection stiffness and ultimate capacity. The first UC prototype was modified and optimized using finite element (FE) techniques (Mosallam et al. 1994). To minimize the number of design variables required for producing the optimum UC, the Taguchi statistical method for quality control was incorporated in the optimization procedure. Among the different parameters selected were the UC geometry, composite lay-up, and thickness of the various elements. Optimum UC is shown in Fig. 7-36. Figure 7-37 shows the dimensions and the geometry of the modified version of the UC connector. The FRP connector prototype was designed and fabricated from an E-glass/vinylester composition. The UC element (Fig. 7-38) can be used for the majority of PFRP connections for different shapes, such as exterior and interior beam-to-column connections, column-base connections, continuous beam connections, beam-to-girder connections, and others.

To verify the performance of this *engineered* composite connector, a comprehensive experimental program to evaluate quasi-static, dynamic creep, and low-fatigue cyclic behavior of connections constructed using the UC element(s) was conducted by Mosallam et al. (1994). The experimental program was composed of five major phases: (1) characterization of quasi-static behavior of UC *exterior* beam-to-column connections; (2) characterization of dynamic and damping characteristics of UC *exterior* beam-to-column connections; (3) characterization of cyclic behavior of UC *exterior* beam-to-column connections; (4) performance of UC beam-to-column connections under sustained loads or creep performance (at

| Run 1 | Run 2 | Run 3 | Run 4 | Run 5 |
| Run 6 | Run 7 | Run 8 | Run 9 | Run 10 |

| 0.375" wall thickness | 0.5" wall thickness | 0.375" wall thickness | 0.375" wall thickness | 0.75" wall thickness |

(a) No diagonal webs

(b) Central diagonal web

(c) Two outboard diagonal webs

(d) Three diagonal webs
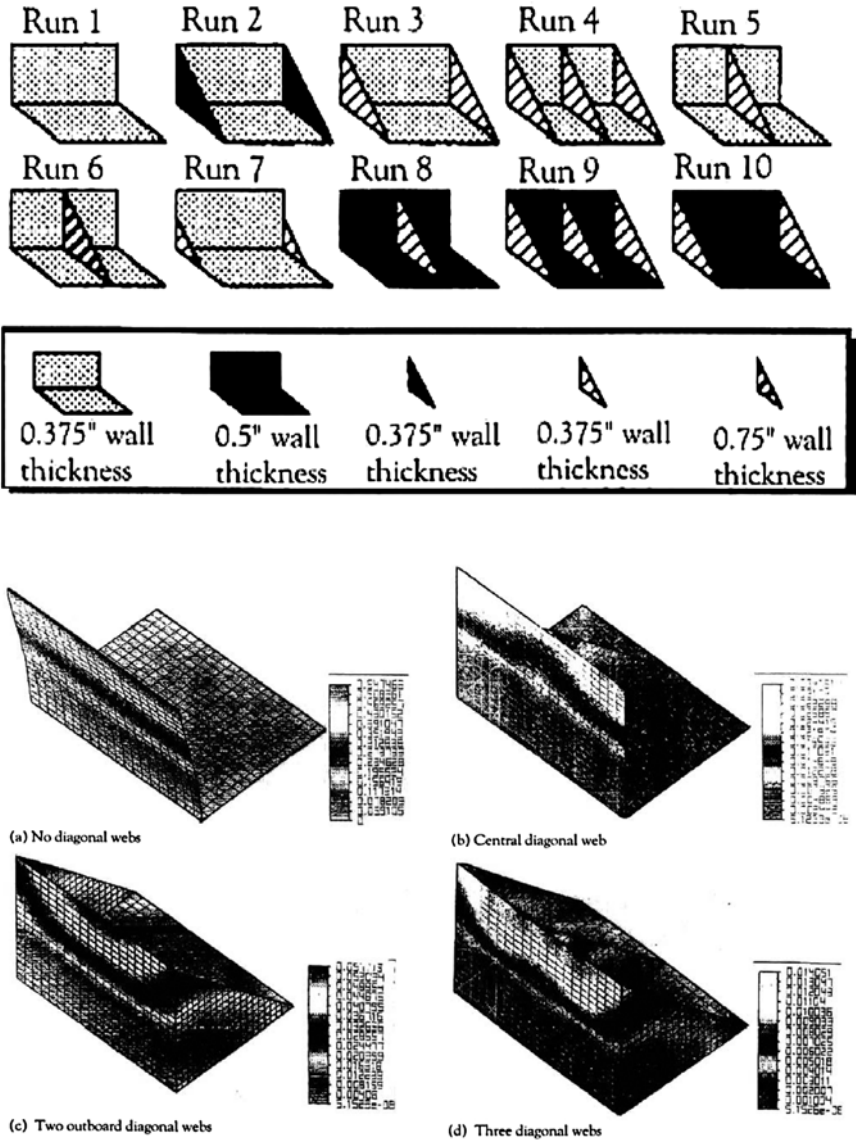
Figure 7-36. A sample of the FE analysis runs used in developing optimum UC design.

ambient room conditions); and (5) quasi-static and full reversed cyclic fatigue behavior of UC *interior* beam-to-column connections. In addition, several coupon tests characterizing both short- and long-term mechanical properties of the UC material were conducted in this program.
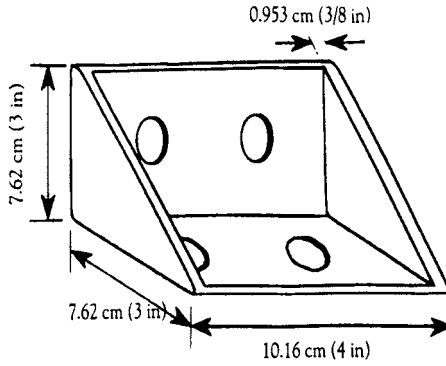
Figure 7-37. Dimensions and geometry of the modified UC.
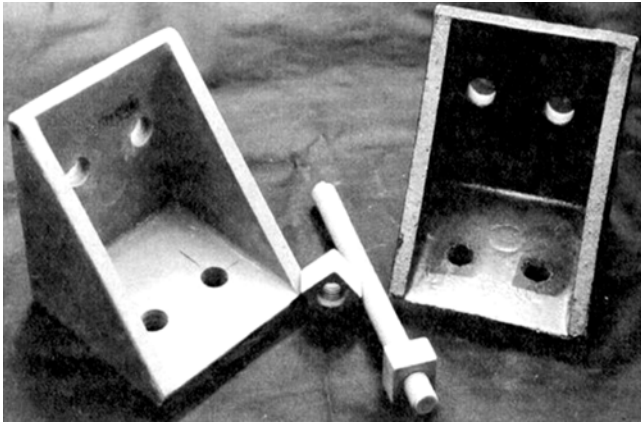
Figure 7-38. The universal connector.

7.5.6 Quasi-Static Behavior of UC Connections

Three types of PFRP exterior beam-to-column connections were tested in this program. All beams and columns were constructed from "off-the-shelf" 4 in. × 4 in. × 1/4 in. (101.6 mm × 101.6 mm × 6.35 mm) PFRP E-glass/vinylester H-profiles manufactured by Bedford Reinforced Plastics, Inc. The connecting elements used for these connections were a combination of the following: high-strength epoxy adhesive (Magnobond 56), 1/2 in. (12.7 mm) pultruded threaded rods and nuts (supplied by Bedford Reinforced Plastics, Inc.), UC No. 4, PFRP 3 in. × 3 in. × 3/8 in. (76.2 mm × 76.2 mm × 9.53 mm) equal-leg unidirectional angles. The objective of testing these connection details was to (1) experimentally determine both the rotational stiffness and the ultimate strength of each connection detail; (2) evaluate the performance of the newly designed and developed
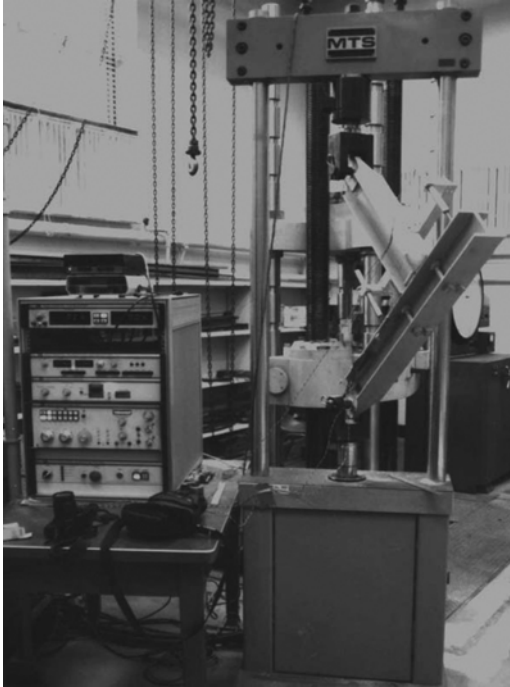
Figure 7-39. Test setup for both quasi-static and cyclic UC exterior frame connections.

prototype of the UC; (3) identify the different failure mechanisms of each connection; and (4) investigate the impact of using high-strength adhesive in both the strength and the stiffness of beam-to-column connections. Figure 7-39 shows the test setup used for the moment–rotation tests. To characterize the rotational stiffness of PFRP connections, two measurements had to be obtained from the test. The first quantity was the applied moment at the connection, and the second quantity was the relative angle of rotation between the beam and the column. Due to the statically determinate nature of the setup, the corner moment at any load (P) could be calculated by knowing the fixed dimension (l). The relative rotation was measured by using two deflection readings, which were measured at two fixed points on the column flange as shown in Fig. 7-40. The deflection readings were measured using a rigid rotational bar fixture that was attached to the flanges of the beam. Details of these calculations can be found in Bank et al. (1992).

Figure 7-41 shows the details of the PFRP beam-to-column connection details tested in this program. The same connection designation system used by Bank et al. (1992) was adopted by Mosallam et al. (1993) to assist the reader in relating and comparing the behavior of each connection and
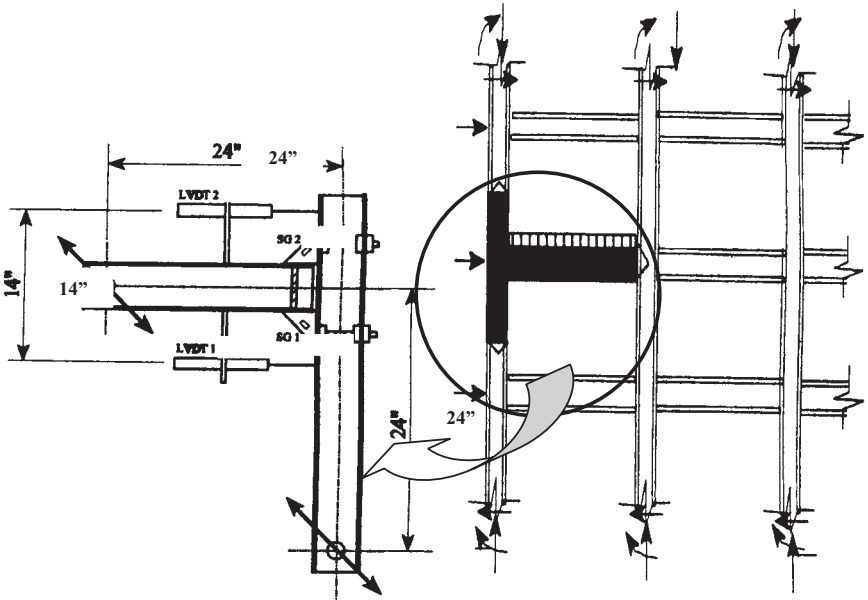
Figure 7-40. Typical geometry, dimensions, and details of the PFRP exterior frame connection specimens.

to add continuity to the research subject. Accordingly, the three PFRP connections developed in this study were designated as Types v, vi, and vii. The design of the three connections included PFRP threaded rod stiffeners.

As discussed earlier, the addition of these threaded rod stiffeners is recommended to prevent the premature separation of the web and flanges of the PFRP H-sections (this recommendation applies to all open-web PFRP unidirectional profiles). Furthermore, this stiffening technique will ensure the integrity of the three composite plates (the flanges and the web) forming the H-shape. Consequently, an efficient utilization of the PFRP sections will be achieved by both enhancing the stiffness characteristics and increasing the ultimate strength of the connection. Based on past experience, this stiffening detail is strongly recommended at any high tensile stress concentration zones of PFRP open-web, thin-walled structural shapes (e.g., H, I). The locations of high stress concentration are likely found near the connections (maximum shear and maximum negative moments), near the girder mid-span (maximum positive moments), and at the locations of concentrated loads (maximum shear). The need for this stiffening detail is especially important when minimum fiber reinforcement at the web-flange junction is provided (most commercially produced PFRP H-shapes contain negligible fibers in the transverse direction). Unlike connection detail Types vi and vii, no UC element was

Type v
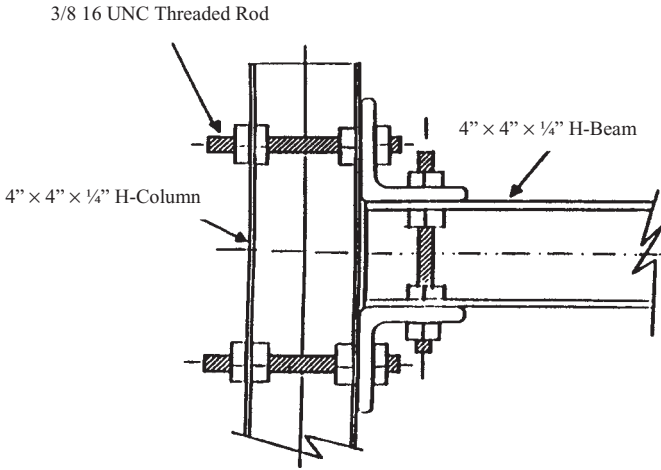
Type vi and vii
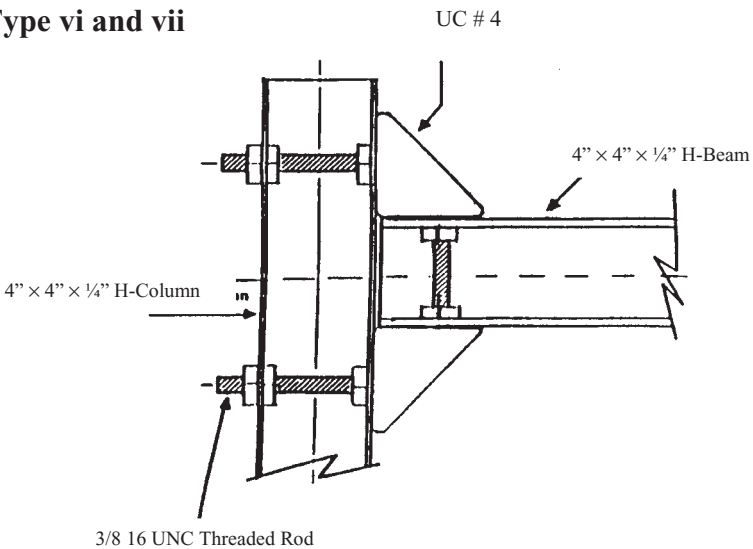
Figure 7-41. Details of the PFRP exterior frame connection, Types v, vi, and vii. Source: Mosallam et al. (1993).

employed in connection detail Type v. Instead, two PFRP unidirectional angles [3 in. × 3 in. × 3/8 in. (76.2 mm × 76.2 mm × 9.53 mm)] were placed at both the top and the bottom of the beam. The connection was stiffened by PFRP threaded rods and FRP molded nuts.

To investigate the effect of using adhesive in the overall performance of the connection, connection detail Type vii was designed. This connection has the same details as connection Type vi except for the addition of
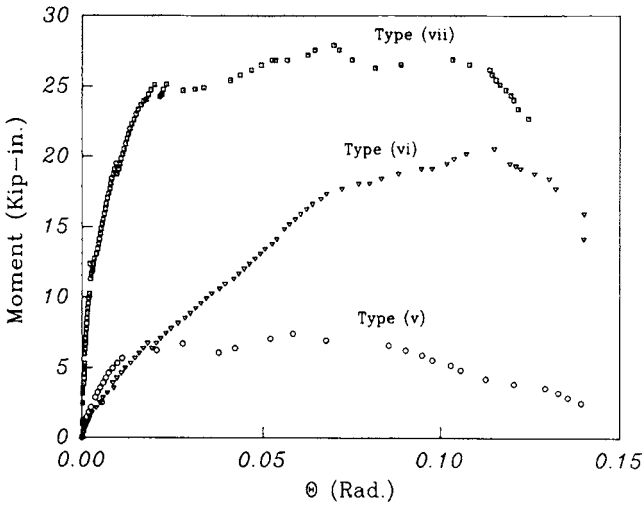
Figure 7-42. Experimental moment–rotation curves for the three PFRP exterior frame connections, Types v, vi, and vii.

thin films of high-strength epoxy adhesive (Magnobond 56 supplied by Bedford Reinforced Plastics, Inc.) between the contacting surfaces between the UCs and both the beam and the column. A torque of approximately 30 ft-lb (40.67 N-m) was applied to all bolts of the three connections. The experimental moment–rotation (M/Θ) curves of the three connection details are shown in Fig. 7-42. A linearized version of these curves is shown in Fig. 7-43. In this section, detailed descriptions and evaluations of different test results are presented.

7.5.6.1 Type v.   The initial behavior of the connection was linear and this linearity was continued until the occurrence of the local failure at the top clip angle. The through-the-thickness cracks and the delimitation failure mode of the top clamp angle were expected and were unavoidable. The origin of this failure is generally associated with three factors: (1) the tensile flexural stresses which are mainly carried by the matrix (fibers are running in the wrong direction); (2) a large radial tensile stress occurred generally at the curved corner of the PFRP clip angle; and (3) the low through-the-thickness strength of the commercially produced PFRP sections (Mosallam and Bank 1992). The ultimate failure mode of this connection was due to a combination of radial stress delimitation and the nuts punching through the thickness of the PFRP top angle. No catastrophic failure occurred.

7.5.6.2 Type vi.   In general, the behavior of this connection exhibited little nonlinearity up to the ultimate moment capacity (refer to Fig. 7-42).
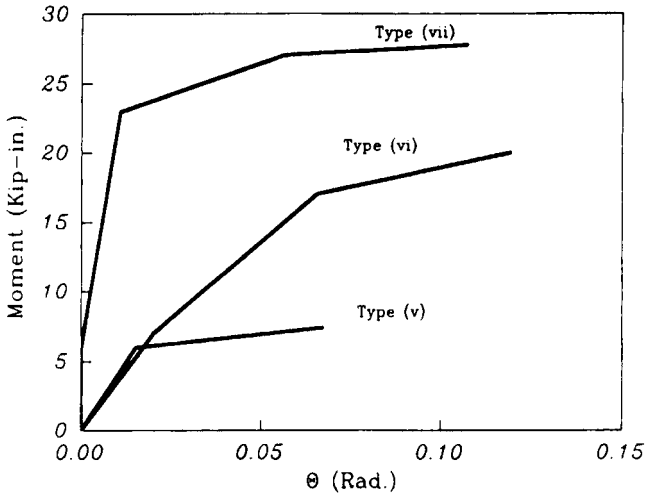
Figure 7-43. Linearized moment–rotation curves for the three PFRP exterior frame connections, Types v, vi, and vii.

The failure of this connection was very gradual and was in the form of punching shear by the nuts at the column-side. Generally, the square shape of the FRP nuts is undesirable and has always been a contributing factor in the punching shear failure mode due to the stress concentration at the sharp corners. As noted in Chapter 6, proper selection of washers may alleviate the problem and minimize damage but a hexagonal nut would also represent an improvement. No failure occurred in the PFRP threaded rods. However, hair cracks were formed at the left nut of the topside of the beam. When the ultimate strength of the top UC was reached, the majority of the load was carried by the bottom UC. An appreciable loss in the connection stiffness was observed at this point. Following this moment transfer, the connection stiffness was provided by the bottom UC and the M/θ curve became similar to the connection detail reported by Zahr et al. (1993). The moment–rotation curve in Fig. 7-42 shows the near-linear behavior of the connection up to 18 kip-in. (2 kN-m) (about 80% of the connection ultimate flexural capacity). The large deformation due to the failure of the top UC can also be inferred from the loss of stiffness (decrease in the slope of M/θ curve) until the ultimate moment. No catastrophic failure occurred.

7.5.6.3 Type vii.   Both the stiffness and the strength of this connection were improved compared to the other two connection details. A "complete fixity" (rigid assumption) was achieved up to a moment of approximately 5 kip-in. (0.56 kN-m) (20% of the ultimate moment

capacity). In this regard, both the beam and column rotated rigidly with no, or with negligible, relative rotation. Although the shape and the characteristics of the M/θ curve for this connection were similar to Type vi, an appreciable increase in both stiffness and strength was achieved. The first failure occurred in the adhesive at the right side of the interface of the top UC and the column. This local failure occurred at a moment of approximately 6 kip-in. (0.68 kN-m). Following this localized failure, the connection behavior continued to be linear until the connection reached its ultimate moment capacity (Fig. 7-42). A similar "nut-punching" failure mode gradually took place at the bolt-line of the column top side. At this stage, noticeable loss in the flexural stiffness was observed due to the local damage of the bottom UC. The ultimate failure for this connection detail was similar to the failure of the Type vi connection.

7.5.6.4 Analysis. Careful analysis of the three moment–rotation curves shown in Fig. 7-42 reveals the following facts: (1) the behavior of the three connections was "near-linear" up to about 80% of the ultimate moment capacity; (2) a premature failure of connection Type v was due to the duplicating metallic connection detail; (3) the use of the UC improved greatly both the overall stiffness and the ultimate flexural strength of the two UC connections (Types vi and vii); and (4) a complete fixity was achieved in the initial loading history of connection Type vii by using a combination of bolts and high-strength epoxy adhesive.

For analysis and design purposes, the M/θ relationships of the three connections are expressed by the following polynomial equations, which describe the full M/θ history of each connection detail. These expressions are essential for performing nonlinear/semi-rigid analysis of PFRP frame structures (Mosallam 1990).

Type v:
$$M_v = 0.22 + 875\ \theta - 5 \times 10^4\ \theta^2 + 1.4 \times 10^6\ \theta^3$$
$$- 2.15 \times 10^7\ \theta^4 + 1.93 \times 10^8\ \theta^5 - 1.03 \times 10^9\ \theta^6$$
$$+ 3.19 \times 10^9\ \theta^7 - 5.32 \times 10^9\ \theta^8 + 3.70 \times 10^9\ \theta^9 \qquad (7\text{-}5)$$

Type vi:
$$M_{vi} = 0.23 + 466\ \theta + 10^3\ \theta^2 - 10^6\ \theta^3$$
$$+ 4.7 \times 10^7\ \theta^4 - 1.00 \times 10^9\ \theta^5 + 1.15 \times 10^{10}\ \theta^6$$
$$- 7.36 \times 10^{10}\ \theta^7 + 2.50 \times 10^{11}\ \theta^8 - 3.42 \times 10^{11}\ \theta^9 \qquad (7\text{-}6)$$

Type vii:
$$M_{vii} = 2.65 + 4.0 \times 10^3\ \theta - 4.1 \times 10^5\ \theta^2 + 2.55 \times 10^7\ \theta^3$$
$$- 9.42 \times 10^8\ \theta^4 + 2.08 \times 10^{10}\ \theta^5 - 2.75 \times 10^{11}\ \theta^6$$
$$+ 2.15 \times 10^{12}\ \theta^7 - 9.13 \times 10^{12}\ \theta^8 + 1.62 \times 10^{13}\ \theta^9 \qquad (7\text{-}7)$$

For simplified design purposes, linearized forms of these equations are presented in Table 7-6.

In addition, the following experimental information is important for the structural engineer in the design and the selection process of PFRP frame connection details: (1) the ultimate capacity of the connection; and (2) the service and the ultimate deformation of the connection. This rotational information can be obtained using both the average rotational stiffness (K_a) and the ultimate angle of rotation (θ_{ult}). For moderate loading conditions, an initial rotational stiffness (k_i) can be used (Gerstle 1985; Mosallam 1990). This essential design information is presented in Table 7-7. From these data, one can see the tremendous improvement in both
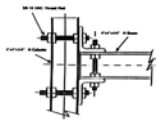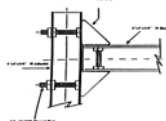
Table 7-6. Linearized Expressions for Connections
Details Types v, vi, and vii[a]

Connection	$\Theta = f(M)$	
Type v	$\Theta = -10^{-3} \times 10^{-3}M$	$(0 < M < 6)$
	$\Theta = -192.0 \times 10^{-3} + 35 \times 10^{-3}\ M$	$(6.0 \leq M < 7.4)$
Type vi	$\Theta = 2.85 \times 10^{-3}\ M$	$(0 < M < 7.0)$
	$\Theta = -1.271 \times 10^{-2} + 0.46 \times 10^{-2}\ M$	$(7 \leq M < 17)$
	$\Theta = -21.43 \times 10^{-2} + 1.667 \times 10^{-2}\ M$	$(17 \leq M < 20.5)$
Type vii	$\Theta = 0$ (no rotation)	$(0 < M < 6.0)$
	$\Theta = -3.0963 \times 10^{-3} + 0.6024 \times 10^{-3}\ M$	$(6.0 \leq M < 23.0)$
	$\Theta = -267.96 \times 10^{-3} + 12 \times 10^{-3}\ M$	$(23.0 \leq M < 27.0)$
	$\Theta = -1780 \times 10^{-3} + 68 \times 10^{-3}\ M$	$(27.0 \leq M < 28.0)$

[a]1 kN-m/rad = 0.112 kip-in./rad.
Source: Mosallam et al. (1993).

Table 7-7. Connection Flexural Design Data

Connection Type	K_e (kip-in./rad)	K_f (kip-in./rad)	$M_{ult.}$ (kip-in.)	$\Theta_{ult.}$ (rad)	Connection Detail
Type v	970.00	620.00	7.4	0.1380	
Type vi	737.00	600.00	20.5	0.1400	
Type vii	23,570.00	2500	28.0	0.1247	

Source: Mosallam (1993d).

the stiffness and the ultimate strength of connection Type vii. An increase in the ultimate moment capacity of *up to 300%* over the corresponding capacity of connection Type v was achieved. In addition, an increase of about 40% in connection strength was achieved compared to the strength of connection of Type vi. The average stiffness of connection Type vii was approximately *25 times* the average stiffness of the other connections. This is attributed to the use of both the UC stiffened detail and the application of the high-strength epoxy adhesive. Test results also showed that the maximum rotational deformations for the three connections were in the same range (0.14 rad). Unlike the Type v and vi connections, connection detail Type vii demonstrated exceptional performance and exhibited a desirable failure behavior which provided enough warning before the total collapse of the joint. Unlike connection Type iv reported by Bank et al. (1992), tremendous gain in the area under the curve was achieved. This proves the energy absorption capability of the connection and also demonstrates that the gain in the flexural strength of UC connections was not at the expense of the ductility and connection safety.

Based on the experimental M/Θ results, a "fixed" or "rigid" assumption for PFRP frame analysis is valid and can be utilized for structures with connection detail Type vii. However, this assumption has its limitations and is only recommended *if a factor of safety of 4 or more* is used. The proposed connection factor of safety (*SF*) is given by:

$$SF = \frac{M_u}{M_n} \tag{7-8}$$

where M_u = the ultimate flexural capacity of the connection, and M_n = the nominal design moment. To use the full range of the flexural capacity of the connection (*SF* = 1.0), semi-rigid analysis is recommended to achieve a cost-effective design of PFRP frame structures. Another reason for recommending the semi-rigid model in designing PFRP frame structures is because the major part of the connection initial rigidity depends, to a large extent, on the quality and reliability of the adhesive. However, the application, curing, and quality inspection of the adhesive are difficult tasks to achieve and control at the construction site.

Based on experimental observations, and to satisfy the deflection limitation of 1/250 of the beam span, a relative rotation of 0.013 rad was proposed as a serviceability limit if the partial safety factor is taken to be 1.0.

7.5.7 Cyclic Behavior of Exterior Universal Connector PFRP Connections

The objectives of these tests were to (1) identify both the rotational stiffness and strength of each connection under cyclic loading; (2) identify

the connection failure modes under cyclic loading and compare these modes to those observed from the quasi-static tests performed in previous studies; (3) evaluate the performance of the modified molded connectors under low cycle fatigue conditions; and finally, (4) to investigate the impact of using high-strength epoxy adhesives (in combination with pultruded threaded rods and molded nuts) on strength, stiffness, and ductility of these connections as compared to bolted-only connection details.

In performing experimental work on the seismic performance of frame connections, progressively increasing cyclically reversing loads are applied. In earthquake situations, the rate at which such loadings occur on individual members is relatively slow, and, for this reason, it is possible to perform experiments by subjecting the connection specimen to a slow cyclically reversing force or displacement.

Figure 7-44 shows the loading history that was used for these connections. This loading history was selected to simulate the behavior of these connections under cyclic loading due to an earthquake and associated aftershocks. However, the results of this study may be different under a different cyclic loading history. The loading history consisted of 36 cycle groups. Each cycle group, represented in Fig. 7-44 as one compressed cycle, represents five cycles with the same amplitude. The relative rotation was gradually increased for the first six cycle groups (total of 30 cycles). The load was decreased for the next three cycle groups (7, 8, and 9). The load was gradually increased again for eight cycle groups (total of 40 cycles) up to cycle group 17 with amplitude of 0.04 rad. The maximum amplitude was achieved at cycle group 36 (total number of cycles = 180)
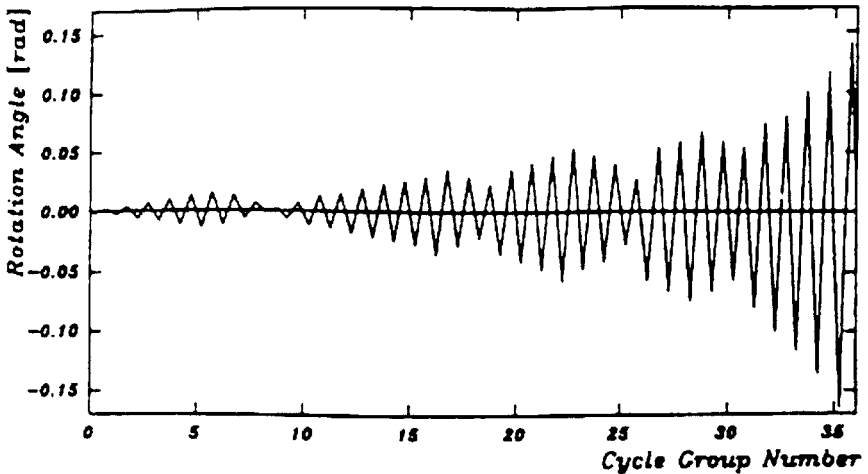
Figure 7-44. Loading history selected to simulate the behavior of exterior UC PFRP connections under cyclic loading due to an earthquake and associated aftershocks.

with maximum rotation value of about 0.16 rad. For all specimens, the test was conducted under displacement control, that is, over the course of the five cycles, the rotation angle (Θ) was held at a certain value. Reverse cyclic displacements were applied to each connection detail. The shape of the loading signal was selected to be a negative sine wave (i.e., compression first, then tension). The loading frequency for all tests was 0.1 Hz. Load, rotation angle (Θ), and strain data were measured continuously throughout the experiment. For each test—a total of 36 cycle groups—each five cycles were investigated (refer to Figure 7-44). Cycle groups 23, 27, 31, and 35 were selected for more detailed evaluation, to be discussed later in this section.

For the bolted-only specimen (BO), the connection failed due to fatigue loading in a brittle manner. The main cause of the sudden failure of the threaded rods was the excessive decrease in the cross section (about 30%) of the rod due to the failure of the outermost glass fibers because of the cyclic bending load with superimposed tension. Figure 7-45 shows a close-up photograph of one of the failed rods. From this figure, one can see the fiber degradation of the threaded rod and the reduction of the effective cross section of the composite bolt. The figure shows also the shaved thread mode of failure, as described earlier.

For the combined bolted/adhesive specimen (BA), the first crack in the adhesive material was clearly visible at cycle group 5 (after 25 cycles). The crack line started from the edge of the H-beam top flange. As the load increased, hair cracks were observed at the corner of the UC as well as at the bolts. For the BO connection specimen, similar behavior was observed. However, in specimen BA higher relative moments were measured compared to specimen BO, especially at the early stage of the test. A major
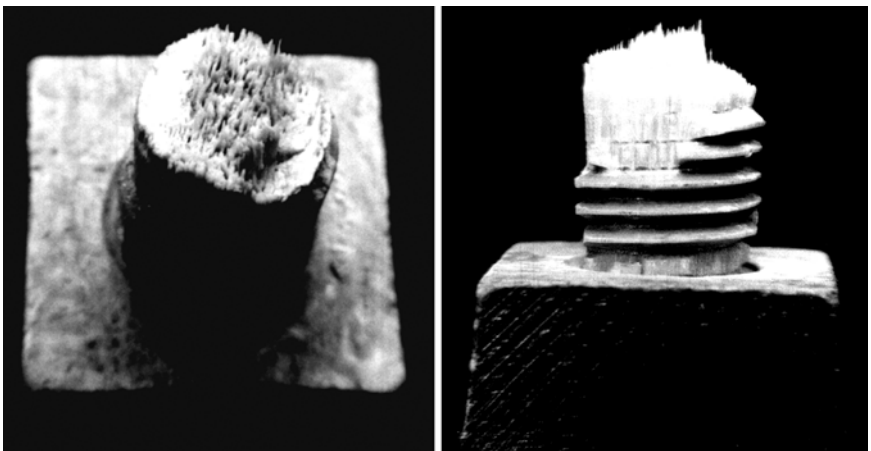
Figure 7-45. Close-ups of the typical failure modes of composite threaded rods.

failure of the adhesives occurred at around cycle group 14 (±0.022 rad amplitude). At this stage, the UC was no longer bonded by the adhesive to either the column or the beam flanges. However, the stiffness was still relatively higher than that for specimen BO. As the experiment progressed, and after the failure of the adhesive of specimen BA, the behavior of the two specimens became increasingly similar such that both specimens began to exhibit similar lower rotational stiffness. Starting with cycle group 31, the connection behaved merely as a bolted-only with an average rotational stiffness of 250 kip-in./rad (28.24 kN-m/rad) for both specimens (the experimental cyclic results are summarized in Table 7-8). The major local failure of the threaded rod/nut system occurred at cycle group 35 (same as for specimen BO). At this stage, both bolts connecting the lower UC to the beam section failed in a flexural fatigue failure mode. As a result, the rotational stiffness was decreased, especially in compression; hence, the connection moment capacity dropped dramatically.

Figure 7-46 shows the moment–rotation hysteresis for the three cycle groups, 23, 27, and 31, for both specimens. From this graph, one can see that these three cycle groups had the same amplitude of ±0.07 rad. The response of the two specimens on cycle groups 23 and 27 was not very different, and in the case of specimen BO it was even identical. This indicates that the two specimens were not significantly damaged in-between these cycle groups. Cycle group 31, however, showed an obvious loss in stiffness coupled with relative strength degradation. The apparent damages under the repeated load increased gradually. This happened in the form of hair cracks at the UC and progressive failure of the adhesive, progressive shaving of the rods, and progress of the cracks in the rods. The maximum moment was achieved at cycle group 23 for specimen BA and at cycle group 35 for specimen BO (Table 7-8). For the BA specimen, and following the major local failure of the threaded rods, the maximum moment resisted in compression was less than 50%, and the moment in tension was about 10%, compared to the moment before the local failure occurred. This behavior is seen in Figure 7-47, where a large drop in the rotational stiffness is shown.

The rotational stiffness dropped from 185 kip-in./rad (20.9 kN-m/rad) to approximately 155 kip-in./rad (17.51 kN-m/rad). This allowed the beam to rotate relative to the column by a large angle under lower moment. As the thread shaving progressed, the nuts moved about 1/8 in. This slip was blocked because the shaved material filled the undamaged threads. This made it harder for the composite nut to move farther. At this stage, the threaded rods were under reversal bending and the outer fibers of these rods began to fail progressively. This continued until the remaining cross section of the threaded rod was insufficient to carry the applied cyclic load. Another interesting mode of local failure was also observed: the appearance of delamination hair cracks in the composite nuts. *The behavior*

Table 7-8. Summary of Experimental Cyclic Results[a]

		Bolted Only					Bolted with Adhesive				
		Max. Moment (kip-in.)		k (kip-in./ rad)	Max. Strain (%)		Max. Moment (kip-in.)		k (kip-in./ rad)	Max. Strain (%)	
Cycle Group	θ (rad)	Tension	Compression		Tension	Compression	Tension	Compression		Tension	Compression
2	±0.004	2.61	−2.2	430	0.08	−0.16	6.30	−6.4	2200	0.26	−0.26
23	±0.07	22.08	−23.41	320	0.49	−0.61	29.38	−33.48	580	0.85	−1.13
27	±0.07	20.88	−22.60	260	0.52	−0.7	26.8	−30.90	470	0.51	−1.45
31	±0.07	16.36	−18.40	220	0.86	−1.01	18.77	−20.59	260	0.14	−1.65
35 Before Failure	±0.14	23.93	−27.64	180	1.03	−1.22	27.34	−30.41	190	0.4	−1.86
35 After Failure	±0.14	2.33	−12.54	150	—	−1.10	3.10	−13.21	160	—	−1.56

[a]1 kN-m/rad = 0.112 kip-in./rad.
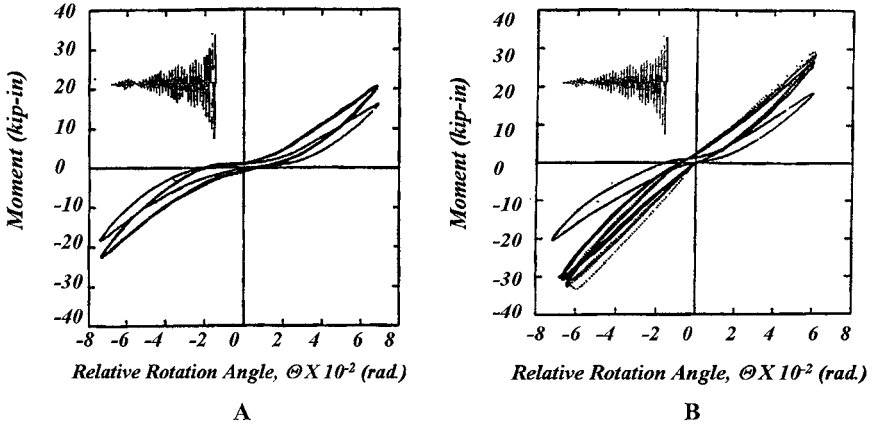
Figure 7-46. Hysteresis curves for specimens BO (A) and BA (B) at cycle groups 23, 27, and 31.
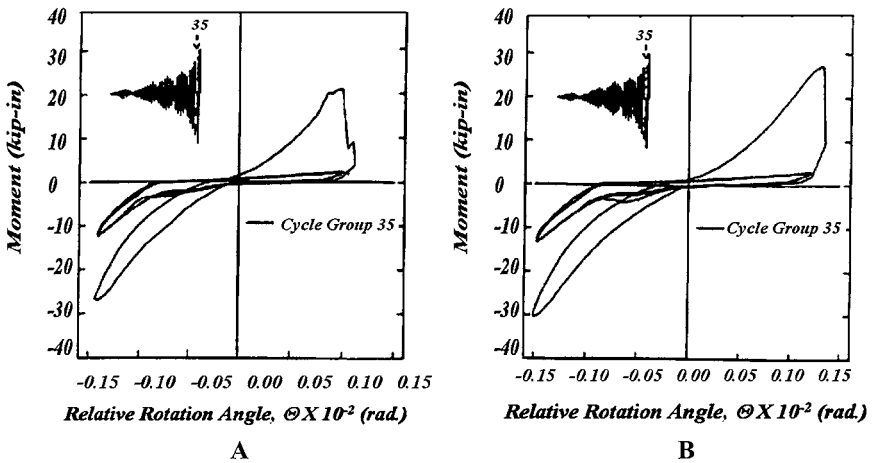
Figure 7-47. Hysteresis curves for BO (A) and BA (B) at cycle group 35.

of the pultruded composite threaded rods and molded nut system requires more in-depth evaluation. For this reason, additional experimental studies are required to investigate other possible modes of failure by changing the geometry and locations of the threaded rods as well as the loading history.

There are two types of commercially produced threaded rods, and both have major design problems. The first type of these composite rods is made of smooth pultruded rods and the threads are cut similar to steel threaded bolts. In this case, the longitudinal fibers are damaged with the depth of the thread and become discontinuous. The other commercially produced composite threaded rods are composed of smooth pultruded

rods, and the threads are made from another material that is molded on the outer skin of the smooth pultruded composite rod. The latter type was used in this experiment. For this reason, it was expected to see the thread-shaving mode of failure due to the lack of bond and homogeneity of the rod core and the outer threaded shell. This is also the main reason for the limited torque that could be applied to the tested bolted joints. The "maximum safe" torque (T_{max}) recommended by the manufacturer for this size was applied to all bolts [T_{max} = 15 lb-ft (20.3 N-m)]. According to the manufacturer, the 1/2 in. (12.7 mm)-diameter bolts used in this program have ultimate thread shear strength of 4,000 lb/in (700 N/mm) of thread engagement. The maximum design tensile load these rods is 2,000 lb (8.9 kN), and the compression and flexural strength values are 55 ksi (379 MPa) and 60 ksi (413 MPa), respectively.

Cyclic test results indicate that the PFRP connections exhibited ductile failure and that enough warnings were given before the ultimate failure of connection. In all cases, the major local failure occurred at the lower UC. Hence, since the upper UC was still able to carry load, local failure occurred but the structure was still capable of carrying the load. The test results also indicate that the combined (bolted with adhesive) connection had a relatively higher initial stiffness. This was valid until the epoxy adhesive has failed. A common mode of failure was observed for both bolted and bolted/adhesive connections. This was in the form of threaded rods bending fatigue failure. The inefficient design of commercially produced threaded rods was identified through the "shaving" failure mode of the threaded shell.

The design of a composite element or structure must not be a copy of a steel structure. The properties are too different and, to develop more efficient designs, the anisotropic material properties must be considered. One must "think composites" to come up with a proper connection design. It should be noted that these results were obtained from only four specimens with specific details and loading history. A larger number of specimens are required to confirm these results.

7.5.8 UC/PFRP Connection Response under Sustained Loads (Creep Tests)

Due to the viscoelastic nature of pultruded polymer composites, it is essential to evaluate the effect of the long-term loading of composite connections. Several studies have been conducted on the creep behavior of PFRP structures. Results of comprehensive experimental and theoretical study on creep behavior of PFRP portal frames were reported by Mosallam (1990) (refer to Fig. 7-48). A detailed review on this subject can be found in Mosallam and Chambers (1995). Connection creep is a function of time and temperature, connection configuration, stress level, orientation of the composite adherend, and types of adhesive.
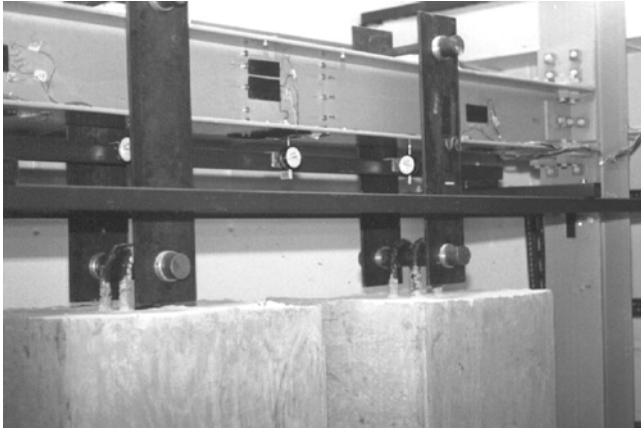
Figure 7-48. 10,000-hour full-scale creep test of a PFRP composite portal frame with semi-rigid connection details (Type i).
Source: Mosallam (1990).

As mentioned earlier, no experimental information on the creep behavior of pultruded frame connections is available. To model and include rotational creep effects, full-scale creep tests are required to precisely predict the actual behavior of each class of composite connections. For this reason, Mosallam (1995b) undertook an experimental program related to creep, which involved testing several adhesively bonded and bolted coupon specimens, as well as a bolted-only full-scale connection specimen that was subjected to a sustained load. The creep specimen was identical to those used in previously described cyclic studies. Accordingly, the test fixture and instrumentation was the same as that shown in Figs. 7-41 and 7-49, which was used in those programs. The connection specimen was tested under ambient environmental conditions. The average temperature was 75 °F (23.8 °C), and the average relative humidity was 73%. The specimen was instrumented with six 120 Ω electrical strain gages. M-coating coated all strain gages for environmental protection, and strain gages were connected to a strain indicator and switch box system. For the static and cyclic test specimens, the relative rotation angle (θ) was measured using two deflection creep readings. All readings were taken manually. Both rotational and strain readings were taken every hour for the first few hours, and twice a day thereafter. Both temperature and humidity were recorded at each reading. Creep data up to 1,400 h were reported. The load was applied at the two ends using a special 20,000-lb (88,964 N)-capacity lever arm creep tester (refer to Fig. 7-49).

Unlike the static loading compression mode, the creep test was in the tension mode (the lower UC was in tension). The sustained moment was taken as 0.33 M_u [10.18 kip-in. (1.15 kN-m)]. This load level was considered to be the working moment for this particular connection detail

Figure 7-49. PFRP connection creep test setup.
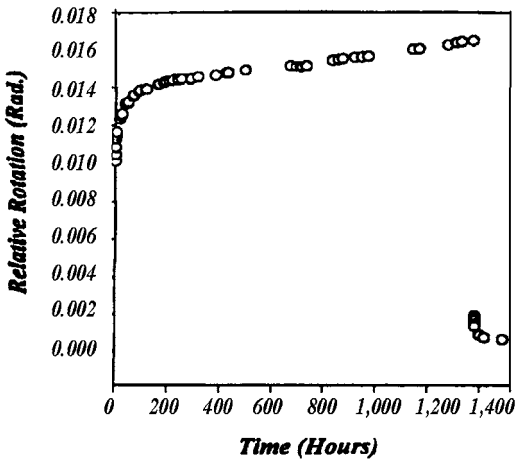
Figure 7-50. Rotation angle (Θ) vs. time (creep and recovery).

[M_u = 30 kip-in. (3.39 kN-m)]. The creep data were recorded for compression and tension strains at different locations. In addition, the relative rotation angle (Θ) creep was also recorded as described earlier. Figure 7-50 shows the rotational creep and recovery curves of the bolted-only connection specimen. Upon loading, the instantaneous rotation angle (Θ) of

0.0098 rad was observed. After a continuous loading for 420 h, the rotational angle reading was 0.0143 rad, an increase of about 46%. After 1,400 h of loading ($\cong$2 months), the relative rotation had increased to about 0.0165 rad. This increase represented about a 70% loss in the initial rotational stiffness of the connection. This loss can be attributed to the creep of the pultruded sections and the relaxation of the composite threaded rods and nuts. The load was carefully removed after 1,400 h. The instantaneous relative rotational angle (Θ) at the unloading dropped to about 0.002 rad. This represented a recovery of about 80%. The recovery process (delayed elasticity) continued and the original rotational stiffness was recovered at about 200 h after unloading (refer to Fig. 7-50). From this figure, one can see that a significant portion of the creep occurred during the first 200 hours (Mosallam 1990). Upon loading, the instantaneous rotation angle was 0.0098 rad. The rotation after 420 h was 0.0143 rad. Therefore, the net rotation was 0.0045 rad., a 46% increase. This indicates that the connection creep could be significant and must be considered in the design of any PFRP frame structure.

Figure 7-51 shows the strain creep of the top UC (compression). The instantaneous compression creep was 340 microstrain. The compression strain after 420 h of loading was increased slightly (422 microstrain). This was expected for compression creep. Similar experimental results were reported earlier by Mosallam (1990).

A simplified protocol to include the creep deflection of pultruded composites is presented in the ASCE *Structural Plastics Design Manual* (ASCE 1984) using linear viscoelastic modulus. This expression is derived from a linear form of Findley's power law. The usefulness of this viscoelastic modulus was validated through a 10,000-h full-scale test conducted by Mosallam in 1990. To include the long-term deformation of polymeric
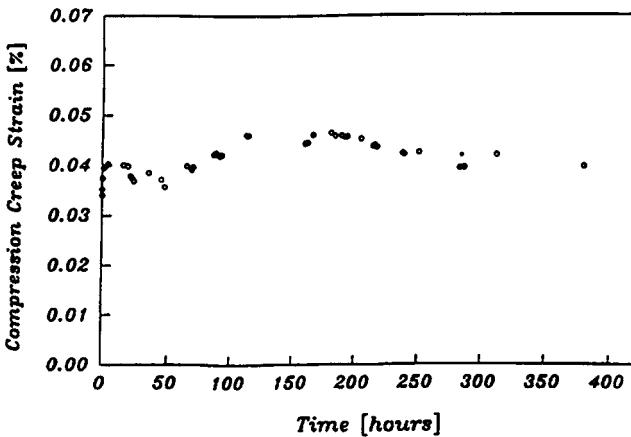
Figure 7-51. Compression strain creep curve.

composite connections, the following simple linear viscoelastic modulus expression (K_v) was proposed by Mosallam (1997a):

$$K_v = \frac{K_o K_t}{K_t + K_o (t/t_o)^{n_k}} \qquad (7\text{-}9)$$

where
$K_o = M_o/\Theta$
$K_t = M/m_k$
t = unit time (hours)
M = applied moment
n_k = material-dependent rotational creep parameter
m_k = stress-dependent creep parameter.

The two creep coefficients can be determined experimentally for different stress levels by plotting the creep curves on a log-log scale, as shown in Fig. 7-52.

The creep test results also indicated that the connection's rotational creep cannot be ignored. For example, in a period of 1,400 h, the rotational stiffness dropped more than 70% from the initial stiffness. This will affect the moment capacity, end restraint modeling, and stress distribution of any frame structure built from this pultruded composite material. Subsequently, the creep behavior can affect the stability, long-term deflection, and, ultimately, the failure mode of frame structures, especially when higher moments are applied. More in-depth studies in this area are essential in order to understand the long-term behavior of such connections when subjected to higher stress levels that may lead to a catastrophic failure due to creep rupture.
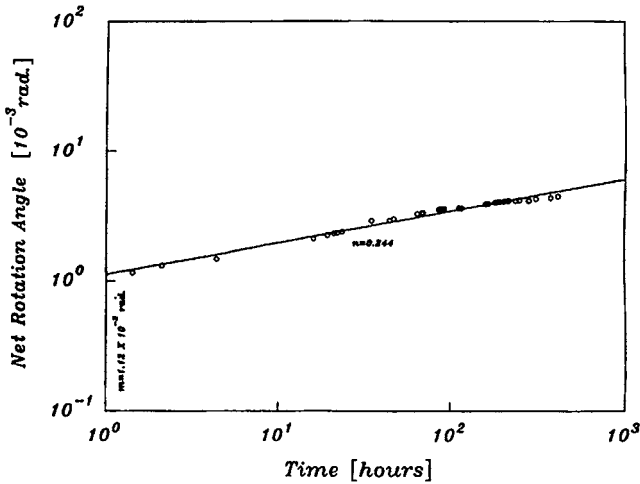
Figure 7-52. Determination of creep parameters m_k and n_k.

7.5.9 Vibration and Damping Evaluation of UC/PFRP Frame Connections

In 1993, Mosallam et al. (1993) conducted a pilot study on characterizing the dynamic and damping behavior of both bolted and combined (bolted/bonded) PFRP frame connections utilizing the UC as the principal connecting element. The study consisted of three parts, including (1) coupon-level dynamic characterization, (2) member-level dynamic characterization, and (3) connection-level dynamic characterization.

Two types of beam-to-column pultruded frame connections were evaluated (designated as Type vi and Type vii in the quasi-static evaluation program described earlier). The beam and the column sections for the two connections were identical to those tested in the quasi-static, cyclic, and creep programs described earlier [4 in. × 4 in. × 1/4 in. (101.6 mm × 101.6 mm × 6.35 mm] H-sections with UC No. 4. Both bolted and bolted/bonded beam-to-column connections (Types vi, vii) were tested to investigate the effect of using the high-strength adhesive on the dynamic performance of PFRP frame joints. The connections were attached from the column end to a steel fixture which was mounted on heavy steel plates using steel threaded rods and nuts. The beam side acted as a cantilever from the column, as shown in Fig. 7-53.

A vibration exciter was used to apply a sine-sweep force to the free end of the beam. The vibration was monitored by piezoelectric accelerometers positioned at points spaced evenly at a distance of 3 in. along the axes of both the beam and column. At the coupon level, coupons from the webs and flanges of pultruded profiles identical to those used in building the connection specimens were analyzed. For the web coupons, the results of
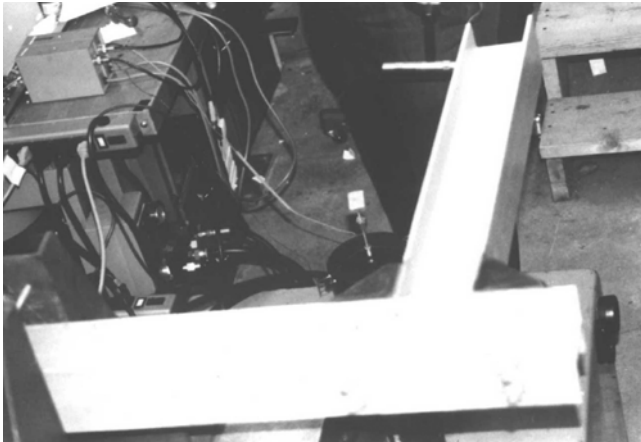
Figure 7-53. Experimental setup for vibrations tests.
Source: Mosallam et al. (1993).

circle fitting (Ewins 1989) indicated that the first and the second resonance of x/f were 27.73 and 174.2 Hz, respectively, with a modal loss factor of 1.8%. For the flange coupon, the experimental frequency values of the first and second bending modes were 25.56, and 167.2 Hz, respectively. The corresponding modal damping coefficient was in the same range of 1.8% as for the web coupon specimens. Results from the two coupon tests showed little variation in the mechanical properties of both the flange and web of pultruded shapes.

At the member level, PFRP profiles identical to those used in building the connection specimens were analyzed. Analysis of the data was focused on two bands of frequency. At the very low frequency range, the characteristics were considered pseudo-static ($1/k_{ij}$, where j is the applied force and i is the resulting displacement). Generally, the pseudo-static characteristics should show a constant receptance line since k_{ij} is independent of frequency. This was not necessarily true, as was seen from the receptance plots. The deviation was attributed to the limited low-frequency performance of the transducers that were used. The second band of the analysis was that of the first resonance. The first natural frequency was derived from a circle fit at the resonance range. When the first natural frequency was considered and was separated from the second frequency (by a factor of one octave), the modal residue of the first mode was used to provide a second estimate of the static characteristics of the material. The circle fit also provided the modal damping, which was in the same range of 1.8% as determined from the coupon tests. The estimated values for the first natural frequencies for both the H-beam and the box-beam were 96 Hz and 57.8 Hz, respectively. Compared to the results obtained from the H-beam test, a relatively lower value for the box-beam loss factor was obtained ($\zeta = 1.5\%$).

At the beam-to-column connection level (Type vi), the first natural frequency resulting from the modal test was 48.8 Hz. The loss factor for this joint was about 4%. Test results showed an increase in the overall damping characteristics of the PFRP frame structure. This increase in damping can be attributed to the friction provided by the PFRP bolts and nuts. Compared to the loss factor of the beam element, the structure's apparent modal damping was doubled (1.8% vs. 4%). The static compliance of the beam-to-column connection was estimated from the low-frequency band to be 1.02×10^{-4} ft-lb (7×10^{-6} N-m). For the bolted/glued beam-to-column connection (Type vii), the first natural frequency occurred at 51.3 Hz. The relatively higher frequency indicates the effect of the high-strength epoxy adhesive on increasing the rotational stiffness of the joint. The corresponding loss factor was 2%. Frequency response functions for the two connections are shown in Fig. 7-54. Prior to each frequency, a very loud acoustical resonance was heard which lasted until the end of the test.
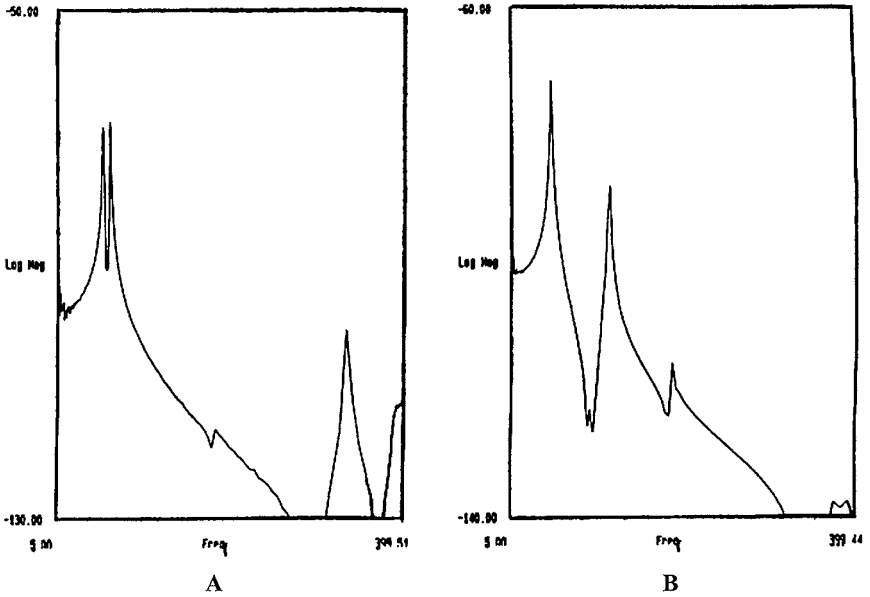
Figure 7-54. Frequency response plots for bolted (A) and combined (B) PFRP beam-to-column frame connections.

Identical sound was noticed for all test specimens, and the loudness was proportional to the size of the specimens.

In the same study (Mosallam et al. 1993), a finite element (FE) model was developed for both web and flange specimens. An ANSYS (1989) *Stiff 99* (composite shell) finite element was selected (refer to Chapter 9 of this manual for more details on appropriate finite elements and methods). This eight-node composite shell element has six degrees of freedom per node. The FE flange model consisted of 24 elements (2×12 elements) with fixed/free boundary conditions. A finite element model of the coupon was generated using the *Stiff 99* elements to calculate the natural frequencies. The first natural frequency obtained from the FE analysis occurred at 26.6 Hz compared to the experimental value of 27.7 Hz. The second natural frequency obtained from the FE analysis was 163 Hz, which was relatively lower than the experimental value of 182.2 Hz. For the flange coupon model, the FE analysis estimated the first mode to be at 26 Hz and the second mode at 163 Hz. From the FE results, it was concluded that the material properties and assumed lay-up of the material were appropriate for modeling both the flange and the web coupons.

An FE model was also developed for a PFRP cantilever H-beam using the same material properties and lay-up used in modeling the coupon specimens. From the FE analysis, a third mode shape occurred at a

frequency of 129 Hz, which corresponds to the experimental value of 96 Hz. The difference between the experimental and FE model results can be attributed to the difficulty in providing a complete fixity to the beam end. The flexibility of the support fixture resulted in a reduction in the measured value of the natural frequency of the PFRP H-beam. Better results from the FE model can be achieved by considering a lumped spring at the steel fixture to account for the relative flexibility of the bolted steel end support.

A similar FE analysis was performed for a cantilever PFRP box-beam. Satisfactory agreement between the FE results and the experimental results was achieved. The first four mode shapes occurred at 60.23, 60.28, 335.20, and 341.80 Hz. It is noted that the modes were repeated due to the symmetry of the cross section of the PFRP square tube. The effect of the relative flexibility of the fixed end was minimum. This was due to the relatively lighter weight of the box beam as compared to the H-profile (the weights of the box-beam and the H-beam were 1.274 lbm/ft (1.9 kg/m) and 2.10 lbm/ft (3.12 kg/m), respectively).

The results of this study confirmed the validity of using both the material properties and the lay-up of the coupons in modeling PFRP beams and frame structures. From the test and FE results, the effect of the relative flexibility of the end support was identified. This relative flexibility resulted in lower values for the measured natural frequencies. This effect was proportional to the weight of the specimen. For example, the FE analysis results for the square box section agreed well with the modal test results. On the other hand, discrepancies between the measured and the predicted results were observed in the case of the relatively heavier H-beam section. As a result, it is recommended that a fixed/free test configuration for coupon and light specimens be used. For larger and heavier specimens, a free/free test configuration is recommended.

An attempt was made to dynamically excite beam-column joints. The results showed that the bolted PFRP beam-to-column connection (Type vi) was relatively flexible compared to the bolted/bonded connection (Type vii). Consequently, the damping capabilities of connection Type vi with friction PFRP threaded rods and nuts only were higher than the connection specimen with both bolts and adhesive. The identical loud noise near the resonance was noticeable and repeatable. Further studies on the acoustical properties of the PFRP sections are needed. A sample of the results obtained from the circle-fitting technique (Ewins 1989) for different specimens along with the corresponding factors are given in Table 7-9.

A similar investigation on characterizing the dynamic response of PFRP connections was performed by Cunha et al. (2008). This study followed the footsteps of an earlier study that was reported by Wong et al. (1996) on steel frame connections. In this study, both experimental and analytical evaluations were presented. In the experimental program,

E-glass/polyester PFRP UTILO 150 × 74.5 × 5.5-mm I-beams, manufactured by Exel Composites of Belgium, were used to construct the beam-column frame connection specimens. The PFRP equal-leg angles used to connect the beam and the column were PFRP UTILO 50 mm × 50 mm × 5 mm. Figure 7-55 shows the details of the connection evaluated in this study, which was similar to connection detail that was initially utilized by Mosallam (1990) and identical to the one reported by Wong et al. (1996)

Table 7-9. Dynamic Tests Summary

Specimen	Frequency (Hz)	Loss Factor (%)
Web	27.73	1.80
Flange	25.56	1.80
Beam	96.00	1.80
Type vi	48.80	4.00
Type vii	51.30	2.00

Source: Ewins (1989).
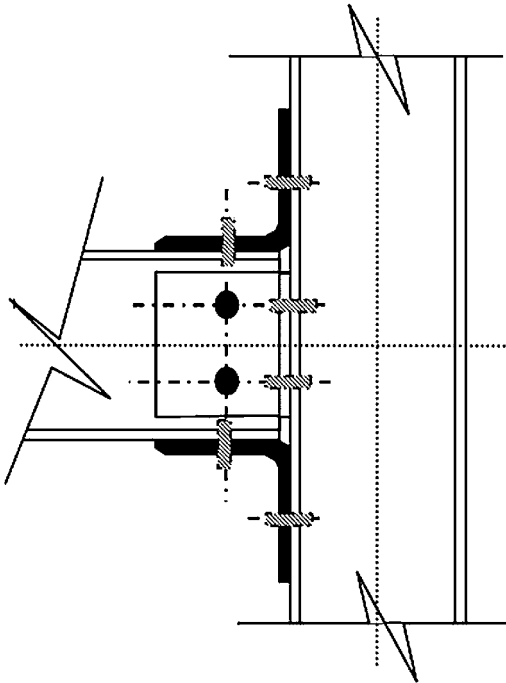
Figure 7-55. Beam-column connection evaluated by Cunha et al. (2008).

for steel frames. Although this research succeeded Mosallam (1990), which confirmed the deficiency of "steel-like" joint detail, the authors still used the deficient "steel-like" joint detail. As indicated by Mosallam (1990), the strength of this connection detail transfers the entire load through the web-flange junction. In the absence of sufficient transfer elements, as described by Mosallam and others in the early 1990s, a premature failure would be unavoidable at the web flange junction, as shown in Fig. 7-56. Also, it is not clear what type of bolts is used, but it is believed that 0.24 in. (6 mm) steel bolts were utilized in all tests. Figure 7-57 illustrates the typical test setup adopted in Cunha et al. (2008).

As indicated in the previously mentioned studies, PFRP connections behave in a semi-rigid fashion and that the source of the flexibility of such connections is not only due to rotational flexibility but also to translational flexibility (shear). However, as compared to the major effect of the rotational flexibility of the connections and its effect on the overall stability, strength, and stiffness of PFRP frame structures, semi-rigid translation should have a minor impact on the overall behavior of PFRP frame structures. This may occur due to a faulty design or detail, material creep, creep and relaxation of bolt threaded rods, or due to oversized bolt holes, which should be avoided. The study also presented results of analytical study on using model updating techniques to evaluate the connection flexibility.

Numerical treatment of the dynamic response of PFRP semi-rigid connections was performed by Harte and McCann (2001). In this study, a
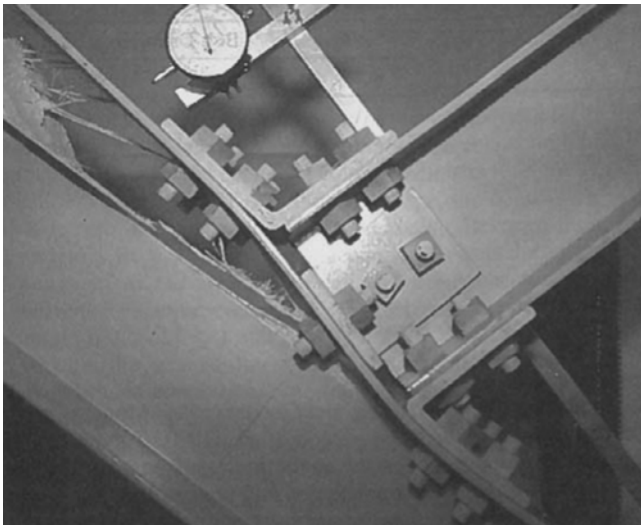
Figure 7-56. Premature failure of PFRP beam-column connections without web-flange transfer elements.
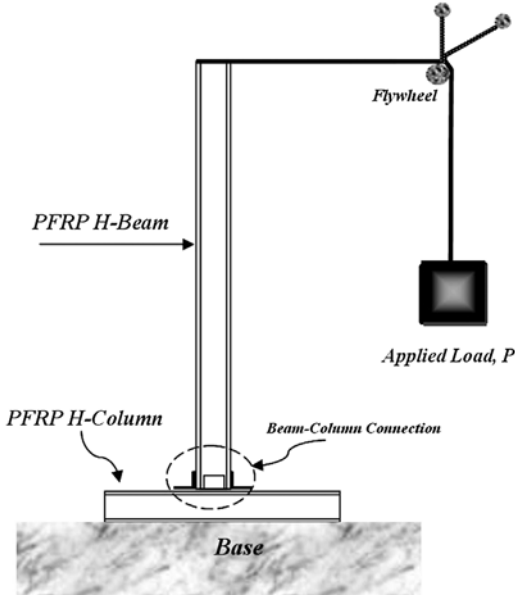
Figure 7-57. *Exterior connection dynamic test setup adopted in Cunha et al. (2008).*

two-dimensional FE model was developed using ANSYS commercial software. Numerical results were compared to the experimental results reported earlier by Turvey and Cooper (1998). From the FE results, one can see that the predicted failure mode does not agree with the typical premature web/flange junction failure that was reported by many researchers (refer to Fig. 7-56).

7.5.10 Mechanically Fastened PFRP Exterior *Flexible* Connections

As an extension of this program, a new flexible "seated" detail of a beam-to-column connection was evaluated (Zahr et al. 1993). Details and test setup of this connection are shown in Figs. 7-58 and 7-59, respectively. The "flexible" connection specimen was tested under a quasi-static loading regime. The failure was due to a large deformation on the top side (tension) of the connection. As expected, and due to the flexible nature of this connection detail, as the load increased, a large horizontal relative rotation between the beam and the column flange was observed (acting as a hinged support as intended). The ultimate failure of the connection was due to a local failure of the web-flange junction at the top of the open-web H-beam (high tensile stress concentration). This mode failure provides additional evidence of the importance of using reinforcing details such as a threaded rod/nut system (Mosallam 1994b) or transfer members such
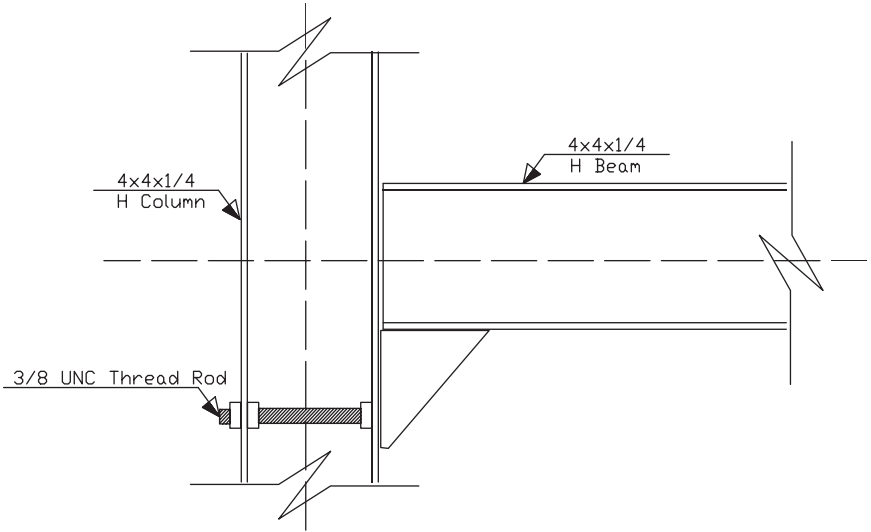
Figure 7-58. Details of the PFRP flexible connection Type viii.

Figure 7-59. UC PFRP "flexible" frame connection test setup of Zahr et al. (1993).

as angles at the junction with high stress concentration (Bank and Mosallam 1991). Figures 7-60 and 7-61 present the experimental and bilinear representation of the moment–rotation behavior of this flexible detail.

The moment–rotation behavior of this connection can be incorporated in the analysis using the following equation extracted by a curve-fitting technique of the experimental data:

$$M = 0.12 + 59.6\theta - 5190\theta^2 + 2368.9\theta^3 \tag{7-10}$$
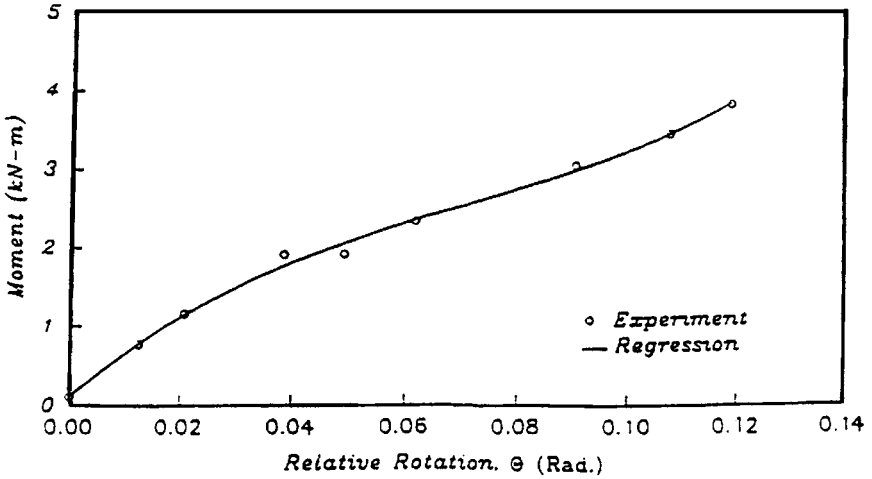
Figure 7-60. Experimental moment–rotation curve for UC PFRP "flexible" frame connection Type viii.
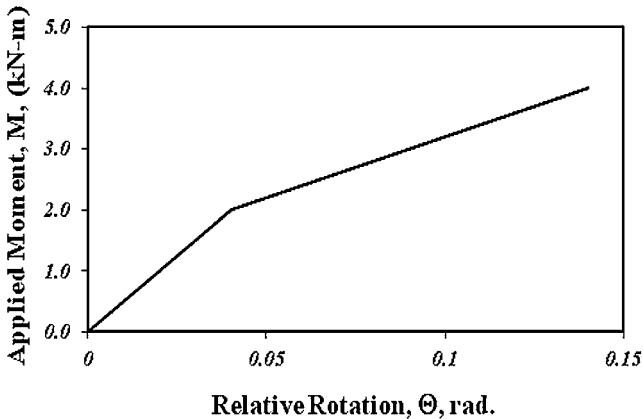
Figure 7-61. Bilinear representation for UC PFRP "flexible" frame connection Type viii.
Source: Zahr et al. (1993).

For design purposes, the polynomial expression of Eq. 7-10 can be replaced by the following two linear equations:

$$M = 0.107 + 30.84\theta \ (0 \leq \Theta \leq 0.39 \text{ rad}) \tag{7-11a}$$

$$M = 2.980 + 22.91\theta \ (0.39 \leq \Theta \leq 0.14 \text{ rad}) \tag{7-11b}$$

where M is the applied moment (kN-m), and Θ is the resulting relative rotation between the beam and column axes (radian). It should be noted that this empirical formula is units-sensitive, and unit conversions must be performed when other units are used (e.g., kip-in.).

As discussed earlier, the use of a simple representation of the initial rotational stiffness by a single stiffness coefficient (k_i) or an average stiffness coefficient (k_e) is acceptable in simple design calculations. Table 7-10 presents these values.

Comparing the stiffness and strength information presented in Table 7-10 with the results of connection details Types vi and vii listed in Table 7-7, one can see the great difference in behavior. For example, the initial stiffness of this flexible detail is about 39% of the corresponding stiffness of connection Type vi, and about 1.2% of the initial stiffness of connection Type vii (fixed vs. hinged). As shown in Table 7-10, this type of connection has negligible moment capacity of 0.45 kip-in. (0.051 kN-m) as compared to 20.50 kip-in. (2.31 kN-m) and 28 kip-in. (3.36 kN-m) of connection Types vi and vii discussed earlier. For this reason, this detail is recommended for a shear-type connection.

7.5.11 Quasi-Static and Cyclic Behavior of Interior PFRP Frame Connections

In 1998, a comprehensive program to evaluate the structural performance of different types of interior PFRP frame connections was conducted by Mosallam (1998a). In this study, several full-scale cyclic tests were conducted on several pultruded framing elements. This included box and H-beam profiles with different sizes. The emphasis of this study

Table 7-10. Design Information for Universal Connector-Seated Flexible Beam-to-Column Connection Detail

Initial Stiffness Flexural Coefficient, k_i [kip-in./rad (kN-m/rad)]	Average Stiffness Flexural Coefficient, k_e [kip-in./rad (kN-m/rad)]	Ultimate Moment Capacity, M_u [kip-in. (kN-m)]	Plastic Relative Rotation at Failure (rad)
290 (32.78)	470 (53.23)	0.45 (3.98)	0.12

was on interior framing connections with both flange and web attachments. In addition to high-strength adhesives, both FRP and steel mechanical fasteners were studied. Bolted-only, adhesively bonded-only, and combined joint details were evaluated using both metallic and nonmetallic bolts. Strain, deflection, and load information was collected using a computerized data acquisition system. M/θ and P/θ hysteresis curves were developed and analyzed. For FRP mechanical fastener bolted-only connections, a common mode of failure was observed for all specimens. This was a combination of bolt thread shaving and flexural fatigue-type failure of pultruded threaded rods. Other local failures of the pultruded thin-walled beam sections were observed at the ultimate moment. Delamination cohesive failures were also observed for adhesively bonded connection details.

The objective of this program was to generate detailed design information for different details of composite connections for pultruded shapes. These included:

- Similar and dissimilar connected profiles
- Moment and shear connections
- Bolted connections (composites and noncomposite bolts)
- Adhesively bonded frame connections (different types of adhesives)
- Combined framing connections (bolted/bonded)
- Web and flange attachment frame connections
- Quasi-static loading
- Cyclic loading (low-cycle and high-cycle fatigue)
- Traditional "unidirectional" clip angles details
- UC-type connection details
- Full-scale frame tests and analyses

Twenty five specimens were tested under both quasi-static and cyclic loading regimes. The purpose of the quasi-static tests was to measure the moment–rotation characteristics of each detail and to monitor any premature failure.

In general, three connection details were evaluated:

- Mechanical (bolted) connections: (1) metallic fasteners, and (2) FRP threaded rods and nuts
- Adhesively bonded connections (no fasteners)
- Combined connections (adhesives and mechanical fasteners)

The connecting elements used in building the connection specimens included unidirectional pultruded angles, UCs, and continuous universal connectors (CUCs), also developed by the author (see Fig. 7-62). Commercially produced PFRP were used for both beam and column sections.

The test matrix included different standard sizes 4 in. (101.6 mm), 6 in. (152.4 mm), 8 in. (203.2 mm), 10 in. (254 mm), and 12 in. (304.8 mm) pultruded H-beam and box-section profiles.

Coupon specimens from different locations from each section were tested to determine the average mechanical properties of each member. All connections were fabricated, and instrumented by strain gages at different critical locations. The connection specimens were tested in a 30-ft (9.15-m), 2-D test frame. This test frame was equipped with dual hydraulic actuators and each actuator had a capacity of ±50,000 lb (±222.40 kN). Figures 7-63 and 7-64 show the typical test setup for interior and exterior connections, respectively. Reversal loads of ±50 kips (±222.40 kN) were applied to the top of the column along the centerline. During the load control regime, load increments of 2 kips (8.9 kN)/cycle were used. For the displacement control portion of all tests, a load increment of 0.25 in. (63.50 mm) was used. Samples of M/θ hysteresis are shown in Figs. 7-65 through 7-72. From these figures, one can see the difference in behavior
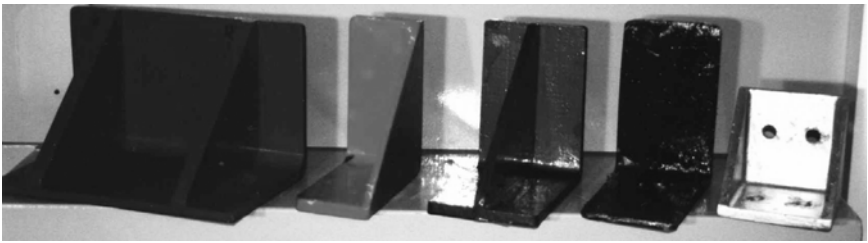
Figure 7-62. The continuous universal connector (CUC).
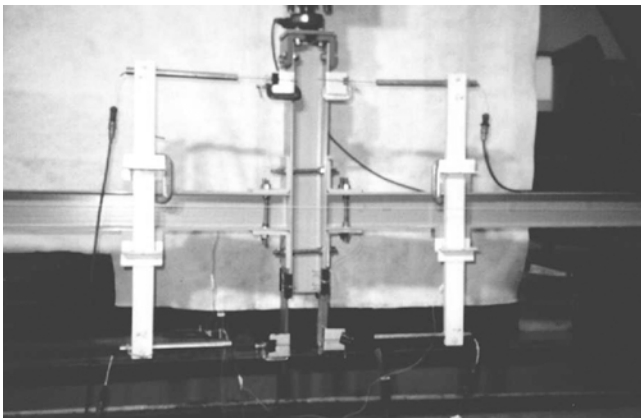
Figure 7-63. Test setup for interior connections.
Source: Mosallam (1998a).
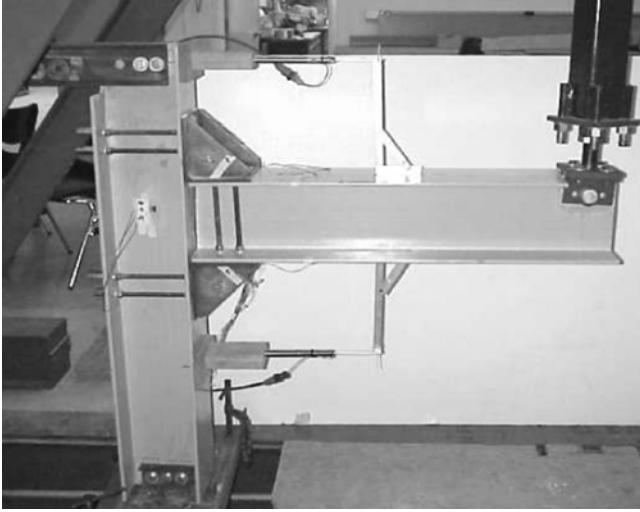
Figure 7-64. Test setup for exterior connections.
Source: Mosallam (1998a).
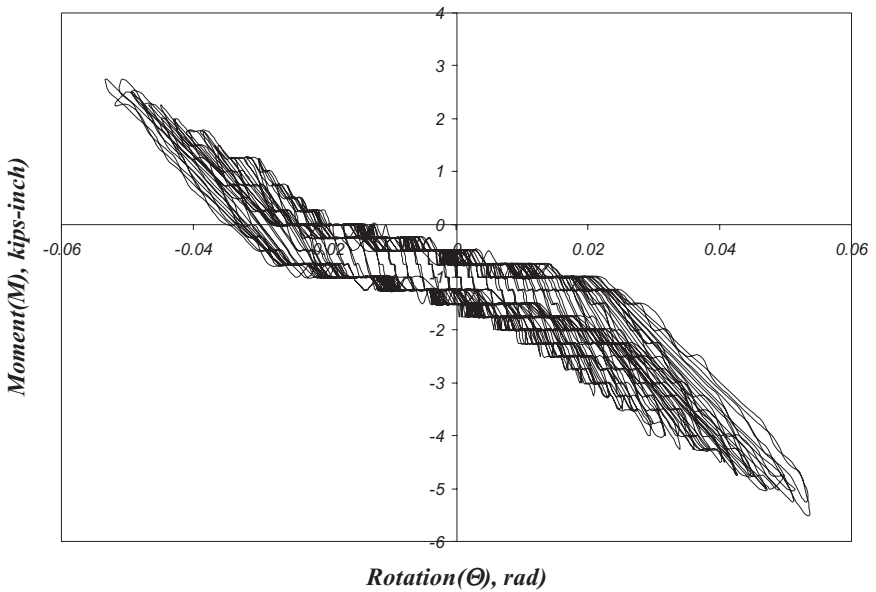
Figure 7-65. Moment–rotation hysteresis for interior box connection SQ4-LFB
(4 in. × 1/4 in. PFRP angle, FRP bolts, PFRP 4 in. × 1/4 in. box-profiles).
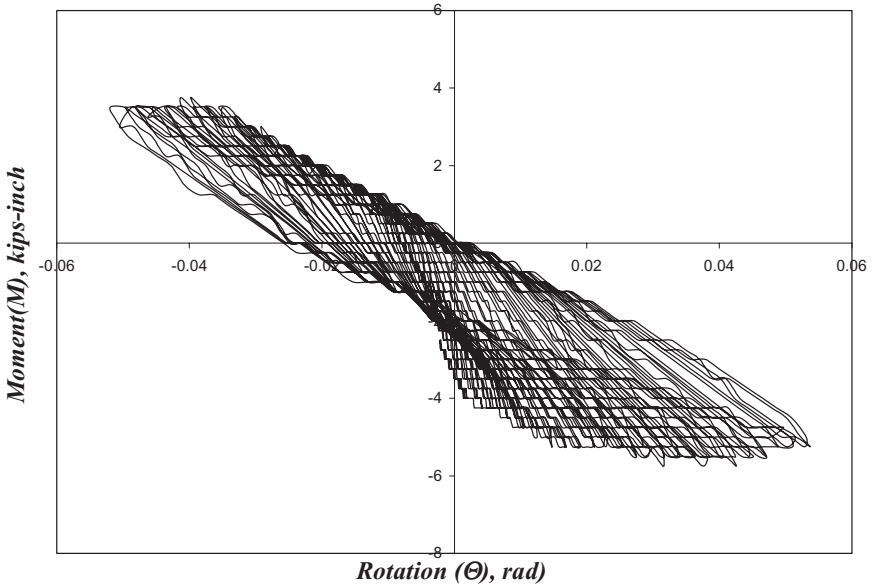
Figure 7-66. Moment–rotation hysteresis of interior box connection SQL4-SS (4 in. × 1/2 in. PFRP angle, SS bolts, PFRP 4 in. × 1/4 in. box-profiles).
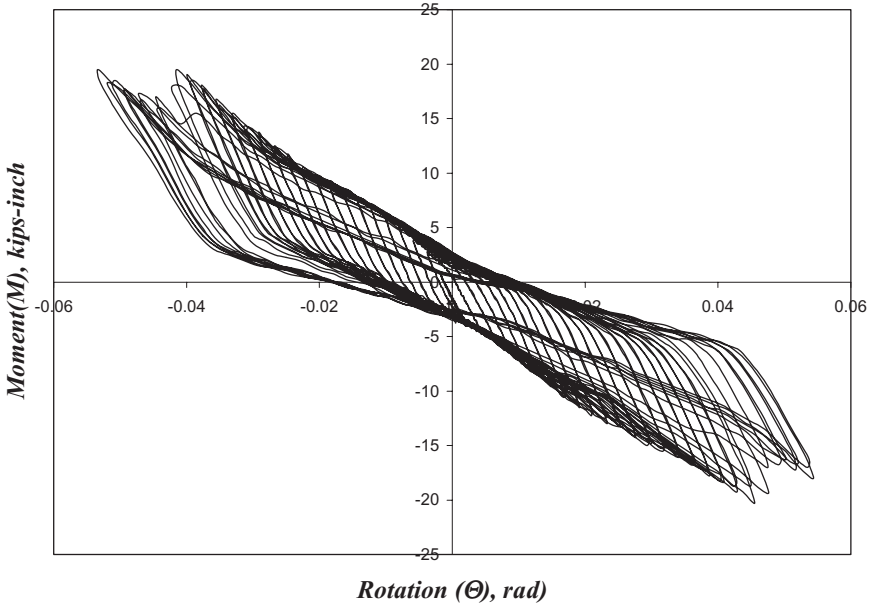
Figure 7-67. Moment–rotation hysteresis of interior box connection SQU4-SS (UC, SS bolts, PFRP 4 in. × 1/4 in. box-profiles).
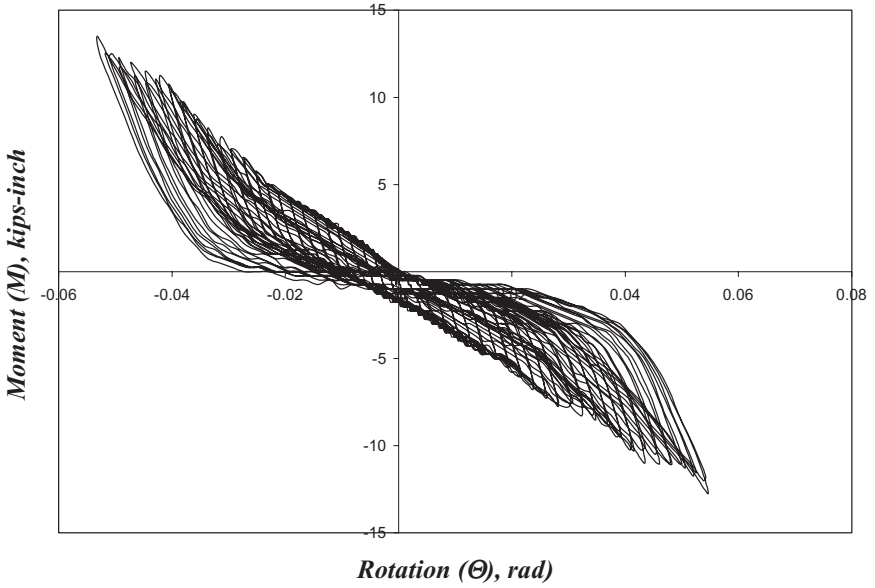
Figure 7-68. *Moment–rotation hysteresis of interior box connection SQU4-FRP (UC, FRP bolts, PFRP 4 in. × 1/4 in. box-profiles).*
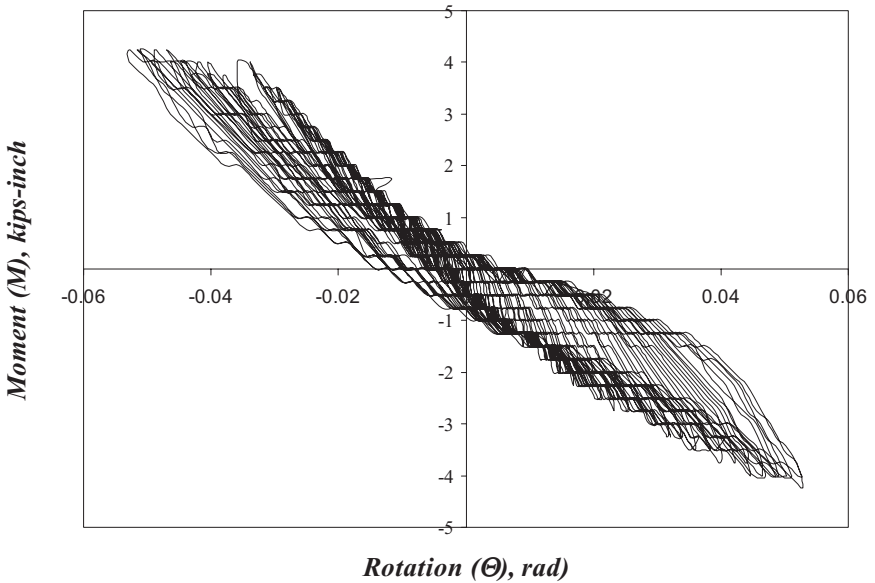
Figure 7-69. *Moment–rotation hysteresis for interior H-profiles connection HL4-DL (4 in. × 1/2 in. PFRP angle, FRP bolts, 4 in. × 1/4 in. PFRP H-profiles).*
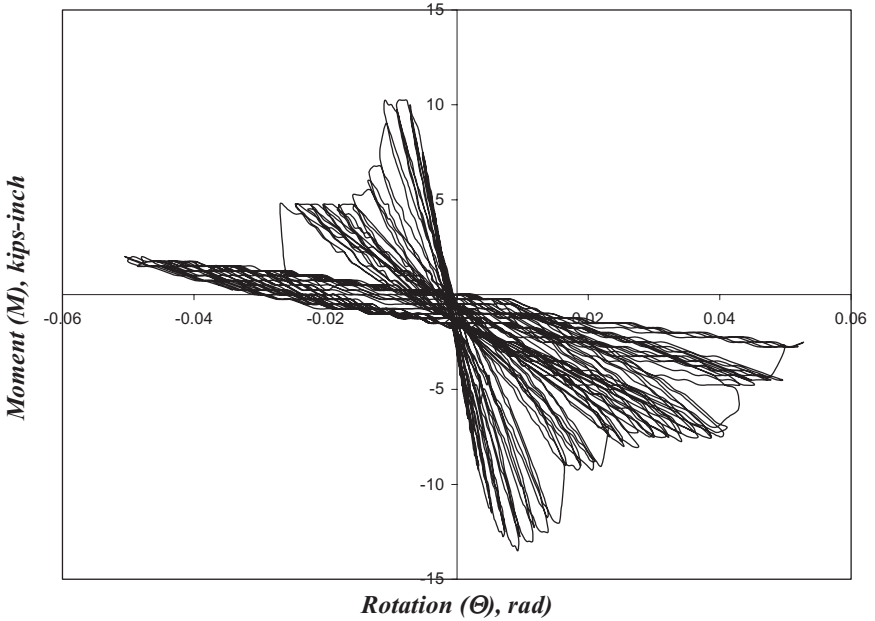
Figure 7-70. Moment–rotation hysteresis for interior H-profiles connection H44LAd1 (4 in. × 1/2 in. PFRP angle, adhesives only, 4 in. × 1/4 in. PFRP H-profiles).
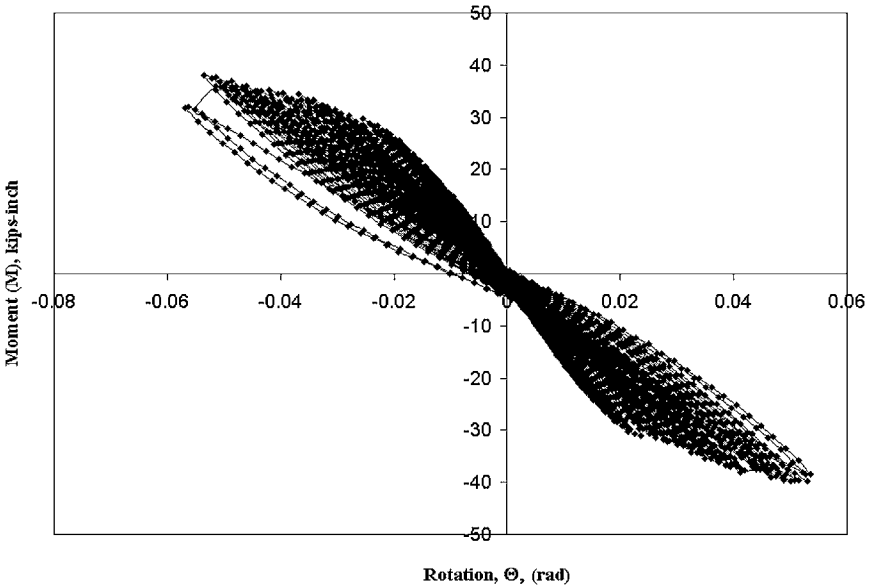
Figure 7-71. Moment–rotation hysteresis for interior H-profiles connection H6U-ADS (CUC, SS bolts, adhesives, 6 in. × 3/8 in. PFRP H-profiles).
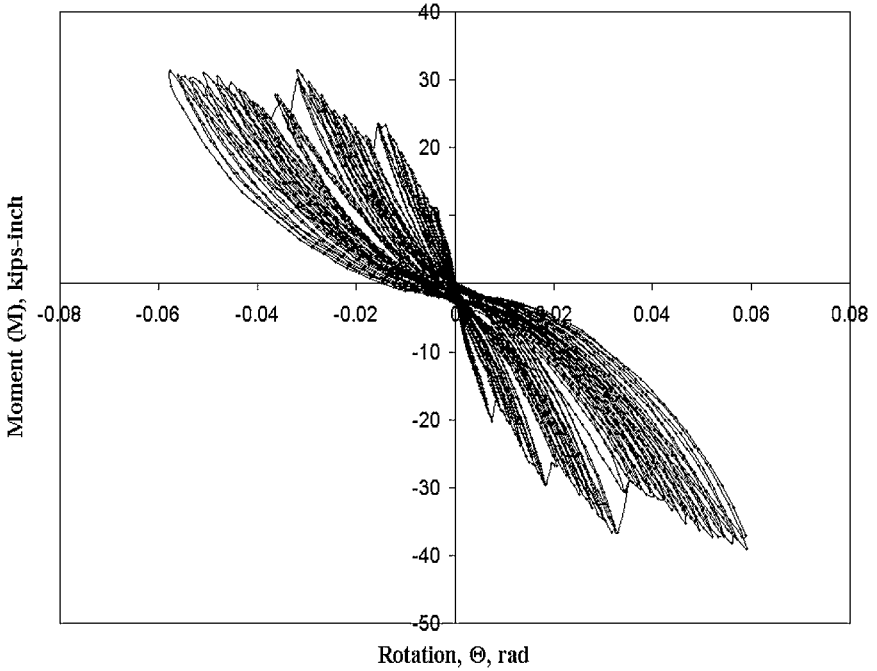
Figure 7-72. Moment–rotation hysteresis for interior H-profiles connection H6U-SS (CUC, SS bolts only, 6 in. × 3/8 in. PFRP H-profiles).

of bolted, adhesively bonded, and combined details. The benefit of using multidirectional composite connectors such as UCs and CUCs can be seen by comparing the experimental results shown in Figs. 7-66 and 7-67 for connection details with unidirectional angles and UC elements, respectively.

Several failure modes were identified for bolted, adhesively bonded, and combined beam-to-column interior and exterior connections. Figure 7-73 shows an interesting local mode of failure of the unidirectional box beam at the junction of the web and the flange. This local failure resulted in an appreciable loss in both stiffness and strength of the connection under the applied cyclic loads. This mode failure is attributed to insufficient fiber continuity between the thin walls of the pultruded box profile (similar to the reason behind the premature failure of the web-flange junction reported earlier for open-web profiles such as H, I, C, etc.). Figures 7-74 and 7-75 show that using the proper adhesive and following a proper surface pretreatment (as discussed in Chapter 4) can result in a cohesive failure rather than the catastrophic brittle failure as was reported earlier by Merkes and Bank (1999). In addition, this figure shows the low strength of the unidirectional pultruded angles due to the wrong direction of the
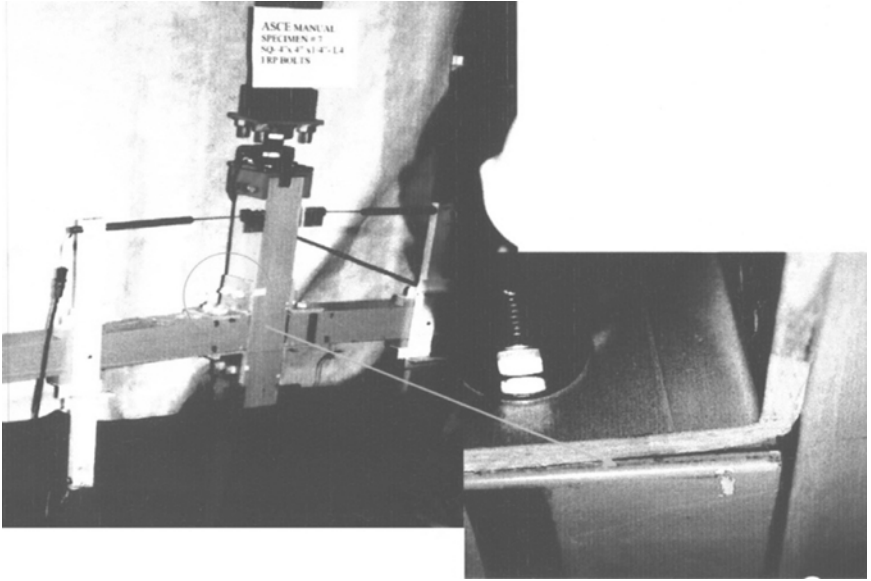
Figure 7-73. Local failure of box beam at the corner.
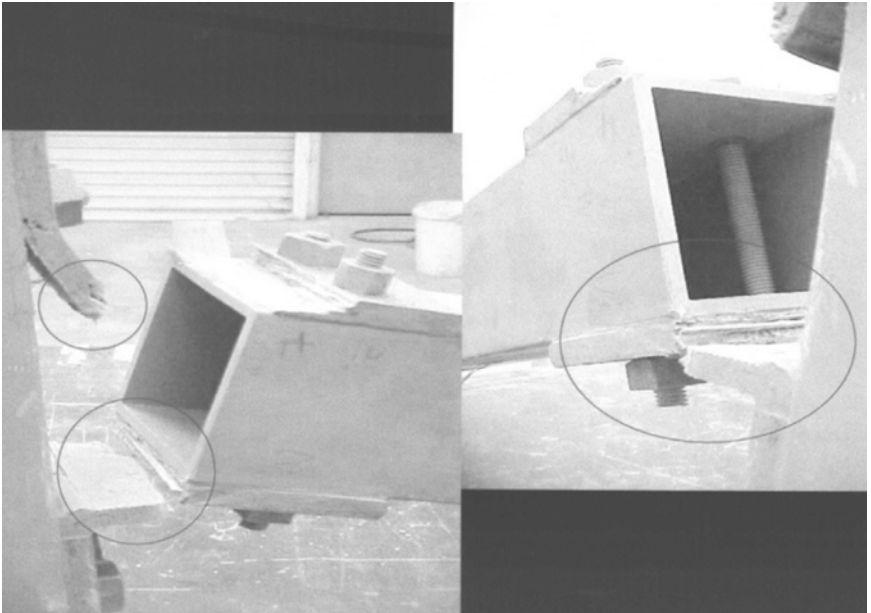
Figure 7-74. Cohesive failure of the combined (PFRP threaded rods and molded nuts and high-strength epoxy), box-to-box interior connections.
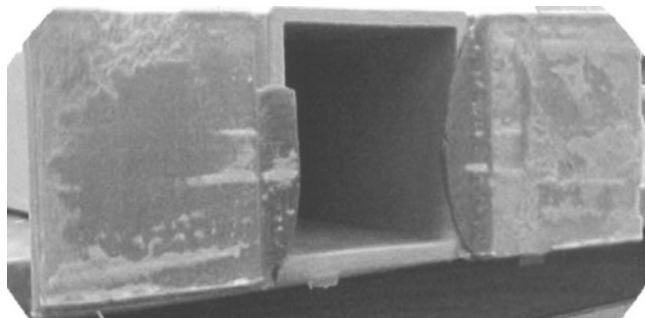
Figure 7-75. Cohesive failure of the adhesively bonded, box-to-box interior connections.

major reinforcements (the major reinforcement is perpendicular to the load path, as discussed earlier).

7.5.12 Seismic Behavior of PFRP Frame Connections

A pilot experimental program has been initiated by the author on the seismic behavior of PFRP 3-D frame structures (Fig. 7-76). In this program, both one- and two-story 3-D frames made entirely from PFRP composites and gratings were evaluated under ground motion. The tests focus on evaluating the effect of different connection details on the dynamic response of the PFRP frame structure. Samples of the experimental results were reported by Mosallam (2000).

7.5.13 Examination of Rigid Beam/Column Connections

Bruneau and Walker (1994) undertook simple experimental investigations of PFRP specimens that examined the material behavior of epoxied joints, subjected rigid PFRP column connections to cyclic loads, and ultimately evaluated the seismic worthiness of PFRP structures. The study found that epoxied connections alone were not sufficient to exploit the high strength potential of pultruded constructs. Further, delamination of components appeared to be more problematic than the inherent brittleness of the material. Cyclic flexural tests revealed the particular delamination weakness of the flange to web core. Figure 7-77 describes the load curvature relationship and load deflection relationship of the tested rigid beam column connection. The loading followed a path in which the specimen was taken to a nominal positive load that corresponded to initial cracking, unloaded, and then reloaded until delamination of the bottom T-stub occurred, without permanent deformations. From here the specimen was manually rotated 180 degrees and reloaded so that the behavior would correspond to an actual reversal or compression of the member.

Figure 7-76. Seismic evaluation of 3-D PFRP frame structure with PFRP gratings.
Source: Mosallam (2000).
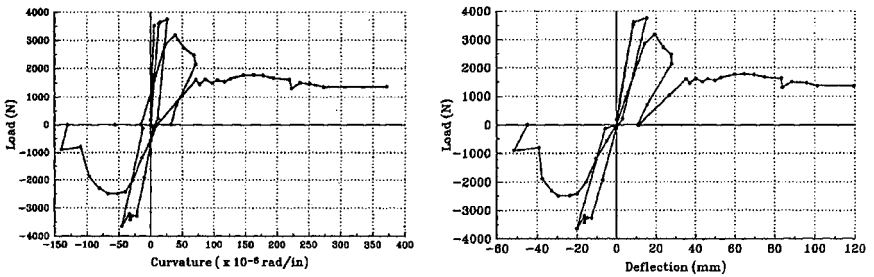
Figure 7-77. Experimental load–curvature and load–deflection of tested rigid beam-column connection.
Source: Brunei and Walker (1994).

The resulting behavior lead to the separation of the flange from the web and confirmed that the utilization of steel detail as ineffective.

Figure 7-78 shows the initial delamination and sizeable deformations before failure. The research exposed the inherent weakness of the web-to-flange interaction surface and the need to redesign and optimize connectors rather than mimic existing steel details. In addition, the study confirmed the need for alternative bonding and detailing techniques germane to PFRP construction in order to achieve near-full moment capacity and improve ductility related to seismic-resistance worthiness.

7.5.14 Examination of PFRP Interior Frame Connections

Bass and Mottram (1994) presented experimental results of five flange-cleated subassemblies. All connection details were steel-like. Commercially produced pultruded profiles, similar to those tested by Bank et al. (1992), were used. Figure 7-79 shows the different details tested in this program. Of the five full-scale interior connection tests, three major-axis (i.e., the beam connected to the column flanges) H-profile connection details were tested. Both steel mechanical fasteners and adhesives were used in building these connections.

The pultruded profiles used in both beams and columns were EXTREN 525 series, manufactured by the Strongwell Company. Equal lengths of 4.92-ft (1.50-m) pultruded beams and columns were used. The column and beam members for all specimens were 8 in. × 8 in. × 3/8 in. (203 mm × 203mm × 9.5 mm). The unidirectional connecting equal-leg angles were 6 in. × 6 in. × 1/2 in. (152 mm × 152 mm × 2.7 mm). A two-part, cold-cure adhesive system was used (Araldite 2015). The steel mechanical fasteners were M16 Grade 8.8 steel and were tightened to a torque of approximately 173.5 lb-in. (19.60 N-m). Figure 7-80 shows the test setup used in testing all connections. The two quasi-static end loads were applied at a distance of 1 m from the connection region. The relative rotation was measured using electronic inclinometers. The load was applied in increments of 112.41 lbf (0.50 kN).
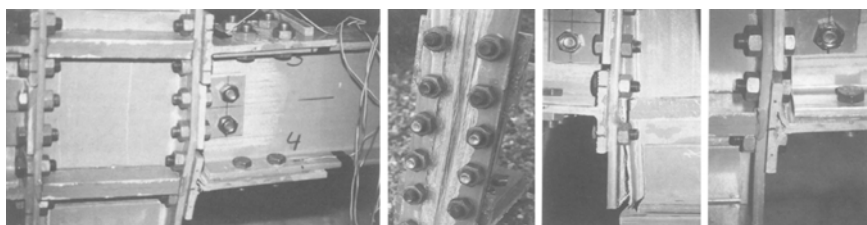
Figure 7-78. Local and global failure modes of PFRP interior connections due to lack of reinforcement continuity at the web/flange junctions of unidirectional pultruded profiles.
Source: Brunei and Walker (1994).
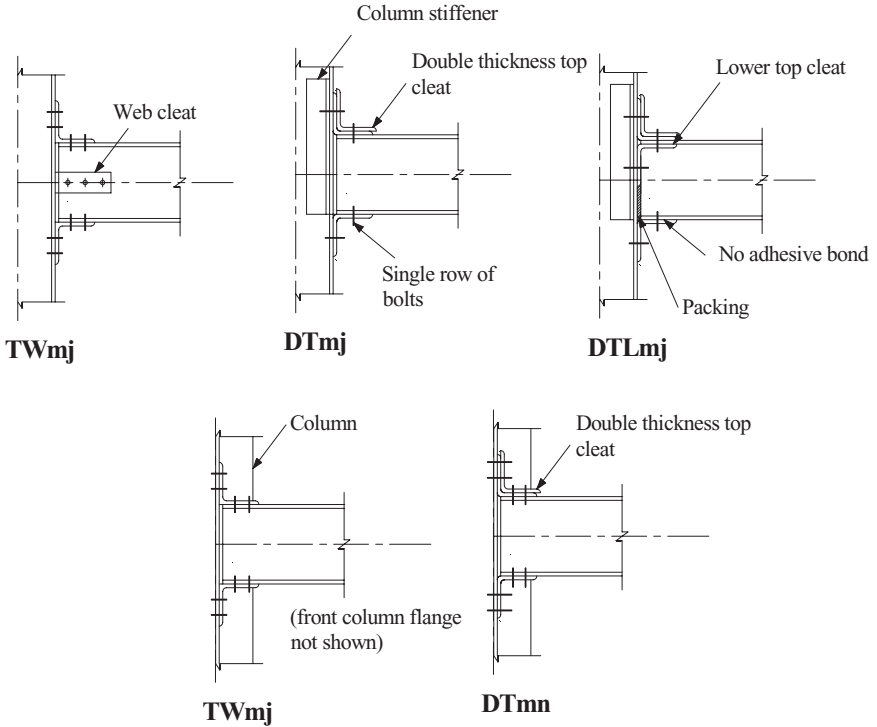
Figure 7-79. Interior frame connection details tested by Bass and Mottram (1994).
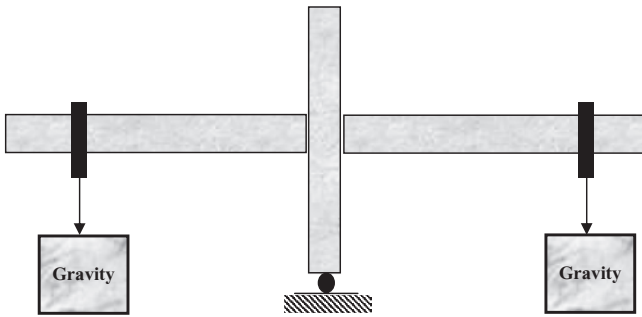
Figure 7-80. Bass and Mottram (1994) test setup.

7.5.15 Examination of Pinned and Semi-Rigid Connections

Mottram and Zheng (1996) presented a comprehensive state-of-the-art review on connection design for pultruded structures. In this review, the researchers divided the test program into two connection groups similar to the classification adopted by the steel industry (AISC-ASD/LRFD

2005). These two groups were Type I: pinned connections, and Type II: semi-rigid connections.

7.5.15.1 Type I Connection Details.   Three types of connecting regimes were tested: I (1) bolted only, (2) adhesively bonded only, and (3) combined bolted/bonded connection detail. A summary of the pinned connection test details and labeling is shown in Table 7-11. All connection details were similar to those recommended by the *EXTREN Design Manual* as shown in Fig. 7-81.

The connection details consisted of two back-to-back cantilever beams with a central column (Fig. 7-79). For both connection details *Wmj_bt + bd* and *Wmj_bd,* Araldite 2015 (a Ciba-Geigy product) epoxy adhesives were used. Secant stiffness S_j, moment M_j, rotation Θ_j, ultimate moment M_{ult}, and the rotation relative rotation corresponding to the ultimate moment capacity, Θ_{max} at the first observed local failure of each connection are shown in Table 7-12. From this table, one can see that the adhesively bonded-only connections (*Wmj_bd*) had the highest average rotational stiffness (S_j ^{ave} = 377 kN-m/rad), while the bolted connection details (*Wmj_bt*) exhibited the lowest average stiffness of about 54 kN-m/rad. This is attributed to the contribution of connection slippage of the bolted

Table 7-11. Type I Connection Details Summary Tested by Mottram and Zheng

Label	Details	Column Axis	Connectivity
Wmj_bt	Web Cleats	Major[a]	Bolting (16Φ)
Wmj_bt + bd	Web Cleats	Major	Bolting (16Φ) + Bonding
Wmj_bd	Web Cleats	Major	Bonding

[a] Beams are connected to column flanges.
Source: Mottram and Zheng (1996).
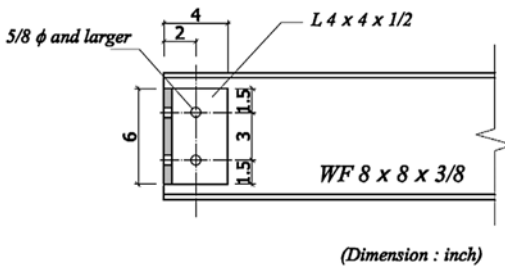
Figure 7-81. Typical Strongwell connection details evaluated by Mottram and Zheng (1996).

Table 7-12. Type I Connection Summary Results Tested by
Mottram and Zheng

Connection	$S_j = M_j/\Theta_j$ (kN-m/ rad)	M_j (kN-m)	Θ_j (micro-rad)	M_{ult} (kN-m)	Θ_{max} (micro-rad)
Wmj_bt Left	52 (68)[a]	1.64	32 (24)	1.72	39
Wmj_bt Right	57 (76)	1.64	35 (22)	1.72	49
Wmj_bt + bd Left	185	1.24	7	2.07	89
Wmj_bt + bd Right	172	1.24	7	2.07	33
Wmj_bd Left	369	1.18	3	1.0	3
Wmj_bd Right	385	1.04	3	1.18	10

[a] Values in parentheses are following unloading.
Source: Mottram and Zheng (1996).

details. Although the combined connection detail, *Wmj_bt + bd*, had a lower stiffness as compared to the bonded connection, its energy dissipation capability was the highest among the three connection details.

In general, the major function of these connections is to transmit the shear forces from beams to columns. However, and as indicated from the experimental results, pinned connections have a limited capability to transmit bending moments to the column. A sudden adhesive failure was observed for bonded-only connection details at a relatively low load level. Based on the experimental results, Mottram and Zheng (1996) recommended avoiding the use of adhesives as the sole connecting media. It was also concluded that when beams are connected to the column web (minor axis attachment), relative rotation would decrease due to the elimination of the deformation resulting from the prying action when connecting the beam to the column flanges. This is particularly significant for commercially produced unidirectional open-web pultruded profiles where minimum fiber continuity exists between the web and flange reinforcements (Mosallam 1993a).

The following points were recommended for pinned beam-column connections:

- Use bolted or combined connection detail.
- Use a 2-mm bolt hole clearance.

- For bolted-only connections, use oversize rounded-edge washers of a diameter 2.5 times the bolt diameter to maintain bearing stresses less than 68 N/mm^2.
- For beam-pinned connections attached to the column web (weak or minor axis), and to improve the ease of fabrication and installation, the centerline of the column web holes may have to be offset from the cleat's leg centerline. In this case, it is recommended to use a connection detail with a combination of bolts and adhesives (only when connection slip is not permitted). In this case, the beam must be lightly loaded because there will be failure of the unidirectional cleats when beam deflection is >1/360 of the beam span.
- Use a bolt clearance of 2 mm and a gap of 10 mm between the beam end and the column face, to increase the rotation at the occurrence of the first local failure.
- Web cleat connection details are recommended, provided that the maximum deflection is ≤1/250 of the beam span.

The above recommendations are valid only for the details and dimensions tested. Generalizing these recommendations to other connection details will require further testing.

7.5.15.2 Type II Connection Details.   The second group tested by Mottram and Zheng (1996) was classified as Type II or "semi-rigid" connection details. A total of five full-scale connection specimens were tested. Both adhesives and metallic mechanical fasteners were used. Beams and column sections were 8 in. × 8 in. × 3/8 in. (203.2 mm × 203.2 mm × 9.53 mm) E-glass/polyester H-pultruded profiles, and unidirectional cleats were cut from 6 in. × 6 in. × 1/2 in. (152.4 mm × 152.4 mm × 12.7 mm) unidirectional pultruded equal-leg angles. Details of these connections are described in Fig. 7-82.

Mottram and Zheng (1996) used double unidirectional cleat angles (Fig. 7-82) to increase the flexural strength of these connections. Again,
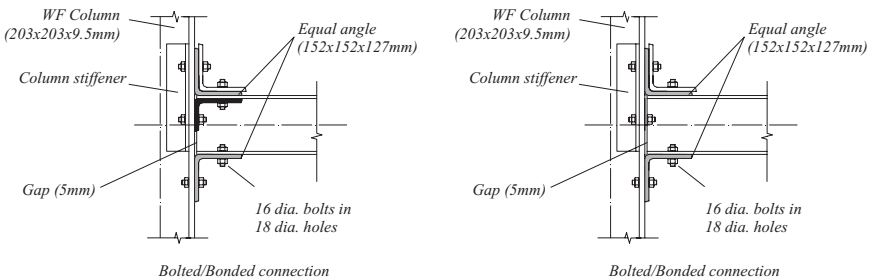
Figure 7-82. Bass and Mottram (1996) double-cleat angle details.

the fibers in both angles were running in the wrong direction, and the only addition was the increase of the matrix cross section by doubling the thickness of the cleat angles. For the same reason, the same expected delamination failure of the top cleat occurred. This common type of failure for steel-like connections was described in detail by Mosallam (1994b). The same stiffening approach was adopted by Sanders et al. (1996) in their experimental study on the behavior of adhesively bonded "steel-like" pultruded connections.

Table 7-13 summarizes the results of three "semi-rigid" connection details tested by Bass and Mottram (1994). Mottram and Zheng (1996) state that adding double thickness to the connection (Detail DTLmj in Table 7-13), as expected, increased the stiffness of the connection. In connection details such as DTLmj, a third unidirectional pultruded angle was attached to the interior of the top flange. Again, by tripling the thickness of the connecting elements, an increase in the rotational stiffness was no surprise. However, these details are not recommended for several reasons, including:

- It will increase the initial cost, since fibers and the composite action are not utilized (the polyester matrix is used as the primary bearing element).
- From a constructability point of view, this arrangement will be difficult at the site because of the space limitation and dimension restrictions of the pultruded profiles.
- Most importantly, this connection can only be used for gravity load application. In cases of cyclic loading conditions, similar details at the bottom should be used.

7.5.16 Examination of Additional Steel-Like Beam Column Connection Assemblies

Mottram and Zheng (1996) tested two other steel-like connection details, referred to as Stmj and TLmj. The letters "mj" refer to "major axis attachment to the column section." The first connection detail was identical to that presented and tested by Mosallam et al. in 1993. In this detail, and to avoid the inherent premature local failure of the column section at the connection zone, the researchers adopted the recommendation of Mosallam (1993a; 1994b) of using prestressing double-nut threaded rods connecting the two flanges of the column at the connection zone. In an effort to increase the rotational stiffness of the connections and to overcome the premature failure of the connecting elements, Mottram and Zheng (1996) used steel angles and added a stiffening detail, which was proposed and validated by Mosallam (1994b). This steel/composite detail is shown in Fig. 7-83A. As described earlier, the use of steel angles as

Table 7-13. Type II Semi-Rigid Connection Summary Test Results by Bass and Mottram

	Lowest Initial		First Failure		Secant	Ultimate Failure	
Connection	Stiffness, S_i (kN-m/rad)	Moment, M_i (kN-m)	Moment, M_j (kN-m)	Rotation, Θ_j (micro-rad)	Stiffness, S_i (kN-m/rad)	Moment, M_{ult} (kN-m)	Rotation, Θ_{max} (micro-rad)
DTLmj	1,380	5.6	7.8[a]	5.6	1,380	14.9	33
Stmj	1,100	5.5	10.0[b]	13.5	740	>12.0[d]	23
TLmj	1,330	9.0	14.6[c]	17.5	830	16.0	30

[a] Mode of failure was delamination in pultruded top cleat.
[b] Mode of failure was flexural rupture of top beam flange.
[c] Mode of failure was delamination in pre-preg top cleat.
[d] Connection did not attain ultimate failure load.
Source: Bass and Mottram (1994).
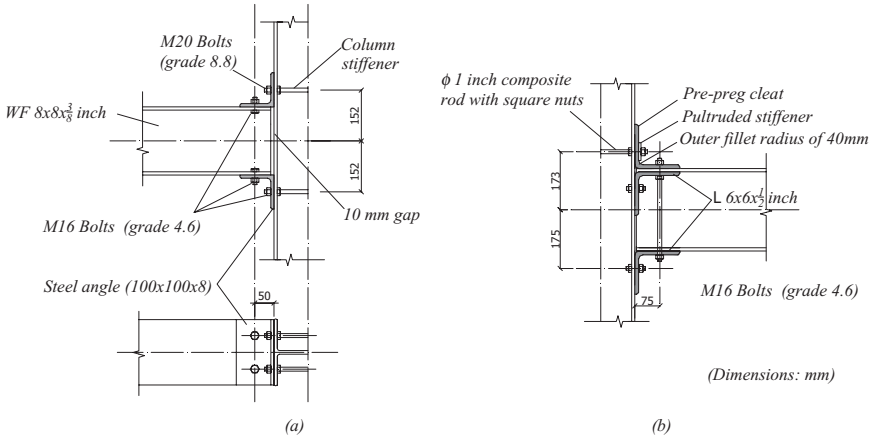
Figure 7-83. A. Steel/composite detail Stmj; B, semi-rigid composite detail TLmj.

connecting elements was reported by Morsi et al. (1984) for column-base connections. The equal-leg steel angle was cut from a 3.94 in. × 3.94 in. × 0.31 in. (100 mm × 100 mm × 8 mm) standard steel section. The steel angles were bolted to the beam and column flanges. No adhesives were used in this detail. The steel bolts were M20 bolts Grade 8.8. The steel bolts with standard washers were tightened to a torque of 885 ft-lb (100 N-m).

A clearance of 2 mm for bolt holes and a gap between the beams and the column flanges of 10 mm were used in this detail (refer to Fig. 7-83B). As compared to other composite-composite connection details, this type of connection exhibited a relatively lower strength and rotational stiffness up to failure. The first observed localized failure was due to flexural rupture of the beam's top flange at the location of the single row of steel bolts. There are several disadvantages of using this hybrid connection detail (metallic-composite), including:

1. Limitation of usage in corrosive or electromagnetic environments.
2. In the case of carbon fiber-reinforced pultruded sections, a phenomenon called "galvanic corrosion" may occur by direct contact of steel to the composite surface (Bellucci and Capobianco 1989). Such corrosion can induce degradation of the composite resin matrix if saponifiable resins such as polyamide and polyesters are used (Boyd et al. 1991).
3. Mechanical properties mismatch (both short- and long-term) between steel and composites.
4. Thermomechanical properties mismatch, including the coefficient of thermal expansions of metallic and nonmetallic connection components.

Mottram and Zheng (1996) proposed another efficient composite detail. In this detail (referred to as TLmj in Fig. 7-83B), the top cleat piece was fabricated using pre-preg materials using a pressure molding process (the cleat was initially fabricated using a vacuum bagging process and had a poor and flexible performance). This approach of multidirectional connectors, which will be revisited later in the chapter, was recently adopted by Lopez-Anido et al. (1999) through the use of quasi-isotropic pultruded angles. The pre-preg material used was GF007/LTM25/300A2S (manufactured by Advanced Composites Group Ltd., UK). The reinforcement used was bi-directional E-glass woven rovings at 850 g/m^2, with a matrix made of epoxy resin at a weight fraction of 32%. The cleat angle cured thickness was 14 mm, constructed by laminating a total of 24 layers. A total of 50% unidirectional reinforcements were used in the direction of the beams axis. A generous fillet with a maximum radius of 40 mm was used at the knee of the two angle legs to alleviate the expected through-the-thickness radial stresses generally responsible for corner delamination, as initially observed by Mosallam (1990) for unidirectional pultruded angles. Similar to the steel-composite hybrid detail (STmj), a local pre-stressing system at the connection zone, composed of 1 in. (25.4 mm) composite threaded rods and square nuts (manufactured by the Strong-well Company), was used. The other bolts used in this connection detail were made of steel. Bolt holes had 2-mm clearance and the steel bolts were tightened by a 28.3 N-m torque. That type of connection was found to be too flexible. For this reason, extra stiffening elements were added (Fig. 7-83B). These stiffening elements were:

- A lower top cleat 1/2 in. pultruded equal-leg angle
- Steel bolts connecting the top and bottom cleats and flanges on the beam side of the connections as tested and recommended by Mosallam et al. (1993a)
- A 2 3/4 in. × 7 7/8 in. (70 × 200 mm) section of 1/2 in. (12.7 mm) pultruded material adjacent to the vertical leg of the top cleat

The first localized failure of this connection detail was due to delamination of the top prepreg cleat at the fillet radius due to the poor through-the-thickness properties of the majority of composites. This common type of failure is caused by the radial stress component as reported by Mosallam (1990). To avoid this type of failure, optimized connector geometry, similar to the optimized universal connector developed by Mosallam (1993d), should be used.

Experimental results indicated that both details, TLmj and Stmj, had higher resistance to initial failure coupled with higher flexibility as compared to connection detail DTLmj, where unidirectional PFRP angles were used. While there was an increase of nearly 100% in the connection *initial*

strength (7 to 8 vs. 14.6 kN-m) as compared to the pultruded angle detail (DTLmj), no significant increase in the connection ultimate moment was achieved (14.9 kN-m vs. 16 kN-m). As noted in Table 7-13, one may conclude that the initial rotational stiffness, S_j, for the three connection details was similar (1,380, 1,100, and 1,330 kN-m/rad).

Mottram and Zheng (1996) performed an analytical study to model the behavior of an isolated beam and the response of a whole pultruded composite plane frame structure. The beam-line method was used to analyze isolated beams with different end restraints. Provided that the connection's stiffness is known, the beam-line method can determine the factor by which the loading can be increased above that when the beam has simple supports and a serviceability condition on deflection is imposed [in their case, a L/250 deflection limit was adopted as per the requirements of the *EUROCOMP Design Code and Handbook* (Clarke 1996). Table 7-14 presents the results of a parametric study of the three connection details DTLmj, Stmj, and TLmj described earlier.

Table 7-14. Beam-Line Parametric Study for Maximum Deflection of 1/250 of Beam Span

Connection	Connection Stiffness, S (kN-m/rad)	Connection Moment, M_e (kN-m)	Connection Rotation, Θ_e (micro-rad)	Load Factor Q_{sr}
Beam span = 4.0 m				
DTLmj				
	1,400 ($S_i@S_j$)	9.1[a,b]	6.5	2.4
Stmj	1,100 (S_i)	8.0[a]	7.3	2.2
Stmj	740 (S_j)	6.3[a]	8.5	2.0
TLmj	1,300 (S_i)	8.7	6.7	2.3
TLmj	830 (S_j)	6.8	8.2	2.0
Beam span = 3.0 m				
	1,300 (S_i)			
TLmj	830 (S_j)	9.1[a]	7.0	2.0
TLmj		7.0	8.4	1.8
Beam span = 5.0 m				
	1,300 (S_i)			
TLmj	830 (S_j)	8.3	6.4	2.6
TLmj		6.5	7.8	2.3

[a] Maximum moment for initial stiffness has been exceeded.
[b] First failure of connection will have occurred.
Source: Mottram and Zheng (1996).

The beam-line concept is a useful analytical tool but it does not provide the overall structural behavior of a pultruded frame structure. For that reason, Mottram and Zheng (1996) developed a linear, elastic frame analysis computer code. The program considers the connection's nonlinear rotational behavior, the second-order deformation effect, as well as the effect of shear deformation. The use of the beam-line concept for pultruded connections was originally developed by Mosallam (1990) through the development of a frame member stiffness matrix that includes both the semi-rigid behavior of the connections as well as the shear deformation effects.

Figure 7-84 shows the dimensions and loading of a three-story, single-bay pultruded plane-frame structure used in the analysis. All members were made of 8 in. × 8 in. × 3/8 in. H-profiles with the following properties:

$I_{xx} = 4.13 \times 107$ mm^4, moment of inertia,
$A_w = 1,750$ mm^2, area of web,
$E_{xx} = 20$ kN/mm^2, longitudinal stiffness,
$G_{xy} = 3$ kN/mm^2, shear modulus.
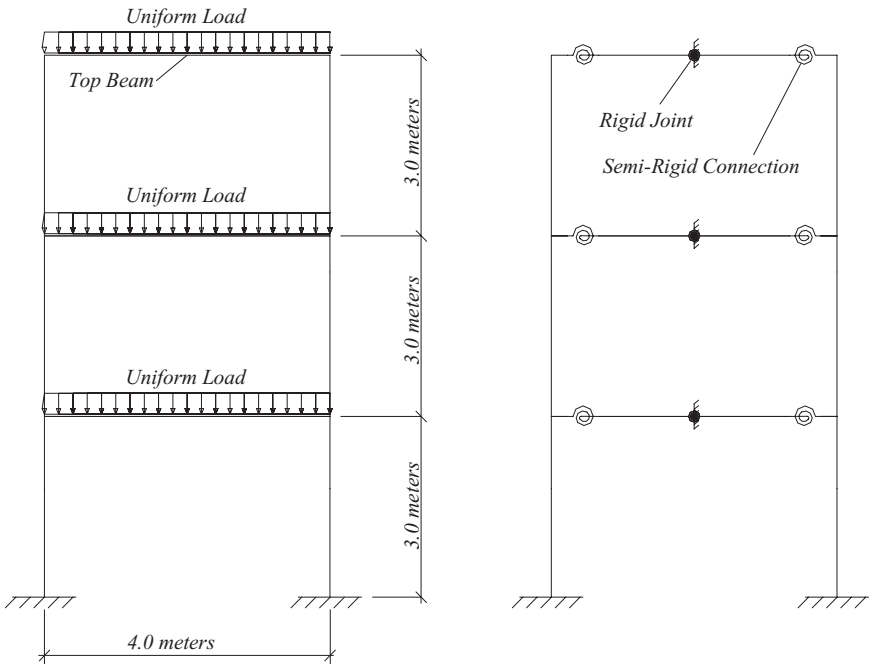
Figure 7-84. Example of plane frame with semi-rigid connections.
Source: Mottram and Zheng (1996), courtesy of Dr. Toby Mottram.

In the analysis, all beam-column connections were considered semi-rigid, while the base-column connections were assumed to be fully fixed. It should be noted that, especially in cases of applications of lateral loads such as earthquake or wind, this concept would significantly underestimate the lateral deflection of the frame structure. Based on this study, Mottram and Zheng (1996) reached the following conclusions:

1. Define standard definitions and design parameters for connection design of pultruded composite structures.
2. Develop standard test methods to determine connection properties under both short- and long-term loading conditions.
3. Consider new connection pieces and/or connection details, such as the UC and CUC developed by Mosallam that will ensure a connection with adequate strength and stiffness for primary pultruded load-bearing frame structures.

Another study of beam-to-column connections for pultruded frame structures was reported by Mottram and Zheng (1999b). In this study, three full-size tests were conducted on 10 in. (254-mm) proprietary web-cleated connections. For the first two connection details, the beams were connected to the column major axis (column flange attachment), while in the third detail the beams were connected to the column minor axis (column web attachment). The centerline of the beams was at a height of 35 in. (900 mm) from the column base. The two concentrated loads were applied at an equal distance of 40 in. (1.016 m) from the column centerline. The height of the hinged-base column was 35 in. (900 mm). Relative rotation measurements were captured using electronic inclinometers and displacement transducers. The major axis connection detail was adopted from the Strongwell (2004) design manual. Both beam and column sections were constructed from 10 in. × 10 in. × 1/2 in. (254 mm × 254 mm × 12.7 mm) H-profiles manufactured by Creative Pultrusions, Inc. The unidirectional pultruded angles were cut from 6 in. × 6 in. × 1/2 in. (152 mm × 152 mm × 12.7 mm) equal-leg unidirectional pultruded angles manufactured by the Strongwell Company. The details of these connections are shown in Fig. 7-85, and their labeling explained in Table 7-15. For all connection specimens, bolting was accomplished by using M16 Grade 8.8 steel bolts with standard-size steel washers of 1 3/8 in. (30 mm) diameter. The torque used to tighten the steel bolts was increased to 100 N-m as compared to the applied torque of 23.6 N-m described earlier for 8 in. × 8 in. × 3/8 in. (203.2 mm × 203.2 mm × 9.53 mm) connection details (Mottram and Zheng 1996). The reason behind the 400% increase of the torque load was an attempt to eliminate possible connection slip when adhesive bonding was not present. A clearance of 0.08 in. (2 mm) was used for all bolt holes in all connection details tested in this study.
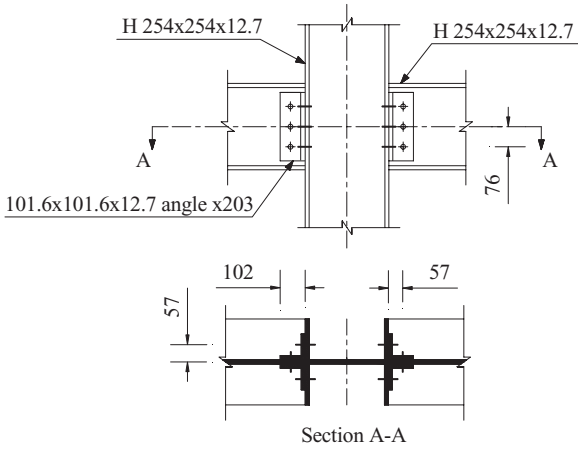
Figure 7-85. Details for major-axis connections Wmj10_bt and Wmj10_bt+bd (all dimensions in mm).
Source: Mottram and Zheng (1999), courtesy of Dr. Toby Mottram.

Table 7-15. Connection Details and Labeling Summary,
Mottram and Zheng

Label	Details	Column Axis	Connectivity
Wmj10_bt	Web Cleats	Major[a]	Bolting (16Φ)
Wmj10_bt + bd	Web Cleats	Major	Bolting (16Φ) and Bonding
Wmn_bt	Web Cleats	Minor[b]	Bolting (16Φ)

[a] Beams are connected to column flanges.
[b] Beams are connected to column web.
Source: Mottram and Zheng (1999).

7.5.17 Examination of Exterior Beam Column Connections for Pultruded Sections

Smith et al. (1996) presented a study on the behavior of exterior beam-to-column connections using both pultruded rectangular tubes and I-profiles. The study focused on the static behavior of two full-scale connection details. The testing protocol followed that adopted by Mosallam (1990), as shown in Fig. 7-86. The two pultruded cross sections used in building the full-scale connection specimens are shown in Fig. 7-87.

7.5.17.1 I-Beam: Standard Connection Detail.   Two connection specimens were fabricated and tested. The failure modes of the two specimens were similar. The failure was initiated at the column face of the clip angles
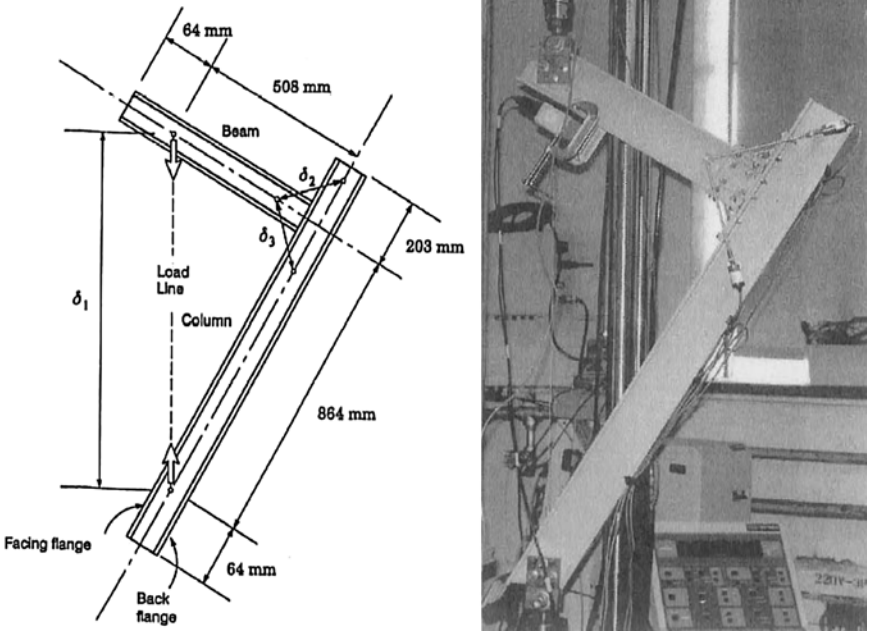
Figure 7-86. Test setup, Smith et al. (1999).
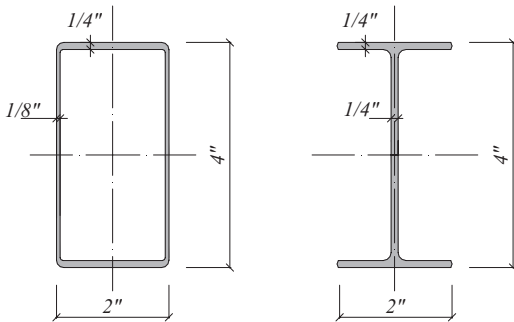
Figure 7-87. Geometry of the I-beam and box pultruded profiles.
Source: Smith et al. (1999).

as the outer surfacing veil delaminated from the uni-axial reinforcement region. Immediately following this local failure, the unidirectional top angle failed, resulting in collapse of the frame. Figures 7-88 and 7-89 show typical M/Θ curves for the front and the back of the connection, respectively.

Smith et al. (1996) indicated that their technique for measuring the relative rotation (Θ) between the beam element and the column allowed them
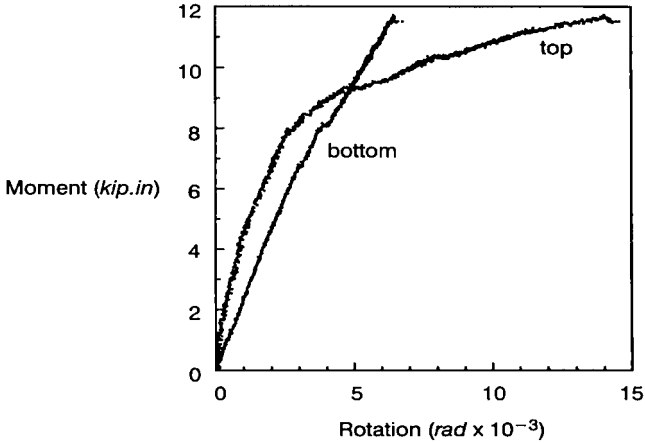
Figure 7-88. Moment–rotation curves for front of the I-beam joint.
Source: Smith et al. (1999).
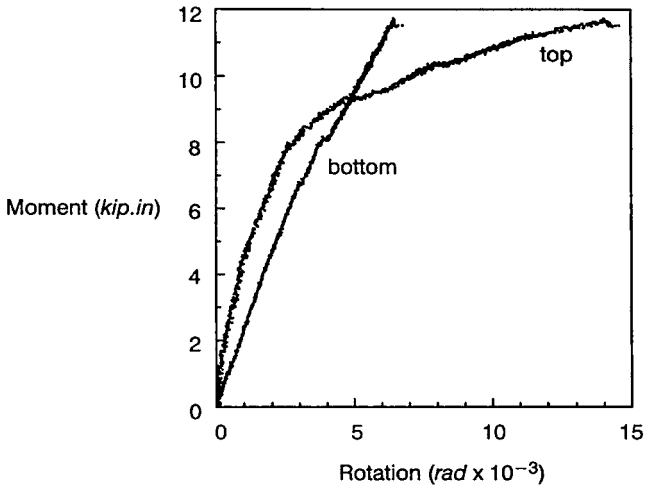
Figure 7-89. Moment–rotation curves for back of the I-beam joint.
Source: Smith et al. (1999).

to measure the opening and the closing rotational stiffness independently. The reader should be aware of the fact that the deformation of a pultruded unidirectional angle behaves differently in tension and in compression. This is due to the anisotropic nature of the composite materials. For example, and as readily seen from the M/Θ curves presented by the researchers, one can notice that the top (tension) pultruded composite angle has a lower stiffness as compared to the pultruded angle exposed to compressive stresses at the bottom. This is due to the weak

through-the-thickness properties of pultruded composites. In fact, all laminated curved members exposed to tensile loading will develop hair cracks at the curved area (at the junction of the pultruded angle's legs), and delamination local failure is generally unavoidable except for parts with 3-D reinforcement, (Mosallam 1998b).

7.5.17.2 I-Beam: Thick Seats Connection Detail.   This detail is similar to the standard connection detail reported earlier. The result of the first test indicated that the bottom seat pultruded angle contributed the overall stiffness of the connection. For this reason, a thicker pultruded angle was used in this detail. Again, the reader should be aware of the fact that the fibers are still running in the wrong direction and that the stiffness increase was gained by increasing the thickness of the "unreinforced" plastic section. In this case, the thickness of the seated angle was increased to 9.5 mm (3 in. × 3 in. × 3/8 in. vs. 3 in. × 3 in. × 1/4 in. equal-leg pultruded angle). A slight increase in the ultimate moment capacity of the connection was reported. However, this detail did not solve the problem associated with premature failure of the open web pultruded sections of both the column and the beam element due to the lack of adequate fiber continuity between the flanges and web elements of the commercially produced I-profile, as mentioned earlier. For this reason, extensive cracking along the column web-flange interface was observed. It should be noted that there is a direct relationship between the overall stiffness of the connection and the individual stiffness of the connected member. The failure mode of this detail was sudden and ultimately occurred at the "thick" top angle as shown in Fig. 7-90.

It really does not matter how stiff the connecting element is as long as the individual members exhibit flexible behavior, whether due to inherent low modulus or to faulty member fiber architecture design [as in the case of unidirectional (90-degree) pultruded angle connectors used in this detail]. This will be clearly proven by observing the behavior of the next connection detail, where steel angles with higher stiffness were used. In addition, it should be noted that only a single connection test was conducted.

7.5.17.3 I-Beam: Steel Connection Detail.   In this test, two connection details were tested. The sections of both column and beam were pultruded I-profiles. The beam was connected to the column by two mild steel angles. This hybrid system followed the concept reported by Morsi et al. (1984) for base-column connection details. As expected, the overall stiffness of the connection was increased due to the higher stiffness of the steel angles. The ultimate moment capacity was also increased.

The failure was in the form of separation of the column inner flange from the adjacent web interface. This failure mode should be avoided. In joint design for other materials such as steel and concrete, designers
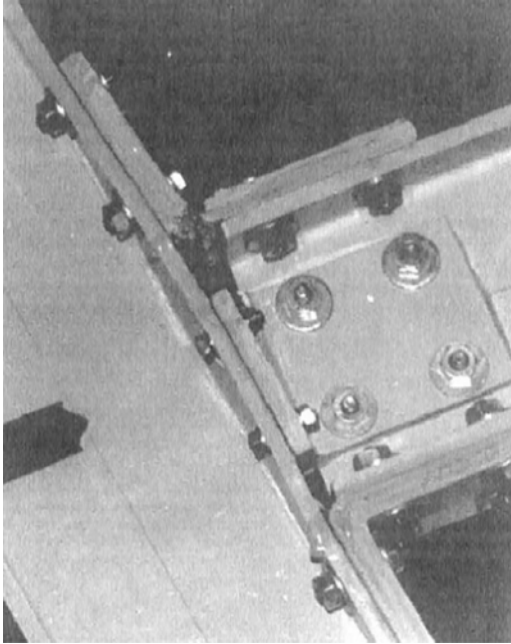
Figure 7-90. I-beam: thick seats connection failure.
Source: Smith et al. (1999).

follow a concept called the "weak beam/strong column" concept. The idea is to ensure the occurrence of the ultimate failure away from the column and the joint region. Preventing this type of column failure, as reported in several papers by Mosallam (e.g., Mosallam 1994b), can be accomplished by introducing prestressing threaded rod elements to avoid the inherent premature failure of web-flange junctions of the commercially produced open-web pultruded sections. Another important problem associated with this steel/composite hybrid connection is the mechanical and thermal properties mismatch ($E_{steel} = 29 \times 10^6$ psi vs. $E_{FRP} = 2$ to 3×10^6 psi). This can result in both short- and long-term serviceability and strength problems.

7.5.17.4 Box: Standard Connection Detail.   This connection detail is composed of two 3 in. × 3 in. × 1/4 in. (76.2 mm × 76.2 mm × 6.35 mm) equal-leg unidirectional pultruded angles placed at the top and bottom of the FRP box beam. Two connection specimens were tested in this program. A combination of adhesives and steel bolts were used. In addition, two side plate elements were attached to the sides of both beam and column, as shown in Fig. 7-91. The plates were commercially produced unidirectional plates with 1/4 in. (6.35 mm) thickness.
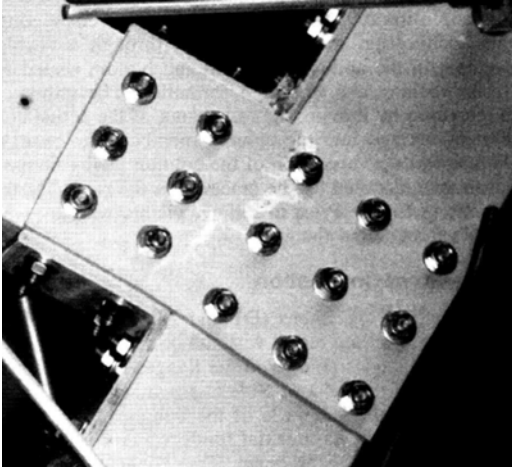
Figure 7-91. Failure of standard box connection detail.
Source: Smith et al. (1999).

Failure of this detail was sudden with no warning. The failure was initiated by a brittle fracture of one of the side plates at the bolt hole closest to the facing flange. This failure was propagated along the entire plate, resulting in a complete failure of one of the side plates and then of the top unidirectional pultruded angle, as shown in Fig. 7-91. The failure mode of the second specimen occurred at the beam side wall. The side wall separated completely from the rest of the beam member leading to immediate failure of the pultruded angle. Smith et al. (1996) attributed this type of failure to a combination of a relatively thin side wall thickness of the tubular profile as well as to the inadequacy of the uniaxial reinforcement at this region. Figures 7-92 and 7-93 show typical M/Θ curves for the front and the back of the connection, respectively.

7.5.17.5 Box: Gusset Connection Detail.   The detail of this connection is shown in Fig. 7-94. In addition to the two top and bottom unidirectional angles, two side pultruded gusset plates were added. The plates were bolted via steel bolts to the sides of the box beam and column sections. The gusset plates were aligned so that the fibers were running at 45 degrees relative to both the pultruded box beam and the column axes. Test results indicated that these plates contributed significantly to the connection stiffness (a 30% increase as compared to the standard box connection detail described earlier). In addition, the ultimate moment capacity of the connection was increased. The mode of failure was similar to the standard connections initiated by a tensile failure of the sides of the beam box section at the top of the beam side, as shown in Fig. 7-95. The longitudinal cracks propagated along the length of the beam section. This
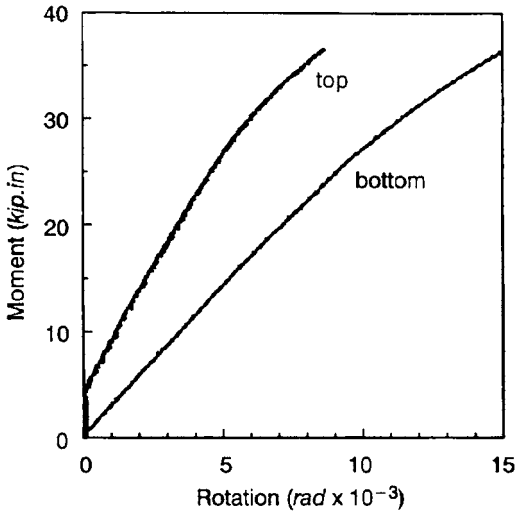
Figure 7-92. Moment–rotation curves for front of box connection.
Source: Smith et al. (1999).
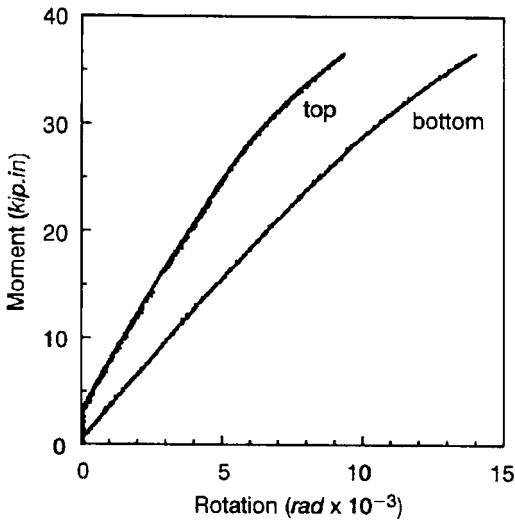
Figure 7-93. Moment–rotation curves for back of box connection.
Source: Smith et al. (1999).

local failure was expected due to the unidirectional nature of the pul-
truded box beam and the mechanical property mismatch of the steel bolts
and the pultruded composite materials. When compared to all other con-
nection details tested by Smith et al. (1996), this connection detail achieved
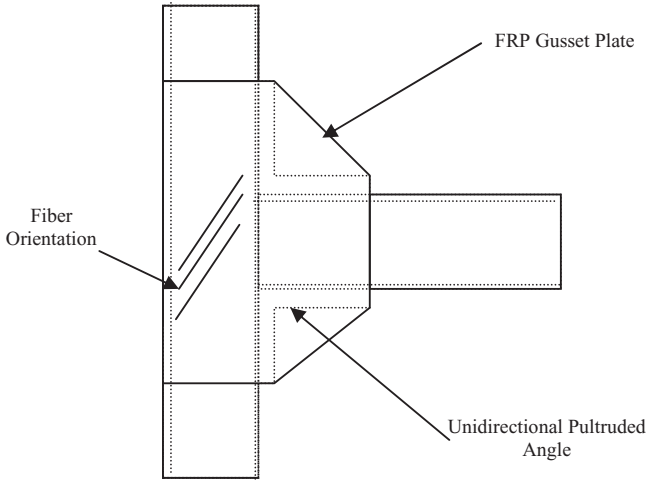
Figure 7-94. Details of the gusset connection.
Source: Smith et al. (1999).
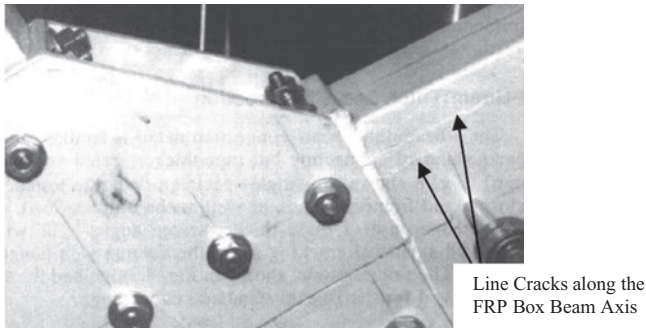
Figure 7-95. Local failure of the FRP gusset plate connection detail.
Source: Smith et al. (1999).

the highest *opening* stiffness of 3,100 kN-m/rad. The ultimate moment capacity was 5.80 kN-m.

7.5.17.6 Box: Cuff Connection Detail. Figure 7-96 shows a conceptual design of what is called a "cuff connection." Smith et al. (1999) suggested the use of this type of connection. They recommended that this part be fabricated as a single monolithic unit fully utilizing the entire column section. The primary fabrication difficulty of bolting closed section connections would be resolved by using the boltless nature of the proposed cuff connector. Ideally, using this connector, the beam and column can fit into the hollow section and then be bonded using epoxy adhesives

without the need of mechanical fasteners. However, no prototype for this connection was reported by Smith et al. (1999).

Figure 7-97 shows the closest attempt to the proposed cuff design. A built-up cuff section was constructed by using four unidirectional pultruded angles. One leg of these angles was cut, and the cut portions were attached to the column side wall by means of two steel bolts at each side of the column. At the beam section, the complete two-leg angles wrapped the outer box beam side and top flange, as shown in Fig. 7-97. The legs attached to the top and the bottom flanges of the box section were connected to the column inner flange via bolted pultruded angles. The
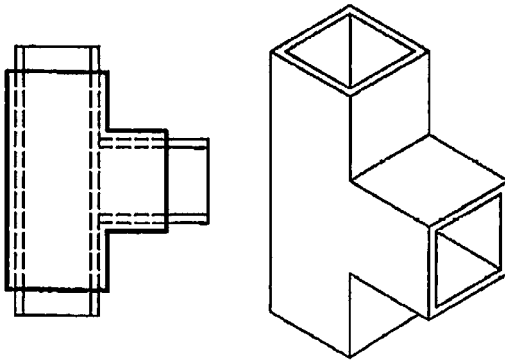
Figure 7-96. Idealized cuff connection.
Source: Smith et al. (1999).
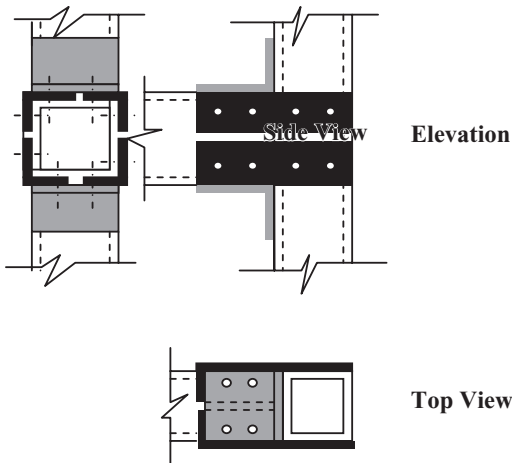
Figure 7-97. Details of built-up cuff connection.
Source: Smith et al. (1999).

specimen was subjected to a quasi-static loading regime until failure. The opening stiffness of this connection was about 42% of the corresponding stiffness of the FRP gusset connection detail described earlier. However, this detail achieved the highest ultimate moment capacity among all connection details tested in this program, with an ultimate value of 54.87 kip-in. (6.2 kN-m). The ultimate mode of failure was in the form of web-flange junction separation of the upper portion of the pultruded box column, as shown in Fig. 7-98. As shown in this figure, one side wall separated from the facing flange and the other side wall also separated from the back flange. This typical mode of failure was reported earlier for open-web pultruded profiles such as H-sections due to the lack of fiber continuity between the webs and flanges (Mosallam 1994b). As discussed earlier, this premature failure could have been avoided by using Mosallam's recommendations for using a threaded rod prestressing rod extended through the box section at the connection zone.

7.5.17.7 Box: Steel Connection Detail.   This hybrid connection detail is identical to the standard box section details except that the PFRP plate was replaced with steel plate, as shown in Fig. 7-99. While the highest opening stiffness was achieved by the FRP gusset detail, this connection detail achieved the highest *closing s*tiffness of 1,300 kN-m/rad. However, for some reason, no value was reported for the opening stiffness of this
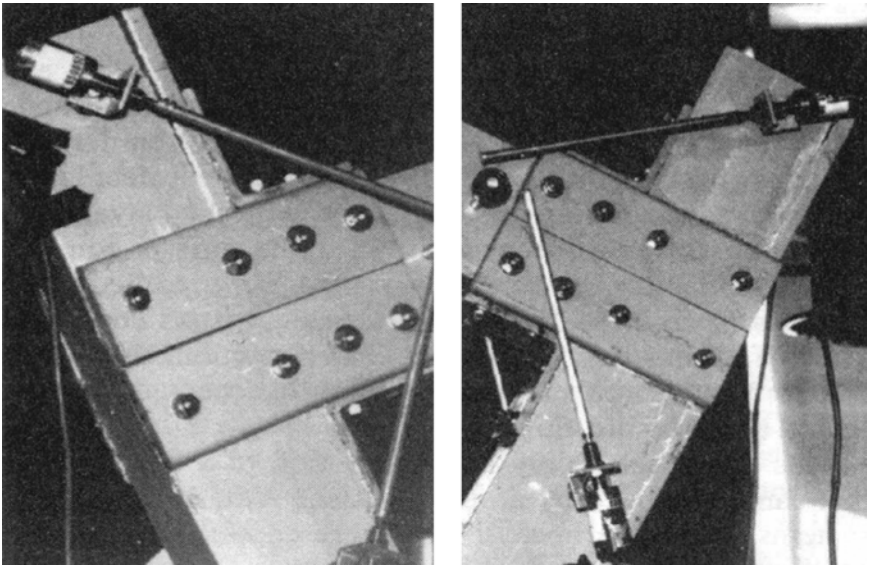
Figure 7-98. Ultimate failure mode due to web-flange separation at the column section.
Source: Smith et al. (1999).
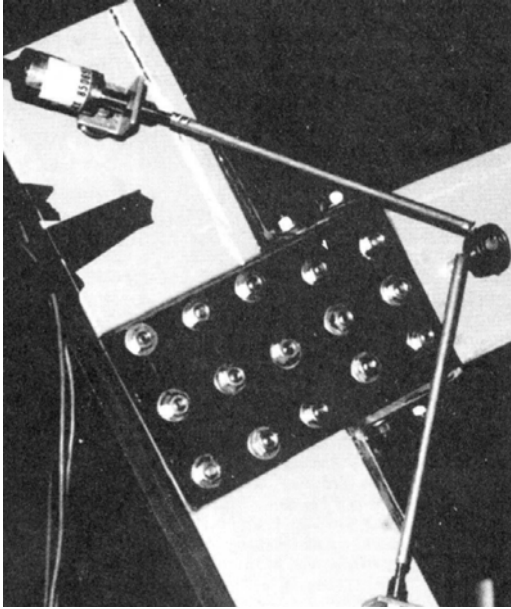
Figure 7-99. Box steel connection detail.
Source: Smith et al. (1999).

connection detail, which is expected to be relatively higher as compared to other details due to the major increase in the stiffness resulted from the use of the steel plate (E_{11}^{FRP} = 3 Msi, E^{steel} = 29 Msi). The failure mode was a combination of both localized beam failure and web-flange junction separation of the column-facing flange. Due to these premature local failures of the unidirectional pultruded composite profiles, the ultimate moment capacity was slightly lower than the ultimate moment value achieved by the FRP plate detail (4.60 kN-m vs. 4.80 kN-m). Based on the poor performance of this hybrid detail, it was concluded that, regardless of the added capacity of the individual connection elements, this detail did not succeed in overcoming the weakness of the local failure of the commercially produced unidirectional pultruded profiles. Unless the load path is modified or the load is redistributed, the steel detail will have a limited strength contribution. However, an appreciable increase in the connection rotational stiffness can be achieved by using metal parts, bearing in mind that, as mentioned earlier, the use of metal parts is associated with several problems, including lower resistance to corrosion environments as compared to FRP materials, and the mechanical incompatibility due to both the mechanical and thermal properties mismatch.

7.5.17.8 PFRP Box Profile Monolithic Cuff Connection Detail.   As an extension to the work reported by Smith et al. (1999), Carrion et al. (2005)

proposed a similar beam-column connection detail for PFRP box profiles; it utilizes a monolithic cuff connector with three thicknesses that was produced using the vacuum-assisted resin-transfer-molding (VARTM) fabrication method that was bonded to both beam and column members. In this study a total of 12 connection specimens were tested under either cyclic or monotonic loadings regimes until failure. Test results indicated that monolithic cuff connections of moderate thickness were capable of developing the flexural capacity of a pultruded FRP box beam, and that these cuffs exhibited somewhat ductile failure modes. Furthermore, the results of the study indicated that the flexibility of the monolithic cuff connection had higher strength and stiffness as compared to those that were reported by Smith et al. (1999).

7.5.18 Adhesively Bonded Exterior Beam-Column Frame Connections

Sanders et al. (1996) presented results of experimental and numerical studies on the behavior of FRP adhesively bonded *exterior* beam-to-column frame connections. In the experimental program, only two specimens were tested. Standard PFRP I-profiles were used in fabricating the beam-to-column connection specimens. However, for some unclear reason, the matrix materials for the column, beam, and the pultruded angles were different. For example, the matrix for the beam sections was ISO-polyester; the pultruded angles were made of isophthalic polyester resin, while the matrix of column sections was made of vinlyester resin. All pultruded materials were pultruded by Creative Pultrusions, Inc. Only epoxy adhesives were used to attach the pultruded angles to the flanges of the PFRP beam and column sections. The adhesives used in this study were manufactured by the Lord Corp. of Cary, NC, and the two-part epoxy product was labeled as FUSOR 320/322. As reported, the FUSOR 320/322 is a two-part (1:1 mixing ratio by weight) epoxy adhesive with a relatively high strength and higher workability. Per the manufacturing specifications, the pot life of this system is 15 min at 77 °F (25 °C). This is a relatively short pot life and it would be very difficult at the construction site to have efficient use of the epoxy in this short time frame, especially for complex connection details. Also, in high-temperature environments [e.g., 110 °F (43 °C)], it is expected that the pot life would decrease rapidly to only a few minutes, which could complicate the construction process.

In this study, surface preparation involved sanding off the glossy surface (nonstructural polymeric veils) followed by solvent surface cleaning.. The adhesives were then applied and glass beads were used to control the adhesive film thickness to 25 μm. The bonded parts were clamped and allowed to cure for 16 h.

Unlike the majority of the test setups used in most of the published work on exterior beam-to-column connections (Bank and Mosallam 1992;

Bass and Mottram 1994; Mosallam et al. 1993; Smith et al. 1996), a reaction wall was used to mount the column section. This arrangement aimed at preventing any bending or rotational freedom to the column section. Figure 7-100 shows a sketch of the test setup. In this program, two connection details were tested (Fig. 7-101). The first detail was similar to bolted connection Type i tested by Bank et al. (1994). The second detail was similar to the concept proposed by Bass and Mottram (1994) for connection DTLmj. This concept was accomplished by adding additional angle(s) in an effort to stiffen the pultruded angles. It should be noted that in the case of connection DTLmj tested by Bass and Mottram (1994), the additional angle was added at the top beam flange side, while in
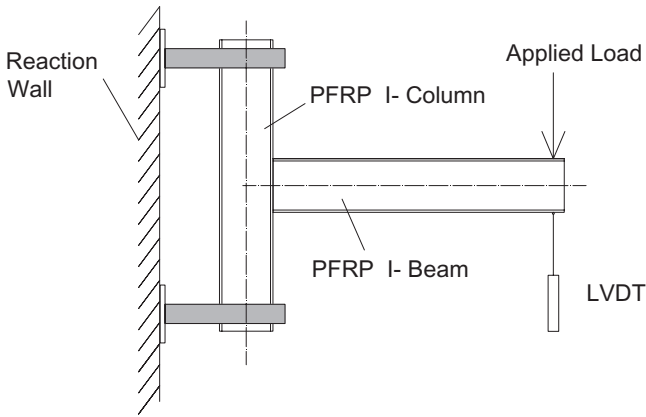
Figure 7-100. Exterior PFRP beam-to-column bonded connection setup.
Source: Sanders et al. (1996).
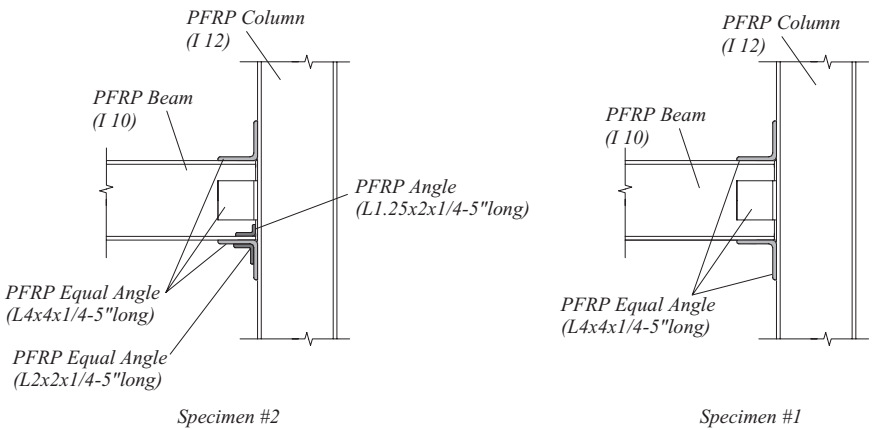
Figure 7-101. Beam-to-column bonded specimens details.
Source: Sanders et al. (1996).

this detail the additional angles were placed at the bottom side of the connection.

The ultimate load for specimen 1 was slightly above 630 lb (2,800 N). This load was translated to 28.98 kip-in. (3.27 kN-m) with an ultimate deflection of 0.3 in. (7 to 62 mm). A crackling sound was heard during the experiment but no external cracks were observed until a load of 600 lb (2,700 N). At this load level, a crack was visible on the surface of the bottom bonded pultruded angle. At the ultimate load of 630 lb (2,800 N), the lower pultruded angle delaminated, resulting in a load drop to 536 lb. Up to this point, no adhesive failure was observed. Loading was continued and the load was increased up to 604 lb (2,685 N). At this load, the lower pultruded angle delaminated heavily. As a result, the load was dropped and the test was stopped.

This type of connection was a typical moment connection, but no moment–rotation (M/Θ) curve was reported. However, the authors calculated the vertical or frame stiffness (the slope of the P/δ curve) as 6,050 lb/in. This was translated to 280,000 lb/rad (1,245 kN/rad) by multiplying the frame vertical stiffness by the moment arm of 46 in. ($P/\Theta = \{P/(\delta/l)\} = Pl/\delta$). It should be noted that the deflection was measured at 46 in. (1.17 m) from the column face. In this case, the LVDT was measuring the total deflection, which included:

1. Bending deflection of the beam member
2. Shear deformation effect
3. The relative rotation between the beam member (free to rotate), and the restrained column (attached to the reaction wall)

So, determining the relative rotation was not a simple conversion of the vertical deflection. For that reason, precise measurements for the relative rotational angle would have provided better understanding to the joint rotational stiffness. Assuming a simple conversion, one can calculate the approximate rotational stiffnes k_{approx} as:

$$k_{approx} = \frac{Pl^2}{\delta_f} \tag{7-12}$$

where
P = applied load
l = moment arm
δ_f = frame vertical deflection.

Using Eq. 7-12, we can calculate the approximate value for the connection rotational stiffness as 12,888 kip-in./rad (1,456 kN-m/rad). This value is slightly higher than the initial rotational stiffness reported by Bass

and Mottram (1994) and discussed earlier, for the connection detail DTLmj (1,320 kN-m/rad).

Based on the results of the first specimen test, modification was introduced in a second similar bonded connection detail. As mentioned earlier, it was observed that the premature local delamination failure of the bottom-seated angle was the major factor in determining both the strength and stiffness of connection specimen 1. For that reason, two stiffening FRP angles were added to the bottom portion of the connection, as shown in Fig. 7-101. Note that the location of the additional angles was opposite to the one used in the Bass and Mottram DTLmj connection detail. However, the addition of the reinforcing angles in both cases was an effort to overcome the low stiffness of the pultruded angles due to the wrong fiber architecture (fibers were perpendicular to the load path). Essentially, the addition of these angles was to increase the stiffness by increasing the thickness of the "unreinforced" plastic section. The same delamination mode of failure did occur to the lower angle but at a higher load of 1,067 lb (4,750 N) as compared to 600-lb load of specimen 1. At a load of 1,169 lb (6,200 N), the reinforcing angles at the bottom suffered from heavy delamination and adhesive failure. As a result, the load was dropped and the test was stopped. The vertical frame stiffness was 7,010 lb/in. 325,000 lb/rad (1,450 kN/rad). This can be approximately converted to a rotational stiffness of 14,950 kip-in./rad (1,676 kN-m/rad). This is about a 16.5% increase in the stiffness and an 86% increase in the ultimate load-carrying capacity of the connection. Table 7-16 summarizes the findings of this study.

Bank et al. (1994) extended the work initiated by Bank and Mosallam in 1990. In this program, three connection details were designed and developed. A total of five full-scale quasi-static tests were performed to evaluate the performance of each new design. All the connections tested were fabricated from 8 in. × 8 in. × 3/8 in. (203.2 mm × 203.2 mm × 9.53 mm) commercially produced unidirectional E-glass/vinylester H-

Table 7-16. Summary of Results, Sanders et al.

Detail	Rotational Stiffness[a] [kip-in./rad (kN-m/rad)]	Frame Vertical Stiffness [kip-in. (kN-m)]	Ultimate Load [kip (kN)]	Ultimate Moment [kip-in. (kN-m)]	Ultimate Displacement (mm)
Specimen 1	12,888 (1,456)	6 (1,052)	0.63 (2.8)	28.98	0.25 (6.4)
Specimen 2	14,950 (1,676)	7 (1,227)	1.169 (5.2)	53.8	0.3 7-6)

[a]Approximate values for rotational stiffness were obtained using Eq. 7-12.
Source: Sanders et al. (1996).

profiles manufactured by Creative Pultrusions, Inc. The test setup followed the earlier work performed by Mosallam (1990) and Bank et al. (1992; 1994).

7.5.19 Multicell Molded Connector Detail

A hand-fabricated E-glass/polyester connecting element was fabricated using hand lay-up. The connector was composed of three separate parts: a square and two triangles. The three parts were then connected together to produce the multicell connector. The beam and the column pultruded members were connected together using two connectors placed at the top and at the bottom of the beam flanges.

A total of eight 3/4 in. pultruded threaded rods and molded square nuts were used to connect the beam to the pultruded column. The threaded rods were extended through the depth of the beam and column H-section as a prestressing element, as recommended by Mosallam (1994b). In addition, pultruded stiffener plates were placed between the flanges of both the column and the beam open-web sections. These stiffener plates were bonded to the flanges and the webs of both the column and beam sections. This stiffening detail was identical to those used in steel connections using welded steel plates. However, in the current detail, a very small adhesive surface area was available. In addition, the epoxy was subjected to not only shear but also tensile and compressive stresses. For these reasons, *these details are not recommended*. This connection detail is shown in Fig. 7-102.

As described by the authors, this connection detail was "massive" as compared to three connection details reported earlier by Bank et al. (1994).
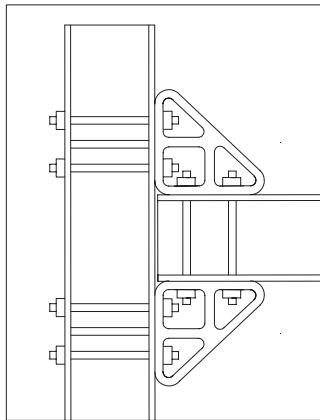
Figure 7-102. Details of multicell molded connection details.
Source: Bank et al. (1994).

During the test, no failure was observed in the multicell connectors. However, local failure was due to damage of the FRP threaded rods and nuts. The pultruded threaded rods failed by "threaded stripping or shaving" and by bending failure in the connection zone. This typical mode of premature failure of FRP pultruded threaded rods was observed during other research investigations (e.g., Mosallam 1994b; 1995a; 1995b; 1995c; 1995e; 1996a; 1996b; 1999). Due to use of the prestressing threaded rods/nuts system, no failure of the pultruded open-web beam or column was observed. Adhesive local failure to one of the bonded FRP plates occurred. As expected, the connection failed at a higher moment of approximately 270 kip-in. (30.5 kN-m), which was 100 kip-in. (11.30 kN-m) higher than the slotted T-connection detail previously reported by Bank et al. (1994).

7.5.20 Back-to-Back 6 in. (152.4 mm) Pultruded H-Section

This connection detail was constructed using two pieces of 6 in. H-sections that were cut at 45 degrees with respect to the beam axis (refer to Fig. 7-103). The two pieces were then bonded back-to-back using EPON 828 epoxy adhesives (currently produced by Hexion Specialty Chemicals, Inc.) to form a right-angle "brace" as shown in Fig. 7-104. The two bonded pieces were attached to the 8 in. (203.2 mm) H-beam and column flanges using two 3/4 in. (19 mm) FRP treaded rods and FRP molded square nuts at each side of the connection. As shown in Fig. 7-103, the fiber orientation
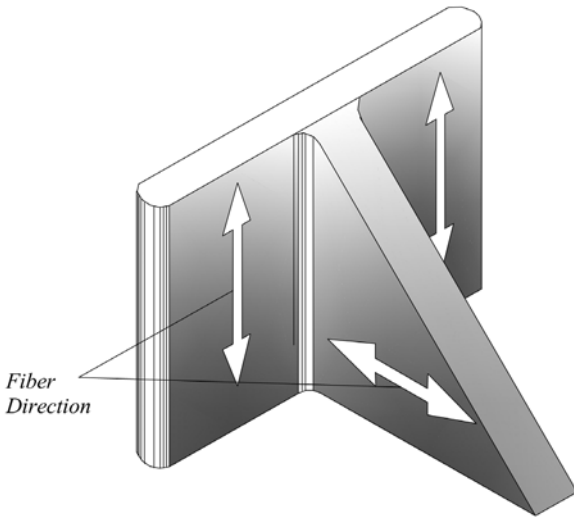
Figure 7-103. 6 in. H-sections cut at 45 degrees with respect to the beam axis. Source: Bank et al. (1994).
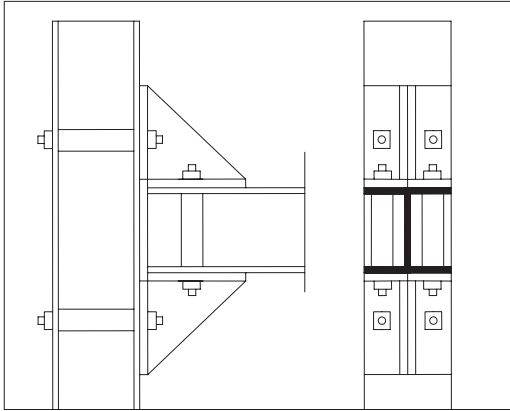
Figure 7-104. Back-to-back 6 in. brace connection detail.
Source: Bank et al. (1994)

of these pieces was not optimum for the connection load path. The connection specimen was subjected to a similar loading regime. It is clear from Fig. 7-104 that the lack of fiber continuity between the flange and the web of the right angle H-profile piece contributed to the development of this premature local failure. Test results indicated that this detail performed very poorly, and the ultimate mode of failure was due to through-the-thickness tensile failure of the wide flange section used to construct the right brace, as shown in Fig. 7-103. The ultimate moment capacity of this connection was only about 14% (40 kip-in.) as compared to the multicell connection detail described earlier.

7.5.21 Back-to-Back 8 in. (203.2 mm) Pultruded H-Section

This connection detail is identical to the previous back-to-back 6 in. detail except that the thickness of the pieces was 8 in. (203.2 mm) instead of 6 in. (152.4 mm). In this case, and due to the larger available area for the placement of four bolts [instead of two bolts in the case of the 6 in. (152.4 mm) version], added stiffness was observed. As expected, a similar ultimate mode of failure occurred. However, and due to the increase of both the thickness of the connecting pieces and the increase in the number of threaded rods and nuts, this detail was able to carry slightly more load [75 kip-in. (8.47 kN-m)]. The local failure was in the top brace subjected to tension. At the compression side, the FRP brace also showed signs of local failure and contributed in the overall poor performance of this detail.

7.5.22 6 in. × 1/2 in. (152.4 mm × 12.7 mm) Wrapped Angle Connection

Figure 7-105 shows the details of this connection specimen. The connecting elements were constructed by wrapping a unidirectional E-glass/
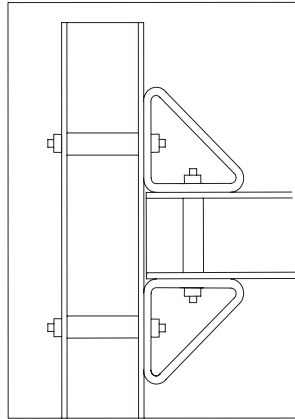
Figure 7-105. Wrapped angle detail.
Source: Bank et al. (1994).

vinlyester pultruded 6 in. × 1/2 in. (152.4 mm × 12.7 mm) equal-leg angle with two layers of fabric mat (Fabmat 2415). In this case, the open-web pultruded angles were converted to a closed thin section with diagonal fibers following the load path. These closed section angles were connected to the flanges of the H-beam and column using 3/4 in. (19 mm) pultruded threaded rods and molded square nuts at each side of the joint. The failure of this detail occurred in two interrelated stages. Initially, and under a relatively low load level, the diagonal membrane of the bottom (compression) wrapped angle buckled locally. This can be attributed to the stiffness mismatch between the "thicker" pultruded angle with fibers running in the wrong direction and the "thinner" membrane wrapped around the angle with fibers following the load path. In this regime, and as the load increased, excessive deformation occurred to the pultruded angle (closing mode) and axial forces developed at the ends of the thin-walled diagonal membrane, causing it to buckle. It is expected that this initial mode of failure would be avoided by increasing the thickness of the wrap material and by ensuring complete adhesion between the wrapping materials and the pultruded angle skin.

Also, due to the limited area for bolting, only two bolts were used, which allowed for more flexibility to the seated wrapped member. In this case, combining both bolts and adhesives may delay the initial local failure and improve the overall performance of this innovative and simple connection detail. As a result of the initial local buckling mode of failure, the top (tension) brace was activated and performed well, reaching an ultimate load of 100 kip-in. (11.3 kN-m) with a large plastic rotation. The ultimate failure was due to the failure of threaded rods connecting the top flange of the beam to the inner flange of the column, as shown in Fig. 7-106. Compared to connection detail Type iii tested by Bank et al. (1994),

the stiffness and the strength of this wrapped angle detail were slightly less. However, the Type iii connection detail was more complicated and composed of several parts. Table 7-17 summarizes the results obtained from the different details.

7.5.23 Impact of Shear on Pultruded Beam-Column Connections

Lopez-Anido et al. (1999) investigated the behavior of shear beam-column pultruded connection details. This is one of the more common connection details used by the industry, where two clip angles are used to attach the webs of the beams to the flanges of the pultruded columns (Fig. 7-107). The test program focused on examining the structural behavior of beam-column connections using pultruded FRP angles transversely reinforced with multi-axial stitched fabrics. The beam and column profiles used in this program were pultruded by Creative Pultrusions, Inc. Both the beams and columns were 8 in. × 8 in. × 3/8 in. (203.2 mm × 203.2 mm × 9.52 mm) E-glass/vinlyester pultruded H-profiles. The clip angles were
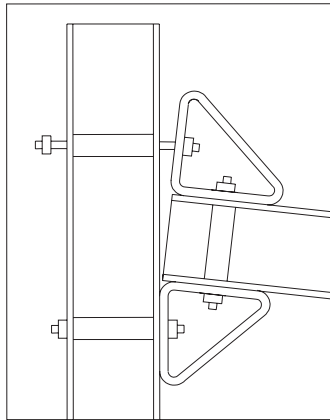
Figure 7-106. Local failure of 6 in. × 1/2 in. wrapped angle connection detail. Source: Bank et al. (1994).

Table 7-17. Summary of Results

Detail	Initial Stiffness (kip-in./rad)	Ultimate Moment (kip-in.)	Ultimate Rotation (rad)
Multicell	5,950	270	0.044
6 in., 2 bolts	1,910	40	0.019
8 in., 4 bolts	10,400	75	0.035
6 in. wrapped angle	600	100	0.086
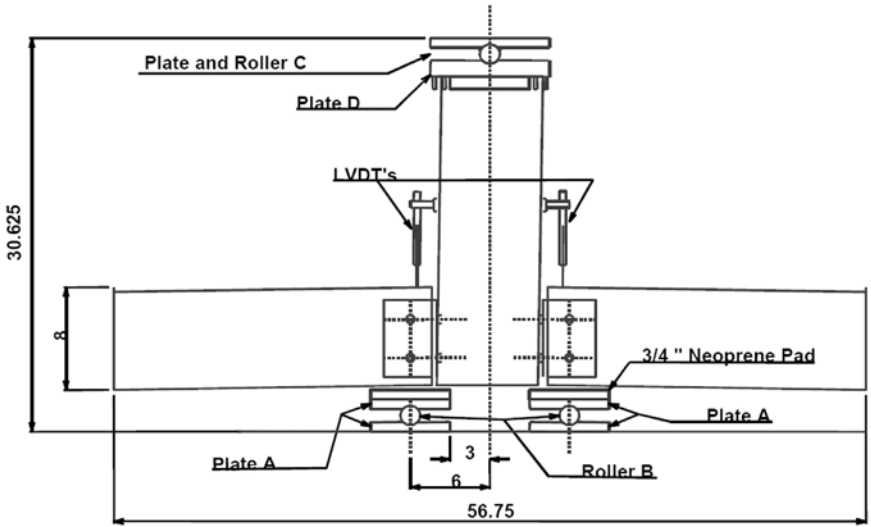
Figure 7-107. Details and dimensions of the PFRP shear connection specimen. Source: Lopez-Anido et al. (1999).

cut from 4 in. × 4 in. × 3/8 in. (101.6 mm × 101.6 mm × 9.52 mm) equal-leg pultruded angle profiles with a length of 6 in. (152 mm). All mechanical fasteners were ASTM 325 Grade 5 coarse-threaded bolts with a 1½ in. (12.7 mm) shoulder length [proof strength 75 ksi (517 MPa)]. The washers were Grade 8 hardened, oversized washers (2.5 times the hole diameter). The two-part epoxy adhesive used in this study was Magnobond 56 (manufactured by Magnolia Plastics Inc.) with a pot life of 1.5 h and a cure time of 48 h. Three variables were investigated in this study: (1) bolt diameters 1/2 in. (12.7 mm) and 5/8 in. (15.9 mm); (2) torque pressure (37.5% and 75% of bolt proof load); and (3) combined connectivity (bolted-only, and combined bolted and adhesively bonded details). The different torque values and corresponding clamping pressures used in this study are presented in Table 7-18. The listed torque values were selected such that the crushing strength of the pultruded materials was not exceeded.

7.5.24 Clip Angles Bearing Tests

Initially, four individual bearing tests were performed on the multiaxial-reinforced FRP pultruded clip angles. The bearing tests were conducted in the lengthwise direction. In these tests, a compression load was applied to a central steel plate connected to a pair of clip angles. Figure 7-108 shows the relation between the bearing stress and the relative bearing deformation (ratio of deformation/hole diameter). The test setup

Table 7-18. Torque and Clamping Pressure Used in the Connections

Bolt [dia - pitch]	Low Torque: 37.5% of Bolt Proof Load		High Torque: 75% of Bolt Proof Load	
	Torque [ft-lb (N-m)]	Clamping Pressure [psi (MPa)]	Torque [ft-lb (N-m)]	Clamping Pressure [psi (MPa)]
1/2 in.—13	29 (39)	4,740 (32.7)	57 (77)	9,316 (64.2)
5/8 in.—11	57 (77)	4,719 (32.5)	113 (153)	9,356 (64.5)

Source: Lopez-Anido et al. (1999).
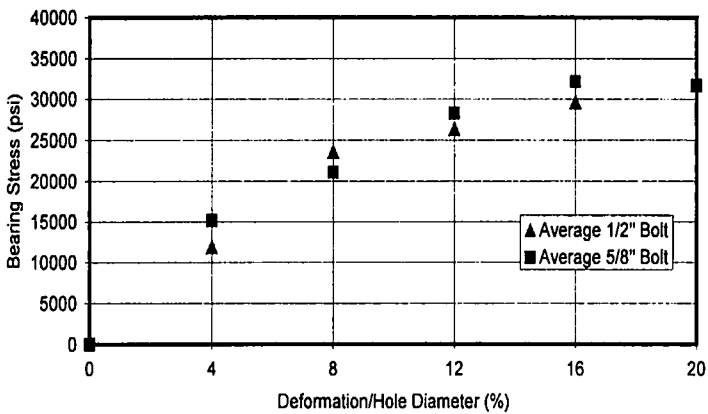
Figure 7-108. Bearing stress vs. relative bearing deformation.
Source: Lopez-Anido et al. (1999).

for all connections is shown in Fig. 7-109. As shown in the figure, a double-cantilever configuration was used to evaluate the shear strength of both bolted and combined connection details.

According to Lopez-Anido et al. (1999), this test setup was designed to minimize the load eccentricity in the beam-column shear connection. Two hinge supports were placed directly below the bolt line of the clip angles of the beam side. As shown in Fig. 7-107, identical hinge supports were placed at the top of the column beneath the load cell. The load was applied at the column top and the vertical displacement was measured using two LVDTs clamped on both sides of the column center flanges. This setup is somewhat impractical and does not reflect the actual loading conditions expected during service. Placing the hinges at a distance of 2 in. (50.8 mm) from the column face [6 in. (152.4 mm) from the column centerline] will prohibit the rotational freedom of the connection, which in reality will never occur. Another observation is that, since the test ignored
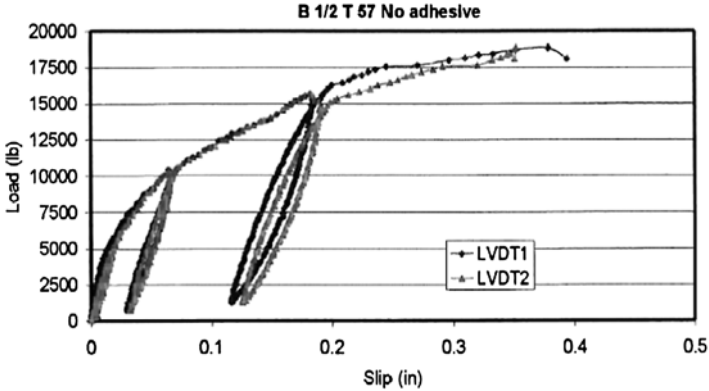
Figure 7-109. Load–slip curves for bolted-only connection detail.
Source: Lopez-Anido et al. (1999).

the rotational capacity of the connection and the load was applied at a distance of 2 in. (50.8 mm) from the column face, there was justification for using longer beam pieces [only 6 in. to 8 in. (152.4 mm to 203.2 mm) cantilever pieces would have been satisfactory]. Designating this detail as a shear connection does not imply that, during service, the connection will not undergo a large rotation. In contrast, these connections are flexible and the resulting rotation will affect the overall behavior ultimate failure mode of these joints (J. T. Mottram, personal communication via e-mail, 1999).

Each connection detail was subjected to several loading and loading cycles. For bolted-only connection details, test results indicated that the common mode of failure was delamination of the pultruded angle in combination with bearing damage in the beam web. A prying action was also observed and resulted in the clip angles being flattened or pulled away from the column flanges. Test results for bolted-only connection details also indicated that for 1/2 in. (12.7 mm)-diameter steel bolts, increasing the bolt torque from 29 ft-lb (39.3 N-m) to 57 ft-lb (77.24 N-m) resulted in an increase of 10% of the connection strength. However, for 5/8 in. (15.88 mm)-diameter steel bolts, increasing the bolt torque from 57 ft-lb (15.88 N-m) to 113 ft-lb (153.12 N-m) contributed to a slight increase in the connection strength (about 4%). It should be noted that tightening the bolts to a high torque increases the possibility of increasing through-the-thickness creep. Over time, this type of creep will contribute to a decrease in the original torque. Mottram (1999) suggested that the design of these connections should be based on connection properties when bolts are finger-tight only. It should be noted that for a shear force of 8,093 lbs (36 kN), the moment is 5.472 kN-m [based on a 6 in. (0.1524 m) lever arm to the column centerline, or 1.82 kN-m based on a 2 in. (0.0508 m)

to the column face] (Mottram (1999). These maximum moment values are similar to or greater than those obtained by Mottram in earlier web-cleated connections with a 1-m lever arm (in this case, the effect of the shear force was neglected). Mottram (1999) confirmed that the presence of the applied moment will affect the connection mode of failure. Figure 7-109 shows the loading and loading versus slip curves for bolted-only connection detail. The average load–slip curves for each bolted-only connection detail for load increments up to 8,250 lbs (36.7 kN) are shown in Fig. 7-110.

For the combined (bolted/bonded) connection detail tested by Lopez-Anido et al. (1999), it was observed that no appreciable increase in the connection ultimate strength was gained by adding the adhesives. This finding is somewhat different than that observed and reported by Mosallam in numerous moment connection tests (1993; 1994; 1999). The average strength gain reported by Mosallam ranged from 40% to 50%. It was also observed for this type of connection detail that the mode of failure did not depend on the steel bolt diameter. For example, a slight average gain of 300 lb (1.3 kN) was achieved when using 5/8 in. bolts instead 1/2 in. steel bolts. Also, it was observed that varying the torque pressure did not affect the mode of failure. The average maximum slip for bonded connection detail was 0.42 in. (10.70 mm) while for the combined detail; the slip was reduced to only 0.1 in. (2.5 mm). This translates to about a 300% increase of the connection slip resistance. The average load–slip curves for each combined connection detail for load increments up to 8,250 lb (36.7 kN) as shown in Fig. 7-111. It was also concluded that the bearing strength of FRP pultruded materials has little effect on the ultimate
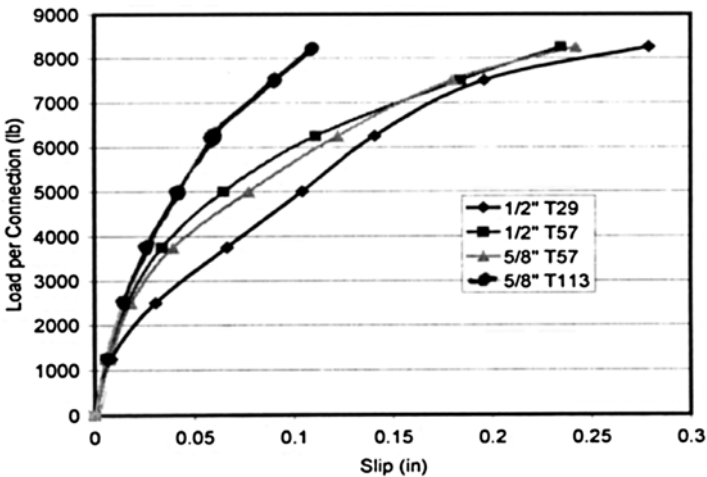
Figure 7-110. Load–slip curves for different bolted-only connection details. Source: Lopez-Anido et al. (1999).
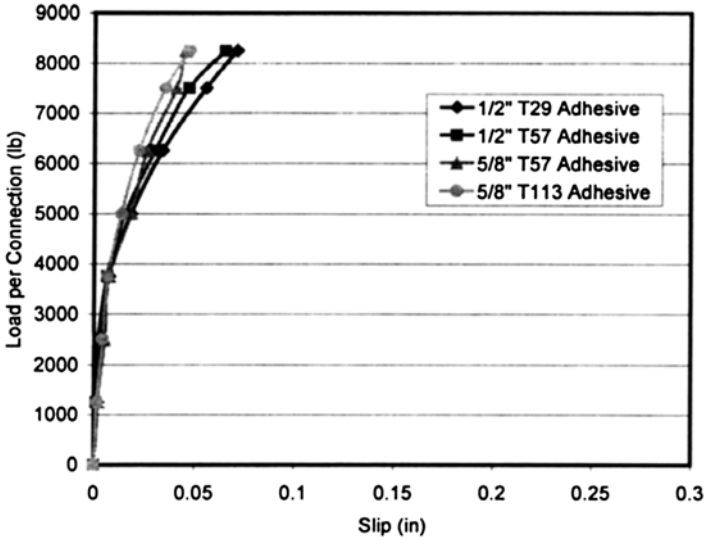
Figure 7-111. Load–slip curves for different combined connection details.
Source: Lopez-Anido et al. (1999).

strength of steel-like connection details since local delamination failures usually occurred prior to achieving the full bearing strength of the pultruded composite materials.

Lopez-Anido et al. (1999) recommended the use of epoxy adhesives only for slip-critical connections. However, based on the research conducted by others (e.g. Mosallam 1993–1999) and Sanders et al. (1996), this recommendation is questionable. It should be noted that, as described earlier, Lopez-Anido et al. (1999) ignored the fact that the bending exposure is unavoidable and that the adhesives would help increase both the shear and the rotational stiffness and strength of these connections in addition to providing an even stress distribution at the bondline. Lopez-Anido et al. (1999) also concluded that the use of multi-axial fabric reinforcements prevented splitting or shear separation of mechanically fastened connection details.

7.5.25 Tension, Moment–Rotation and Uplift on Pultruded Frame Connections

Turvey (1998) conducted tension, moment–rotation, and uplift full-scale tests on frame connections for commercially produced pultruded composite frame structures constructed from H-profiles. This work is considered one of the most comprehensive research programs in the area of pultruded moment frame connections under quasi-static loading conditions.

- *Materials Characterization Tests:* A total of 29 coupon specimens cut from the webs and flanges of EXTREN (product of the Strongwell Company) pultruded profiles were tested under both tension and compression. This part of an experimental program is always necessary to verify the data supplied by the pultruders on the mechanical properties of the sections. Results of this study showed that the pultruder's information was conservative.
- *Bolted Single-Bolt, Double-Lap Tension Joint Tests:* A total of 63 single-bolt, double-lap tension joint tests were conducted under this program. The joint specimens were cut from 4 in. × 4 in. × 1/4 in. (102 mm × 102 mm × 6.4 mm) and 8 in. × 8 in. × 3/8 in. (203 mm × 203 mm × 9.5 mm) pultruded H-profiles (parallel to the pultrusion axis). The summary of this work was described in Chapter 2 of this manual.
- *Beam-to-Column Connection Tests:* In this part of the study, two series of bolted beam-to-column connection tests were performed on different sizes of commercially produced unidirectional H-profile specimens. Two types of connecting elements were used in these tests. The first connecting elements were composed of pultruded unidirectional angles, while the other tests were conducted on connections with a combination of pultruded angles, pultruded plates, and special resin-injected composite elements. Two test rigs were employed in this program. Figures 7-112 and 7-113 show the two test setups for evaluating the structural behavior of interior beam-to-column connections. In this program, a total of seven
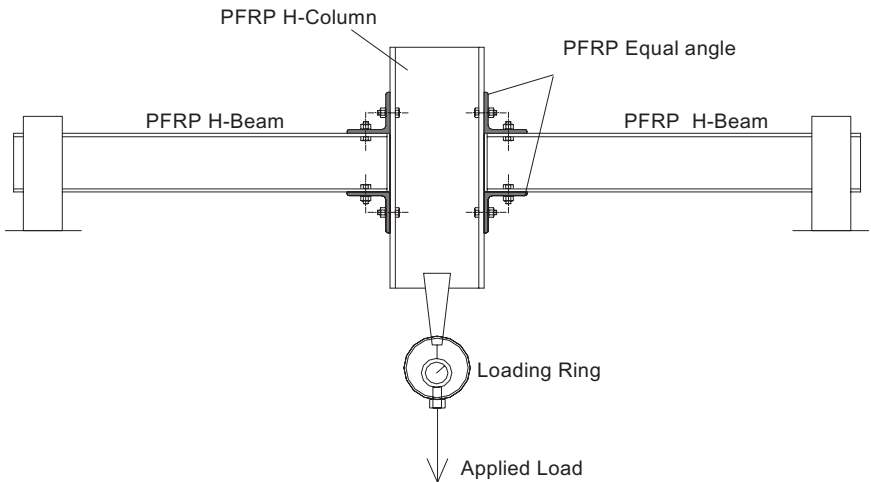
Figure 7-112. Turvey's simply supported beam test rig.
Source: Turvey (1998).

conventional beam-to-column pultruded connection specimens were evaluated, three of which with small-size H-profiles were used and the specimens were tested in a quasi-static mode, as shown in Fig. 7-112. Two of the connections tested were web cleat connections, while the third was detailed to have both web and flange cleats. The mechanical fasteners used in this study were 0.39 in. (10 mm) mild steel bolts in close-tolerance holes. All bolts were torqued to 22.14 ft-lb (30 N-m). The large specimens were tested in the test rig shown in Fig. 7-113. In addition, a total of six "unconventional" beam-to-column details were also evaluated under quasi-static loading conditions. Figure 7-114 shows the cruciform
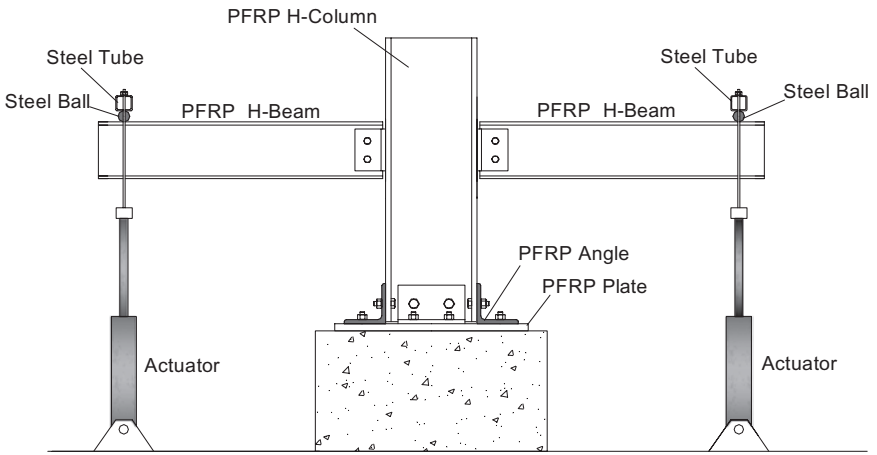
Figure 7-113. Turvey's subframe test rig (double cantilever mode).
Source: Turvey (1998).
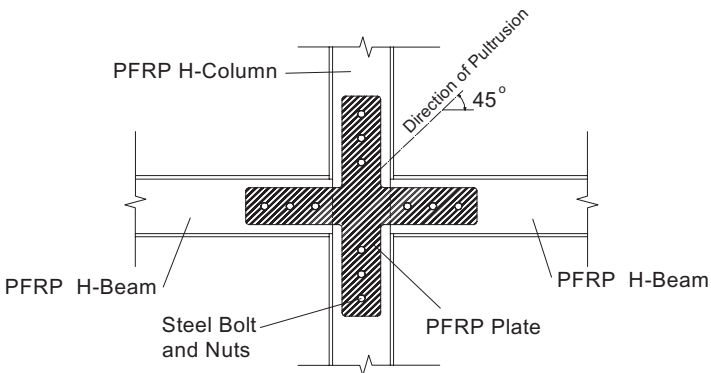
Figure 7-114. Turvey's cruciform beam-to-column detail.
Source: Turvey (1998).

beam-to-column detail. As shown in this figure, the pultruded plates were bolted to the column and beam webs using steel bolts. The plates were cut so that the major reinforcements (pultrusion axis) were at ±45 degrees with respect to beam and column centerlines. It was reported that fabricating this type of detail is cumbersome and that the initial rotational stiffness (k_i) of the connection was somewhat lower than the conventional cleat angle connection detail. In addition, two exterior beam-to-column connections were tested in this program. Figure 7-115 shows the test setup for the exterior PFRP connection evaluation.

• *Beam-to-Base Connection Tests:* The beam-to-base connection tests conducted by Turvey (1998) are considered to be the second published data on beam-to-base connection evaluation (the first pilot tests were reported by Morsi et al. in 1984, as discussed earlier in this chapter). In this pilot program, two moment–rotation tests were performed on PFRP web and flange cleat specimens, as shown in Fig. 7-116. For small-size pultruded H-profiles, both minor axis details and major axis details were tested. For larger H-profiles, two major axis tests were performed on web cleat and web and flange cleat details. A third minor axis test was also performed. In addition, four uplift tests were conducted on both web cleats and web and flange cleats. The test setup for this group is shown in Fig. 7-117. An analytical model was developed and was verified by the experimental results. Closed-form formulae were also derived which can possibly be used in design of pultruded frame structure connections.
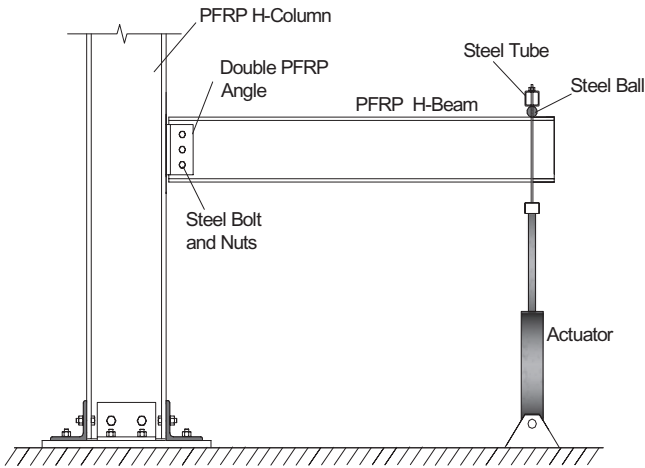
Figure 7-115. Turvey's subframe test rig for exterior connections.
Source: Turvey (1998).
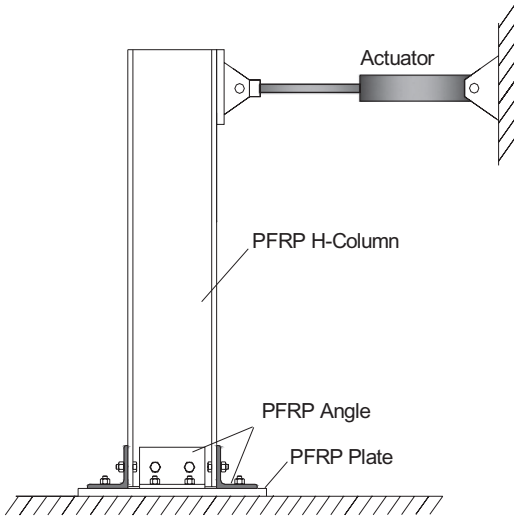
Figure 7-116. *Turvey's test rig for moment–rotation base-to-column connection.*
Source: *Turvey (1998).*
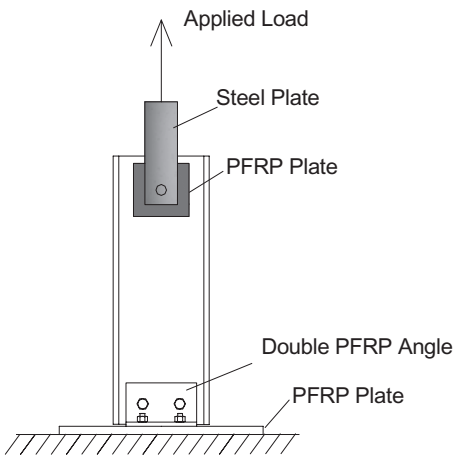
Figure 7-117. *Turvey's test rig for uplift base-to-column connections.*
Source: *Turvey (1998).*

7.5.26 Re-examination of Tension, Moment–Rotation, and Uplift

In a re-examination of the work of Turvey, Mosallam et al. (2010) examined three commercially produced PFRP unidirectional E-glass/polyester connection sections in a traditional column-to-base test program. The first specimen consisted of a 6 in. × 6 in. × 3/8 in. PFRP H-profile column that

was connected to a steel base with the assistance of 4 in. × 4 in. × 3/8 in. PFRP L profiles using 3/8 regular steel bolts, as shown in Figs. 7-118, 7-121, 7-122, and 7-123. In the second specimen, the column was once again a 6 in. × 6 in. × 3/8 in. PFRP H-profile connected to the steel base by way of 4 in. × 4 in. × 3/8 in. PFRP L-profiles that 3/8 in. regular steel bolts that passed between both flanges of the column. Images of the specimen are provided in Figs. 7-119 and 7-126. Finally, the third connection specimen consisted of 6 in. × 6 in. × 3/8 in. PFRP H-profile column that was connected to a steel base by way of two 5 in. × 5 in. × 3/8 in. steel L- profile using 3/8 regular steel bolts, as shown in Figs. 7-120 and 7-129.
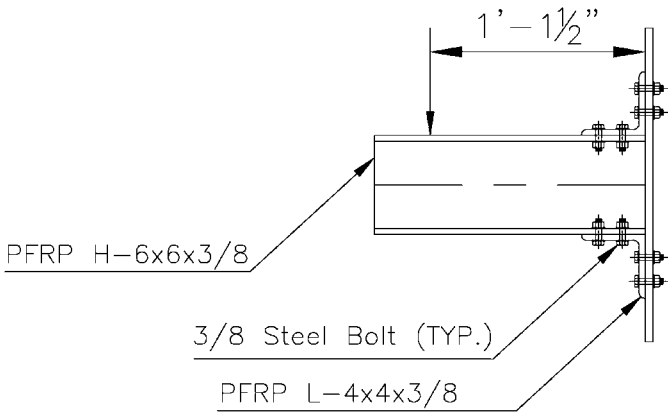
Figure 7-118. Schematic setup of base connection 1.
Source: Mosallam et al. (2010a).
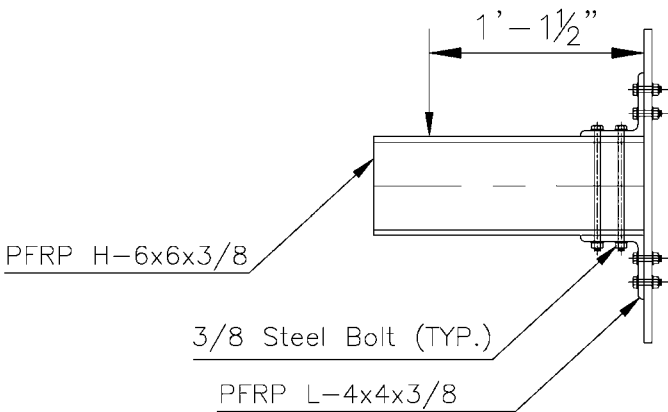
Figure 7-119. Schematic setup of base connection 2.
Source: Mosallam et al. (2010a).
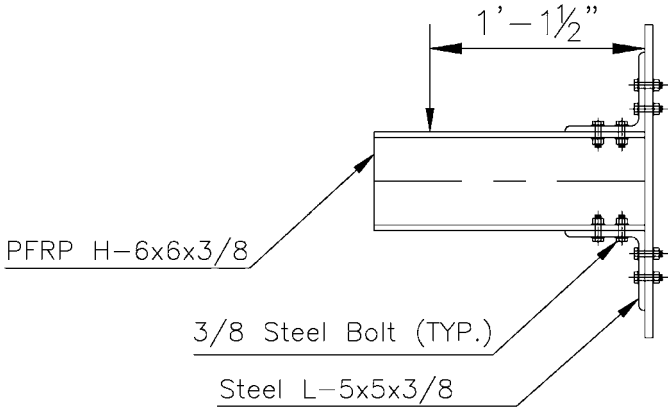
Figure 7-120. Schematic setup of base connection 3.
Source: Mosallam et al. (2010a).
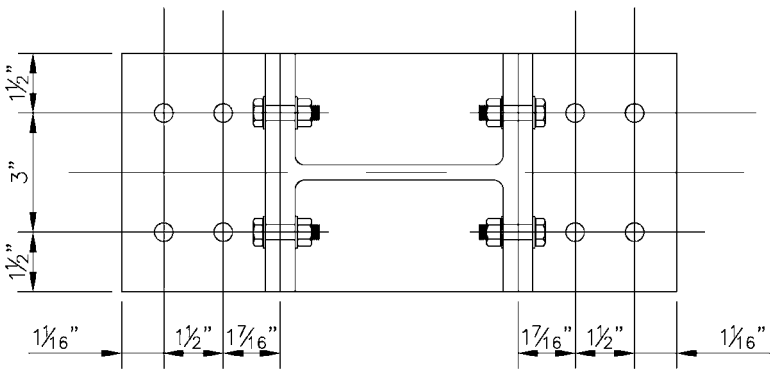
Figure 7-121. Schematic typical bolts spaces.
Source: Mosallam et al. (2010a).

7.5.26.1 Test Description.   The test program was undertaken in the Structural Engineering Testing Hall on the campus of the University of California, Irvine. The load was monotonic up to failure. For all specimens, the load was applied using a calibrated MTS 55-kip servo-hydraulic actuator. Similarly, a calibrated data-acquisition system was used to continuously collect all information including load and displacement. The load was applied at 13.5 in. from the steel base (Figs. 7-118, 7-119, and 7-120).

7.5.26.2 Results.   The main objective of the tests was to generate moment rotation curve (M-θ) for different type of base connections. For
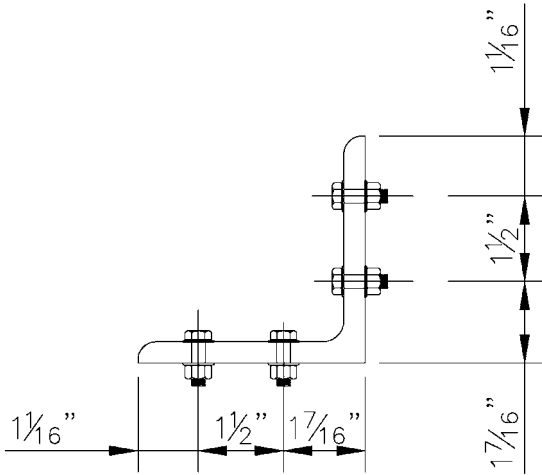
Figure 7-122. Schematic typical angle.
Source: Mosallam et al. (2010a).
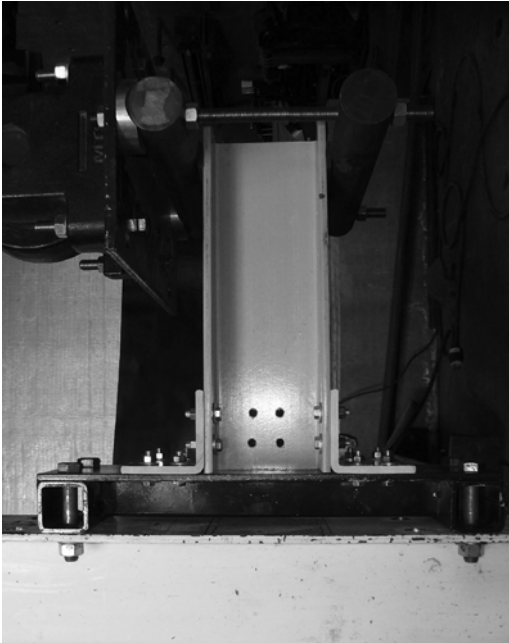
Figure 7-123. Connection 1 test setup.
Source: Mosallam et al. (2010a).
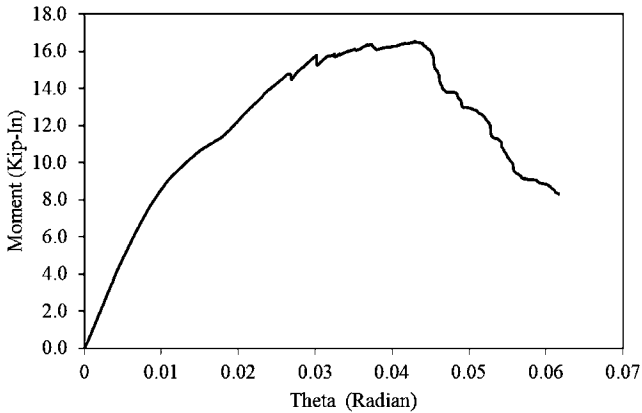
Figure 7-124. Moment-rotation curve for connection 1.
Source: Mosallam et al. (2010a).

the first connection specimen, the load was linear up to a moment equal to 8.0 kip-in. At a rotation equal to 0.0085 radian. After this point, the relationship between moment and rotation remained linear while the slope of the curve and overall stiffness decreased up to moment 16 kip-in. And rotation 0.03 radian. Beyond this point, failure intiated as shown in Fig. 7-124. The failure occured in the top (opening) angle as shown in Fig. 7-125.

For the second connection (Fig. 7-126), the load was linear up to moment 16.5 kip-in. At rotation 0.012 radian. After this point, the relationship between moment and rotation remained linear although the stiffness decreased until moment 20 kip-in. And rotation 0.017 radian. After this final point, failure initiated as shown in Fig. 7-127. The failure occured in the top (opening) angle as shown in Fig. 7-128.

For the third connection (Fig. 7-129), the load was linear up to moment 40 kip-in. and rotation 0.012 radian. Once again, the relationship between moment and rotation remained linear while stiffness decreased. A second inflection point ocurred at moment 120 kip-in. and rotation equal to 0.055 radian. Beyond this pont, failure initiated as shown in Fig. 7-130. The failure occured in steel bolts as shown in Fig. 7-131. Table 7-19 summarizes the initial stiffness for each specimen. Similarly, regression analysis yielded three equations that describe the behavior of each curve. These equations are presented in Table 7-20.

7.5.27 Dynamic Behavior of Pultruded Framed Structures

Ahmadian and Mantena (1996) analyzed and compared the dynamic behavior of pultruded framed structures. In this study, pultruded flat
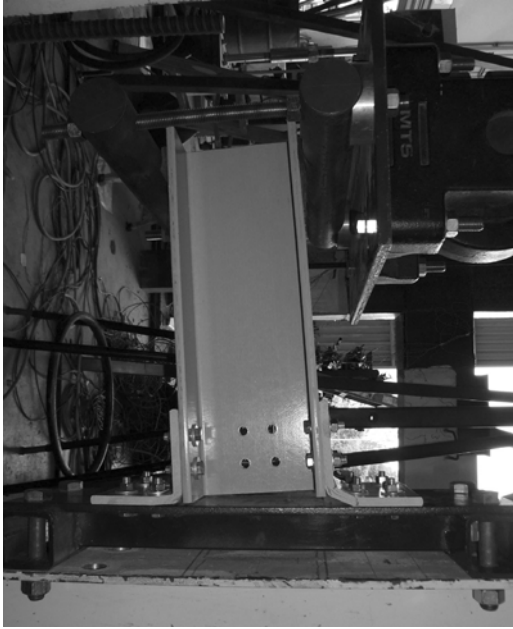
Figure 7-125. Failure of connection 1.
Source: Mosallam et al. (2010a).
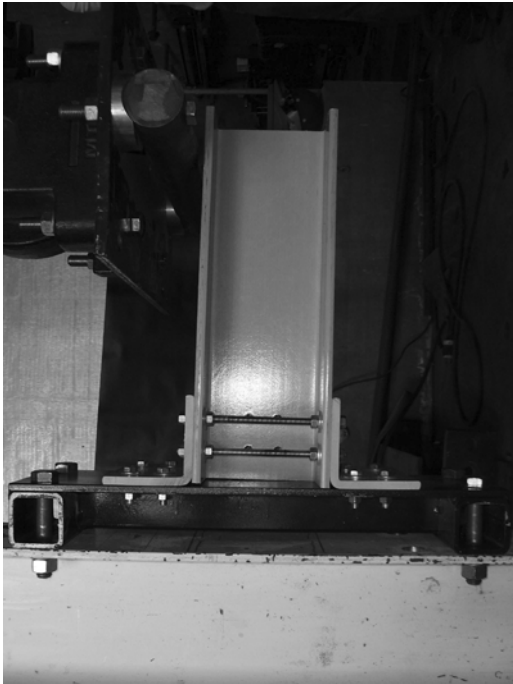
Figure 7-126. Connection 2 test setup.
Source: Mosallam et al. (2010a).
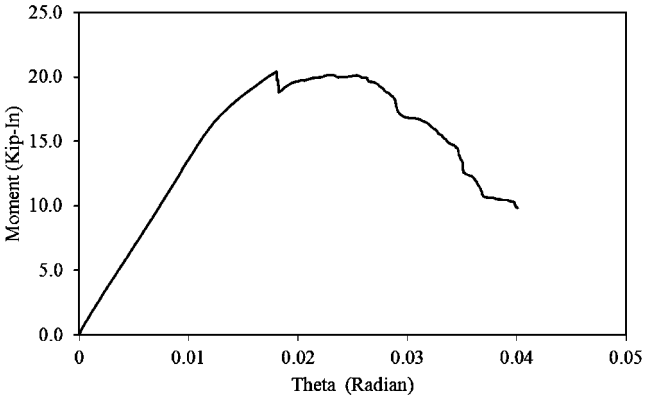
Figure 7-127. Moment-rotation curve for connection 2.
Source: Mosallam et al. (2010a).
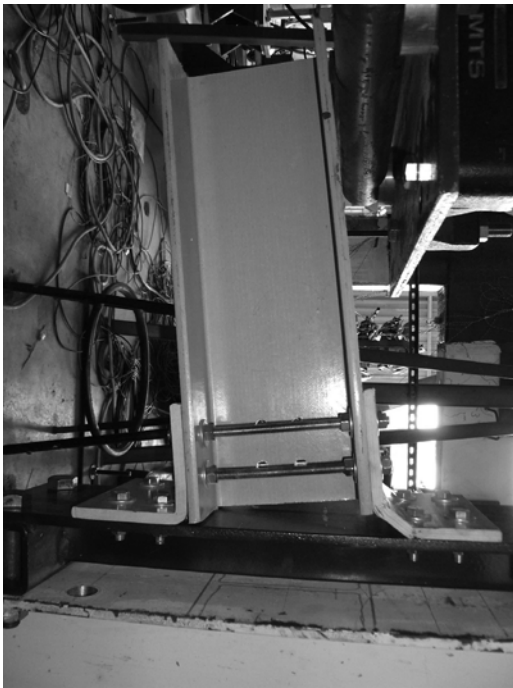
Figure 7-128. Failure of connection 2.
Source: Mosallam et al. (2010a).
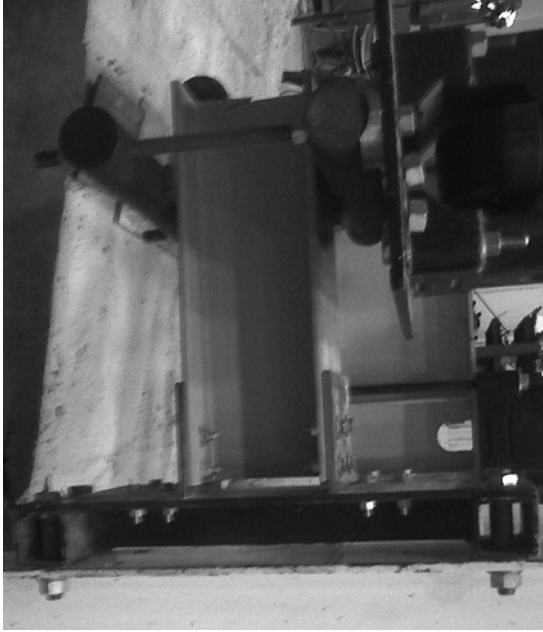
Figure 7-129. Connection 3 test setup.
Source: Mosallam et al. (2010a).
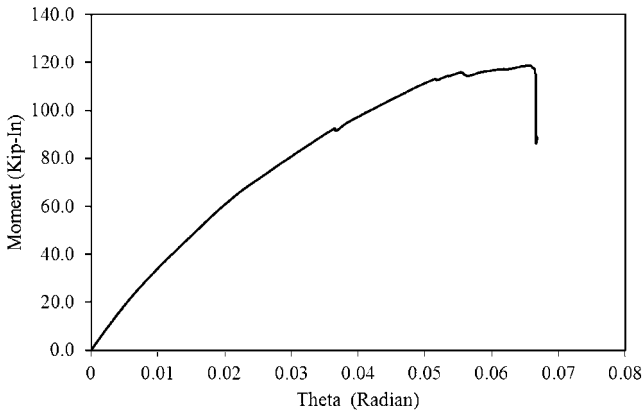
Figure 7-130. Moment-rotation curve for connection 3.
Source: Mosallam et al. (2010a).

beams made of glass/epoxy, graphite/epoxy, and various lay-up combinations of hybrid glass-graphite/epoxy were used to produce high-modulus and lightweight, L-shaped portal frame and other composite material structures. An experimental modal analysis technique was utilized to determine the dynamic properties of the decoupled and mechanically

Figure 7-131. Failure of connection 2.
Source: Mosallam et al. (2010a).

Table 7-19. Initial Rotational Stiffnesses

Connection	First	Second	Third
Intial Stiffness (kip-in./rad)	935	1360	3470

Source: Mosallam et al. (2010).

Table 7-20. Curve Fitting Equations

Specimen	Approximate Polynomial Expression
First Connection	$y = 4E+08x^5 - 6E+07x^4 + 3E+06x^3 - 75{,}558x^2 + 1{,}341.1x$
Second Connection	$y = 3E+07x^4 - 3E+06x^3 + 18{,}340x^2 + 1{,}392.4x$
Third Connection	$y = -26{,}612x^2 + 3{,}532.5x$

Source: Mosallam et al. (2010a).

fastened coupled structures. The structural properties identification process for each of the beam and lumped systems consisted of generating the frequency response functions (FRFs), estimation of natural frequencies, damping, and the associated mode shapes. A measurement chain comprising a dual-channel dynamic signal analyzer, corresponding instruments, and a modal analysis software package was used for identifying the modal parameters. The experimental results demonstrated the applicability and dynamic superiority of structures made with pultruded hybrid composite materials.

7.5.28 Multistory Pultruded Frames

Experimental and analytical results of a recent study on the quasi-static behavior of large-scale multistory pultruded frame structures were reported by Na (2008). Full-scale lateral loading tests on 2-D single-bay, multistory PFRP composite frames, with different brace configurations and different beam-to-column framing connections, were conducted. The overall height of all frames was 22 ft (6.7 m) with girder span of 14 ft (4.26 m). Each frame was composed of three levels with different heights. The bay heights were 10 ft, 8 ft, and 4 ft for the lower, middle, and upper bays, respectively, as shown in Fig. 7-132. No justification for this special geometry and dimensions of the PFRP was provided, but it appears that this was specifically targeting a cooling tower project for a company. Six loading regimes were used to determine the performance of PFRP frames, as shown in Fig. 7-132. However, none of the tests included any gravity loading or cyclic lateral loading regimes.

Several connection details were utilized in this study which were typical "steel-like" details that are still being used by the industry. However, one of the recommendations that was reported by Mosallam (1994b) for extending the threaded rods through the pultruded profiles was adopted to avoid the premature failure that will potentially occur at the web flange junction (refer to Fig. 7-98). Experimental load–displacement curves for different types of connections were developed. However, no moment–rotation curves were provided by the author. It should be also noted that stainless steel angles were used in the details of the examined pultruded frames. A frame analysis method that accounts for the anisotropic nature of PFRP composites was adopted to predict the performance of the tested frames. A comparison between the test results and those obtained from analysis were made and showed reasonable agreement. The results of this study indicated that three major parameters govern the overall lateral performance of the PFRP frames: the effective mechanical material properties of members, the type of beam-to-column connections, and the details and arrangement of diagonal bracings that logically will increase the lateral stiffness of any frame structure subjected to lateral loads.
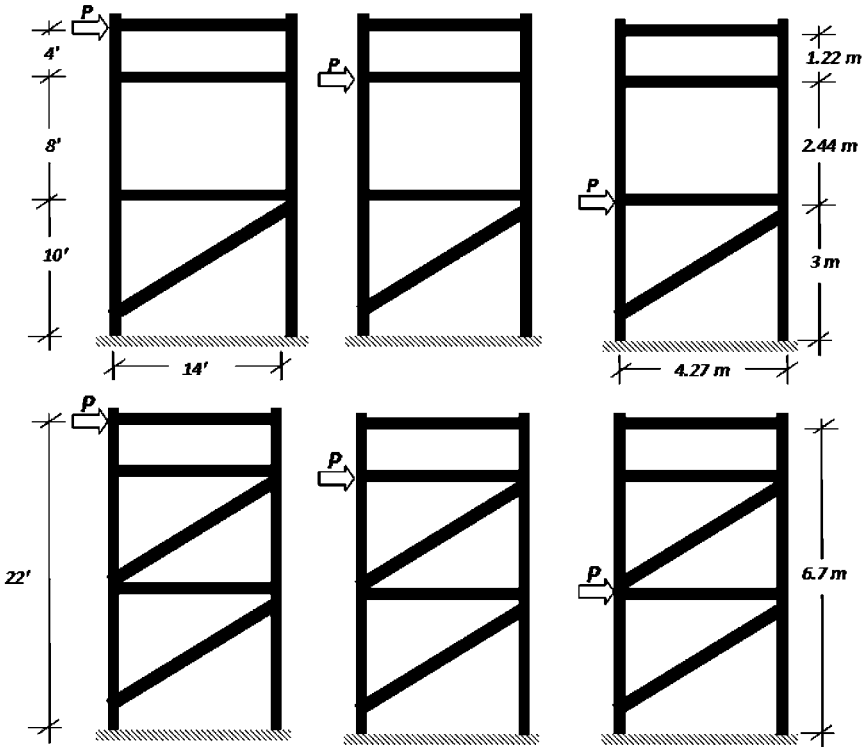
Figure 7-132. Dimensions, configurations, and loading schemes of PFRP 2-D multistory frames.
Source: Na (2008).

7.5.29 The Web-Flange Junction

Understanding and designing in response to micromechanical behavior of the web-flange junction is critical to the successful application of PFRP composite connections. However, as has been previously indicated, there is a dearth of experimental data related to this subject and, accordingly, a limited set of empirical formulations to provide the basis for design. For that reason, Mosallam et al. (2010b, c) initiated a pilot program that examined the rotational and pull-out behavior of web-flange junctions without ignoring the anisotropic and the viscoelastic nature of open-web pultruded composites.

7.5.29.1 Pull-Out Behavior of the Web-Flange Junction.   The first study, Mosallam et al. (2010b), evaluated the axial stiffness of web-flange junctions that affect both the buckling and uniaxial strength of PFRP profiles. In the study, three H-profiles (Fig. 7-133) were tested under both

service and ultimate pull-out loads. Data from the experimental effort included P-δ relations, which were then used to establish design limit-states for the PFRP structures. Figure 7-134 provides a detailed image of the junction between the web and flange of FRP I-beam. As can be seen from the diagram, the area is relatively rich in resin and poor in fibers (matrix-dominated), which represents a critical weak point in the design of the structure.

In the experimental program, a commercially produced PFRP unidirectional E-glass/polyester open-web H-profile was examined. The overall dimensions and details of the profile are presented in Table 7-21. During testing, a uniform pull load was applied on the flange of PFRP profile; however, the location of the pull force varied. In the first series of tests,

Figure 7-133. PFRP profiles and products.
Source: Mosallam et al. (2010b).
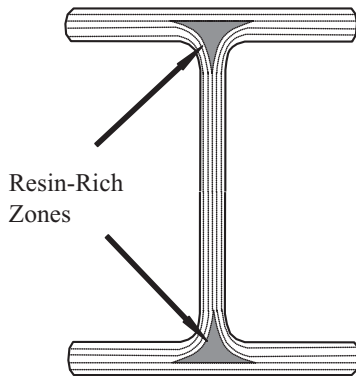
Figure 7-134. Resin-rich zones at web-flange junction of PFRP profile.
Source: Mosallam et al. (2010b).

load was applied at the mid-point of the PFRP specimen, as shown in Fig. 7-135a. Similarly, in the second series of tests, load was applied at a distance of l/4 in. from the longitudinal edge of the specimen, as shown in Fig. 7-135b. For all specimens, the pull load was applied using an MTS 55-kip servo-hydraulic actuator (Figs. 7-136 and 7-137) under a force-controlled loading protocol. Standard peripheral hardware was used to capture load, displacements, and strains.

The main objective of the pullout tests was to observe and define both serviceability and strength limit states of the web/flange junctions. In the case of mid-point loading, the displacement of the H–10 in. × 10 in.

Table 7-21. PFRP H-and L-Profiles Used in the Tests

Profile	Web Length— H in. (mm)	Flange Length— W in. (mm)	Web-Flange Thickness— t in. (mm)
H − 10″ × 10″ × 1/2″	10 (254)	10 (254)	1/2 (12.7)
H − 8″ × 8″ × 3/8″	8 (203.2)	8 (203.2)	3/8 (9.53)
H − 6″ × 6″ × 3/8″	6 (152.4)	6 (152.4)	3/8 (9.53)
L − 6″ × 6″ × 1/2″	6 (152.4)	6 (152.4)	1/2 (12.7)
L − 4″ × 4″ × 3/8″	4 (101.6)	4 (101.6)	3/8 (9.53)

Source: Mosallam et al. (2010b).

a) Mid-point Loading Test Setup

b) Eccentric Loading Test Setup
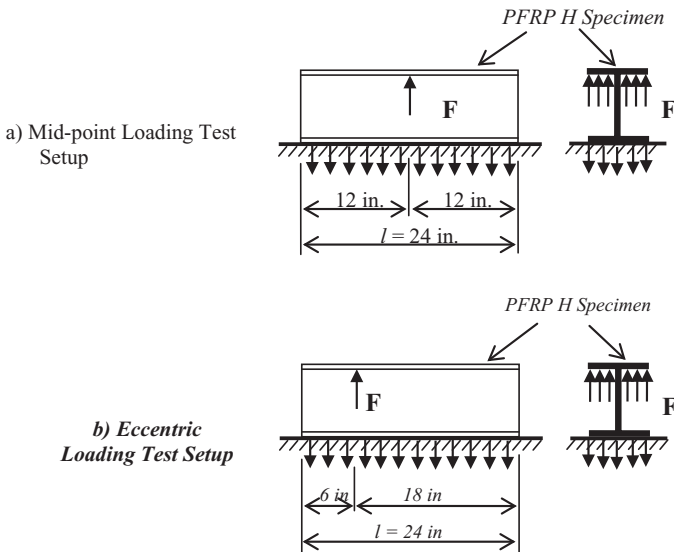
Figure 7-135. Schematic setup of web-flange junction pullout test.
Source: Mosallam et al. (2010b).

× 1/2 in. PFRP specimen increased linearly with increasing load up to an axial displacement of 0.25 in. and a load level of 4.7 kips (20.91 kN). From here, stiffness degradation was observed even though load-displacement behavior followed a near-linear behavior until a 0.42-in. displacement at
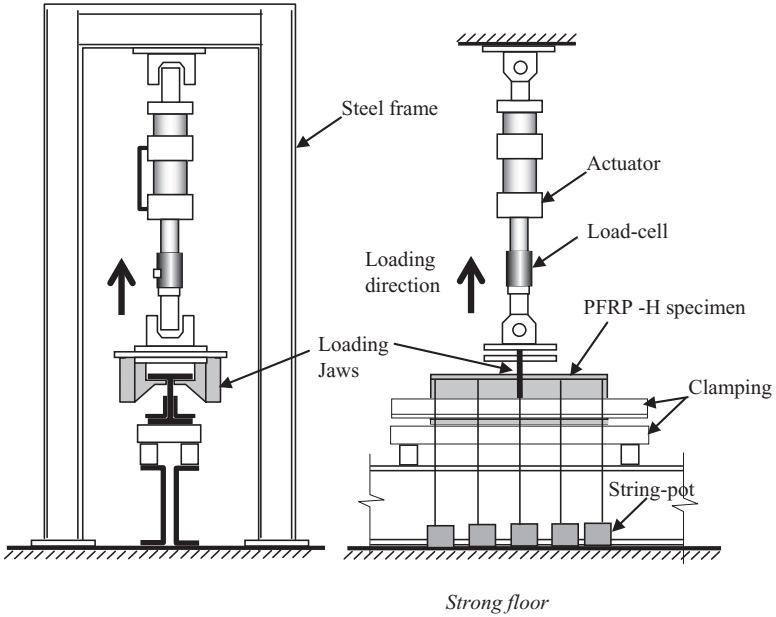
Figure 7-136. Schematic views of pull-out test setup.
Source: Mosallam et al. (2010b).
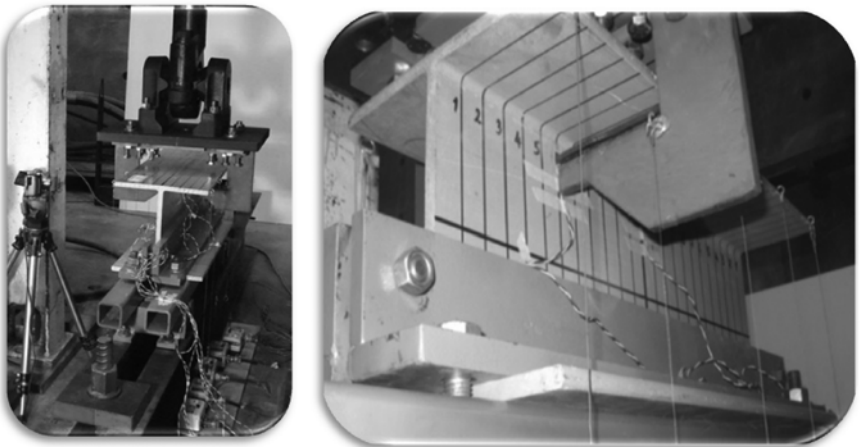
Figure 7-137. Pull-out test setup.
Source: Mosallam et al. (2010b).

an axial load of 5.5 kips. Beyond this point, failure started to occur. Figure 7-138 shows the load-displacement curve for mid-point loaded specimen, while an approximate linearized version of the same curve is shown in Fig. 7-139. Continuing in this vein, smaller specimens produced relatively similar results. In most cases, signs of failure were observed prior to a complete separation of the flange from the web, which usually began at the location of the pull load line and propagated to the rest of the junction length. Results are summarized in Table 7-22.

In the case of eccentric loading, the H–10 in. × 10 in. × 1/2 in. profile experienced a linear growth in displacement in relation to applied load. After 0.4-in. displacement and 5.8 kips, the loaded profile started to fail. For the H–8 in. × 8 in. × 3/8 in. specimen, failure initiated at 0.35 in. and 3.5 kips. The H–6 in. × 6 in. × 3/8 in. specimen exhibited similar behavior to that of the H–8 in. × 8 in. × 3/8 in. profile. Here, failure initiated at 0.275 in. and 2.8 kips.

The results of this study confirmed the inherent weakness of the resin-rich zone at the point web-flange junction, which precluded the possibility of "steel-like" behavior. This also suggested that in the realm of computational analysis web-flange junction for the open section should be modeled as a flexible junction.

7.5.29.2 Rotational Behavior of the Web-Flange Junction.   In the second paper, Mosallam et al. (2010c) evaluated the rotational behavior
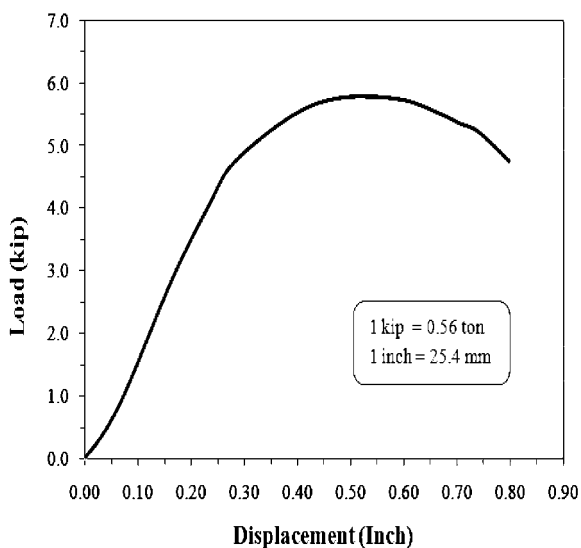
Figure 7-138. *Load-displacement curve for H–10 in. × 10 in. × 1/2 in. profile: mid-point loading.*
Source: Mosallam et al. (2010b).
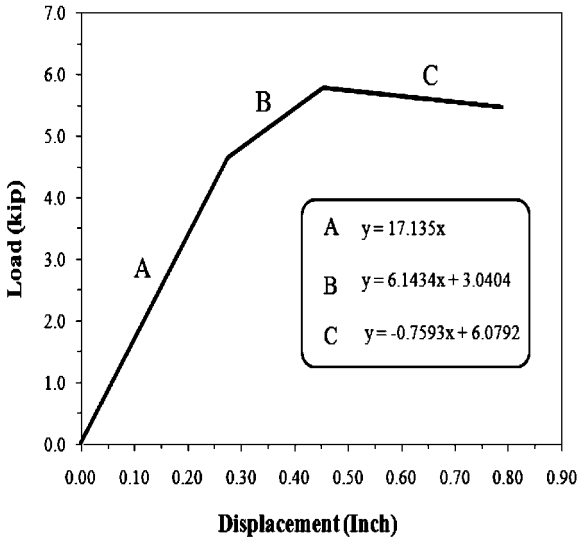
Figure 7-139. Linearized load–displacement curve for H–10 in. × 10 in. × 1/2 in. profile: mid-point loading.
Source: Mosallam et al. (2010b).

Table 7-22. Pull Out Test

Profile	Mid Point Test	Eccentric Point Test
H − 6″ × 6″ × 3/8″	$y = -264.4x^3 + 35.087x^2 + 18.89x$	$y = -516.63x^6 + 1178.3x^5 - 699.55x^4 + 75.261x^3 + 5.3031x^2 + 11.626x$
H − 8″ × 8″ × 3/8″	$y = 14555x^5 - 10829x^4 + 2419.3x^3 - 191.25x^2 + 23.218x$	$y = 232.53x^6 - 1816x^5 + 1259.5x^4 - 301.64x^3 + 27.326x^2 + 9.2388x$
H − 10″ × 10″ × 1/2″	$y = -295.44x^5 + 603.77x^4 - 433.91x^3 + 107.69x^2 + 9.0454x$	$y = 1783.6x^6 - 3659.9x^5 + 2880.9x^4 - 1125.3x^3 + 211.94x^2 - 0.0659x$

Source: Mosallam et al. (2010b).

of web/flange junctions of open web pultruded fiber reinforced polymer composite (PFRP) profiles. The purpose of the study was to establish M-θ relations, measure axial flexibility, assess rotational stiffness, which is a critical variable when considering buckling and post-buckling performance, and develop empirical formulas to describe behavior and define design limit states. In addition, measurements of rotational stiffness were compared to methodologies available from two PFRP design guides that
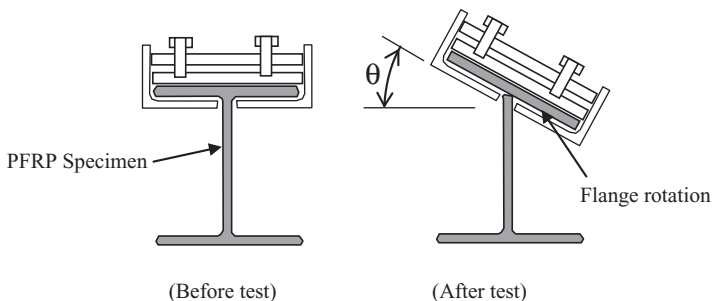
Figure 7-140. Schematic view of flange rotation.
Source: Mosallam et al. (2010c).

provide formulas to calculate rotational stiffness. Examples from these guides, Kollar's (2003) approach and the *Guide for the Design and Construction of Structures made of FRP Pultruded Elements* by the National Research Council of Italy, were presented in the text.

In the study, three H-profiles and two L-profiles, whose dimensions were previously presented in Table 7-21, were subjected to service and ultimate loads using a novel test rig. To generate the desired behavior, specimens were securely held at the lower flange and web, while rotation was applied on the upper flange, as shown in Fig. 7-140. For all specimens, load was applied using a servo-hydraulic actuator and a transfer arm to generate the required rotation, as shown in Fig. 7-141. A displacement-controlled protocol was adopted in all tests. Web/flange relative rotation was captured by two string potentiometers placed on either side of the specimen and two inclinometers positioned on the extreme ends of the PFRP specimen. Strain gauges were used to measure strain at the web/flange junction and a common data-acquisition system was used to simultaneously collect all loads, displacements, rotations, and strains.

Test results for the H-10 specimen displayed a very small rotation up to moment of 1.5 kip-in. and continued linear behavior up to 3.55 kip-in. and 0.025 radian rotation angle. After this point, stiffness degradation started, which was followed by failure at 5.4 kip-in. and 0.48 radians. Figure 7-142 shows failure in the specimen, while Figs. 7-143 and 7-144 show the actual and linearized moment-rotation curves. Similar results were secured for the remaining H-profile specimens. Those curves are presented in Figs. 7-145 through 7-148.

As mentioned previously, measurements of rotational stiffness for the web/flange junction are compared (Table 7-23) to calculated values based on Kollar's approach, as presented by the ASCE *Standard for Load Resistance Factor Design (LRFD) of Pultruded Fiber Reinforced Polymer (FRP) Structures*, and the *Guide for the Design and Construction of Structures made*
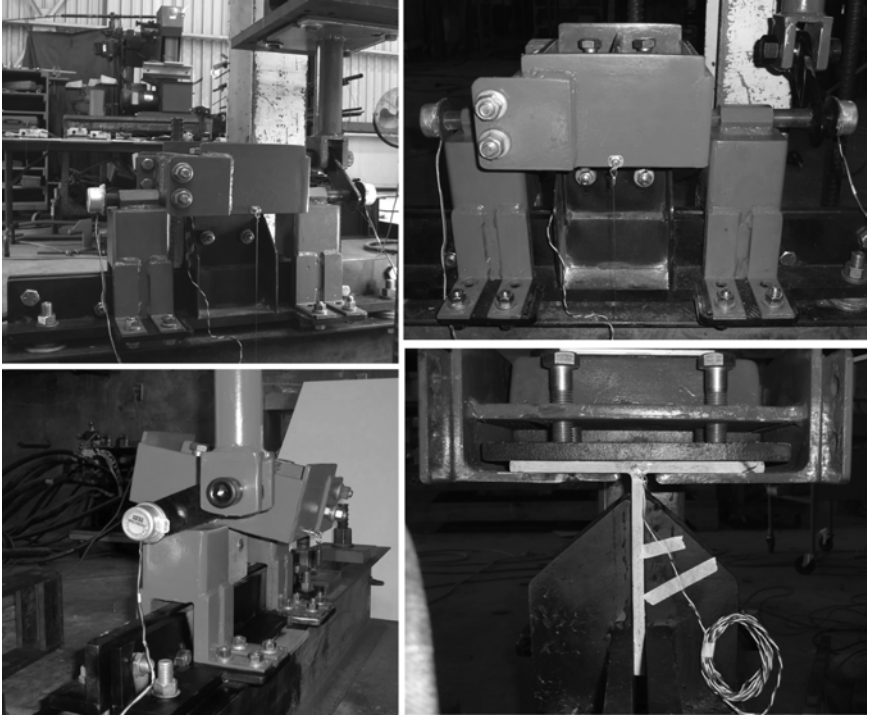
Figure 7-141. Views from rotation test setup.
Source: Mosallam et al. (2010c).
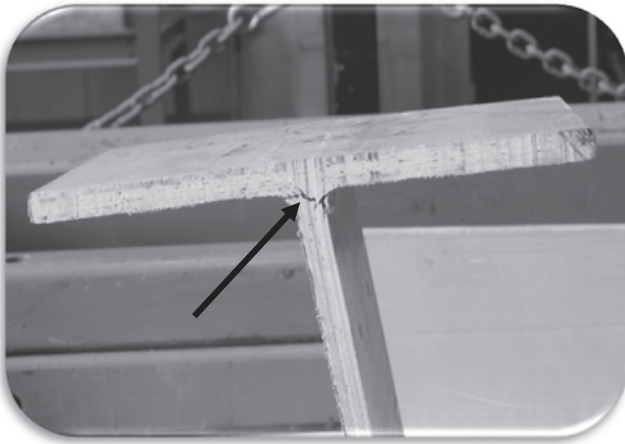
Figure 7-142. Failure of H–10 in. × 10 in. × 1/2 in. profile.
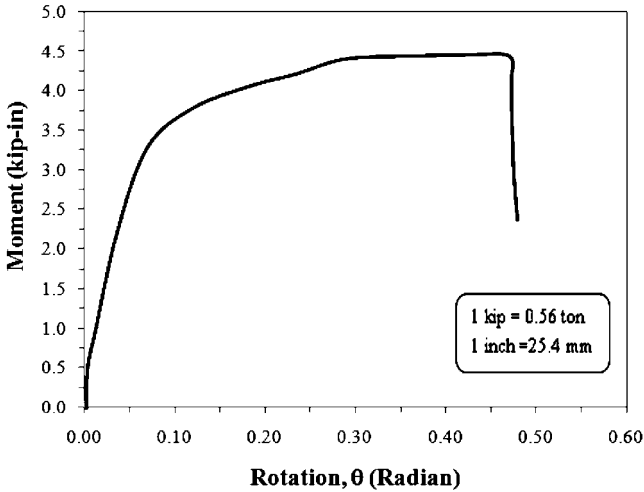*Source: Mosallam et al. (2010c).*
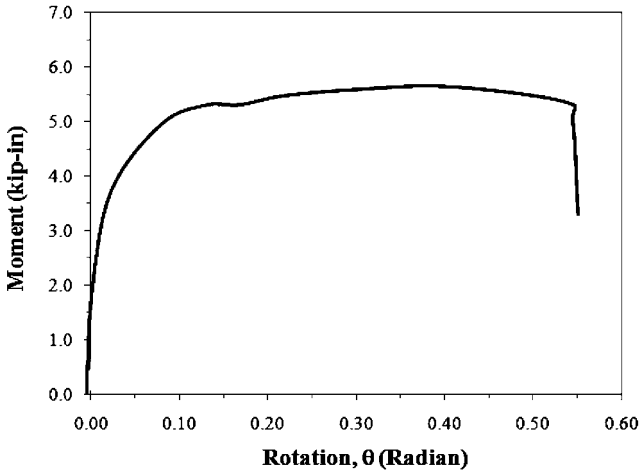
Figure 7-143. Moment-rotation curve for H–10 in. × 10 in. × 1/2 in. profile.
Source: Mosallam et al. (2010c).
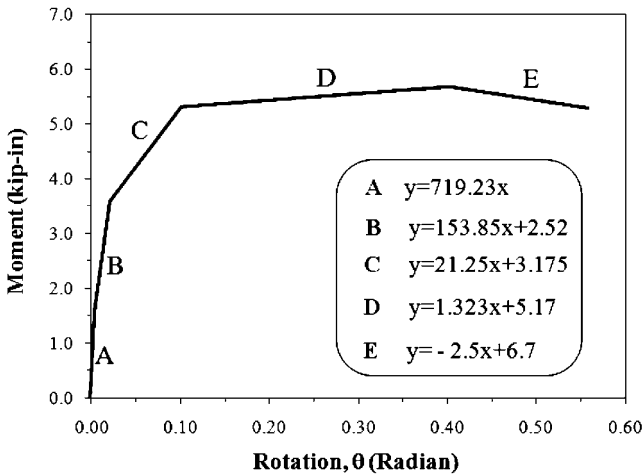
Figure 7-144. Linearized moment-rotation curve for H–10 in. × 10 in.
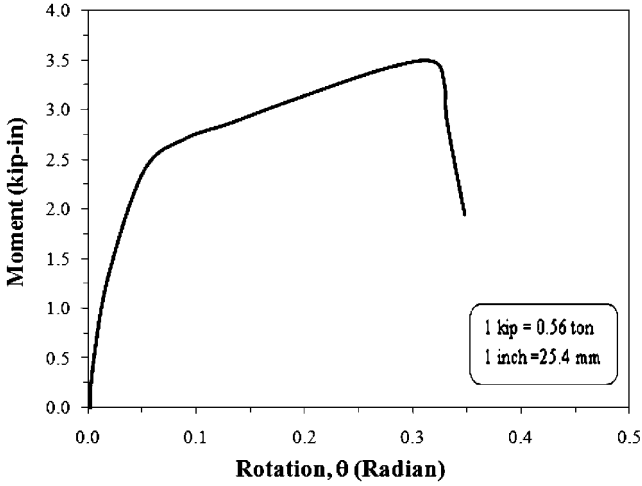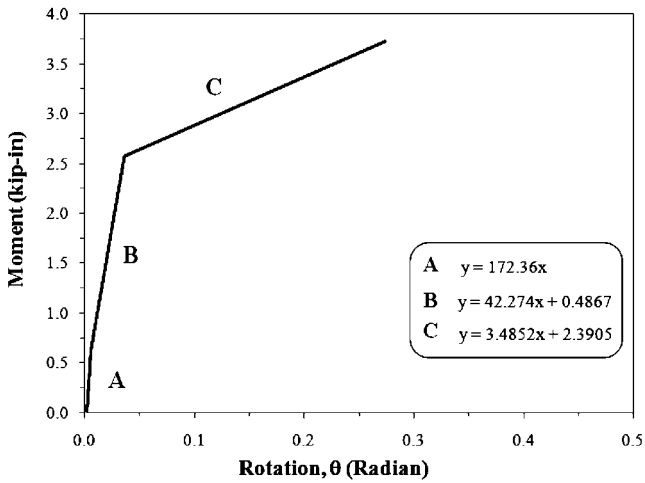*× 1/2 in. profile.*
Source: Mosallam et al. (2010c).

of FRP Pultruded Elements by the National Research Council of Italy. Based on the limited data presented in the table, the guide from the National Research Council of Italy provided the better estimations of rotational stiffness.

L-shaped profiles were tested in open mode, in which the profile angle increased, and closed mode, in which the profile angle decreased. For the

L–6 in. × 6 in. × 1/2 in. open mode specimen, it was observed that rotation was very small up to 1.0 kip-in.; however, beyond this point, the relation between moment and rotation angle was strongly linear up to 2.0 kip-in. and 0.03 radian. After this point, large increases in rotation angle were accompanied by small increases in moment until total rotation has reached 0.4 radian. Failure occurred soon after. Figure 7-149 shows failure in the

Figure 7-145. *Moment-rotation curve for H–8 in. × 8 in. × 3/8 in. profile.*
Source: *Mosallam et al. (2010c).*
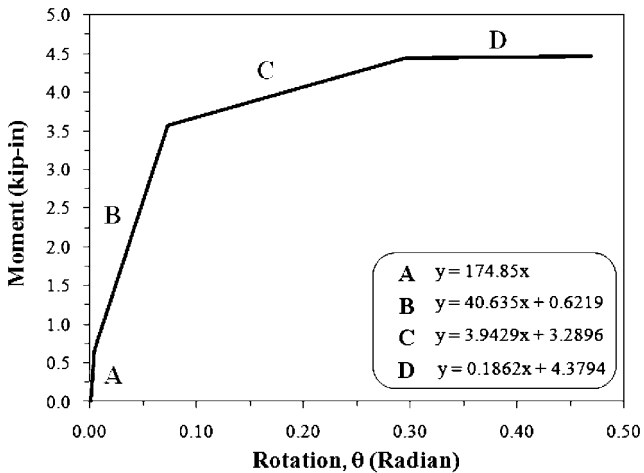
Figure 7-146. *Linearized moment-rotation curve for H–8 in. × 8 in. × 3/8 in. profile.*
Source: *Mosallam et al. (2010c).*

*Figure 7-147. Moment-rotation curve for H–6 in. × 6 in. × 3/8 in. profile.
Source: Mosallam et al. (2010c).*

*Figure 7-148. Linearized moment-rotation curve for H–6 in. × 6 in. × 3/8 in.
profile.*

Table 7-23. Rotational Stiffness Values

Profile	Kollar's Approach	Italian Guide	Experimental Results
H − 10″ × 10″ × 1/2″	2083	653	720
H − 8″ × 8″ × 3/8″	1099	345	175

Source: Mosallam et al. (2010c).
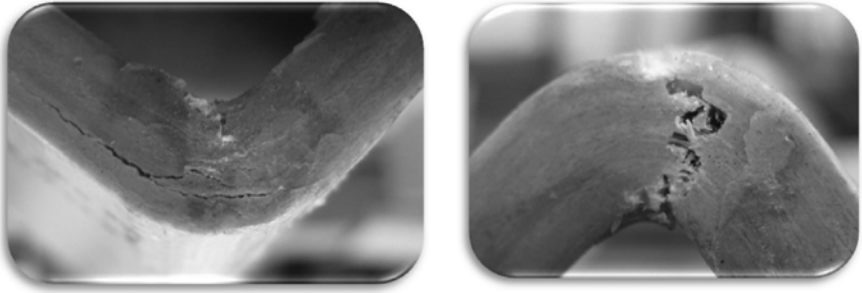
Figure 7-149. Typical web-flange junction failures in rotation tests for PFRP L-profiles. Left, open; right, closed.
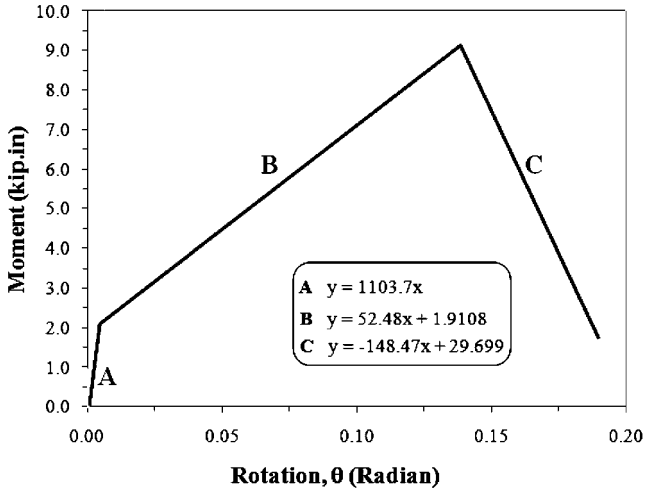*Source: Mosallam et al. (2010c).*
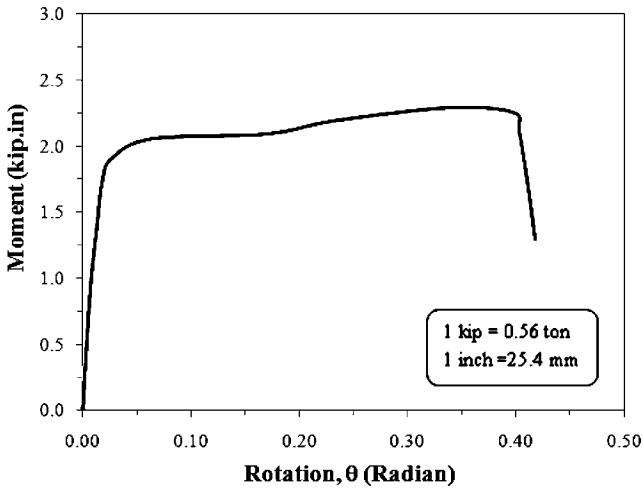
Figure 7-150. Moment-rotation curve for opening mode of L–6 in. × 6 in. × 1/2 in. profile.
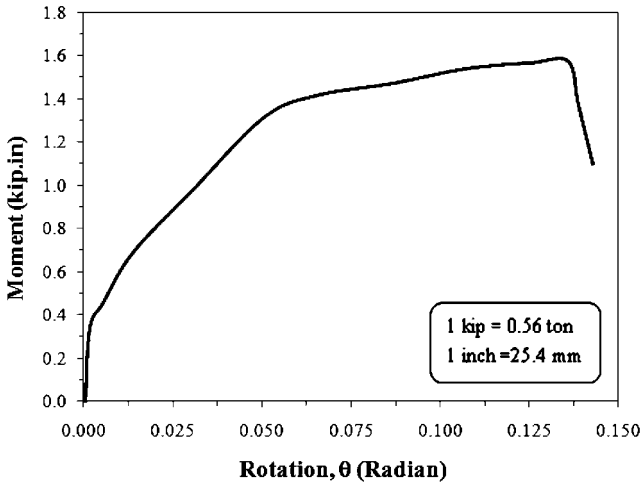*Source: Mosallam et al. (2010c).*

joint, while Figs. 7-150 and 7-151 show actual and linearized moment–rotation curves for open mode L– 6 in. × 6 in. × 1/2 in. profile. For close mode, it was observed that the rotation was very small and the material was quite stiff—up to 2.0 kip-in. As stiffness began to degrade, the relation between moment and rotation angle remained linear up to 9.0 kip-in. and 0.14 radian rotation angle. After this point, failure occurred as depicted in Fig. 7-149. Figure 7-152 shows the actual moment–rotation curve and Fig. 7-153 depicts the linearized version.

Similar behavior was observed for both open mode and close mode L–4 in. × 4 in. × 3/8 in. profile specimens. In the case of the L–4 in. × 4 in.
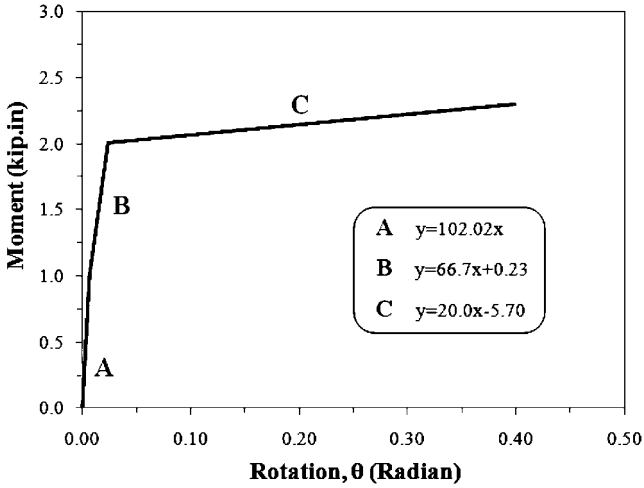
Figure 7-151. Linearized moment-rotation curve for opening mode of L–6 in. × 6 in. × 1/2 in. profile.
Source: Mosallam et al. (2010c).
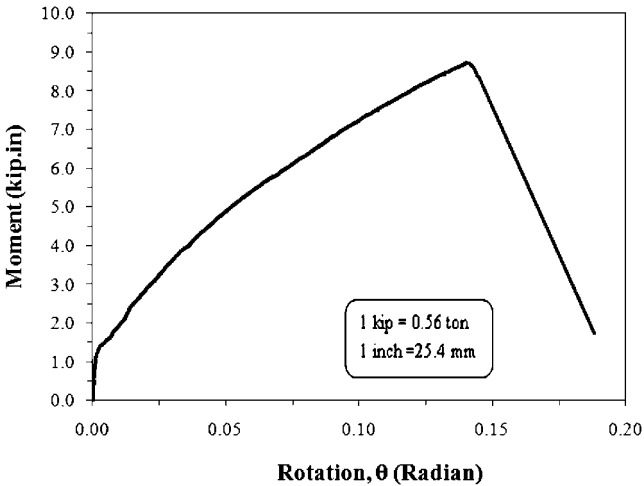
Figure 7-152. Moment-rotation curve for closing mode of L–6 in. × 6 in. × 1/2 in. profile.
Source: Mosallam et al. (2010c).

× 3/8 in. open mode specimen, very limited rotation was observed up to an applied moment of 0.5 kip-in. The relationship between moment and rotation angle remained linear up to 1.4 kip-in. and 0.05 radian rotation angle. After this point, increases in rotation angle were accompanied by small increases in moment until rotation equaled 0.13 radian. Beyond this

Figure 7-153. Linearized moment-rotation curve for closing mode of L–6 in.
× 6 in. × 1/2 in. profile.
Source: Mosallam et al. (2010c).

Figure 7-154. M-Θ curve for opening mode of L–4 in. × 4 in. × 3/8 in. specimen.
Source: Mosallam et al. (2010c).

point, there was a sudden failure in the specimen. Figure 7-154 shows the moment–rotation curve for open mode, while the linearized curve is shown in Fig. 7-155. In the case of the close mode specimen, it was observed that rotation was very small up to moment equal to 0.75 kip-in.
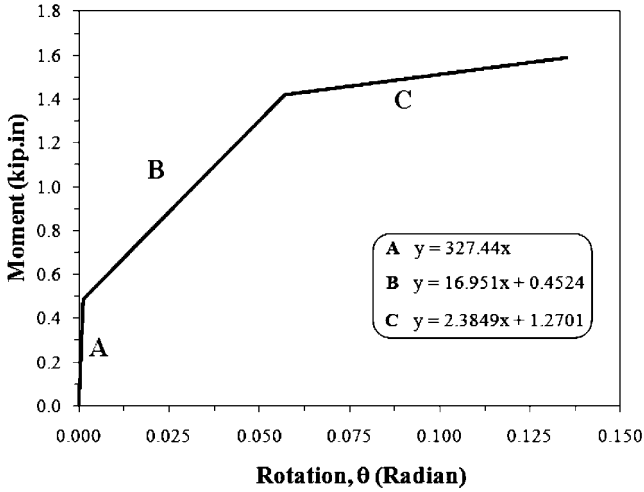
Figure 7-155. *Linearized M-Θ curve for opening mode of L–4 in. × 4 in. × 3/8 in. specimen.*
Source: *Mosallam et al. (2010c).*
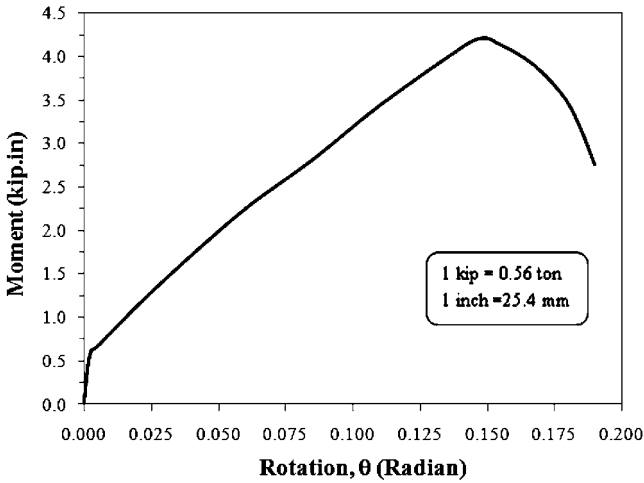
Figure 7-156. *M-Θ curve for closing mode of L–4 in. × 4 in. × 3/8 in. specimen.*
Source: *Mosallam et al. (2010c).*

The relationship between moment and rotation angle remained linear up to 4.3 kip-in. and 0.15 radian and failure occurred just after this point. Figure 7-156 shows the moment–rotation curve for close mode for the L–4 in. × 4 in. × 3/8 in. profile, while the linearized curve is shown in

A   y = 350.83x
B   y = 25.138x + 0.6531
C   y = -23.344x + 7.7823
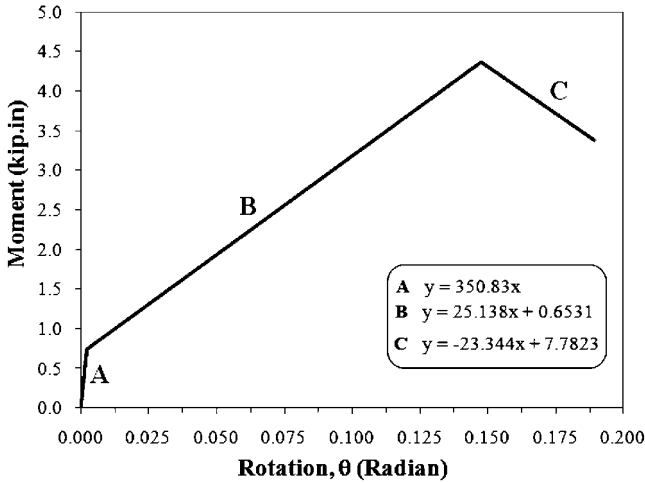
Figure 7-157. Linearized M-Θ curve for closing mode of L–4 in. × 4 in. × 3/8 in. specimen.
Source: Mosallam et al. (2010c).

Table 7-24. Rotation Test

Profile	Equation
H – 6″ × 6″ × 3/8″	$y = -7184.8x^6 + 14425x^5 - 11269x^4 + 4282.9x^3 - 821.92x^2 + 77.76x$
H – 8″ × 8″ × 3/8″	$y = -7800x^6 + 14871x^5 - 11182x^4 + 4218.3x^3 - 844.32x^2 + 88.744x$
H – 10″ × 10″ × 1/2″	$y = -25238x^4 + 12962x^3 - 2389.5x^2 + 183.01x$
L – 6″ × 6″ × 1/2″ (Open)	$y = -546078x^6 + 523957x^5 - 196107x^4 + 36029x^3 - 3332.6x^2 + 140.44x$
L – 6″ × 6″ × 1/2″ (Close)	$y = -85256x^4 + 27516x^3 - 3172.1x^2 + 199.52x$
L – 4″ × 4″ × 3/8″ (Open)	$y = -2E+07x^6 + 9E+06x^5 - 1E+06x^4 + 108753x^3 - 4351.6x^2 + 97.26x$
L – 4″ × 4″ × 3/8″ (Close)	$y = -26930x^4 + 9018.6x^3 - 1051.8x^2 + 73.572x$

Source: Mosallam et al. (2010c).

Fig. 7-157. Table 7-24 specifies the approximating polynomial equations that have been defined to capture the behavior the tested profiles.

Based on the study, it was concluded that (1) the PFRP web-flange interface for the open section must be modeled as a flexible junction; (2) the PFRP L profiles exhibit different behaviors in open and close mode; and (3) the calculation for rotational stiffness of the web/flange junction requires additional research and investigation.

7.6 A CASE STUDY OF DURABILITY OF PULTRUDED FIBER-REINFORCED POLYMER COMPOSITES IN HARSH ENVIRONMENTS

7.6.1 General

In designing composite framing structures, the structural engineer should consider the effect of the surrounding environment on the long-term behavior of the structure. This includes appropriate selection of row materials, including additives and fillers. In addition, the effect of temperature, freeze–thaw cycles, humidity, and other corrosive agents should be considered when predicting the creep behavior of such structures, so as to avoid catastrophic failures due to creep rupture. To demonstrate the significance of this issue, a case study conducted by the author is described in the following paragraphs.

Mosallam (1997a) reported details of a field survey related to the long-term behavior of pultruded composite structures under corrosive environments. The impact of several design and construction factors on the long-term performance of pultruded composite structural systems is presented. These factors included structural detailing, material selection and its interrelationship with the surrounding environment, as well as fabrication and construction procedures. The results of the field survey indicated that the majority of the structural members were severely damaged due to the combined effects of (1) faulty structural design and detailing of both members and connections; (2) wrong selection of the resin system used in manufacturing these pultruded composites; and (3) poor quality control and quality assurance during the fabrication and construction processes. Recommendations for repair of existing structures as well as for strengthening details and procedure for new structures are presented both at the end of this section and in detail in Section 7.7 of this chapter.

7.6.2 The Field Survey

In August 1997, the author conducted a field survey in a major industrial site in the United States. The purpose of the site visit was to inspect and evaluate the pultruded composite framing structures at these two facilities which suffered from structural and corrosion damages at different locations. In addition to the damage assessment and analysis of structural damages, recommendations for repair and structural upgrade were provided to the owner. In general, it was observed that the majority of the pultruded composite structural members at both facilities had serious corrosion damages due to continuous exposure to the surrounding harsh environment. The inadequate connection details and deficient fiber architecture of unidirectional structural pultruded members amplified the corrosion problem.

7.6.3 Major Factors Affecting the Long-Term Performance of Existing Pultruded Structural Systems

In addition to the sulfuric acid and copper plating solution vapors environment surrounding the pultruded frame structures at these facilities, other major factors contributed to local and overall failures observed during the site visit. These factors can be summarized as follows:

1. *Member corrosion due to poor selection of resin, and lack of quality control during the fabrication and construction processes*: During the inspection, it was observed that the majority of the load-carrying pultruded members (e.g., H-beams, I-beams, angles, channels, and gratings) were deteriorating due to matrix corrosion caused by the attack of the sulfuric acid and other corrosive agents that led to a premature delamination of the composite members in some locations, as shown in Fig. 7-158. The resin system used in manufacturing these profiles was isophthalic polyester. Several factors contributed to the corrosion and premature local failure of several pultruded composite, such as:

   a. *Poor performance of the isophthalic polyester matrix* which contained about 30% by volume of fillers such as clay, calcium carbonate, etc., especially at this site with relatively high concentration of sulfuric acid coupled with high temperature and wet environment. In this case, a special resin system should have been recommended by the supplier and selected by the engineer to accommodate the existing harsh environment. The question was
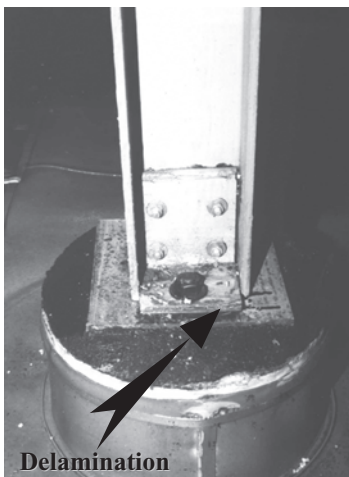
Figure 7-158. Examples of corroded pultruded members.

raised about why polyester resin was selected over vinlyester resin, which has a better corrosion performance in such environments. The answer was that the manufacturer had recommended the isophthalic polyester and that the decision was based on the information presented in recommendation tables listed in the manufacturer's design guide. To verify this claim, four pultrusion design manuals* were reviewed. Using the corrosion selection tables of these design guides and knowing that the concentration of sulfuric acid was about 17% by weight with maximum site temperature of about 110 °F (43.33 °C), two design guides allowed the use of polyester, while the other two disqualified the use of isophthalic polyester for temperatures higher than 80 °F (26.67 °C). It should be noted that the source of all information contained in the tables listed in the pultruders' manuals was provided or copied directly from the resin suppliers' manuals, which contained environmental results generated by using ASTM test standards such as ASTM C 581. (ASTM C 581 determines the loss in laminate mechanical properties with immersion time. The degradation of composite mechanical properties is generally the result of deterioration of the matrix resin by hydrolysis or oxidation, and fiber degradation is due to sulfuric acid attack. These tests are usually conducted on *resin-rich* specimens and not on commercially pultruded composite specimens, which generally have variable thickness, fillers, and void contents.) For this reason, the listed information and recommendations *did not* reflect the actual material response and, therefore, should only have been used as a rough guideline. This fact was not explained clearly in any of the available pultruders' guides. To make the correct selection decisions, results from environmental tests performed on typical pultruded specimens should be used.

The absence of such critical durability information raises a big question: *Who was responsible in this case*? Was it the pultruder or the resin supplier, or both? Regardless of the answer, the *engineer-of-record* will bear the ultimate responsibility in specifying the appropriate resin system. This issue should seriously be addressed by the composite industry, and these selection tables should be verified by establishing a reliable environmental test program to be performed on an appropriate number of pultruded specimens according to a special ASTM standard procedure for pultruded composites. In addition, it is proposed that these tests should be a part of the quality control and quality assurance protocol of

---

*The four guides were Strongwell, Creative Pultrusions, Bedford Reinforced Plastics, and Fiberline A/S.

each pultrusion facility, especially for corrosive environment applications.

b. Careful inspection indicated that, during the construction and installation of the pultruded members, *exposed cut edges were not sealed with polyester, epoxy, or any other compatible sealant to prevent migration of acids and other agents through the voids of these members*. In addition, and according to the information provided by the contractor, *drilled holes were not sealed during the fabrication process*. Proper fabrication and construction practice calls for the use of sealant on all exposed areas. Although it was stated in the engineering drawings that "Any scratches, cut edges or drilled holes shall be resin-sealed to prevent excessive attack of the laminate," this critical step was ignored during fabrication and construction. In addition, physical inspection of several failed pultruded sections indicated that the *void ratio* was relatively high, which facilitated the penetration of the surrounding acid vapor and other corrosive agents into these unsealed areas. This directly related to the amount and type of filler materials used in the matrix system of the pultruded materials used. No information on the average void ratio was available in any of the design guides reviewed during this investigation. Again, some *minimum standard* procedure should be used by all pultruders to determine an average values for their products. The aforementioned factors were the major cause of the rapid and continuing deterioration of these pultruded members.

2. *Local failure of web-flange junction of open-web pultruded members:* As discussed earlier, because of the unidirectional characteristics of off-the-shelf open-web pultruded structural profiles, and due to the lack of fiber continuity at the web and the flanges of the majority of these members, local failure of flange/web junctions at stress concentration zones was inescapable, especially when *inappropriate* connection structural details were used (Mosallam 1993a; 1994b; 1995a). This type of local failure can also occur at *non-connection* regions such as the mid-span of beams and/or along the column height where high stress concentration exists.

During the inspection, web-flange junction local failures of several pultruded H-columns were identified. These local failures occurred at the connection zone (Fig. 7-159). As shown in this figure, the separation of the inner flange from the column web was extended about 2 ft from the connection centerline. If no immediate repair was performed, the primary crack would propagate along the corner length, parallel to the junction, and ultimately would cause a complete failure of the supported beams and gratings. It should be noted that although only a few columns suffered a complete separation at the
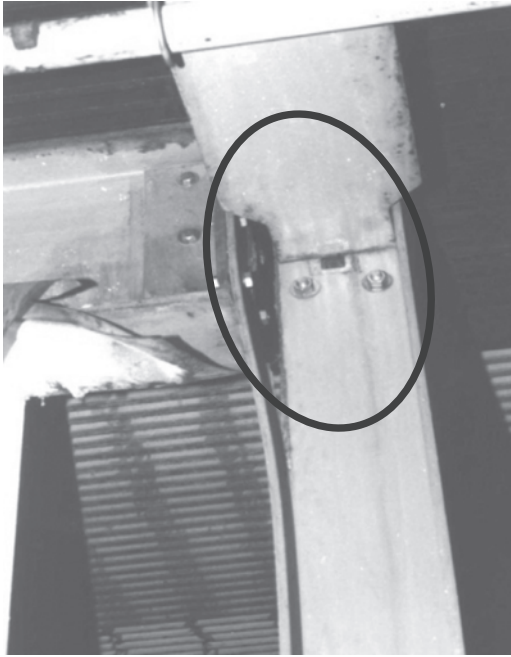
Figure 7-159. Column local failure initiated at the web-flange junction.

web-flange junction, it was the author's experience that the majority of the existing columns had already developed "internal cavities" which would lead to the same type of failure in the near future if no stiffening details were added. The development of internal cavities was reported earlier through several full-scale test results performed by Mosallam (1994b). The initiation of local failure in these cases is invisible to the naked eye because of the existence of the finishing Nexus veil layer covering the top surface of pultruded profiles. Introducing special repair and retrofit engineering details can control this deficiency, such as those proposed by Mosallam (1994b) and described in Section 7.7 of this chapter.

3. *Improper "steel-like" connection details:* One of the major direct causes of rapid stiffness and strength degradation of pultruded members is the use of inadequate connection details. In this case, careful review of the engineering drawings revealed the fact that the majority of the connection details were improper and were a complete duplication of standard isotropic steel connection details. Steel-like or isotropic connection details (refer to Figs. 7-158 and 7-159) used in building types of structures will have both direct and indirect negative effects on both the short- and long-term overall

performance of PFRP structures. These inadequate connection details result in loss of the rotational stiffness of the frame structure, and ultimately will result in a complete brittle failure as cracks propagate and enlarge over time.

In this case, for all FRP connection details, unidirectional pultruded angles with the majority of glass fibers running in the *wrong* direction relative to the applied loads were used as the primary connecting framing elements. In this regime, the isophthalic polyester and fillers matrix (which was designed to act only as a binder to the load-carrying glass fibers) were exposed to the majority of applied stresses. The isophthalic polyester matrix used in manufacturing the PFRP members had a weak resistance to the facility chemical environment and temperature, as discussed earlier. As a result, failure was unavoidable due to the low tensile and low flexural moduli and strengths of the isophthalic polyester matrix.

The mechanical properties degradation was generally due to the deterioration of the matrix by hydrolysis or oxidation, in addition to the degradation of the E-glass fibers due to acid attack. This usually starts in the form of minor hair cracks (environmental stress cracking, ESC) at the pultruded clip angles corners. ESC attacks PFRP members in the presence of a corrosive agent, extreme temperature, and sustained loading. As the stress crack nucleus is formed, rapid growth of the nucleus will occur due to the presence of sustained loads and harsh environment surrounding the member. The rapid degradation in the member's strength is commonly attributed to corrosion attack on both the fibers and the matrix material. The common size of the corrosion micro-cracks is on the order of 500 Å in length in E-glass/polyester composites. The formation of these micro-cracks enables acid diffusion into the matrix, which will accelerate the corrosion process. This was confirmed by an experimental investigation on four different types of polyester resin laminates (Fuji et al. 1994). The results of this study indicated that the stress corrosion failure was due to penetration of acid through the loaded composite specimens, which caused micro-cracking in the resin or resulted in debonding at the resin/fiber interfaces.

In the case of the unidirectional clip angles used in the two facilities being discussed here, the hair cracks grew and propagated in the longitudinal direction of unidirectional continuous loading as a result of a continuous exposure to the facilities' harsh environment (refer to Fig. 7-160). After a certain period of loading and exposure (a function of the loading level and exposure type), chances of static fatigue failure (creep rupture) of the isophthalic polyester matrix may rapidly increase. In the case under consideration here, this occurred in the majority of the connections where out-of-plane angle
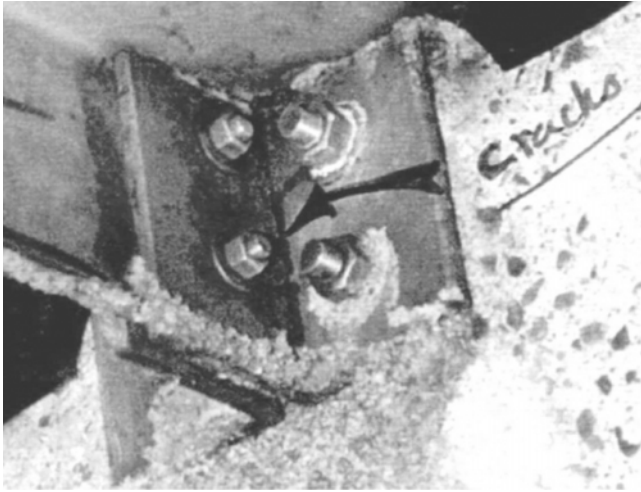
Figure 7-160. Typical corroded PFRP connection with longitudinal cracks.

legs, along with the supported members, separated entirely from the other wall-side legs (refer to Fig. 7-161). During the inspection, it was noticed that some of the failed connections had been replaced with stainless steel connectors. This solution was acceptable for immediate repair but there is a short- and long-term compatibility drawback (stiffness mismatch) in using this type of connection, which will be discussed in the recommendation section immediately below.

7.6.4 Conclusions and Recommendations

Site inspection indicated that there was an immediate need for providing remedies to several problems in the existing FRP structural systems at the two facilities. It was equally important to take into consideration these incorrect details when building the new extensions. The following are some of the lessons learned from this case:

1. Avoid the use of steel-like connection details.
2. Use stiffeners and prestressing elements at high stress concentration zones.
3. Ensure that all scratches, cuts, and member ends are carefully sealed with the same resin system.
4. Provide the manufacturer with complete details of the chemical environment, including temperature, in order to select the appropriate resin system for the section. Also specify a low voids ratio for your sections.
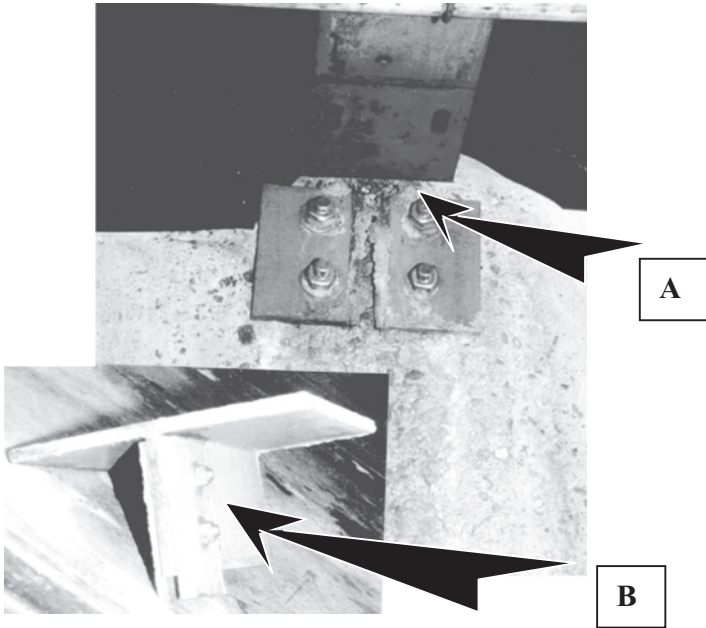
Figure 7-161. Typical failure of steel-like connection details (out-of-plane angle leg separated from the leg attached to concrete wall). A, The as-built position; B, position after separation failure.

5. Avoid the use of metallic parts as connectors for several reasons, including strength, stiffness, and thermal coefficient of expansion mismatch.

7.7 CONNECTION AND REINFORCEMENT DETAILS FOR PFRP COMPOSITE STRUCTURES

7.7.1 Connection Details

In this section, several connection details are presented. These details are grouped into two categories: (1) existing, and (2) new construction. The term "existing" refers to PFRP structures already in service that were designed using inadequate steel-like connection details. Although not highly recommended by the author for new construction, these details may still be appropriate design alternatives in the absence of proper connecting element(s).

These details are described in Figs. 7-162 and 7-163. From these figures, one notices that the following details are added to conventional connection details often used by the industry:
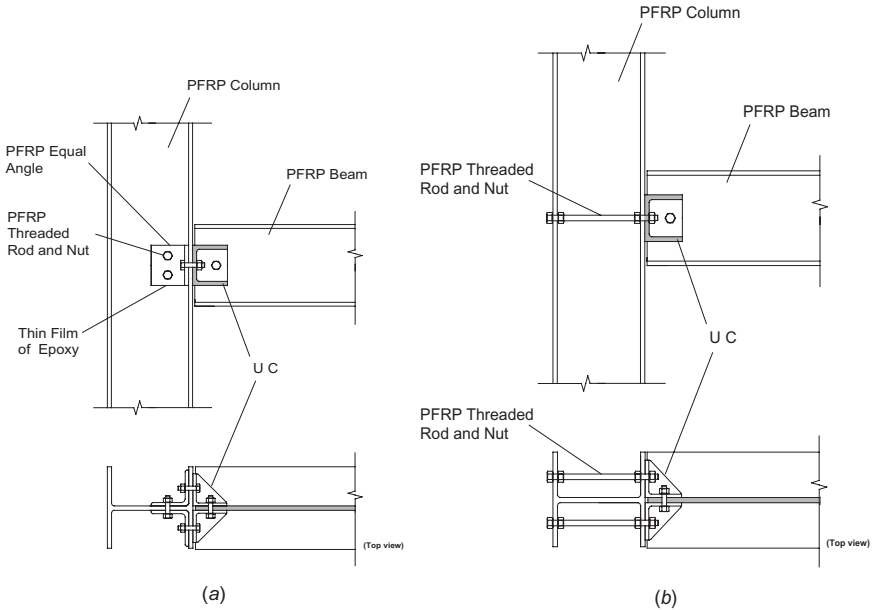
Figure 7-162. Hinged (shear) PFRP beam-to-column connection details.

1. *Transfer elements (PFRP angles) at the column location:* The purpose of these angles is to transfer applied tensile forces from the beam to the column's web for both open-web and closed-web profiles. In this detail, the majority of the tensile forces will bypass the weak junction between the web and flanges of the pultruded profile (refer to Fig. 7-160). This will result in a relatively higher stiffness due to the reduction of localized deformation at the tension portion of the connection. It is recommended that these pultruded angles be attached using both mechanical fasteners and high-strength adhesives. Applications for this system are shown in Figs. 7-162A, 7-167A, and 7-169D.

2. *Transfer elements (PFRP angles) at the beam location:* As discussed earlier, these bolted/bonded transfer elements are needed at high stress concentration locations. Due to the presence of negative bending moments at the beam-column region, it is recommended that transfer elements be attached to the bottom flange and the web of the beam member. The ultimate mode of failure of a flexible connection studied by Zahr et al. (1993) demonstrated the need of such a stiffening detail. Applications for this system are shown in Figs. 7-162B, 7-165A,F, and 7-166A. It should be noted that although the use of unidirectional pultruded angles as transfer elements has been proven experimentally to increase connection's strength (Bank and

(a)

(b)

(c)
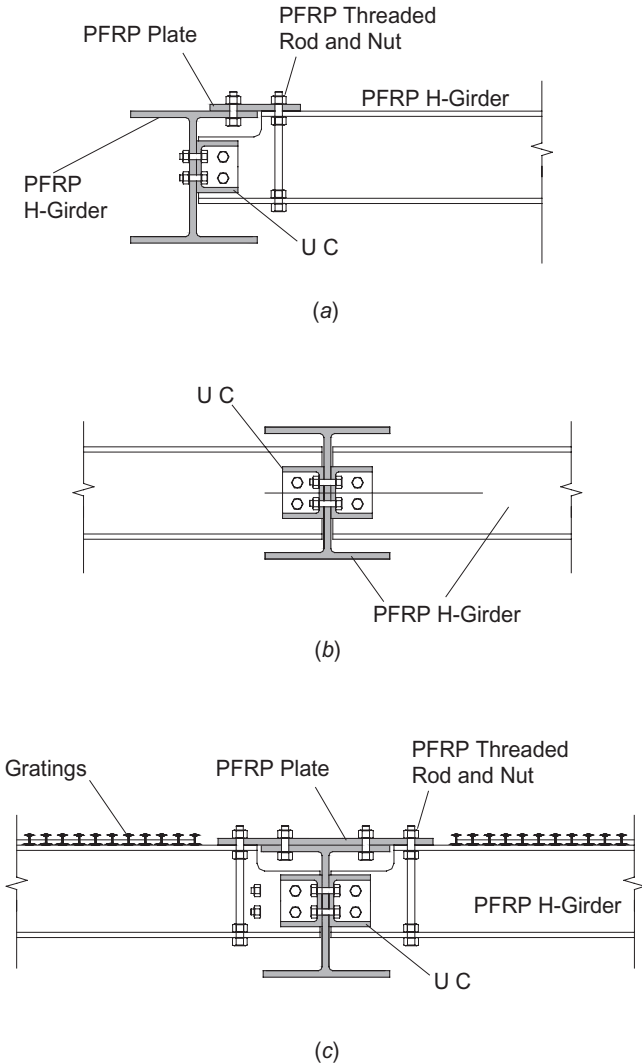
Figure 7-163. Hinged PFRP beam-to-girder connection details for open-web profiles (both interior and exterior).

Mosallam 1991b), the major reinforcements of these angles are still running in the *opposite* direction with respect to the loading path. The optimum performance can be achieved using a special PFRP angle with multidirectional reinforcements for frame connections. For this reason, an alternative approach described in the following paragraph is recommended.
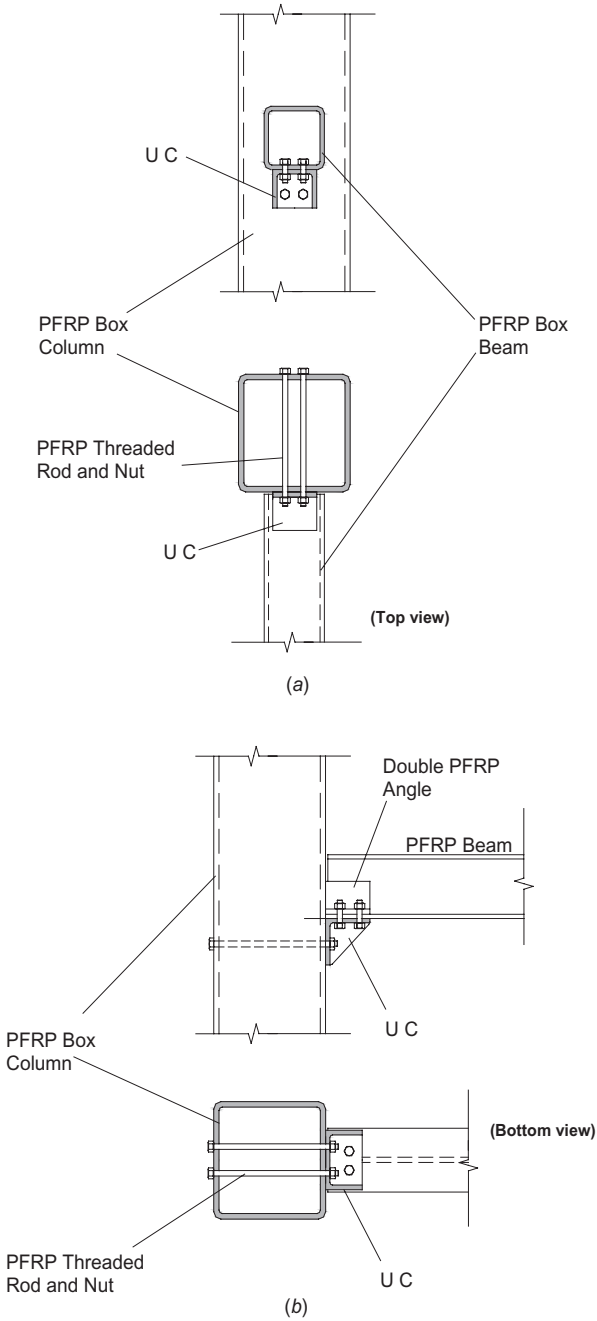
Figure 7-164. Flexible exterior (UC seat) PFRP beam-to-column connection details.
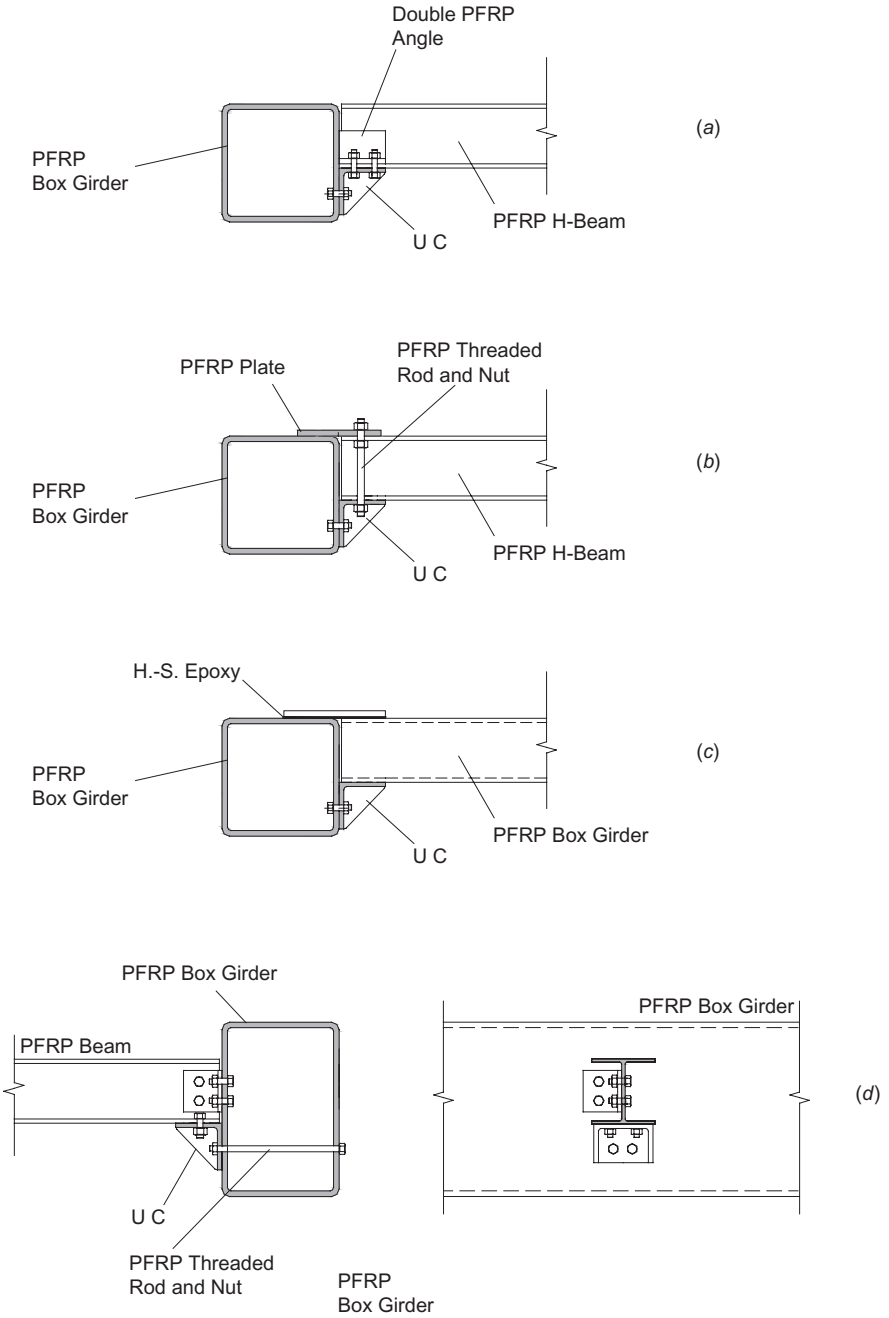
Figure 7-165. Flexible PFRP beam-to-girder and beam-to-beam connection details (exterior).

(e)

(f)
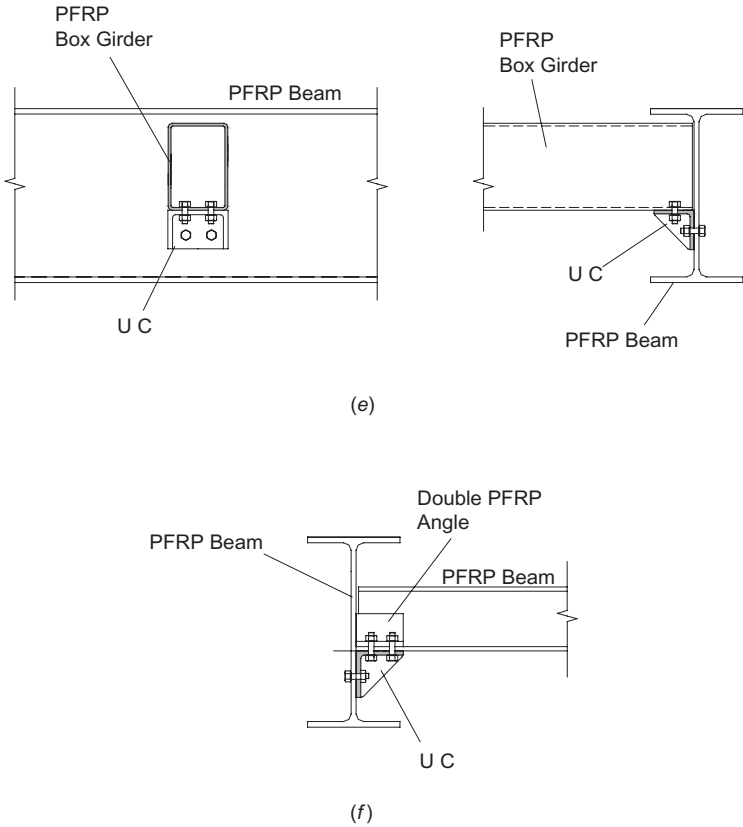
Figure 7-165. (Continued)

3. *Threaded rod/nut stiffener:* In this system, the connection-threaded rods (either FRP or metallic) are extended to the other flange using a double-nut system, as shown in Fig. 7-162B. The function of this system is to prestress and confine the open-web sections at connection locations. This system will ensure the utilization of the full resistance of the pultruded section at high stress concentration locations, and will prevent premature failure at the web-flange junctions. This type of failure can occur at very low stress levels and even during fabrication, as reported by Turvey and Cooper (2000). It should be clear that, by reinforcing the open-web section, failure of the connection would most likely be due to the failure of the connecting elements. Because of the brittle nature of PFRP materials, failure with minimum warning is expected. It should be noted that these extended threaded rod transfer elements will only increase the strength of the connection, with minimum improvement to the

PFRP Column

Double PFRP Angle

U C

PFRP Threaded Rod
and Nut

(*a*)

PFRP Column

U C

PFRP Threaded Rod
and Nut

(*b*)

PFRP Column

U C

PFRP Threaded Rod
and Nut

Closed Web
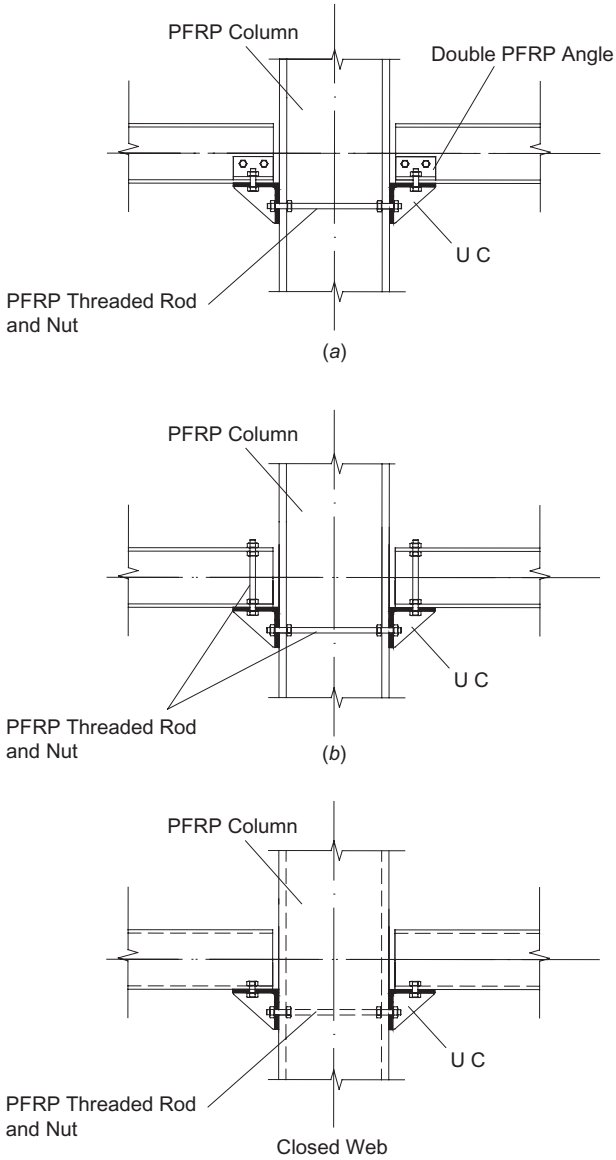
Figure 7-166. Flexible interior (UC seat) PFRP beam-to-column connection details.

connection's rotational stiffness. The stiffness of the connection is determined mainly by the structural capacity of the connecting elements, for example, size, lay-up, and wall thickness of the connector; type of connecting media (bolted only, bolted/glued, glued only); applied torque; and curing. Based on experimental and theoretical
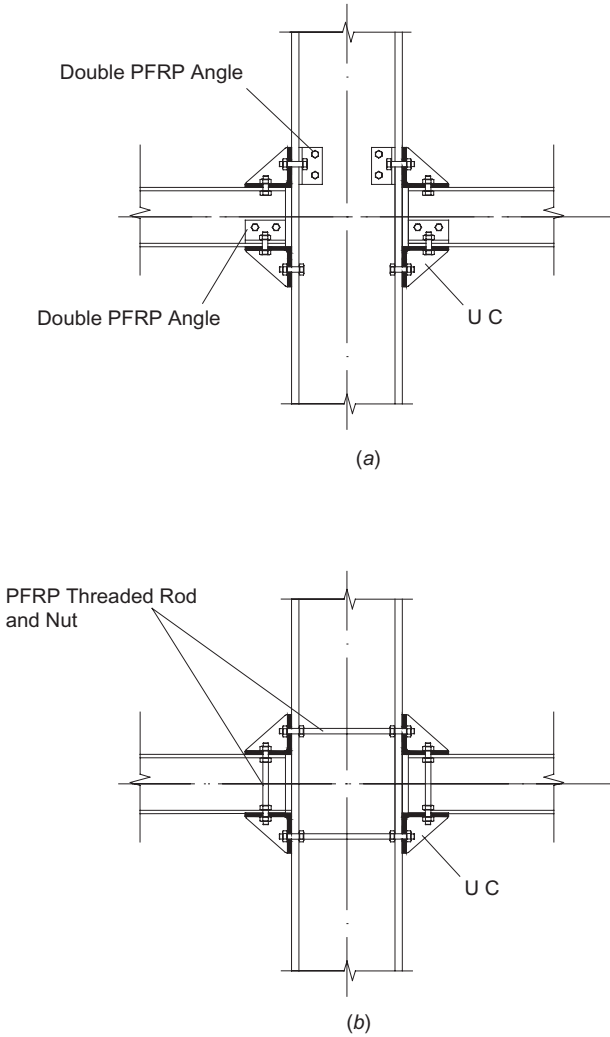
Figure 7-167. Rigid and semi-rigid PFRP beam-to-column connection details.

results obtained by Mosallam (1993a), Mosallam and Abdelhamid (1993), and Bedewi et al. (1993), the geometry and the lay-up of the connector were identified as the major parameters in determining the stiffness of PFRP connections. For this reason, connection details utilizing special connecting elements are expected to achieve a higher flexural stiffness of PFRP frame connections (Mosallam 1993d). This system was adopted by Na (2008), and neglecting the use of such stiffening details was the major deficiency of Bruneau and Walker (1994), as was described earlier in this chapter.

(a)

(b)
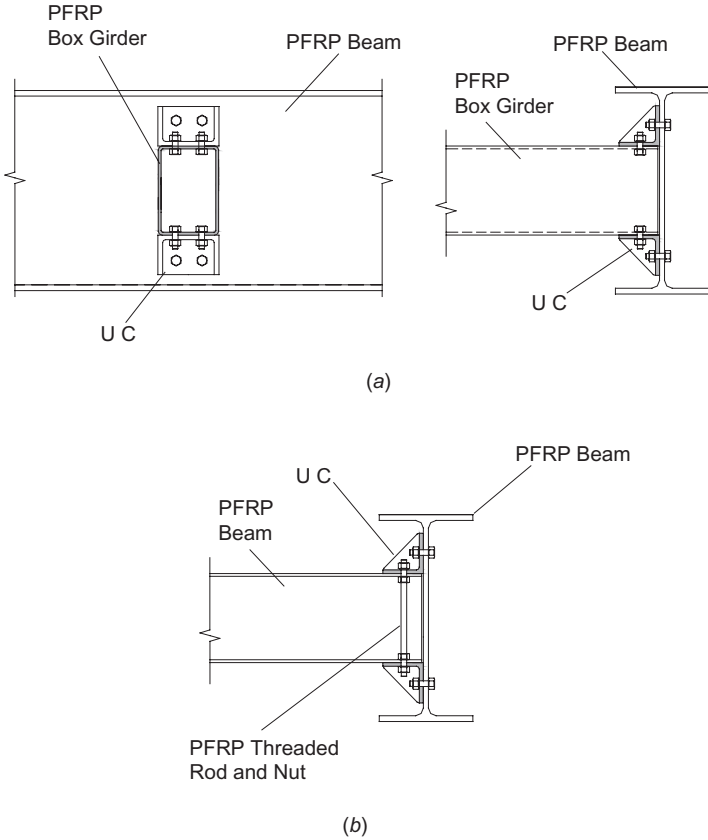
Figure 7-168. Rigid and semi-rigid PFRP beam-to-girder connection details.

The connection details presented herein are classified into three categories: (1) hinged, (2) semi-rigid, and (3) rigid connections:

1. *PFRP hinged connection details (simple framing):* These connections provide minimum rotational stiffness at the member ends (between 0% and 20%). Examples of this type of connection are shown in Figs. 7-162, 7-165, 7-166, and 7-169A. These connection details are used when design calculations are based on a simply-supported beam assumption. An example of this type is the seated UC connection (Zahr et al. 1993) shown in Figs. 7-58 and 7-59.

2. *PFRP fixed connection details (fully restrained):* This type of connection assembly provides 90% (or more) of the rotational stiffness in the linear range of an overall rotational restraint system (i.e., preventing relative rotation between the two attached members). An example
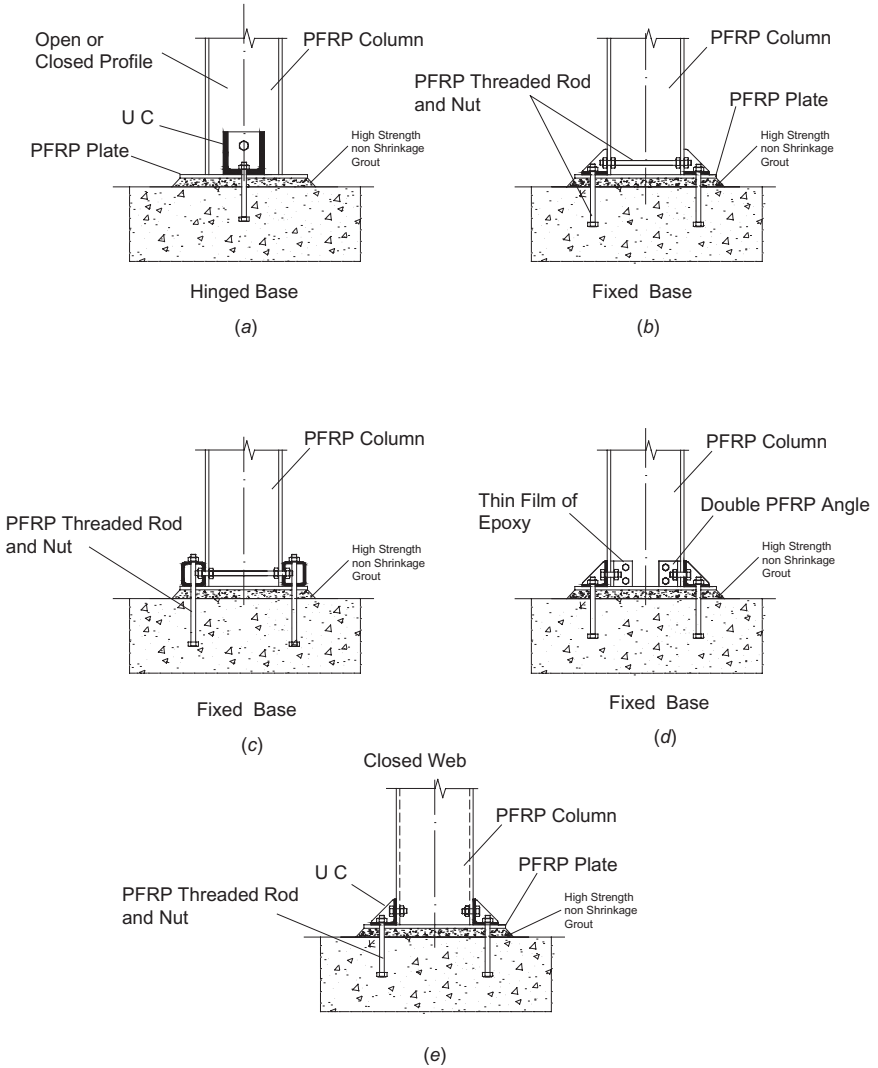
Figure 7-169. Column-to-base PFRP connection details.

of this is connection detail Type vii reported by Mosallam et al. (1993) and shown in Fig. 7-41.

3. *PFRP semi-rigid connection details (partially restrained):* These connections provide partial rotational stiffness ranging from 20% to 90%. The design of these connections requires experimental information describing the rotational stiffness of each connection. Stiffness characteristics of these connection details are obtained from the

corresponding moment–rotation (*M/Θ*) curves as described earlier in this chapter. An example of this is connection detail Type vi reported by Mosallam et al. (1993) and shown in Fig. 7-41.

REFERENCES

Ahmadian, R., and Mantena, P. R. (1996). "Modal characteristics of structural portal frames made of mechanically joined pultruded flat hybrid composites." *Composites*, *Part B, Eng.*, 27(3–4), 319–328.

American Institute of Steel Construction (AISC). (1992). *Manual of steel construction*, Vol. II: Connections, ASD 9th ed./LRFD 1st ed., American Institute of Steel Construction, Chicago, Ill.

American Institute of Steel Construction (AISC). (2005). Allowable Strength Design (ASD)/Load and Resistance Factor Design (LRFD) Steel Construction Manual, Thirteen Edition, Fifth Printing, American Institute of Steel Construction, Chicago, IL, AISC 325-05.

American Society of Civil Engineers (ASCE). (1984). *Structural plastics design manual*. ASCE, New York.

ANSYS (1989). ANSYS Engineering and Analytical System User's Manual. Revision 4.40, Volume I–II. Ed. John Swanson, G.J. DeSalvo, and R. Gorman, TX2-618-229. Pittsburgh, PA.

Bank, L. C., and Mosallam, A. S. (1992). "Creep and failure of a full-size fiber-reinforced plastic pultruded frame." *Composites Eng.*, 2(3), 213–227.

Bank, L. C., and Mosallam, A. S. (1991a). "Linear and non-linear response of pultruded FRP frames subjected to static loads." *Plastics and plastic composites: Material properties, part performance, and process simulation*, ASME, New York, pp. 371–386.

Bank, L. C., and Mosallam, A. S. (1991b). "Performance of pultruded FRP beam-to-column connections." *Proc., 49th ASCE Structures Cong.*, April 29–May 1, Indianapolis, Ind., ASCE, New York, pp. 389–392.

Bank, L. C., Mosallam, A. S., and Gonsior, H. E. (1990). "Beam-to-column connections for pultruded FRP structures." *Proc., ASCE Materials Cong.*, August 13–15, Denver, Colo., ASCE, New York, pp. 804–813.

Bank, L. C., Mosallam A. S., and McCoy, G. T. (1994). "Design and performance of connections for pultruded frame structures." *J. Reinf. Plastics and Composites*, 13, 199–211.

Bank, L. C. and Mosallam, A. S., and McCoy, G. T. (1992). "Make connections part of pultruded frame design." *Modern Plastics Magazine*, 69(8), 65–67.

Bass, A. J., and Mottram, J. T. (1994). "Behavior of connections in frame reinforced polymer composite section." *The Structural Engineer*, 72(17), 280–285.

Bedewi, N. E., Mosallam, A. S., and Goldstein, E. (1993) "Parametric analysis on the structural performance of a universal connector for PFRP frame structures." *Proc., 25th International SAMPE Technical Conference,* October 25–28, Philadelphia, Pa., SAMPE, Covina, Calif., pp. 622–629.

Bedford Reinforced Plastics, Inc. (2007). *Bedford Reinforced Plastics design guide,* Bedford Reinforced Plastics, Inc., Bedford, Pa.

Bellucci, F., and Capobianco, G. (1989). "Corrosion characteristics of composite metallic materials couple." *British Corrosion Journal*, 24(219).

Boyd, J., et al. (1991). "Galvanic corrosion effects on carbon fiber composites," *Proc., 36th International Sampe Symposium*, April 15–18, pp. 1217–1231.

Bruneau, M., and Walker, D. (1994) "Cyclic testing of pultruded fiber-reinforced plastic beam-to-column rigid connection." *ASCE J. Struct. Eng.*, 120(9), 2637–2652.

Carrion, J. E., LaFave, J. M., and Hjelmstad, K. D. (2005). "Experimental behavior of monolithic composite cuff connections for fiber-reinforced plastic box sections." *Composite Struct.*, 67, 333–345.

Chambers, R. E., ed. (1993). "Plastics composites for 21st century construction," *Proc., 1993 ASCE Annual Convention and Exposition*, Dallas, TX, October 24–28, p. 80.

Clarke, J. L., ed. (1996). "Structural design of polymer composites." *EUROCOMP design code and handbook*. E & FN Spon/Chapman & Hall, London.

Creative Pultrusions, Inc. (2004). *Creative Pultrusions design guide*, Creative Pultrusions Inc., Alum Bank, Pa.

Cunha, J., Foiltete, E., and Bouhaddi, N. (2008). "Evaluation of stiffness of semi-rigid joints in pultruded profiles from dynamic and static data by using model updating techniques." *Engineering Structures,* 30(4), 1024–1036.

Delta Composites, LLC. (2009). *Delta design guide*, Delta Composites, LLC, Spring, Tex.

Ewins, D. J. (1989). *Modal testing: Theory and practice*, John Wiley & Sons, Inc., New York.

Enduro Systems, Inc. (2009). *Enduro Tuff Span technical data and design guide,* Enduro Systems, Inc., Houston, Tex.

Fiberline Composites A/S. (2004). *Fiberline design manual*, Fiberline Composites A/S, Kolding, Denmark.

Fuji, Y., Murakami, A., and Kato, K. (1994). "A study on the stress corrosion cracking of GFRP: Effect of the toughness of the matrix resin on the fatigue damage and stress corrosion cracking of GFRP." *J. Mat. Sci.*, 29, 4279–4285.

Gerstle, K. H. (1985). "Flexibly connected steel frames." R. Narayagan, ed., *Steel framed structures: Stability and strength*, Elsevier Applied Science, Essex, UK, Chap. 7, pp. 205–239.

Goland, M. and Reissner, E. (1944). "The stresses in cemented joints", *Journal of Applied Mechanics*, 11, 17–27.

Green, A. (1985). *Civil Euugineering*, 55(7).

Harte, A. M., and McCann, D. (2001). "Finite element modelling of the semi-rigid behaviour of pultruded FRP connections." *Journal of Materials Processing Technology*, 119(1–3), 98–103.

Hart-Smith, L. J. (1973a). "Adhesive-bonded single-lap joints." Technical Report NASA CR112234, Contract NAS1-11234, McDonnell Douglas/Douglas Aircraft Company.

Hart-Smith, L. J. (1973b). "Adhesive-bonded double-lap joints." Technical Report NASA CR112235, Contract NAS1-11234, McDonnell Douglas/Douglas Aircraft Company.

Hart-Smith, L. J. (1973c). "Adhesive-bonded scarf and stepped lap joints." Technical Report NASA CR112237, Contract NAS1-11234, McDonnell Douglas/Douglas Aircraft Company.

Hassan, N. K., Mohamedien, M. A., and Rizkalla, S. H. (1997a). "Multi-bolted joints for GFRP structural members." *J. Compos. Constr.*, 1(1), 3–6.

Hassan, N. K., Mohamedien, M. A., and Rizkalla, S. H. (1997b). "Rational model for multibolted connections for GFRP members." *J. Compos. Constr.*, 1(2), 71–78.

Lopez-Anido, R., Falker, E., Mittelstadt, B., and Troutman, D. (1999). "Shear tests of FRP pultruded beam-to-column connections with clip angles." *Proc., 5th ASCE Mat. Eng. Cong.,* May 10–12, Cincinnati, Ohio, ASCE, Reston, Va., pp. 92–99.

Merkes, D., and Bank, L. C. (1999*).* "Longitudinal lap splices for pultruded FRP tubes." *Proc., 5th ASCE Mat. Eng. Cong.*, May 10–12, Cincinnati, Ohio, ASCE, Reston, Va., pp. 60–67.

Morsi, A. A., Wissman, D., and Cook, J. (1984) "Column base connections of fiber-reinforced plastics." *Material selection, design and tooling for structural plastics*, ASCE, New York.

Mosallam, A. S. (1990). "Short and long-term behavior of pultruded fiber-reinforced plastic frame." Ph.D. dissertation, The Catholic University of America, Washington, D.C.

Mosallam, A. S., and Bank, L. C. (1992). "Short-term behavior of pultruded fiber-reinforced plastic frame." *ASCE J. Struct. Eng.*, 118(7), 1937–1954.

Mosallam, A. S. (1993a). "An innovative technique for joining pultruded frame structures." Presented at the Task Force A2C51 (Structural Applications of Fiber-Reinforced Plastics) meeting, Transportation Research Board (TRB) Annual Conference, Washington, D.C., January.

Mosallam, A. S. (1993b). "Pultruded composites: Materials for the 21st century." *Plastics composites for 21st century construction*, ASCE, New York, pp. 23–55.

Mosallam, A. S. (1993c) "Pultruded composites: Applications and future in Egypt." *Arab Roads J.*, 2, 34-67.

Mosallam, A. S., (1993d). "Stiffness and strength characteristics of PFRP UC/beam-to-column connections." *Proc., ASME Energy-Sources Tech. Conf. and Expo*, Texas, January 31–February 4, *Composite Mat. Tech.*, PD-Vol. 53, pp. 275–283.

Mosallam, A. S., and Abdelhamid, M. K. (1993). "Dynamic behavior of PFRP structural sections." *Composite Mat. Tech.*, 53, 37–44.

Mosallam, A. S., Abdelhamid, M. K., and Conway, J. (1993). "Performance of pultruded FRP connections under static and dynamic loads." *J. Reinf. Plastics and Composites*, 13, 386–407.

Mosallam, A. S. (1994a). "Applications of structural composites for developing countries." *Arab Roads J.*, 5, 13–22 [in Arabic].

Mosallam, A. S. (1994b). "Connections for pultruded composites: A review and evaluation." K. D. Basham, ed., *Infrastructures: New materials and methods of repair*, ASCE, New York, pp. 1001–1017.

Mosallam, A. S., Bedewi, N. E., and Goldstein, E. (1994). "Design optimization of FRP universal connectors." *Polymer & Polymer Composites*, 2(2), 115A–123A.

Mosallam, A. S. (1995a). "Behavior of pultruded composites frame structures and connections." J. Colville, and A. Amde, eds., *Research transformed into practice*, ASCE, New York, pp. 96–107.

Mosallam, A. S. (1995b). "Cyclic and creep behavior of UC composite frame connections." *Proc., 2nd Int. Conf. for Composites Eng. (ICCE/2)*, New Orleans, La., pp. 521–522.

Mosallam, A. S. (1995c). "Performance of pultruded composites frame connections under cyclic and sustained loads." *Fiber-reinforced structural plastics in civil engineering*, Tata McGraw-Hill, New Delhi, India, pp. 307–316.

Mosallam, A. S. (1995d). "Seismic performance of pultruded frame structures." *Proc., Composites '95, The Winning Edge*, October 18–21, Anaheim, Calif., Composites Fabricators Association (CFA).

Mosallam, A. S. (1995e). "Semi-rigid behavior of beam-to-column connections for polymer composite frame structures." *Proc., 4th Pan American Cong. Appl. Mech. (PACAM IV)*, January 3–6, Universidad del Salvador, Buenos Aires, Argentina.

Mosallam, A. S., and Chambers, R. E. (1995). "Design procedure for predicting creep and recovery of pultruded composites." *Proc., 50th Ann. Conf.*, January 30–February 1, Composites Institute, Paper No. 6-c.

Mosallam, A. S. (1996a). "Connections and reinforcements design details for PFRP composite structures." *J. Reinf. Plastics and Composites*, 14, 752–784.

Mosallam, A. S. (1996b). "Viscoelastic behavior of semi-rigid composites frame connections." *Proc., 3rd Int. Conf. on Composites Eng. (ICCE/3)*, July 21–26, New Orleans, La.

Mosallam, A. S. (1997a). "Cyclic and long-term behavior of pultruded beam-to-column composite connections." *Proc., Int. Composites Expo '97 Conf.*, January 27–29, Session 14-B, Nashville, Tenn., pp. 1–18.

Mosallam, A. S. (1997b). "Structural evaluation of polymer composite connections for civil engineering structures." *Proc., SAMPE Conf.*, April, Anaheim, Calif., pp. 269–280.

Mosallam A. S. (1998a). "Impact of materials selection, structural detailing, and environment on structural durability of pultruded composites." *Proc., 1998 Int. Composites Expo*, The Composites Institute, Nashville, Tenn., pp. EI6–7.

Mosallam, A. S. (1998b). "State-of-the-art review on connections for pultruded composites." *Proc., EPTA Ann. Conf.*, Vienna, Austria, April, European Pultrusion Technology Association (EPTA).

Mosallam, A. S. (1999). "Cyclic behavior of FRP interior frame connections for pultruded structures." *Proc., ASCE 5th Mat. Cong.*, Cincinnati, Ohio, May 10–12, ASCE, Reston, Va., pp. 84–91.

Mosallam, A. S. (2000). "Fully reversed cyclic performance of pultruded frame structures." *Proc., EPTA 5th Ann. World Conf. and Expo*, April 13–14, Berlin, European Pultrusion Technology Association (EPTA) [CD ROM].

Mosallam, A. S., El Sadek, A., Miraj, R., and Pul, S. (2010a). "Evaluation of pultruded composite column based connections." Report No. SETH-10-FRP-CON1, Structural Engineering Test Hall Report, Department of Civil and Environmental Engineering, University of California, Irvine.

Mosallam, A. S., Pul, S., Elsadek, A. (2010b). "Experimental assessment of web-flange junctions rotational behavior of PFRP profiles." *Proc., 9th Int'l. Cong. on Advances in Civil Engineering*, Trabzon, Turkey [CD ROM].

Mosallam, A. S., El Sadek A. A., and Pul, S. (2010c) "Pull-out behavior of web-flange junctions of open-web pultruded composites." *Proc., 9th International Congress on Advances in Civil Engineering* (ASCE), Osman Turan Congress and Culture Center, Karadeniz Technical University, Trabzon, Turkey, 27–30 September.

Mottram, J. T. (1999b). "Further tests on beam-to-column connections for pultruded frames: Flange-cleated, experimental problems and results." *Research Report CE60*, School of Engineering, University of Warwick, Coventry, UK.

Mottram, J. T. (1999a). "Connection tests pultruded frames." *Research Report CE47*, School of Engineering, University of Warwick, Coventry, UK.

Mottram, J. T., and Turvey, G. J., eds. (1998). *State-of-the-art review on design, testing, analysis and applications of polymeric composite connections*, European Cooperation in the Field of Scientific and Technical Research [now European Cooperation in Science and Technology (COST)], Brussels.

Mottram, J. T., and Zheng, Y. (1996). "State-of-the-art review on the design of beam-to-column connections for pultruded frames." *Composite Struct.*, 15, 387–401.

Mottram, J. T. and Zheng, Y. (1999a). "Further tests on beam-to-column connections for pultruded frames: Flange-cleated." *J. Composites for Construction*, 3(3), 108–116.

Mottram, J. T. and Zheng, Y. (1999b). "Further tests on beam-to-column connections for pultruded frames: Web-cleated." *J. Composites for Construction*, 3(1), 3–11.

Na, G.-S. (2008). "Load-displacement behavior of frame structures composed of fiber-reinforced polymeric composite materials." Ph.D. dissertation, School of Civil and Environmental Engineering, Georgia Institute of Technology, Atlanta, Ga.

Prabhakaran, R., Razzaq, Z., and Devara, S. (1996). "Load and resistance factor design (LRFD) approach for bolted joints in pultruded composites." *Composites: Part B*, Vol. 27B, pp. 351–360.

Sanders, D. H., Gordaninejad, F., and Murdi, S. (1996). "FRP beam-to-column connections using adhesives." *Proc., ICCI '96*, January 15–17, Tucson, Ariz., pp. 596–607.

Smith, S. J., Parsons, I. D., and Hjelmstad, K. D. (1999). "Design models of GFRP connections." *Proc., 5th ASCE Mat. Eng. Cong.*, May 10–12, Cincinnati, Ohio, pp. 100–107.

Smith, S. J., Parsons, I. D., and Hjelmstad, K. D. (1996). "A study of the behavior of joints in GFRP pultruded rectangular tubes and I-beams." *Proc., ICCI '96*, January 15–17, Tucson, Ariz., pp. 583–595.

Stelmack, T. W., Marley, M. J., and K. H. Gerstle (1986). "Analysis and tests of flexibly connected steel frames." *ASCE Struct. J.*, 112, 1573–1588.

Strongwell Company. (2004). *EXTREN design manual*, Strongwell Company (formerly MMFG), Bristol, Va.

Turvey, G. J. (1998). "Recent developments in testing, design, analysis and modeling of bolted connections in pultruded GRP frames made of open-section profiles." *Proc., 4th EPTA Pultrusion Conf.*, April 9–11, Vienna, Austria, Paper 4.

Turvey, G. J., and Cooper, C. (2000). "Semi-rigid column–base connections in pultruded GRP frame structures." *Computers & Structures*, 76, (1–3), 77–88.

Turvey, G. J., and Cooper, C. (1998). "Semi-rigid connections and their effects on the sway response of pultruded GRP columns in low-rise frame structures." *Proc., ICCI '98*, Tucson, Ariz., January, Vol. II, pp. 221–235.

Wong, Y. L., Chan, S. L., and Nethercot, D. A. (1996). "A simplified design method for unbraced frames with semi-rigid connections." *Proc., International Conference on Advances in Steel Structures (ICASS 96)*, Pergamon, pp. 213–220.

Zahr, S., Hill, S., and Morgan, H., (1993). "Semi-rigid behavior of PFRP/ UC beam-to-column connections." *Proc., ANTEC '93 Conf.*, May 9–13, New Orleans, La., Society of Plastic Engineers, pp. 1496–1502.

CHAPTER 8

ANALYSIS AND DESIGN OF SEMI-RIGID PULTRUDED FIBER-REINFORCED POLYMER FRAME CONNECTIONS

8.1 SEMI-RIGID BEHAVIOR OF PFRP CONNECTIONS

The conventional design approach used by most engineers is based on one of two extreme assumptions: the fixed (rigid) connection model and the hinged (pinned) connection model. In reality, the behavior of most frame connections always falls between these two extremes (Fig. 8-1). In the semi-rigid connection analysis (partially restrained), the relative rotation between the beam and column is considered. The most accurate tool in characterizing these connection models is by constructing, experimentally, a moment–rotation (M/θ) curve. The M/θ curve describes the moment transmitted by the joint and the resulting relative rotation of the beam with respect to the column (refer to Fig. 8-2). The slope of these curves represents the *rotational stiffness* (k) for each connection at a specific moment level.

Connection performance can also be characterized by *rotational flexibility* (l/k). For frame structures, the rotational connection flexibility will affect the overall frame deformations, especially the frame sway when subjected to lateral loads. In addition, the reduction in the stiffness of frame structure will affect the natural period of vibration and, consequently, its behavior under seismic or wind loads. The degree of flexibility of the frame connection will also affect the internal force and moment distribution in beams and columns (Gerstle 1988; Ozturk and Catal 2005). A wrong assumption can result in an uneconomical and unsafe design of the structural system. For example, underestimating the rotational stiffness (the resistance of the connection against relative rotation when subjected to moment) will result in overdesign of beam sections and underdesign of the PFRP column. On the other hand, overestimating the
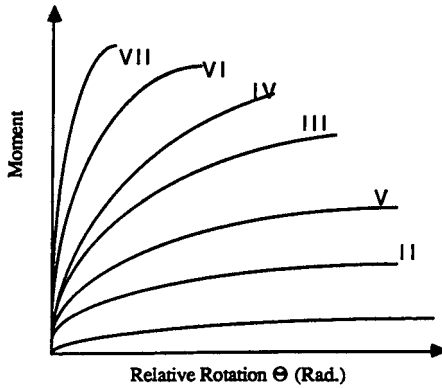
Figure 8-1. *Moment–rotation curves for various degrees of rotational stiffness.*
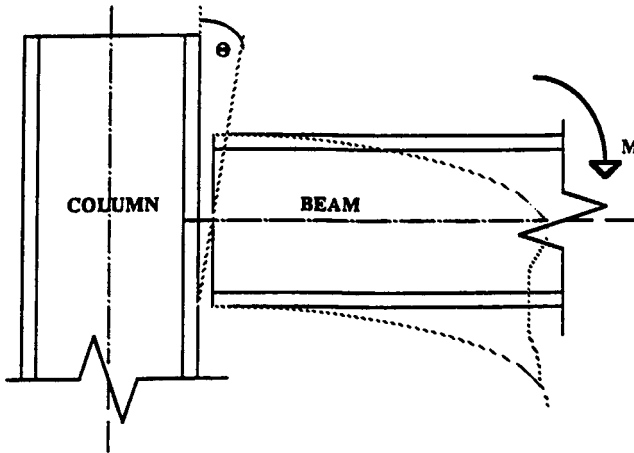
Figure 8-2. *Relative rotation between the beam and column in semi-rigid PFRP connections.*

rotational stiffness of the connection will result in selecting an inadequate beam section and an uneconomical column section. This will indirectly affect the structural performance of structure, including the buckling and post-buckling of PFRP thin-walled sections. Continuing, most available beam selection tables provided by manufacturers are based on the extreme assumption of hinged ends. As discussed earlier, this supposition will result in increasing beam sections or overestimating the capacity of a particular design, and may lead to the selection of undersized column sections.

8.2 MOMENT–ROTATION RELATIONS (*M*/Θ)

Realistic prediction of the degree of rigidity or the rotational stiffness of the connection can only be obtained through experimental results. Connection rotational stiffness is calculated from experimental moment/rotation (M/θ) curves. In these plots, the abscissa represents the relative rotation (θ) and the ordinate represents the applied moment (M). The vertical axis (M) represents the perfectly fixed (rigid) connection, while the horizontal axis (θ) represents the perfectly pinned (hinged) connection. In practice, all PFRP connections fall within the quadrant between these two extremes (Mosallam and Abdelhamid 1993). For steel connections, several earlier experimental and analytical studies describe these relations for different connection details. For example, Frye and Morris (1975), Mosallam (1990), and Zahr et al. (1993) represented the experimental M/θ data using a polynomial expression. Jones et al. (1982) presented a close approximation using a cubic B-spline model, Ang and Morris (1984) used the Ramberg-Osgood exponential function to express the connection standardized behavior, and Lui and Chen (1985) developed an exponential function that includes the strain-hardening stiffness of the connections.

8.3 CONNECTION STIFFNESS EXPRESSIONS

In general, M/θ relations are nonlinear, with decreasing stiffness described by the instantaneous slope (k) as the applied moment increases. To describe the rotational stiffness of PFRP connections, several techniques employed for steel connections are available. Among these methods are:

8.3.1 Initial Connection Stiffness (K$_i$)

This stiffness coefficient is determined from the initial tangent slope of the M/θ curve (refer to Fig. 8-3). In general, this initial stiffness value will result in a relatively high stiffness as compared to the actual stiffness at advanced loading stages. Mosallam and Abdelhamid (1993) has adopted this procedure to predict the long-term response of PFRP frame structure. The predicted results using this initial stiffness coefficient were satisfactory as compared to results obtained from the full-scale frame test. The initial stiffness K_i is expressed as:

$$K_i = \frac{M}{\theta} \tag{8-1}$$
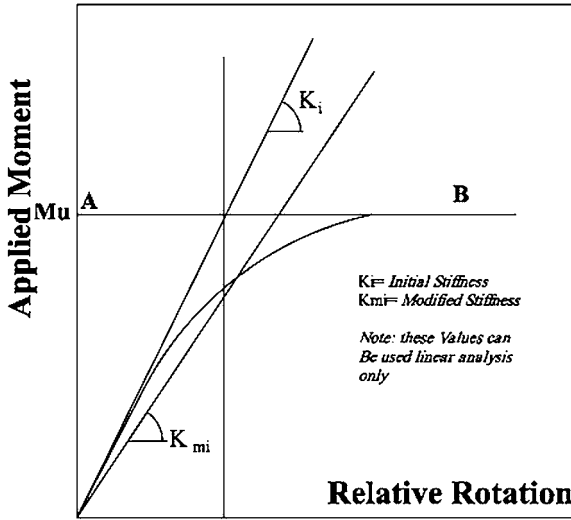
Figure 8-3. Initial and modified initial stiffness coefficients for semi-rigid connections.

8.3.2 Modified Initial Stiffness (K_{mi})

The modified initial stiffness (K_{mi}) is a moderately softer stiffness coefficient as compared to the initial K_i. This modified stiffness is defined as the secant modulus corresponding to the initial rotation (Θ_0). As shown in Fig. 8-3, the value of Θ_0 is determined by calculating the relative rotation corresponding to the intersection point of both the initial stiffness line and the ultimate moment line (AB).

8.3.3 Beam-Line Method

Beyond the service (linear) loading stage, the connection stiffness will decrease in a nonlinear fashion. To account for this decrease in stiffness, the beam-line concept can be used to better describe the connection stiffness. In 1934, Batho proposed a simple graphical approach for determining the angle of rotation and the actual end moment for semi-rigid connections. To illustrate this concept, consider a PFRP beam subjected to a concentrated load at mid-span (refer to Fig. 8-4). The rotation at the end of the beam under any loading condition is a linear function of the applied end moment. The relation can be obtained for any particular span and load pattern. If the end condition of this beam is totally fixed ($\Theta = 0$), then the corresponding end moment is equal to the fixed end moment ($PL/8$). On the other hand, if the beam is simply supported ($M = 0$), the end
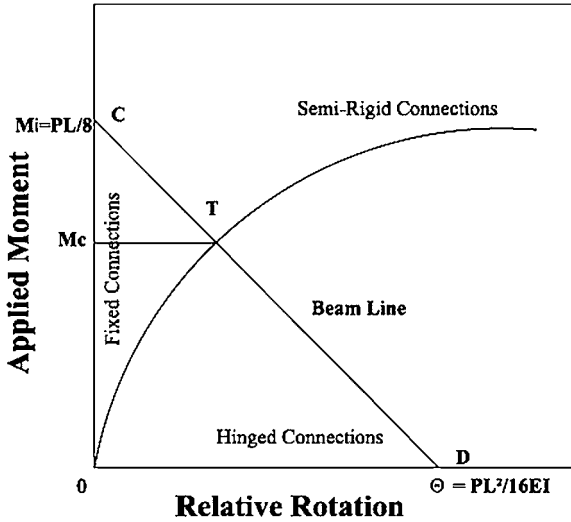
Figure 8-4. *Beam-line method for semi-rigid connections analysis.*

rotation can be calculated using virtual work or other techniques (in this example, $\Theta = PL^2/16EI$ as shown in Fig. 8-4). These two conditions produce two points on the linear M/θ curve of the beam (at the x and y axes). The line connecting these two points (C and D) is called the beam-line, as shown in Fig. 8-4. The intersection of the beam line CD and the connection M/Θ curve gives the moment and rotation that are actually present in the member. It should be noted that, for this procedure, the end deformation of the column was ignored based upon the assumption that a relatively small deformation will occur at the column end. The column-end deformation is prevented from rotation by the beam moment acting on the opposite side. For design, the actual value for the negative beam end moment, M_e, can be determined from the graph. This value falls between zero and $wL^2/12$ for a uniformly loaded beam. See Mosallam (1994) for discussion on the end moment for semi-rigid connections. Mottram and Zheng (1996) have adopted this beam-line technique to describe PFRP interior beam-to-column connections.

8.3.4. Closed-Form Expressions for Beams with Semi-Rigid End Connections

Simple expressions for deflection and end rotations of composite beams with semi-rigid behavior, which accounts for shear deformation, was proposed by Turvey (1998). In developing this closed-form expression, the

moment–rotation behavior was assumed to be linear. This closed-form expression is given by:

$$\delta = \frac{QL^3}{k_1 E_{11} I_{11}}\left(\frac{1 + 48\alpha + k_2\beta + 96\alpha\gamma}{1 + 2\beta}\right) \tag{8-2a}$$

or

$$\delta = \phi\left(\frac{1 + \varpi}{1 + 2\beta}\right) \tag{8-2b}$$

where

$$\phi = \frac{QL^3}{k_1 E_{11} I_{11}} \tag{8-3a}$$

$$\varpi = 48\alpha + k_2\beta + 96\alpha\beta \tag{8-3b}$$

and
δ = mid-span deflection
L = span
Q = total applied load
E_{11} = longitudinal modulus of elasticity of the beam
I_{11} = moment of inertia (major axis)
k_1 and k_2 = constants that depend on the load distribution (refer to Table 8-1)
β = dimensionless connection flexibility parameter expressed as:

$$\beta = \frac{E_{11} I_{11}}{K_i L} \tag{8-4}$$

where
K_i = initial linear rotational stiffness of the connection which is determined from the M/θ experimental curve as described earlier
α = dimensionless shear flexibility parameter expressed as:

$$\alpha = \frac{E_{11} I_{11}}{k^V G_{21} A L^2} \tag{8-5}$$
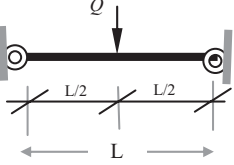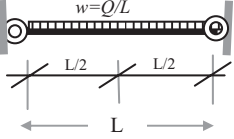
where
k^V = modified shear coefficient. Different expressions for calculating this coefficient can be found in Bank and Bednarczyk (1988) and Mosallam and Chambers (1995).
G_{21} = shear modulus
A = cross-sectional area.

Table 8-1. Values of Coefficients k_1, k_2, k_3, and k_4 for Semi-Rigid PFRP Beams with Semi-Rigid End Connections

Beam Loading Distribution on Beams with Semi-Rigid Ends		k_1	k_2	k_3	k_4
	Point load at mid-span	192	8	8	4
	Uniform load over entire span	384	10	12	5

If the shear deformation effect is ignored (i.e., $\alpha = 0$), Eq. 8-2 will be reduced to the following simpler form:

$$\delta = \frac{QL^3}{k_1 E_{11} I_{11}} \left(\frac{1 + k_2 \beta}{1 + 2\beta} \right) \tag{8-6}$$

Equation 8-6 will reduce to the commonly known mid-span deflection expressions for simply supported beams by setting $K_i = 0$, and consequently, $\beta = \infty$:

$$\delta = \frac{QL^3 k_2}{2 k_1 E_{11} I_{11}} \tag{8-7}$$

Similarly, the mid-span deflection expression for fixed end beams (without a shear deflection component) can be obtained from Eq. 8-6 by setting $K_i = \infty$, and consequently, $\beta = 0$:

$$\delta = \frac{QL^3}{k_1 E_{11} I_{11}} \tag{8-8}$$

Turvey (1997) also developed the following expression for calculating the rotation of the semi-rigid ends of a composite beam:

$$\theta = \frac{QL^2}{k_3 E_{11} I_{11}} \left(\frac{\beta}{1 + 2\beta} \right) \tag{8-9}$$

It should be noted that, as expected, the shear deformation has no effect on Eq. 8-9. Also, for a beam with fixed ends (i.e., $K_i = \infty$, and consequently $\beta = 0$), Eq. 8-8 reduces to zero, and by setting $K_i = 0$, and consequently, $\beta = \infty$, the following expression is obtained from Eq. 8-9 describing the end rotations of a simply supported composite beam:

$$\theta = \frac{QL^2}{2k_3 E_{11} I_{11}} \tag{8-10}$$

8.3.4.1 Performance Indices.   To appreciate the gain of including the partial fixity (semi-rigidity) of commonly used connection details of PFRP frame connections, Turvey (1997) proposed expressions for what are called "performance indices" that relate the mid-span deflection, associated load, and end rotations of composite beams with semi-rigid ends and semi-rigid beams to identical composite beams with simply supported end conditions (which is commonly used today in sizing PFRP frame structures members). These coefficients are similar to the λ-coefficients introduced initially by Mosallam and Chambers (1995) to relate the long-term total deflection to short-term instantaneous deflection of PFRP beams.

8.3.4.1.1 Deflection Reduction Index (λ_δ).   The deflection reduction index is the ratio between the mid-span deflections of a beam with a specific semi-rigid rotational stiffness and a simply supported beam having identical properties, dimensions, and subjected to the same total load (Q). This expression is obtained by dividing Eq. 8-2 by the same equation after setting $\beta = \infty$ (a simply supported case). Introducing a new deflection factor k_4 (refer to Table 8-1) and rearranging, we get:

$$\lambda_\delta = \left(\frac{1 + 48\alpha + k_2\beta + 96\alpha\beta}{k_4 + 48\alpha + k_2\beta + 96\alpha\beta} \right) \tag{8-11}$$

or

$$\lambda_\delta = \frac{1 + \varpi}{k_4 + \varpi} \tag{8-12}$$

If the shear deformation component is neglected (i.e., $\alpha = 0$), Eq. 8-11 will reduce to:

$$\lambda_\delta = \left(\frac{1 + k_2\beta}{k_4 + k_2\beta} \right) \tag{8-13}$$

As expected, λ_δ equals unity for the case of a simply supported beam (i.e., $\beta = \infty$). On the other hand, if the beam's ends are fixed, Eq. 8-11 reduces to:

$$\lambda_\delta = \left(\frac{1}{k_4} \right) \qquad (8\text{-}14)$$

Equation 8-14 results in the known ratio between fixed-end and simply supported mid-span deflections of identical beams subjected to identical loads.

8.3.4.1.2 Load Enhancement Index (λ_Q). The load enhancement index is the ratio between the load capacity of a beam with a specific semi-rigid rotational stiffness and a simply supported beam having identical properties, dimensions, and subjected to the same deflection limit (e.g., $\delta_{max} = L/360$). This can be obtained by rearranging the two forms of Eq. 8-2. It is obvious that this enhancement index is simply the inverse of the deflection reduction index (λ_δ), in general, regardless of the type of end conditions or the inclusion of the shear deformation effects, that is,

$$\lambda_Q = \left(\frac{1}{\lambda_\delta} \right) \qquad (8\text{-}15)$$

As expected, λ_Q equals unity for the case of a simply supported beam (i.e., $\beta = \infty$). On the other hand, if the beam's ends are fixed, Eq. 8-11 reduces to:

$$\lambda_Q = k_4 \qquad (8\text{-}16)$$

Equation 8-16 results in the known ratio between fixed-end and simply supported load capacities of identical beams subjected to identical span/ deflection limits; that is, a fixed beam loading capacity is k_4^{th} the capacity of an identical beam with same span-to-deflection limit.

8.3.4.1.3 Span Enhancement Index (λ_L). The span enhancement index for a composite beam with a prescribed load and a mid-span deflection limit is the ratio between the allowable span of a beam with a specific semi-rigid rotational stiffness and the allowable span of a simply supported beam having identical properties, dimensions, and subjected to the same loads and mid-span deflection limit. This can be determined as the positive root of the following cubic equation:

$$\lambda_L^3 + k_2 \lambda_L^2 \beta - k_4 \lambda_L - k_2 \beta = 0 \qquad (8\text{-}17)$$

For a composite beam with a fixed end, i.e. $K_i = \infty$, and consequently $\beta = 0$, Eq. 8-17 reduces to the following simpler form:

$$\lambda_L^3 + k_4 \lambda_L = 0 \tag{8-18}$$

The roots of Eq. 8-18 are: $\lambda_L = -\sqrt{k_4}$, $\lambda_L = +\sqrt{k_4}$, and $\lambda_L = 0$. Thus, the span enhancement index is $\lambda_L = +\sqrt{k_4}$ (the only positive root). Similarly, for a case of a simply supported beam, i.e. $K_i = 0$, and consequently, $\beta = \infty$, Eq. 8-17 will be simplified to the following form:

$$\lambda_L^2 - 1 = 0 \tag{8-19}$$

Solving Eq. 8-19 yields the following two roots: $\lambda_L = \pm 1$. Using the positive root, the span enhancement index, as expected, is equal to unity.

8.3.4.1.4 Rotational Capacity (θ_c). It is advantageous to express the rotational capacity of a composite beam in terms of the serviceability limit on mid-span deflection, that is, as a function of the prescribed deflection-to-span ratio, κ_c (Turvey 1997). An expression for the rotational capacity, θ_c, is obtained by combining Eqs. 8-2 and 8-8, and replacing $\frac{\delta}{L}$ by the deflection-to-span ratio κ_c. Thus:

$$\theta_c = \frac{k_1}{k_3}\left(\frac{\kappa_c \beta}{1+\varpi}\right) \tag{8-20}$$

If the shear deformation effect is ignored, i.e., $\alpha = 0$, then Eq. 8-20 reduces to:

$$\theta_c = \frac{k_1}{k_3}\left(\frac{\kappa_c \beta}{1+k_2\beta}\right) \tag{8-21}$$

To demonstrate the effectiveness of the aforementioned closed-form equations for determining both the mid-span deflection and the end rotations of a composite beam with semi-rigid end connections, two numerical examples are presented.

Example 8-1: Calculate the mid-span deflection and the end rotations of an 8 in. × 8 in. × 3/8 in. (203 mm × 203 mm × 9.5 mm) PFRP E-glass/vinylester H-beam (Pultex 1625) with semi-rigid end connection details (refer to Fig. 8-5 here and Fig. 7-20D in Chapter 7 for end connection details). The total factored load is 2,500 lb (11,120 N) applied at the mid-span. The total span of the PFRP beam is 9 ft (2.74 m). The initial linear
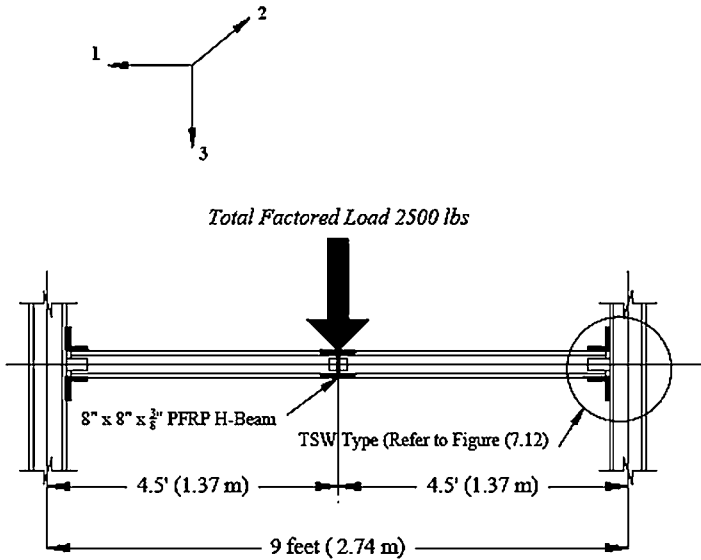
Figure 8-5. Details of the semi-rigid connected PFRP beam of Example 8-1.

rotational stiffnesses of the end connections were determined experimentally [refer to connection detail TSW in Fig. 7-21 and Table 7-3 to be 7,000 kip-in./rad (790.3 kN-m/rad)]. The following are the PFRP beam mechanical properties that were measured experimentally (Mosallam 1990): $E_{11} = 2.35 \times 10^6$ psi (16.20 GPa), $E_{22} = 1.00 \times 10^6$ psi (6.90 GPa), and $G_{21} = 0.54 \times 10^6$ psi (3.72 GPa).

SOLUTION

   i) Section Properties: Using the *Creative Pultrusions Design Guide* tables (Creative Pultrusions, Inc. 2003), the major moment of inertia and the cross-sectional area of the beam pultruded profiles are $I_{11} = 99.18$ in.⁴ (4,127.8 cm⁴); and $A = 8.73$ in.² (56.31 cm²), respectively.
   ii) Calculate the Modified Shear Coefficent (k^v): Due to the anisotropic nature of PFRP composites, mechanical properties are directionally-dependent. As a consequance, the ratio of the in-plane longitudinal modulus, E_{11}, to the in-plane shear modulus, G_{21}, for the pultruded profiles is higher than that of isotropic materials. In our case, $E_{11}/G_{21} = 4.35$ as compared to a ratio of 2.60 for isotropic materials. For this reason, it is recommended to consider the shear deformation component when calculating the total mid-span deflection (Mosallam 1990). The total deflection at any point along the beam span is calculated using the following equation (Mosallam and Bank 1992):

$$\delta_{total} = \frac{f_F}{E_{11}I_{11}} + \frac{f_V}{k^v A G_{21}} \tag{8-22}$$

where

δ_{total} = total deflection due to bending moments and shear forces

f_F and f_V = functions that depend upon the loading and the boundary conditions (refer to Table 8-2). Note that subscript F refers to the flexural term, and subscript V refers to the shear term

k^v = the modified shear correction factor (Bank and Bednarczyk 1988).

For H-beams (*open-web profiles*):
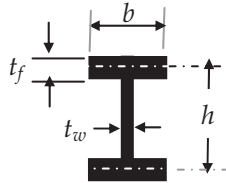
$$k^v = \frac{20(\zeta + 3m)^2}{\left[\dfrac{E_f}{G_f}(60m^2n^2 + 60\zeta mn^2) + \dfrac{E_f}{G_w}(180m^3 + 300\zeta m^2 + 144\zeta^2 m + 24\zeta^3) \right. \\ \left. + \nu_f(60m^2n^2 + 40\zeta mn^2) + \nu_w(30m^2 + 6\zeta m - 4\zeta^2) \right]}$$

$$\tag{8-23}$$

For box-beams (*closed-web profiles*):
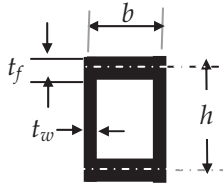
$$k^v = \frac{20(\zeta + 3m)^2}{\left[\dfrac{E_f}{G_f}(60m_b^2n^2 + 60\zeta m_b n^2) + \dfrac{E_f}{G_w}(180m_b^3 + 300\zeta m^2 + 144\zeta^2 m_b + 24\zeta^3) \right. \\ \left. + \nu_f(-30m_b^2n^2 - 50\zeta m_b n^2) + \nu_w(30m_b^2 + 6\zeta m_b - 4\zeta^2) \right]}$$

$$\tag{8-24a}$$

where

$$n = \frac{b}{h}$$

$$m = \frac{2bt_f}{ht_w}$$

$$m_b = \frac{bt_w}{ht_f}$$

t_f = flange thickness
t_w = web thickness
b = flange width
h = distance between the centerlines of the flanges

$$\zeta = \frac{E_w}{E_f}$$

E_w, G_w = longitudinal modulus of elasticity and shear modulus of the web
E_f, G_f = longitudinal modulus of elasticity and shear modulus of the flanges
v_f and v_w = Poisson's ratios for the flanges and the web, respectively.

It should be noted that, for prelimanary analysis, the shear correction factor can be taken as:

$$k^v \cong \frac{A_{web}}{A_{Gross}} \tag{8-24b}$$

where A_{web} = the area of the web(s), and A_{Gross} is the gross sectional area = $A_{web(s)} + A_{flanges}$.

Using Eq. 8-23, we have:

$$k^v = 0.29$$

Note: The approximate value of this coefficient according to Eq. 8-24b is:
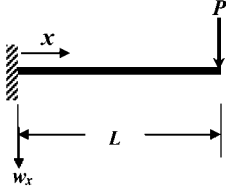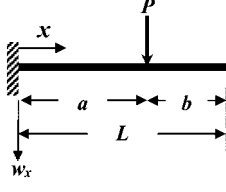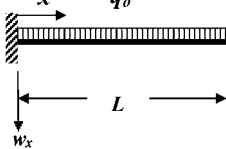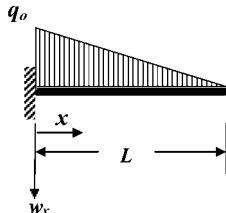
$$k^v \cong \frac{A_{web}}{A_{Gross}} \cong \frac{7.25 \text{ in.} \times 0.375 \text{ in.}}{8.73^2 \text{ in.}^2} = 0.31$$

iii) Calculate the shear flexibility ratio:
Using Eq. 8-5, we get:
For $k^v = 1$:
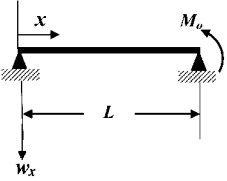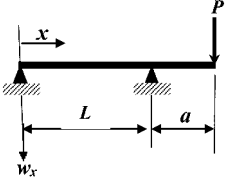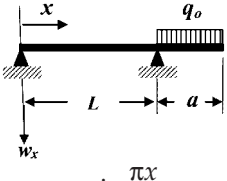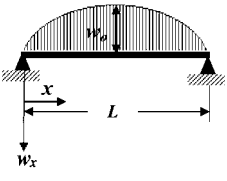
Table 8-2. Flexure and Shear Deformation Functions

Load Case	Boundary & Loading Conditions	$f_1(x)$	$f_2(x)$
Load Case 1		$\dfrac{P}{6}(-x^3 + 3Lx^2)$	Px
Load Case 2		$\dfrac{Px^2}{6}(3a - x); 0 \le x \le a$ $\dfrac{Pa^2}{6}(3x - a); a \le x \le L$	$Px; 0 \le x \le a$ $Pa; a \le x \le L$
Load Case 3		$\dfrac{q_o}{24}(x^4 - 4Lx^3 + 6L^2x^2)$	$\dfrac{q_o}{2}(-x^2 + 2Lx)$
Load Case 4		$\dfrac{q_o x^2}{120L}(10L^3 - 10L^2x + 5Lx^2 - x^3)$	$\dfrac{q_o}{6L}(3L^2x - 3Lx^2 + x^3)$

Load Case 5

$$-\frac{M_o x^2}{2}$$

Zero

Load Case 6

$$\frac{Pbx}{6L}(L^2 - x^2 - b^2); \; 0 \le x \le a$$

$$\frac{Pb}{6L}\left\{\frac{L}{b}(x-a)^3 + x(L^2 - b^2) - x^3\right\}; \; a \le x \le L$$

$$\frac{Pbx}{L}; \; 0 \le x \le a$$

$$Pa\left(1 - \frac{x}{L}\right); \; a \le x \le L$$

Load Case 7

$$\frac{P}{48}(-4x^3 + 3L^2 x)$$

$$\frac{Px}{2}$$

Load Case 8

$$\frac{Px}{6}(3aL - 3a^2 - x^2); \; 0 \le x \le a$$

$$\frac{Pa}{6}(3xL - 3x^2 - a^2); \; a \le x \le (L-a)$$

$$Px; \; 0 \le x \le a$$

$$Pa; \; a \le x \le (L-a)$$

Load Case 9

$$\frac{q_o}{24}(x^4 - 2Lx^3 + L^3 x)$$

$$\frac{q_o}{2(-x^2 + Lx)}$$

Table 8-2. Continued

Load Case	Boundary & Loading Conditions	$f_1(x)$	$f_2(x)$
Load Case 10		$\left(\dfrac{M_o}{6L(-x)^3} - L^2 x\right)$	*Zero*
Load Case 11		$\dfrac{P}{6L}(ax^3 - axL^2);\ 0 \le x \le L$ $\dfrac{P}{6}(-x^3 + 3Lx^2 + 3ax^2 - 4aLx - 3L^2x + aL^2 + L^3);$ $L \le x \le (L+a)$	*Zero*; $0 \le x \le L$ $\dfrac{P}{L}(Lx + ax - aL - L^2);$ $L \le x \le (L+a)$
Load Case 12	$w = w_0 \sin\dfrac{\pi x}{L}$	$\dfrac{q_o a^2}{12L}(x^3 - L^2 x);\ 0 \le x \le L$ $\dfrac{q_o}{24}\left\{(L+a-x)^4 + \left(4La^2x - 4a^3x - 4L^2a^2 + 4a^3L - a^4\right)\right\};$ $L \le x \le (L+a)$	*Zero*; $0 \le x \le L$ $\dfrac{q_o}{2}(x^2 - 2Lx - 2ax + 2La + L^2);$ $L \le x \le (L+a)$
Load Case 13		$\dfrac{L^4}{\pi^4} w_0 \sin\dfrac{\pi x}{L}$	$\dfrac{L^2}{\pi^2} w_0 \sin\dfrac{\pi x}{L}$

Note: For all load cases, $w_x = \dfrac{f_1(x)}{E_b I} + \dfrac{f_2(x)}{kAG}$.

$$\alpha = \frac{(2.35 \times 10^6 \text{ psi})(99.18 \text{ in.}^4)}{(0.54 \times 10^6 \text{ psi})(8.73 \text{ in.}^2)(108^2 \text{ in.}^2)} = 0.0042$$

For $k^v = 0.29$:

$$\alpha = \frac{0.0042}{0.29} = 0.015$$

iv) Calculate the rotational flexability ratio (β):
Using Eq. 8-4, we get:

$$\beta = \frac{(2.35 \times 10^6 \text{ psi})(99.18 \text{ in.}^4)}{\left(7,000,000 \dfrac{\text{lb-in.}}{\text{rad}}\right)(108 \text{ in.})} = 0.31$$

v) Calculate the mid-span deflection:
From Table 8-1, we have:

$$k_1 = 192, \ k_2 = 8, \ k_3 = 8, \text{ and } k_4 = 4$$

Now, substituing in Eq. 8-5, we get:
For $k^v = 1$:
First, calculate the term ϕ (Eq. 8-3a):

$$\therefore \phi = \frac{QL^3}{k_1 E_{11} I_{11}} = \frac{(2,500 \text{ lb})(108^3 \text{ in.}^3)}{(192)(2.35 \times 10^6 \text{ psi})(99.18 \text{ in.}^4)} = 0.07 \ \frac{\text{lb-in.}}{\text{lb}}$$

Calculate the term ω (Eq. 8-3b):

$$\omega = 48\alpha + k_2\beta + 96\alpha\beta = (48)(0.0042) + (8)(0.31) + (96)(0.0042)(0.31) = 2.8$$

Substituting the above value into Eq. 8-2b, we have:

$$\delta = \phi\left(\frac{1+\omega}{1+2\beta}\right) = 0.07\left(\frac{1+2.8}{1+(2)(0.31)}\right) = 0.16 \text{ in. (4.17 mm)}$$

Similarly for $k^v = 0.29$:
Recalculate the term ω (Eq. 8-3b):

$$\omega = 48\alpha + k_2\beta + 96\alpha\beta = (48)(0.015) + (8)(0.31) + (96)(0.015)(0.31) = 3.65$$

Substituting the above values into Eq. 8-2b, we have:

$$\delta = 0.07\left(\frac{1+3.64}{1+(2)(0.31)}\right) = 0.2 \text{ in. (5.12 mm)}$$

The reason for calculating two values for the mid-span deflection is to demonstrate the effect of including the modified shear coefficient. The foregoing results show that mid-span deflection calculated using the modified shear coefficient is 25% higher than assuming $k^v = 1$ ($L/675$ vs. $L/540$).

vi) Calculate end rotations:
Using Eq. 8-8, the end rotations can be calculated as follows:

$$\theta = \frac{QL^2}{k_3 E_{11} I_{11}}\left(\frac{\beta}{1+2\beta}\right) = \frac{(2,500 \text{ lb})(108^2 \text{ in.}^2)}{(8)(2.35\times 10^6 \text{ psi})(99.18 \text{ in.}^4)}\left(\frac{0.31}{1.62}\right) = 0.003 \text{ rad (0.17°)}$$

Example 8-2: For the PFRP beam described in Example 8-1, calculate:

1. The deflection reduction index (λ_δ). Verify the results using Eq. 8-22 and Table 8-2
2. The load enhancement index (λ_q)
3. The rotation capacity (θ_c), assuming that mid-span deflection-to-span ratio (κ_c) should not exceed $L/400$

SOLUTION:

1-a) Calculate the deflection reduction index (λ_δ):
Subsituting in Eq. 8-11, we get:
For $k^v = 1$: ($\alpha = 0.0042$, $\omega = 2.8$, and $k_4 = 4$)

$$\lambda_\delta = \frac{\text{Mid-Span Deflection (semi-rigid)}}{\text{Mid-Span Deflection (simply supported)}} = \frac{1+2.8}{4+2.8} = 0.56$$

That is, the mid-span deflection of this semi-rigid is 56% of the mid-span deflection of an identical PFRP if ends were assumed to be hinges. Using the results obtained from Example 8-1, the mid-span deflection of a simply supported beam with identical physical and mechanical properties and subjected to the same load is calculated as:

$$\delta^{ss} = \frac{\delta}{\lambda_\delta} = \frac{0.16 \text{ in.}}{0.56} = 0.29 \text{ in. (7.37 mm)}$$

For $k^v = 0.29$: ($\alpha = 0.015$, $\omega = 3.65$, and $k_4 = 4$)

$$\lambda_\delta = \frac{\text{Mid-Span Deflection (semi-rigid)}}{\text{Mid-Span Deflection (simply supported)}} = \frac{1+3.65}{4+3.65} = 0.61$$

That is, the mid-span deflection of this semi-rigid is 61% of the mid-span deflection of an identical PFRP beam if the ends were assumed to be hinges. Using the results obtained from Example 8-1, the mid-span deflection of a simply supported beam with identical physical and mechanical properties and subjected to the same load is calculated as:

$$\delta^{ss} = \frac{\delta}{\lambda_\delta} = \frac{0.2 \text{ in.}}{0.61} = 0.32 \text{ in. (8.33 mm)}$$

1-b) Calculate the mid-span deflection of an identical simply supported beam using Eq. 8-22 and Table 8-2:

The mid-span deflection, including the shear deformation component, can be calculated using Eq. 8-22 and substituting by $x = L/2$ in Loading Case 7 of Table 8-2:

For $k^v = 1$:

$$\delta_{total} = \frac{QL^3}{48E_{11}I_{11}} + \frac{QL}{4k^v AG_{21}}$$

$$= \frac{(2,500 \text{ lb})(108^3 \text{ in.}^3)}{(48)(2.35 \times 10^6 \text{ psi})(99.18 \text{ in.}^4)} + \frac{(2,500 \text{ lb})(108 \text{ in.})}{(4)(1)(8.73 \text{ in.}^2)(0.54 \times 10^6 \text{ psi})}$$

$$= 0.28 + 0.014 = 0.29 \text{ in. (7.37 mm)} \quad \leftarrow \text{(same answer)}$$

For $k^v = 0.29$:

$$\delta_{total} = \frac{QL^3}{48E_{11}I_{11}} + \frac{QL}{4k^v AG_{21}}$$

$$= \frac{(2,500 \text{ lb})(108^3 \text{ in.}^3)}{(48)(2.35 \times 10^6 \text{ psi})(99.18 \text{ in.}^4)} + \frac{(2,500 \text{ lb})(108 \text{ in.})}{(4)(0.29)(8.73 \text{ in.}^2)(0.54 \times 10^6 \text{ psi})}$$

$$= 0.28 + 0.048 = 0.32 \text{ in. (8.33 mm)} \quad \leftarrow \text{(same answer)}$$

2) Calculate the load enhancement index (λ_Q):

As stated earlier, the load enhancement index (λ_Q) is the inverse of the deflection reduction index (λ_δ) as indicated by Eq. 8-15. Thus,

For $k^v = 1$:

$$\lambda_Q = \left(\frac{1}{\lambda_\delta}\right) = \frac{1}{0.56} = 1.78$$

That is, including the partial fixity (semi-rigidity) of the PFRP beam in the analysis results in an increase in the load capacity (for the same deflection-to-span limit) limit of 78% as compared to assuming that the same PFRP beam has simply supported end connections. This, of course, will make a great difference in estimating the initial materials cost of the structure and the associated weight reduction.

For $k^v = 0.29$:

$$\lambda_Q = \left(\frac{1}{\lambda_\delta} \right) = \frac{1}{0.61} = 1.64$$

That is, including the partial fixity (semi-rigidity) of the PFRP beam in the analysis and including the modified shear coefficient result in an increase in the load capacity (for the same deflection-to-span limit) of 64% as compared to the hinged ends assumption. It is highly recommended to use the proper modified shear coefficients when calculating deflection and other performance indices, which will result in a more conservative and more realistic design of the PFRP frame structures.

3) Calculate the rotation capacity (θ_c):

In this example, the prescribed maximum span-to-deflection (at mid-span) ratio is $L/400$ ($1/\kappa_c$) or 108 in./$400 = 0.27$ in. (6.86 mm).

First calculate κ_c as follows:

$$\kappa_c = \frac{\text{mid-span deflection}}{\text{span}} = \frac{0.27''}{108''} = 0.0025$$

Using Eq. 8-20, we get:
For $k^v = 1$: ($\alpha = 0.0042$, $\omega = 2.8$, $k_1 = 192$, and $k_2 = k_3 = 8$)

$$\theta_c = \frac{192}{8} \left(\frac{(0.0025)(0.31)}{1 + 2.8} \right) = 0.0049 \text{ rad } (0.28°)$$

For $k^v = 0.29$: ($\alpha = 0.015$, $\omega = 3.65$, $k_1 = 192$, and $k_2 = k_3 = 8$)

$$\theta_c = \frac{192}{8} \left(\frac{(0.0025)(0.31)}{1 + 3.65} \right) = 0.004 \text{ rad } (0.23°)$$

Example 8-3: Caculate the mid-span deflection, end rotations, the deflection reduction index, and the load enhancement index for the beam described in Example 8-1 if the beam is subjected to a uniformaly
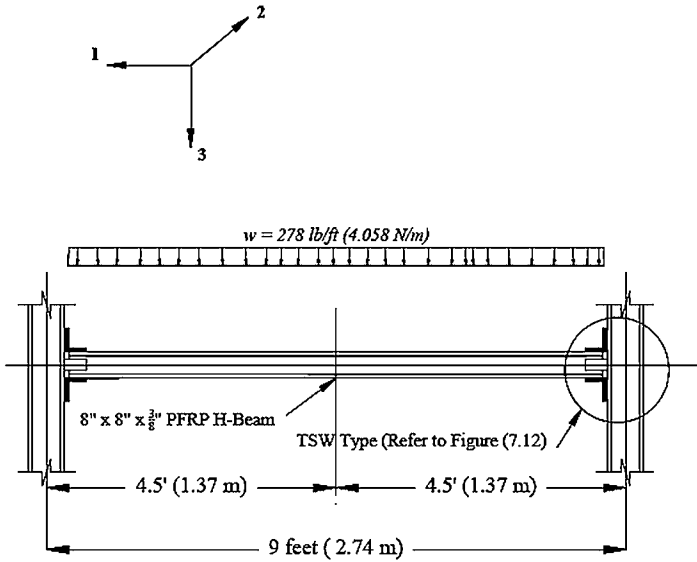
Figure 8-6. Details of the semi-rigid connected PFRP beam of Example 8-3.

distrbuted load of 278 lb/ft (total load $Q = 2,500$ lb) as shown in Fig. 8-6. Also, caculate the mid-span deflection of an identical beam with hinged end supports using Eq. 8-22 and Table 8-2.

SOLUTION:

i) **Calculate the mid-span deflection:**
From Table 8-1, we have:

$$k_1 = 384, k_2 = 10, k_3 = 12, \text{ and } k_4 = 5$$

From Example 8-1, we have:

$$\beta = 0.31, \alpha \text{ (for } k^v = 1) = 0.0042, \text{ and } \alpha \text{ (for } k^v = 0.29) = 0.015$$

For $k^v = 1$:
First, calculate the terms ϕ and ω using Eqs. 8-3a and 8-3b, respectively:

$$\therefore \phi = \frac{QL^3}{k_1 E_{11} I_{11}} = \frac{(2,500 \text{ lb})(108^3 \text{ in.}^3)}{(384)(2.35 \times 10^6 \text{ psi})(99.18 \text{ in.}^4)} = 0.036 \frac{\text{lb-in.}}{\text{lb}}, \text{ and}$$

$$\varpi = 48\alpha + k_2\beta + 96\alpha\beta$$
$$= (48)(0.0042) + (10)(0.31) + (96)(0.0042)(0.31) = 3.43$$

Substituting both values into Eq. 8-2b, we get:

$$\delta = \phi\left(\frac{1+\varpi}{1+2\beta}\right) = 0.036\left(\frac{1+3.43}{1+(2)(0.31)}\right) = 0.098''\,(2.50\text{ mm})$$

For $K^v = 0.29$:

From Example 8-1, it should be recalled that $\beta = 0.31$ and α (for $k^v = 0.29$) = 0.015. Substituting both values into Eq. 8-3b yields the following expression for ω:

$$\varpi = 48\alpha + k_2\beta + 96\alpha\beta = (48)(0.015) + (10)(0.31) + (96)(0.015)(0.31) = 4.27$$

Returning to Eq. 8-2b, we have:

$$\delta = \phi\left(\frac{1+\varpi}{1+2\beta}\right) = 0.036\left(\frac{1+4.27}{1+(2)(0.31)}\right) = 0.12''\,(2.97\text{ mm})$$

The reason for calculating two values for the mid-span deflection is to demonstrate the effect of including the modified shear coefficent. The foregoing results show that mid-span deflection calculated using the modified shear coefficent is 14.6% higher than assuming $k^v = 1$ ($L/125$vs. $L/982$). Also, as compared to the results of mid-span loading of the identical beam analyzed in Example 8-1, one can see that the inclusion of the proper shear deformation coefficent has less impact when the beam is subjected to a uniformaly distributed loading patern with the same total load resultant [$Q = 2,500$ lb (11,120 N) in both cases].

ii) Calculate end rotations:

Using Eq. 8-9, the end rotations can be calculated as follows:

$$\theta = \frac{QL^2}{k_3E_{11}I_{11}}\left(\frac{\beta}{1+2\beta}\right)$$
$$= \frac{(2,500\text{ lb})(108^2\text{ in.}^2)}{(12)(2.35\times10^6\text{ psi})(99.18\text{ in.}^4)}\cdot\left(\frac{0.31}{1.62}\right)$$
$$= 0.002\text{ rad }(0.11°)$$

iii) Calculate the deflection reduction index (λ_δ):

Subsituting in Eq. 8-12, we get:

For $k^v = 1$: ($\alpha = 0.0042$, $\omega = 3.43$, and $k_4 = 4$)

$$\lambda_\delta = \frac{\text{Mid-Span Deflection (semi-rigid)}}{\text{Mid-Span Deflection (simply supported)}} = \frac{1+\varpi}{k_4+\varpi} = \frac{1+3.43}{4+3.43} = 0.6$$

That is, the mid-span deflection of this semi-rigid beam is 60% of the mid-span deflection of an identical PFRP if the ends were assumed to be hinges. Using the results obtained from Example 8-1, the mid-span deflection of a simply supported beam with identical physical and mechanical properties and subjected to the same load is calculated as:

$$\delta^{ss} = \frac{\delta}{\lambda_\delta} = \frac{0.098 \text{ in.}}{0.6} = 0.164'' \, (4.16 \text{ mm})$$

For $k^v = 0.29$: ($\alpha = 0.015$, $\omega = 4.27$, and $k_4 = 4$)

$$\lambda_\delta = \frac{\text{Mid-Span Deflection (semi-rigid)}}{\text{Mid-Span Deflection (simply supported)}} = \frac{1+4.27}{4+4.27} = 0.64$$

That is, the mid-span deflection of this semi-rigid is 64% of the mid-span deflection of an identical PFRP beam if the ends were assumed to be hinges. Using the results obtained from Step (i), the mid-span deflection of a simply supported beam with identical physical and mechanical properties and subjected to the same load is calculated as:

$$\delta^{ss} = \frac{\delta}{\lambda_\delta} = \frac{0.12 \text{ in.}}{0.64} = 0.19'' \, (4.83 \text{ mm})$$

iv) Calculate the mid-span deflection of an identical simply supported beam using Eq. 8-22 and Table 8-2:
The mid-span deflection, including the shear deformation component, can be calculated using Eq. 8-22 and substituting by $x = L/2$ in Loading Case 8 of Table 8-2:
For $k^v = 1$:

$$\delta_{total} = \frac{5wL^4}{384E_{11}I_{11}} + \frac{wL^2}{8k^v AG_{21}}$$

$$= \frac{(5)\left(\frac{278}{12} \text{ lb/in.}\right)(108^4 \text{ in.}^4)}{(384)(2.35\times10^6 \text{ psi})(99.18 \text{ in.}^4)} + \frac{\left(\frac{278}{12} \text{ lb/in.}\right)(108^2 \text{ in.}^2)}{(8)(1)(8.73 \text{ in.}^2)(0.54\times10^6 \text{ psi})}$$

$$= 0.17'' + 0.007'' = 0.177 \text{ in. } (4.5 \text{ mm}) \qquad \leftarrow \text{(same answer)}$$

For $k^v = 0.29$:

$$\delta_{total} = \frac{5wL^4}{384E_{11}I_{11}} + \frac{wL^2}{8k^v AG_{21}}$$

$$= \frac{(5)\left(\dfrac{278}{12}\,\text{lb/in.}\right)(108^4\ \text{in.}^4)}{(384)(2.35\times10^6\ \text{psi})(99.18\ \text{in.}^4)} + \frac{\left(\dfrac{278}{12}\,\text{lb/in.}\right)(108^2\ \text{in.}^2)}{(8)(0.29)(8.73\ \text{in.}^2)(0.54\times10^6\ \text{psi})}$$

$$= 0.17'' + 0.024'' = 0.19\ \text{in. (4.83 mm)} \qquad \leftarrow (\text{same answer})$$

v) Calculate the load enhancement index (λ_Q):

As stated earlier, the load enhancement index (λ_Q) is the inverse of the deflection reduction index (λ_δ) as indicated by Eq. 8-15. Thus,

For $k^v = 1$:

$$\lambda_Q = \left(\frac{1}{\lambda_\delta}\right) = \frac{1}{0.6} = 1.67$$

That is, including the partial fixity (semi-rigidity) of the PFRP beam in the analysis results in an increase in the load capacity (for the same deflection-to-span limit) limit of 67% (slightly less than the corresponding value calculated for the mid-span point loading condition) as compared to assuming that the same PFRP beam has simply supported end connections.

For $k^v = 29$:

$$\lambda_Q = \left(\frac{1}{\lambda_\delta}\right) = \frac{1}{0.64} = 1.56$$

That is, including the partial fixity (semi-rigidity) of the PFRP beam in the analysis and including the modified shear coefficient result in an increase in the load capacity (for the same deflection-to-span limit) of 56% as compared to the hinged ends assumption.

Comments on the Results of Examples 8-1 through 8-3: The reasoning behind the selection of a specific total load, Q = 2,500 lb (11.12 kN) in these examples, and the specific beam cross-section and connection details is to compare the results of these exercises with actual experimental results conducted by Mosallam (1990) and which are described in Chapter 7 of this manual. Although the loading pattern used by Mosallam was four-point loading, some comparision with the results of Example 8-1 (where the load was applied in a three-point configuration) can still be made. For example, the experimental results in the linear
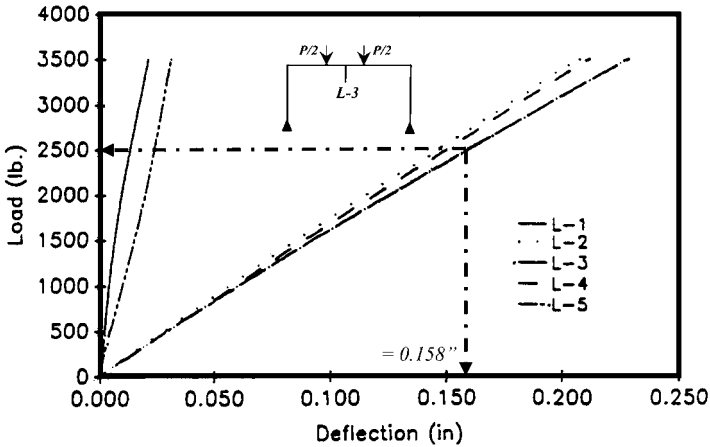
*Figure 8-7. Linear load vs. deflection curves of PFRP frame tested by Mosallam (1990)
Note: L-3 is the mid-span deflection measurements.*

range obtained by Mosallam showed that the mid-span deflection (L-3) corresponding to a total load of 2,500 lb (11.12 kN) was 0.158 in. ($\approx$ 4 mm) as shown in Fig. 8-7. This is almost identical to the results obtaind from Example 8-1 for $k^v = 1$ [$d = 0.16$ in. (4.17 mm)]. However, in reality, one would expect that this value will be slightly less than 0.16 in. (4.17 mm), given the fact that load was applied in a four-point pattern. It is also interesting to see that the inclusion of the modified shear coeffecient overestimated the actual mid-span deflection, contrary to what one would expect. As expected, the results obtained from Example 8-3 for an equivalent total load uniformally distributed along the girder span was much less than the corresponding four-point experimental result [$\delta_{uniform\ load}$ was 0.098 in. (2.5 mm)].

The results are also compared to the finite element models that will be described in Chapter 9 of this manual. For example, the results obtained from Example 8-1 match well with the results of the finite element model C-3 described Chapter 9. As shown in Table 9-11, the mid-span deflection calculated numerically was 0.161 in. (4.09 mm) as compared to 0.16 in. (4.06 mm) obtained from Example 8-1. Figures 8-8 and 8-9 present a comparision between the results of Examples 8-1 and 8-3.

8.3.5 Closed-Form Expressions for PFRP Portal Frames with Semi-Rigid Connections

8.3.5.1 Girder's Mid-Span Deflection. Turvey (1996) developed, and Turvey and Cooper (1996a and 1996b) expanded upon, a simple closed-form expression for mid-span deflection of a PFRP portal frame girder.
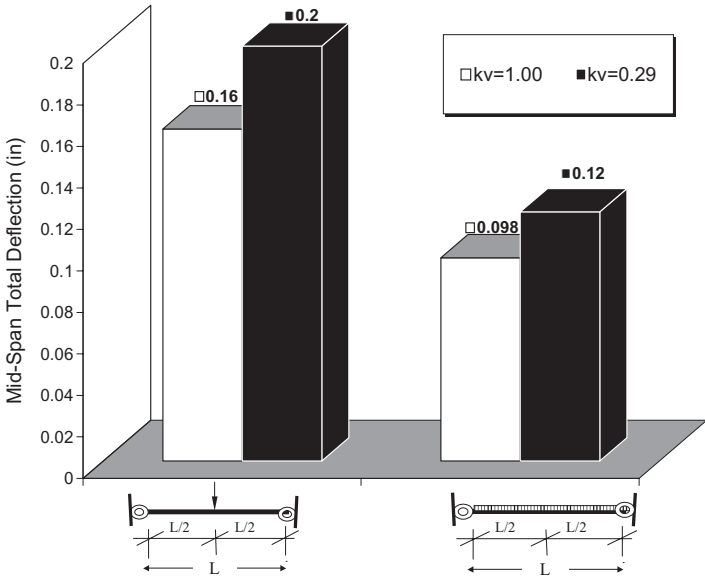
Figure 8-8. Comparison between the mid-span deflection of the two semi-rigid PFRP beams described in Examples 8-1 and 8-3.
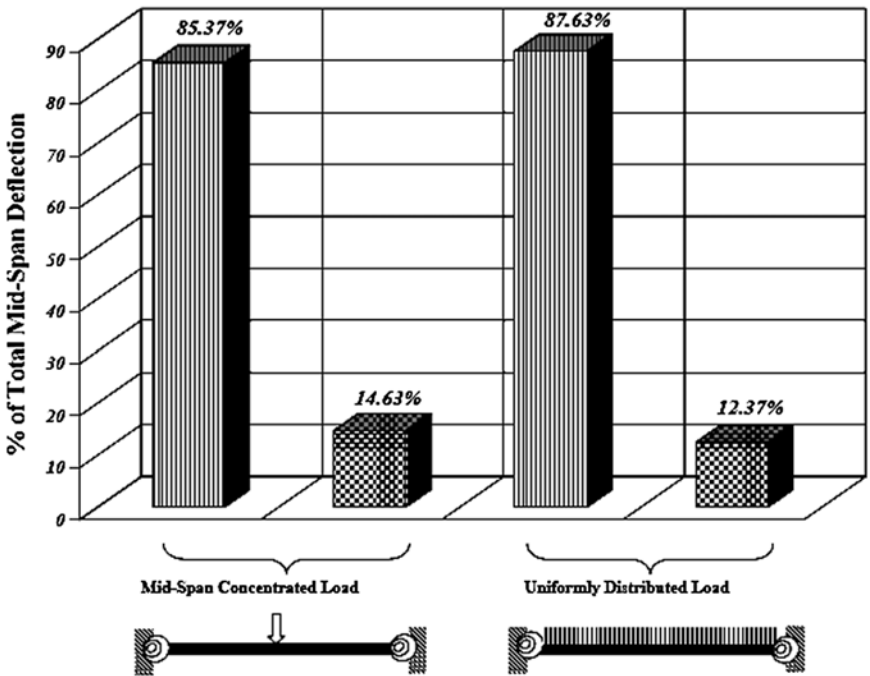
Figure 8-9. Flexural and shear deflection components as a percentage of total mid-span deflection of the two PFRP beams described in Examples 8-1 and 8-3.
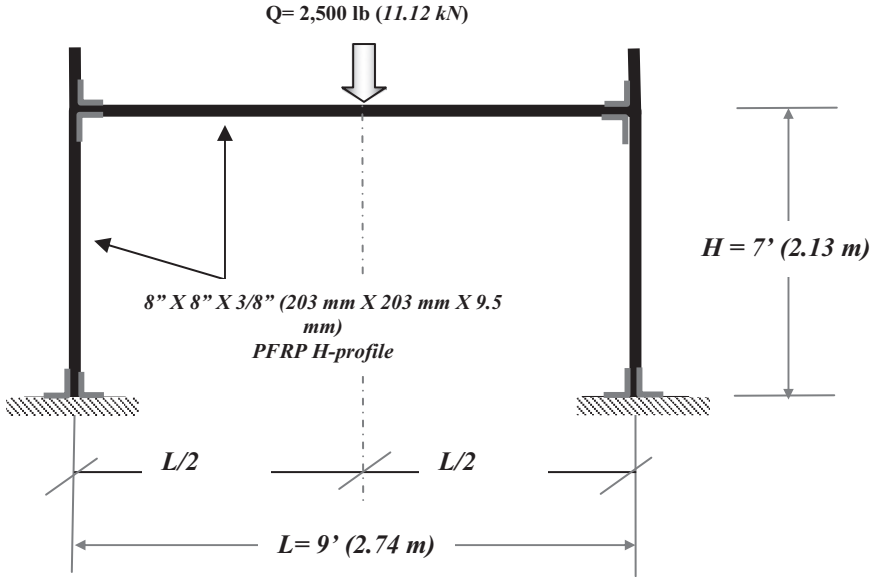
Figure 8-10. Geometry and loading configuration of the PFRP portal frame analyzed by Eq. 8-25 and Example 8-3.

For example, for the PFRP portal frame shown in Fig. 8-10, assuming same PFRP profile for both columns and frame girder, the girder's mid-span deflecton is caculated using the follwing expression:

$$\delta = \frac{QL^3}{k_1 E_{11} I_{11}} \left[4 - \left\{ \frac{9HL}{2H^2 + 3HL + 6\alpha + 6H\beta} \right\} + \frac{48\alpha}{L^2} \right] \qquad (8\text{-}25)$$

or

$$\delta = \phi \left[4 - \left\{ \frac{9HL}{2H^2 + 3HL + 6\alpha + 6H\beta} \right\} + \frac{48\alpha}{L^2} \right] \qquad (8\text{-}26)$$

where k_1 is equal to 192, for three-point lading configuration (refer to Table 8-1, and H and L are the height and span of the frame, respectively.

Example 8-4: Calculate the girder's mid-span deflection for a PFRP portal frame, with identical pultruded profiles for the columns and frame girder. Use the same information of Example 8-1. The hight of the frame (H) is 7 ft (2.13 m), and the span (L) is 9 ft (2.74 m).

SOLUTION:

From Example 8-1, we have:

$\phi = 0.07$, $\beta = 0.31$, $\alpha\ (k^v =1) = 0.0042$, and $\alpha\ (k^v = 0.29) = 0.015$.

Substituting twice in Eq. 8-26 by the two values of α, we get:
For $k^v = 1$ ($\alpha = 0.0042$):

$$\delta = 0.07'' \left[4 - \left\{ \frac{(9)(84'')(108'')}{(2)(84^2\ \text{in.}^2) + (3)(84'')(108'') + (6)(0.0042) + (6)(84'')(0.31'')} \right\} \right. $$
$$\left. + \frac{48(0.0042)}{(108^2\ \text{in.}^2)} \right]$$

or $\delta = 0.142$ in. (3.6 mm)

For $k^v = 0.29$ ($\alpha = 0.015$):

$$\delta = 0.07'' \left[4 - \left\{ \frac{(9)(84'')(108'')}{(2)(84^2\ \text{in.}^2) + (3)(84'')(108'') + (6)(0.015) + (6)(84'')(0.31)} \right\} \right. $$
$$\left. + \frac{48(0.015)}{(108^2\ \text{in.}^2)} \right]$$

or $\delta = 0.142$ in. (3.6 mm)

As compared of the results obtined from Example 8-1 using Eq. 8-2b, the mid-span deflection in this example is less conservative. Also, by examining Eq. 8-26, one can see that the deflection calculated by this equation is *not sensitive* to the shear deformation effect (same deflection for $k^v = 1$ and $k^v = 0.29$). For this reason, it is highly recommended to use Eq. 8-2b to generate a more conservative and relastic prediction for mid-span deflection.

8.3.5.2 Sway Deflection and End Rotations of Semi-Rigid Connected PFRP Columns.   Based on the flexibility method, Turvey (1998) proposed closed-form expressions for calculating the sway deflection (refer to Fig. 8-11), as well as the column's end rotations. Unlike the assumption of equal rotational stiffness of the beam ends used in developing Eq. 8-3, the column end connection rotational stiffnesses were assumed unequal ($K_U \neq 184\ K_L$ as shown in Fig. 8-11).

8.3.5.2.1 Sway Deflection (δ_s).   The expression for the sway deflection, i.e., the in-plane translation of the upper end of the column relative to the lower end (δ_s), is:
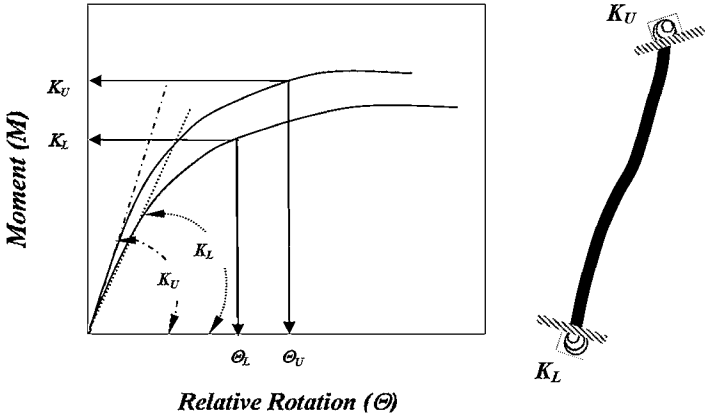
*Figure 8-11. PFRP columns with different rotational stiffness at upper end
(K_U) and lower end (K_L).*

Table 8-3. Values of Coefficients k_5 through k_{10} for Semi-Rigid PFRP
Frame Columns

Load Pattern	k_5	$k_6 = k_4$	k_7	k_8	k_9	k_{10}
Point Load	12	4	4	2	1	2
Uniform Load	24	5	3	6	2	3

$$\delta_s = \frac{QH^3}{k_5E_{11}I_{11}} \frac{\{1+12\alpha(1+\beta_L+\beta_U)+12\beta_L\beta_U+k_6\beta_L+k_7\beta_U\}}{(1+\beta_L+\beta_U)} \quad (8\text{-}27)$$

The symbols E_{11}, I_{11}, Q, α, and β in Eq. 8-27 have the same definition as
those used in Eqs. 8-2 and 8-3. However, the subscripts L and U are used
to refer to the lower and upper column end connections, respectively. The
k-coefficients are described in Table 8-3 for point load and uniformly dis-
tributed loading conditions.

If both ends of the column have same rotational stiffness ($\beta_L=\beta_U=\beta$), then:

$$\delta_s = \frac{QH^3}{k_5E_{11}I_{11}} \frac{\{1+12\alpha(1+2\beta)+12\beta^2+\beta(k_6+k_7)\}}{(1+2\beta)} \quad (8\text{-}28)$$

If the shear deformation effect is ignored (i.e., $\alpha = 0$), Eq. 8-27 will
reduce to the following simpler form:

$$\delta_s = \frac{QH^3}{k_5 E_{11} I_{11}} \frac{\{1 + k_6 \beta_L + k_7 \beta_U + 12 \beta_L \beta_U\}}{(1 + \beta_L + \beta_U)} \tag{8-29}$$

For columns with hinged ends (i.e., $\beta_L = \beta_U = \infty$), the sway displacement δ_s is equal to ∞. On the other hand, if the column base is fixed and the beam-column connection is assumed rigid (i.e., $\beta_L = \beta_U = 0$), Eq. 8-28 reduces to the following classic deflection formula:

$$\delta_s = \frac{QH^3}{k_5 E_{11} I_{11}} \tag{8-30}$$

Likewise, for a column with hinged column-base connection, and a rigid beam-to-column connection (i.e., $\beta_L = \infty$, $\beta_U = 0$), Eq. 8-28 will reduce to the following classical deflection formula:

$$\delta_s = \frac{QH^3 k_6}{k_5 E_{11} I_{11}} \tag{8-31}$$

8.3.5.2.2 End Rotations (θ_L and θ_U).   The rotations at the two ends of the column are given by these two closed-form expressions using Morice's *Linear Structural Analysis: An Introduction to the Influence Coefficients Method Applied to Statically Indeterminate Structures* (1969):

$$\theta_L = \frac{QH^2}{k_8 E_{11} I_{11}} \frac{\{\beta_L(k_9 + k_{10} \beta_U)\}}{(1 + \beta_L + \beta_U)} \tag{8-32}$$

$$\theta_U = \frac{QH^2}{k_8 E_{11} I_{11}} \frac{\{\beta_U(k_9 + k_{10} \beta_L\}}{(1 + \beta_L + \beta_U)} \tag{8-33}$$

For columns with hinged ends (i.e., $\beta_L = \beta_U = \infty$), $\theta_L = \theta_U = \infty$. On the other hand, if the column base is fixed and the beam-column connection is assumed rigid (i.e., $\beta_L = \beta_U = 0$), $\theta_L = \theta_U = 0$. Likewise, for a column with a hinged column-base connection and a rigid beam-to-column connection (i.e., $\beta_L = \infty$, $\beta_U = 0$), Eqs. 8-32 and 8-33 reduce to the following:

$$\theta_L = \frac{QH^2 k_9}{k_8 E_{11} I_{11}} \tag{8-34}$$

$$\theta_U = 0 \tag{8-35}$$

Finally, if the column-base connection is assumed fixed, while the beam-column connection is assumed hinged (i.e., $\beta_L = 0$, $\beta_U = \infty$), Eqs. 8-32 and 8-33 will reduce to the following:

$$\theta_L = 0 \tag{8-36}$$

$$\theta_U = \frac{QH^2 k_{10}}{k_8 E_{11} I_{11}} \tag{8-37}$$

8.3.5.2.3 Performance Indices (λ_δ, λ_Q, and λ_H). Similar to semi-rigid performance described earlier, Turvey and Cooper (1998) proposed three indices for semi-rigid frame columns.

- *Sway-Deflection Increase Index (λ_δ):* This index is defined as the ratio of the sway displacement of a column with semi-rigid ends to an identical column (same height, applied load, cross section) with fixed/rigid end connections. This ratio will always be larger than unity and expressed as:

$$\lambda_\delta = \left(\frac{1 + 12\alpha(1 + \beta_L + \beta_U) + 12\beta_L\beta_U + k_6\beta_L + k_7\beta_U}{(1 + 12\alpha)(1 + \beta_L + \beta_U)} \right) \tag{8-38}$$

If the shear deformation effect is ignored (i.e., $\alpha = 0$), Eq. 8-38 will reduce to the following simpler form:

$$\lambda_\delta = \left(\frac{1 + 12\beta_L\beta_U + k_6\beta_L + k_7\beta_U}{(1 + \beta_L + \beta_U)} \right) \tag{8-39}$$

For a column with a hinged column-base connection and a rigid beam-to-column connection (i.e., $\beta_L = \infty$, $\beta_U = 0$), Eq. 8-38 reduces to:

$$\lambda_\delta = k_6 \tag{8-40}$$

Finally, if the column-base connection is assumed fixed, while the beam-column connection is assumed hinged (i.e., $\beta_L = 0$, $\beta_U = \infty$), Eq. 8-38 reduces to:

$$\lambda_\delta = k_7 \tag{8-40}$$

- *Lateral Load Reduction Index (λ_Q):* If the maximum lateral sway deflection is prescribed for two identical columns with the same height, one with fixed/rigid end connections and the other having semi-rigid end connections, the ratio of the permissible lateral loads of the two columns is defined as the lateral load reduction index, which is less than unity. This index is the inverse of the sway-deflection index (λ_δ):

$$\lambda_Q = \frac{1}{\lambda_\delta} \tag{8-41}$$

- *Height Reduction Index* (λ_H): If the maximum lateral sway deflection is prescribed for two columns, a semi-rigid/semi-rigid and fixed/rigid, subjected to same lateral loads, the ratio between the required column heights to satisfy the design lateral load and lateral displacement limit state is referred to as the height reduction index (λ_H), which is less than unity.

For a column with semi-rigid connections at both ends, and subjected to a point load at the beam-column connection (refer to Fig. 8-11), the cubic equation describing this index is:

$$\lambda_H^3 + (k_6\beta_L + k_7\beta_U)\lambda_H^2 - (1 - 12\beta_L\beta_U)\lambda_H - (\beta_L + \beta_U) = 0 \tag{8-42}$$

Equation 8-42 has only one positive root, which is the height reduction index.

For a column with fixed column-to-base connection and its connection to the beam is assumed rigid (i.e., $\beta_L = \beta_U = 0$), Eq. 8-42 simplifies to the following form:

$$\lambda_H^3 + \lambda_H = 0 \tag{8-43}$$

The roots of Eq. 8-43 are $\lambda_H = -1$, $\lambda_H = +1$, and $\lambda_H = 0$. Thus, the height reduction index is the non-zero positive root, which is 1. Similarly, for a case of a simply supported column, (i.e., $\beta_L = \beta_U = \infty$), Eq. 8-42 will be simplified to:

$$\lambda_H = 0 \tag{8-44}$$

If the column-base connection is assumed fixed, while the beam-column connection is assumed hinged (i.e., $\beta_L = 0$, $\beta_U = \infty$), Eq. 8-42 reduces to the following form:

$$k_7\lambda_H^2 - 1 = 0 \tag{8-45}$$

The two roots of Eq. 8-45 are $\lambda_H = \frac{-1}{\sqrt{k_7}}$ and $\lambda_H = \frac{+1}{\sqrt{k_7}}$. Thus, the height reduction index is the non-zero positive root, which is:

$$\lambda_H = \frac{+1}{\sqrt{k_7}} \tag{8-46}$$

Finally, if the column has a hinged column-base connection at the bottom and a rigid beam-to-column connection at the top (i.e., $\beta_L = \infty$, $\beta_U = 0$), Eq. 8-38 reduces to:

$$k_6 \lambda_H^2 - 1 = 0 \qquad (8\text{-}47)$$

The two roots of Eq. 8-45 are $\lambda_H = \dfrac{-1}{\sqrt{k_6}}$ and $\lambda_H = \dfrac{+1}{\sqrt{k_6}}$. Thus, the height reduction index is the non-zero positive root, which is:

$$\lambda_H = \frac{1}{\sqrt{k_6}} \qquad (8\text{-}48)$$

Equations 8-46 and 8-48 indicate that the heights of columns with semi-rigid end connections are reduced to $\dfrac{1}{\sqrt{k_6}}$ and $\dfrac{1}{\sqrt{k_7}}$ times the height of the corresponding columns with fixed column-base and beam-to-column end connections.

8.3.5.2.4 End Rotation Capacities of Semi-Rigid Columns (θ_L^c and θ_U^c). Closed-form expressions for calculating the required rotational capacities of the two ends of a semi-rigid connected column to achieve a prescribed sway-deflection-to-column-height ratio (κ_{UL}) are obtained by combining Eqs. 8-27, 8-32, and 8-33. The values of θ_L^c and θ_U^c are between 0 and κ_{LU} (Turvey and Cooper 1998):

$$\theta_L^c = \frac{k_5}{k_8} \left[\frac{\kappa_{LU} \beta_L (k_9 + k_{10} \beta_U)}{\{1 + 12\alpha(1 + \beta_{nL} + \beta_U) + 12\beta_L \beta_U + k_6 \beta_L + k_7 \beta_U\}} \right] \qquad (8\text{-}49)$$

$$\theta_U^c = \frac{k_5}{k_8} \left[\frac{\kappa_{LU} \beta_U (k_9 + k_{10} \beta_L)}{\{1 + 12\alpha(1 + \beta_L + \beta_U) + 12\beta_L \beta_U + k_6 \beta_L + k_7 \beta_U\}} \right] \qquad (8\text{-}50)$$

where

$$\kappa_{LU} = \frac{\delta_s}{H} \qquad (8\text{-}51)$$

If the shear deformation effect is ignored, Eqs. 8-49 and 8-50 reduce to the following forms:

$$\theta_L^c = \frac{k_5}{k_8} \left[\frac{\kappa_{LU} \beta_L (k_9 + k_{10} \beta_U)}{\{1 + 12\beta_L \beta_U + k_6 \beta_L + k_7 \beta_U\}} \right] \qquad (8\text{-}52)$$

$$\theta_U^c = \frac{k_5}{k_8} \left[\frac{\kappa_{LU} \beta_U (k_9 + k_{10} \beta_L)}{\{1 + 12\beta_L \beta_U + k_6 \beta_L + k_7 \beta_U\}} \right] \qquad (8\text{-}53)$$

For a column with a fixed column-base connection and its connection to the beam is assumed to be rigid (i.e., $\beta_L = \beta_U = 0$), Eqs. 8-49 and 8-50 generate the following expected results for the required rotational capacities of the column ends:

$$\theta_L^c = \theta_U^c = 0 \tag{8-54}$$

If the connections at the column ends are hinged ($\beta_L = \beta_U = \infty$), Eqs. 8-52 and 8-53 reduce to the following:

$$\theta_L^c = \theta_U^c = \frac{k_5 k_{10}\kappa_{LU}}{12k_8} = \kappa_{LU} \ ^1\text{(the mechanism case)} \tag{8-55}$$

If the column has a hinged column-base connection at the bottom and a rigid beam-to-column connection at the top (i.e., $\beta_L = \infty$, $\beta_U = 0$), Eqs. 8-52 and 8-53 reduce to the following:

$$\theta_L^c = \frac{k_5 k_9 \kappa_{LU}}{k_6 k_8} \tag{8-56}$$

$$\theta_U^c = 0 \tag{8-57}$$

Finally, if the column has a fixed column-base connection at the bottom and a rigid beam-to-column connection at the top (i.e., $\beta_L = 0$, $\beta_U = \infty$), Eqs. 8-52 and 8-53 reduce to the following:

$$\theta_L^c = 0 \tag{8-58}$$

$$\theta_U^c = \frac{k_5 k_{10}\kappa_{LU}}{k_7 k_8} \tag{8-59}$$

Example 8-5: Calculate the sway deflection, end rotations, the sway-deflection increase index, and the load reduction index for the frame shown in Fig. 8-12. If the column top is subjected to a lateral

[1] From Table 8-3, we have:

$$\left(\frac{k_5 k_{10}}{12k_8}\right)_{\text{Point Load}} = \left(\frac{k_5 k_{10}}{12k_8}\right)_{\text{Distributed Load}} = 1$$

or

$$\left(\frac{(12)(2)}{(12)(2)}\right)_{\text{Point Load}} = \left(\frac{(24)(3)}{(12)(6)}\right)_{\text{Distributed Load}} = 1$$
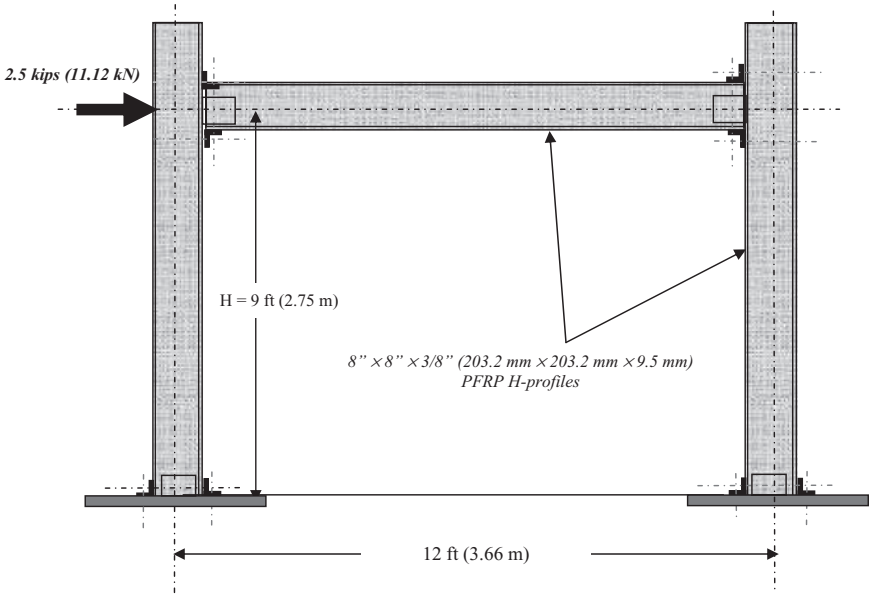
Figure 8-12. Details and loading of the PFRP frame of Example 8-5.

point load of 2.5 kips (11.12 kN), the rotational stiffnesses for the base-column connection and the beam-column connections are 10,000 kip-in./rad (1,130 kN-m/rad) and 7,000 kip-in./rad (791 kN-m/rad), respectively. Use the same me chanical properties as described in Example 8-1.

SOLUTION

i) Calculate β-values for the upper and the lower ends of the column:
For the upper end:
At this end, we have $K_u = 7,000$ kip-in./rad, $H = 108$ in., $E_{11} = 2.35 \times 10^6$ psi, $I_{11} = 99.18$ in.^{2}, and $k_5 = 12$. Substituting in Eq. 8-4, we get:

$$\beta_U = \frac{E_{11}I_{11}}{K_U H} = \frac{(2.35 \times 10^6 \text{ psi})(99.18 \text{ in.}^4)}{\left(7,000,000 \frac{\text{lb-in.}}{\text{rad}}\right)(108 \text{ in.})} = 0.31$$

For the upper end:

$$\beta_L = \frac{E_{11}I_{11}}{K_L H} = \frac{(2.35 \times 10^6 \text{ psi})(99.18 \text{ in.}^4)}{\left(10,000,000 \frac{\text{lb-in}}{\text{rad}}\right)(108 \text{ in.})} = 0.22$$

ii) Calculate sway-deflection for $k^v = 1$ ($\alpha = 0.0042$) and $k^v = 0.29$ ($\alpha = 0.015$) (refer to Example 8-1):

From Table 8-3, we have:

$$k_5 = 12, k_6 = k_7 = 4$$

$$\beta_L + \beta_U = 0.22 + 0.31 = 0.53, \beta_L \cdot \beta_U = (0.22)(0.31) = 0.0682,$$

$$\frac{QH^3}{k_5 E_{11} I_{11}} = \frac{(2,500 \text{ kips})(108^3 \text{ in.}^3)}{(12)(2.35 \times 10^6 \text{ psi})(99.18 \text{ in.}^4)} = 1.12$$

Now, using Eq. 8-27 to calculate the sway-deflection for the two cases:
For $k^v = 1$ ($\alpha = 0.0042$):

$$\delta_s = (1.12) \cdot \frac{\{1 + (12)(0.0042)(1 + 0.53) + (12)(0.0682) + (4)(0.22) + (4)(0.31)\}}{(1 + 0.53)}$$

$$= 2.94 \text{ in. (7.47 cm)}$$

For $k^v = 0.29$ ($\alpha = 0.015$):

$$\delta_s = (1.12) \cdot \frac{\{1 + (12)(0.015)(1 + 0.53) + (12)(0.0682) + (4)(0.22) + (4)(0.31)\}}{(1 + 0.53)}$$

$$= 3.08 \text{ in. (7.83 cm)}$$

iii) Calculate the columns end rotations:

From Table 8-3, we have: $k_8 = k_{10} = 2$, and $k_9 = 1$.

Applying in Eqs. 8-32 and 8-33, the rotations at the lower and upper ends of the columns are calculated as follows:

$$\theta_L = \frac{(2,500 \text{ kips})(108^2 \text{ in.}^2)}{(2)(2.35 \times 10^6 \text{ psi})(99.18 \text{ in.}^4)} \cdot \frac{0.22[1 + (2)(0.31)]}{1.53} = 0.0145 \text{ rad } (0.83°)$$

$$\theta_U = \frac{(2,500 \text{ kips})(108^2 \text{ in.}^2)}{(2)(2.35 \times 10^6 \text{ psi})(99.18 \text{ in.}^4)} \cdot \frac{0.31[1 + (2)(0.22)]}{1.53} = 0.0182 \text{ rad } (\cong 1°)$$

iv) Calculate sway-deflection increase index (λ_δ) for $k^v = 1$ ($\alpha = 0.0042$) and $k^v = 0.29$ ($\alpha = 0.015$):

Using Eq. 8-38, calculate the two values of the λ_δ index:
For $k^v = 1$ ($\alpha = 0.0042$):

$$\lambda_\delta = \frac{\{1 + (12)(0.0042)(1 + 0.53) + (12)(0.0682) + (4)(0.22) + (4)(0.31)\}}{\{1 + (12)(0.0042)\}\{1 + 0.53\}}$$

$$= 2.5$$

For $k^v = 1$ ($\alpha = 0.015$):

$$\lambda_\delta = \frac{\{1+(12)(0.015)(1+0.53)+(12)(0.0682)+(4)(0.22)+(4)(0.31)\}}{\{1+(12)(0.015)\}\{1+0.53\}}$$

$$= 2.33$$

v) **Calculate load reduction index (λ_Q) for $k^v = 1$ ($\alpha = 0.0042$) and $k^v = 0.29$ ($\alpha = 0.015$):**

According to Eq. 8-39, this index is the inverse of the sway-deflection increase index (λ_δ), thus:

For $k^v = 1$ ($\alpha = 0.0042$):

$$\lambda_Q = \frac{1}{\lambda_\delta} = \frac{1}{2.5} = 0.4$$

For $k^v = 1$ ($\alpha = 0.015$):

$$\lambda_Q = \frac{1}{\lambda_\delta} = \frac{1}{2.33} = 0.43$$

Example 8-6: Calculate the required rotaional capacities for the ends of the frame clomns described in Example 8-5 and Fig. 8-12, assuming that the prescribed sway-deflection-to-column-height ratio(κ_{LU}) is 0.009.

SOLUTION

$$\kappa_{LU} = 0.009 = \frac{\delta_s}{H} = \frac{\delta_s}{108''} \text{ from which } \delta_s^{\text{allowable}} = 0.97 \text{ in. (2.47 cm)}$$

From Table 8-3, we have:

$$k_5 = 12, \ k_6 = k_7 = 4, \ k_8 = 2, \ k_9 = 1, \text{ and } k_{10} = 2$$

To fulfill this requirement, and according to Eqs. 8-49 and 8-50, the column ends should possess the following rotational capacities:

For $k^v = 1$ ($\alpha = 0.0042$):

$$\theta_L^c = \frac{12}{2}\left[\frac{(0.009)(0.22)[(1+(2)(0.31)]}{\{1+(12)(0.0042)(1+0.53)+(12)(0.0682)+(4)(0.22)+(4)(0.31)\}}\right]$$

$$= 0.0047 \text{ rad } (0.27°)$$

$$\theta_U^c = \frac{12}{2}\left[\frac{(0.009)(0.31)[(1+(2)(0.22)]}{\{1+(12)(0.0042)(1+0.53)+(12)(0.0682)+(4)(0.22)+(4)(0.31)\}}\right]$$
$$= 0.006 \text{ rad } (0.34°)$$

For $k^v = 1$ ($\alpha = 0.015$):

$$\theta_L^c = \frac{12}{2}\left[\frac{(0.009)(0.22)[(1+(2)(0.31)]}{\{1+(12)(0.015)(1+0.53)+(12)(0.0682)+(4)(0.22)+(4)(0.31)\}}\right]$$
$$= 0.0046 \text{ rad } (0.26°)$$

$$\theta_U^c = \frac{12}{2}\left[\frac{(0.009)(0.31)[(1+(2)(0.22)]}{\{1+(12)(0.015)(1+0.53)+(12)(0.0682)+(4)(0.22)+(4)(0.31)\}}\right]$$
$$= 0.0057 \text{ rad } (0.33°)$$

Now, comparing these allowable maximum rotation with those calculated in Example 8-5, the calculated actual rotation of the upper and the lower ends of the columns in Example 8-5 far exceeded the required allowable rotation for the prescribed sway-deflection-to-height ratio on the order of 3.15 and 3.19 times, respectively, for $\alpha = 0.015$. Based on the prescribed sway-deflection-to-height ratio of Example 8-6, the end connections selected in the frame described in Example 8-5 will not pass, and more rigid end connection details will be required. [Earlier, Eq. 8-55 defined the mechanism case, which occurs when all connections at the column ends are hinged ($\beta_L = \beta_U = \infty$). At this point, both ends reach a rotation of $\kappa_{LU} = 0.009$ rad (0.52 degrees)]. In this case, and to satisfy the design requirement, a lateral bracing system (e.g., diaphragm, end gables) must be designed and attached to the PFRP frame.

Experimental Verification: As was described in Chapter 7, Turvey and Cooper (1998) conducted an experimental program on PFRP column-base connections. In their program, two sizes of H-profiles were examined, namely, 4 in. × 4 in. × 1/4 in. (101.6 mm × 101.6 mm × 6.4 mm), and 8 in. × 8 in. × 3/8 in. (203.2 mm × 203.2 mm × 9.5 mm) PFRP H-profiles (EXTREN 500-Series). Both PFRP equal-leg angles 4 in. × 4 in. × 1/2 in. (102 mm × 102 mm × 12.7 mm) and 0.47 in. (12 mm) steel bolts were used in connecting the 8 in. × 8 in. × 3/8 in. (203.2 mm × 203.2 mm × 9.5 mm) PFRP H-profiles, while PFRP equal-leg angles 4 in. × 4 in. × 3/8 in. (102 mm × 102 mm × 9.5 mm) and 0.39 in. (10 mm) steel bolts were used in connecting the 4 in. × 4 in. × 1/4 in. (101.6 mm × 101.6 mm × 6.4 mm) PFRP H-columns. The base-column experimental rotational stiffnesses along with the corresponding beam-to-column connections information obtained by Turvey and Cooper (1996a; 1996b) were used to

demonstrate the validity of the performance indices discussed earlier in this chapter.

Figures 8-13 and 8-14 present the details of the beam-to-column and the column-base connections, respectively. It should be noted that the details described in these figures are for web + flanges cleats; however, the web cleats details were obtained by removing the upper and bottom angles bolted to the beam and column flanges. Table 8-4 summarizes the linear rotational stiffness values obtained experimentally for the two selected sizes of the PFRP H-profiles for both the columns and the beams. The information presented in this table may be useful in conducting linear analysis of pultruded frame structures. Tables 8-5 through 8-10 present the calculated values of the sway-deflection index (λ_δ) and the required end rotational capacities (θ_L^c and θ_U^c) for two PFRP H-profiles and for different column height-to-depth (H/d) ratios.

The calculations were based on the following:

- Lateral point load applied at the top end of the column (refer to Fig. 8-12)
- The longitudinal elastic modulus, E_{11} [for 8 in. × 8 in. × 3/8 in. (203.2 mm × 203.2 mm × 9.5 mm) PFRP H-profiles] = 17.24 kN/mm^2
- The longitudinal elastic modulus, E_{11} [for 4 in. × 4 in. × 1/4 in. (101.6 mm × 101.6 mm × 6.4 mm) PFRP H-profiles] = 17.93 kN/mm^2
- The transverse shear modulus, G_{21}, for both PFRP H-profiles = 2.93 kN/mm^2
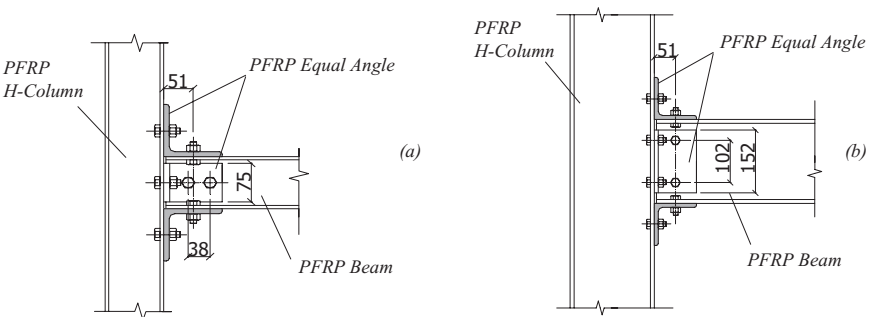
Figure 8-13. Beam-to-column connection details tested by Turvey and Cooper. A, 4 in. × 4 in. × 1/4 in. (101.6 mm × 101.6 mm × 6.4 mm) H-profiles; B, 8 in. × 8 in. × 3/8 in. (203.2 mm × 203.8 mm × 9.5 mm) H-profiles. Source: Turvey and Cooper (1998).
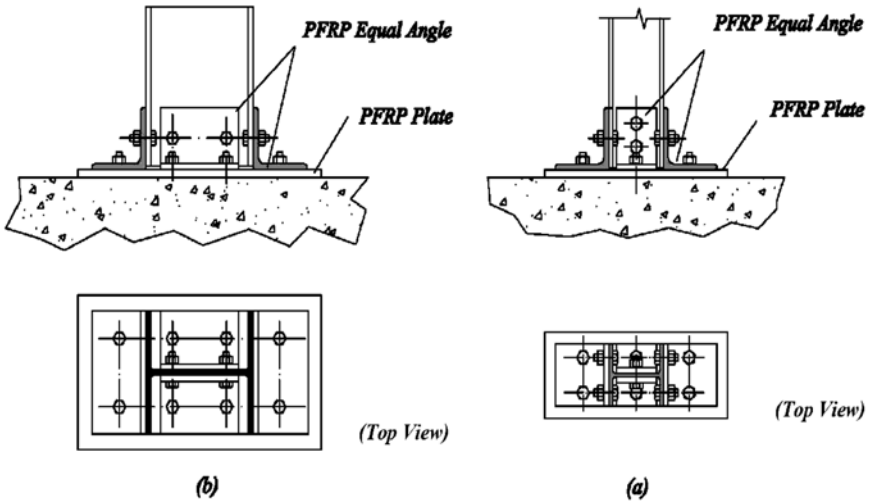
Figure 8-14. Column-base connection details tested by Turvey and Cooper.
A, 8 in. × 8 in. × 3/8 in. (203.2 mm × 203.8 mm × 9.5 mm) H-profiles;
B, 4 in. × 4 in. × 1/4 in. (101.6 mm × 101.6 mm × 6.4 mm) H-profiles.
Source: Turvey and Cooper (1998).

8.4 RIGOROUS ANALYSIS OF PFRP STRUCTURES WITH SEMI-RIGID CONNECTIONS
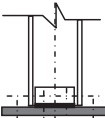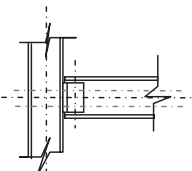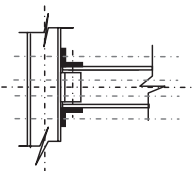
For a more precise analysis of the semi-rigid behavior of PFRP connections, both the nonlinear rotational stiffness behavior and the shear deformation effect must be considered. Mosallam (1990) developed the modified stiffness matrix, which includes both effects:

$$
k = \frac{1}{\lambda}
\begin{bmatrix}
\xi & 0 & 0 & -\xi & 0 & 0 \\
 & 12\mu(1+R) & 6\mu Lj & 0 & -12\mu(1+R) & 6\mu L \\
 & & \mu L^2 m & 0 & 0 & 2\mu L^2[1-(\psi/2)] \\
 & & & \xi & 0 & 0 \\
 & \text{symmetric} & & & 12\mu(1+R) & -6\mu L \\
 & & & & & 4\mu L^2[1+(\psi/4)]
\end{bmatrix}
$$

(8-60a)

where

$$
\lambda = \frac{1}{m(1+R)-3j^2}
$$

(8-60b)

Connection End Detail	Connection Description	PFRP Column and Beam Profiles	Initial Linear Rotational Stiffness [kips-in./rad (kN-m/rad)][a]
	Web Cleats [*L*] (*Column-Base End Connection*)	**H-Profile:** 4 in. × 4 in. × 1/4 in. (101.6 mm × 101.6 mm × 6.4 mm)	123 (14)
		H-Profile: 8 in. × 8 in. × 3/8 in. (203.2 mm × 203.2 mm × 9.5 mm)	3,186 (360)
	Web Cleats [*U*] (*Beam-Column End Connection*)	**H-Profile:** 4 in. × 4 in. × 1/4 in. (101.6 mm × 101.6 mm × 6.4 mm)	123 (14)
		H-Profile: 8 in. × 8 in. × 3/8 in. (203.2 mm × 203.2 mm × 9.5 mm)	1,132 (128)
	Web + Flange Cleats [*L*] (*Column-Base End Connection*)	**H-Profile:** 4 in. × 4 in. × 1/4 in. (101.6 mm × 101.6 mm × 6.4 mm)	744 (84)
		H-Profile: 8 in. × 8 in. × 3/8 in. (203.2 mm × 203.2 mm × 9.5 mm)	11,770 (1,330)
	Web + Flange Cleats [*U*] (*Beam-Column End Connection*)	**H-Profile:** 4 in. × 4 in. × 1/4 in. (101.6 mm × 101.6 mm × 6.4 mm)	832 (94)
		H-Profile: 8 in. × 8 in. × 3/8 in. (203.2 mm × 203.2 mm × 9.5 mm)	6,177 (698)

[a] About the section's major axis.
Source: Turvey and Cooper (1996a, 1996b).

Table 8-5. Sway-Deflection Increase Index Values (λ_δ) for 8 in. × 8 in. × 3/8 in. (203.2 mm × 203.2 mm × 9.5 mm) PFRP H-Columns with Semi-Rigid Ends and Subjected to a Lateral Point Load

| Height-to-Depth Ratio (H/d) | Deflection Increase Index (λ_δ) Based On: | | | | | |
| | Gross Cross-Sectional Area (A_{Gross}) | | Web Cross-Sectional Area (A_{Web}) | | Shear-Rigid ($\alpha = 0$) | |
	Web Cleat	Web + Flange Cleats	Web Cleat	Web + Flange Cleats	Web Cleat	Web + Flange Cleats
4.92	12.9	3.89	7.80	2.65	19.10	5.39
9.84	9.22	2.98	7.56	2.58	10.3	3.23
14.80	6.97	2.42	6.33	2.27	7.32	2.50
19.70	5.67	2.10	5.36	2.03	5.82	2.13
24.60	4.83	1.89	4.66	1.85	4.91	1.91
29.50	4.25	1.75	4.15	1.73	4.29	1.76
34.40	3.82	1.65	3.76	1.63	3.85	1.65
39.40	3.50	1.57	3.45	1.56	3.52	1.57

Table 8-6. Sway-Deflection Increase Index Values (λ_δ) for 4 in. × 4 in. × 1/4 in. (101.6 mm × 101.6 mm × 6.4 mm) PFRP H-Columns with Semi-Rigid Ends and Subjected to a Lateral Point Load

| Height-to-Depth Ratio (H/d) | Deflection Increase Index (λ_δ) Based On: | | | | | |
| | Gross Cross-Sectional Area (A_{Gross}) | | Web Cross-Sectional Area (A_{Web}) | | Shear-Rigid ($\alpha = 0$) | |
	Web Cleat	Web + Flange Cleats	Web Cleat	Web + Flange Cleats	Web Cleat	Web + Flange Cleats
4.92	34.40	6.26	19.70	3.95	51.80	9.00
9.84	23.50	4.54	18.80	3.80	26.40	5.00
14.80	17.00	3.52	15.20	3.24	17.90	3.67
19.70	13.30	2.94	12.50	2.81	13.70	3.00
24.60	11.00	2.57	10.50	2.50	11.20	2.60
29.50	9.34	2.32	9.08	2.27	9.46	2.33
34.40	8.18	2.13	8.00	2.11	8.25	2.14
39.40	7.30	1.99	7.18	1.97	7.35	2.00

Table 8-7. Required End Rotational Capacities of Bolted Web Cleat End Semi-Rigid Connections for (θ_L^c and θ_U^c) for 8 in. × 8 in. × 3/8 in. (203.2 mm × 203.2 mm × 9.5 mm) PFRP H-Profile Connections under Point Lateral Load ($\kappa_{LU} = 0.005$)

Height-to-Depth Ratio (*H/d*)	Required End Rotational Capacities (θ_L^c and $\theta_U^c \times 10^{-3}$) Based On:					
	Gross Cross-Sectional Area (A_{Gross})		Web Cross-sectional Area (A_{Web})		Shear-Rigid ($\alpha = 0$)	
	θ_L^c	θ_U^c	θ_L^c	θ_U^c	θ_L^c	θ_U^c
4.92	4.3	4.9	4.1	4.7	4.4	5.1
9.84	3.9	5.0	3.8	4.9	4.0	5.1
14.80	3.6	5.0	3.5	4.9	3.6	5.0
19.70	3.3	4.9	3.3	4.9	3.3	4.9
24.60	3.1	4.8	3.1	4.8	3.1	4.9
29.50	2.9	4.7	2.9	4.7	2.9	4.8
34.40	2.7	4.6	2.7	4.6	2.7	4.7
39.40	2.6	4.6	2.6	4.5	2.6	4.6

Table 8-8. Required End Rotational Capacities of Bolted Web Cleat End Semi-Rigid Connections for (θ_L^c and θ_U^c) for 4 in. × 4 in. × 1/4 in. (101.6 mm × 101.6 mm × 6.4 mm) PFRP H-Profile Connections under Point Lateral Load ($\kappa_{LU} = 0.005$)

Height-to-Depth Ratio (*H/d*)	Required End Rotational Capacities (θ_L^c and $\theta_U^c \times 10^{-3}$) Based On:					
	Gross Area (A_{Gross})		Web Area (A_{Web})		Shear-Rigid ($\alpha = 0$)	
	θ_L^c	θ_U^c	θ_L^c	θ_U^c	θ_L^c	θ_U^c
4.92	4.9	4.9	4.7	4.7	4.9	4.9
9.84	4.8	4.8	4.7	4.7	4.8	4.8
14.80	4.7	4.7	4.7	4.7	4.7	4.7
19.70	4.6	4.6	4.6	4.6	4.6	4.6
24.60	4.5	4.5	4.5	4.5	4.6	4.6
29.50	4.5	4.5	4.4	4.4	4.5	4.5
34.40	4.4	4.4	4.4	4.4	4.4	4.4
39.40	4.3	4.3	4.3	4.3	4.3	4.3

Table 8-9. Required End Rotational Capacities of Bolted Web + Flange Cleats End Connections for (θ_L^c and θ_U^c) for 8 in. × 8 in. × 3/8 in. (203.2 mm × 203.2 mm × 9.5 mm) PFRP H-Profile Connections under Point Lateral Load ($\kappa_{LU} = 0.005$)

Height-to-Depth Ratio (H/d)	Required End Rotational Capacities (θ_L^c and $\theta_U^c \times 10^{-3}$) **Based On:**					
	Gross Cross-Sectional Area (A_{Gross})		Web Cross-Sectional Area (A_{Web})		Shear-Rigid ($\alpha = 0$)	
	θ_L^c	θ_U^c	θ_L^c	θ_U^c	θ_L^c	θ_U^c
4.92	3.2	4.2	2.7	3.5	3.5	4.6
9.84	2.7	3.9	2.5	3.6	2.8	4.1
14.80	2.3	3.6	2.2	3.4	2.4	3.6
19.70	2.0	3.2	1.9	3.1	2.0	3.3
24.60	1.8	2.9	1.7	2.9	1.8	3.0
29.50	1.6	2.7	1.6	2.6	1.6	2.7
34.40	1.5	2.5	1.4	2.4	1.5	2.5
39.40	1.3	2.3	1.3	2.3	1.3	2.3

Table 8-10. Required End Rotational Capacities of Bolted Web + Flange Cleats End Connections for (θ_L^c and θ_U^c) for 4 in. × 4 in. × 1/4 in. (101.6 mm × 101.6 mm × 6.4 mm) PFRP H-Profile Connections under Point Lateral Load ($\kappa_{LU} = 0.005$)

Height-to-Depth Ratio (H/d)	Required End Rotational Capacities (θ_L^c and $\theta_U^c \times 10^{-3}$) Based On:					
	Gross Cross-Sectional Area (A_{Gross})		Web Cross-Sectional Area (A_{Web})		Shear-Rigid ($\alpha = 0$)	
	θ_L^c	θ_U^c	θ_L^c	θ_U^c	θ_L^c	θ_U^c
4.92	4.3	4.1	3.8	3.7	4.5	4.4
9.84	4.0	3.8	3.8	3.6	4.1	3.9
14.80	3.7	3.5	3.6	3.4	3.7	3.5
19.70	3.4	3.2	3.3	3.1	3.4	3.2
24.60	3.2	2.9	3.1	2.9	3.2	3.0
29.50	3.0	2.7	2.9	2.7	3.0	2.7
34.40	2.8	2.5	2.7	2.5	2.8	2.6
39.40	2.6	2.4	2.6	2.4	2.6	2.4

$$m = 4 + 12R + \psi \qquad\qquad (8\text{-}60\text{c})$$

$$\psi = \frac{12EI}{L^2 kAG} \qquad\qquad (8\text{-}60\text{d})$$

$$j = 1 + 2R \qquad\qquad (8\text{-}60\text{e})$$

$$\xi = \lambda\gamma \qquad\qquad (8\text{-}60\text{f})$$

$$\gamma = \frac{EA}{L} \qquad\qquad (8\text{-}60\text{g})$$

The nondimensional rotational stiffness term, R, is given by:

$$R = \frac{E_{11}I}{LK_c} \qquad\qquad (8\text{-}61)$$

where K_c is the stiffness of the connection-end rotational spring, which can be calculated from experimental results as:

$$K_c = \frac{M}{\theta} \qquad\qquad (8\text{-}62)$$

Note that the R ratio described in Eq. 8-61 is similar to the β ratio described in Eq. 8-4.

The fixed-end vertical force, f_5, and fixed-end moment, f_6, at the right end of the frame element with flexible connection at its right end (due to a concentrated downward force, P, acting at a distance, a, from the left end), are given by:

$$f_5 = \frac{Pa^2}{L^3}(a + 3b\lambda) \qquad\qquad (8\text{-}63)$$

$$f_5 = \frac{Pa^2 b}{L^2}\left[\lambda\left(1 - \frac{\psi}{2}\right)\right] \qquad\qquad (8\text{-}64)$$

where $b = L - a$. The remaining fixed-end forces and moments can be obtained from static equilibrium. Note that the frame element stiffness matrix (Eq. 8-4) and fixed-end reactions without the effects of connection rotational flexibility and shear deformation effect are obtained by setting R and ψ equal to zero. The validity of this analytical tool was verified by Mosallam and Bank (1992). A detailed description of the iterative procedures commonly used in the nonlinear analysis of PFRP with semi-rigid connections can be found in Mosallam (1990).

Chapter 9 of this manual presents a comprehensive finite element treatment for analyzing PFRP with semi-rigid connections under different loading conditions.

8.5 DESIGN OF SEMI-RIGID BOLTED FRAME CONNECTIONS

The following design examples for PFRP bolted beam-to-column con-
nections follow, to a large extent, the design philosophy adopted by the
EUROCOMP Design Code and Handbook (Clarke 1996) that was developed
at the University of West Virginia.

Example 8-7: Design a semi-rigid beam-to-column connection shown in
Fig. 8-15 to resist a moment of 16.2 ft-kips and a shear load of 5.7 kips.
Use 1/2-in.-diameter, A325N high-strength steel bolts in standard holes.
Design this using allowable stress design (ASD) methodology.

SOLUTION
Step 1: *Reduction of fixed end moment* (*semi-rigid approximation*)
The fixed end moment of 16.2 ft-kips is reduced to 9.68 ft-kips assuming
50% flexibility in the connection.
Step 2: *Design with A325N high-strength bolts*
a. *Bolt Shear: Connected Leg* (*double-shear at beam leg*):
  Allowable shear strength in one bolt $F_v = 10$ ksi [per the AISC *Steel
Construction Manual* (AISC 2006)]
  Assume $d_{bolt} = 1/2$ in.; area of one bolt = 0.196 in.^{2}
  Therefore, allowable shear per bolt = $2 \times 10 \times 0.196 = 3.92$ kips and
therefore the number of bolts required is $n = 5.7/3.92 = 1.45$. Use a
minimum of two bolts.
b. *Bolt Shear: Outstanding Leg* (*single-shear at column flange*)
  $F_v = 10$ ksi [per the AISC *Steel Construction Manual* (AISC 2006)]
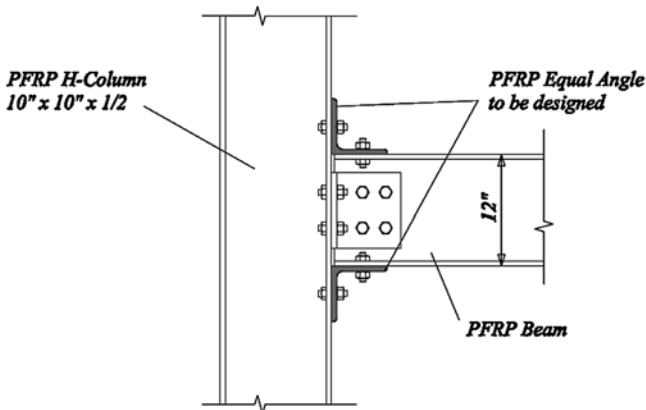
Figure 8-15. Connection details, Example 8-7.

Assume $d_{bolt} = 1/2$ in.; area of one bolt = 0.196 in.^{2}

Therefore, allowable shear per bolt = $10 \times 0.196 = 1.96$ kips and the number of bolts required is $n = 5.7/1.96 = 2.9$. Use a minimum of four bolts, two on each side, for symmetry.

Step 3: *Bolt bearing (in the web of the beam)*

Assume thickness of the web = 1/2 in.

Using a safety factor $SF = 2.5$, we have $F_{bearing} = 34{,}500/2.5 = 13{,}800$ psi

Bolt bearing area = thickness of web × bolt diameter = 0.5 in. × 0.5 in. = 0.25 in.^{2}

Therefore, the allowable bearing per bolt = $13{,}800/4 = 3{,}450$ psi and the required number of bolts is $5.7/3.45 = 1.65$. Use two 1/2-in.-diameter bolts on all sides.

Step 4: *Sizing of the PFRP angle*

Check shear on the gross angle area:

Use $F_v = 7{,}000/2.5 = 2{,}800$ psi

Assume 2 in. clearance at the top

Max angle length = height of the beam-thickness of the web clearance

Therefore, maximum PFRP angle length = $(12 - 1 - 4) = 7$, and thickness = $5.7 / (7 \times 2{,}800) \approx 0.3$. Therefore, use a 3/4-in.-thick PFRP angle.

Step 5: *Number of bolts through the beam flanges and the top and bottom angles*

The capacity of one bolt in shear is 9.3 kips (AISC 2006)

The minimum capacity of one bolt in bearing = 32.6 kips

The force in each flange of the beam is calculated as follows:

$T = C =$ moment/(height of the beam) = $(9.68 \times 12)/12 = 9.68$ kips

Number of bolts required is $9.68/9.3 = 1.04$. Use four bolts, two on each side (i.e., top and bottom flange of beam) for symmetry.

Step 6: *Bolts through the column flanges*

Capacity of one bolt in tension = 19.44 kips (AISC 2006)

Therefore, number of bolts = $9.68/19.44 = 0.5$ (use a minimum of two bolts)

Use a 6 in. × 6 in. × 3/4 in. × 9 in. PFRP equal-leg angle to accommodate the required number of bolts (refer to Fig. 8-16).

Now, find the contraflexure point located at the top angle. The distance from the bolt in tension to the top of the horizontal leg of the angle, assuming angle thickness of 3/4 in.:

$x = 3 - 0.75 = 2.25$ in.

Determining the tensile force, using the actual vertical distance between T and C:

$T = C = (9.68 \times 12)/18 = 6.45$ kips

$M = 6.45 \times (2.25/2) = 8.25$ in.-kips

Solving for the required thickness (t), and recalling that for a rectangular shape the section modulus is given by:
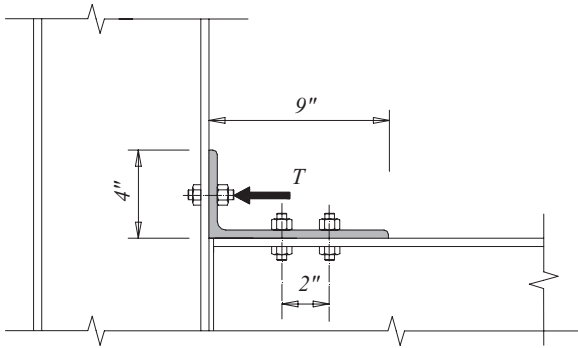
Figure 8-16. Analysis of the top cleat angle.

$S = bt^2/6$ and $S = M/F_b$, where F_b = bending stress, the required thickness of the PFRP is calculated using the following expression:

$$t = \sqrt{\frac{6M}{F_b b}}$$

where $F_b = 19{,}900/2.5 = 7{,}960$ psi and $b = 9$ in.

Therefore, the required thickness $t = 0.78$ in.

Thus, use PFRP equal-leg 6 in. $\times$ 6 in. $\times$ 3/4 in. $\times$ 9 in. top and bottom angles.

Step 7: *Shear-out and bearing strengths compliance check*

I. Taking into consideration the web of the beam and assuming that the bolts in the web of the beam are taking 40% of the total shear load:

First, assume number of steel bolts = 4.

a) Calculate the induced shear-out strength in PFRP material:

$$\tau_{sh,s} = \frac{0.59\times0.25\times5.7\times0.4}{0.5\times0.75} = 0.898 \text{ ksi}$$

b) Calculate induced bearing strength in PFRP material:

$$\sigma_{r,s} = \frac{1.35\times0.25\times5.7\times0.4}{0.5\times0.75} = 2.052 \text{ ksi}$$

c) Compute the resisting shear-out strength of the composite material: $\tau_{sh,k} = 24.07$ ksi [this particular value for the shear-out strength has been

taken from the *EUROCOMP Design Code and Handbook* (Clarke 1996) due to insufficient test data for shear-out strength values].

Dividing the above value by a safety factor of 2.5, we have $\tau_{sh,k}$ = 9.63 ksi. Furthermore, dividing the shear-out value by a stress concentration factor of 1.2 and multiplying it by an aging factor of 0.4, we have:

$$\tau_{sh,k} = 3.2 \text{ ksi}$$

Therefore,

$$\tau_{sh,s} = 0.898 \text{ ksi} \le \tau_{sh,k} = 3.2 \text{ ksi; hence acceptable.}$$

d) Calculate resisting bearing strength of PFRP material:

For bearing, we have $\sigma_{r,k}$ = 38,000 psi.

Dividing this stress value by a safety factor of 2.5 produces $\sigma_{r,k}$ = 15,200 psi.

To account for nonuniform stress distribution through the thickness of the laminate due to nonsymmetry, bolt bending, and loss of lateral restraint, we will divide by a factor C_m = 1.2 in., resulting in a further reduction of $\sigma_{r,k}$ ($\sigma_{r,k}$ = 12,666.67 psi). Furthermore, $\sigma_{r,k}$ is divided by a stress concentration factor of 1.6, and multiplying by an aging factor of 0.4, we have in bearing, $\sigma_{r,k}$ = 3.16 ksi.

Therefore, we have $\sigma_{r,s}$ = 2.052 ksi $\le \sigma_{r,k}$ = 3.16 ksi; hence acceptable.

II. Consider the top angle attached to the column flange (single shear), assuming the number of bolts is four. In this example, the remaining 60% of the shear load is shared by the top and bottom angles, assuming that each is taking 30%.

a) Calculate induced shear-out strength in PFRP material:

$$\tau_{sh,s} = \frac{0.59 \times 0.25 \times 5.7 \times 0.3}{0.5 \times 0.75} = 0.673 \text{ ksi}$$

b) Calculate induced bearing strength in PFRP material:

$$\sigma_{r,s} = \frac{0.59 \times 0.25 \times 5.7 \times 0.3}{0.5 \times 0.75} = 1.54 \text{ ksi}$$

c) Calculate resisting shear-out strength of the composite material:

$\tau_{sh,k}$ = 24.07 ksi [this particular value for the shear-out strength has been taken from the *EUROCOMP Design Code and Handbook* (Clarke 1996), due to insufficient test data for shear-out strength values].

Dividing the above value by a safety factor of 2.5, we have $\tau_{sh,k}$ = 9.63 ksi.

Similar to the last step, $\tau_{sh,k}$ is further divided by a factor $C_m = 2$ to account for bending effects due to the eccentricity in the single-lap joint configuration (Clarke 1996). Thus, $\tau_{sh,k} = 4.82$ ksi. Furthermore, the shear-out value is divided by a stress concentration factor of 1.2, and multiplying it by an aging factor of 0.4, we have:

$$\tau_{sh,k} = 1.61 \text{ ksi}$$

Therefore, $\tau_{sh,s} = 0.673$ ksi $\leq \tau_{sh,k} = 1.61$ ksi; hence acceptable.

d) Calculate resisting bearing strength of PFRP material. In bearing, we have $\sigma_{r,k} = 38{,}000$ psi. Dividing by a safety factor of 2.5, we have $\sigma_{r,k} = 15{,}200$ psi.

Dividing by a factor $C_m = 2$ to account for bending effects due to eccentricity in the single-lap joint; we have $\sigma_{r,k} = 7{,}600$ psi.

Dividing by a stress concentration factor of 1.6 and multiplying by an aging factor of 0.4, we have in bearing, $\sigma_{r,k} = 1.9$ ksi.

Therefore, $\sigma_{r,s} = 1.54$ ksi $\leq \sigma s_{r,k} = 1.9$ ksi; hence acceptable.

Note that the above computations for shear-out and bearing strengths will hold good for the bottom angle, too.

Step 8: *Check maximum force in bolt group* (for bolts in the web when subjected to a combination of induced moment and shear)

The torsional moment is $M = 9.68$ ft-kip $= 116{,}160$ in.-lb

The polar moment of inertia is calculated as:

$$\Sigma x^2 = 8\,(1)^2 + 8\,(3)^2 + 8\,(5)^2 = 280 \text{ in.}^2$$
$$\Sigma y^2 = 12\,(1)^2 + 12\,(3)^2 = 120 \text{ in.}^2$$

Therefore:

$$\Sigma x^2 + \Sigma y^2 = 400 \text{ in.}^2$$

The torsional load (Q_{mu}), acting at a unit distance from the center of gravity of the bolt group, is:

$$Q_{mu} = M\,/\,[\Sigma x^2 + \Sigma y^2] = 116{,}160\,/\,400 = 290.4 \text{ lb/ft}$$

Torsional load on the critical bolt is $Q_{mu} = 290.4 \times \sqrt{34} = 1{,}693$ lb

Horizontal component of $Q_{mu} = 1{,}452$ lb

Vertical component of $Q_{mu} = 580$ lb

The force on the bolt due to the 5.7 kips shear load applied at the center of gravity is determined for the most critical bolt using the load distribution table given in the *EUROCOMP Design Code and Handbook* (Clarke 1996). Accordingly, the shear load acting on the most critical bolt is 432 lb.

Therefore, the load in the most critical bolt in the bolt group is R, which is:

$$R = \sqrt{(432+580)^2 + 1,452^2} = 1,768 \text{ lb}$$

The induced strength in shear-out due to this load is:
$(R \times K_s) / (d_{bolt} \times t) = (1,763 \times 0.59) / (0.5 \times 0.75) = 2.78 \text{ ksi}$

This induced strength, however, is lower than the allowable shear strength of 3.2 ksi. Notice that if the induced moment and the shear are taken by the web of the beam, the result will be an uneconomical design, which may pose problems in terms of angle selection, beam depth, and so forth.

Step 9: *Checking block-shear in the web of the beam* (refer to Fig. 8-17)

The capacity of the connection based on web tear-out (block shear) is calculated as follows:

The thickness of the web is 0.5 in.

The block shear load $P_{block} = A_v \times \tau_{sh} + A_t \times \sigma_n$

The shear area $A_v = 2[4 - 1.5 \,(0.5)] \times 0.5 = 3.25 \text{ in.}^2$

The tension area $A_t = 2[2 - 0.5 \,(0.5)] \times 0.5 = 1.75 \text{ in.}^2$

The allowable value of stress in shear = $[7,000/(2.5 \times 1.2)] \times 0.4 = 933.33 \text{ psi}$

The allowable value of stress in tension = $[7,6250/(2.5 \times 2.3)] \times 0.4 = 5,304.34 \text{ psi}$

Therefore, the block shear load $P_{block} = [3.25 \times 933.33 + 1.75 \times 5,304.34] = 12.3 \text{ kips.}$
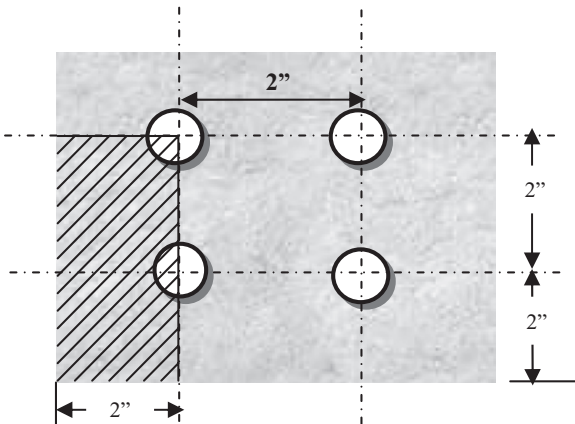
Figure 8-17. Web tear-out (block shear).

Example 8-8: Design the same semi-rigid connection as in Example 8-7, with a flexibility of 75%. Use all assumptions adopted in Example 8-7. Due to a fixity factor of 0.75 or a flexibility of 75%, the value of the semi-rigid moment is now equal to 13.23 ft-kips.

Proceed for the solution by following Steps 1 through 4 as shown in Example 8-1. This procedure ensures that there is no change in the amount of shear load coming onto the beam web and the column flanges; hence, the procedure remains the same.

Step 5: *Bolts through the beam flanges and the top and bottom angles*
The capacity of one bolt in shear is 9.3 kips (AISC 2006).
The minimum capacity of one bolt in bearing = 32.6 kips
The force in each flange of the beam is calculated as follows:
$T = C$ = moment/(height of the beam) = $(13.23 \times 12)/12 = 13.23$ kips
The number of required bolts = $13.23/9.3 = 1.42$. Therefore, use four bolts, two on each side (i.e., top and bottom flange of the beam) for symmetry.

Step 6: *Bolts through the column flanges*
The capacity of one bolt in tension = 19.44 kips (AISC 2006). Therefore, the number of bolts = $13.23/19.44 = 0.68$.

Use a minimum of two bolts and PFRP equal-leg L 6 in. $\times$ 6 in. $\times$ 3/4 in. $\times$ 9 in. angles to accommodate the required number of bolts.

Finding the contraflexure point located at the top angle: The distance from the bolt in tension to the top of the horizontal leg of the angle, assuming 3/4 in. thickness angle, is:

$$x = 2.5 - 0.75 = 1.75 \text{ in.}$$

Now determine the tensile force using the actual vertical distance between T and C:
$T = C = (13.23 \times 12)/18 = 8.82$ kips, and the moment $M = 8.82 \times (1.75/2)$ = 8.72 in.-kips
Solving for the required thickness, recall that for a rectangular shape:
$S = (bt^2/6)$ and $S = M/F_b$
where F_b = bending stress.
The required thickness of the angle is calculated as follows:

$$t = \sqrt{\frac{6M}{F_b b}}$$

$F_b = 19,900/2.5 = 7,960$ psi; $b = 9$ in.
Therefore, the required $t = 0.76$ in.
Use L 6 in. $\times$ 6 in. $\times$ 3/4 in. $\times$ 9 in. top and bottom PFRP angles.

REFERENCES

American Institute of Steel Construction (AISC). (2006). *Manual of steel construction: Allowable stress design and plastic design,* 13th ed., AISC, Chicago, Ill.

Ang, K. M., and Morris, G. A. (1984). "Analysis of three-dimensional frames with flexible beam-column connections." *Can. J. Civil Eng.,* 11(2), 245–254.

Bank, L. C., and Bednarczyk, P. J. (1988). "A beam theory for thin-walled composite beams." *Composite Sci. Tech.*, 32, 265–277.

Clarke, J. L., ed. (1996). "Structural design of polymer composites." *EURO-COMP design code and handbook*. E & FN Spon/Chapman & Hall, London.

Creative Pultrusions, Inc. (2004). *Creative Pultrusions design guide*, Creative Pultrusions, Inc., Alum Bank, Pa.

Frye, M. J., and Morris, G. A. (1975). "Analysis of flexibly connected steel frames." *Can. J. Civil Eng.,* 2(3), 280–291.

Gerstle, K. H. (1988). "Effect of connection on frames." *J. Const. Steel Res.*, 10, 241-268.

Jones, S. W., Kirby P. A., and Nethercot, D. A. (1982). "Columns with semi-rigid joints." *ASCE J. Struct. Div.*, 108(ST2), 361–372.

Lui, E. M., and Chen, W. F. (1985). "Joint flexibility in steel frame." *Proc., ASCE Convention*, October 24, Detroit, Mich., pp. 77–100.

Morice, P. B. (1969). *Linear structural analysis: An introduction to the influence coefficients method applied to statically indeterminate structures,* Thames and Hudson Publishers, London.

Mosallam, A. S. (1994) "Connections for pultruded composites*:* A review and evaluation." K. D. Basham, ed., *Infrastructure: New materials and methods of repair*, ASCE, New York, pp. 1001–1018.

Mosallam, A. S. (1990). "Short- and long-term behavior of pultruded fiber-reinforced plastic frame." Ph.D. dissertation, The Catholic University of America, Washington, D.C.

Mosallam, A. S., and Abdelhamid, M. K. (1993). "Dynamic behavior of pultruded PFRP structural sections." *Composite material technology,* PD-Vol. 53, *Proc., ASME Energy-Sources Tech. Conf. and Expo*, Texas, January 31–February 4, pp. 37–44.

Mosallam, A. S., and Bank, L. C. (1992). "Short-term behavior of pultruded fiber-reinforced plastic frame." *ASCE J. Struct. Eng.*, 118(7), 1937–1954.

Mosallam, A. S., and Chambers, R. E. (1995). "Design procedure for predicting creep and recovery of pultruded composites." *Proc., 50th Ann. Conf. of the Composite Inst.*, Society of the Plastics Industry (SPI), January 30–Feburary 1, Cincinnati, Ohio, Session 6-C, pp. 1–13.

Mottram, J. T., and Zheng, Y. (1996). "State-of-the-art review on the design of beam-to-column connections for pultruded frames." *Composite Struct.,* 35(4), 354, 387–401.

Ozturk, A. U., and Catal, H. H. (2005). "Dynamic analysis of semi-rigid frames." *Math. and Comput. Apps.*, 10(1), 1–8.

Turvey, G. J. (1998). "Recent developments in testing, design, analysis and modeling of bolted connections in pultruded GRP frames made of open-section profiles." *Proc., EPTA Conference*, Vienna, Austria, April 9–10.

Turvey, G. J. (1997). "Analysis of pultruded glass reinforced plastic beams with semi-rigid end connections." *Composite Struct.*, 38(1–4), 3–16.

Turvey, G. J. (1996). "Testing of a pultruded GRP pinned base rectangular portal frame for the EUROCOMP Project." J. L. Clarke, ed., *Structural design of polymer composites: EUROCOMP design code and handbook*, E & FN Spon/Chapman & Hall, London, pp. 719–741.

Turvey, G. J., and Cooper, C. (1998). "Semi-rigid connections and their effects on the sway response of pultruded GRP columns in low-rise frame structures." *Proc., 2nd Int. Conf. on Composites in Infrastructure* (*ICCI '98*), University of Arizona, Tucson, Ariz., Vol. II, pp. 221–235.

Turvey, G. J., and Cooper, C. (1996a). "Semi-rigid pultruded GRP frame connections: Tests to determine static characteristics*." Proc., 7th European Conf. on Composite Mat.* (*ECCM-7*), May 14–17, London, Woodhead Publishing Co., Cambridge, UK, Vol. 2, pp. 295–300.

Turvey, G. J., and Cooper, C. (1996b). "Characteristics of the short term static moment-rotation of bolted connections between pultruded GRP beam and column WF-sections." *Proc., 2nd Int. Conf. on Adv. Composite Mat. in Bridges and Structures* (*ACMBS II*), August 11–14, Montréal, pp. 927–934.

Zahr, S., Hill, S., and Morgan, H. (1993). "Semi-rigid behavior of PFRP/UC beam-to-column connections." *Proc., ANTEC Conf.*, New Orleans, La., May 9–13, Society of Plastic Engineers, pp. 1496–1502.

This page intentionally left blank

CHAPTER 9

FINITE ELEMENT MODELING OF PULTRUDED FIBER-REINFORCED POLYMER FRAME CONNECTIONS

9.1 INTRODUCTION

Numerical analysis methods such as finite element (FE) are considered powerful analytical and design tools for the structural engineer. Great advances in computer software and computer hardware contributed to the development of more efficient and user-friendly FE codes.

FE methods are particularly important when designing complex structures in general and composite structures in particular. Commonly, the performance of fiber-reinforced polymer (FRP) composite joints are analyzed using such methods, which enables the engineer to monitor the local deformation, stresses, and progressive failure at specific critical locations.

In the preliminary design phase, the engineer should use simple and approximate methods, such those presented in Chapters 4, 5, and 6 of this manual, to develop the conceptual design of the joint. Parametric or trade-off studies using FE methods can be extremely costly and may offer little or no logical rationale for the trends (Kedward 1990). The engineer should also carefully evaluate the feasibility of conducting linear analysis versus nonlinear analyses, since nonlinear analyses are cumbersome and often involve several hours to several days of computer and operator time. In this chapter, a case study is presented to demonstrate this critical issue. In some composites, depending on the fiber architecture, it is also acceptable to assume homogeneous orthotropy (e.g., in the case of laminates with many angle-ply or cross-ply structures for which the bending stiffness coupling terms D_{16} and D_{26} have a little impact in the analysis).

9.2 ORTHOTROPIC PROPERTIES IN PLANE STRESS OF LAMINATED COMPOSITES

Pultruded shapes can be simulated as laminated composites (Davalos et al. 1996; Neto and La Rovere 2007). Because structural members made of pultruded fiber-reinforced polymer (PFRP) I/H/C/L-profiles are thin in the through-the-thickness direction, the two-dimensional orthotropic properties are frequently used (Jones 1999). This can be obtained by setting $\sigma_3 = \tau_{13} = \tau_{23} = 0$ (a plane stress assumption) to get:

$$
\begin{pmatrix} \varepsilon_1 \\ \varepsilon_2 \\ \varepsilon_3 \end{pmatrix} := \begin{bmatrix} \dfrac{1}{E_1} & -\dfrac{v_{21}}{E_2} & 0 \\ -\dfrac{v_{12}}{E_1} & \dfrac{1}{E_2} & 0 \\ 0 & 0 & \dfrac{1}{G_{12}} \end{bmatrix} \cdot \begin{pmatrix} \sigma_1 \\ \sigma_2 \\ \sigma_3 \end{pmatrix}
\tag{9-1}
$$

There are four independent material properties, E_1, E_2, G_{12}, and v_{12}, in addition to the following reciprocal relation:

$$
\frac{v_{12}}{E_1} = \frac{v_{21}}{E_2}
\tag{9-2}
$$

9.3 MODELING OF PFRP COMPOSITES

To build a finite element model for any composite element, material properties of the fibers and matrix material, as well as the lay-up, must be defined. For commercially produced PFRP materials, the first two pieces of information are defined. However, it is very difficult to precisely identify the material lay-up due to the irregularity of the fiber positions along the beam. This may be attributed to two factors: the nature of the pultrusion process, and the quality control of the available commercially produced PFRP sections. For this reason, the available mechanical properties of the materials are only provided as effective moduli which are determined experimentally. The apparent modulus of this material is given as an average value.

The variation of the lay-up along the cross section of the PFRP test specimens can be detected by the naked eye. This observation indicates the possibility of deviation between the results calculated from the FE model and those obtained from the test. The effect of the irregularity in the fiber positioning is minimum in the case of in-plane loading condition (Mosallam et al. 1993). This is due to the fact that the axial stress distribution is uniform throughout the section; consequently, positioning of the

fibers in the section will have little impact on the overall stiffness charac-
teristics of the PFRP section. However, under combined loading condi-
tions [e.g., tensile/flexural (out-of-plane), and/or torsional loads], the
stress distribution is nonuniform, and the inaccurate positioning of the
fibers will greatly affect the stress distribution along the section. Conse-
quently, the stiffness will be altered.

Although PFRP shapes are not produced by lamination lay-up, the
arrangement of the constituent materials can be simulated as a layered
system. The stiffness properties of each panel can be predicted by lamina-
tion theory in terms of the ply stiffness computed through micro-mechan-
ics by estimating the fiber volume fractions (V_f) of the constituents. The
analysis of the V_f of the constituents and the ply stiffness is not within the
scope of this manual and thus will not be discussed any further. However,
the reader is referred to several excellent textbooks dealing with this
subject, including Barbero (1998), Danial and Ishai (2006), Jones (1999),
and Tsai and Hahn (1980).

As an example, Fig. 9-1 shows an approximation for the material lay-up
and fiber architecture of a typical open-web unidirectional PFRP H-profile
(Liu 2000). The materials data are listed in Table 9-1. The material informa-
tion presented in Table 9-1 was supplied by the manufacturer (Bedford
Reinforced Plastics, Bedford, Pa.), while the ply stiffness in terms of engi-
neering constants of laminae (e.g., E_{11}, E_{22}, G_{12}, and v_{12}) were directly taken
from Davalos et al. (1996) as an approximation.
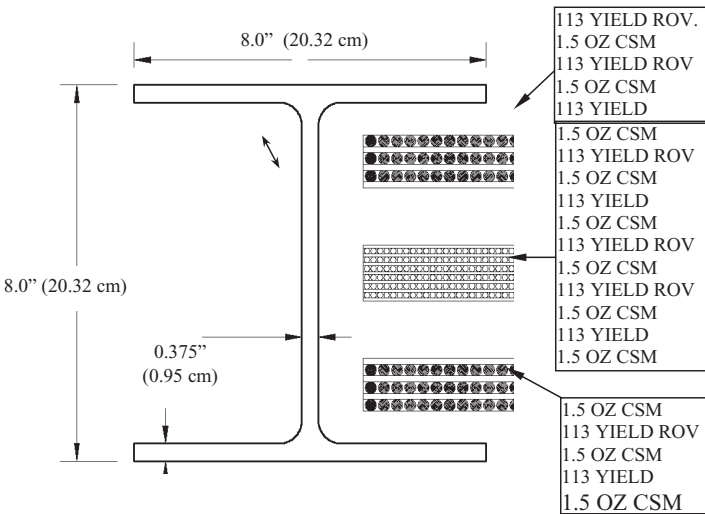
Figure 9-1. Cross-sectional dimensions and fiber architecture of an 8 in.
× 8 in. × 3/8 in. (20.32 cm × 20.32 cm × 0.95 cm) PFRP profile.
CSM, continuous strand mat.

Table 9-1. Engineering Constants for Pultruded H-Profile
Shown in Fig. 9-1

Mechanical Properties	1.5 oz CSM [psi (GPa)]	113 Yield Roving [psi (GPa)]
E_1	1,716,000 (11.83)	4,320,000 (29.79)
E_2	1,716,000 (11.83)	959,000 (6.61)
E_3[a]	10 (0.00007)	10 (0.00007)
G_{12}	605,000 (4.17)	371,000 (25.58)
G_{23}[a]	10 (0.00007)	10 (0.00007)
G_{31}[a]	10 (0.00007)	10 (0.00007)
υ_{12} (dimensionless)	0.419	0.293
υ_{21} (dimensionless)[b]	0.419	0.065

[a] These were assumed engineering constants for the orthotropic materials needed for FEA input.
(Note that these values are negligible as compared properties at other directions.)
[b] These values were calculated per the reciprocal relation $\upsilon_{12}/E_1 = \upsilon_{21}/E_2$.
CSM, continuous strand mat.
Source: Bedford Reinforced Plastics, Inc.

9.4 FINITE ELEMENT ANALYSIS CODES FOR COMPOSITE STRUCTURES

Several FE codes have the capability of analyzing laminated composites structures. The degree of suitability of some of these codes depends on the user's desired convenience features, such as the ability to input lamina properties and output layer-by-layer stresses at specific locations. A comprehensive list and an evaluation of different FE computer codes suitable for FRP composites are presented by Brown (1987) and Kedward (1990), and Brown and Nachlas (1985), respectively.

The following are some commonly available FE codes (in alphabetical order) that are suitable for analysis of composite structures:

ABAQUS
ANSYS
COSMOS
GENOA
I-DEAS
MARC
NASTRAN
NISA II

PATRAN
LUSAS

Brief descriptions of some of these FE codes are given in the following sections.

9.4.1 ABAQUS FE Code

This FE code was developed by Hibbitt, Karlsson & Sorensen, Inc., Pawtucket, Rhode Island. This code is considered to be very efficient in performing nonlinear analysis of structures, including composites. ABAQUS code has several modules, including:

- *ABAQUS/Explicit:* This module is capable of performing nonlinear, transient, dynamic analysis of solids and structures using explicit time integration.
- *ABAQUS/Standard:* This module is a general-purpose FE analysis software that includes all analysis capabilities except nonlinear dynamic analysis using explicit time integration.
- *ABAQUS/Design:* This module is an add-on analysis capability for ABAQUS/Standard that allows the user to perform design sensitivity analysis (DSA). The derivatives of the output variables are calculated with respect to specified design parameters.
- *ABAQUS/Safe:* This module uses the results from ABAQUS analyses to determine the fatigue life of a component.

9.4.2 ANSYS FE Code

This code was developed by Swanson Analysis Systems Inc. and currently available from ANSYS, Inc., Canonsburg, Pa. There are several products of ANSYS, including:

- *ANSYS/Structural:* This software has an extensive element library that includes linear and nonlinear elements as well as a comprehensive set of nonlinear and linear material laws. For laminated composites, only one element, STIF 53 (a flat triangular shell element) featuring laminated orthotropic layer-by-layer properties, is available. The majority of the other elements offer orthotropic material properties, and in some of these elements the user can specify an arbitrary angle of orientation of the principal material directions. Table 9-2 provides a summary of different elements suitable for laminated composite analysis.
- *ANSYS/LS-DYNA:* This software is extremely useful for simulating explicit structural dynamic problems, including composite structures and joints.

Table 9-2. ANSYS FE Elements for Analysis of Composite Structures

Subroutine Name	Description	Properties	Orientation of Principal Material Axes
Plane Elements			
STIF 42	2-D isoparametric, plane stress or strain	Orthotropic	Either (1) parallel to global or (2) parallel to element U side/face
STIF 82	2-D isoparametric, multi-node, plane	Orthotropic	Parallel to global reference axis
Plate Bending Elements			
STIF 6	2-D triangular plate	Orthotropic	Parallel to global reference axis
STIF 26	2-D triangular plate (plastic)	Orthotropic (elastic) isotropic (plastic)	Parallel to global reference axis
STIF 46	2-D rectangular plate	Orthotropic	Parallel to global reference axis
Shell Elements			
STIF 41	Quadrilateral membrane shell	Orthotropic	Arbitrary angle (θ) to U side
STIF 43	Rectangular shell	Orthotropic	Arbitrary angle (θ) to U side
STIF 48	Triangular shell (plastic)	Orthotropic isotropic (plastic)	Parallel to U side
STIF 53	Laminated triangular shell (15-ply limit)	Laminated orthotropic layers	Arbitrary angle (θ) to U side
STIF 63	Quadrilateral shell	Orthotropic	Parallel to U side
STIF 94	16-node isoparametric shell	Orthotropic	Parallel to U side

Solid Elements

STIF 45	3-D isoparametric solid	Orthotropic	Parallel to global reference axis
STIF 95	20-node, isoparametric solid	Orthotropic	Parallel to global reference axis

Axi-Symmetric Elements

STIF 11	Axi-symmetric shell	Orthotropic	Parallel to shell meridian
STIF 25	Axi-symmetric solid	Orthotropic	Either (1) parallel to global reference axis or (2) parallel to U face.
STIF 42	Axi-symmetric solid	Orthotropic	Either (1) parallel to global reference axis or (2) parallel to U face.
STIF 61	Axi-symmetric shell (harmonic)		Parallel to shell meridian

Specialty Elements

STIF 27	2-node matrix input (stiffness, mass, damping)	6 × 6 stiffness matrix coefficients	Parallel to nodal coordinate directions
STIF 85	Crack tip solid	Orthotropic	Parallel to global reference axis

Source: ANSYS, Inc., Canonsburg, Pa.

9.4.3 COSMOS/M FE Code

COSMOS/M version 2.0 is an FE analysis code developed by Structural Research and Analysis Corporation (SRAC), Santa Monica. As defined in the User Guide developed by SRAC (2004), COSMOS/M has several unique elements that are suitable for analyzing composite structures in general and composite joints in particular. Some of the important elements that were used by several researchers modeling pultruded composite frame connections, including Mosallam (2000) and Bank et al. (1996), are:

- *Linear Quadrilateral Plate and Shell Element (SHELL4L):* SHELL4L is a four-node multilayer quadrilateral shell element with membrane and bending capabilities for the analysis of 3-D structural and thermal models. Up to 50 layers can be used. Six degrees of freedom (DOF) (three translations and three rotations) are considered per node. Each layer can be associated with different isotropic or orthotropic material properties (Fig. 9-2).
- *Linear Quadrilateral Thick Shell Element (SHELL4T):* SHELL4T is a four-node quadrilateral thick shell element with membrane bending
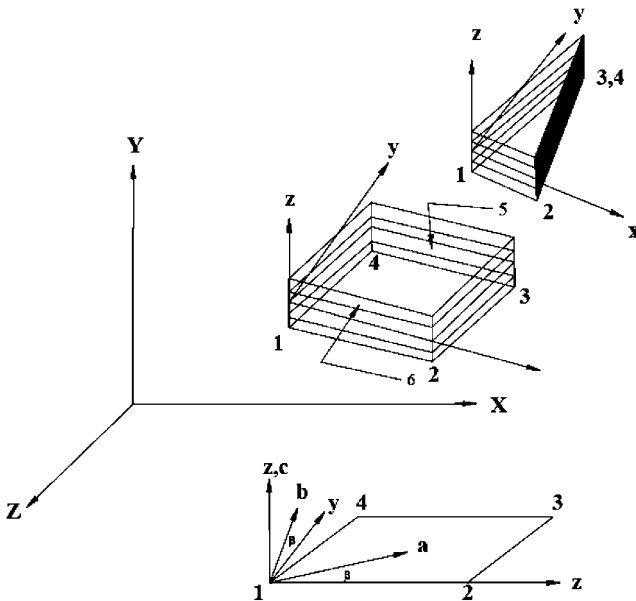
Figure 9-2. COSMOS/M composite quadrilateral plate and shell (SHELL4L). xyz, global Cartesian coordinate system; xyz, element coordinate system; bc, material coordinate system.

capabilities for the analysis of 3-D structural and thermal models. The element accounts for shear deformation effects. Six DOF per node (three translations and three rotations) are considered for structural analysis. Only one DOF per node, representing the temperature, is used for the thermal module. A triangular element is considered if the third and fourth nodes are assigned the same global node number. The element is assumed to be isotropic with constant thickness for structural problems and orthotropic for thermal problems. For orthotropic structural materials, SHELL4T is recommended used for problems involving thin plates or shells, as determined by standard guidelines (refer to Figs. 9-3 and 9-4).

- *Linear 3-D Elastic Beam (BEAM3D):* BEAM3D is a two-node uni-axial element for 3-D structural and thermal models. For structural analysis, six DOF (three translations and three rotations) are considered per node. One DOF per node, representing the temperature, is used for the thermal module. A third node is required only for the element orientation, as shown in Figs. 9-5 and 9-6.
- *Nonlinear Spring Element (SPRING):* SPRING is a one-node or two-node massless uni-axial element for the analysis of nonlinear structural models. Two DOF (one translation and one rotation) are considered for each node in the element local coordinate system.
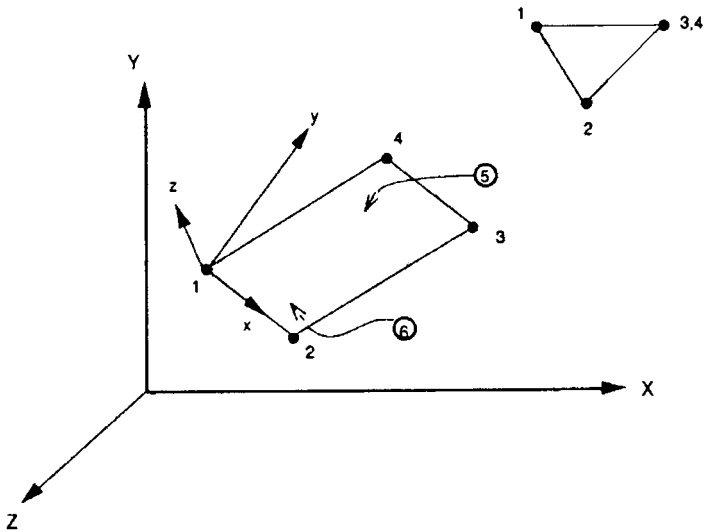
Figure 9-3. COSMOS/M quadrilateral thick shell.
XYZ, global Cartesian coordinate system; xyz, element coordinate system; 0, face number for pressure application (positive when applied inward).
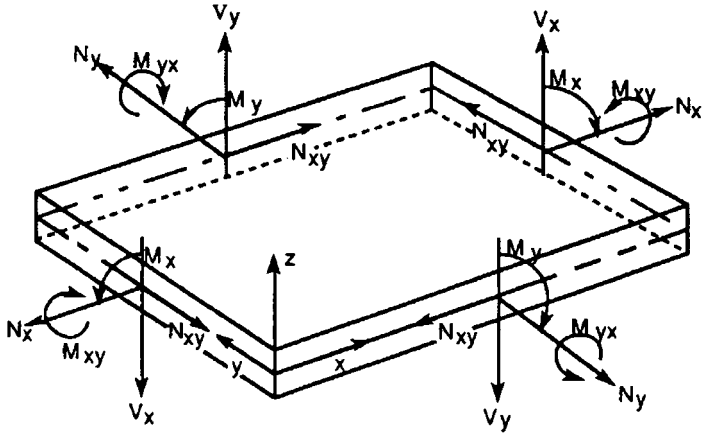
Figure 9-4. *Direction of force and moment components per unit length as defined by COSMOS/M thick shells.*
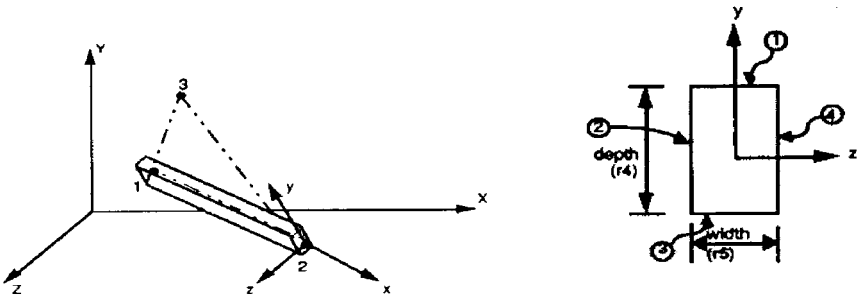
Figure 9-5. *COSMOS/M 3-D symmetric elastic beam.*
xyz, global Cartesian coordinate system; xyz, element coordinate system;
0, face number for pressure application (positive when applied inward).

The one-node element has its DOF specified in the global Cartesian directions. The element can be used as a longitudinal and/or torsional spring in 1-, 2-, or 3-D applications. Note that large displacement effects can only be considered for translation, or axial spring (refer to Figs. 9-7 and 9-8).

• *Linear Gap–Friction Element (GAP):* Gap is a two-node element for 2-D or 3-D interface problems in structural models. The element behaves similarly to a rigid link, which can resist either compression or tension in the direction normal to the interface. A compressive gap resists compression once the relative contraction between the two nodes exceeds the defined gap distance (refer to Fig. 9-9).
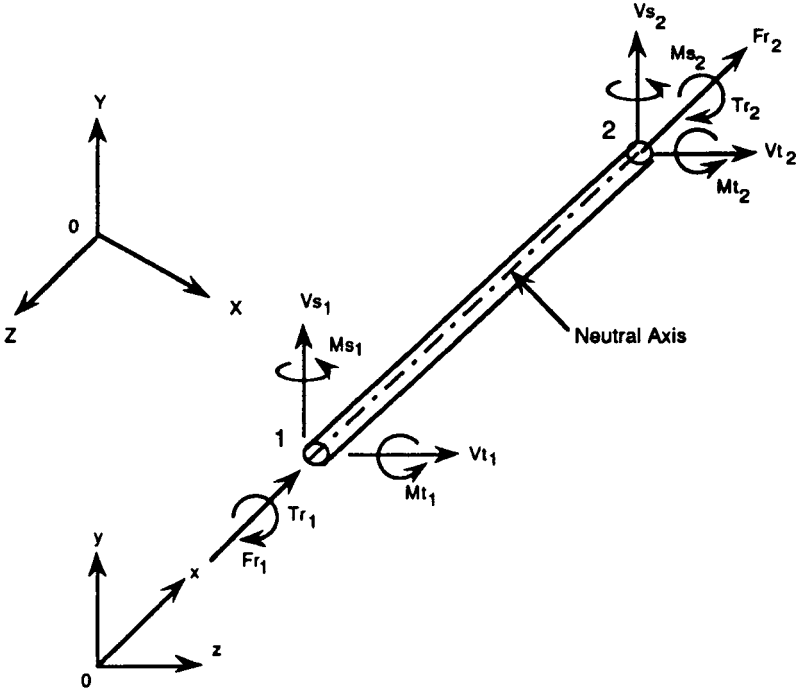
Directions of Forces and Moments in the element coordinate system

Figure 9-6. COSMOS/M directions of forces and moments in the element coordinate system.

XYZ: Global Cartesian Coordinate System
xyz: Element Coordinate System
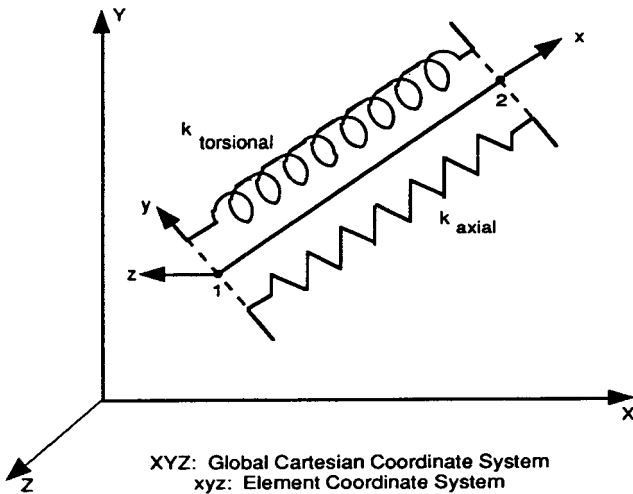
Figure 9-7. COSMOS/M 3-D spring element.
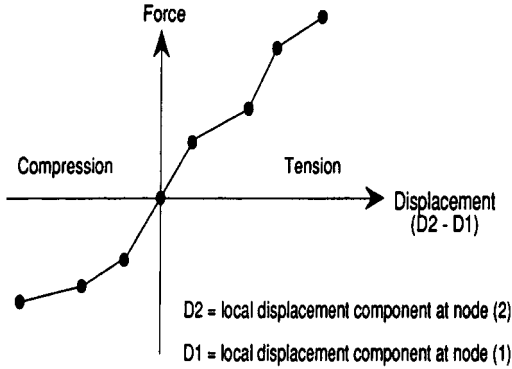
Figure 9-8. COSMOS/M user-defined nonlinear force–displacement curve.
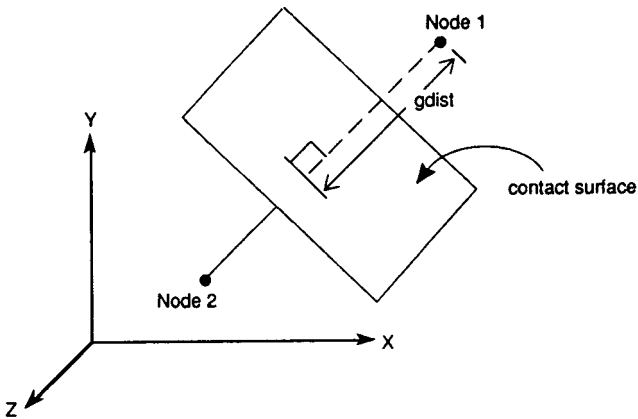
Figure 9-9. COSMOS/M node-to-node gap element.

9.4.4 GENOA Progressive Failure Analysis Code

The GENOA Progressive Failure Analysis (PFA) software package was developed by NASA-Glenn and NASA-Langley in conjunction with the Alpha Star Corp., Long Beach, Calif.

GENOA produces a 3-D structural and material model predicting strength, progressive failure, reliability, and durability of polymer composites, ceramics, and metallic structural components at the design stage, with minimal experimental support. GENOA makes the manufacturing process of composites extremely cost- and time-effective. GENOA is the only software that predicts damage initiation, propagation and residual strength of laminated, 3-D, woven, braided, stitched, z-pin, T-pin, and honeycomb composite structures, from the micro-mechanics to the

structural level, under various environmental and service conditions. GENOA PFA can be used to investigate the deterioration of 2-D or 3-D composite structure and joints subjected to static cycle and random fatigue, creep, and impact loadings under hygrothermal environments. GENOA can be expected to facilitate targeting of changes in design parameters for greatest effectiveness in reducing the probabilities of given failure modes.

PFA simulation involves (1) ply layering methods using FEM with through-the-thickness representation and adaptive meshing; (2) effects on global structure of static, cyclic, and cyclic fatigue strengths, and material conditions relative to voids, fiber waviness, and residual stress; (3) non-linear periodic Lagrangian updating of material property and geometrical parameters; (4) simulation of the initiation and growth of cracks to failure under random static, cyclic fatigue, creep, and impact loads; (5) identification of various material failure modes involved in critical damage events; and (6) determining sensitivities of failure modes to design parameters such as fiber volume fraction, ply thickness, fiber orientation, and thickness of adhesive bonds.

The methodology builds on extending the progressive failure analysis to partitioned components: (1) durability and damage tolerance based on degradation of material properties due to crack initiation location and growth of damage under in-service operations and environments; (2) the contributions of various possible failure modes to failure; (3) predictions of optimum inspection intervals; (4) incipient damage locations; (5) margin of safety; (6) probabilistic failure by determination of sensitivities to identified progressive damage parameters; (7) evaluation of uncertainty of material parameters; (8) determination of sensitivities of failure modes to design parameters to facilitate targeting design parameter changes that will be most effective in reducing the probability of a given failure mode occurring; (9) the probability of failure; and (10) evaluation of material fracture toughness without the need for conducting standard testing. The concept of the PFA is shown in Table 9-3 and the process flow of GENOA's principal elements shown in Fig. 9-10.

Virtual testing simulations can predict accurate results of experimental testing, reduce the test matrix, predict the results of expensive tests, and be utilized for calibration of previously performed experimental tests. For example, the generally accepted strategy for verifying an aircraft structural design for Federal Aviation Administration (FAA) certification is a building-block testing approach consisting of coupon, sub-element, and full-scale prototype experimental testing. Building a comprehensive virtual testing database of building blocks that conform to certification requirements will put at the designer's disposal a readily available compendium of certified designs that can be beneficially interrogated relative to the certification potential of a newly proposed design.

Table 9-3. Concept and Functionality of GENOA-PFA

Methodology	Functionality
Updated/total Lagrangian	Geometrical nonlinearity
Material property degradation at (1) fiber/ matrix level; (2) fiber/ matrix/interface; (3) lamina	Material nonlinearity
Adaptive meshing	Singularity conditioning
Mixed iterative FEM	Minimize residual error conditioning
14 failure mechanisms	Flexibility for crack growth (3-D) space
Percent contribution of failure modes to fracture	Identify fracture for each mode
Strain energy rate: local and global	Damage and fracture monitoring
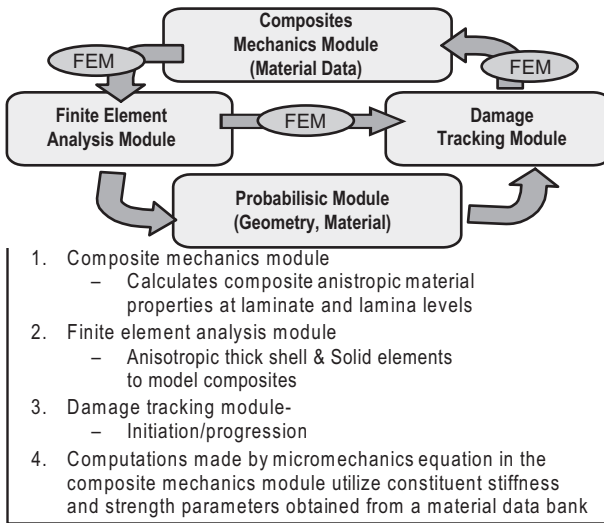
Figure 9-10. Principal elements of the GENOA progressive failure analysis (PFA) software.

9.4.5 MARC FE Code

MARC is a general-purpose FE program for advanced engineering analysis. MARC was one of the original commercial finite element analysis (FEA) codes. Back in 1965 a team of researchers at Brown University

initiated the development of the technology behind the MARC program, the first commercial general-purpose nonlinear FEA program. MARC Analysis Research Corp. was subsequently founded in 1971, and the first version of the MARC program was introduced in 1972. Since June 1999, MARC has been maintained by MSC Software, Santa Ana, CA.

MARC code offers sophisticated capabilities based on a wide range of high-order elements. Due to its sophistication, MARC is more difficult to use as compared to other FE software, especially when specifying boundary conditions in models composed of higher-order curved shell elements. Specifying the anisotropic properties of composites in MARC FE code involves the use of the ANELAS and ORIENT subroutines. These subroutines may be used in conjunction with most of the plane or continuum elements in the MARC library.

MARC offers several alternative methods of modeling composite structures, including:

- *Sub-Element Model:* This method involves the superposition of two sub-elements, one representing the fiber reinforcement material, and another isotropic element representing the matrix material (refer to Fig. 9-11).
- *Linked Layer Model:* This is a commonly used model for laminated composites. In this model, a stack of orthotropic membrane elements is interconnected by a system of rigid links that enforce the nondeformable normal condition at each series of node points, as shown in Fig. 9-12.
- *Solid Elements:* In this method, a series of continuum solid elements representing each individual ply of a composite laminate can be used. This technique is available in most general-purpose FE codes but is usually very expensive.
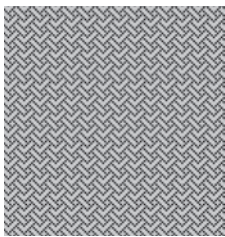
Stiffness of Composite   Stiffness of Fibers   Stiffness of Matrix

Figure 9-11. The "sub-element" concept for modeling composites in MARC FE code.
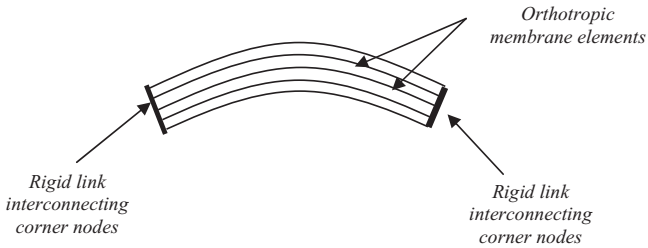
Figure 9-12. Linked layer modeling of composites in MARC FE code.

9.4.6 MSC-NASTRAN FE Code

MSC-NASTRAN FE code is also maintained by MSC.Software Corp., Santa Ana, CA. It is a general-purpose FE program to analyze strength and performance characteristics of structures. MSC-NASTRAN can be used to analyze static as well as dynamic behavior of composites. It has nonlinear analysis capabilities that are useful in solving a wide range of static and dynamic problems exhibiting both material and geometric non-linear behavior. This code contains an extensive element library, but its nonlinear capability is rather limited as compared to other codes such as ABAQUS. The code includes a laminated composite element as well as a sandwich shell element.

Composite laminate properties are specified for isoparametric plate or shell elements (QUAD 4, TRIA 3, QUAD 8, TRIA 6) by the use of a matrix format in the property and material cards. The code has the capability to transition from a coarse to a fine mesh in regions of high stress concentration, which is particularly important in highly anisotropic composites where through-the-thickness stress prediction is required in a very localized regions near free edges and joints. An example of a PFRP frame structure analyzed using MSC-NASTRAN is presented in Section 9.5.

9.4.7 NISA II/COMPOSITES FE Code

NISA II/COMPOSITES is an integrated part of the general-purpose FE program NISA II. The elements of NISA II/COMPOSITES can be used with all the elements of NISA, including isotropic (or orthotropic) shells, solids, beams, spars, mass, and spring elements, and thus complete analysis capability is available for all composite and hybrid structures. The NISA II/COMPOSITE element library includes several elements. These elements have no restriction on the number of layers, and each layer may have different thickness, orientation angle, and material properties. The lamination may be symmetric or nonsymmetric. For shell elements, transverse (interlaminar) shear deformation and "bending extensional" coupling are included.

- *3-D Layered Composite Shell*: This element is composed of several layers of orthotropic materials with varying thicknesses and material properties. The Tsai-Wu and Hill-von Mises failure theories are available for these elements.
- *3-D Sandwich Shell:* In sandwich composite elements, the face sheets are thin, which resist extensional and in-plane shear deformation, with a thick core material, which resists transverse shear. The face sheets themselves can be made of laminated composites and the core may be orthotropic. Multiple cores of more than two face sheets are allowed and the sandwich construction need not be symmetrical.
- *3-D Composite Solid (Overlay) Element:* In this element, solid is assumed to be composed of several plies, and each ply may have different material properties and lamination angles. Each ply group is considered as a solid element. The normal stress and interlaminar shear stress are most accurately determined at any desired location. The element is capable of accurately predicting displacement and stress variations, including edge effects.

9.4.8 PATRAN Laminate Modeler FE Code (MSC-PATRAN)

This FE code is currently maintained by MSC.Software Corp., Santa Ana, Calif. MSC-PATRAN is an engineering analysis software package offering an FE-based grid generator, several analysis modules, links to other popular analysis software packages, and a graphical post-processor. It provides a graphical user interface from which the user may create engineering designs or modify designs imported from computer-aided design packages; create FE meshes; assign materials to designs; assign loads, forces, temperatures, and so on to designs; automatically prepare input files to all major FE analysis programs (such as ABAQUS or MSC-NASTRAN); and perform visualization and analysis of results from FE analysis programs.

There are several preprocessors for MSC-PATRAN, including:

- *P3/PATRAN:* This is the graphical preprocessor, primarily used for generating input decks for FE analysis. This includes grid generation, setting boundary conditions, and loads. The input decks created can be used with a variety of analysis codes or solvers.
- *P3/FEA:* This is MSC-PATRAN's analysis module. It is an FE-based solver code developed in collaboration with Hibbitt, Karlsson & Sorensen, Inc. (the ABAQUS software vendor).
- *PAT3/ABAQUS:* Generates input decks compatible with the ABAQUS analysis software.

- *PAT3/ANSYS:* Generates input decks compatible with the ANSYS analysis software.
- *PAT3/MSC-NASTRAN:* Generates input decks compatible with the MSC-NASTRAN software.

MSC-PATRAN Laminate Modeler provides the designer an intuitive means for specifying laminate designs using existing geometric models. Laminate Modeler helps improve the communication of structural details and material definitions. This saves time, which can thus be applied to the process of design verification and optimization. Laminate Modeler also provides complete manufacturing data, including the cut-out shapes for each layer. This eliminates trial-and-error prototyping and minimizes material waste.

9.4.9 LUSAS Composite FE Code

LUSAS Composite code was developed and is maintained by Finite Element Analysis Ltd., Surrey, UK. This code can perform both linear and nonlinear analysis of composite structures. As defined in the Software User Manual, provided by Finite Element Analysis Ltd (2010), LUSAS Composite offers simple composite lay-ups independent of the component to be analyzed. The properties of each laminate are defined in a table and each layer given a unique name for use in results processing— extremely useful where ply drop-off occurs. A lay-up icon provides a useful visual check before the lay-up is automatically assigned to the underlying geometry.

In addition to shell elements, the LUSAS 3-D solid composite element reduces the model size by allowing a number of laminates to be modeled by a single element. Where complex 3-D components are built from a number of composite blocks butted together, LUSAS Composite can be used to automatically generate constraint equations to tie dissimilar meshes together. LUSAS code utilizes four commonly used composites failure criteria, including Tsai-Hill, Hoffman, Tsai-Wu (with Cowin extension), and Hashin (fiber and matrix). An example of analyzing a composite bonded joint with dissimilar adherends, taken from Pickett and Hollaway (1985), is discussed in Section 9.5.

9.5 NUMERICAL MODELING EXAMPLES FOR COMPOSITE JOINTS AND FRAME CONNECTIONS

This section presents several applications of the use of FE techniques in modeling composite joints and frame structures. These examples are selected to demonstrate the capabilities of some of the FE codes described in Section 9.4 of this chapter.

9.5.1 Numerical Modeling of Composite Joints

9.5.1.1 Analysis of PFRP Single- and Multi-Bolted Joints Using ANSYS FE Code.
In this study by Hassan et al. (1996), a 3-D FE analysis using ANSYS FE code was conducted on both single- and multi-bolted double-shear lap PFRP joints. The strength analysis was based on the Tsai-Wu tensor polynomial failure criterion (Tsai and Wu 1971), which was applied to the laminate as a whole (refer to Eq. 9-3). This study was interrelated to the experimental study by the principal author (Hassan 1994) that was described in Chapter 3 of this manual. The joint details used in this study are described in Tables 3-5 and 3-6 in Chapter 3.

$$\left(\frac{1}{X}+\frac{1}{X'}\right)\sigma_x + \left(\frac{1}{Y}+\frac{1}{Y'}\right)\sigma_y + \left(\frac{1}{Z}+\frac{1}{Z'}\right)\sigma_z - \frac{\sigma_x^2}{XX'} - \frac{\sigma_y^2}{YY'} - \frac{\sigma_z^2}{ZZ'} +$$

$$\frac{\sigma_{xy}^2}{S^2} + \frac{\sigma_{yx}^2}{Q^2} + \frac{\sigma_{xz}^2}{R^2} + \frac{F_{xy}\sigma_x\sigma_y}{\sqrt{XX'YY'}} + \frac{F_{yz}\sigma_y\sigma_z}{\sqrt{YY'ZZ'}} + \frac{F_{xz}\sigma_x\sigma_z}{\sqrt{XX'ZZ'}} = \Phi \qquad (9\text{-}3)$$

where

F = output of Tsai-Wu failure criterion
X and X' = tension and compression failure stress in X-direction
Y and Y' = tension and compression failure stress in Y-direction
Z and Z' = tension and compression failure stress in Z-direction
F_{xy} = X-Y coupling coefficient
F_{xz} = X-Z coupling coefficient
F_{yz} = Y-Z coupling coefficient.

In this analysis, the eight-node layered shell element (ANSYS Stiff 99) was used to model the PFRP composite plate and high-strength bolts (refer to Fig. 9-13). The bolt/hole contact problem can be modeled using several approaches, including:

1. Assume a certain contact pressure distribution (e.g., a cosine distribution) acting along the boundaries of the loaded hole(s).
2. Assume that the radial displacements are equal to zero at the hole boundary. This assumption will result in a distributed contact reaction to the applied load.
3. Perform a complete analysis for the joint.

In this study, the first approach was adopted. Contact stresses and stresses in the vicinity of the hole were calculated. The clearance between the hole and the steel bolt was represented by a 3-D gap element (refer to Fig. 9-14). The contact element (ANSYS Stiff 55) represents two surfaces which may maintain or break the physical contact and may slide relative to each other. This element is defined by two nodes (I and J in Fig.
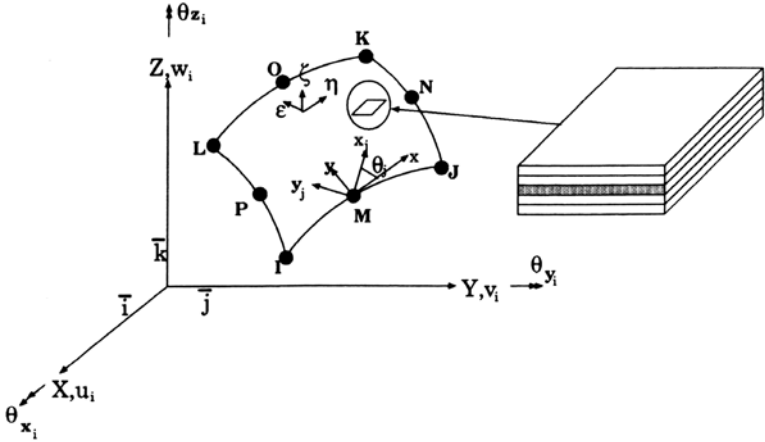
Figure 9-13. ANSYS shell element Stiff 99.
Source: Hassan et al. (1996)
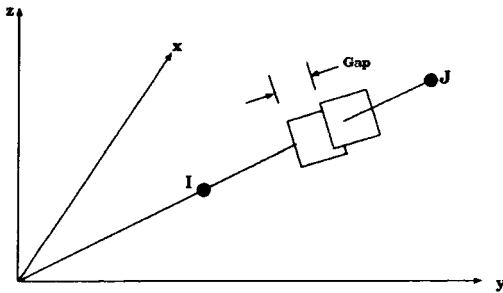
Figure 9-14. ANSYS gap element Stiff 55.
Source: Hassan et al. (1996)

9-14) and the interface is assumed to be orthogonal to the I-J line as shown in Fig. 9-14.

A 3-D axial spring element (ANSYS Stiff 14) of a very small stiffness was used with each gap element to simulate the initial open status of the gap elements. Figure 9-15 shows the geometry and node locations for this element. For more details on these elements, the reader is referred to the ANSYS manual.

Figure 9-16 shows the stress contours (σ_y) in the fiber direction for a single-bolted joint generated from the FE analysis. A comparison between the numerical and experimental results for three bolted composite joints is shown in Fig. 9-17.
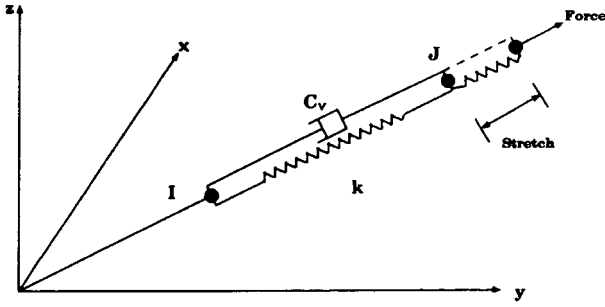
Figure 9-15. ANSYS spring element Stiff 14.
Source: Hassan et al. (1996)
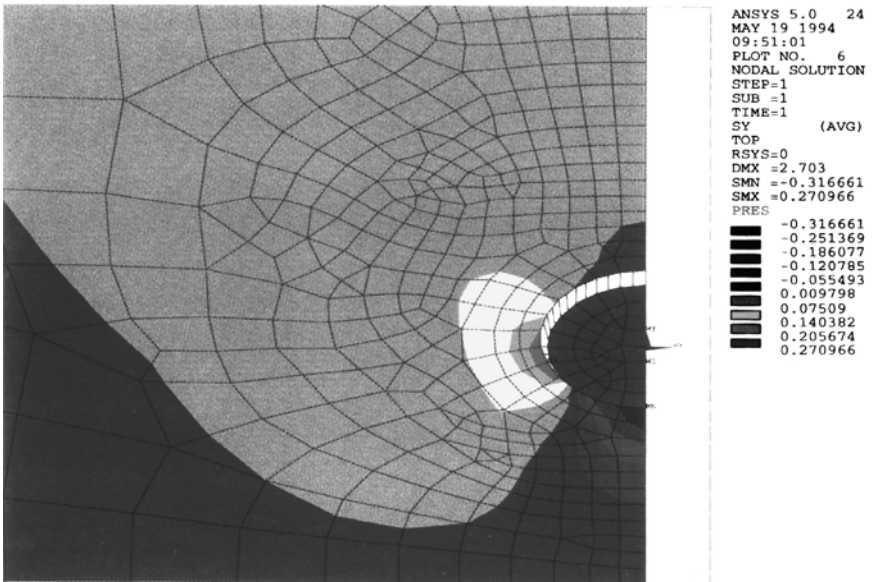
Figure 9-16. Stress in the fiber direction (S_y) for a single-bolted PFRP joint.
Source: Hassan et al. (1996)

9.5.1.2 Analysis of PFRP Pin-Loaded Joints Using ABAQUS FE Code. Steffen et al. (1999) conducted a 3-D FE analysis to predict the behavior of a single pin-loaded PFRP joint. Similar to Hassan et al.'s (1996) approach, the analysis accounted for variable contact regions through a sliding contact formulation. In this study, ABAQUS FE code was used in modeling the PFRP bolted joint as a sliding problem. A 3-D, 20-node brick element was used in modeling joints made of pultruded materials parallel

and normal to the pultrusion axis (major reinforcement axis). Only one-fourth of the joint was modeled due to the symmetry of the loading, hole location, and the lay-up. Figure 9-18 shows the dimensions and geometry of the PFRP joint.

The steps followed in performing the FE analysis were:

1. Incremental uniform displacements were applied at the bottom edge of the PFRP plate.
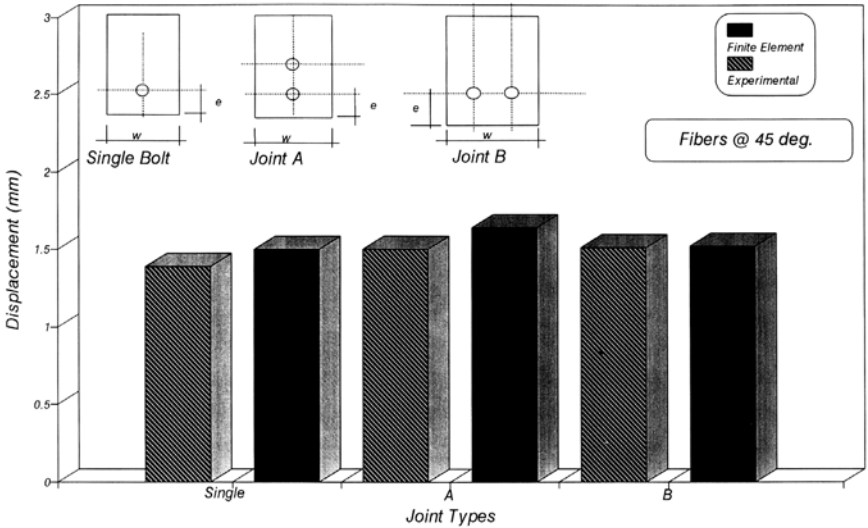
Figure 9-17. *Experimental versus FE displacement results PFRP bolted joints loaded at 45 degrees.*
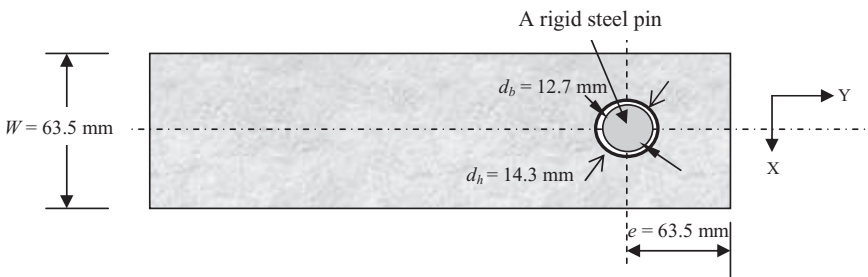
Figure 9-18. *Details of single, pin-loaded PFRP joint.*
Source: *Steffen et al. (1999)*

2. The steel pin was modeled as rigidly attached at the circular section (refer to Fig. 9-18).
3. Due to the difference between the diameters of the rigid pin and the hole [clearance = 0.03125 in. (0.794 mm)], the first displacement increment forced the plate to displace rigidly a distance equal to the clearance, after which the PFRP plate rested upon the steel pin and established a stable initial contact condition.
4. 0.006 in. (0.15 mm) displacement increments were then applied to the PFRP plate up to a final total displacement of 0.06 in. (1.5 mm).
5. The applied force was calculated by multiplying the remote axial stresses by the PFRP plate cross-sectional area for each displacement increment.
6. The force–displacement curves generated from the FE analysis were compared with experimental force–displacement curves, as shown in Fig. 9-19.
7. Computed elastic stresses (based on linear elastic material properties) were compared to both Tsai-Wu failure criteria (Eq. 9-3) and Hashin cumulative failure criteria evaluated at each elements
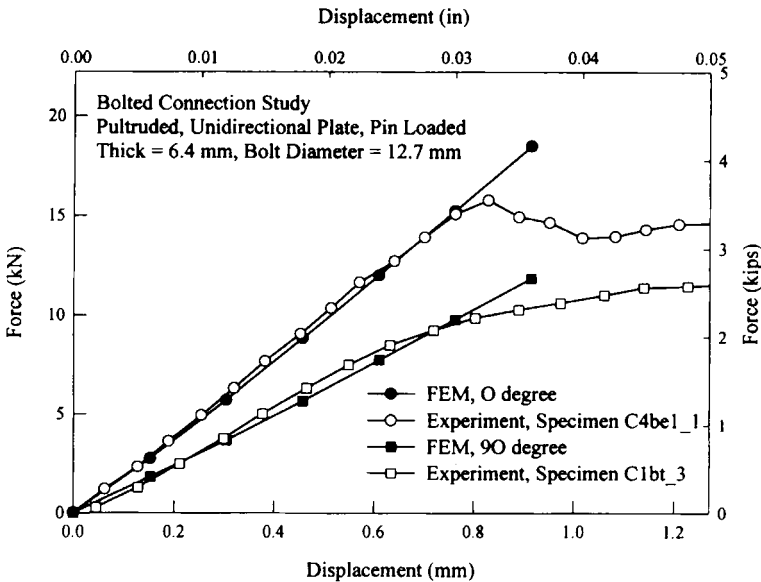
Figure 9-19. Comparison between numerical and experimental results for single pin-loaded PFRP joints.
Source: Steffen et al. (1999)

integration points (refer to Fig. 9-20). It should be noted that in the FE analysis, material degradation schemes due to failure were not used. For this reason, the FE analysis was used only to identify failure zones and not to predict the ultimate joint failure load. Other progressive failure FE codes, such as GENOA PFA, can be used to predict the ultimate failure mode and load.
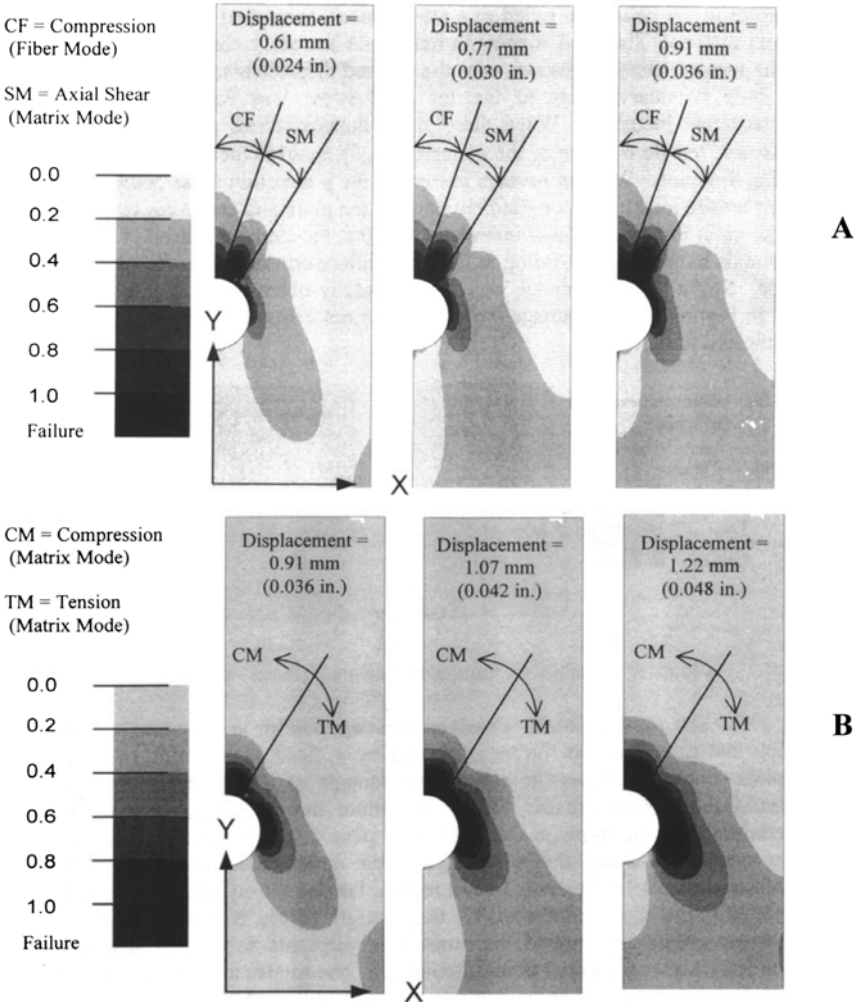
Figure 9-20. *Hashin's cumulative failure criteria. A, 0-degree specimen; B, 90-degree specimen.*
Source: *Steffen et al. (1999)*

9.5.1.3 Progressive Damage and Nonlinear Analysis of PFRP Joints using ABAQUS Material Subroutine (UMAT).   Kilic and Haj-Ali (2003) used the ABAQUS material subroutine (UMAT) to perform progressive damage and nonlinear analysis of PFRP joints. The micro-mechanical models were implemented at the through-the-thickness Gaussian integration points of the pultruded cross section. In this analysis, Tsai-Wu failure criteria were calibrated separately for the continuous filament mats (CFM) and roving layers using ultimate stress values from off-axis pultruded coupons under uni-axial loading. When failure was detected at any ply, the micro-model of such ply was no longer used; instead, an elastic degrading material model was activated for the failed layer to simulate the post-ultimate response. Damage variables for in-plane modes of failure were considered in computing the effective anisotropic strain energy density of each ply, and degraded secant stiffness was employed in the FE analysis. In this study, damage analyses were performed to simulate the response of two previous tests reported earlier by Steffen (1998) and Steffen et al. (1999) on bolted E-glass/vinylester PFRP pultruded composites with thickness of 1/4 in. (6.4 mm). In the analysis, plane stress models were used with eight-node reduced integration elements. Good agreement between experimental and numerical results was achieved.

9.5.1.4 Analysis of Composite Bonded Joints with Dissimilar Adherends Using LUSAS FE Code.   Pickett and Hollaway (1985) used two analytical techniques, namely, the classical and FE methods, to model single, double and tubular lap bonded joints with similar and dissimilar adherends. In each joint model, an eight-node quadrilateral element was used. This higher-order quadratic element was selected to allow stress and strain variation across the element, which enabled the high-stress gradients and localized stress concentrations that are typical in adhesively bonded joints to be represented. To accurately model the lap joint, a large-displacement FE program was used based on the "initial stress method" advocated by Zienkiewicz (1971). However, the usual small-displacement theory that assumes a linear relationship between the applied loads and displacements was adopted for both the double and the tubular lap joint configurations. Two case studies were performed for each joint configuration; one had stiffness-balanced aluminum adherends, and the other had stiffness-mismatched FRP/aluminum adherends. Details and FE meshes of these joints are shown in Fig. 9-21.

9.5.1.5 Examples of Durability and Damage Tolerance Analysis of Composite T-Joint Using GENOA Progressive Failure Analysis Code.   The analysis summary presented in this section, from work by Alpha Star Corporation (2001), demonstrates the advantages of
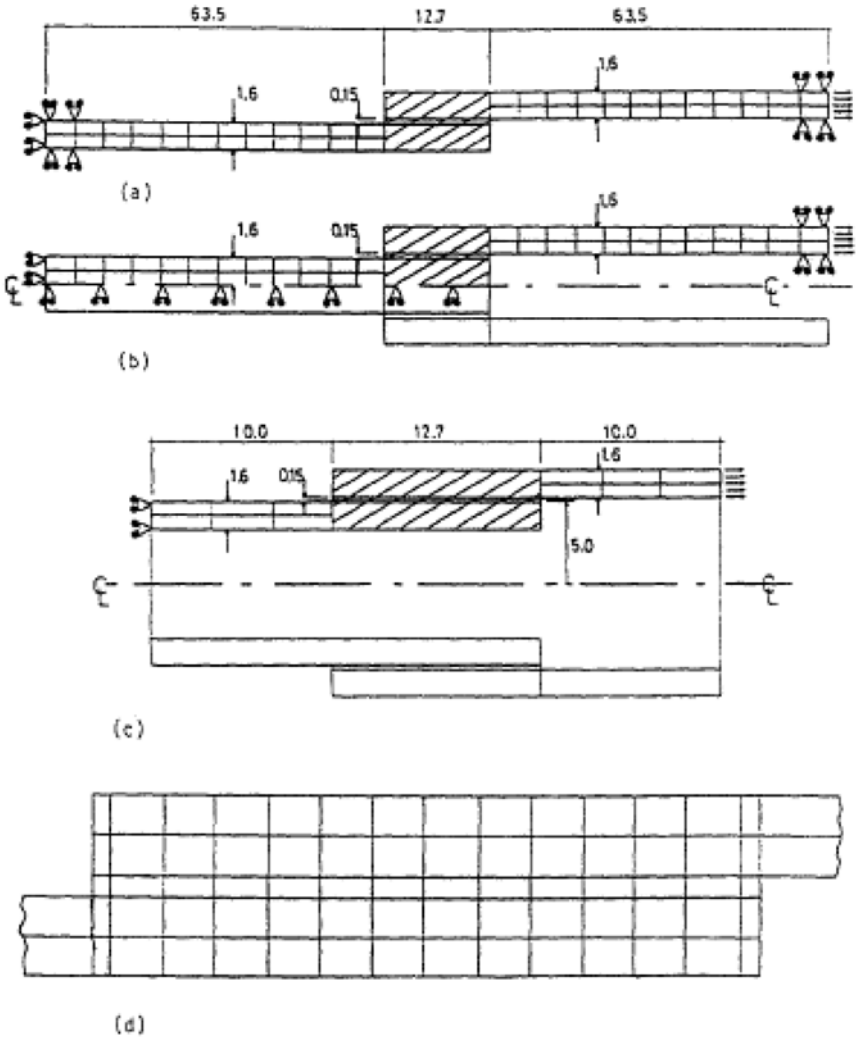
Figure 9-21. *The geometries and finite element meshes for the a) single lap joint, b) double lap joint, c) tubular lap joint, and d) common overlap region. Source: Pickett and Holloway (1985).*

progressive failure analysis and virtual testing simulations of complex composite joints, including Carbon/Silicon Carbide (C/SiC) T-joints, using GENOA PFA software. Designers can gain valuable insight, compared to conventional analysis, with structural simulations evaluating life performance based on composite micro-mechanics. Virtual testing simulations can investigate a wide variety of joint geometries and strength,

stitched joints configurations, bonded, or co-cured T-joint subassemblies to panels.

Design schemes of these joint structures should yield simple designs that can lend themselves to more economical and durable repairs. Effects of fillet and ply drop-off, and laminate stacking sequence, shown in Fig. 9-22A can be optimized to yield a durable joint. Figure 9-23A shows the robustness of stitching reinforcement, which postpones the onset of damage in the fillet region. A field repair test simulation of a reinforcement patch under a proof bond test is shown in Fig. 9-24A. In each case, variation of the T-joint model was used to simulation the T-joint performance under design loads.
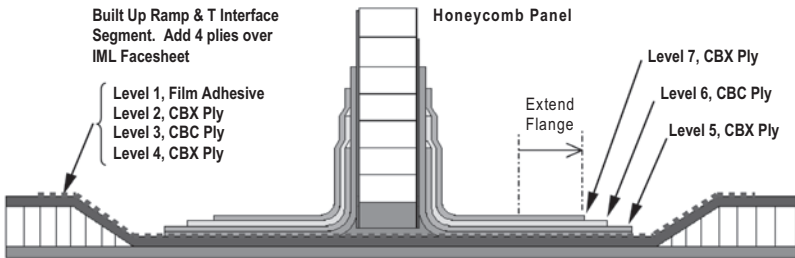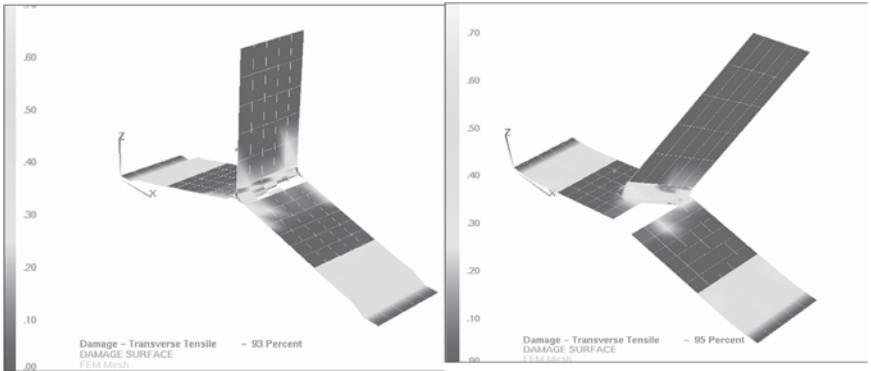
Figure 9-22. Classic T-joint transition in a honeycomb panel. Fillet areas are sensitive to manufacturing processes and will require that provisions be made for generous radii, avoidance of resin starvation or richness, and bridging. A, optimized joint for pull loads; B, fillet sensitivity—damage initiation; C, damage propagation.
Source: ASC (2001).
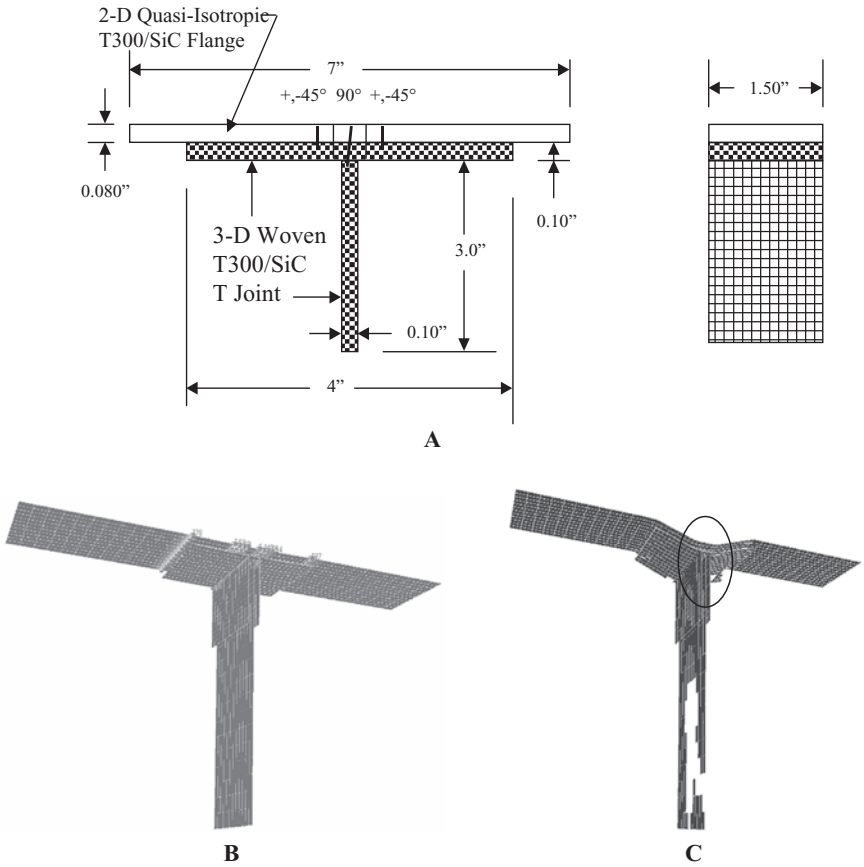
Figure 9-23. Stitched solid laminate T-joint virtual testing simulation. In shear, stitches in the web help postpone the occurrence of the fracture. In pull-off, stitches prevent the T-joint from breaking. For both pull-off and shear simulations, the damage energy release rate in the case with stitches is higher than that without stitches. Thus, breaking the T-joint with stitches takes more energy than breaking the T-joint without stitches. A, stitched C/SiC T-joint; B, damage initiation in pull-off; C, final failure.
Source: ASC (2001).

Further studies can be performed to evaluate the sensitivity of design selected parameters using probabilistic progressive failure analysis (Fig. 9-25). This figure shows the assessment of the stitched T-joint to determine the range of residual strength under random design variables: (1) fiber volume fraction (5% variation), (2) fiber tensile strength (5% variation), (3) matrix tensile strength (5% variation), and (4) matrix shear strength (5% variation).

A

B

C

D

E
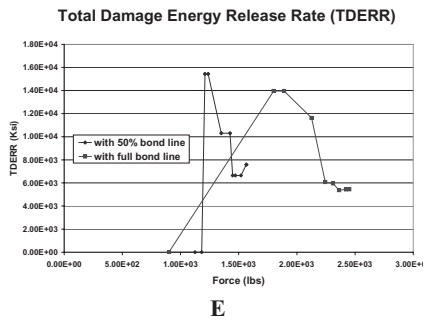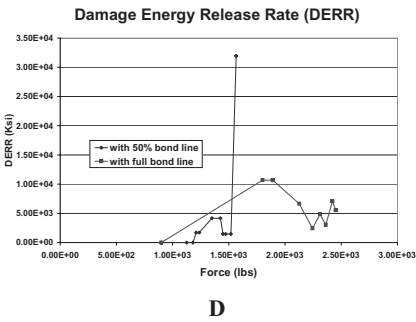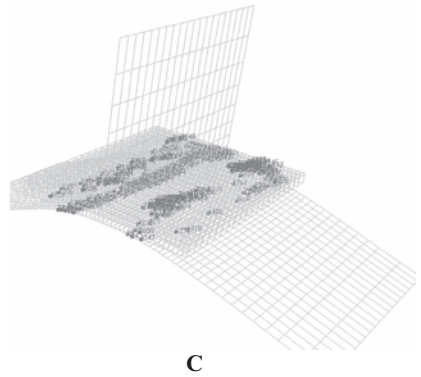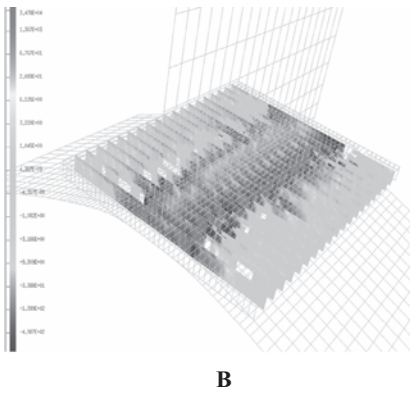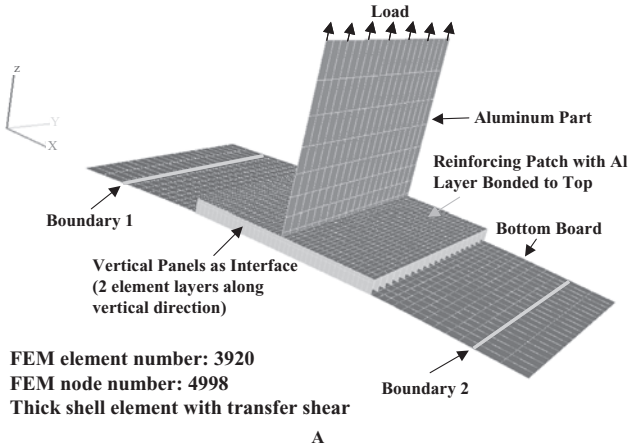
Figure 9-24. T-patch repair bonding virtual testing simulation. With 50% bondline area effective, the delamination starts from the corner of reinforced area, and then propagates to the center (B). The final failure of the T-joint is caused by the fracture of the interface (C). Comparisons between relative bond line strength are shown in D and E. A, T-Proof bond virtual test simulation; B, btress distribution in the matrix resin interface; C, damages at final failure; D, DERR vs. force; E, TDERR vs. force.
Source: Abdi (2001).
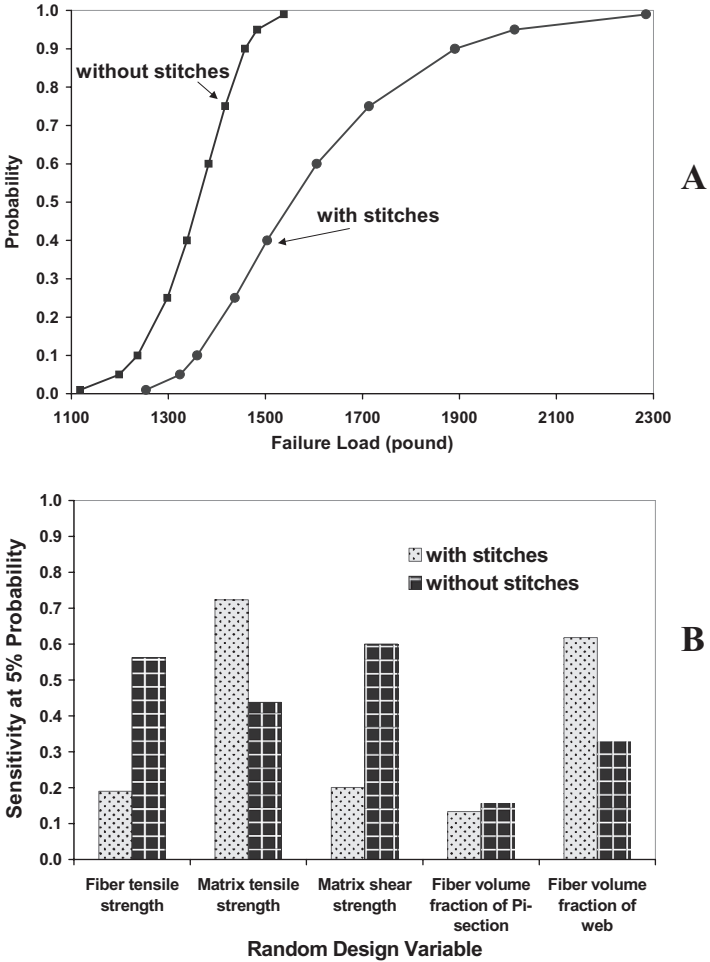
Figure 9-25. Cumulative distribution functions/sensitivities in shear of C/SiC T-joint. For the C/SiC T-joint with stitches, matrix tensile strength and fiber volume fraction of web have a significant effect on the failure load. For the C/SiC T-joint without stitches, fiber volume fraction, and fiber and matrix strengths have similar influence on the failure load. 5% variation of fiber volume fraction. A, cumulative distribution functions; B, sensitivities. Source: ASC (2001).

9.5.2 Numerical Modeling of PFRP Composite Frame Connections

9.5.2.1 Analysis of PFRP Frame Connections Using I-DEAS FE Code. Reimer and Sorby (1998) presented the results of a comprehensive FE analysis on simulating the structural behavior of PFRP beam-

to-column connections. The model used in this study was based on con-
nection detail Type i [also known as TSW, as shown in Fig. 7-12 taken
from Mosallam (1990)]. Figure 9-29 shows the detail of this connection
and the corresponding FE model, from Reimer and Sorby (1998).

In this study, a full 3-D FRP bolted connection was modeled using
I-DEAS Master Series 3.0 software. The model consists of 4,572 eight-node
linear brick elements as the main elements, with three DOF assigned to
each node. The interface between the connecting elements and the beam
or column and the bolts and bolt holes was modeled by a contact set
without frictional analysis. Several approximations were used in the
model, including the use of rigid elements to model steel bolts, and
neglecting the effect of friction between the connecting pultruded angles
and the beam or column. Six models were investigated. This included
Model 1 (the original TSW detail) as the base of comparison.

**9.5.2.2 Linear Analysis of PFRP Exterior Connections Using COSMOS
FE Code.**   Bank et al. (1996) conducted an FE study to model the rota-
tional stiffness of exterior PFRP beam-to-column connections using
COSMOS FE code. Three different connection models were investigated
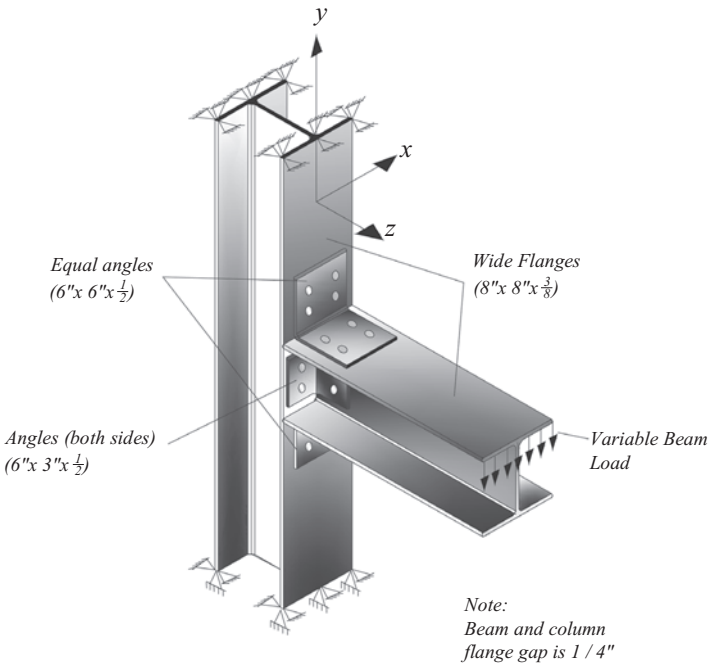
*Figure 9-26. Details of Reimer and Sorby (1998) FEM connection model
(TSW, or Type i).*

in this study. The reader is referred to Chapter 7 for background information on different connection details tested in this study. In the analysis, the loads were applied in the same configurations used in the testing program described in Chapter 7 of this manual. It should be noted that the FE analysis was limited to the linear behavior of PFRP connections, and that buckling and local failure were not included.

The following connection models were investigated in this study:

- *Case 1. No connecting element:* In this model, the PFRP beam and column were connected at the the intersecting nodes.
- *Case 2. Exterior connection model with a gusset plate element:* In this model, the PFRP beam and column were connected by a triangular gusset plate in the plane of the web. This model is similar to the 8 in. (203.2 mm) back-to-back pultruded H-section connection type described in Section 7.5.
- *Case 3. Exterior connection model with angle brace connecting element:* In this model, the PFRP beam and column were connected by a brace at 45 degrees to both the beam and the column axes. This model is similar to the wrapped angle connection details described in Fig. 7-105. However, this FE model was based on an 8 in. (203.2 mm) brace configuration, while the brace dimensions tested in the experimental program, were based on a 6 in. (152.4 mm) brace, discussed in Section 7.5.

Table 9-4 presents a comparison between FE analysis and experimental results. From this table, one can see that there is a large deviation between the predicted and the experimental values. This can be attributed to several factors, including:

- In Case 1, the authors did not model any connecting elements such as unidirectional angles and FRP bolts and nuts. Instead, the beam and column were connected at the intersecting nodes, which does not reflect the actual connectivity of the tested specimen.
- In Case 2, the beam and the column in the FE model were connected by triangular gusset plates. However, in the actual test, the connecting elements were composed of parts that were cut from a unidirectional H-profile, with unidirectional vertical attachment (refer to Fig. 7-103). Again, this is not an actual representation of the specimen described in the experimental program.
- In Case 3, the beam and the column in the FE model were connected by 45-degree braces, while in the actual test, top and bottom unidirectional PFRP angles were wrapped with two layers of unidirectional laminates. The laminates were weak in the closing mode due to deformation of the inner angle, which led to a premature buckling of the wrap material. For this reason, the predicted values were

Table 9-4. A Comparison between Finite Element Analysis and
Experimental Results Performed by Bank et al. (1996)

Finite Element Results		Experimental Results		
Model Description	Initial Rotational Stiffness, $k_{initial}$ (kip-in./rad) $\times 10^{-3}$	Model Description	Initial Rotational Stiffness, $k_{initial}$ (kip-in./rad) $\times 10^{-3}$	Error[a], e (%)
Case 1	2.82	Type i[b]	6.99	+59.6
Case 2	4.65	Back-to-back 8 in. (203.2 mm) H-section	6.00	+22.5
Case 3	5.84	6 in. × 1/2 in. (152.4 mm × 12.7 mm) wrapped unidirectional angle	2.10	−178

[a] $\text{Error} = e = \dfrac{k_{initial}^{Experimental} - k_{initial}^{FEM}}{k_{initial}^{Experimental}} \times 100$

[b] Bank et al. (1994).

much higher than the actual experimental values, with a deviation up to 178%.

This example illustrates the importance of developing an FE model that reflects the actual detail of the connection in order to avoid discrepancies between actual and predicted behavior.

9.5.2.3 Linear Analysis of PFRP Exterior Connections Using ABAQUS FE Code. Smith et al. (1999a; 1999b) conducted an FE study using ABAQUS FE code to predict the linear behavior of seven connection details that were previously tested by the authors (refer to Figs. 7-97 through 7-100 of Chapter 7 for details on the experimental program). The overall dimensions and geometry of typical PFRP beam-to-column connections are shown in Fig. 9-27. The material properties of the PFRP profiles were obtained from full-section, four-point load tests. These properties were: E_{xx} = 22.1 GPa, E_{yy} = 12.4 GPa, E_{ss} = 6.9 GPa, and v_{xy} = 0.33.

In modeling the different connection details, eight-node shell elements that included transverse shear deformation were used for the detailed model, while in developing the condensed model, two-node shear beam
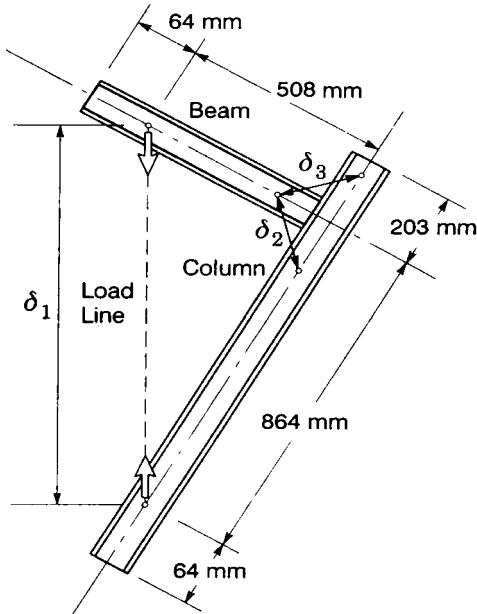
Figure 9-27. Dimensions and test setup of exterior PFRP beam-to-column connections.
Source: Smith et al. (1999).

elements with a connection element developed from the connection region of the shell model were used. For each connection detail, two types of meshes were investigated, namely, detailed mesh (refer to Fig. 9-28) and condensed mesh (refer to Fig. 9-29). Table 9-5 details the errors in the detailed and condensed FE model as compared to the experimental results described in Chapter 7 of this manual.

Based on the information described in Chapter 7, three values of the linear stiffness, k, were used in this study, namely, opening stiffness (k_o) closing stiffness (k_c), and stiffness of the frame (k_f). These stiffness values were determined by the following equations:

$$k_o = \frac{M}{\Delta\alpha} \tag{9-4}$$

$$k_c = \frac{M}{\Delta\beta} \tag{9-5}$$

$$k_f = \frac{P}{\delta_1} \tag{9-6}$$

(a) all I-beams   (b) box: standard   (c) box: gusset   (d) box: cuff
                       and box: steel
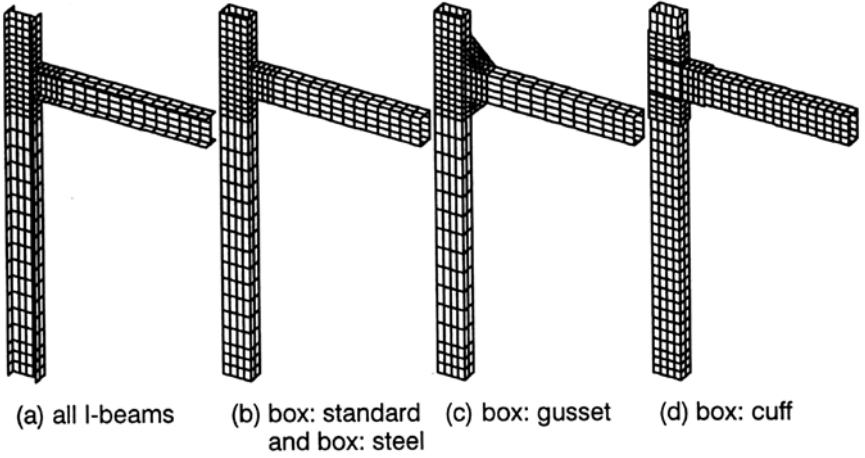
Figure 9-28. Detailed FE meshes for exterior PFRP beam-to-column connections.
Source: Smith et al. (1999).
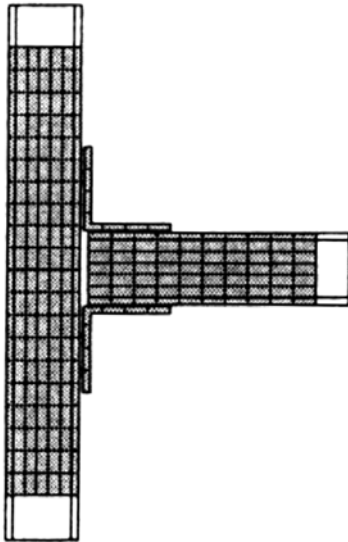
Figure 9-29. Condensed FE mesh for exterior PFRP beam-to-column connections.
Source: Smith et al. (1999).

Table 9-5. Errors in the Detailed and Condensed Finite Element Models

Connection Specimen	Detailed Finite Element Model			Condensed Finite Element Model		
	$e^a{}_{open}$ (%)	$e^a{}_{closed}$ (%)	$e^a{}_{frame}$ (%)	$e^a{}_{open}$ (%)	$e^a{}_{closed}$ (%)	$e^a{}_{frame}$ (%)
I: Standard	+26	−5	−6	−18	0.00	−3
I: Thick Seat	—	+4	−6	—	0.00	−5
I: Steel	+18	−3	−8	+18	−0.06	−5
Box: Standard	−33	−2	−8	−44	−0.13	−10
Box: Gusset	+27	−8	−1	+30	−0.13	−2
Box: Cuff	−6	−9	−3	+0.11	+14	−2
Box: Steel	—	16	−5	—	+6	−4

^{a} $e = \text{Error} = \dfrac{k_{initial}^{Experimental} - k_{initial}^{FEM}}{k_{initial}^{Experimental}} \times 100$

where

M = applied moment
α = angle between the beam and column axes above the joint
β = angle between the beam and column axes below the joint
$\Delta\alpha$ = the change in angle $\alpha = \alpha - \dfrac{\pi}{2}$
$\Delta\beta$ = the change in angle $\beta = \dfrac{\pi}{2} - \beta$
P = applied vertical load (refer to Fig. 9-27)
δ_l = the change in length of the line load (refer to Fig. 9-27).

9.5.2.4 FEM Analysis of PFRP Column-Base Connections Using GTSTRUDL Code. The experimental part of this study by Na (2008) was described in Chapter 7; it focused on evaluating the lateral response of multistory PFRP frames with and without bracing elements. The column supports were modeled with finite elements using the GTSTRUDL Stretching and Bending Hybrid Quadrilateral (SBHQ6) plate finite elements in order to account for the stiffness characteristics of the column base support in the analysis (Fig. 9-30). Unlike the FE models developed by Liu et al. (1998) and Mosallam (2000) that will be presented in Section 9.6 and includes both the web/flange junction and actual rotational flexibility of PFRP connections used in the multistory frames, this study did not consider these major effects and did not use
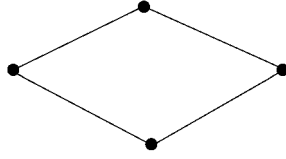
*Figure 9-30. GTSTRUDL stretching and bending hybrid quadrilateral
(SBHQ6) plate finite element.*
Source: Na (2008).

the equivalent isotropic mechanical properties. For these reasons, no
definitive prediction of the frame performance was possible, and only
upper and lower bounds were used to compare the behavior of the large-
scale PFRP frame tests.

**9.5.2.5 FEM Modeling of Semi-Rigid PFRP Connection Using ANSYS
FE Code.**   Based on the "web line approach," Harte and McCann (2001)
developed 2-D FE models for PFRP semi-rigid connections. The numerical
models were based on low-load beam-column connection tests performed
by Turvey and Cooper (1998). Details of these connections are described
in Chapter 7 of this manual. The plane of the model was taken parallel
to the plane passing through the mid-thickness of the PFRP profiles
webs. The FE models were analyzed using ANSYS v. 5.3 software. PFRP
columns, beams, and angles were modeled using 2-D bilinear quadrilat-
eral solid plane stress elements. The FE mesh had 690 nodes with 918
solid elements. Each element was assigned to an appropriate thickness
and materials property. Average orthotropic materials properties based
on manufacturers' reported data were used in the analysis. Using sen-
sitivity analysis, a contact stiffness value of 86 kN/mm was used. In
modeling steel bolts, two methods were considered for bolt representa-
tion, including:

1. *2-D Link Element:* In this modeling approach, the link element was a
   two-noded element with two displacement DOF. This link element
   was connected to nodes representing bolt head and nut positions.
   The number of link elements to represent a single bolt ranged from
   1 to 5. Numerical results indicated that as the number of link ele-
   ments increased, the connection stiffness increased.
2. *Plane Stress Elements:* In this approach, the bolt shank was modeled
   using a single bilinear quadrilateral plane stress element, and the
   area of each bolt was converted to an equivalent rectangular area.
   The equivalent area was assumed to be spread across the beam
   width as a rectangle.

The bolt pretensioning force was modeled by introducing a specified amount of temperature to each bolt. As the steel bolt temperature decreased, a contraction displacement equal to

$$\delta = \alpha. L. \Delta T \qquad (9\text{-}7)$$

occurred, where

δ = bolt contraction displacement
α = steel bolt coefficient of thermal expansion (12×10^{-6} °C^{-1})
L = bolt length
ΔT = temperature difference (°C)

When a steel bolt is restrained at either end, a tensile force will be induced in the bolt which will create an equal but opposite clamping force, P, in the surrounding composite materials. Although this technique may be suited for steel bolts, FRP bolts that are commonly used are made from E-glass/polyester or E-glass/vinylester with relatively low coefficient of thermal expansion (1×10^{-6} °C$^{-1} \approx 1/12$ of steel) and much lower stiffness as compared to steel. Adopting this approach may create some problems through the introduction of creep displacement in the FRP threaded rod and the surrounding polymeric matrix. Numerical results showed that introduction of a bolt prestress force had insignificant impact on the connection stiffness.

Unlike the FE models developed by Liu et al. (1998) and Mosallam (2000) that will be presented in Section 9.6, which included both the web-flange junction and actual rotational flexibility of PFRP connections, this study did not consider either of those major effects.

9.6 RECOMMENDED MODELING PROCEDURES FOR SEMI-RIGID PFRP FRAME CONNECTIONS

To achieve satisfactory numerical results when analyzing a semi-rigid behavior of a pultruded composite frame structure, the moment–rotation characteristics should be included in the analysis. As mentioned in Chapter 8, this can be accomplished by either the use of the connection initial stiffness for preliminary design purposes, or by including the nonlinear characteristics of the connection for a more accurate modeling. In both cases, the rotational stiffness can be introduced via either a rotational spring or two sets of extensional springs (Liu et al. 1998; Mosallam 2000). Other inherent characteristics of PFRP profiles, such as the flexible web-flange junctions of open-web sections, and shear deformation effects, will result in a more precise modeling of the frame

connection. However, the engineer should evaluate the benefit of conduct-
ing a sophisticated analysis that includes all variables versus a more
moderate analysis that includes only the parameters that have major
effects on the predicted performance. This also applies to whether or not
a nonlinear analysis is needed. These concepts are illustrated in the fol-
lowing examples.

9.6.1 Linear Analysis Using MSC-NASTRAN FE Code

9.6.1.1 Description of the Finite Element Models.   Typical analysis
of thin-walled frame structures assumes a rigid connection between the
beam and columns. In addition, the junction between the flanges and the
web of an open-web PFRP sections is commonly assumed to be rigid.
Although these assumptions may be applicable to steel connections and
open-web sections made of steel, it is not satisfactory for unidirectional
PFRP open-web profiles. To illustrate the impact of ignoring these inher-
ent characteristics of PFRP connections and thin-walled open-web profiles
on predicting the overall structural behavior of PFRP frame structures,
the following models were developed.

1. *Model I. Rigid frame assumptions:* This model was developed using
   the rigid frame assumption. The MSC-NASTRAN composite shell
   element (LAMINATE) was used in building this model. The flanges
   and web of the PFRP beam were connected directly through common
   nodes with six DOF. This regime was also used to connect both ends
   of the PFRP to the frame columns. In the experimental program, 2 in.
   (5.08 cm)-diameter steel rods were used as rollers to apply the loads
   to the top flange of the frame girder (Mosallam and Bank 1992). To
   ensure a uniform load distribution and to prevent the possible web
   crippling of the thin-walled section under the load points, two 6 in.
   × 8 in. × 1/2 in. (15.24 cm × 20.32 cm × 1.27 cm) PFRP bearing plates
   were placed (not bonded) under the steel rollers. This was also
   incorporated in the FE model for accurate comparison with the
   experimental results. In the experimental program, the column was
   connected to the base via two equal-leg PFRP angles 6 in. × 6 in. ×
   1/2 in. (15.24 cm × 15.24 cm × 1.27 cm) using FRP threaded rods and
   nuts (refer to Fig. 9-31).
2. *Model II. Flexibility of web-flange junction and semi-rigid beam to column
   connection:* In this model, the flexibility of the web-flange junction
   and the semi-rigid characteristics of the beam-to-column connec-
   tions of the PFRP frame are considered.
   a. *Web-flange junction modeling:* The connection between the flanges
      and the web of the H-beam was modeled with MSC-NASTRAN
      rigid elements in T_x, T_z, R_x, and R_y DOF (refer to Fig. 9-32). The
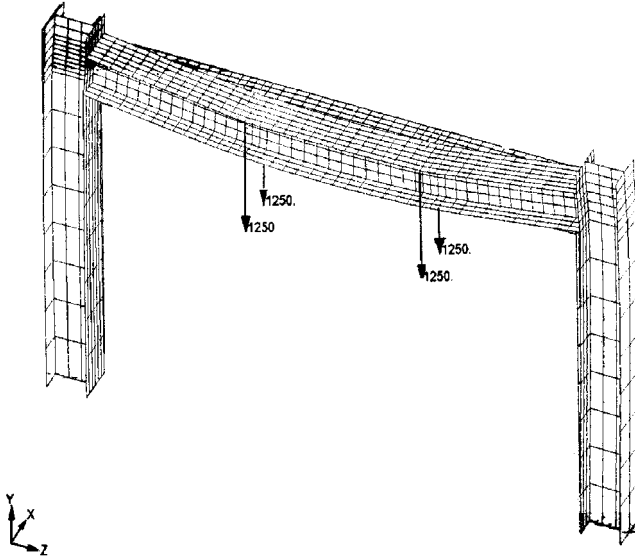
Figure 9-31. An isometric view of FEA Model I (with deformed shape shown).
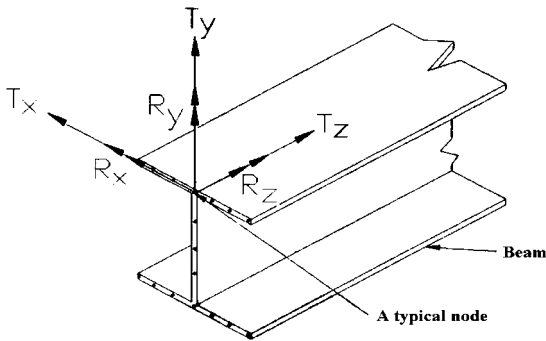
Figure 9-32. A sketch showing the six DOF used in the FEA Model II relative to the global coordinate system.

flexibility of the web-flange junction was modeled using two spring elements, as follows:

- A single DOF extensional spring element in the T_y direction, and
- A single DOF spring element with rotational stiffness in the DOF of R_z. Both the axial and rotational stiffness were obtained from full-scale test results (Figs. 9-33 and 9-34). The bilinear
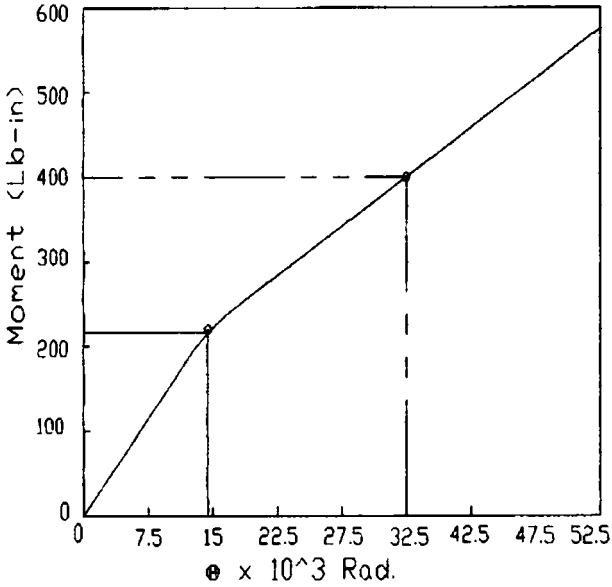
Figure 9-33. Moment–rotation curve of flange and web connection. (100 in.-lb = 11.3 N-m)
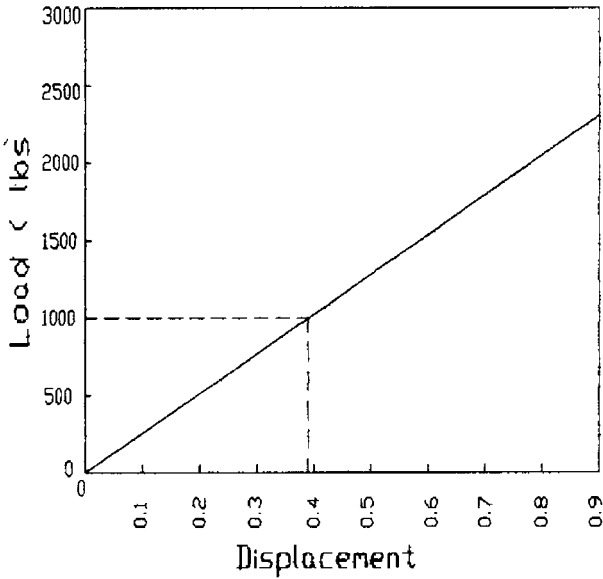
Figure 9-34. Pulling load vs. displacement for flange and web separation. (100 in.-lb = 11.3 N-m.)

behavior of the M/θ relationship of the connections was considered in this model.

b. *Beam-to-column connection modeling:* The beam-to-column connections were modeled using MSC-NASTRAN Rigid Elements connected in the DOF of T_x, T_y, R_z, R_y. The rotational flexibility of the connection in the DOF of R_x was introduced indirectly using equivalent extensional spring stiffness of 14 spring elements located at the upper and lower flanges of the beam ends (7 on the upper flange and 7 on the lower flange). The axial stiffness of these springs was indirectly obtained from a full-scale experimental connection test obtained by Mosallam (1990) (refer to Fig. 9-35). Loading and frame support conditions were identical to those of Model I.

3. *Model III. Semi-rigid beam to column connection:* As a part of a sensitivity analysis, a third model was developed to measure the effect of the web-flange flexibility of the thin-walled beams on the linear behavior of the frame structure. This model was identical to Model II except that a rigid connection was assumed between the web and flanges.

9.6.1.2 Comparisons of Experimental and Numerical Analysis Results.   To verify the validity of the numerical models, a comparison between full-scale experimental test results (Mosallam 1990) with the closed-form solution results was performed. Figure 9-36 shows the experimental, theoretical, and numerical deflection values at the mid-span of
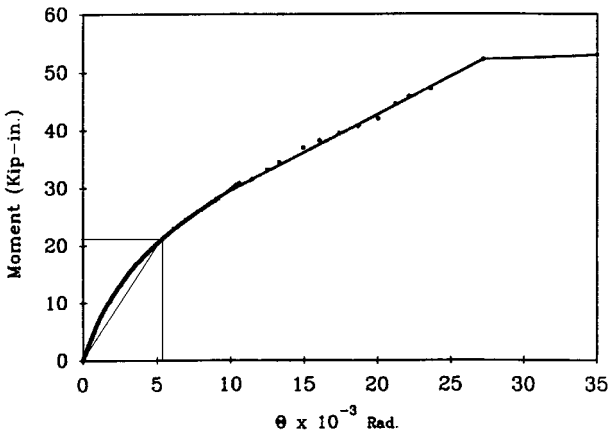
Figure 9-35. Moment–rotation curve for beam-to-column connection Type TSW. (1 kip-in. = 113 kN-m.)
Source: Mosallam (1990).
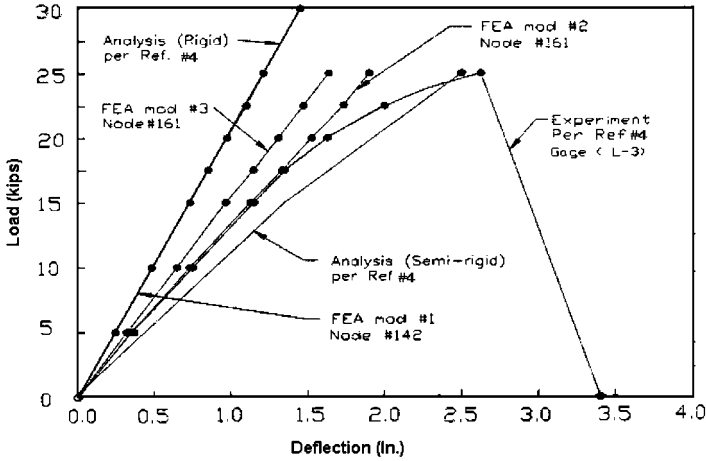
Figure 9-36. Comparison between theoretical and experimental mid-span frame deflection. (1 kip = 4.45 kN; 1 in. = 2.54 cm.)
Source: Mosallam (1990).

the PFRP frame girder tested by Mosallam (1990). Because the numerical analysis was conducted in the linear range, without including the effects of both geometrical and buckling nonlinearities, an expected deviation from the experimental buckling load was noticed in this plot. However, there was good agreement between the experimental and the numerical deflection results using Model II, up to a total load of 17,500 lb (77.78 kN). Both Model I and III resulted in relatively stiffer behavior as compared to both Model II and the experimental results in the linear range. The strain distribution along the depth of the mid-span section of the PFRP frame girder is shown in Fig. 9-37. Figure 9-38 shows that the compression strain on the top surface of middle span on all three models was stiffer than the analytical (both rigid and semi-rigid assumptions) and the experimental results. Due to the inherent semi-rigid behavior of PFRP column-base connections, a realistic modeling of this support can be achieved by introducing a rotational spring with rotational stiffness obtained from a full-scale connection M/θ diagram. Experimental data on the rotational stiffness of the base-column connections is unavailable. Therefore, the best approach in modeling these supports is by connecting only the column's webs directly to the PFRP base plate.

9.6.2 Nonlinear Analysis Using COSMO/M FE Software

To capture the nonlinear behavior of the PFRP frame, a more sophisticated model is required. In this example, a nonlinear analysis for the same
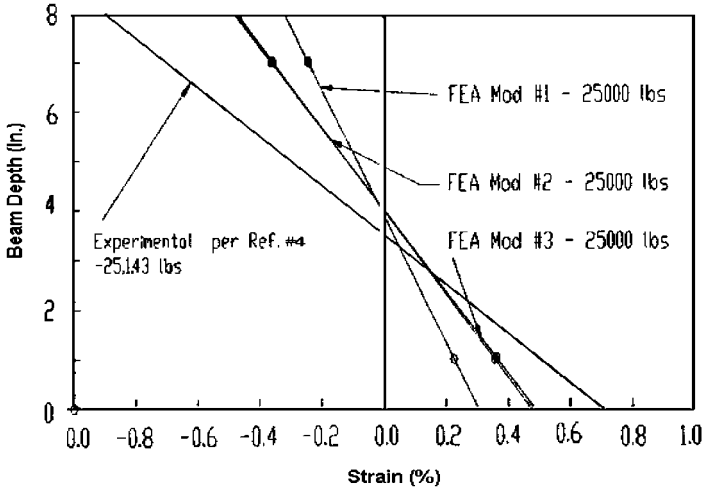
Figure 9-37. Strain distribution along the web depth at frame girder's mid-span. (1 in. = 2.54 cm.)
Source: Mosallam (1990).
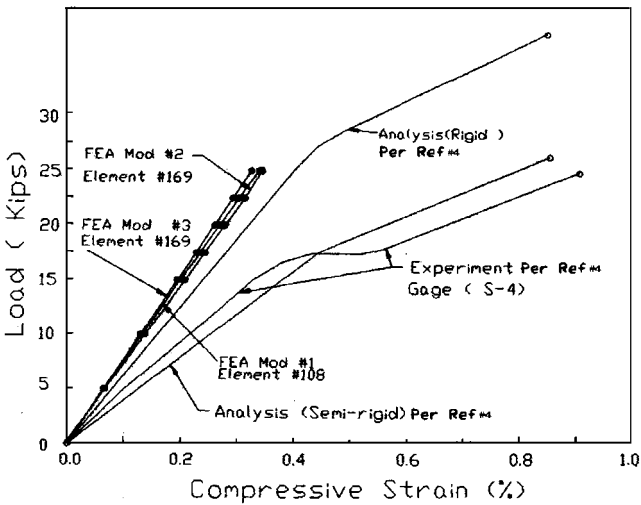
Figure 9-38. Load versus girder's compression strain (mid-span top flange). (1 kip = 4.45 kN;1 in. = 2.54 cm.)
Source: Mosallam (1990).

PFRP portal frame described in Section 9.6.1 (which was analyzed using MSC-NASTRAN FE code) is re-analyzed using COSMOS/M FE code.

9.6.2.1 A Case Study of COSMOS/M Nonlinear Spring Elements.   To simulate the flexibility between the flanges and web, and the semi-rigid nature of the beam-to-column connection, it is recommended to use the COSMOS/M tensional and/or rotational nonlinear springs elements in the following FE modeling.

Six cases were included in this study to demonstrate the applicability of the use of nonlinear spring elements (both axial and rotational) in modeling the flexibility between the flanges and the web junction, and the semi-rigid behavior of the beam-to-column connection.

Case I. A beam with both ends fixed under bending and shear: Case I was needed to evaluate and validate the FEA modeling of the BEAM3D elements. This model, shown in Fig. 9-39, consists of a group of BEAM3D elements directly jointed together for all six DOF at adjacent nodes. In this case, the beam is fixed at both ends and subjected to bending and shear because of an arbitrarily positioned vertical load, or $P_y = -100,000$ lb (-444.44 kN). The cross-sectional properties of the beam were assumed to be: area $= 3.14$ in.^{2} (20.25 cm^2), and $I_{xx} = 0.7854$ in.^{4} (32.69 cm^4). As shown in Fig. 9-40, and based on the FEA, the maximum displacement was found to be 0.158 in. (0.40 cm), which matched the maximum displacement of the same beam obtained by Mosallam (1990) using a computer code that was based on a closed-form solution [which was also 0.158 in. [0.40 cm)].

Case II. A beam with middle hinge and both ends fixed under bending and shear: This model, as shown in Fig. 9-41, is identical to Case I except a hinge was used to join the two middle span elements at the middle span

$Z = 7"$ (17.78 cm)
$L = 21"$(53.34 cm)

$E = 30,000,000$ psi
    (207 GPa)
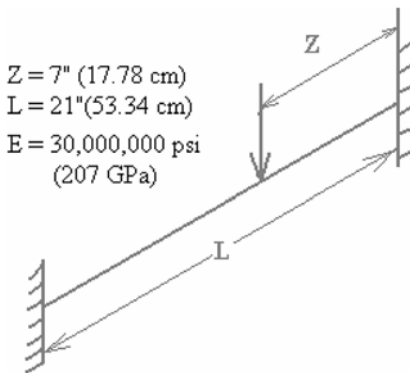
Figure 9-39. Idealized diagram for study Case I: A beam with both ends fixed under bending and shear.
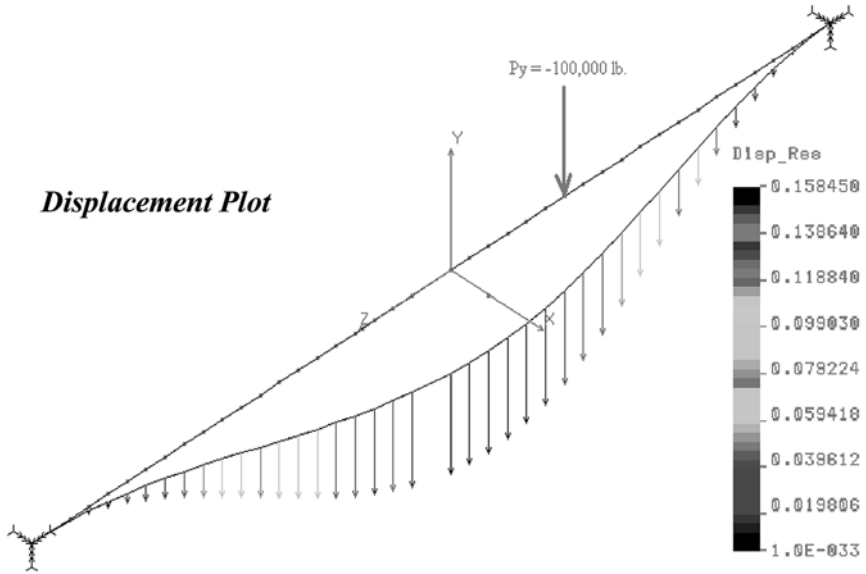
Figure 9-40. Case I: A beam with both ends fixed under bending and shear (Model I).
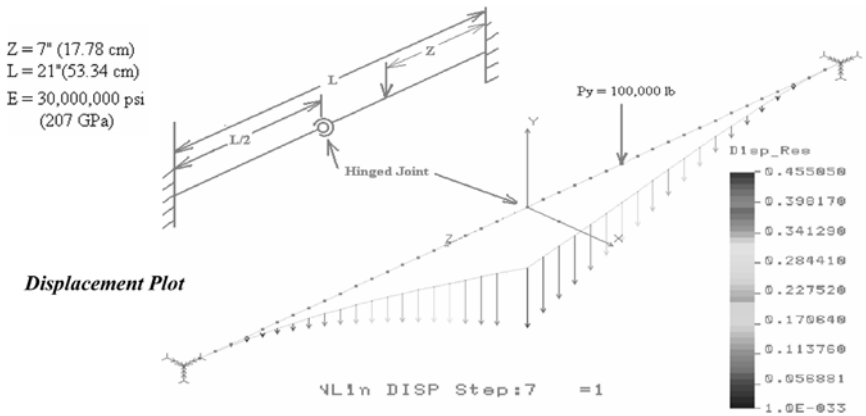
Figure 9-41. Case II: A beam with a middle hinge and both fixed ends under bending and shear.

point. (The DOF of R_x at the middle point was released.) As shown in Fig. 9-41, and based on the FE nonlinear analysis, the maximum displacement was found to be 0.455 in. (1.156 cm).

Case III. A beam jointed together in the middle span with one one-node rotational spring element and both ends fixed under bending and shear: This model,

as in Fig. 9-41, is identical to Case II except a one-node rotational spring element joined the two middle span elements at the middle span point. The nonlinear rotational stiffness of the one-node rotational spring element was defined via the COSMOS/M Material Property Curve (MPC) per the M/θ curve that was described earlier in Fig. 9-35. As shown in Fig. 9-42, and based on the FEA, the maximum displacement was found to be 0.382 in. (0.97 cm).

Case IV. A beam jointed together in the middle span with two nonlinear axial spring elements, under bending and shear: This model, as shown in Fig. 9-43, is identical to Case III except two one-node nonlinear axial spring elements joined the two middle span elements at the middle span point. The two axial tensile and compressive forces of the two nonlinear axial spring elements form a couple, as shown in the enlarged view of Fig. 9-43, which is equivalent to the rotational stiffness of the one one-node nonlinear rotational spring element used in Case III. As shown in this figure, the maximum displacement was found to be 0.382 in. (0.97 cm), which was identical to that of Case III.

Case V. A beam jointed together in the middle span with one one-node rotational spring element and both ends fixed, under bending, shear and axial loads: This model, shown in Fig. 9-44, is identical to Case III except for the loading configuration and the restraint condition. This beam is subjected to both vertical load, P_y = −100,000 lb (444 kN), and axial load, P_z = −10,000,000 lb (44,444 kN). To apply all of the axial loads onto the connection, the DOF of T_z of the right-hand end of the beam was released. In this case, the maximum displacement was found to be 1.404 in. (3.57 cm).
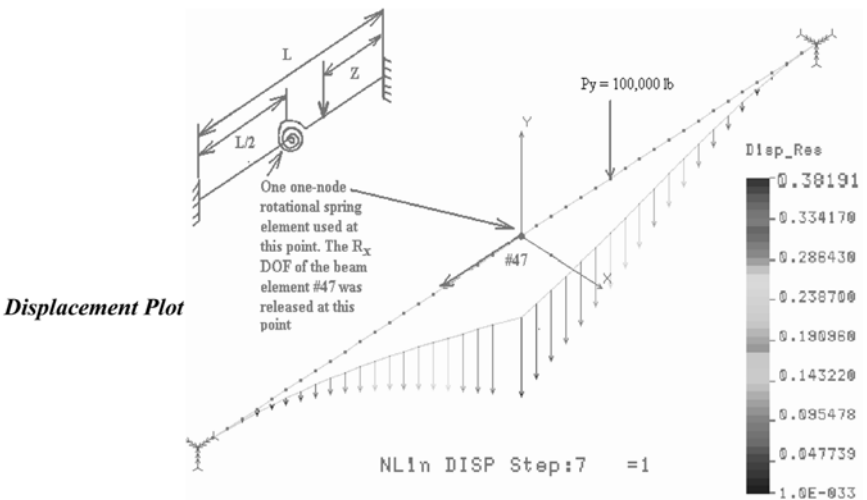
Figure 9-42. Case III: A beam jointed together at mid-span with one single-node rotational spring element and both ends fixed under bending and shear.
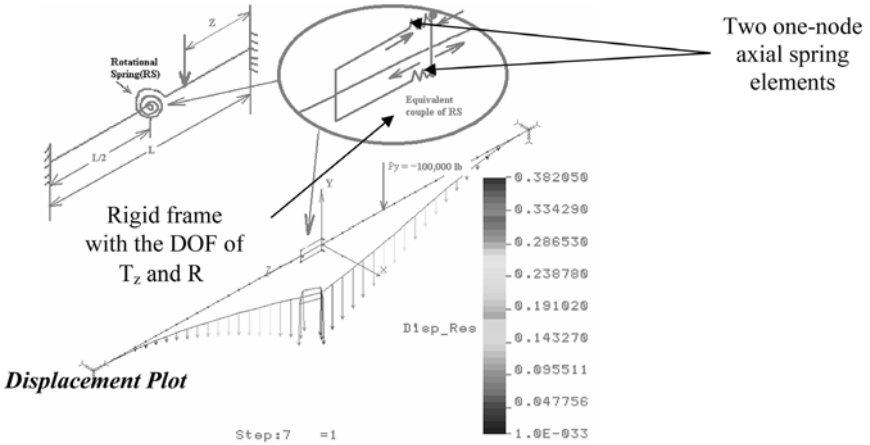
Figure 9-43. Case IV: A beam jointed together in the middle span with two nonlinear axial spring elements, under bending and shear.
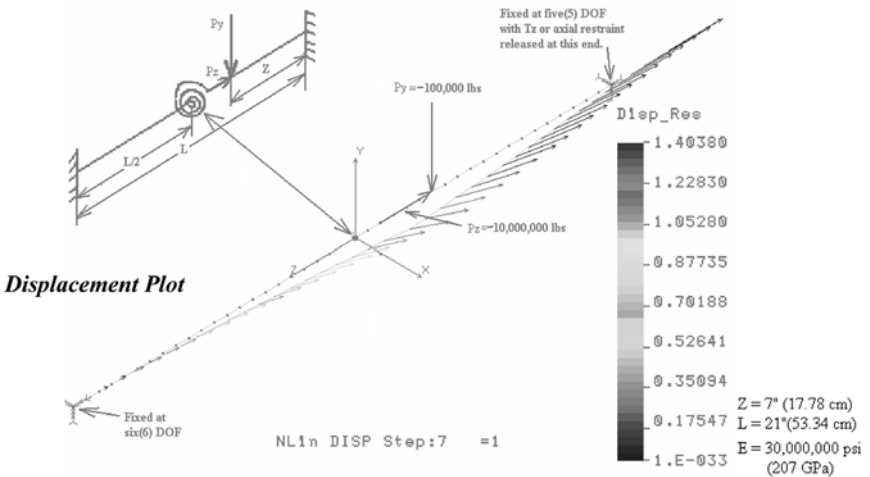
Figure 9-44. Case V: A beam jointed by one-node rotational spring element at mid-span and both ends are fixed, under bending, shear, and axial loads.

Case VI. A beam jointed together in the middle span with by two one-node axial spring elements and both ends fixed, under bending, shear and axial loads: This model, shown in Fig. 9-45, is identical to Case IV except for the loading configuration and the end restraining condition. In this case, the PFRP beam is subjected to both vertical (P_y = −100,000 lb or 444 kN), and axial loads (P_z = −10,000,000 lb or 44,444 kN). To apply all the axial
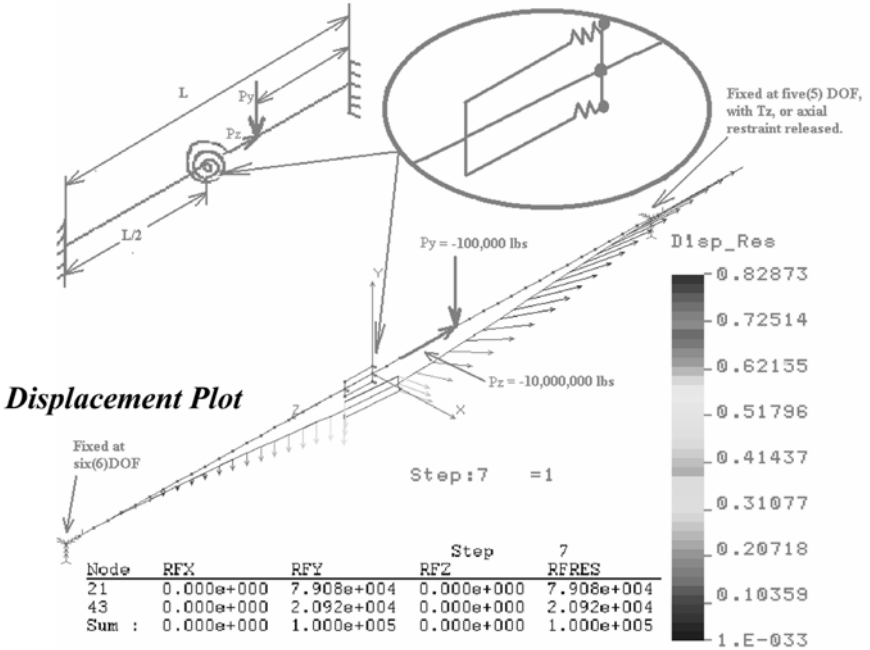
Figure 9-45. Case VI: A beam jointed together, at mid-span, with two one-node axial spring elements under bending, shear, and axial loads.

loads to the connection, the DOF of T_z of the right-hand end of this beam was released. The results indicated that the analysis was not convergent to the solution. The total reaction force in the Z-direction was equal to zero, and not equal to the applied load P_z of −10,000,000 lb or 44,444 kN, as it should be.

9.6.2.2 Conclusions on the Preliminary Evaluations of Different Modeling Approaches for Using Nonlinear Spring Elements.   Evaluation of the preliminary analytical results presented in this section indicates that:

- Both the nonlinear rotational spring element and axial spring element introduced at the middle span were equally good in modeling of the semi-rigid joint behavior, provided that the element is subjected to no axial loads.
- Only the rotational spring element can be used to model the flexibility and the semi-rigid joint when the element is subjected to axial loads.
- In the modeling approaches described earlier, a fixed-fixed beam example was used to demonstrate and evaluate the different

approaches. However, the same approaches can be applied generally, for different loading and geometry conditions.

9.6.3 Nonlinear FE Modeling of PFRP Portal Frames

9.6.3.1 Model C-1: Rigid Beam/Column Connection and Rigid Web-Flange Junction (Continuous Rigid Connectivity).

9.6.3.1.1 General Description.   This model was developed using rigid frame assumptions as described in the Model I of Section 9.6.1.1. In this model, the COSMOS/M SHELL4T composite element was used. The flanges and web of the PFRP beam were connected directly through common nodes with six DOF. This regime was also followed when connecting both ends of the PFRP beam to the frame columns. The FEA model of the portal frame is shown in Figs. 9-46 and 9-47.

9.6.3.1.2 Symmetrical Boundary Condition.   Because of the symmetrical nature of the structure and loading, and in order to optimize the use of the computing time, only half of the portal frame structure was modeled
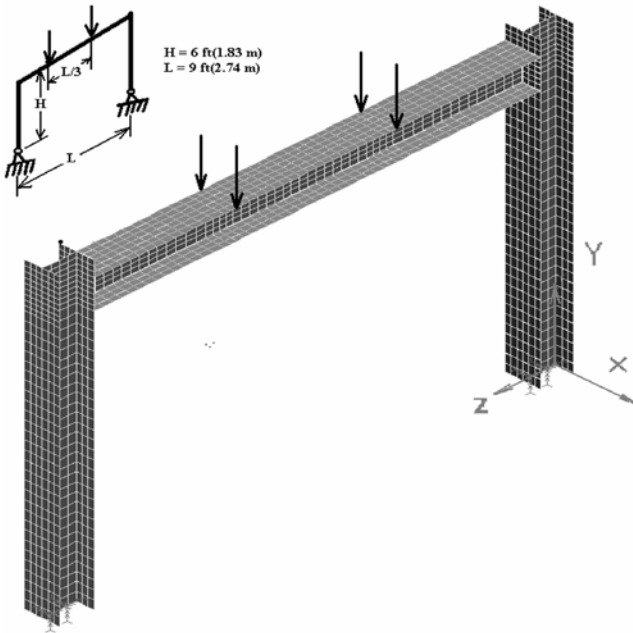
Figure 9-46. Model C-1: Continuous rigid connectivity.

and analyzed. The symmetrical boundary restraints, U_z, R_x, and R_y, shown in Figs. 9-48 and 9-49, were introduced into the symmetrical plan at the mid-span section. The application of the symmetrical boundary reduces the computation time. The boundary restraints U_z, R_x, and R_y are associated with the 6 DOF used in the FEA Model II relative to the global coordinate system that is presented in Fig. 9-32.

9.6.3.1.3 Loading Rod and Bearing Plate.   To simulate the loading regime performed in the experimental program (Mosallam 1990), a 2 in. (5.08 cm) steel loading rod and bearing plate were introduced, as shown in Fig. 9-50.

9.6.3.1.4 The Column-Base Connection.   In the experimental program the bottom end of the column's web was connected to the base via two equal-leg 6 in. × 6 in. × 1/2 in. (15 cm × 15 cm × 12.7 cm) back-to-back PFRP connections (Mosallam and Bank 1992). Figure 9-51 shows a
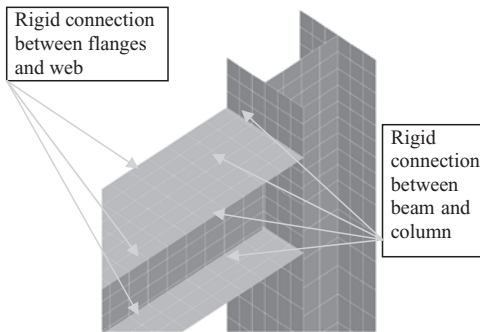
Figure 9-47. Model C-1: Direct connected joint.
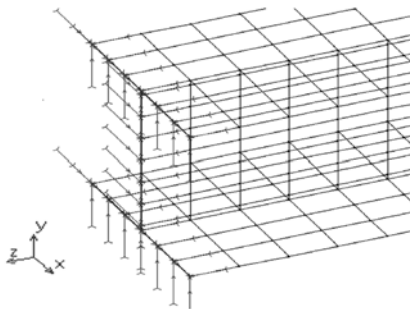
Figure 9-48. Symmetrical boundary restraints.
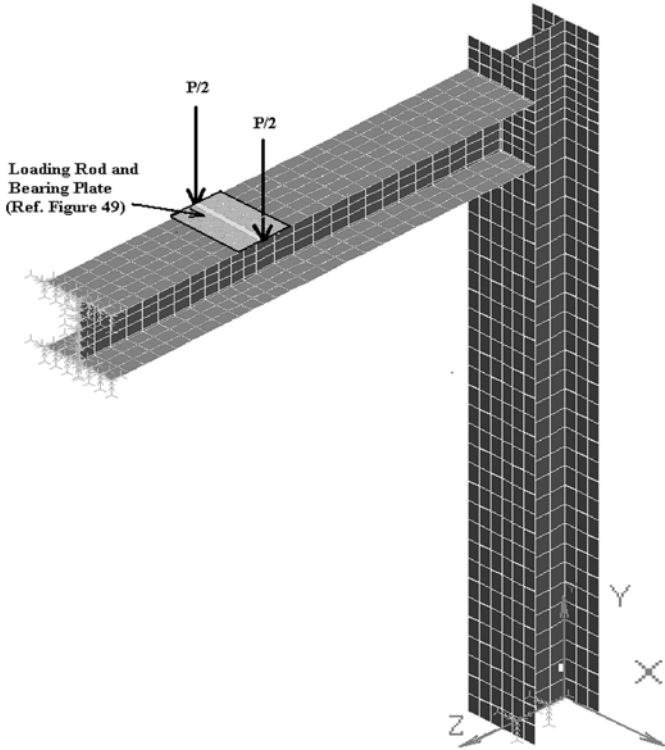
Figure 9-49. Half model with symmetrical restraint condition.
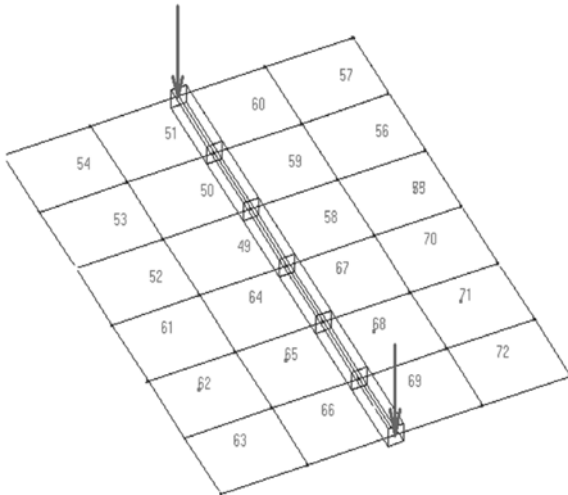
Figure 9-50. Loading rod and bearing plate (enlarged view).

M_x - Applied bending moment, P_y -- Applied down force

R_{y1} and R_{y2} -- Reaction forces by the column-base mounting bracket
due to M_x

R_{y3} and R_{y4} -- Reaction forces by the column-base mounting bracket
due to F_y
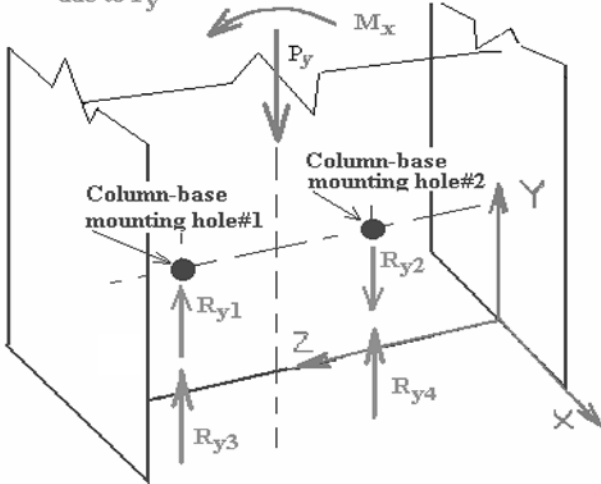
Figure 9-51. A free-body diagram of column-base connection under compression force, P_y, and bending moment M_x without the consideration of possible flange-base bearing or prying action.

free-body diagram of the column-base connection under compression force P_y and bending moment M_x without consideration of the possible flange-base bearing or prying action. Figure 9-52 shows a free-body diagram of the column-base connection under compression force P_y and bending moment M_x with the possible flange-base bearing or prying action considered. To simplify the modeling, the column and base connection of the Model C-1 was restrained as shown in Fig. 9-53.

9.6.3.1.5 Modeling of Flanges/Web of the PFRP Frame Members. The COSMOS/M SHELL4L composite element was used to model the flanges and web of the PFRP profiles. The ply engineering constants of the pultruded H shape, as listed in Table 9-1, was used as in the Model C-1. The engineering constants of the 1.5 oz /sq. yd (33.9 g/m²) continuous strand mat (CSM) was used as material Set 1, and that of the 113 yield roving as listed in Table 9-1 was used as material Set 2 in the Model C-1. The flanges of both the beam and column were modeled as six layer-composite elements and were designated as Element Group 1 (refer to Table 9-6). The web of the beam and column was modeled as 13

Mx - Applied bending moment, Py -- Applied down force
Ry1 -Reaction forces by the bearing action of the base due to Mx
Ry2 -Reaction forces by the column-base mounting bracket due to Mx
Ry3 -Reaction forces by the bearing action of the base due to Fy
Ry4 -Reaction forces by the column-base mounting bracket due to Fy
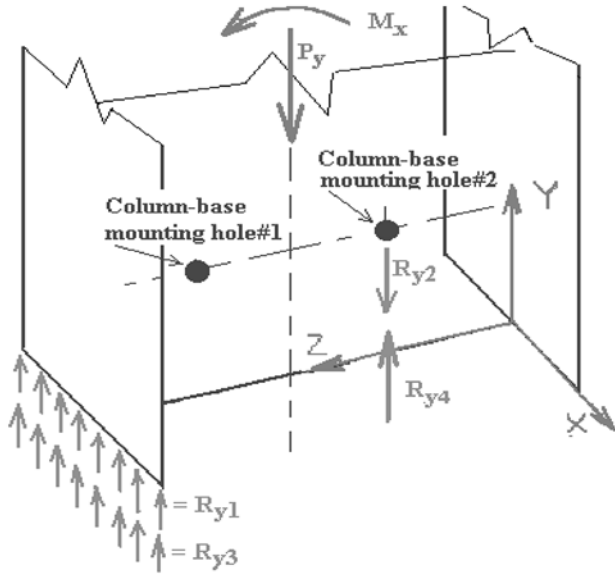
Figure 9-52. A free-body diagram of column-base connection under compression force, P_y, and bending moment, M_x, that considers possible flange-base bearing or prying action.

The web of column was restrainted against six(6) DOF at these two nodes
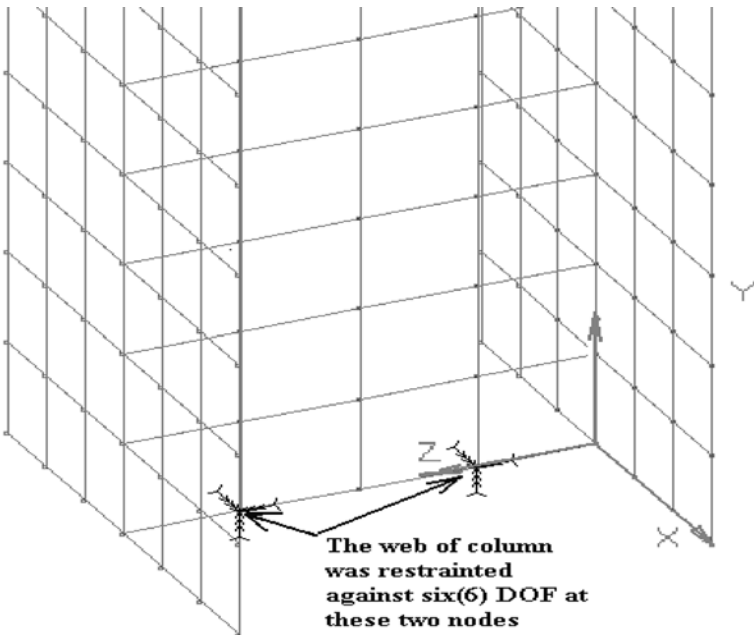
Figure 9-53. The column and base connection of FEA Model C-1.

Table 9-6. Element Group and Real Constant Sets
for the Flanges of the PFRP H-Profiles

```
Element Group :   1  ( SHELL4L )

  Op1: Type :0=QUAD2;1=QUAD4;2=QUAD . . . . . . . . . =   1
  Op2: Number of Layers . . . . . . . . . . . . . . =   6
  Op3: Stress Dir :0=Global;1=Local;2=Mat . . . . . . . . =   2
  Op4: Unused option . . . . . . . . . . . . . . . =   0
  Op5: Failure Analysis 0=LE;7=Tsai Wu . . . . . . . . =   0
  Op6: Disp. Formulation:0=Small;1=Large  . . . . . . . =   0
  Op7: Unused option . . . . . . . . . . . . . . . =   0
  Op8: Unused option . . . . . . . . . . . . . . . =   0

                      Real Constant Sets

Real Constant Set :   1
Associated Element Group :   1  ( SHELL4L )

  Rc1  : Dist. from ref. plane to top surface  . . . . =  1.875000e-001
  Rc2  : Temperature gradient . . . . . . . . . . =  0.000000e+000
  Rc3  : Thickness of layer 1 . . . . . . . . . . =  2.500000e-002
  Rc4  : Material number for layer 1  . . . . . . =            1
  Rc5  : Material angle for layer 1 . . . . . . . . =  9.000000e+001
  Rc6  : Thickness of layer 2 . . . . . . . . . . =  1.000000e-001
  Rc7  : Material number for layer 2  . . . . . . =            2
  Rc8  : Material angle for layer 2 . . . . . . . . =  9.000000e+001
  Rc9  : Thickness of layer 3 . . . . . . . . . . =  2.500000e-002
  Rc10 : Material number for layer 3  . . . . . . =            1
  Rc11 : Material angle for layer 3 . . . . . . . . =  9.000000e+001
  Rc12 : Thickness of layer 4 . . . . . . . . . . =  1.000000e-001
  Rc13 : Material number for layer 4  . . . . . . =            2
  Rc14 : Material angle for layer 4 . . . . . . . . =  9.000000e+001
  Rc15 : Thickness of layer 5 . . . . . . . . . . =  2.500000e-002
  Rc16 : Material number for layer 5  . . . . . . =            1
  Rc17 : Material angle for layer 5 . . . . . . . . =  9.000000e+001
  Rc18 : Thickness of layer 6 . . . . . . . . . . =  1.000000e-001
  Rc19 : Material number for layer 6  . . . . . . =            2
  Rc20 : Material angle for layer 6 . . . . . . . . =  9.000000e+001
```

layer-composite elements and designated as Element Group 2 (refer to Table 9-7).

9.6.3.1.6 *Loading.*   Total loads of 12,500 lb (6,250 lb at each node) were applied onto the half model as shown in Fig. 9-49. This load was equivalent to the 25,000 lb of the total loads for the complete model.

9.6.3.1.7 *The Nonlinear Analysis.*   Although nonlinear analysis may yield a slightly better result, in our case both linear and nonlinear analysis are expected to produce similar results because of the linear properties of the composite laminate and the expected small deflection under the loading conditions. The experimental program indicated that the maximum mid-span deflection of the portal frame under the action of the 25,000 lb (111 kN) total load was less than 2.5 in. (6.35 cm), or about l/43 (Mosallam and Bank 1992). However, nonlinear analysis was performed in order to make better comparisons with the nonlinear analyses of other models that follow.

Table 9-7. Element Group and Real Constant Sets for the
Web of PFRP H-Profiles

```
                         Element Groups
Element Group :    2  ( SHELL4L )

   Op1: Type :0=QUAD2;1=QUAD4;2=QUAD  .  .  .  .  .  .  .  .  .  .  =    1
   Op2: Number of Layers .  .  .  .  .  .  .  .  .  .  .  .  .  .  =   13
   Op3: Stress Dir :0=Global;1=Local;2=Mat .  .  .  .  .  .  .  .  =    2
   Op4: Unused option .  .  .  .  .  .  .  .  .  .  .  .  .  .  .  =    0
   Op5: Failure Analysis 0-LE;7-Tsai Wu .  .  .  .  .  .  .  .  .  -    0
   Op6: Disp. Formulation:0=Small;1=Large  .  .  .  .  .  .  .  .  =    0

                       Real Constant Sets
Real Constant Set :    2
Associated Element Group :    2  ( SHELL4L )

   Rc1  : Dist. from ref. plane to top surface   .  .  .  = 1.875000e-001
   Rc2  : Temperature gradient .  .  .  .  .  .  .  .  .  = 0.000000e+000
   Rc3  : Thickness of layer 1 .  .  .  .  .  .  .  .  .  = 2.500000e-002
   Rc4  : Material number for layer 1  .  .  .  .  .  .  =            1
   Rc5  : Material angle for layer 1 .  .  .  .  .  .  .  = 9.000000e+001
   Rc6  : Thickness of layer 2 .  .  .  .  .  .  .  .  .  = 3.333000e-002
   Rc7  : Material number for layer 2  .  .  .  .  .  .  =            2
   Rc8  : Material angle for layer 2 .  .  .  .  .  .  .  = 9.000000e+001
   Rc9  : Thickness of layer 3 .  .  .  .  .  .  .  .  .  = 2.500000e-002
   Rc10 : Material number for layer 3  .  .  .  .  .  .  =            1
   Rc11 : Material angle for layer 3 .  .  .  .  .  .  .  = 9.000000e+001
   Rc12 : Thickness of layer 4 .  .  .  .  .  .  .  .  .  = 3.333000e-002
   Rc13 : Material number for layer 4  .  .  .  .  .  .  =            2
   Rc14 : Material angle for layer 4 .  .  .  .  .  .  .  = 9.000000e+001
   Rc15 : Thickness of layer 5 .  .  .  .  .  .  .  .  .  = 2.500000e-002
   Rc16 : Material number for layer 5  .  .  .  .  .  .  =            1
   Rc17 : Material angle for layer 5 .  .  .  .  .  .  .  = 9.000000e+001
   Rc18 : Thickness of layer 6 .  .  .  .  .  .  .  .  .  = 3.333000e-002
   Rc19 : Material number for layer 6  .  .  .  .  .  .  =            2
   Rc20 : Material angle for layer 6 .  .  .  .  .  .  .  = 9.000000e+001
   Rc21 : Thickness of layer 7 .  .  .  .  .  .  .  .  .  = 2.500000e-002
   Rc22 : Material number for layer 7  .  .  .  .  .  .  -            1
   Rc23 : Material angle for layer 7 .  .  .  .  .  .  .  = 9.000000e+001
   Rc24 : Thickness of layer 8 .  .  .  .  .  .  .  .  .  = 3.333000e-002
   Rc25 : Material number for layer 8  .  .  .  .  .  .  =            2
   Rc26 : Material angle for layer 8 .  .  .  .  .  .  .  = 9.000000e+001
   Rc27 : Thickness of layer 9 .  .  .  .  .  .  .  .  .  = 2.500000e-002
   Rc28 : Material number for layer 9  .  .  .  .  .  .  =            1
   Rc29 : Material angle for layer 9 .  .  .  .  .  .  .  = 9.000000e+001
   Rc30 : Thickness of layer 10   .  .  .  .  .  .  .  .  = 3.333000e-002
   Rc31 : Material number for layer 10 .  .  .  .  .  .  =            2
   Rc32 : Material angle for layer 10  .  .  .  .  .  .  = 9.000000e+001
   Rc33 : Thickness of layer 11   .  .  .  .  .  .  .  .  = 2.500000e-002
   Rc34 : Material number for layer 11 .  .  .  .  .  .  =            1
   Rc35 : Material angle for layer 11  .  .  .  .  .  .  = 9.000000e+001
   Rc36 : Thickness of layer 12   .  .  .  .  .  .  .  .  = 3.333000e-002
   Rc37 : Material number for layer 12 .  .  .  .  .  .  -            2
   Rc38 : Material angle for layer 12  .  .  .  .  .  .  = 9.000000e+001
   Rc39 : Thickness of layer 13   .  .  .  .  .  .  .  .  = 2.500000e-002
   Rc40 : Material number for layer 13 .  .  .  .  .  .  -            1
   Rc41 : Material angle for layer 13  .  .  .  .  .  .  - 9.000000e+001
```

9.6.3.1.8 Results Presentations and Interpretations.   Displacement: From the following figures, the following observations are made:

• The displacement plot shown in Figs. 9-54 through 9-57 show that the maximum displacement was 1.23 in. (3.12 cm) that occurred at the middle span of the beam, as expected.
• The displacement contour at the plane of symmetry confirmed the validity of using symmetrical boundary restraints in the FEA model.
• Figures 9-58 through 9-61 show that the rotation of the top end of the column was rather significant (as much as 1.7 degrees). To evaluate
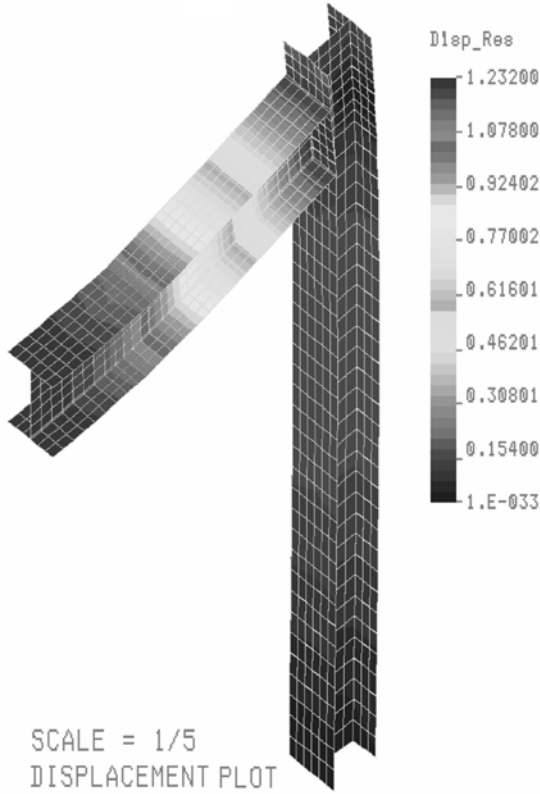
Figure 9-54. Displacement contour plot of Model C-1.

the existing rotational stiffness contribution of the frame's column, the deflection was calculated based on total fixity assumption at the ends. Figures 9-60 and 9-61 show that if the beam ends are assumed fixed, the resulting mid-span deflection is 0.58 in. (1.47 cm) as compared to the 1.23 in. (3.12 cm) obtained from Model C-1.

Stresses: The following are some discussions on the stress results of Model *C-1*:

- Stress vector plots shown in Figs. 9-62 through 9-65 and Figs. 9-67 through 9-69 show that the middle portion of the beam (between the two loading points) was under pure bending, as expected, with zero shear components.
- Figures 9-62 through 9-65 and Figs. 9-67 through 9-69 show that the negative bending moments at the ends of the girder were relatively small due to the flexibility of the connections.
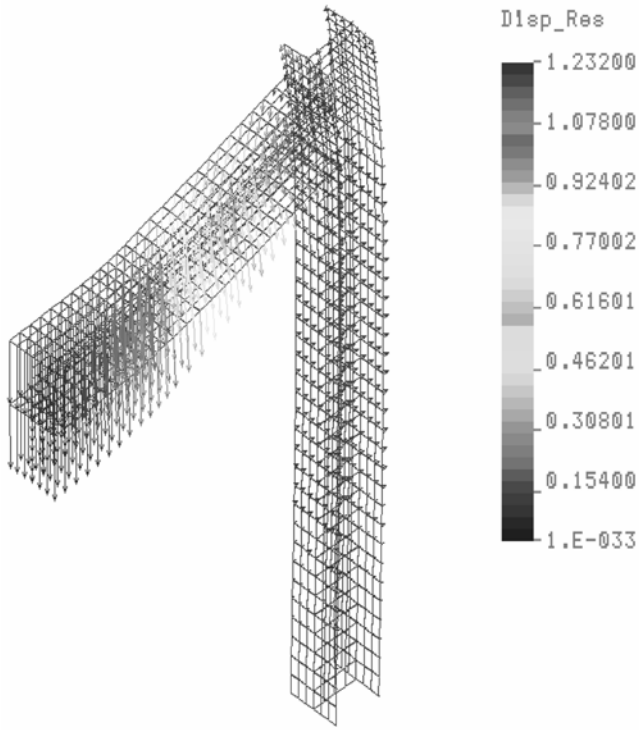
Figure 9-55. Displacement vector plot of Model C-1.
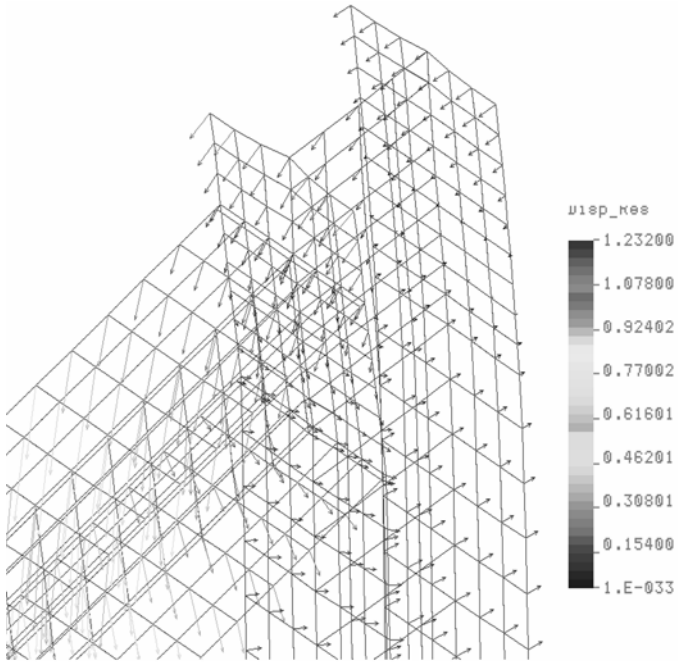
Figure 9-56. Enlarged isometric view of displacement vector plot of beam-column connection model used in Model C-1.

DISP Step:20 =1

Disp_Res

| 1.23200 |
| 1.07800 |
| 0.92402 |
| 0.77002 |
| 0.61601 |
| 0.46201 |
| 0.30801 |
| 0.15400 |
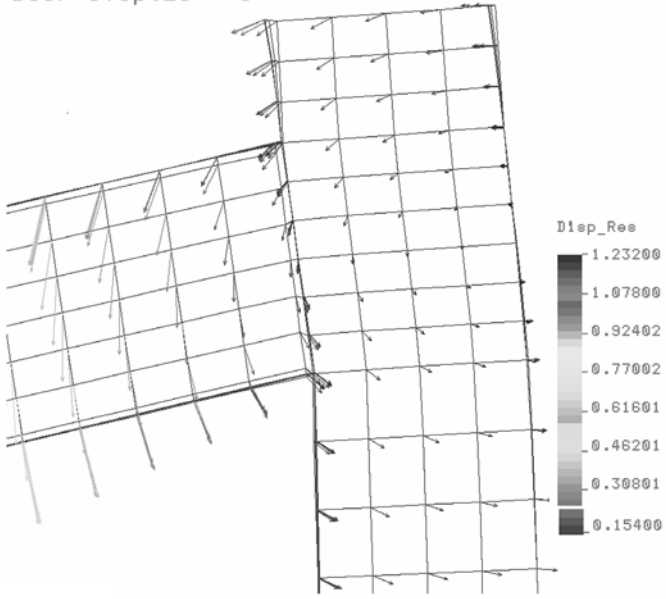
Figure 9-57. Enlarged normal view of displacement vector plot of beam-column connection model used in Model C-1.

NL1n DISP Step:20   =1

Rot_X

| 0.04146000 |
| 0.03561500 |
| 0.02976900 |
| 0.02392300 |
| 0.01807800 |
| 0.01223200 |
| 0.00638610 |
| 0.00054042 |
| -0.0053053 |
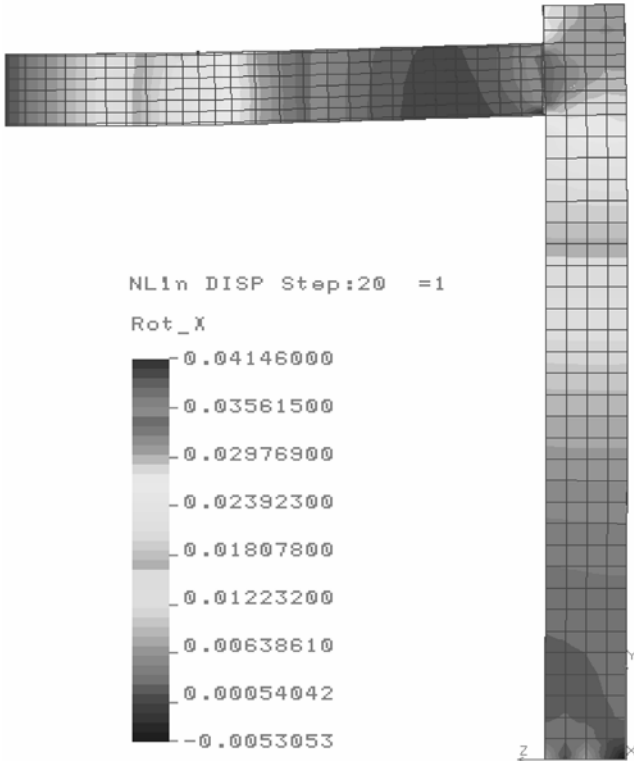
Figure 9-58. Rotation R_x contour plot of Model C-1.

NL1n DISP Step:20

Rot_X

-0.04146000
-0.03561500
-0.02976900
-0.02392300
-0.01807800
-0.01223200
-0.00638610
-0.00054042
--0.0053053
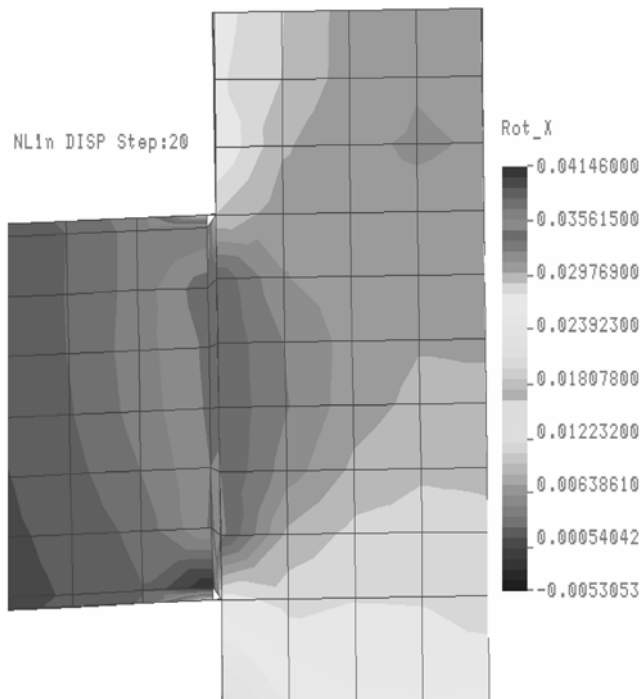
Figure 9-59. Enlarged view of rotation R_x contour plot of the beam-column connection of Model C-1.

DISP Step:7   =1

Disp_Res

-0.579130
-0.506740
-0.434350
-0.361960
-0.289570
-0.217170
-0.144780
-0.072391
--1.0E-033
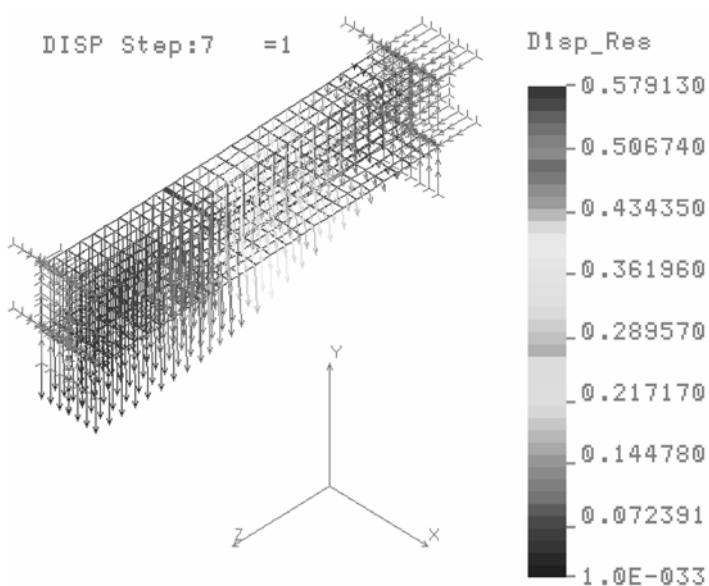
Figure 9-60. Displacement vector plot of the beam with both ends fixed.
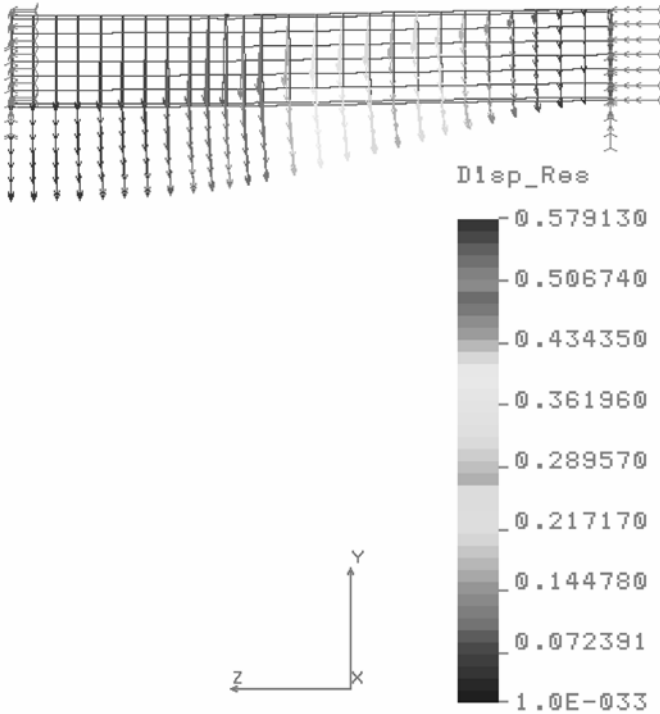
Figure 9-61. Displacement vector plot of the beam with both ends fixed (normal view).

- The lower values of the tensile and compressive stresses on the flanges of the beam between the loading points and the end of the beam, as shown in Figs. 9-62 through 9-64 and 9-67 through 9-69 illustrate that the restraint condition of the beam was indeed qualified to be a semi-rigid restraint condition; however, it was very close to a hinged support.
- The in-plane shear stress plots, shown in Fig. 9-70, show that the shear stress of the web of the beam was higher than that of the column, with the highest occurring at the loading point.
- To further validate the FEA model, the normal (or σ_x) stress of each layer of the top and bottom flanges of the beam at the mid-span (pure bending) is shown in Figs. 9-71 through 9-73 and Table 5. To simplify the presentation, only the σ_x stress of the layers 5 and 6 of the web are presented in Fig. 9-73 and Table 9-8. There were 13 layers in total in the web and layer 6 was in the middle plane. The σ_x stress distribution (Fig. 9-73) shows that the PFRP H profiles were simulated reasonably well by the FEA modeling.
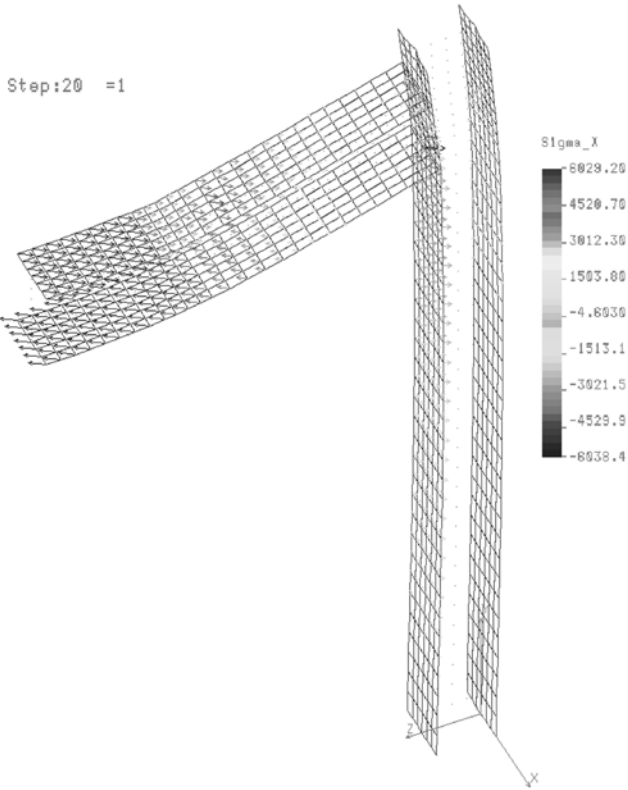
Step:20 =1

Sigma_X

- 6029.20
- 4520.70
- 3012.30
- 1503.80
- -4.6030
- -1513.1
- -3021.5
- -4529.9
- -6038.4

Figure 9-62. σ$_x$ stress vector plot of flanges, layer 1 (typical).

Sigma_X

- 6029.20
- 4520.70
- 3012.30
- 1503.80
- -4.6030
- -1513.1
- -3021.5
- -4529.8
- -6038.4
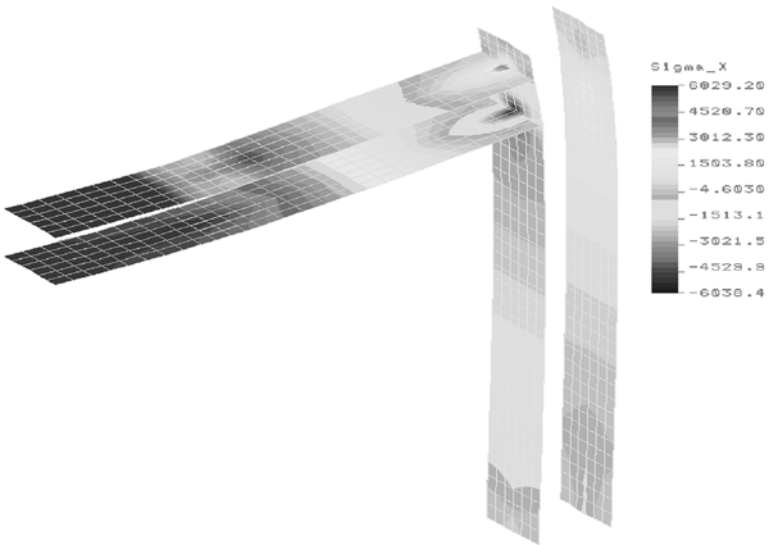
Figure 9-63. σ$_x$ stress contour plot of flanges, layer 1 (typical).
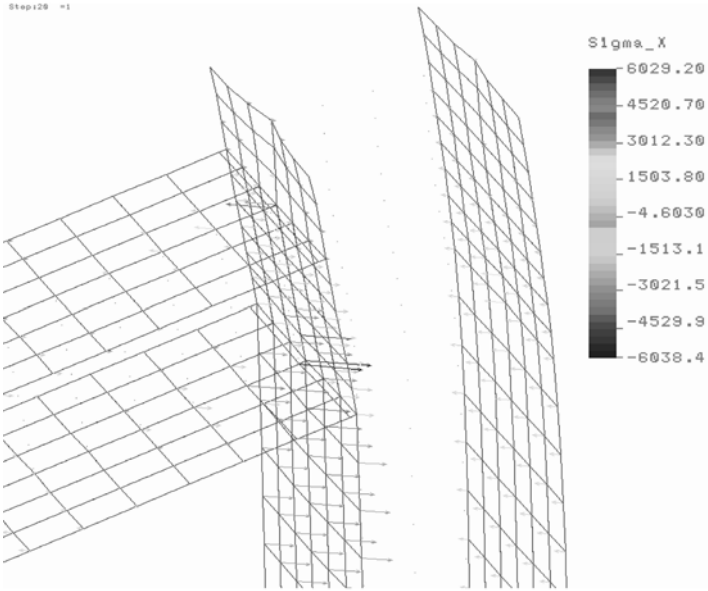
Figure 9-64. σ_x stress vector plot of flanges at the connection.
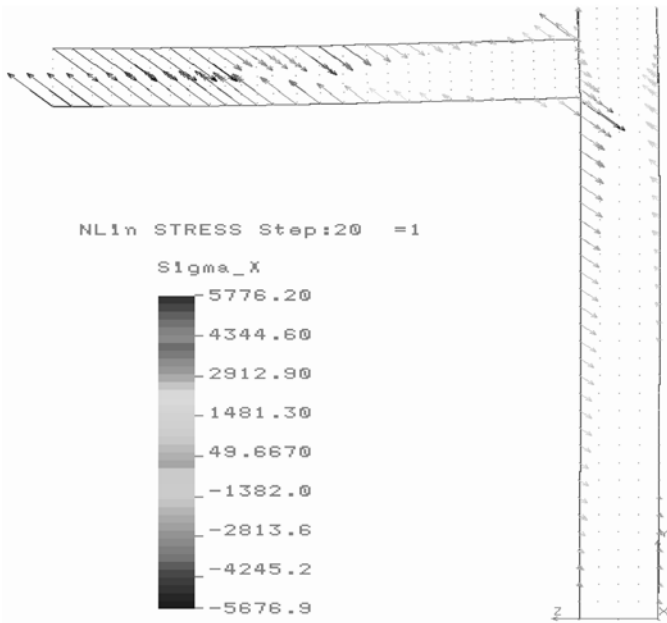
Figure 9-65. σ_x stress vector plot of the PFRP frame flanges (mid-layer 3).
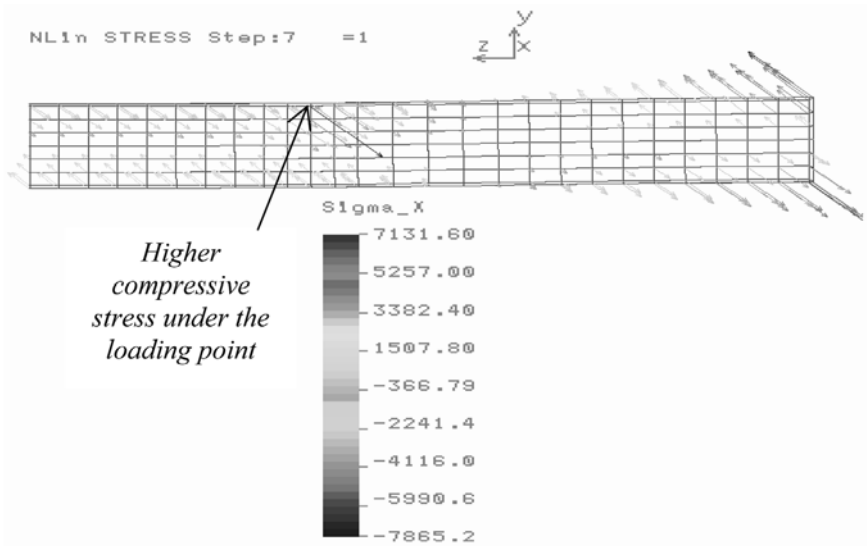
Figure 9-66. Normal stress σ_x vector plot of the beam with both ends fixed (normal view).
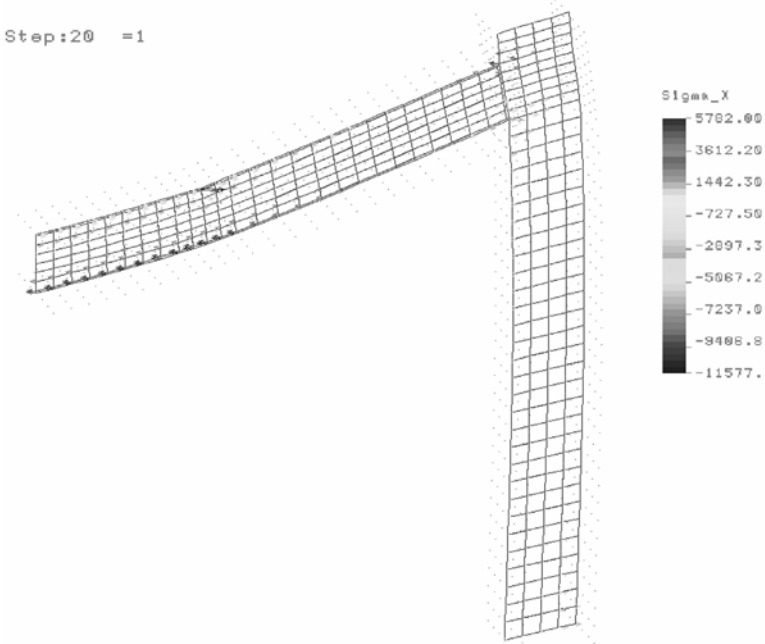
Figure 9-67. σ_x stress vector plot of web, layer 1 (typical).
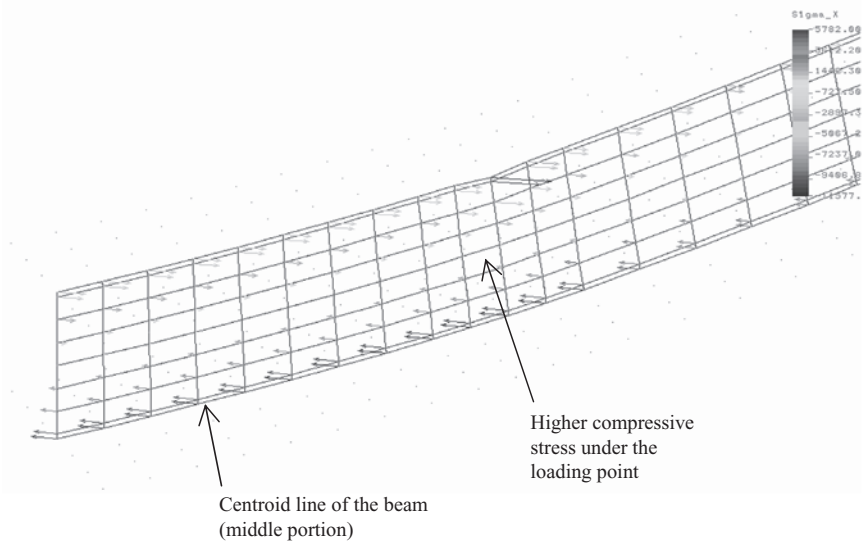
Figure 9-68. Enlarged view of σ_x stress vector plot of the web, layer 1 (typical).
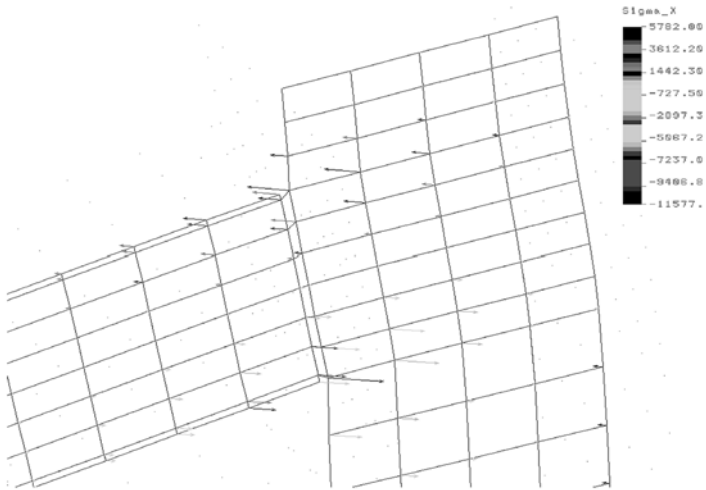
Figure 9-69. Enlarged view of σ_x stress vector plot of web at the connection, layer 1 (typical).
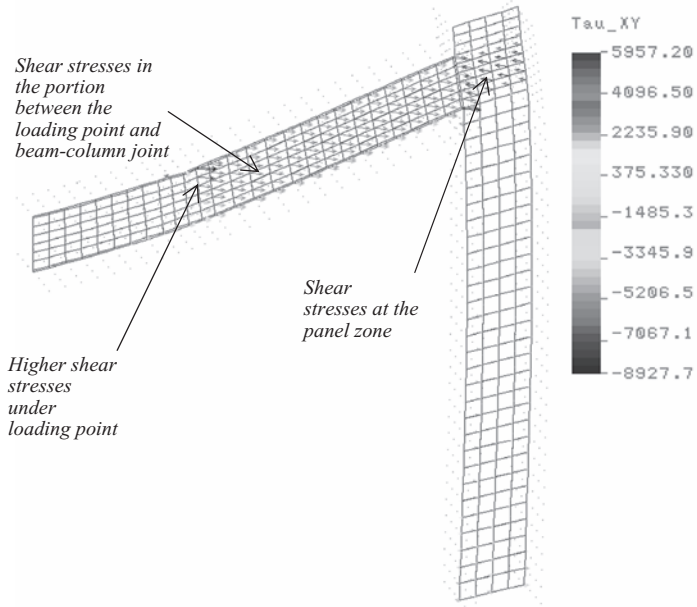
Figure 9-70. The in-plane shear stress, σ_{xy}, vector plot of the web.
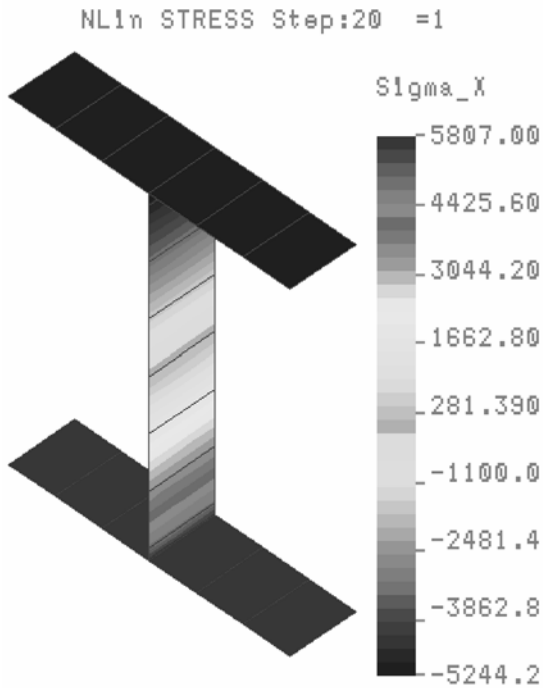
Figure 9-71. σ_x stress contour plot of a typical section of the beam at the mid-span, layer 1.
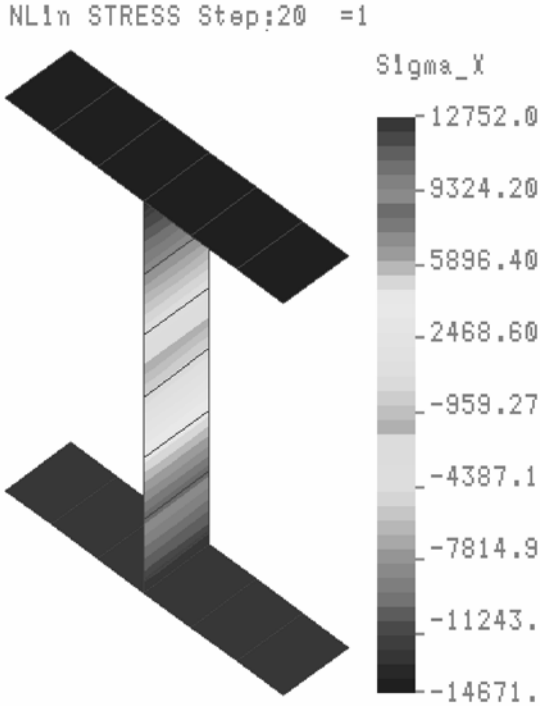
Figure 9-72. σ_x stress contour plot of a typical section of the beam at the mid-span, layer 6.
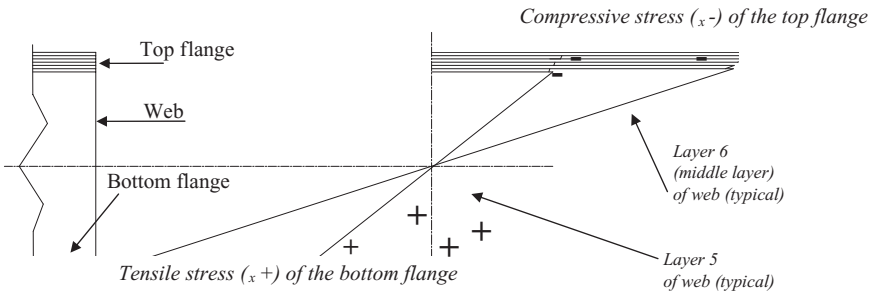
Figure 9-73. Beam cross-sectional σ_x, or normal stress distribution.

9.6.3.2 Model C-2: Hinged Beam-to-Column Connections Using Axial Spring Elements.   This model is identical to Model C-1 except for the change of beam end restraint at the column location to be hinged, as shown in Fig. 9-74A. The hinged beam-column assumption was introduced in order to investigate the lower bounds of the connection

Table 9-8. Beam Cross-Sectional σ_x, or Normal Stress Distribution[a]

Flange	Layer 1		Layer 2		Layer 3		Layer 4		Layer 5		Layer 6	
	Top	Bottom	Top	Bottom	Top	Bottom	Top	Bottom	Top	Bottom	Top	Bottom
Top (−ve)	5,284	5,244	13,531	13,132	5,522	5,461	14,243	13,674	5,826	5,765	14,955	14,671
Bottom (+ve)	5,750	5,807	13,703	14,286	5,469	5,526	13,037	13,557	5,223	5,259	12,562	12,752

Web	Layer 5 (typ.)	Layer 6 (typ.)
Top Edge (−ve)	5,422 (membrane) (membrane)	13,486 (membrane)
Bottom Edge (+ve)	5,242 ((membrane) (membrane)	13,039

[a] Units are psi.
[b] ±ve positive or negative stress.

flexibility and its effect on the overall behavior of the portal frame structure.

In this model, the beam-column connection was represented by two one-node nonlinear axial spring elements with close-to-zero axial stiffness (refer to Figs. 9-74B and 9-75). The close-to-zero axial stiffness was employed to avoid the possibility of any singularity of the stiffness matrix when performing the FEA.
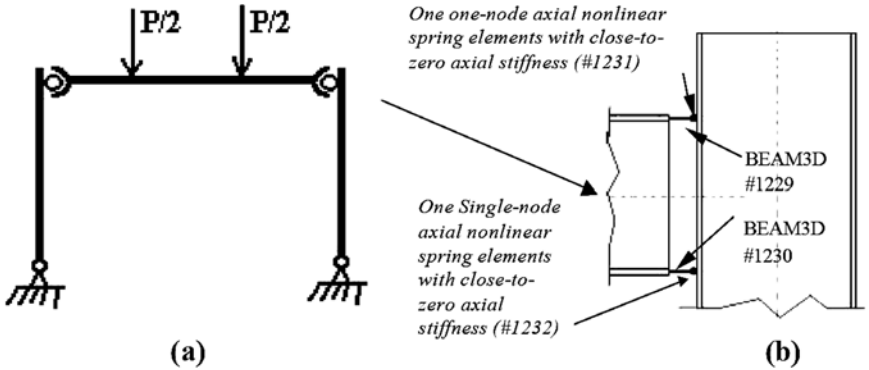
Figure 9-74. A. Ideal diagram of Model C-2 (hinged beam-column connection assumption); B. graphical illustration of beam-column connection.

Figure 9-75. Two one-node axial springs element with almost zero stiffness (K-Linear = 288/0.38 = 758 lb/in. or 133 kN/m, which is 1% of the actual stiffness).

Both the degrees of freedom of translation in the Z-direction (T_z) and the rotation in the X-direction (R_x) at the far ends of Elements 1229 and 1230 were released (Figs. 9-74B and 9-75). This modeling approach enabled the two beam elements to transfer shear force between the beam and column without introducing any additional axial and rotational stiffness into the beam-to-column connection. Samples of displacement and stress results are shown in Figs. 9-76 through 9-85.

9.6.3.3 Model C-3: Semi-Rigid Beam-to-Column Connection Using Axial Spring Elements. This model is identical to Model C-2 except that the beam end restraint at the column location was a semi-rigid beam-to-column connection (refer to Fig. 9-86). The purpose of introducing the semi-rigid beam-to-column connection assumption was to investigate the effect of the connection flexibility over the overall behavior of the portal frame structure. This semi-rigid beam-to-column connection stiffness was applied to the connection by using two one-node nonlinear axial spring elements (refer to Fig. 9-87).

The nonlinear force–displacement curve of the two one-node spring elements was converted from the M/θ curve shown in Fig. 9-35. This conversion was made based on the following two assumptions:
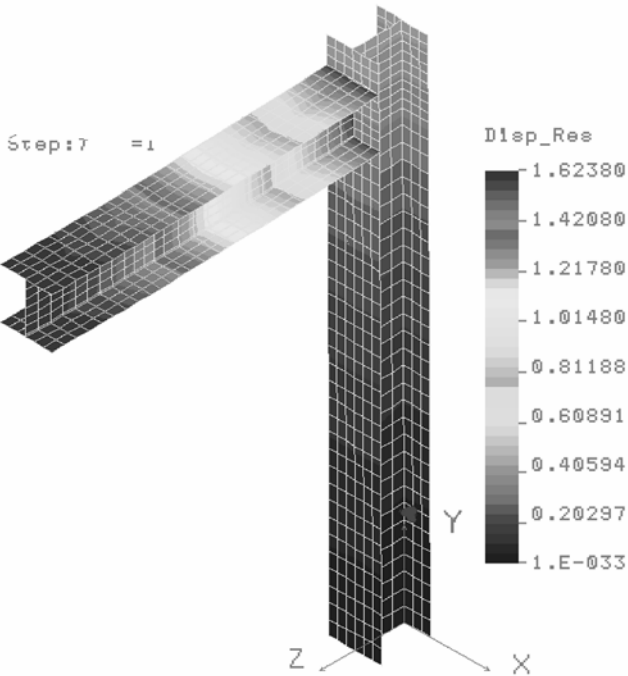
Figure 9-76. Displacement contour plot of Model C-2.
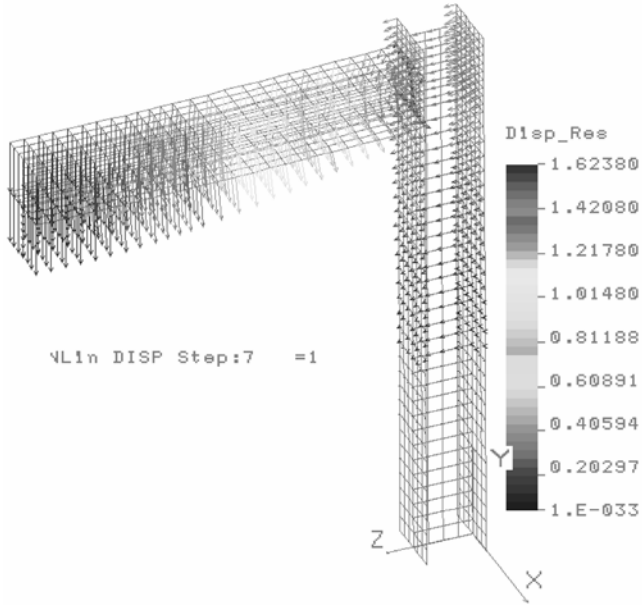
Figure 9-77. Displacement vector plot of Model C-2.
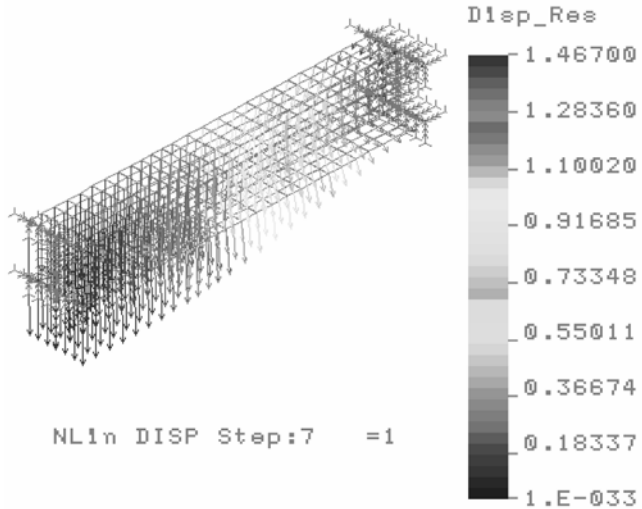
Figure 9-78. Displacement vector plot of the same beam (as Model C-2) with both ends hinged, or simply supported.
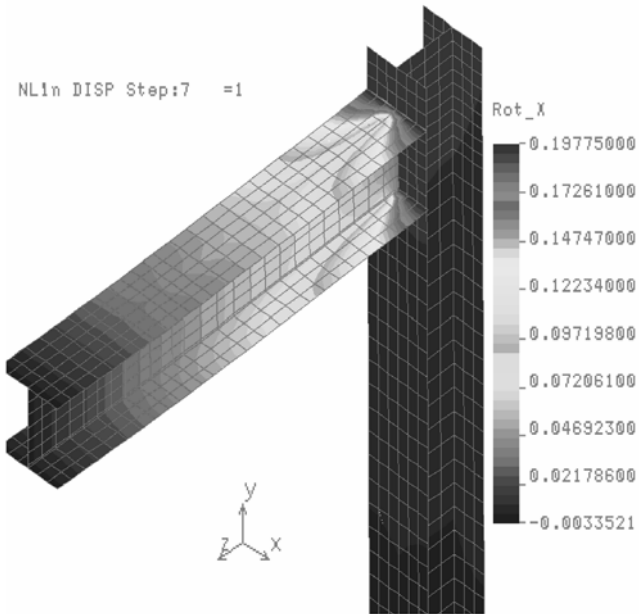
Figure 9-79. Rotation R_x contour plot of Model C-2.
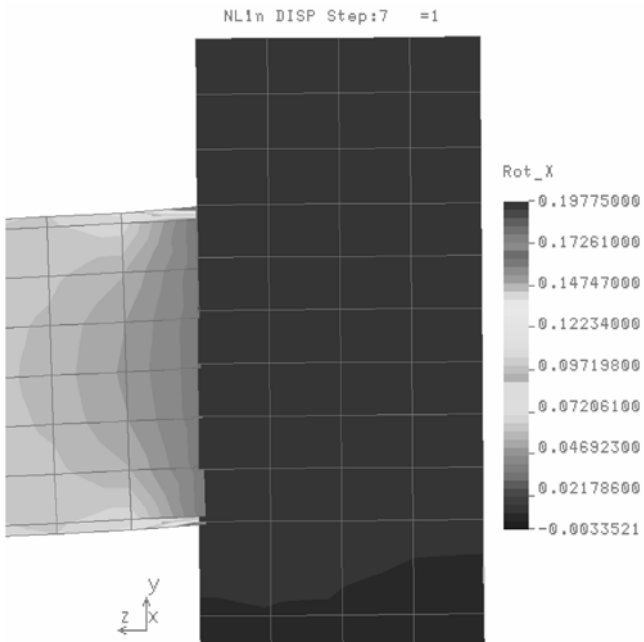
Figure 9-80. Rotation R_x contour plot of Model C-2, enlarged view of the connection.
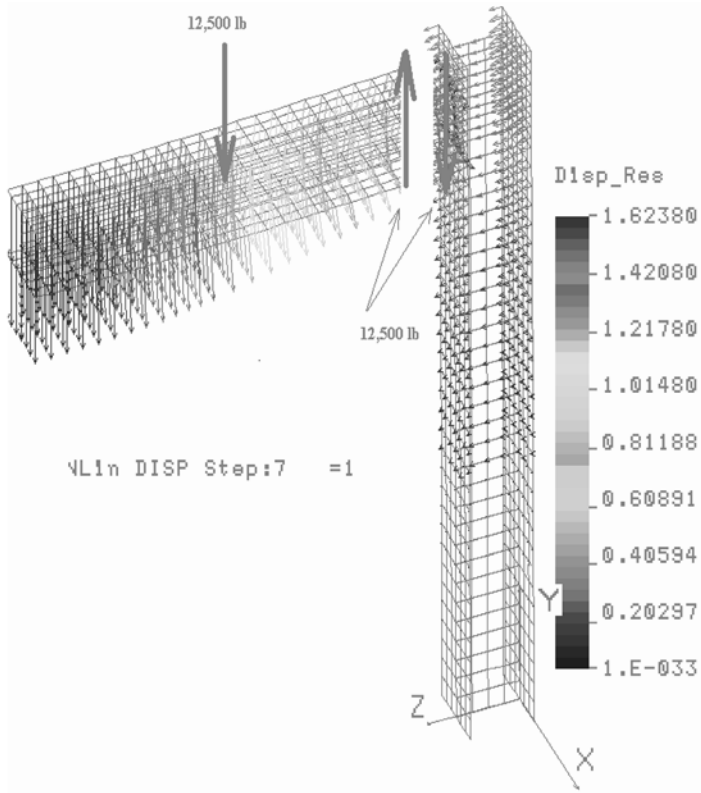
Figure 9-81. Shear force applied onto the inner flange of column and its overall axial effect on the column.

1. The beam will rotate around the bottom flange of the beam, as shown in Fig. 9-88.
2. The flexibility of the beam-to-column connection solely contributed to the M/θ curve shown in Fig. 9-35. In reality, the M/θ curves produced experimentally reflect the flexibility of both the connection and rest of the structure. In other words, the connection will undergo a total rotation, θ_{total}, which can be expressed as

$$\theta_{total} = \theta_c + \theta_r \qquad (9-8)$$

where θ_{total} is the total rotational displacement of the beam relative to the base at the location of the connection; θ_c is the rotational displacement of the column relative to the base at the location of the connection; and θ_r is the rotational displacement of the beam relative to the column at the location of the connection as shown in Fig. 9-89.
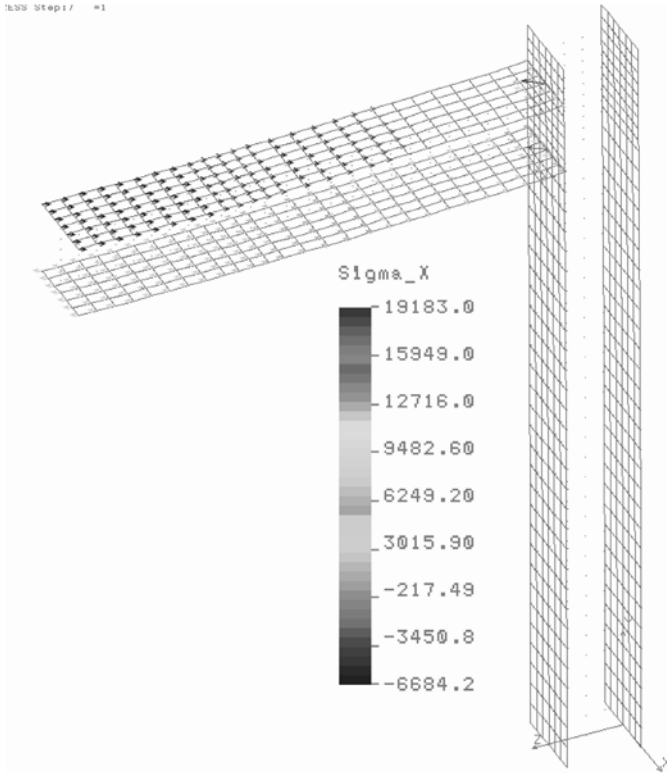
Figure 9-82. Normal stress σ_x vector plot of Model C-2.

Figure 9-90 shows the conversion calculation along with the nonlinear force–displacement curve of the axial spring that was presented earlier in Fig. 9-35. The maximum displacement at the middle span was found to be 1.605 in. (4.08 cm), which was slightly less than the 1.624 in. (4.12 cm) of Model C-2. The maximum rotation angle occurred at the beam-to-column connection and was found to be 0.198 rad (11.33 degrees), which was the same as that of Model C-2 except that the pattern of rotation at different locations was not exactly the same. Samples of the FE results are shown in Figs. 9-91 through 9-101.

9.6.3.4 Model C-4: Simulating the Semi-Rigid Beam-to-Column Connection and Web-to-Flange Junction by Using Nonlinear Axial and Rotational Spring Elements. This model is identical to Model C-3 as previously described except that the modeling of the pultruded open web profiles of the beam used a semi-rigid web-to-flange junction. The semi-rigid web-to-flange junction was introduced to investigate the effect
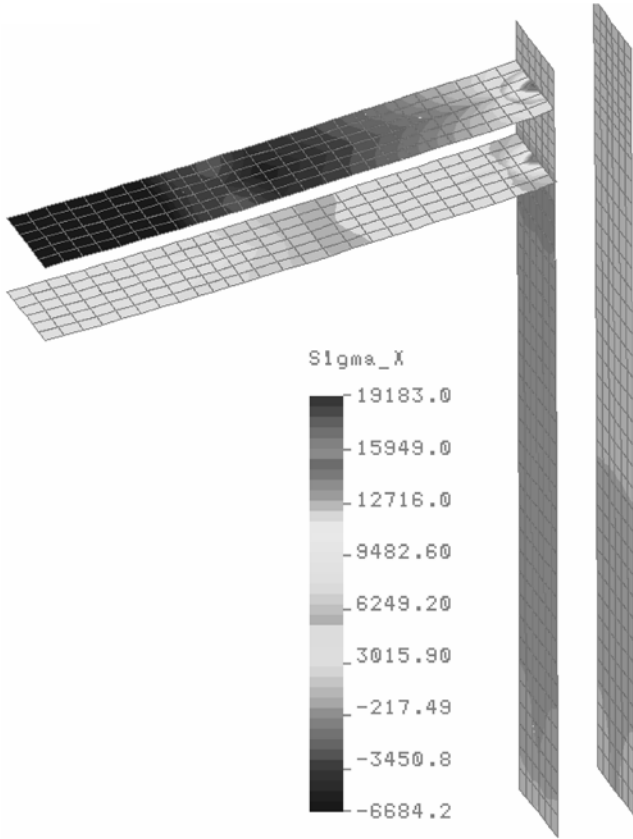
Figure 9-83. *Normal stress σ_x contour plot of Model C-2.*

of the flexibility of the web-to-flange junction on the overall behavior of the portal frame structure. This semi-rigid rotational stiffness of the web-flange junction was introduced by using 54 units of single-node nonlinear rotational spring elements, shown in Fig. 9-95. Figure 9-96 shows a typical modeling arrangement of the web-to-flange junction. The nonlinear force–displacement curve of the 54 pieces of the one-node spring elements was converted from the M/θ curve shown in Fig. 9-35. The conversion was made by simply dividing the total rotational stiffness of the whole length of the beam over 27 pieces of spring elements (refer to Fig. 9-97). Based on this model, the maximum displacement at the mid-span is 1.76 in. (4.47 cm) as shown in Fig. 9-98. The maximum rotation angle that occurred at the beam-to-column joint 0.040 rad (2.34 degrees) (refer to Fig. 9-99). This was much smaller than that of Model C-3, which did not consider the flexibility of the web-to-flange junction.
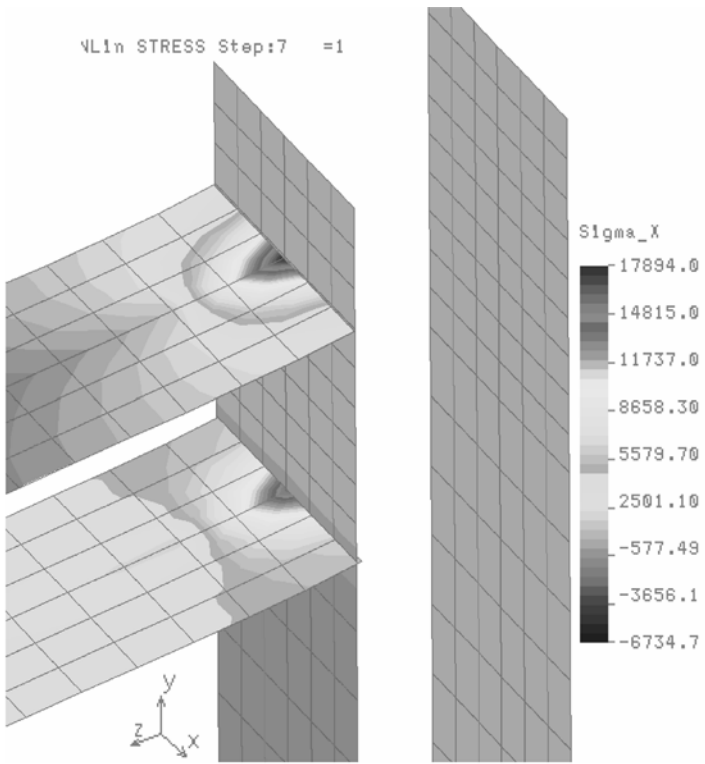
Figure 9-84. Normal stress σ_x vector plot of Model C-2, enlarged view of the beam-to-column connection.
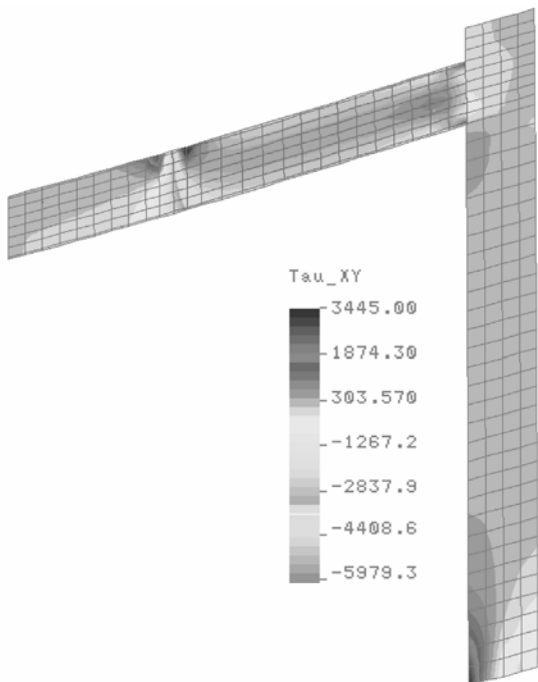
Figure 9-85. In-plane shear stress τ_{xy} contour plot of Model C-2.
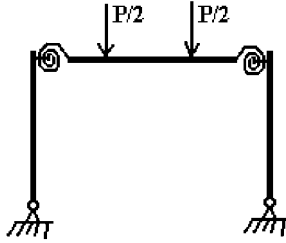
Figure 9-86. *The ideal diagram of Model C-3.*
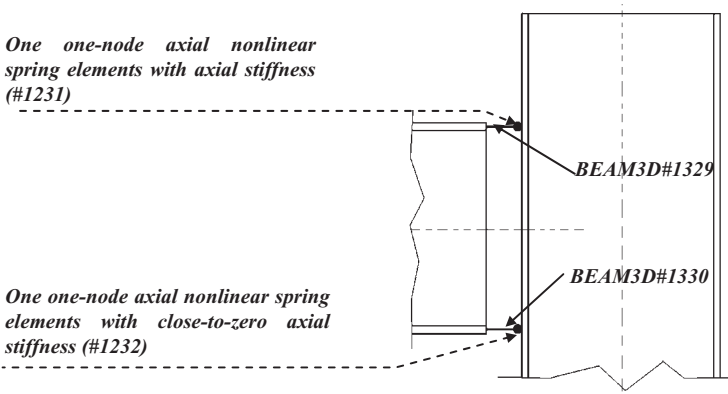
Figure 9-87. *Graphical illustration of beam-column connection of Model C-3.*
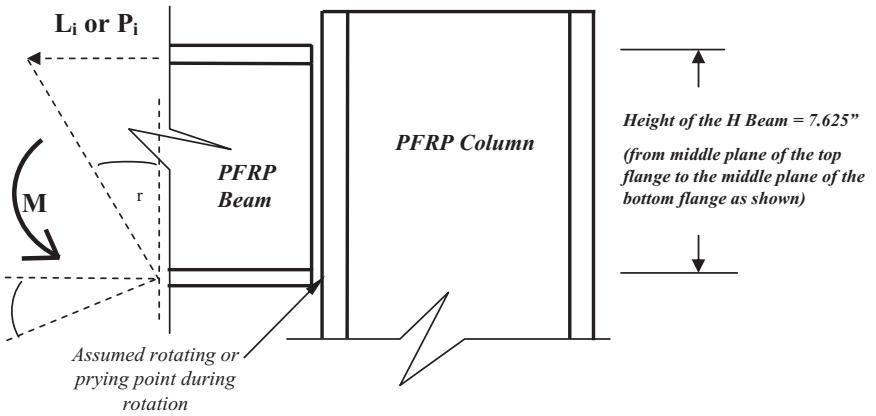
Figure 9-88. *Axial spring element stiffness conversion illustration.*
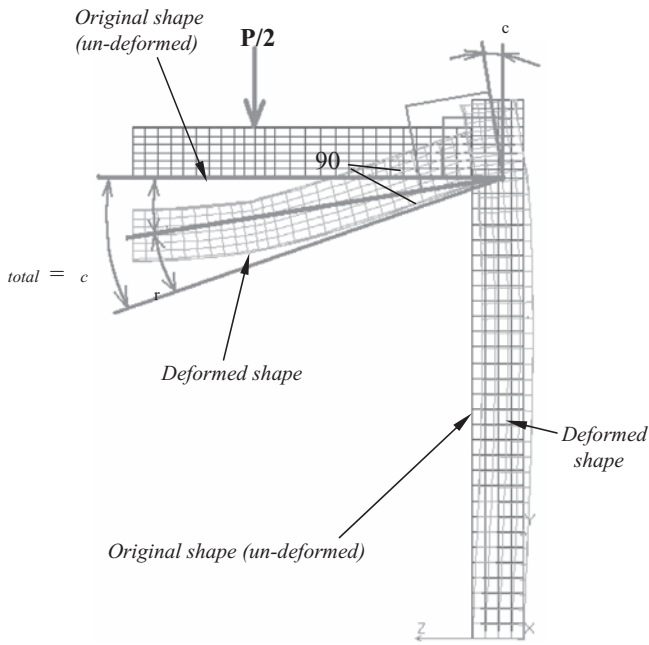
Figure 9-89. The rotational displacement relationship at the beam-to-column connection.

H := 7.625	inches			
M1 := 22000	inch – lbs	θ1 := 0.005	rad	
L1 := H·tan(θ1)		L1 = 0.038	inch	
$P1 := \dfrac{M1}{H}$		$P1 = 2.885 \cdot 10^3$	lbs	
M2 := 52000	inch – lbs	θ2 := 0.0275	rad	
L2 := H·tan(θ2)		L2 = 0.21	inch	
$P2 := \dfrac{M2}{H}$		$P2 = 6.82 \cdot 10^3$	lbs	
M3 := 53000	inch – lbs	θ3 := 0.035	rad	
L3 := H·tan(θ3)		L3 = 0.267	inch	
$P3 := \dfrac{M3}{H}$		$P3 = 6.951 \cdot 10^3$	lbs	
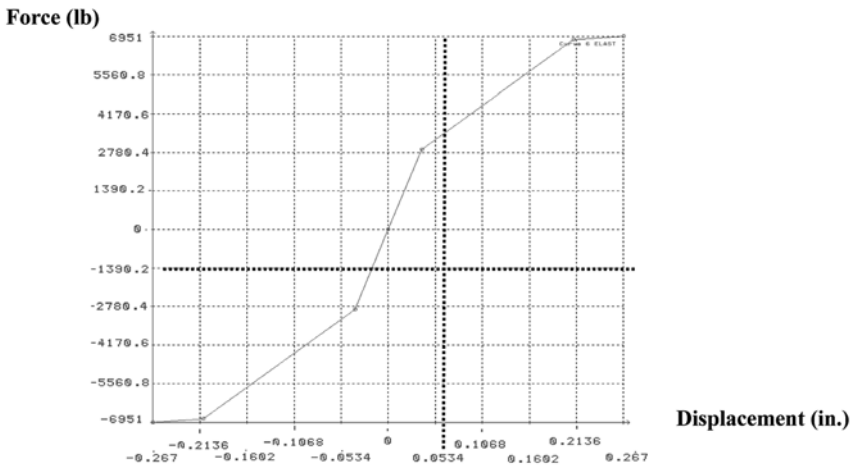
Figure 9-90. Full-range nonlinear force–displacement curve for axial spring elements converted from the linearized M/θ curve of Fig. 9-41.
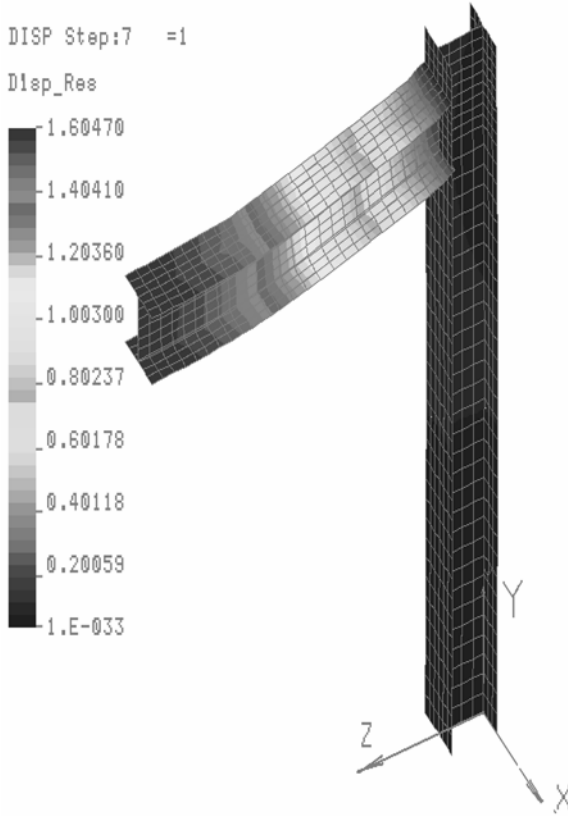
Figure 9-91. Displacement contour plot of Model C-3.

To evaluate the effect of the column stiffness, another model, Model C-4A, was developed by simply removing the column from Model C-4. In this model, the frame girder was treated as a beam with flexible end support, while still considering the web-flange junction flexibility. Figure 9-100 shows that the maximum displacement of the beam in this case was reduced to 1.713 in. (4.35 cm), which was 1.7% less than the 1.76 in. (4.47 cm) displacement of Model C-4. This 1.7% or 0.03 in. (0.76 cm) difference in displacement may have been due to the column's flexibility, which was negligible in this case.

The reduction of R_x rotation at the beam-to-column junction as compared to Model C-3 can be attributed to the increase of the R_x rotation at the loading effective zone, shown in Fig. 9-99. The excessive R_x rotation at the loading effective zone may be attributed to the discontinuity of the model at the flange-to-web junction. Although the study of the
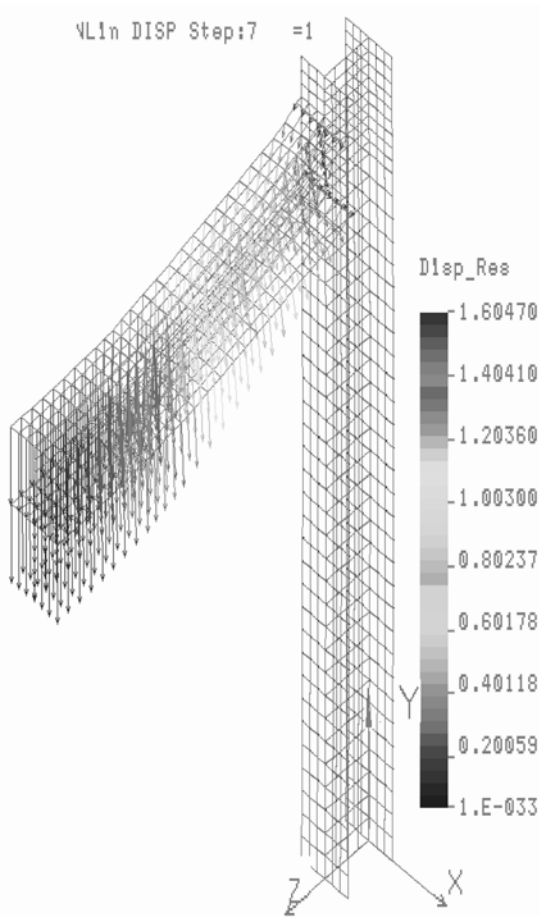
Figure 9-92. Displacement vector plot of Model C-3.

COSMOS/M spring elements, as presented earlier, validated the applicability of the use of the rotational spring element, the modeling of the flange-web junction with the rotational spring element was found to be a difficult task. The rigid beam elements used to connect the web to the flanges seemed to be capable of transferring loads between the flanges and web as intended.

9.6.3.5 Model C-5: Simulating the Semi-Rigid Web-to-Flange Junction Assumption Using a Rotational Spring Element and Beam-to-Column Connection by Using PFRP Angles and Gap Elements.   This model is identical to Model C-4, as previously described, except for the modeling
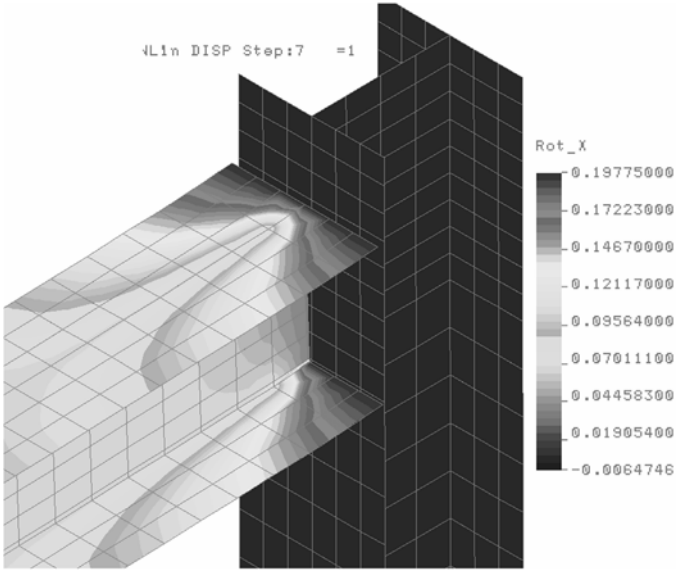
Figure 9-93. Rotation R_x contour plot of Model C-3.
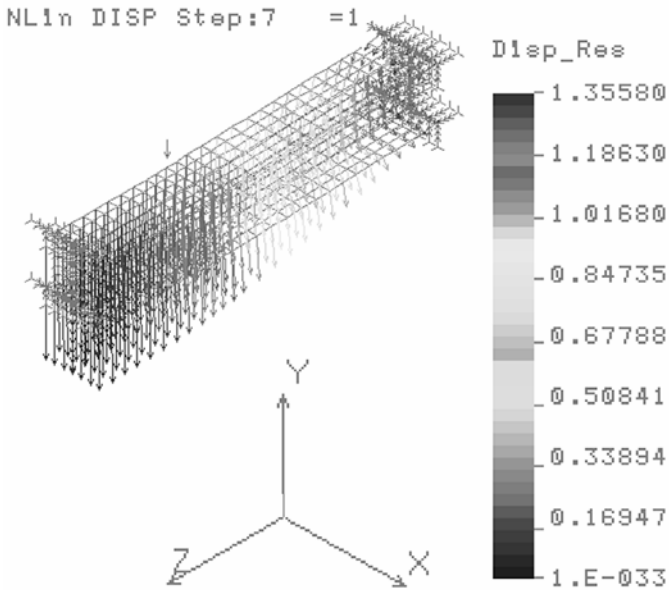
Figure 9-94. Displacement vector plot of the same beam (as Model C-3) with the column removed and the same two one-node axial spring included.

54 pieces of the rotational spring elements used on the top and bottom of the web, jointing the top and bottom edges of the web to the flanges (27 pieces on the top and 27 pieces on the bottom).

```
Element Groups

Element Group :   3  ( BEAM3D )

    Op1: Beam Type:0=Sym;1=UnSym;2=SymTapered  .  .  .  .  .  =   0
    Op2: Unused option .  .  .  .  .  .  .  .  .  .  .  .  .  =   0
    Op3: Unused option .  .  .  .  .  .  .  .  .  .  .  .  .  =   0
    Op4: Integration Type:0=Gauss;1=N-Cotes .  .  .  .  .  .  =   0
    Op5: Material Type:0=LE;1=VMI;2=VMK;4=NLE;8=VEM  .  .  .  =   0
    Op6: Displ. Formulation:0=Small;1=Large .  .  .  .  .  .  =   0
    Op7: Unused option .  .  .  .  .  .  .  .  .  .  .  .  .  =   0
    Op8: Unused option .  .  .  .  .  .  .  .  .  .  .  .  .  =   0

Element Group :   8  ( SPRING )   (ACTIVE)

    Op1: Spring Type:0=Axial;1=Rot;2=Both  .  .  .  .  .  .  =   1
    Op2: Number of nodes:1=1-Node;2=2-Node .  .  .  .  .  .  =   1
    Op3: Dof:1-3=Trans;4-6=Rot;7-9=Both  .  .  .  .  .  .  .  =   6
    Op4: Unused option .  .  .  .  .  .  .  .  .  .  .  .  .  =   0
    Op5: Spring behavior:0=Linear;1=NonLinear;2=Viscoelastic =   1
    Op6: Disp formulation:0=Small;1=Large  .  .  .  .  .  .  =   0
    Op7: Unused option .  .  .  .  .  .  .  .  .  .  .  .  .  =   0
```

Figure 9-95. Fifty-four units of the COSMOS/M BEAM3D and rotational spring elements (refer to Fig. 9-112 for graphical illustration of typical modeling arrangement).

0.25"

A typical rigid BEAM3D element (element group 3) with the rotational stiffness, R_z released at the flange end, connecting the flange to the web.

Flange

Web

A typical one-node rotational spring element (element group 8) connecting the rigid beam to the flange.
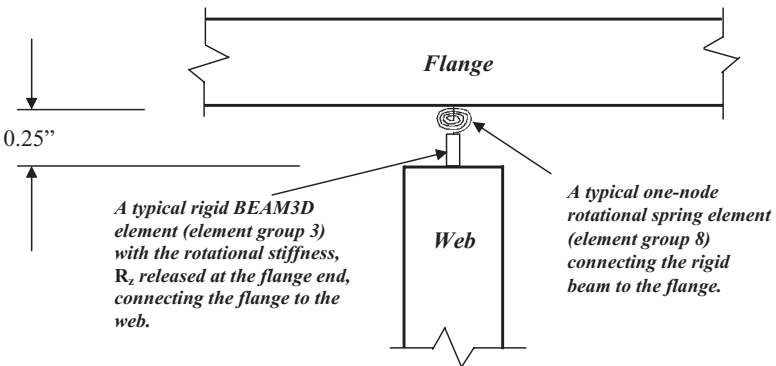
Figure 9-96. A typical web and flange arrangement (1 in. = 25.4 mm).

For example, for a rotational angle of 0.014 rad, a moment of 220 Inch-lbs will be required per Figure 2.3.3--3, thus a conversion can be made as follows:

Width_test_specimen := 4 inches   Length_beam := 50   inches

Number_element := 27   Pcs   M1_Specimen := 220   Inch_lbs

$$M1\_Per\_Spring := \frac{M1\_Specimen}{(\,Width\_test\_specimen\,)} \cdot \frac{Length\_beam}{Number\_element}$$

M1_Per_Spring = 102   Inch lbs
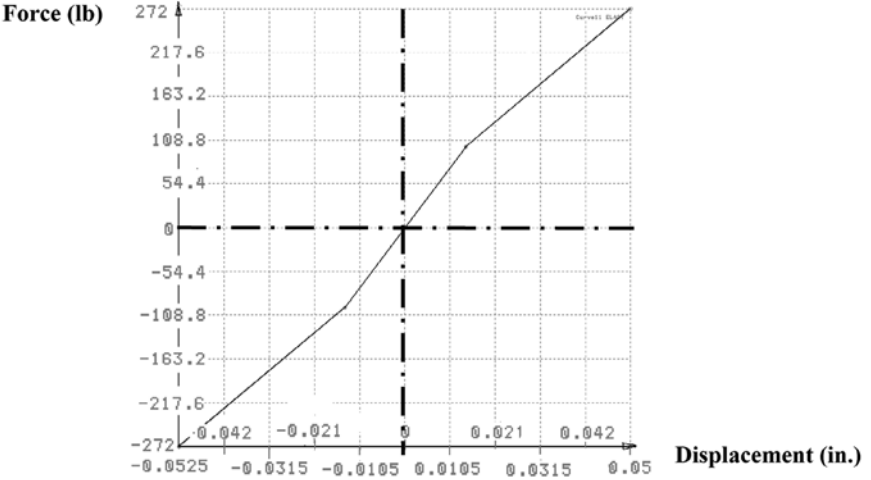
Figure 9-97. Full-range force–displacement curve of rotational spring element used in web-flange junction modeling (1 lb = 4.44 n; 1 in. = 2.54 cm).
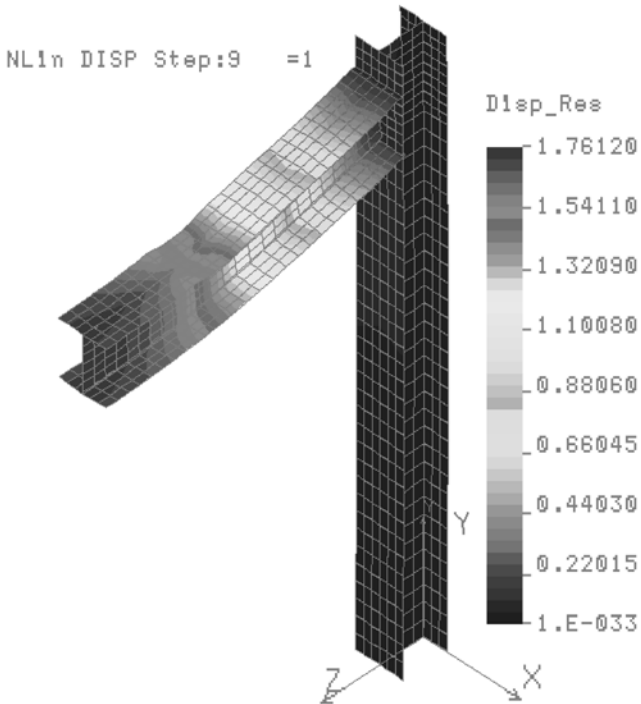
Figure 9-98. Displacement contour plot of Model C-4.
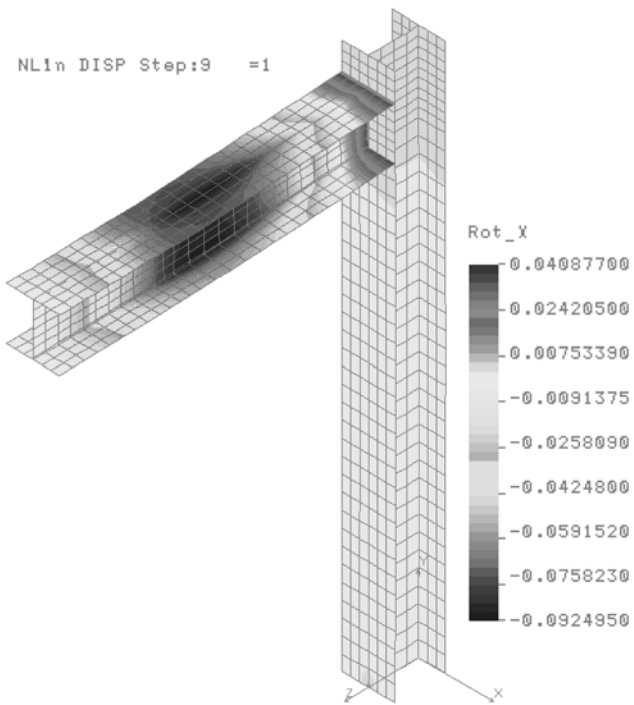
Figure 9-99. R_x rotation plot of Model C-4.
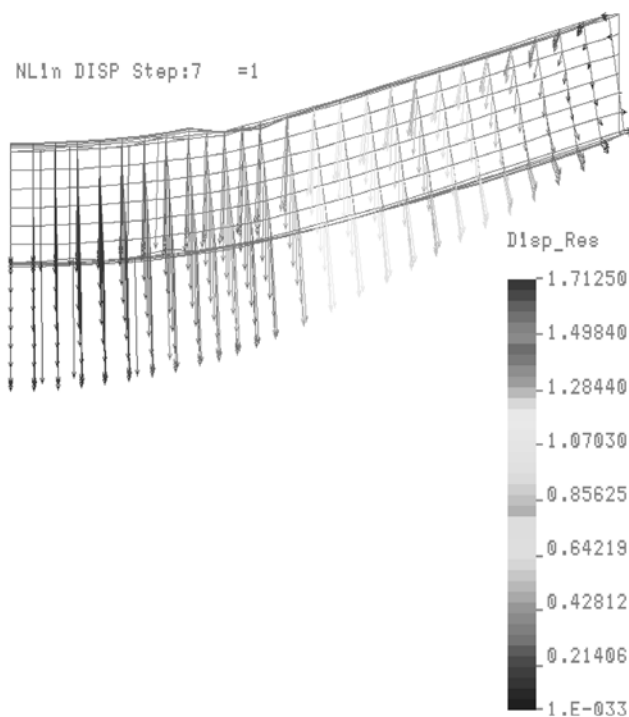
Figure 9-100. Displacement vector plot of Model C-4A, beam with the column removed.

of the semi-rigid beam-to-column connection assumptions. Instead of using two single-node axial spring elements, the semi-rigid beam-to-column connection was modeled with PRFP angles and compressive gap elements.

As described earlier, in the experimental program performed by Mosallam (1990), unidirectional pultruded equal-leg angles (6 in. × 6 in. × 1/2 in. or 15.24 cm × 15.24 cm × 1.27 cm) together with pultruded 3/4 in. (1.91 cm) and 1 in. (2.54 cm)-diameter threaded rods and compression-molded FRP nuts were used to join the beam and columns. In the FEA Model C-5, the 6 in. × 6 in. × 1/2 in. (15.24 cm × 15.24 cm × 1.27 cm) PFRP angles were modeled with COSMOS/M composite SHELL4L elements. These SHELL4L elements were basically the same as those used in the modeling of the flange and web, in terms of mechanical properties and general lamination arrangement. The only difference was the thickness and the number of layers of the PFRP angle, for which 1/2 in. (1.27 cm) thickness was used in the FE model.

In modeling the PFRP girder and columns, the fiberglass roving layer contained continuous unidirectional fiber bundles, which contributed the most to the stiffness and strength of a section (Davalos et al. 1996). The
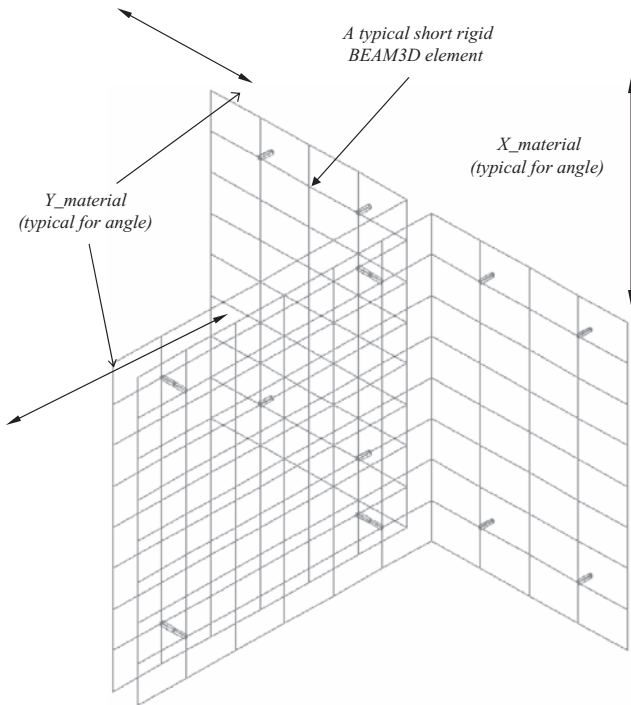
Figure 9-101. Modeling the two back-to-back PFRP angles in Model C-5.

PFRP equal angles that were used in the experimental program were cut off from standard off-the-shelf L-type PFRP profiles, where all the unidirectional fiber layers were laid in the lengthwise direction. In the FE modeling of the PFRP angle, the orientation of the fiber roving layers, or the unidirectional fiber bundles layer, was arranged in the lengthwise direction to simulate the real stiffness of the PFRP angles. Figure 9-101 shows a typical material coordinate system for the four angle brackets.

Figure 9-102 shows an isometric view of Model C-5. Among the four PFRP angles used in Model C-5, shown in Figs. 9-101 and 9-102, one angle was used on the top of the connection, connecting the top (upper) flange of the beam to the inner flange of the column. Another PFRP angle was used on the bottom, connecting the bottom (lower) flange of a beam to the inner flange of the column. Two angles were used to connect the web of the beam to the inner flange of the column, one on each side of the web of the beam. For easy modeling, a ¼ in. (0.635 cm) gap (clearance) was kept between the angles and their mating flanges or web. Each angle was connected with its mating flange by eight rigid beam elements, four on each side leg of angle (refer to Figs. 9-102 and 9-103).

The possible contact or prying action between the angles and their mating flange or web was modeled using a group of gap elements. Four gap elements were used for the top angle, two of which were used between the vertical leg of the top angle and the inner flange of the column, while the other two were used between the horizontal leg of the angle and the top flange of the beam. Eight gap elements were used for the bottom
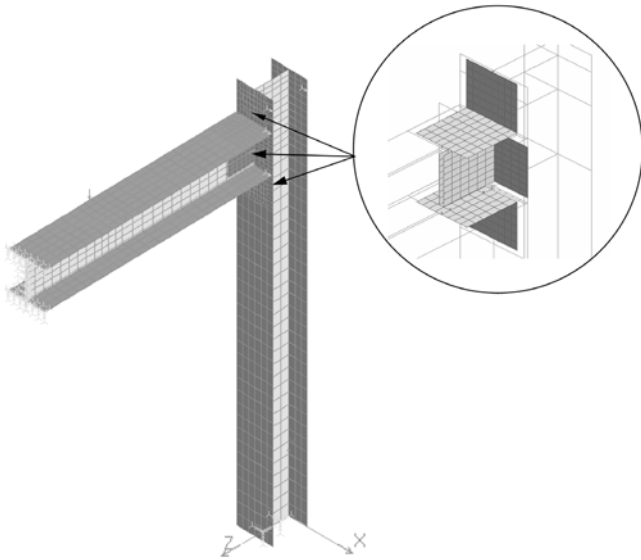
Figure 9-102. Isometric view of Model C-5.

angle, four of which were used between the vertical leg of the bottom angle and the inner flange of the column, while the other four were used between the horizontal leg of the angle and the bottom flange of the beam. All gap elements were placed in the areas where any compressing or prying actions were expected, and where greater supporting stiffness existed due to the existence of the webs of the beam and column. Table

A typical rigid
COSMOS/M BEAM3D
element
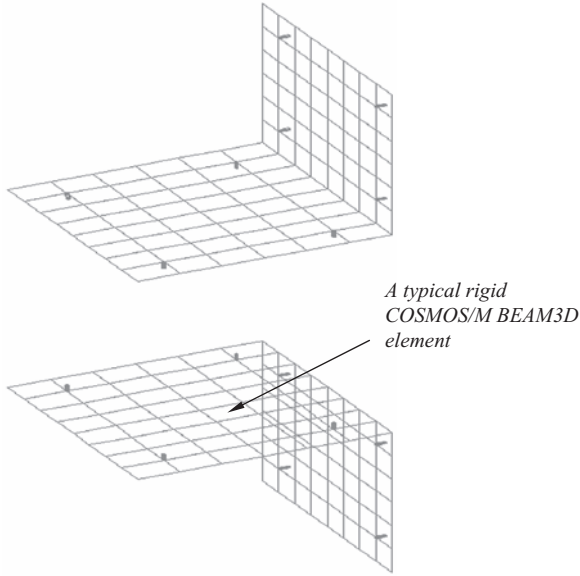
Figure 9-103. Modeling the top and bottom PFRP angles of Model C-5.

Table 9-9. Element Group and Real Constant Set Input Data
of the Gap Elements

```
Element Group :  10  ( GAP )
  Op1: Surface coord. update:0=No;1=Yes   . . . . . . . .  =   1
  Op2: Friction:0=No;1=Yes;2=Yes & Slide  . . . . . . . .  =   0
  Op3: Frict. outside X-Y plane:0=No;1=Yes   . . . . . . .  =   0
  Op4: Gap Type:0=N-N;1=N-L;2=N-S   . . . . . . . . . . .  =   0
  Op5: Unused option .  . . . . . . . . . . . . . . . . .  =   0
  Op6: Compressive gap measurement:0=User 1=Auto   . . . .  =   0
  Op7: Unused option .  . . . . . . . . . . . . . . . . .  =   0
  Op8: Unused option .  . . . . . . . . . . . . . . . . .  =   0
Real Constant Set :  19   (ACTIVE)
Associated Element Group :  10  ( GAP )

  Rc1  : Relative displ. between 2 nodes  . . . . . . =  0.000000e+000
  Rc2  : Coefficient of friction . . . . . . . . . . =  0.000000e+000
  Rc3  : Gap stiffness 0=No Spring k=Stiffness  . . . =  0.000000e+000
  Rc4  : Spring pre-load   . . . . . . . . . . . . . =  0.000000e+000
  Rc5  : Maximum spring deflection  . . . . . . . . . =  1.000000e+008
  Rc6  : Damping constant (c) . . . . . . . . . . . . =  0.000000e+000
  Rc7  : Damping constant (p) . . . . . . . . . . . . =  1.000000e+000
  Rc8  : Source stiffness in X-direction  . . . . . . =  0.000000e+000
  Rc9  : Source stiffness in Y-direction  . . . . . . =  0.000000e+000
  Rc10 : Source stiffness in Z-direction  . . . . . . =  0.000000e+000
```
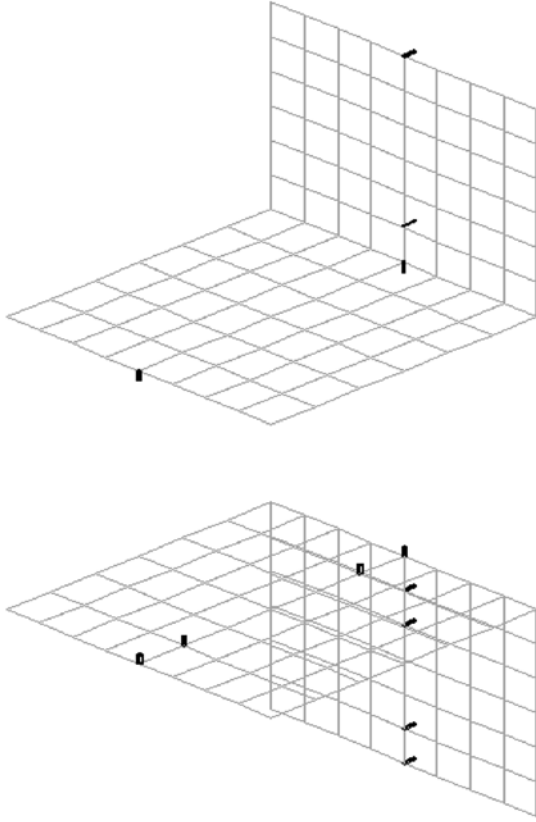
Figure 9-104. Modeling the two top and bottom angles of Model C-5.

9-9 presents the element groups and real constant set definitions of the gap elements. The arrangement of the gap elements appears in Fig. 9-104. According to this model, the maximum displacement at the girder mid-span was found to be 1.814 in. (4.61 cm) as shown in Fig. 9-105. The maximum rotational angle that occurred at the beam-to-column connection was found to be 0.048 rad (2.72 degrees), which was similar to that of Model C-4 (refer to Fig. 9-106).

Figure 9-107 shows the contours of the R_x rotational displacements of the connecting PFRP angles. The pattern of the R_x rotational displacement suggested that there was a need to stiffen the flange of both the beam and column at the beam-to-column connection. It is highly likely that the advantages of a stiffened connector would be greatly reduced due to the flexibility of the flanges of the PFRP open profiles.

The σ_x and τ_{xy} stress contour and vector plots of Model C-5 appear are shown in Figs. 9-108 and 9-109. The σ_x, σ_y stress plots of the four angle
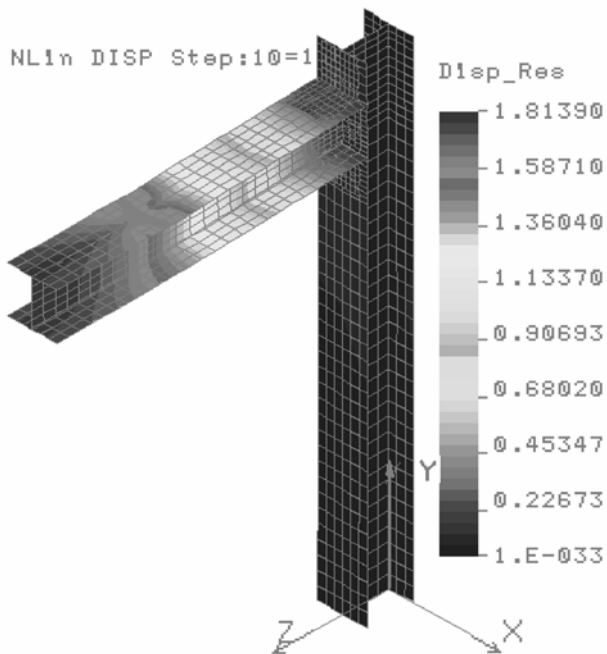
Figure 9-105. Vertical displacement contour (D_y) plot for Model C-5.
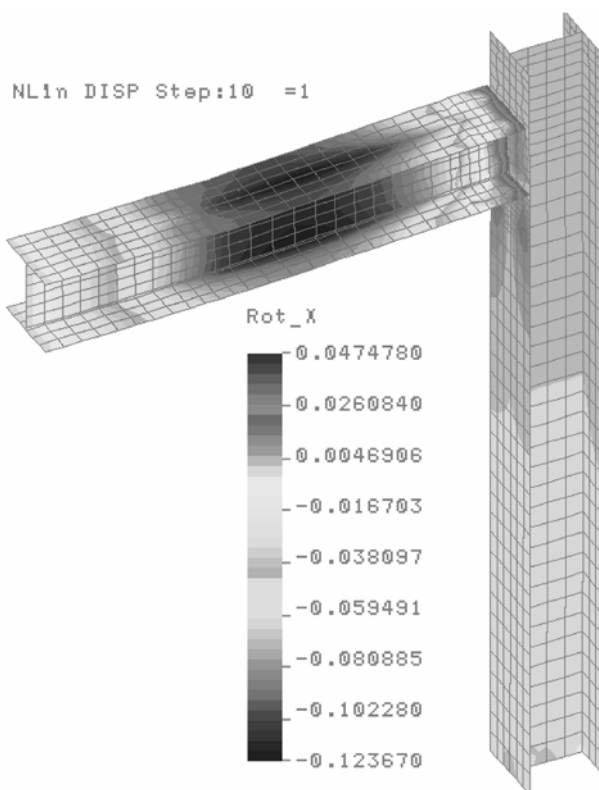
Figure 9-106. Rotational displacement contour (R_x) plot for Model C-5.
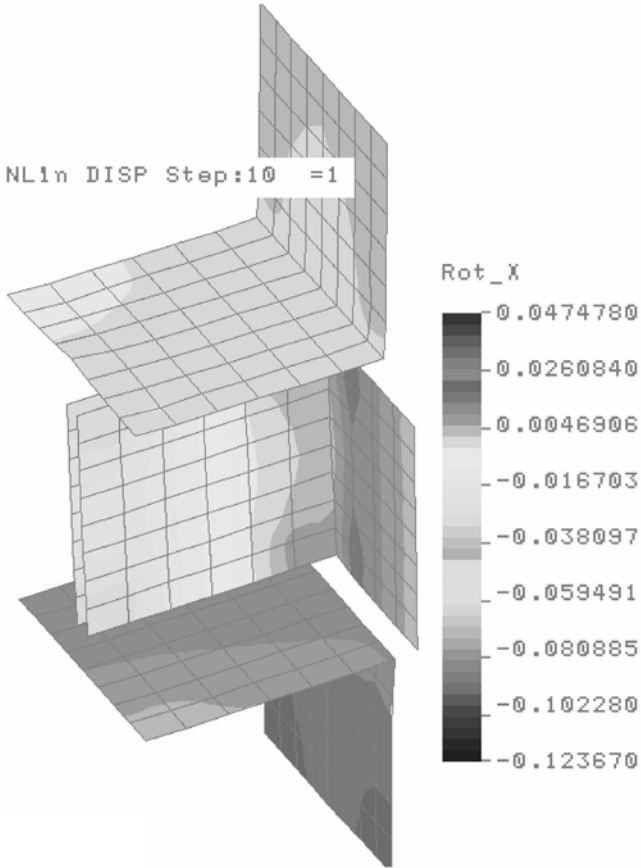
Figure 9-107. Rotational displacement (R_x) contour plot for the PFRP connecting angles (enlarged view).

brackets are shown in Figs. 9-110 through 9-113. The σ_y stress, which was in the weak material direction, was more than three times higher than the σ_x stress, which was in the stronger material direction. It is expected that the bending stiffness of the connecting elements (PFRP unidirectional angles) would be significantly increased if the fiber were used in the Y-direction (rather than the X-direction as used in the experimental program) as shown in Fig. 9-101. Figures 9-114 through 9-118 show, in detail, the σ_x stress distribution of a typical layer (layer 3) of the PFRP girder. The near-zero bending moment at the beam-to-column connection indicates that the beam-to-column connection was qualified for a hinged condition instead of a semi-rigid condition, as originally was assumed.
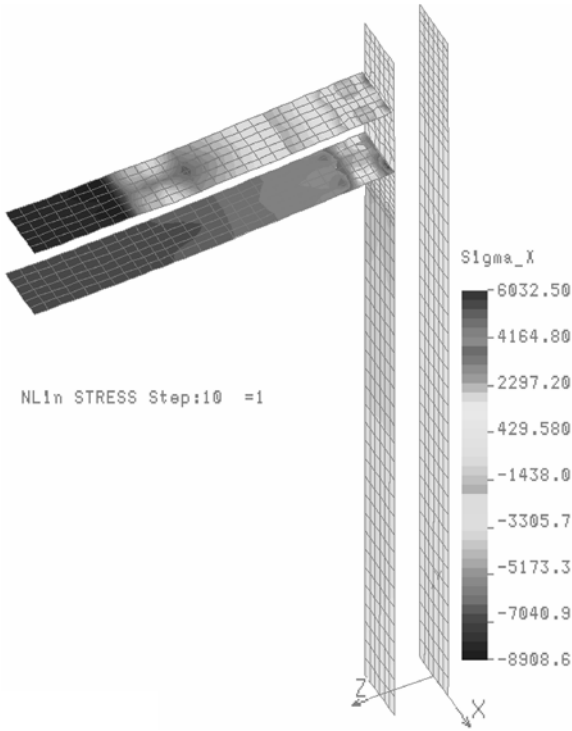
Figure 9-108. σ_x stress contour plot of the girder flange of Model C-5.

To isolate the effect of the semi-rigid beam-to-column connection over the behavior of the frame, an additional model, Model C-5A, was developed by directly connecting the flanges and web of the beam. This approach was the same as Model C-1 in dealing with the flanges and web junction. The beam-to-column connection was modeled the same way as in Model C-5 (with angle brackets and gap elements). Figure 9-119 shows the maximum displacement was reduced from the 1.814 in. (4.61 cm) of Model C-5 to the 1.497 in. (3.80 cm) of Model C-5A. It is obvious that the 0.317 in. (=1.814 in. − 1.497 in.) (0.805 cm) reduction of the maximum displacement was caused by the rigid or direct web-to-flange connectivity used in Model C-5A. However, the R_x rotational displacement at the beam-to-column connection area was increased from 0.048 rad (2.75 degrees) in Model C-5 to 0.062 rad (3.55 degrees) in Model C-5A (refer to Fig. 9-120). The increment of the R_x rotational displacement at the beam-to-column connection area may be attributed to the stiffened web-to-column junction (direct), which resulted in a larger bending moment at the beam-to-column connection. The displacement vector plot of Model

```
NL1n STRESS Step:10  =1
```

Tau_XY

	3142.10
	1636.60
	130.960
	-1374.6
	-2880.2
	-4385.8
	-5891.4
	-7397.0
	-8902.6
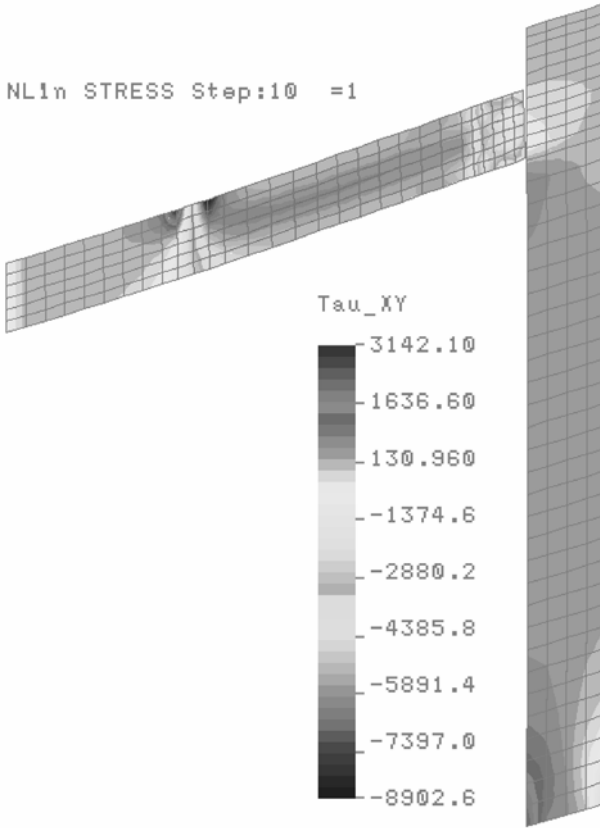
Figure 9-109. τ_{xy} stress contour plot of the girder web of Model C-5.

C-5A, shown in Fig. 9-119, indicates that displacement of the top of column, due to bending, was increased when compared with that of Model C-5, as shown in Fig. 9-105. The σ_x stress plot of Model C-5A appears in Fig. 9-121.

To evaluate the effect of the flexibility of the column on the behavior of the beam, an FEA model of the beam (Model C-5B) was developed by simply removing the column from Model C-5 and modeling the beam alone with both ends supported by the same angle brackets as used in Model C-5. Figure 9-122 shows that the maximum displacement of the beam reduced from the 1.814 in. (4.61 cm) of Model C-5 to the 1.764 in. (4.48 cm) of Model C-5B. This 2.8% or 0.05 in. (=1.814 in. − 1.764 in.) (0.127 cm) reduction of the maximum displacement may have been caused by the flexibility of the column, which was negligible in this case.
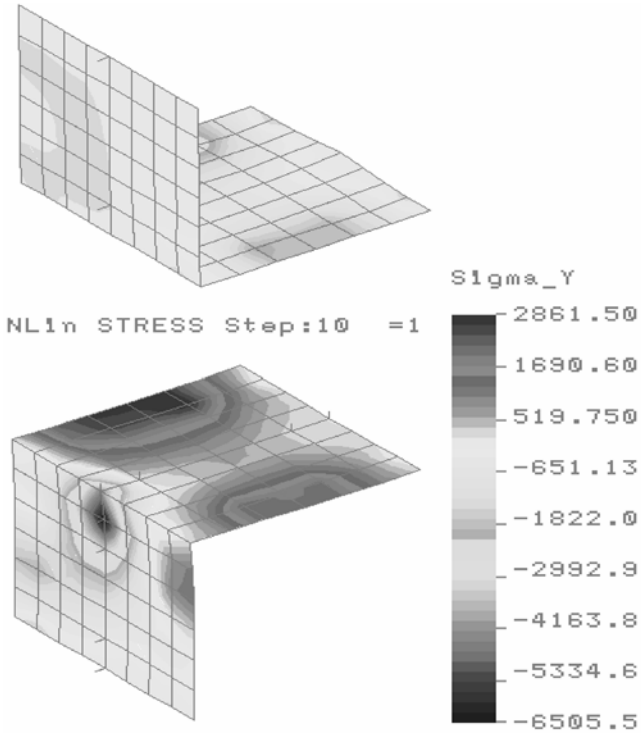
Figure 9-110. σ_y stress contour plot of top and bottom angles (moment connectors).

9.6.3.6 Model C-6: Simulating the Semi-rigid Beam-to-column Connection Assumptions by Using Rotational Spring Elements. This model was identical to Model C-3 as previously described, except for changing the modeling of the semi-rigid beam-to-column connection by using a single one-node rotational spring element.

Instead of using two one-node axial spring elements as in Model C-3, the semi-rigid beam-to-column connection was modeled with a single one-node rotational spring element, as previously presented in the study Case III of Section 9.6.2.1. The experimental M/θ curve shown in Fig. 9-35 was used directly as the rotational stiffness for the one-node rotational spring element, which represents the rotational stiffness of the beam-to-column connection. A description of this model is illustrated in Figs. 9-123 through 9-125. Figure 9-126 shows the full-range material property curve (MPC) defined for the one-node rotational spring element.

A single rigid COSMOS/M BEAM3D element was used to connect the web of beam to the flange of column. as shown in Fig. 9-124. This rigid
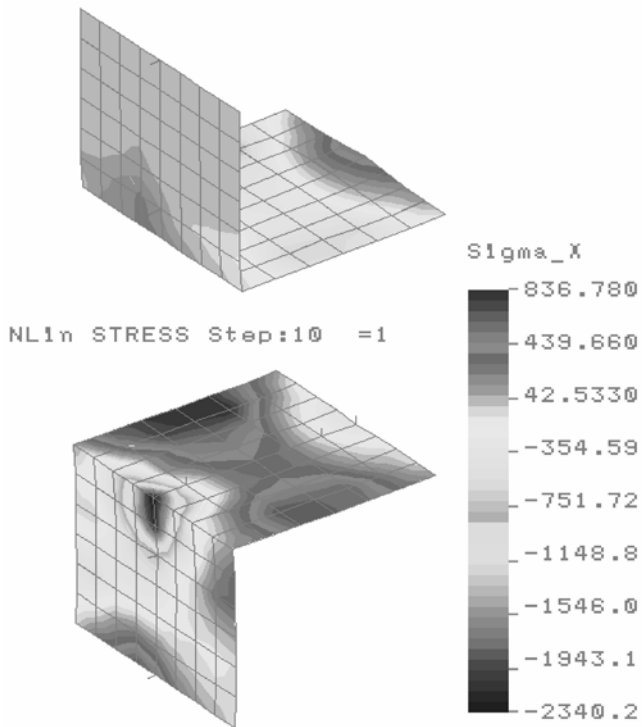
Figure 9-111. σ_x stress contour plot of the top and bottom angles (moment connectors).
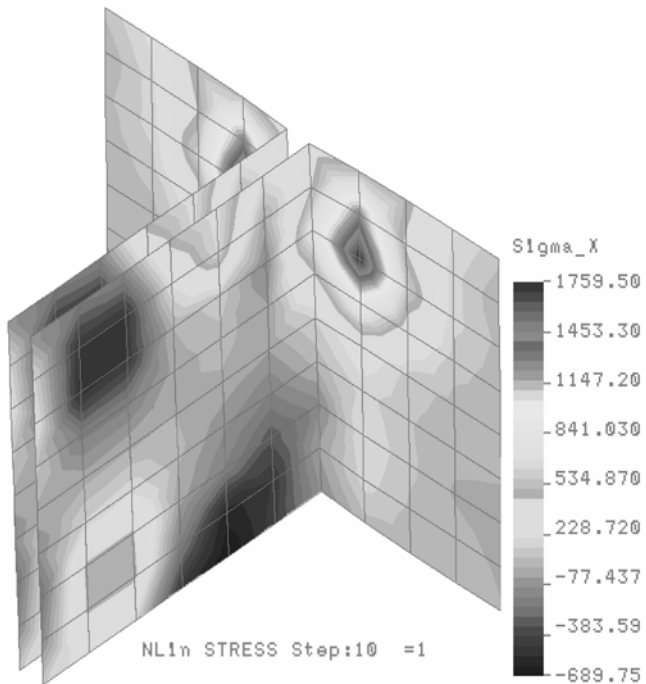
Figure 9-112. σ_x stress contour plot of the middle back-to-back angle (shear connector angles).
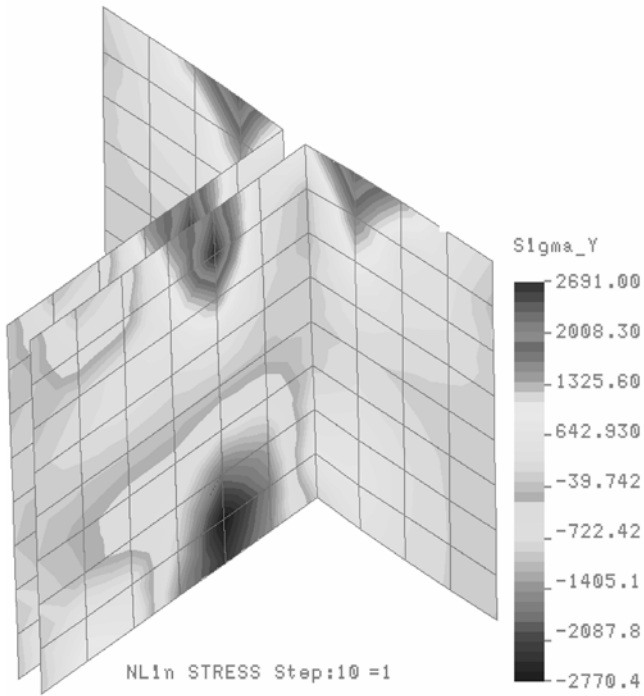
Figure 9-113. σ_y stress contour plot of the middle back-to-back angle (shear connector angles).

Figure 9-114. Model C-5.

NL1n STRESS Step:10   =1
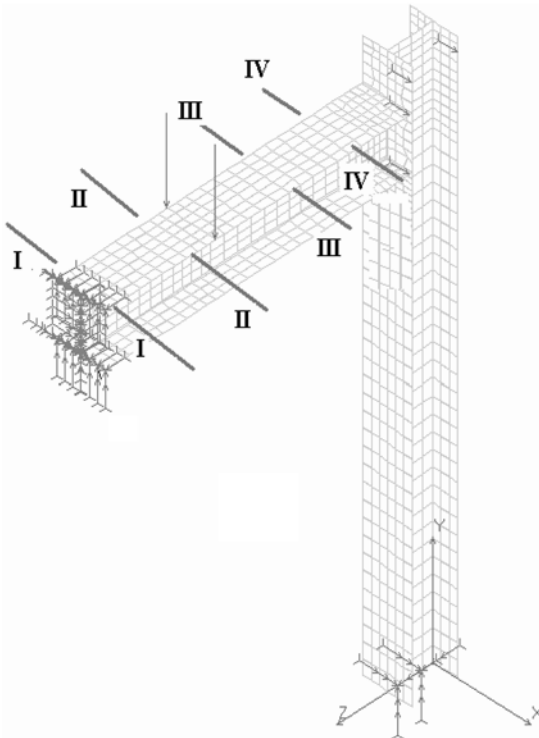
Sigma_X
8746.10
7280.80
5815.50
4350.20
2884.90
1419.60
-45.729
-1511.0
-2976.3
-4441.6
-5906.9
-7372.2
-8837.5
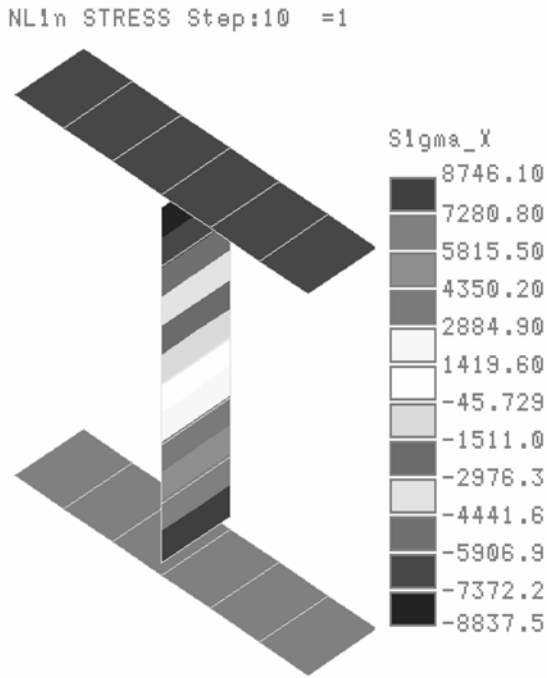
Figure 9-115. Layer 3 σ_x stress contour plot of Section I-I (refer to Fig. 9-120 for section location).

NL1n STRESS Step:10   =1

Sigma_X
9014.90
7533.20
6051.60
4569.90
3088.30
1606.60
124.960
-1356.7
-2838.3
-4320.0
-5801.6
-7283.3
-8764.9
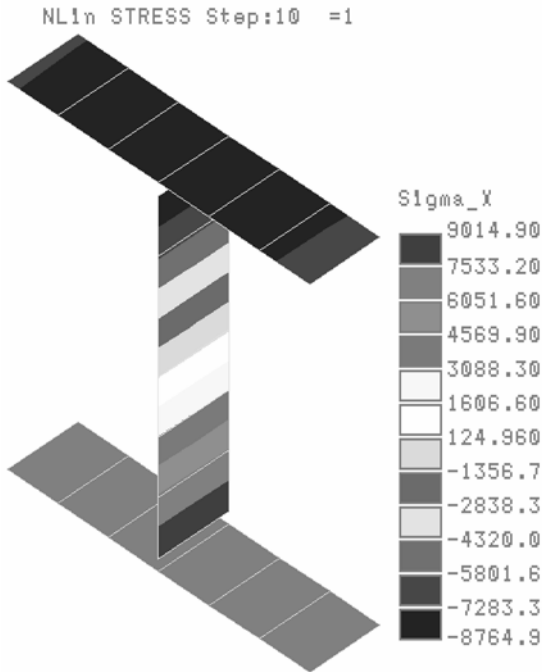
Figure 9-116. Layer 3 σ_x stress contour plot of Section II-II (refer to Fig. 9-120 for section location).
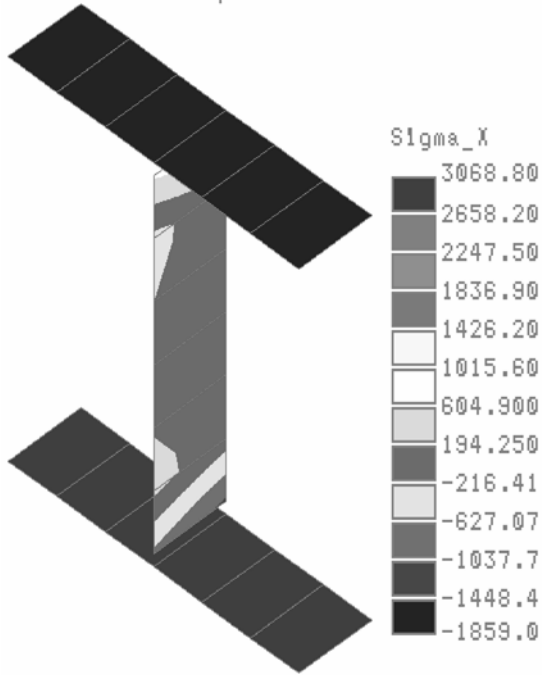
Figure 9-117. Layer 3 σ_x stress contour plot of Section IV-IV (refer to Fig. 9-120 for section location).
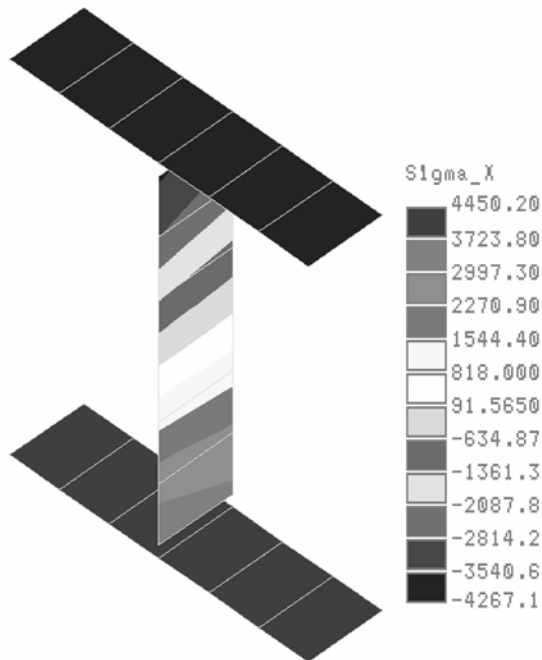
Figure 9-118. Layer 3 σ_x stress contour plot of Section III-III (refer to Fig. 9-120 for section location).

NL1n DISP Step:10 =1

Disp_Res

- 1.49650
- 1.30940
- 1.12230
- 0.93529
- 0.74823
- 0.56117
- 0.37411
- 0.18706
- 1.E-033
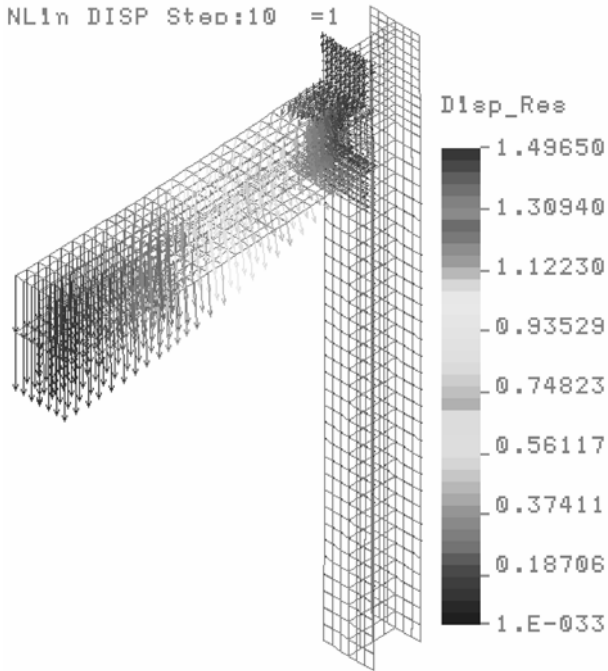
Figure 9-119. Displacement vector plot of Model C-5A (direct flange-web junction).

NL1n DISP Step:10 =1

Rot_X

- 0.06197600
- 0.05349000
- 0.04500300
- 0.03651700
- 0.02803100
- 0.01954400
- 0.01105800
- 0.00257140
- -0.0059149
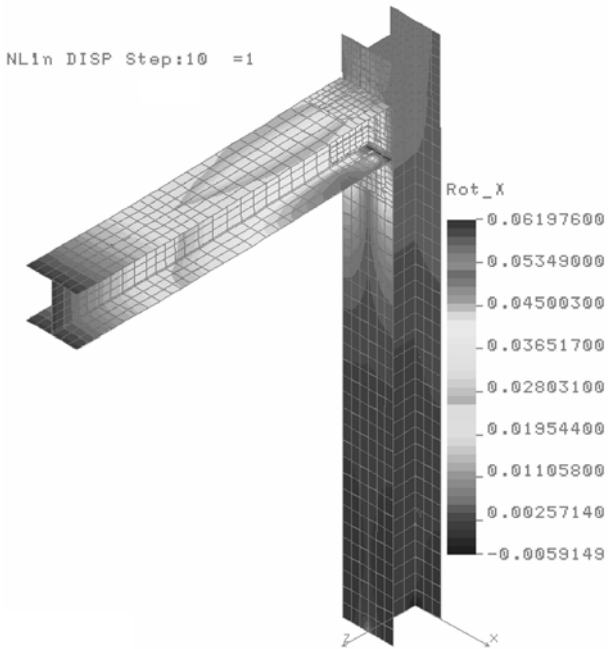
Figure 9-120. Rotational displacement (R_x) contour plot of Model C-5A (direct flange/web junction).
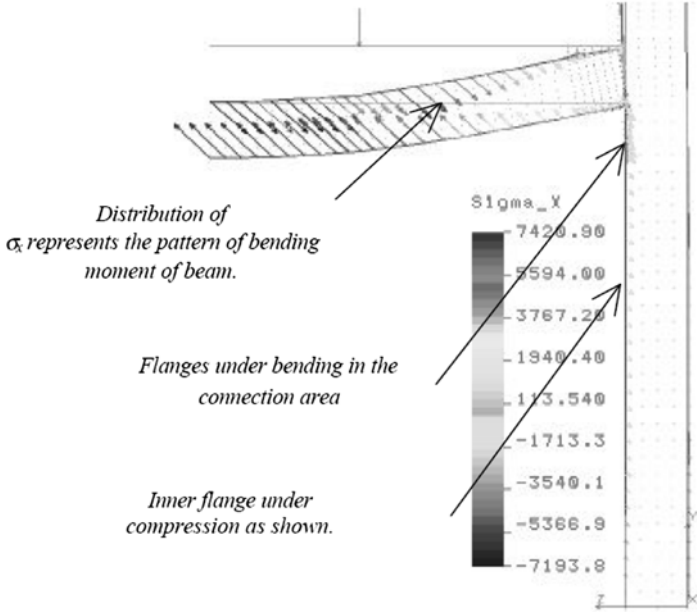
Figure 9-121. σ_x vector plot of Model C-5A (direct flange-web junction).
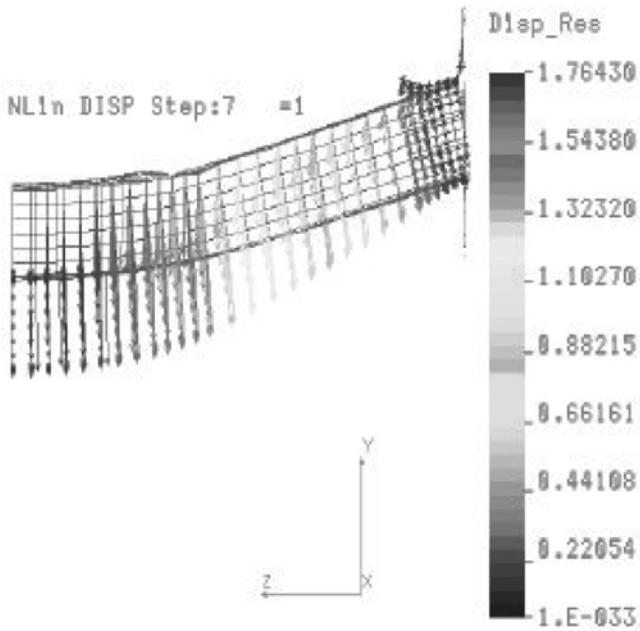
Figure 9-122. Displacement vector plot of Model C-5B (angle brackets are shown while columns removed).

Figure 9-123

$P/2$ $P/2$

Dummy
BEAM3D
elements

One one-node
rotational
spring element
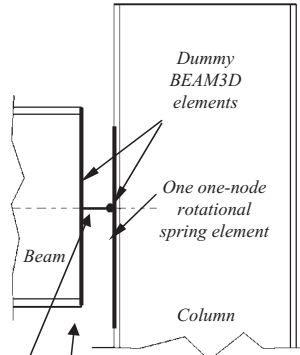
Beam

Column

Figure 9-124

One rigid BEAM3D element with R_x rotational DOF
at the right-hand end released, where the one-node
rotational spring element was located.
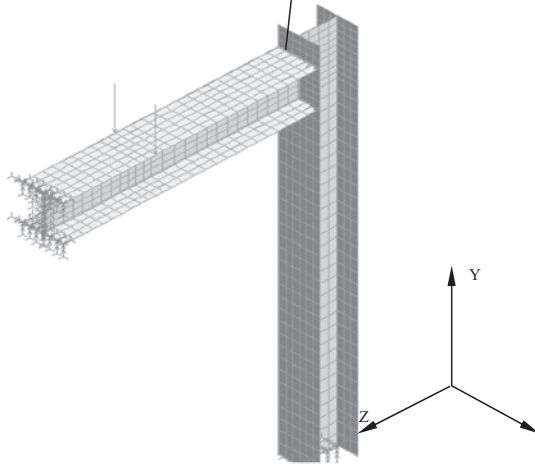
Figure 9-125

Figure 9-123 (top left). Idealized diagram of Model C-6 (semi-rigid beam-column connection assumed). Figure 9-124 (top right). Graphical illustration of the beam-column connection. Figure 9-125 (bottom). Isometric view of Model C-6.
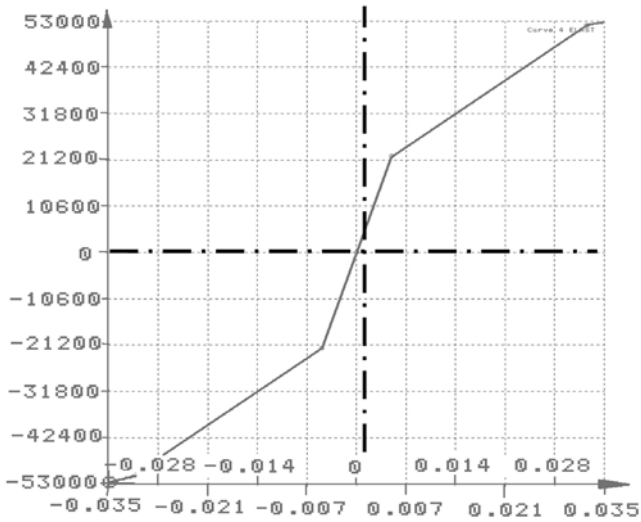
Figure 9-126. Full-range material property curve (MPC) of the one-node rotational spring element defined from the M/θ curve shown in Fig. 9-35.

BEAM3D element was released at the R_x rotational DOF at the right-hand end, where a one-node rotational spring element was located. To ensure the moment-bearing capability at the beam-to-column connection, some dummy BEAM3D elements with limited amount of stiffness for all six degrees of freedom were used (Fig. 9-123).

Based on this model, the maximum displacement at the girder's midspan was found to be 1.555 in. (3.95 cm) as shown in Fig. 9-127. The maximum rotation angle (R_x) was found to be 0.1342 rad (7.69 degrees), which was less than the 0.198 rad (11.345 degrees) obtained from Model C-2, as shown in Figs. 9-128 and 9-129. The maximum rotational angle occurred at the location of the one-node rotational spring element of the beam-to-column connection. Evaluation of the output file indicated that the rotational moment of the one-node rotational spring element was found to be 323 lb-in. (0.0365 kN-m), which was almost equivalent to a hinged beam-column connection condition [when compared with the 300,000 lb-in. (33.87 kN-m) of the maximum bending moment at the fixed ends]. It should be noted that the 323 lb-in. accounts for about 0.1% of a rigid support condition. As mentioned earlier, the maximum displacement of Model C-2, under a hinged beam-to-column connection assumption, was 1.624 in. (4.12 cm). The hinged-like behavior of Model C-6 can be attributed to the limited rotational stiffness (R_x) of the thin-walled cross section of the beam and column at the beam-to-column connection.
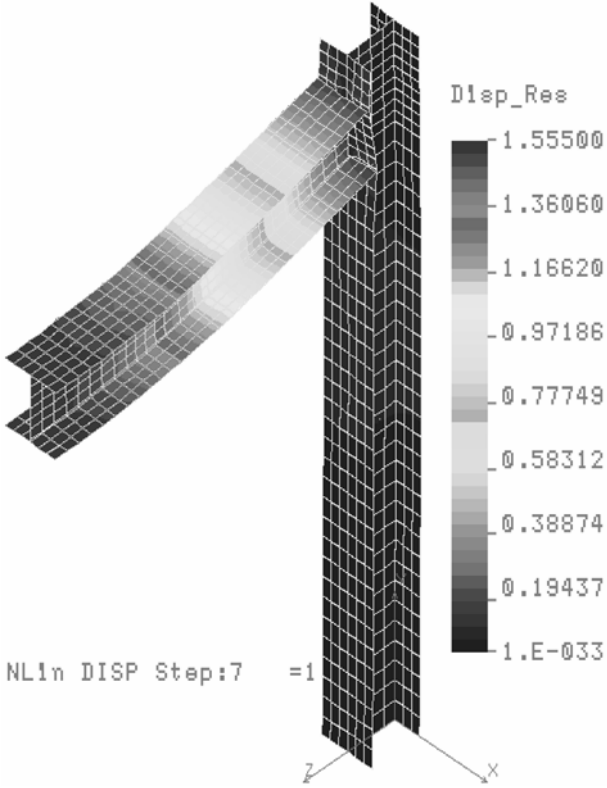
Figure 9-127. Displacement contour plot of Model C-6 (40-color contour).

Model C-6A was developed to investigate the effect of the rotational stiffness (R_x) of the thin-walled web of the beam at the beam-to-column connection. This model was developed by replacing the dummy BEAM3D element on Model C-6 with the rigid BEAM3D elements. The maximum displacement of Model C-6A was reduced from the 1.56 in. (3.95 cm) of Model C-6 to 1.49 in. (3.79 cm), as shown in Fig. 9-130. The most significant change of Model C-6A over Model C-6 was that the R_x rotational displacement was reduced from the 0.1342 rad (7.69 degrees) of Model C-6 to 0.0466 rad (2.67 degrees) of Model C-6A, as shown in Fig. 9-131. As shown in Fig. 9-131, the maximum relative rotational displacement (R_x) between the tips of the flanges and the web of the beam at the beam-to-column connection was found to be 0.013 rad (0.38 rad − 0.25 rad), or 0.74 degrees. The large relative rotational displacement (R_x) between the tips of the flanges and the web of the beam was caused by the rigid BEAM3D elements used at the end of web, which made the web of the beam behave as a rigid body when it rotated around the one-node rotational spring element.
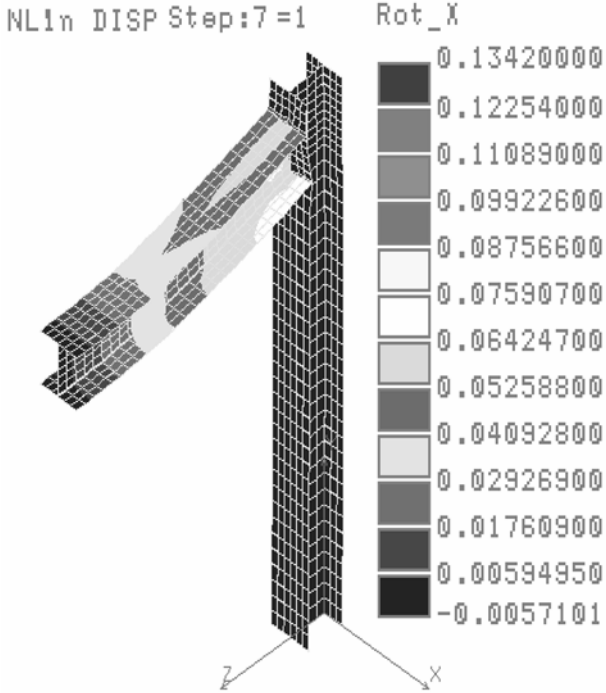
Figure 9-128. R_x rotational displacement contour plot of Model C-6—View 1.
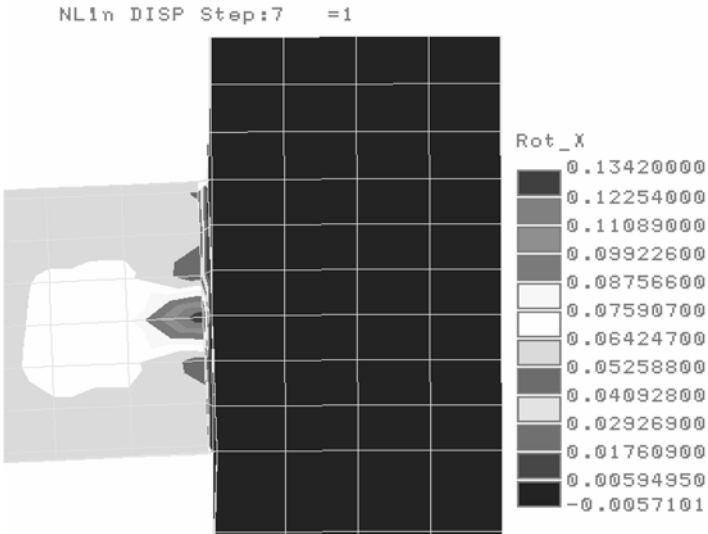
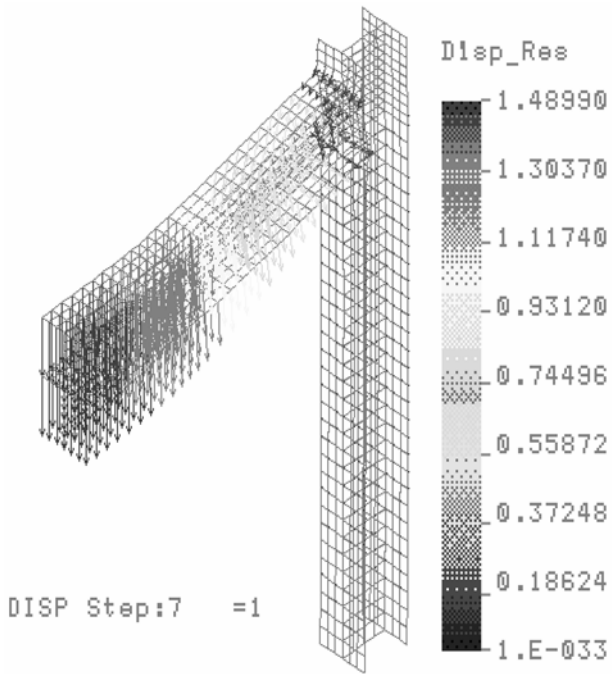*Figure 9-129. Rotational displacement (R_x) contour plot of Model C-6—View 2.*

Figure 9-130. Displacement vector plot of Model C-6A (dummy beam elements replaced with rigid beam element).
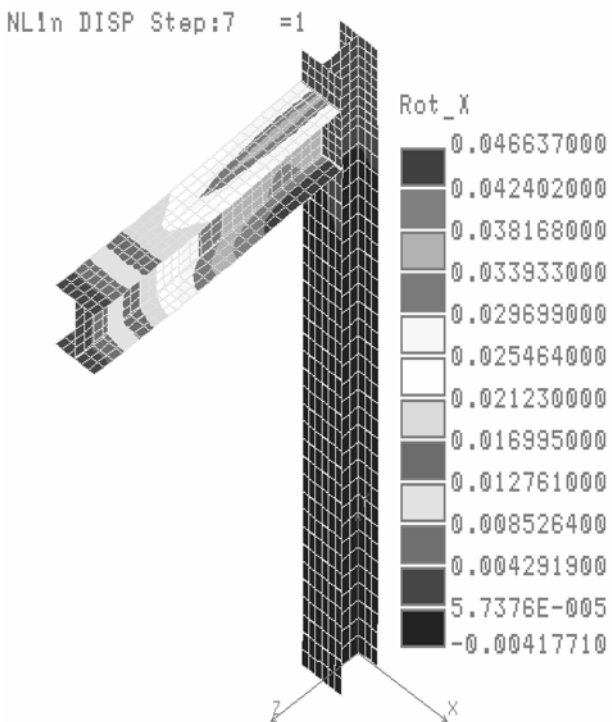

Figure 9-131. Rotational displacement contour plot of Model C-6A (dummy beam elements replaced with rigid beam element).

Model C-6B was developed to evaluate the effect of the stiffness of the thin-walled flange of the beam at the beam-to-column connection. This model was developed by adding additional rigid BEAM3D elements, shown in Fig. 9-132. The maximum displacement of Model C-6B was found to be 1.456 in. (3.70 cm), which was 0.10 in. (0.254 cm) less than that of Model C-6. The rotational displacement (R_x) of the girder at the beam-to-column connection was further reduced to 0.0364 rad (2.09 degrees) from the 0.0466 rad (2.67 degrees) of Model C-6A (refer to Fig. 9-133).

To evaluate the effect of the column on the behavior of the beam, Model C-6C (a beam of Model C-6) was developed by removing the column from Model C-6 and analyzing the beam with flexible end supports. The maximum displacement of the beam was found to be 1.481 in. (3.76 cm), shown in Fig. 9-134, which was 0.074 in. (0.188 cm), or 5% less than that of Model C-6. The difference in displacement between the column, Model C-6, and that of the beam,Model C-6C, may be attributed to the flexibility of the column under the specified boundary conditions.

9.6.4 Comparison of Experimental and Nonlinear Numerical Analysis Results Using COSMOS/M Finite Element Code with Experimental Results. For ease of evaluation and comparison, all of the FE models developed and analyzed earlier have been summarized and presented in Table 9-10.
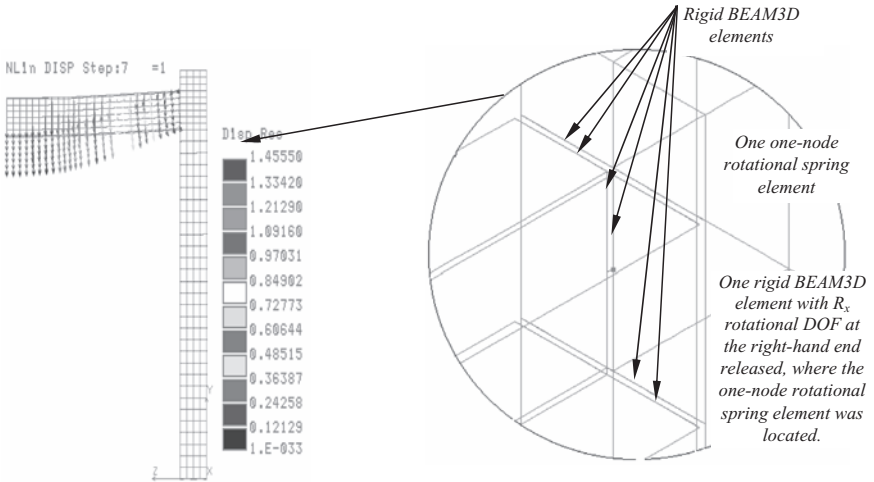

Figure 9-132. The maximum displacement contour plot of Model C-6B (dummy beam is replaced with rigid beam and additional rigid BEAM3D elements added on the top and bottom).
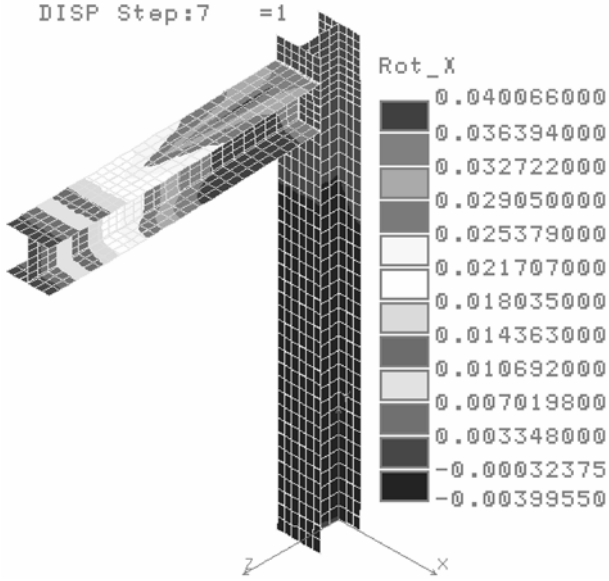
Figure 9-133. Rotational displacement (Rₓ) contour plot of Model C-6B (dummy beam is replaced with rigid beam and additional rigid BEAM3D elements added on the top and bottom).
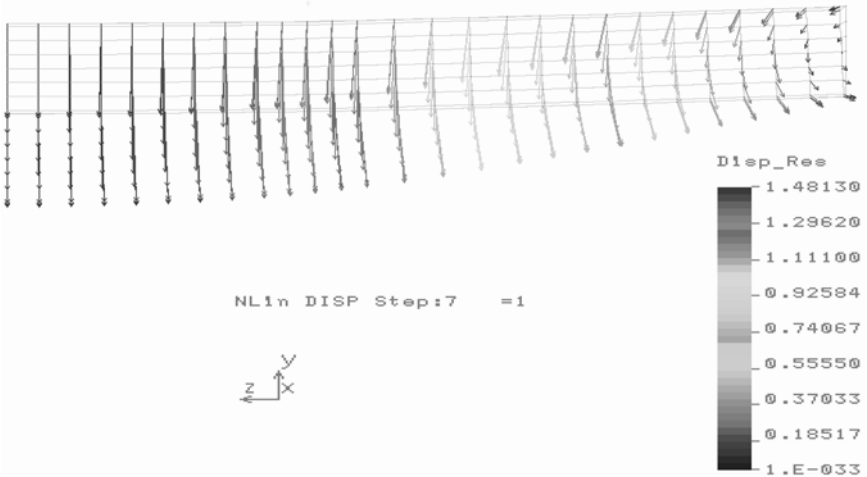

Figure 9-134. Displacement vector plot of Model C-6C (or beam of Model C-6, with column being removed).

Table 9-10. List of All the Finite Element Models

Name of Model	Flange-to-Web Junction	Beam-to-Column Connection
Model C-1	Direct connection	Direction connection
Model C-1A (beam)	Direct connection	Direction connection
Model C-2	Direct connection	Hinged
Model C-2A (beam)	Direct connection	Same as Model C-2
ModelC-3	Direct connection	Semi-rigid connection by using two one-node axial spring elements with real stiffness or experimental M/θ curve
Model C-3A (beam)	Direct connection	Same as Model C-3
Model C-4	Semi-rigid connection by using 54 pieces of nonlinear rotational spring elements	Same as Model C-3
Model C-4A (beam)	Same as Model C-4	Same as Model C-4
Model C-5	Same as Model C-4	Four PFRP angle brackets modeled, and 10 gap elements
Model C-5A	Direct connection	Same as Model C-5
Model C-5B (beam)	Direct connection	Same as Model C-5
Model C-6	Direct connection	One nonlinear rotational spring element (with dummy BEAM3D elements)
Model C-6A	Direct connection	One nonlinear rotational spring element (with rigid BEAM3D elements)
Model C-6B	Direct connection	Same as Model C-6 with rigid BEAM3D elements added on the top and bottom flanges
Model C-6C (beam)	Direct connection	Same as Model C-6

To verify the numerical models, a comparison of full-scale experimental test data and the closed-form solution results was performed (Mosallam 1990). Table 9-11 and Figs. 9-136 through 9-142 show the experimental, analytical, and numerical deflection values at the mid-span of the frame girder, or node 33, identified in Fig. 9-135.

The following conclusions are based on the results presented in Table 9-11 and Figs. 9-136 through 9-142:

- Model C-1 can be used for a simple and rigid analysis for PFRP frame structure under any loading conditions.
- Model C-2 can be used for more accurate analysis of frame structures with hinged beam-to-column connection under pure bending.
- Model C-4 can be used for even more accurate results of a limited-size frame structure with hinged beam-to-column connection under pure bending.
- Model C-5 can be used for the most accurate results of a limited-size frame structure connection study, for example, under any loading conditions.
- Model C-6 can be used for more accurate analysis of frame structures with hinged beam-to-column connection under any loading conditions.

Table 9-11. Comparison of Experimental Maximum
Mid-Span Displacement with Theoretical Results from Different
Finite Element Models

Loads, lb.		Displacement, inch										
	0	2500	5000	7500	10000	12500	15000	17500	20000	22500	25000
Experimental(L3)[4]	0	0.175	0.35	0.525	0.7	0.9	1.1	1.35	1.65	2	2.45
Analytical-Rigid[4]	0	0.125	0.25	0.375	0.5	0.625	0.75	0.875	1	1.125	1.25
Analytical-Semi-Rigid[4]	0	0.225	0.45	0.675	0.9	1.125	1.35	1.6375	1.925	2.2125	2.5
Model C-1@node33	0	0.123	0.246	0.37	0.4928	0.616	0.7392	0.8624	0.9856	1.1088	1.232
Model C-1A*	0	0.058	0.116	0.174	0.2316	0.2895	0.3474	0.4053	0.4632	0.5211	0.579
Model C-2@node33	0	0.162	0.325	0.487	0.6496	0.812	0.9744	1.1368	1.2992	1.4616	1.624
Model C-2**	0	0.147	0.293	0.44	0.5868	0.7335	0.8802	1.0269	1.1736	1.3203	1.467
Model C-3@node33	0	0.161	0.321	0.482	0.642	0.8025	0.963	1.1235	1.284	1.4445	1.605
Model C-3***	0	0.127	0.253	0.38	0.5133	0.6467	0.78	0.9205	1.061	1.2015	1.342
Model C-4@node33	0	0.176	0.352	0.528	0.704	0.88	1.056	1.232	1.408	1.584	1.76
Model C-4	0	0.171	0.343	0.514	0.6852	0.8565	1.0278	1.1991	1.3704	1.5417	1.713
Model C-5@node33	0	0.181	0.363	0.544	0.7256	0.907	1.0884	1.2698	1.4512	1.6326	1.814
Model C-5A@node33	0	0.15	0.299	0.449	0.5988	0.7485	0.8982	1.0479	1.1976	1.3473	1.497
Model C-5	0	0.176	0.353	0.529	0.7056	0.882	1.0584	1.2348	1.4112	1.5876	1.764
Model C-6@node33	0	0.156	0.311	0.467	0.622	0.7775	0.933	1.0885	1.244	1.3995	1.555
Model C-6A@node33	0	0.149	0.298	0.447	0.596	0.745	0.894	1.043	1.192	1.341	1.49
Model C-6B@node33	0	0.146	0.291	0.437	0.5824	0.728	0.8736	1.0192	1.1648	1.3104	1.456
Model C-6C	0	0.148	0.296	0.444	0.5924	0.7405	0.8886	1.0367	1.1848	1.3329	1.481

[a] [4] refers to experimental and analytical work undertaken in relation to the extensive simulation program.
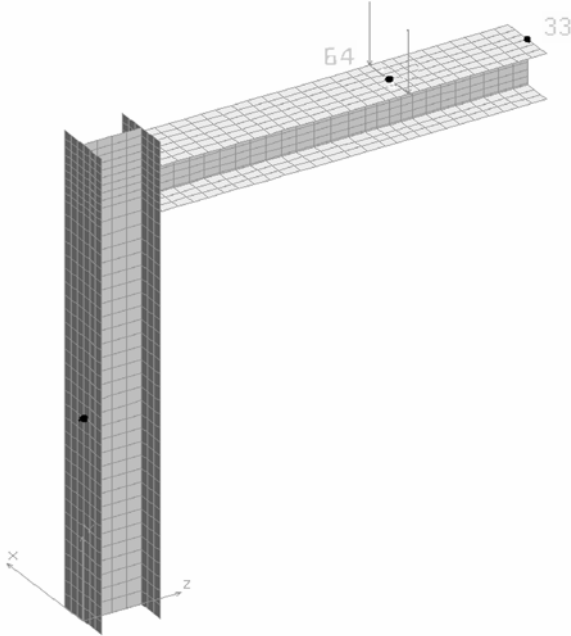
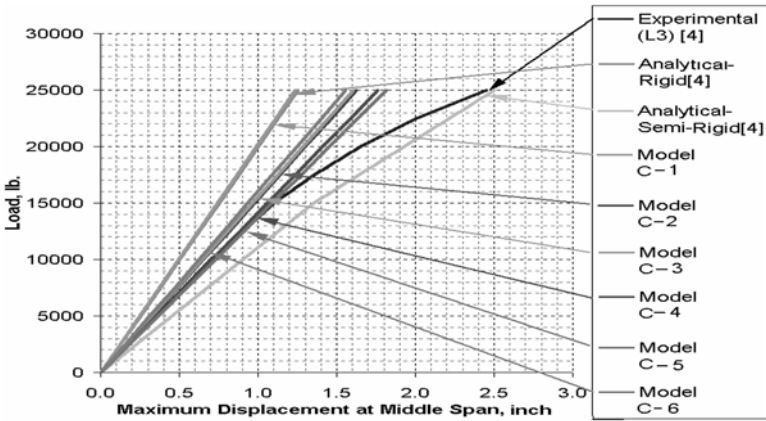*Figure 9-135. Location of node 33 (middle span) and node 64 (loading point).*

Figure 9-136. Maximum displacement comparison of all models.

- Linear analysis may yield results similar to nonlinear analysis.
- The use of FE investigation will save significant resources in future PFRP research.
- The use of FE techniques allows the user to easily evaluate the effect of structural modifications on the measured response (e.g., load–displacement).
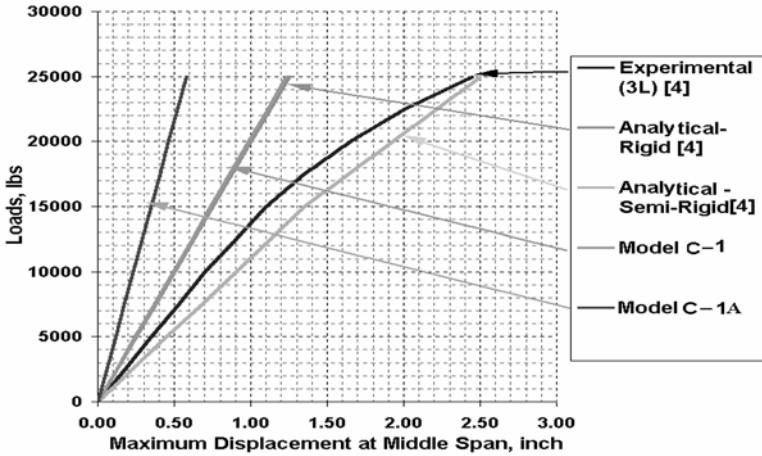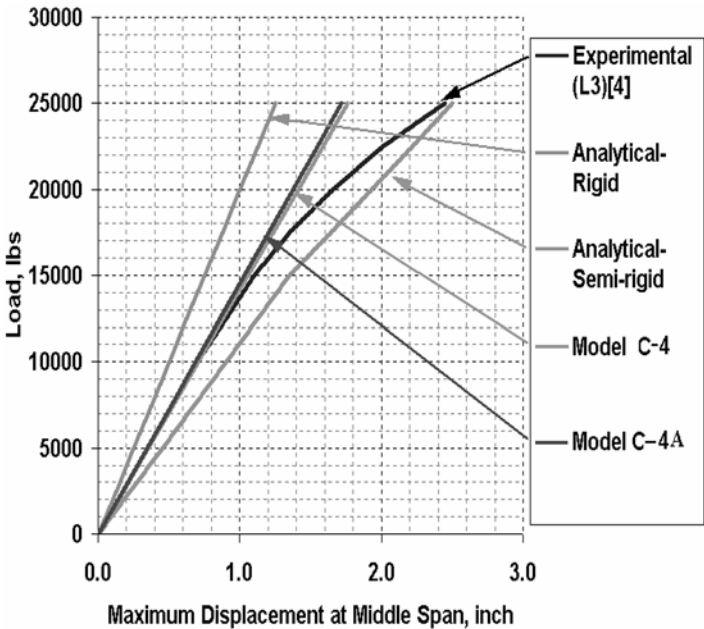
Figure 9-137. Maximum displacement comparison between Models C-1 and C-1A.
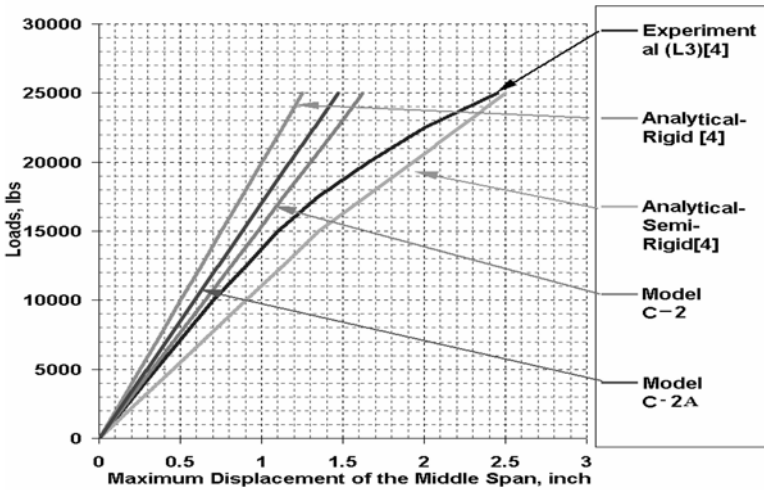
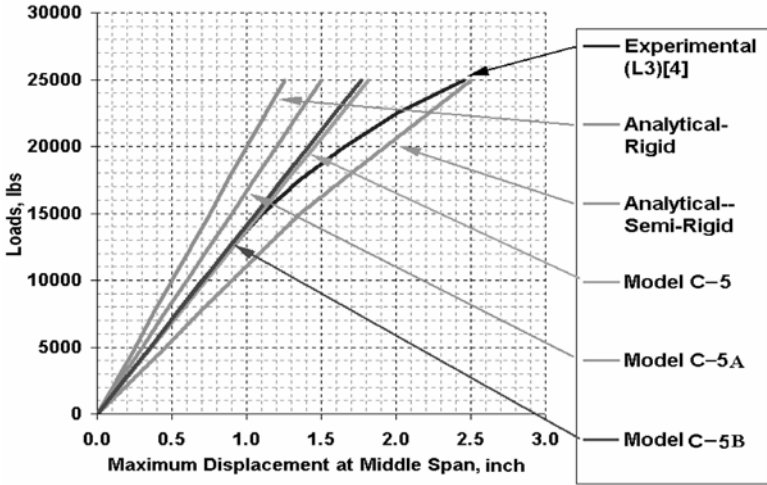*Figure 9-138. Maximum displacement comparison between Models C-2 and C-2A.*

9.6.5 A Parametric Study. Using similar modeling techniques adopted for the single-bay/single-story PFRP portal frame described earlier (Model C-1 and Model C-6), several runs were performed in other PFRP frames with different geometries. Figures 9-143 through 9-152 present results of these runs. To validate the numerical results, full-scale tests are needed.
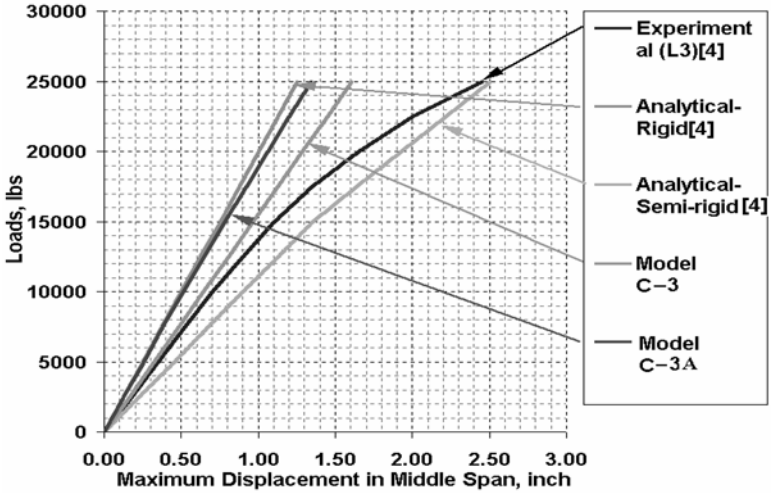
Figure 9-139. Maximum displacement comparison between Models C-3 and C-3A.

Figure 9-140. Maximum displacement comparison between Models C-4 and C-4A.

Figure 9-141. Maximum displacement comparison between Models C-5, C-5A, and C-4B.
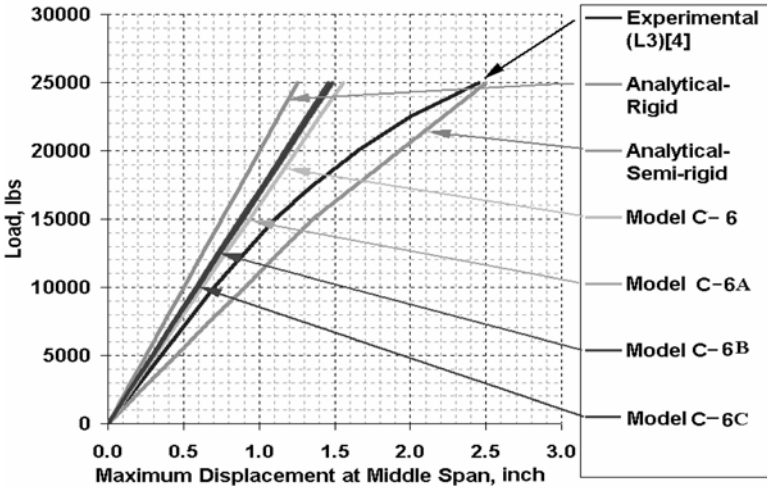

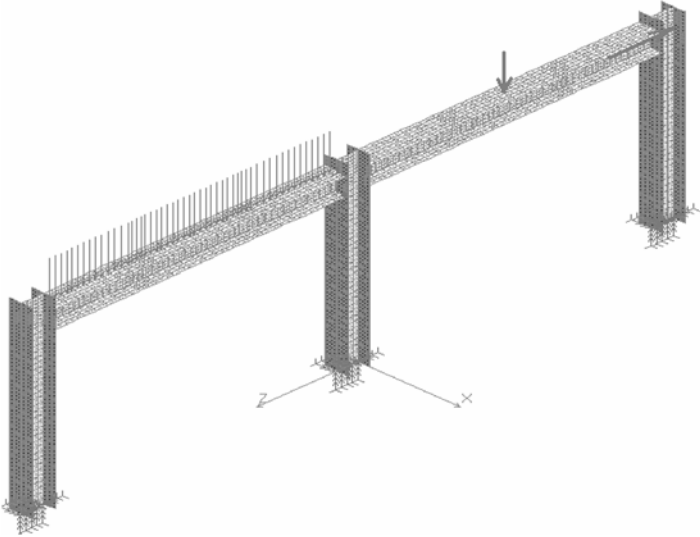*Figure 9-142. Maximum displacement comparison between Models C-6, C-6A, and C-6B.*

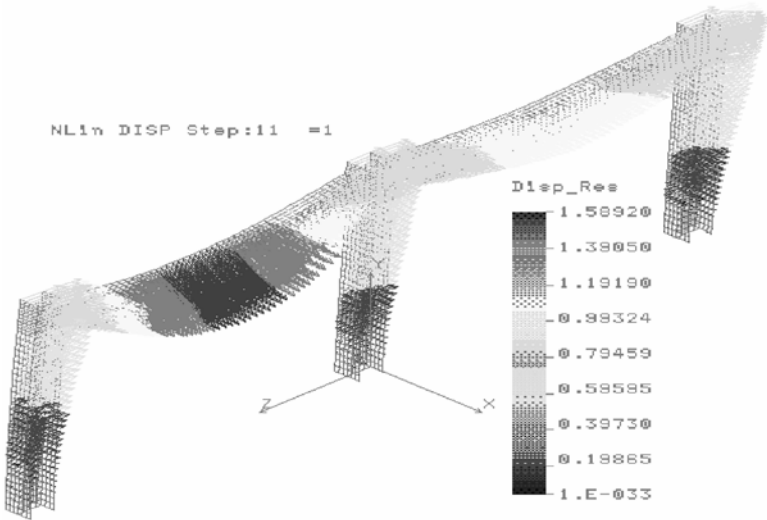*Figure 9-143. Two-bay/single-story PFRP frame modeled using Model C-6 approach.*

Figure 9-144. Deformed shape and displacement vector plot of the two-bay/single-story PFRP frame.
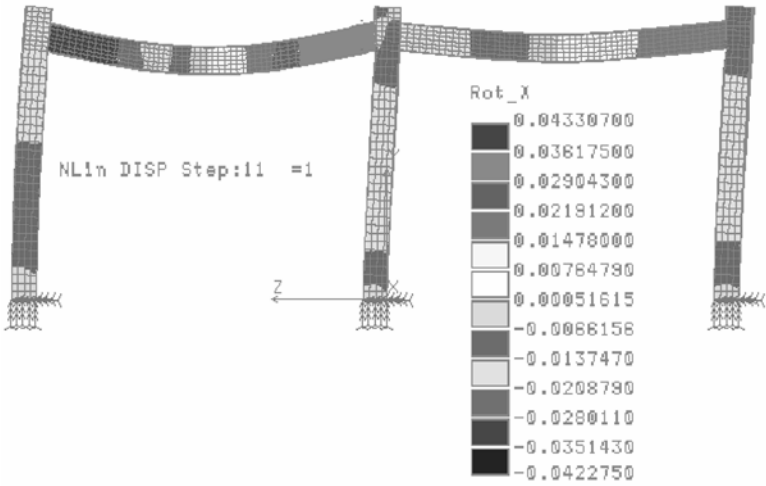
Figure 9-145. Rotational displacement (R_x) contour plot of two-bay/single-story PFRP frame (normal view).
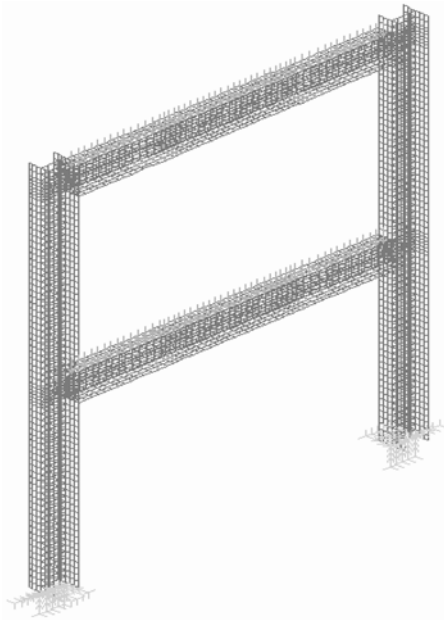

Figure 9-146. Single-bay/two-story PFRP frame modeled using Model C-6 approach (gravity load only).
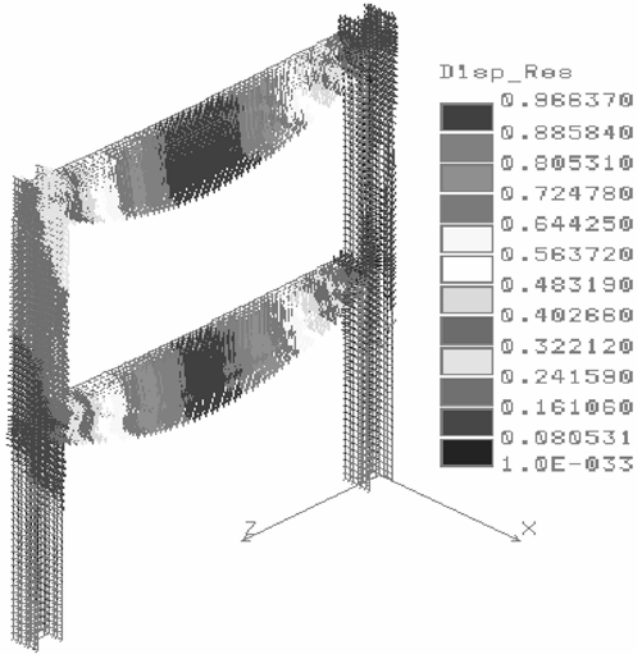
Figure 9-147. Deformed shape and displacement vector plot of the single-bay/two-story PFRP frame (gravity load only).
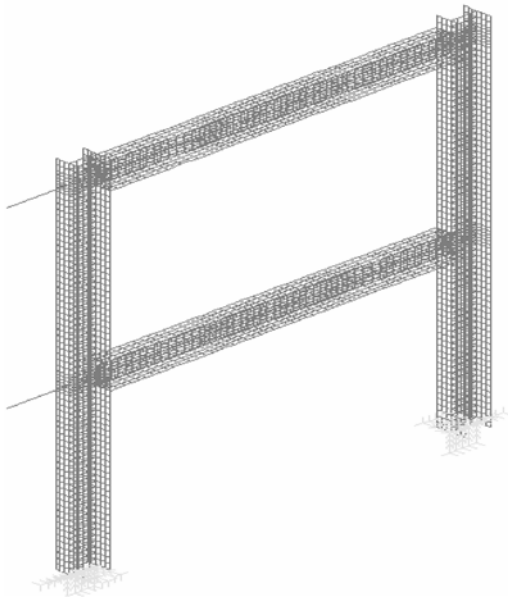

Figure 9-148. Single-bay/two-story PFRP frame modeled using Model C-6 approach (lateral load only).
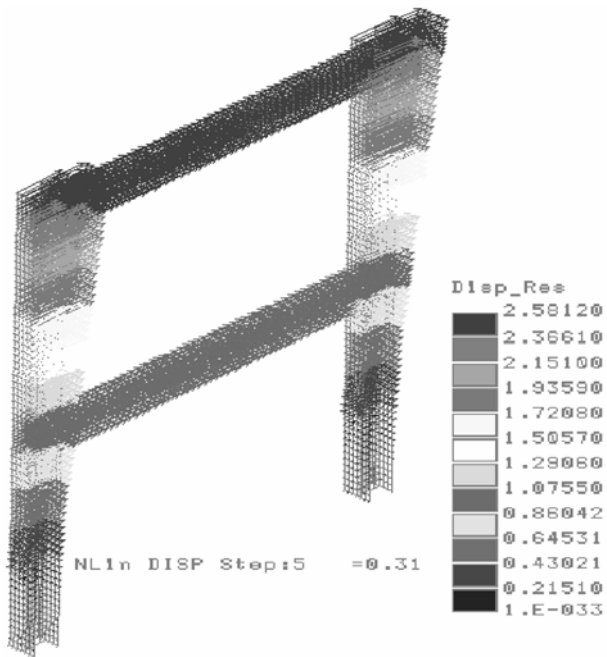
Figure 9-149. Deformed shape and displacement vector plot of the single-bay/two-story PFRP frame (lateral load only).

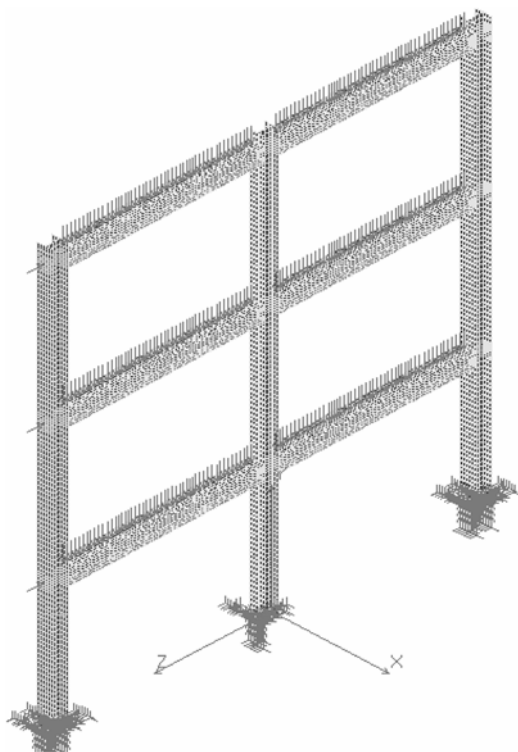Figure 9-150. Two-bay/three-story PRFP frame modeled using Model C-1 approach (direct connection) (gravity and lateral combined loads).
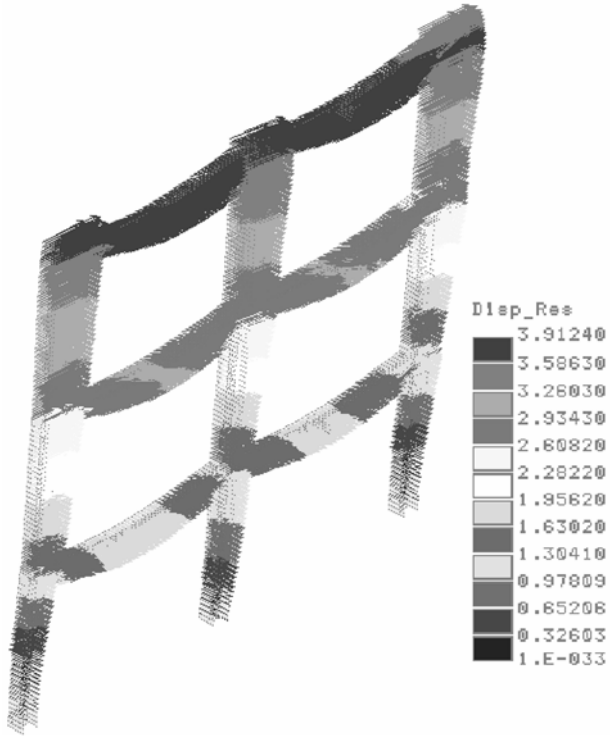
Figure 9-151. Deformed shape and displacement vector plot of the two-bay/three-story PRFP frame (gravity and lateral combined loads).
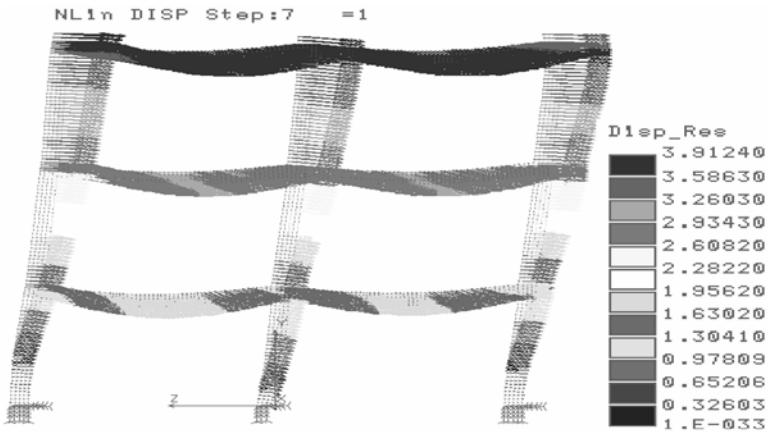

Figure 9-152. A normal view of the deformed shape and displacement vector plot of the two-bay/three-story PRFP frame (gravity and lateral combined loads).

REFERENCES

Alpha Star Corp. (ASC). (2001). "Fire resistance simulation of horizontal flat sandwich panel and deck-bulkhead T-joint assembly with temperature and pressure loads." Alpha STAR Report to ONR, Contract No: N00014-02-M-0213, April 30.

Bank, L. C., Yin, J., and Moore, L. (1996). "Experimental and numerical evaluation of beam-to-column connections for pultruded structures." *J. Reinf. Plastics and Composites*, 15, 1052–1067.

Barbero, E. J. (1998). *Introduction to composite materials design*. Taylor & Francis, New York.

Brown, R. T. (1987). "Computer programs for structural analysis." *Engineering materials handbook: Composites*, ASTM International, West Conshohocken, Pa., pp. 1–268.

Brown, R., and Nachlas, J. (1985). "Criteria for structural code selection." I. H. Marshal, ed., *Composite structures*, Applied Science Publishers, London.

Danial, I., and Ishai, O. (2006). *Engineering mechanics of composite materials*, Oxford University Press, New York.

Davalos, J. F., and Qiao, P. (1998). "Engineering design analysis equations for local buckling of FRP structural shapes." *Proc., 2nd Int. Conf. on Composites in Infrastructure (ICCI '98)*, January 12–14, Tucson,. Ariz., pp. 467–480.

Davalos, J. F., Salim, H. A., Qiao, P., and Lopez-Anido, R. (1996). "Analysis and design of pultruded FRP shapes under bending." *Composites, Part B: Eng. J.*, 27B(3–4), 295–305.

Finite Element Analysis Ltd. (2010). *LUSAS Software User Manual*, Finite Element Analysis Ltd., Kingston upon Thames, Surrey, U.K.

Harte, A. M., and McCann, D. (2001). "Finite element modelling of the semi-rigid behaviour of pultruded FRP connections." *Journal of Materials Processing Technology*, 119(1–3), 98–103.

Hassan, N. K. (1994). "Evaluation of multibolted connections for GFRP members." Ph.D. dissertation, Dept. of Civil Engineering, University of Manitoba, Winnipeg, Canada.

Hassan, N. K., Mohamedien, M. A., and Rizkalla, S. H. (1996). "Finite element analysis of bolted connections for PFRP composites." A. Mosallam, D. Hui, and P. Dutta, eds., *Composites: Part B*, 27B(3–4), 339–349.

Jones, R. M. (1999). *Mechanics of composite materials*, 2nd ed., Taylor & Francis, New York.

Kedward, K. T. (1990). "Application of numerical methods to composite structures." *Delaware composites design encyclopedia: Design studies*, Vol. V, Section 5.3, CRC Press, Boca Raton, Fla.

Kilic, H., and Haj-Ali, R. (2003). "Progressive damage and nonlinear analysis of pultruded composite structures." *Composites: Part B*, 34, 235–250.

Liu, X. (2000). "A linear and nonlinear numerical investigation on static behavior of pultruded composite (PFRP) portal frame structures." Master's thesis, Dept. of Mechanical Engineering, California State University at Fullerton, Fullerton, Calif.

Liu, X., Mosallam, A. S., and Kreiner, J. (1998). "A numerical investigation on static behavior of pultruded composite (PFRP) portal frame structures." *Proc., 43rd Int. SAMPE Symp.*, May 31–June 1, Anaheim, Calif.

Mosallam, A. S. (2000). "Experimental and numerical investigation on the behavior of pultruded composite interior joints." *SAMPE's Materials & Processes Tech.*, 45(1), 870–879.

Mosallam, A. S. (1990). "Short- and long-term behavior of pultruded fiber-reinforced plastic frame." Ph.D. dissertation, The Catholic University of America, Washington, D.C.

Mosallam, A. S., and Bank, L. C. (1992). "Short-term behavior of pultruded fiber-reinforced plastic frame." *ASCE J. Struct. Eng.*, 118(7), 1937–1954.

Na, G. S. (2008). "Load-displacement behavior of frame structures composed of fiber-reinforced polymeric composite materials." Ph.D. dissertation, School of Civil and Environmental Engineering, Georgia Institute of Technology, Atlanta, Ga.

Neto, A. B., and La Rovere, H. L. (2007). "Flexural stiffness characterization of fiber-reinforced plastic (FRP) pultruded beams." *Composite Struct.*, 81, 274–282.

Numerical Algorithms Group Ltd. (NAG). (2010), *NAG library manual*, Numerical Algorithms Group Ltd., Oxford, UK.

Pickett, A. K., and Hollaway, L. (1985). "The analysis of elastic adhesive stresses in bonded lap joints in FRP structures." *Composite Struct.*, 3, 55–79.

Reimer, W. L., and Sorby, S. A. (1998*).* "A finite element study of a PFRP beam/column connection." *Proc., 2nd Int. Conf. on Composites in Infrastructure (ICCI '98)*, January 5–7, Tucson, Ariz., pp. 533–547.

Smith, S. J., Parsons, I. D., and Hjelmstad, K. D. (1999a). "Design models of GFRP connections." *Proc., 5th ASCE Mat. Eng. Cong.*, May 10–12, Cincinnati, Ohio, pp. 100–107.

Smith, S. J., Parsons, I. D., and Hjelmstad, K. D. (1999b). "Finite-element and simplified models of GFRP connections," *J. Struct. Eng.*, 125(7), 749–756.

Steffen, R. E. (1998). "Behavior and design of fiber-reinforced polymeric composite angle struts and their connections." Ph.D. dissertation, School of Civil and Environmental Engineering, Georgia Institute of Technology, Atlanta, Ga.

Steffen, R. E., Haj-Ali, R., and Zureick, A. H. (1999). "Analysis and behavior of pultruded FRP bolted connections." *Proc., 5th ASCE Mat. Eng. Cong.*, May 10–12, Cincinnati, Ohio, pp. 76–83.

Tsai S. W., and Hahn, H. T. (1980). *Introduction to composite materials*, Technomic Publishing Company, Inc., Lancaster, Pa.

Tsai, S.W., and Wu, E. M. (1971). "A general theory of strength for anisotropic materials." *J. Composite Mat.*, 5, 58–80.

Turvey, G. J., and Cooper, C. (1998). "Semi-rigid connections and their effects on the sway response of pultruded GRP columns in low-rise frame structures." *Proc., 2nd Int. Conf. on Composites in Infrastructure (ICCI '98)*, Tucson, Ariz., Vol. II, pp. 221–235.

Zienkiewicz, O. C. (1971). *The finite element method in engineering science*, McGraw-Hill, New York.

GLOSSARY

A-Stage—An early stage in the polymerization reaction of certain thermosetting resins (especially phenolic) in which the material, after application to the reinforcement, is still soluble in certain liquids and is fusible; sometimes referred to as "resole." (See **B-Stage** and **C-Stage**.)

Abhesive—A film or coating that is applied to one solid to prevent (or greatly decrease) the adhesion to another solid with which it is to be placed in intimate contact, e.g., a "parting" or "mold-release" agent.

Accelerator—A material that, when mixed with a catalyzed resin, will speed up the chemical reaction between the catalyst and resin, either in polymerizing of resins or vulcanization of rubbers. Also known as a "promoter."

Acrylic Resin—One of a group of thermoplastic resins formed by polymerizing the esters or amides of acrylic acid; used in concrete construction as a bonding agent or surface sealer.

Activator—An additive used to promote the curing of matrix resins and reduce curing time. (See **Accelerator**.)

Additive—Any substance added to another substance, usually to improve properties, such as plasticizers, initiators, light stabilizers, and flame retardants.

Adherend—A body that is held to another body by an adhesive.

Adhesion—The state in which two surfaces are held together at an interface by forces or interlocking action, or both.

Adhesion, Mechanical—Adhesion between surfaces in which the adhesive holds the parts together by interlocking action.

Adhesive, Contact—An adhesive which requires, for satisfactory bonding, that the surfaces to be joined shall be no further apart than about 0.1 mm.

Adhesive Film—A synthetic resin adhesive, usually of the thermosetting type, in the form of a thin, dry film of resin, used under heat and pressure as an interleaf in the production of laminated materials (particularly plywood and densified wood).

Adhesiveness—The property defined by the adhesion stress $A = F/S$ where F is the perpendicular force to the glue line and S its surface. It is expressed in kg/mm^2.

Adhesives—The group of materials used to join or bond similar or dissimilar materials; for example, in concrete work, the epoxy resins.

AFRP—Aramid fiber-reinforced plastic.

Aging—The effect, on materials, of exposure to an environment for an interval of time. The process of exposing materials to an environment for an interval of time.

Air-Bubble Void—Air entrapment within and between the plies of reinforcement; non-interconnected, spherical in shape.

Ambient Temperature—The environmental temperature surrounding the object under construction.

Anisotropic—Exhibiting different properties when tested along axes in different directions.

Anisotropic Laminate—One in which the properties are different in different directions.

Antioxidant—A substance that, when added in small quantities to the resin, prevents its oxidative degradation and contributes to the maintenance of its properties.

Aramid—A type of highly oriented organic material derived from polyamide (nylon) but incorporating an aromatic ring structure. Used primarily as a high-strength, high-modulus fiber. Kevlar and Nomex are examples of aramids.

Aramid Fiber—Highly oriented organic fiber derived from polyamide incorporating an aromatic ring structure.

Aspect Ratio—The ratio of length to diameter of a fiber or filler.

Autoclave—A closed vessel for conducting a chemical reaction or other operation under pressure and heat.

Autoclave Molding—A process in which, after lay-up, winding, or wrapping, an entire assembly is placed in a closed vessel, under both temperature and pressure control for additional curing or processing. Pressure is normally maintained between 340 to 1,380 kPa (50 to 200 psi). Additional pressure ensures higher density, higher reinforcement loadings, and increased removal of volatiles and air from the resin. Frequently, lay-ups are vacuum-bagged with a bleeder and release cloth. (Modification of **Pressure bag** method.)

B-Stage—Intermediate stage in the polymerization reaction of thermosets, following which the material will soften with heat and is plastic and fusible. The resin of an uncured prepreg or premix is usually in B-stage. (See **Prepreg**.)

Bag Molding—A technique in which the consolidation of the material in the mold is effected by the application of fluid pressure through a flexible membrane.

Balanced Construction—Plywood that has an odd number of plies and is symmetrical on both sides of its centerline.

Barcol Hardness Test—Test to determine the degree of cure by measuring resin hardness (ASTM D 2583).

Bearing Strength—The maximum bearing stress that can be sustained. Also, the bearing stress at that point on the stress–strain curve where the tangent is equal to the bearing stress divided by n% of the bearing hole diameter.

Bearing Stress—The applied load in pounds divided by the bearing area. Maximum bearing stress is the maximum load in pounds sustained by the specimen during the test, divided by the original bearing area.

Bidirectional Laminate—A reinforced plastic laminate with the fibers oriented in two directions in its plane. A cross-laminate.

Binder—The resin or cementing constituent (of a plastic compound) that holds the other components together. Also, the agent applied to a fiber mat or performs to bond the fibers before laminating or molding.

BMC—Bulk molding compound.

Bond—The adhesion and grip of a matrix material to reinforcement or to other surfaces against which it is placed, including friction due to shrinkage and longitudinal shear.

Bond Area—The nominal area of interface between two elements across which adhesion develops or may develop.

Bond Breaker—A layer or coating that is applied to a specific area of a substrate, such that, when a subsequent layer or coating is applied over the bond breaker, it will not bond or adhere in that area.

Bond Strength, 1—Resistance to the separation of two materials which are in contact.

Bond Strength, 2—Resistance to the separation of composites from concrete.

Bond Strength, 3—The amount of adhesion between bonded surfaces; a measure of the stress required to separate a layer of material from the base to which it is bonded (See **Peel Strength**.)

Bond Strength, 4—The amount of adhesion between bonded surfaces. The stress required to separate a layer of material from the base to which it is bonded, as measured by load/bond area.

Bond Stress—The force per unit area necessary to rupture a bond.

Braided String or Rope—String or rope made by braiding continuous fibers or strands.

Braiding, 1—Intertwining of fibers in an organized fashion.

Braiding, 2—Weaving of fibers into a tubular shape instead of a flat fabric, as for graphite fiber-reinforced golf club shafts.

Buckling—Crimping of the fibers in a composite material, often occurring in glass-reinforced thermosets due to resin shrinkage during cure.

C-Stage—The final stage in the reaction of certain thermosetting resins in which the material is practically insoluble and infusible.

Carbon—The element that provides the backbone for all organic polymers. Graphite is a more ordered form of carbon. Diamond is the densest crystalline form of carbon.

Carbonation—The conversion of calcium hydroxide in hardened cementitious material to calcium carbonate by reaction with atmospheric carbon dioxide.

Carbon Fiber—Fiber produced by the prolysis of organic precursor fibers, such as rayon, polyacrylonitrile (PAN) carbon, and mesophase pitch carbon, in an inert environment. Used interchangeably with graphite.

Catalyst, 1—Organic peroxide used to activate polymerization.

Catalyst, 2—A substance that initiates a chemical reaction and enables it to proceed under milder conditions than otherwise required, and which does not, itself, alter or enter into the reaction. (See **Initiator**, the more common term for "addition polymerization.")

Catastrophic Failures—Totally unpredictable failures of a mechanical, thermal, or electrical nature.

Catenary—The property of creating or maintaining equal tension in parallel fibers.

Cathode—The electrode at which chemical reduction occurs.

CFRP—Carbon fiber-reinforced plastic (includes graphite fiber-reinforced plastic).

Chemical Bond—Bond between materials that is the result of cohesion and adhesion developed by chemical reaction.

Coating—Material applied to a surface by brushing, dipping, mopping, spraying, toweling, etc., to preserve, protect, decorate, seal, or smooth the substrate; also refers to foreign or deleterious substances found adhering to aggregate particles.

Coefficient of Linear Expansion—The change in length per unit resulting from a 1-degree rise in temperature.

$$\alpha_L = \frac{1}{L}\left(\frac{\delta L}{\delta T}\right)$$

where L = length and T = temperature.

Coefficient of Thermal Expansion (α_V)—The change in volume per unit volume produced by a 1-degree rise in temperature.

$$\alpha_V = \frac{1}{V}\left(\frac{\partial L}{\partial T}\right) = \frac{\partial \ln V}{\partial T}$$

where V = length and T = temperature.

Cohesion—The propensity of a single substance to adhere to itself. The internal attraction of molecular particles toward each other. The ability to resist partition of itself. The force holding a single substance together.

Cold-Setting Adhesive—A synthetic resin adhesive capable of hardening at normal room temperature in the presence of a hardener.

Commingled Yarn—Hybrid yarn made with two types of materials intermingled in a single yarn; for example, thermoplastic filaments intermingled with carbon filaments to form a single yarn.

Compatibility—The ability of two or more substances combined with one another to form a homogeneous composition of useful plastic properties; for example, the suitability of a sizing or finish for use with certain general resin types.

Composite—A combination of one or more materials differing in form or composition on a macroscale. The constituents retain their identities (i.e., they do not dissolve or merge completely into one another, although they act in concert). Normally, the components can be physically identified and exhibit an interface between one another. (See **FRP Composite.**)

Compression Mold—A mold that is open when the material is introduced, and that shapes the material by heat and by the pressure of closing. Also "compression molding."

Compressive Modulus (*E*)—Ratio of compressive stress to compressive strain below the proportional limit. Theoretically, equal to Young's modulus determined from tensile experiments.

$$E = \frac{\sigma}{\varepsilon}$$

Condensation Polymerization—A process in which water or some other simple substance separates from two or more of the polymer molecules upon their combination. Examples of resins made by this process (condensation resin) are alkyds, phenolaldehydes and urea-formaldehydes, polyesters, polyamides, polyacetals, and polyphenylene.

Conductivity—Reciprocal of volume resistivity. The electrical or thermal conductance of a unit cube of any material (conductivity per unit volume).

Construction Joint—The surface where two successive placements of layers meet, across which it may be desirable to achieve bond and through which reinforcement may be continuous.

Construction Loads—The loads to which a permanent or temporary structure is subjected during construction.

Contact Adhesive—An adhesive which requires that the surfaces to be joined shall be no farther apart than about 0.1 mm for satisfactory bonding.

Continuous Fiber Reinforcement—Any construction of resin-bound continuous fibers used to reinforce a concrete matrix. The construction may be in the shape of continuous fiber bars, tendons, or other shapes.

Continuous Filament—Fiber that is made by spinning or drawing into one long, continuous entity.

Continuous Filament Yarn—Yarn formed by twisting and or plying two or more continuous filaments into a single continuous strand.

Continuous Roving—Parallel filaments coated with sizing, drawn together into single or multiple strands and wound into a cylindrical package.

Contraction—The immediate shrinkage that a molded part undergoes when it is removed from a mold and cooled to room temperature.

Copolymer—A long-chain molecule formed by the reaction of two or more dissimilar monomers.

Corrosion, 1—Degradation of concrete or steel reinforcement by electrochemical or chemical attack.

Corrosion, 2—Destruction of metal by chemical, electrochemical, or electrolytic reaction with its environment.

Corrosion Resistance—The ability of a material to withstand contact with ambient natural factors or those of a particular artificially created atmosphere, without degradation or change in properties. For metals, this could be pitting or rusting; for organic materials, this could be crazing.

Coupling Agent—Part of a surface treatment or finish that is designed to provide a bonding link between the fiber surface and the laminating resin; any chemical substance designed to react with both the reinforcement and matrix phases of a composite material to form or promote a stronger bond at the interface; a bonding link.

Crack—An actual separation of molded material, visible on opposite surfaces of the part, and extending through the thickness; a fracture.

Crazing—Region of ultra-fine cracks which may extend in a network on or under the surface of a resin, polymer material, or plastic material, and which may also appear as a white band; often found in a filament-wound pressure vessel or bottle. The development and/or pattern of ultra fine cracks existing in a surface.

Creel—A device for holding the required number of roving balls (spools) or supply packages of reinforcement in desired position for unwinding onto the next processing step, which is weaving, braiding, or filament winding.

Creep—The change in dimension of a material under sustained load over a period of time, not including the initial instantaneous elastic deformation. The time-dependent part of strain resulting from an applied load. Creep at room temperature is called "cold flow."

Creep, Non-Recoverable—The permanent deformation in a material which remains after a prolonged application of stress that is still below the elastic limit of the material.

Creep, Rate of—The slope of the creep–time curve at a given time. Deflection with time under a given static load.

Crimp—Waviness of a fiber, a measure of the difference between the length of the unstraightened and straightened fibers.

Cross-Laminated—Laminated so that some of the layers of material are oriented at right angles to the remaining layers with respect to the grain or strongest direction in tension. Balanced construction about the centerline of the thickness of the laminate is normally assumed.

Crosswise Direction—Crosswise refers to the cutting of specimens and to the application of load. For rods and tubes, crosswise is the direction perpendicular to the long axis. For other shapes or materials that are stronger in one direction than in another, crosswise is the direction that is *weaker*. For materials that are equally strong in both directions, crosswise is an arbitrarily designated direction at right angles to the lengthwise direction.

Cure—To irreversibly change the properties of a thermosetting resin by chemical reaction, that is, condensation, ring closure, or addition. Cure may be accomplished by addition of curing (cross-linking) agents, with or without heat and pressure.

Cure Cycle—The time/temperature/pressure cycle used to cure a thermosetting resin system or prepreg. (See **Prepreg**.)

Curing—The maintenance of humidity and temperature of freshly-placed concrete during some definite period following placing, casting, or finishing to assure satisfactory hydration of the cementitious materials and proper hardening of the concrete.

Curing Agent—A catalytic or reactive agent that, when added to a resin, causes polymerization. Also called "hardener."

Curing Temperature—Temperature at which a cast, molded, or extruded product, or a resin-impregnated reinforcement, an adhesive, etc., is subjected to curing.

Curing Time—The period of time during which a part is subjected to heat or pressure, or both, to cure the resin; interval of time between the instant of cessation of relative movement between the moving parts of a mold and the instant that pressure is released. (Further cure may take place after removal of the assembly from the conditions of heat or pressure.)

Curling—The distortion of a member that was originally essentially linear, into a curved shape due to differences in temperature or moisture content in the zones adjacent to its apposing faces.

D-Glass—A high-boron-content glass made especially for laminates requiring a precisely controlled dielectric constant.

Damping (Mechanical)—Mechanical damping gives the amount of energy dissipated as heat during the deformation of a material. Perfectly elastic materials have no mechanical damping. Damping terms may be calculated by many methods, including use of the logarithmic decrement, the area of hysteresis loops, and others.

Deflection—Movement of a point on a structure or variation in the position or shape of a structure that is measured as linear displacement transverse to a reference line or axis.

Deformation—A change in dimension or shape due to stress. (See also **Contraction; Creep; Deformation, Elastic; Deformation, Inelastic; Deformation, Time-Dependent; Expansion; Length Change; Shrinkage; Volume Change**.)

Deformation, Elastic—Deformation proportional to the applied stress. (See also **Deformation**.)

Deformation, Inelastic—Deformation not proportional to the applied stress. (See **Deformation; Creep; Deformation, Time-Dependent**.)

Deformation, Nonreversible—See **Creep, Non-Recoverable**.

Deformation, Residual—See **Creep, Non-Recoverable**.

Deformation, Time-Dependent—Deformation resulting from effects such as autogenous volume change, thermal contraction or expansion, creep, shrinkage, and swelling, each of which is a function of time.

Delaminate—To split a laminated plastic material along the plane of its layers. (See **Laminate**.) Physical separation or loss of bond between laminate plies.

Delamination—A separation along a plane parallel to a surface, as in the separation of a coating from a substrate or the layers of a coating from each other; or in the case of a concrete slab, a horizontal splitting, cracking, or separation in a plane roughly parallel to, and generally near, the upper surface.

Denier—A yarn and filament numbering system in which the yarn number is numerically equal to the weight in grams of 9,000 m (used for continuous filaments). The lower the denier, the finer the yarn.

Design Life—The planned life of a structure at the time it was engineered and constructed.

Design Load—Obsolete term for factored load. (See **Factored Load**).

Design Strength—Nominal strength of a member multiplied by a strength reduction (Phi) factor. (See also **Nominal Strength** and **Phi (φ) Factor**.)

Design, Working-Stress—See **Elastic Design** and **Working-Stress Design**.

Deterioration—The disintegration or chemical decomposition of a material during test or service exposure.

Dimensional Stability—Ability of a plastic part to retain the precise shape to which it was molded, cast, or otherwise fabricated.

Discoloration—Variance of a color from that which is normal or desired.

Distortion—See **Deformation**.

Distress—Physical manifestation of cracking and distortion in a concrete structure as the result of stress, chemical action, or both.

Doff—Roving package, i.e., the final product made by roving or pulling together fibers into a bundled cake that is available for delivery or use.

Ductility—That property of a material by virtue of which it may undergo large, permanent deformation without rupture. The ability of a material to deform plastically before fracturing.

Durability—Ability of a system to maintain its properties with time and the ability to resist weathering action, chemical attack, abrasion, and other conditions of service.

Dynamic Modulus of Elasticity—The modulus of elasticity computed from the size, weight, shape, and fundamental frequency of vibration of a test specimen, or from pulse velocity. (See also **Static Modulus of Elasticity** and **Pulse Velocity**.)

E-Glass—A family of glasses with a calcium alumina borosilicate composition and a maximum alkali content of 2.0%. A general-purpose fiber that is most often used in reinforced plastics, and is suitable for electrical laminates because of its high resistivity.

Elastic Design—A method of analysis in which the design of a member is based on a linear stress–strain relationship and corresponding limiting elastic properties of the material.

Elasticity—The ability of a material to return to its original shape after removal of a force causing deformation (load).

Elastic Limit—The limit of stress beyond which the strain is not wholly recoverable.

Elastomer—A material that substantially recovers its original shape and size at room temperature after removal of a deforming force.

Elongation—Increase in length. (See also **Expansion, Shortening,** and **Swelling**.)

Elongation at Break—Elongation recorded at the moment of rupture of the specimen, often expressed as a percentage of the original length.

Environment—The aggregate of all conditions (such as contamination, temperature, humidity, radiation, magnetic and electric fields, shock, and vibration) that externally influence the performance of an item.

Epoxy, 1—A class of organic chemical bonding systems used in the preparation of special coatings or adhesives for concrete, or as binders in epoxy mortars and concretes.

Epoxy, 2—A polymerizable thermoset polymer containing one or more epoxide groups and curable by reaction with amines, alcohols, phenols carboxylic acids, acid anydrides, and mercaptans. An important matrix resin in composites as a structural adhesive.

Epoxy Resin—Resin formed by the chemical reaction of epoxide groups with amines, alcohols, phenols, and others.

Expansion—An increase of a given dimension as a result of load or thermal effects.

Extrusion—A finely divided inert mineral added to provide economical bulk in paints, synthetic resins and adhesives, or other products without extensive lessening of properties.

Fabric—Arrangement of fibers held together in two dimensions. A fabric may be woven, nonwoven, or stitched.

Fabric, Nonwoven—A textile or material structure formed by bonding or interlocking fibers or yarns without interlacing, which may be accomplished by mechanical, chemical, thermal, or solvent means.

Fabric, Woven—Material constructed of interlaced yarns, fibers, or filaments.

Factored Load—Load, multiplied by appropriate load factors, used to proportion members by the strength design method.

Factor of Safety—The ratio of the ultimate load, moment, or shear of a structural member over the service safe permissible load, moment, or shear

Fatigue—The failure or decay of mechanical properties after repeated or alternating applications of stress (loads). Fatigue tests give information on the ability of a material to resist the development of cracks, which eventually bring about failure as a result of a large number of cycles.

Fatigue Failure—The phenomenon of rupture of a material when subjected to repeated loadings.

Fatigue Life—The number of cycles of deformation required to bring about failures of the test specimen under a given set of oscillating conditions (stresses and strains).

Fatigue Limit—The stress level below which a material can be stressed cyclically for an infinite number of times without failure.

Fatigue Strength—The maximum cyclical stress a material can withstand for a given number of cycles before failure occurs. The residual strength after being subjected to fatigue.

FEM—Finite element modeling.

Fiber—General term for a filamentary material. Any material whose length is at least 100 times its diameter, the latter typically being 0.10 to 0.13 mm.

Fiber Content—The amount of fiber present in a composite. This is usually expressed as a percentage volume fraction or weight fraction of the composite.

Fiber Direction—The orientation or alignment of the longitudinal axis of the fiber with respect to a stated reference axis.

Fiberglass—An individual filament made by drawing molten glass. A continuous filament is a single glass fiber of great or indefinite length. A staple fiber is a glass fiber of relatively short length—generally less

than 17 in. (430 mm); the length is related to the forming or spinning process used.

Fiberglass Reinforcement—Major material used to reinforce plastic. Available as mat, roving, fabric, and so forth, it is incorporated into both thermosets and thermoplastics.

Fiber Pattern—Visible fibers on the surface of laminates or molding. The thread size and weave of glass cloth.

Fiber-Reinforced Polymer (FRP)—A general term for a composite that is reinforced with cloth, mat, strands, or any other fiber form.

Filament—Smallest unit of a fibrous material. A fiber made by spinning or drawing into one long, continuous entity.

Filament Winding—A process for fabricating a composite structure in which continuous reinforcements (filament, wire, yarn, tape, or other), either previously impregnated with a matrix material or impregnated during the winding, are placed over a rotating and removable form or mandrel in a prescribed way to meet certain stress conditions. Generally, the shape is a surface of revolution and may or may not include end closures. When the required number of layers is applied, the wound form is cured and the mandrel removed.

Filler—A relatively inert substance added to a material to alter its physical, mechanical, thermal, electrical, and other properties or to lower cost or density. Sometimes the term is used specifically to mean particulate additives.

Fire Resistance—The property of a material or assembly to withstand fire or give protection from it; as applied to elements of buildings, it is characterized by the ability to confine a fire or to continue to perform a given structural function, or both.

Fire Retardants—Certain chemicals that are used to reduce the tendency of a resin to burn.

Flammability—Measure of the extent to which a material will support combustion.

Flexural Modulus—The ratio, within the elastic limit, of the applied stress on a test specimen in flexure to the corresponding strain in the outermost fibers of the specimen. [See also **Modulus of Elasticity**.]

Flexural Strength—A property of a solid, which indicates its ability to withstand bending.

Flexural Strength—The maximum stress that can be borne by the surface fibers in a beam in bending. The flexural strength is the unit resistance to the maximum load before failure by bending, usually expressed in force per unit area.

Form Oil—A substance used on the contact surface of a wooden or metal form to prevent one compound, material, or component from sticking to another.

Fracture—The separation of a body. Defined both as rupture of the surface without complete separation of laminate, and as complete separation of a body because of external or internal forces.

Fracture Stress—The true, normal stress on the minimum cross-sectional area at the beginning of fracture.

Fracture Toughness—A measure of the damage tolerance of a material containing initial flaws or cracks. Used in aircraft structural design and analysis.

FRP—Fiber-reinforced polymer (plastic).

FRP Composite—A polymer matrix, either thermoset or thermoplastic, reinforced with a fiber or other material with a sufficient aspect ratio (length to thickness) to provide a discernable reinforcing function in one or more directions. (See **Composite**).

Gel—The initial jellylike solid phase that develops during the formation of a resin from a liquid. A semisolid system consisting of a network of solid aggregates in which liquid is held.

Gel Coat—A quick-setting resin applied to the surface of a mold and gelled before lay-up. The gel coat becomes an integral part of the finished laminate, and is usually used to improve surface appearance and performance.

Gelation—The point in a resin cure when the resin viscosity has increased to a point such that it barely moves when probed with a sharp instrument. Also known as "vitrification."

Gelation Time—The time required to change an easily flowing resin into a non-flowing substance whose viscosity has increased so much that the resin barely moves and can only be probed by a sharp instrument.

GFRP—Glass-fiber-reinforced polymer (plastic).

Glass Fiber—Fiber drawn from an inorganic product of fusion that has cooled without crystallizing.

Glass Fiber-Reinforced Cement (GFRC)—A composite material consisting essentially of a matrix of hydraulic cement paste or mortar reinforced with glass fibers; typically precast into units less than 1 in. (25 mm) thick.

Glass Fiber, Types—Alkali-resistant (AR-glass), general-purpose (E-glass), high-strength (S-glass).

Glass-Transition Temperature—The midpoint of the temperature range over which an amorphous material changes from (or to) a brittle, vitreous state to (or from) a plastic state. (See **Heat-Deflection Temperature**.)

Graphite Fiber—A fiber made from a precursor by oxidation, carbonization, and graphitization, which consists of more than 99% elemental carbon.

Grating—Large cross-sectional area construction, usually in two axial directions, fabricated using continuous filaments.

Grid—Large cross-sectional area construction in two or three axial directions fabricated using continuous filaments.

Grout—A mixture of cementitious material and water, with or without aggregate, proportioned to produce a pourable consistency without segregation of the constituents; also a mixture of other composition but of similar consistency. (See also **Neat Cement Grout** and **Sanded Grout**.)

Hand Lay-Up—Fabrication method in which successive of plies of reinforcement materials, pre-impregnated or coated afterwards, are placed or positioned in a mold by hand, then cured to the formed shape.

Hardener—Substance added to thermoset resin to cause a curing reaction. Usually applies to epoxy resins. (1) A chemical (including certain fluosilicates or sodium silicate) applied to concrete floors to reduce wear and dusting; (2) in a two-component adhesive or coating, the chemical component which causes the resin component to cure.

Heat-Deflection Temperature—The temperature at which a plastic material has an arbitrary deflection when subjected to an arbitrary load and test condition; this is an indication of the **Glass-Transition Temperature**.

Heat Resistance—The property or ability of plastics and elastomers to resist the deteriorating effects of elevated temperatures.

High-Pressure Laminates—Laminates molded and cured at pressures not lower than 6.9 MP (1.0 ksi), and more commonly in the range of 8.3 to 13.9 Mpa (1.2 to 2.0 ksi).

Homogeneity—Uniformity of composition throughout the material.

Homogeneous—Descriptive term for a material of uniform composition throughout.

Hybrid—A composite laminate consisting of laminae of two or more composite material systems. A combination of two or more different fibers, such as carbon and glass or carbon and aramid, into a structure.

Hysteresis—The energy absorbed in a complete cycle of loading and unloading. This energy is converted from mechanical to friction energy (heat).

Impact—The single instantaneous stroke or contact of a moving body with another, either moving or at rest.

Impact Resistance—Ability of a resin system to absorb energy when it is applied at high rates of strain.

Impact Strength—The ability of a material to withstand shock loading.

Impact Test—Measure of the energy necessary to fracture a standard sample by an impulse load.

Impregnate—In reinforced plastics, to saturate the reinforcement with a resin.

Impregnation—Saturation of voids and interstices of a reinforcement with a resin.

Inhibitor—A substance that retards a chemical reaction. Also used in certain types of monomers and resins to prolong storage life.

Initiator—Peroxides used in free radical polymerization as cross linking agents for elastomers and polyethylene during the curing thermosetting resins.

Inorganic Pigments—Natural or synthetic metallic oxides, sulfides, and other salts that impart heat and light stability, weathering resistance, color, or migration resistance to plastics.

Interface—The boundary or surface between two different, physically distinguishable media. On fibers, the contact area between fibers and sizing or finish. In a laminate, the contact area between the reinforcement and the laminating resin.

Interlaminar—Descriptive term pertaining to an object (for example, voids), event (for example, fracture), or potential field (for example, shear stress) referenced as existing or occurring between two or more adjacent laminae.

Interlaminar Shear—Shearing force tending to produce a relative displacement between two laminae in a laminate along the plane of their interface.

Isophthalic Polyester—High-quality polyester resin (good thermal, mechanical, chemical resistance).

Izod Impact Test—A test for shock loading in which a notched specimen bar is held at one end and broken by striking, and the energy absorbed is measured.

Joint—The location at which two adherends are held together with a layer of adhesive; the general area of contact for a bonded structure.

Joint, Butt—A type of edge joint in which the edge faces of the two adherends are at right angles to the other faces of the adherents.

Joint, Edge—A joint made by bonding the edge faces of two adherends.

Joint, Lap—A joint made by placing one adherend partly over another and bonding together the overlapped portions.

Joint, Scarf—A joint made by cutting away similar angular segments of two adherends and bonding them with the cut areas fitted together.

Knits—Construction made by knitting.

L/D Ratio—A term used to define an extrusion screw, which denotes the ratio of the screw length to the screw diameter.

Laminate, 1—Two or more layers of fiber, bound together in a resin matrix.

Laminate, 2—To unite layers with a bonding material, usually with pressure and heat (normally used with reference to flat sheets, but also rods and tubes). Also, a material consisting of layers bonded together.

Lap—In filament winding, the amount of overlay between successive windings, usually intended to minimize gapping; in textiles, a matted sheet of cotton wound on a spindle, produced by the picker. (Cotton

lap is used extensively in preparing asbestos-cotton mixes in the carding machine.)

Lay-Up—The reinforcing material placed in position in the mold. The process of placing the reinforcing material in position in the mold.

Length Change—Longitudinal extension of a structure.

Light-Fastness—Satisfactory resistance to light, particularly the colorants or other additives entering into the composition of a plastic material; light resistance.

Live Load—Any load that is not permanently applied to the structure.

Load Factor—A factor by which a service load is multiplied to determine a factored load used in the strength design method. (See **Phi (φ) Factor**.)

M-Glass—A high-beryllia-content glass designed especially for high modulus of elasticity.

Mat—A fibrous material for reinforced plastic consisting of randomly oriented chopped filaments, short fibers (with or without a carrier fabric), or swirled filaments loosely held together with a binder.

Matrix, 1—In the case of mortar, the cement paste in which the fine aggregate particles are embedded; in the case of concrete, the mortar in which coarse aggregate particles are embedded.

Matrix, 2—The essentially homogeneous resin or polymer material in which the fiber system of a composite is embedded. Both thermoplastic and thermoset resins may be used, as well as metals, ceramics, and glasses.

Mean Stress—The average of the maximum and minimum stress in one cycle of fluctuating loading (as in a fatigue test); tensile stress is considered positive and compressive stress, negative.

Mechanical Adhesion—Adhesion between surfaces in which the adhesive holds the parts together by interlocking action.

Microcracking—Cracks formed in composites or concrete when stresses locally exceed the strength of the matrix.

Micron—An obsolete term designating a unit of length equal to one thousandth of a millimeter or one millionth of a meter; superseded by micrometer (μm).

Modulus—A number that expresses a measure of some property of a material: modulus of elasticity, shear modulus, etc.; a coefficient of numerical measurement of a property. (Note: The use of the word without modifying terms may be confusing and such use is discouraged.

Modulus in Shear—The ratio of the shear stress to the strain in the material, over the range for which this value is constant.

Modulus in Tension—The ratio of the tension stress to the strain in the material over the range for which this value is constant.

Modulus of Elasticity—The ratio of stress (nominal) to corresponding strain below the proportional limit of a material that is expressed in force per unit area.

Modulus of Elasticity in Torsion—The ratio of the torsion stress to the strain in the material, over the range for which this value is constant.

Modulus of Resilience—The energy that can be absorbed per unit volume without creating a permanent distortion. Calculated by integrating the stress–strain curve from zero to the elastic limit and dividing by the original volume of the specimen.

Modulus of Rigidity—The ratio of unit shearing stress to the corresponding unit shearing strain; referred to as "shear modulus" and "modulus of elasticity in shear," denoted by the symbol G. (See **Modulus of Elasticity**.)

Modulus of Rupture—A measure of the ultimate load-carrying capacity of a beam; sometimes referred to as "rupture modulus" or "rupture strength." It is calculated for apparent tensile stress in the extreme fiber of a transverse test specimen under the load, which produces rupture. (See also **Flexural Strength**.) (Note: The actual stress in the extreme fiber is less than the apparent stress since the flexure formula employed in the calculation is valid only for stresses within the proportional limit of the material; nevertheless, the nominal rupture strength so obtained is considered the rupture modulus.)

Moisture Content—The amount of moisture in a material determined under prescribed conditions and expressed as a percentage of the mass of the moist specimen, that is, the mass of the dry substance plus the moisture present.

Neat Cement Grout—A mortar made from a mixture of cement and water.

Nesting—In reinforced plastics, the placing of plies of fabric so that the yarns of one ply lie in the valleys between the yarns of the adjacent ply (nested cloth).

Netting Analysis—The analysis of filament-wound structures which assumes that the stresses induced in the structure are carried entirely by the filaments, and the strength of the resin is neglected; it is also assumed that the filaments possess no bending or shearing stiffness, and carry only the axial tensile loads.

Nominal Strength—The strength of a structural member calculated in accordance with provisions and assumptions of design method, applicable code, and related reduction factors.

Nonrigid Plastic—A plastic that has a stiffness of apparent modulus of elasticity of not more than 10,000 psi at 23 °C, when determined in accordance with ASTM D 747.

Nonwoven Fabric—A planar textile structure produced by loosely compressing together fibers, yarns, rovings, and so forth, with or without a scrim cloth carrier.

Novolak—A phenolic-aldehyde resin which, unless a source of methylene groups is added, remains permanently thermoplastic; a linear thermoplastic B-stage phenolic resin. (See **Thermoplastic**.)

Orthotropic—Having three mutually perpendicular planes of elasticity symmetry.

Overlap—A simple adhesive joint in which the surface of one adherend extends past the leading edge of another.

Oxidation—The formation of an oxide; the act or process of oxidizing, combining or increasing the proportion of oxygen.

PAN Carbon Fiber—Carbon fiber made from polyacrylonitrile (PAN) fiber.

Peeling—A process in which thin flakes of mortar are broken away from a concrete surface, such as by deterioration or by adherence of surface mortar to forms, as forms are removed. The disbanding of the FRP plate from the parent substrate (see ASTM D 3167).

Peel Ply—A layer of open-weave material, usually fiberglass or heat-set nylon, applied directly to the surface of a prepreg lay-up. (See **Prepreg**.)

Peel Strength—Bond strength, in pounds per inch of width, obtained by peeling the layer. (See **Bond Strength**.)

Permeability—The passage or diffusion (or rate of passage) of a gas, vapor, liquid, or solid through a barrier without physically or chemically affecting it.

PET—Thermoplastic polyester resin (polyethylene terephthalate).

pH (Hydrogen Ion Concentration)—The negative logarithm (to the base 10) of the hydrogen ion concentration of a solution.

Phenolic (Phenolic Resin)—A thermosetting resin produced by the condensation of an aromatic alcohol with an aldehyde, particularly of phenol with formaldehyde. (See **A-Stage, B-Stage, C-Stage,** and **Novolak.)**

Phi (ϕ) Factor—A strength reduction variable.

Pitch Carbon Fiber—Carbon fiber made from petroleum pitch.

Plain Weave—A weaving pattern in which the warp and fill fibers alternate; that is, the repeat pattern is warp/fill/warp/fill, and so on.

Plastic—A material that contains as an essential ingredient an organic substance of large molecular weight; is solid in its finished state; and, at some stage in its manufacture or its processing into finished articles, can be shaped by flow. Made of plastic.

Ply—In general, fabrics or felts consisting of one or more layers (laminates, and so forth). The layers that make up a "stack."

Polyamide—A polymer in which the structural units are linked by amide or thioamide groupings. Many polyamides are fiber-forming.

Polyester—Resin produced by the polycondensation of dihydroxy derivatives and dibasic organic acids or anhydrides yielding resins that can be compounded with vinyl monomers to give highly cross-linked thermoset resins.

Polyesters—Thermosetting resins produced by dissolving unsaturated, generally linear, alkyd resins in a vinyl-type active monomer such as styrene, methyl styrene, and diallyl phthalate. Cure is effected through

vinyl polymerization using peroxide catalysts and promoters, or heat, to accelerate the reaction. The resins are usually furnished in solution form, but powdered solids are also available.

Polyethylene—A thermoplastic high-molecular-weight organic compound used in formulating protective coatings or, in sheet form, as a protective cover for concrete surfaces during the curing period, or to provide a temporary enclosure for construction operations.

Polyimide—A polymer produced by heating of polyamic acid. It is a highly heat-resistant resin (600 °F +) suitable for use as a binder or as an adhesive.

Polymer, 1—A compound formed by the reaction of simple molecules having functional groups, which permit their combination to proceed to high molecular weights under suitable conditions.

Polymer, 2—A high-molecular-weight organic compound, natural or synthetic, whose structure can be represented by a repeated small unit, the "mer"; for example, polyethylene, rubber, cellulose. Synthetic polymers are formed by addition or condensation polymerization of monomers. Some polymers are elastomers, and some are plastics. When two or more monomers are involved, the product is called a "copolymer."

Polymerization—A chemical reaction in which the molecules of monomers are linked together to form large molecules whose molecular weight is a multiple of that of the original substances. When two or more monomers are involved, the process is called "copolymerization" or "heteropolymerization." (See **Condensation Polymerization**.)

Polystyrene Resin—Synthetic resins, varying from colorless to yellow, formed by the polymerization of styrene on heating with or without catalysts, that may be used in paints for concrete, or for making sculptured molds, or as insulation.

Polyurethane—A family of resins produced by reacting a diisocyanate with an organic compound containing two or more active hydrogen atoms (polyols, polyamides, alkyd polymers, and polyether polymers) to form polymers having free isocyanate groups.

Polyvinyl Acetate—Colorless, permanently thermoplastic resin. Usually supplied as an emulsion or water-dispersible powder characterized by flexibility, stability toward light; transparency to ultraviolet rays; high dielectric strength, toughness, and hardness. The higher the degree of polymerization, the higher the softening temperature; may be used in paints for concrete.

Polyvinyl Chloride—A synthetic resin prepared by the polymerization of vinyl chloride, used in the manufacture of nonmetallic water-stops for concrete.

Porosity—The ratio of the volume of air or void contained within the boundaries of a material to the total volume (solid material plus air or void), expressed as a percentage.

Pot Life—The length of time that a catalyzed polymeric resin system retains a viscosity low enough to be used in processing. (See also **Working Life**.)

Precursor—For carbon or graphite fiber, the rayon, PAN, or pitch fibers from which carbon and graphite fibers are derived.

Preform—A preshaped fibrous reinforcement formed by distribution of chopped fibers or cloth by air, water flotation, or vacuum over the surface of a perforated screen to the approximate contour and thickness desired in the finished part.

Pregel—An unintentional extra layer of cured resin on part of the surface of a reinforced plastic (not related to **Gel Coat**.)

Preimpregnation—The practice of mixing resin and reinforcement and effecting partial cure before use or shipment to the user. (See **Prepreg**.)

Prepolymer—A chemical intermediate whose molecular weight is between that of the monomer or monomers and the final polymer or resin.

Prepreg, 1—Semi-hardened construction made by soaking strands or roving with resin or resin precursors.

Prepreg, 2—Either ready-to-mold material in sheet form or ready-to-wind material in roving form, which may be cloth, mat, unidirectional fiber, or paper impregnated with resin and stored for use. The resin is partially cured to a "B" stage and supplied to the fabricator who lays up the finished shape and completes the cure with heat and pressure.

Pressure Bag Molding—A process for molding reinforced plastics in which a tailored, flexible bag is placed over the contract lay-up on the mold, sealed, and clamped in place. Fluid pressure, usually provided by compressed air or water, is placed against the bag and the part is cured.

Pultinsion—Process by which a molten or curable resin and continuous fibers are pulled through a die of a desired structural shape of constant cross section, usually to form a rod or tendon.

Pultrusion—A reversed "extrusion" of resin-impregnated roving in the form of continuous process for manufacturing composites that have a permanent cross-sectional shape, such as rods, tubes, and other structional shapes. The roving, after passing through the resin dip tank, is drawn through the die to form the desired cross section, where the resin is subsequently cured.

Quality Assurance, 1—A system of proceeding that ensures that the intended levels of quality on a project are obtained.

Quality Assurance, 2—Actions taken by an owner or his representative to provide assurance that what is being done and what is being provided are in accordance with the applicable standards of good practice for the work.

Quality Control—Actions taken by a producer or contractor to provide control over what is being done and what is being provided so that the applicable standards of good practice for the work are followed.

Release Agent—Material used to prevent bonding of resin or concrete on a surface. (See also **Bond Breaker** and **Form Oil**.) Also called "parting agent" and "mold release agent."

Resilience—The ratio of energy returned on recovery from deformation, to the work input required to produce the deformation (usually expressed as a percentage); the ability to quickly regain an original shape after being strained or distorted.

Resin—A natural or synthetic viscous liquid, solid, or semisolid organic material of indefinite and often high molecular weight having a tendency to flow under stress; usually has a softening or melting range, and usually fractures conchoidally. Polymeric material (usually) that is rigid or semi-rigid at room temperature, usually with a melting point or glass-transition temperature above room temperature.

Resin Content—The amount of resin in a laminate, expressed as either a percent of total weight or total volume.

Resin-Rich Area—Localized area filled with resin and lacking reinforcing material.

Resin Transfer Molding (RTM)—A process whereby catalyzed resin is transferred or injected into a closed mold in which the fiberglass reinforcement has been placed.

Retardation—A reduction on the rate of hardening or setting, i.e., an increase in the time required to reach initial and final set, or to develop early strength of fresh concrete, mortar, or grout.

Retarder—An admixture that delays the setting of mixtures.

Rockwell Hardness Number—A value derived from the increase in depth of an impression as the load on an indenter is increased from a fixed minimum value to a higher value, and then returned to the minimum value. Indenters for the Rockwell test include steel balls of specific diameters and a diamond cone penetrator having an included angle of 120 degrees with a spherical tip having a radius of 0.2 mm. Rockwell hardness numbers are always quoted with a prefix representing the Rockwell scale corresponding to a given combination of load and indenter.

Room Temperature Curing Adhesives—Adhesives that set (to handling strength) within an hour of temperatures from 60 °F to 86 °F, and later reach full strength without heating.

Roving—A number of yarns, strands, tows, or ends collected into a parallel bundle with little or no twist.

S-Glass—A magnesium alumina silicate composition that is especially designed to provide very high-tensile-strength glass filaments.

Safety Hardener—A curing agent that causes only a minimum of toxic effect on the human body, either on contact with the skin or as concentrated vapor in the air.

Sanded Grout—A polymer-modified grout that produces hard, dense joints that are resistant to shrinking, cracking, and wear. Formulated with proprietary technology to ensure durability, color consistency, and quick setting.

Sandwich Panel Constructions—Panels composed of a lightweight core material, such as honeycomb, foamed plastic, and so forth, to which two relatively thin, dense, high strength-of-stiffness faces or skins are adhered.

Saturation—In general, the condition of coexistence in stable equilibrium of either a vapor and a liquid, or a vapor and solid phase of the same substance at the same temperature.

SCRIMP—Acronym for Seeman Composites Resin Infusion Molding Process, a vacuum process to combine resin and reinforcement in an open mold.

Sealing Compound—A liquid that is applied as a coating to the surface of hardened concrete to either prevent or decrease the penetration of liquid or gaseous media (e.g., water, aggressive solution, or carbon dioxide) during service exposure.

Self-Extinguishing Resin—A resin formulation that will burn in the presence of a flame but will extinguish itself within a specified time after the flame is removed.

Set—To convert into a fixed or hardened state by chemical or physical action, such as condensation, polymerization, oxidation, vulcanization, gelation, hydration, or evaporation of volatiles. Or, the irrecoverable deformation or creep usually measured by a prescribed test procedure and expressed as a percentage of the original dimension.

Shear Modulus (G)—The ratio of shearing stress t to shearing strain within the proportional limit of a material.

$$G = \frac{\tau}{\gamma} = \frac{\sigma}{\varepsilon}$$

When measured dynamically with a torsion pendulum, the shear modulus of a solid rectangular beam is given by:

$$G = \frac{5.588 \times 10^{-4} LI}{CD^3 \mu P^2} \text{ (psi)}$$

where
L = length of specimen between the clamps, in inches
C = width of specimen, in inches

D = thickness of specimen, in inches

I = polar moment of inertia of the oscillating system, in g cm^2

P = period of oscillations, in seconds

μ = a shape factor depending upon the ratio of the width to thickness of the specimen

Shear Strength—The maximum shearing force a flexural member can support at a specific location as controlled by the combined effects of shear forces and bending moment.

Sheet Molding Compound (SMC)—A composite of fibers, a liquid thermosetting resin (usually polyester), and pigments, fillers, and other additives that have been compounded and processed into sheet form to facilitate handling in the molding operation.

Shelf Life—The length of time a material, substance, product, or reagent can be stored under specified environmental conditions and continue to meet all applicable specification requirements and/or remain suitable for its intended function.

Short Beam Shear Strength—The interlaminar shear strength of a parallel fiber-reinforced plastic material as determined by three-point flexural loading of a short segment cut from a ring-type specimen.

Shortening—The breaking of a molecular bond causing the loss of a side group or reduction of the overall chain; reduction in size per unit length caused by compressive forces.

Shrinkage—Decrease in either length or volume. (Note: May be restricted to effects of moisture content or chemical changes.)

Size—Any treatment consisting of starch, gelatin, oil, wax, or other suitable ingredient that is applied to yarn or fibers at the time of formation to protect the surface and aid the process of handling and fabrication, or to control the fiber characteristics. The treatment contains ingredients that provide surface lubricity and binding action but, unlike a finish, contains no coupling agent. Before final fabrication into a composite, the size is usually removed by heat-cleaning, and a finish is applied.

Sizing—Applying a material on a surface, or coating, in order to fill pores and thus reduce the absorption of the subsequently applied adhesive, modify the surface properties of the substrate to improve adhesion, or improve the filament-to-resin bond and to impart processing and durability attributes.

Sizing Content—The percent of the total strand weight made up by the sizing; usually determined by burning off the organic sizing ("loss on ignition").

SMC—See **Sheet Molding Compound**.

Solvent—A liquid in which another substance may be dissolved.

Solvent Resistance—The nonswelling of a material and, of course, the impossibility for it to be dissolved by the solvent in question.

Specific Heat—The quantity of heat required to raise the temperature of a unit mass of a substance 1 degree under specified conditions.

Standard Deviation—The root mean square deviation of individual values from their average.

Staple—Short fibers of uniform length usually made by cutting continuous filaments. **Staple may be crimped or uncrimped.**

Static Modulus of Elasticity—The slope of the chord drawn between any two specified points on the stress-strain curve.

Starved Area—An area in a plastic part that has an insufficient amount of resin to wet out the reinforcement completely.

Starved Joint—An adhesive joint that has been deprived of the proper film thickness of adhesive due to insufficient adhesive spreading or due to the application of excessive pressure during the lamination process.

Static Fatigue—Failure of a part under continued static load; analogous to **Creep-Rupture** failure in metals testing, but often the result of **Aging** accelerated by stress.

Stiffness—The relationship of load and deformation; a term often used when the relationship of stress to strain does not conform to the definition of Young's modulus. (See **Stress–Strain**.)

Storage Life—The period of time during which a liquid resin, packaged adhesive, or prepreg can be stored under specified temperature conditions and remain suitable for use. (See **Shelf Life)**.

Strand, 1—A prestressing tendon compound of a number of wires twisted around a center wire or core.

Strand, 2—Normally an untwisted bundle or assembly of continuous filaments used as a unit, including slivers, tows, ends, yarn, and so forth. (See **Tow** and **Turns Per Inch**.)

Stress Concentration—On a macro-mechanical level, the magnification of the level of an applied stress in the region of a notch, void, hole, or inclusion.

Stress Corrosion—Corrosion of a metal, either initiated or accelerated by stress.

Stress-Corrosion Cracking—Preferential attack resulting in cracking that requires the simultaneous action of a corrodent and sustained tensile stress. (This excludes corrosion-reduced sections that fail by fast fracture; also excludes intercrystalline or transcrystalline corrosion that can disintegrate an alloy without either applied or residual stress.)

Stress Relaxation—The time-dependent decrease in stress in a material held at constant strain.

Stress–Strain—The curve that results from plotting the applied stress on a test specimen in tension versus the corresponding strain that results in a stiffness, expressed in $lb/in.^2$ or kg/cm^2.

Structural Adhesive—A bonding agent used for transferring required loads between adherents exposed to service environments typical for the structure involved.

Structural Bond—A bond that joins basic load-bearing parts of an assembly. The load may be either static or dynamic.

Surface Treatment—A material applied to fibrous glass during the forming operation or **in subsequent processes (e.g., size or finish).**

Swelling—Volumetric increase due to rise in temperature or absorption of moisture. This change in dimensions, transversely and axially, of a fiber due to absorption of water can be expressed in terms of increase in diameter, transverse area, length, or volume.

Synthetic Resin—A complex, substantially amorphous, organic semi-solid or solid material (usually a mixture) built up by chemical reaction of comparatively simple compounds, approximating the natural resins in luster, fracture, comparative brittleness, insolubility in water, fusibility or plasticity, and some degree of rubber-like extensibility. Synthetic resins commonly deviate widely from natural resins in chemical constitution and behavior with reagents.

Tack—Stickiness of an adhesive or filament-reinforced resin prepreg material.

Tack Range—The period of time in which an adhesive will remain in the tacky-dry condition after application to the adherend, and under specified conditions of temperature and humidity.

Tack Stage—The interval of time during which a deposited adhesive film exhibits stickiness or tack, or resists removal or deformation of the cast adhesive.

Textile—Fabric, usually woven.

Thermal Conductivity—Ability of a material to conduct heat. The physical constant for quantity of heat that passes through a unit cube of a substance in time when the difference in temperature of two faces is 1 degree.

Thermal Diffusivity—Thermal conductivity divided by the product of specific heat and unit weight—an index of the facility with which a material undergoes temperature change.

Thermal Expansion—Expansion caused by increase in temperature.

Thermoplastic—Resin that is not cross-linked and therefore, is capable of being repeatedly softened by an increase of temperature and hardened by a decrease in temperature, i.e. remelted and recycled.

Thermoplastic Polyesters—A class of thermoplastic polymers in which the repeating units are joined by ester groups.

Thermoset—Resin that is formed by cross-linking polymer chains. A thermoset cannot be melted and recycled because the polymer chains form a three-dimensional network. A plastic that, when cured by application

of heat or chemical means, changes into a substantially infusible and insoluble material.

Thermosetting Polyesters—A class of resins produced by dissolving unsaturated, generally linear, alkyd resins in a vinyl-type active monomer such as styrene, methyl styrene, or diallyl phthalate.

Toughness—A property of a material for absorbing work or registering fracture by impact or shock. The energy or actual work per unit volume or unit mass of material that is required to rupture or break the material. Toughness is proportional to the area under the stress-strain curve or load–elongation curve, i.e., from the origin to the breaking point.

Tow—An untwisted bundle of continuous filaments. Commonly used in referring to man-made fibers, particularly carbon and graphite, but also glass and aramid. A tow designated as 140 K has 140,000 filaments.

Transition Temperature—The temperature at which the properties of a material change.

Turns Per Inch (TPI)—A measure of the amount of twist produced in a yarn during its conversion from a strand.

Ultimate Elongation—The elongation at rupture.

Ultimate Tensile Strength—The ultimate or final stress sustained by a specimen in a tension test; the stress at moment of rupture.

Ultra-Violet (UV)—Zone of invisible radiations beyond the violet end of the spectrum of visible radiations. Since UV wavelengths are shorter than the visible, their photons have more energy, enough to initiate some chemical reactions and to degrade most plastics.

Ultra-Violet (UV) Stabilizer—Any chemical compound that, when admixed with a thermoplastic resin, selectively absorbs UV rays.

Unidirectional Laminate—A reinforced plastic laminate in which substantially all of the fibers are oriented in the same direction.

Unsaturated Polyester—Product of a condensation reaction between dysfunctional acids and alcohols, one of which, generally the acid, contributes olefinic unsaturation.

V-RTM (VA-RTM)—Acronym for Vacuum Resin Transfer Molding, a vacuum process to combine resin and reinforcement in an open mold. (See **SCRIMP**.)

Vacuum Bag Molding—A process in which a sheet of flexible transparent material plus bleeder cloth and release film are placed over the lay-up on the mold and sealed at the edges. A vacuum is applied between the sheet and the lay-up.

Veil—An ultra-thin mat similar to a surface mat often composed of organic fibers as well as glass fibers.

Vinyl Esters—A class of thermosetting resins containing ester of acrylic and/or methacrylic acids, many of which have been made from epoxy resin. They are characterized by reactive unsaturation located primarily

in terminal positions, which can be compounded with sterol monomers to give highly cross-linked thermoset copolymers.

Viscosity—The internal friction resistance of an adhesive to flow when that resistance is directly proportional to the applied force.

Void Content—The percentage of voids in a laminate can be calculated by the use of the following formula:

Percent voids = $100 - x$,

$$x = \frac{ad}{c} + \frac{ae}{b}$$

where
x = total calculated volume of laminate
a = specific gravity of laminate (Method 5011 of Federal Specification LP-406B, National Bureau of Standards)
b = specific gravity of glass = 2.57
c = specific gravity of cured resin
d = resin content, expressed as a decimal (in accordance with Method 7061 of Federal Specification LP-406B)
e = glass content, expressed as a decimal = $1 - d$

If the laminate or a molding contains a filler:

$$x = \frac{ad}{c} = \frac{ae}{b} = \frac{ar}{g}$$

where
e = glass content = $1 - d - f$
f = filler content, expressed as a decimal
g = specific gravity of filler

Voids—Gaseous pockets that have been trapped and cured into laminate; an unfilled space in a cellular plastic substantially larger than the characteristic individual cell.

Volume Change—An increase or decrease in volume.

Volume Fraction—Fraction of a constituent material based on its volume.

Volatiles—Materials in a sizing or a resin formulation that are capable of being driven off as a vapor at room or slightly elevated temperature.

Volatile Content—The percent of volatiles that are driven off as a vapor from a plastic or an impregnated reinforcement.

Water Absorption—Ratio of the weight of water absorbed by a material to the weight of the dry material.

Weathering—Changes in color, texture, strength, chemical composition or other properties of a natural or artificial material due to the action of the weather.

Weave—The particular manner in which a fabric is formed by interlacing yarns, and usually assigned a style number.

Web—A textile fabric, paper, or a thin metal sheet of continuous length handled in roll form, as contrasted with the same material cut into sheets; a thin sheet in process in a machine; (in extrusion coating) the molten web is that which issues from the die, and the substrate web is applied to the substrate material (which is being coated.)

Weft—The transverse threads or fibers in a woven fabric; those fibers running perpendicular to the warp. Also "filler," "filler yarn," "woof."

Wet Flexural Strength (WFS)—The flexural strength after water immersion; usually after boiling the test specimen for 2 h in water.

Wet Lay-Up—A method of making a reinforced product by applying the resin system as a liquid when the reinforcement is put in place.

Wet-Out—The condition of an impregnated roving or yarn in which substantially all voids between the sized strands and filaments are filled with resin.

Wetting Agent—A substance capable of lowering the surface tension of liquids, facilitating the wetting of solids surfaces and permitting the penetration of liquids into the capillaries.

Whisker—A very short fiber form of reinforcement, usually of crystalline material.

Working Life—The period of time during which a liquid resin or adhesive, after mixing with a catalyst, solvent, or other compounding ingredients, remains usable. (See **Gelation Time, Pot Life**.)

Working Stress Design—A method of design in which structures or members are proportioned for prescribed working loads at stresses that are well below their ultimate values; linear distribution of flexural stresses is assumed. **Woven Fabric**—A material (usually a planar structure) constructed by interlacing yarns, fibers, or filaments to form such fabric patterns as plain, harness satin, or leno weaves.

Woven Fabrics—Those produced by interlacing strands at more or less right angles.

Woven Roving—A heavy glass fiber fabric made by weaving roving.

Wrinkle—A surface imperfection in laminated plastics that has the appearance of a crease or wrinkle in one or more outer sheets of the paper, fabric, or other base which has been pressed in.

Yarn—An assemblage of twisted fibers or strands, either natural or manufactured, to form a continuous yarn suitable for use in weaving or otherwise interweaving into textile materials. (See **Continuous Filament**.)

Yarn—Group of fibers held together to form a string or rope.

Young's Modulus—The ratio of normal stress to corresponding strain for tensile or compressive stresses less than the proportional limit of the material**.** (See **Modulus of Elasticity**).

Conversion Factors from U.S. (Imperial) Units to SI (Metric) Units

To Convert From:	To:	Multiply By:
inches (in.)	millimeters (mm)	25.4
inches (in.)	meters (m)	0.0254
foot (ft)	meters (m)	0.3048
square inches (in.^{2})	square meters (m^2)	0.000645
cubic feet (ft^3)	cubic meters (m^3)	0.028317
cycles per second (cps)	Hertz (Hz)	1.0
pound-mass (lbm)	kilogram (kg)	0.453
pound-mass per foot (lbm/ft)	kilogram per meter (kg/m)	1.488
pound-force (lbf)	newton (N)	4.448
pound-force per foot (lbf/ft)	newton per meter (N/m)	14.59
kilopound-force (kip)	kilonewton (kN)	4.448
kilogram-force (kip)	newton (N)	9.806
pound-force per square foot (psf)	newton per square meters (N/m^2 = Pa)	47.88
pound-force per square inch (psi)	kilonewton per square meters (kN/m^2 = kPa)	6.895
pound force-inch (lbf-in.)	newton-meter (N-m)	0.1129
pound force-foot (lbf-ft)	newton-meter (N-m)	1.356
horsepower [hp = 550 lbf-ft/second (s)]	newton-meter per second (N-m/s = watt (w)	745.7

- Gravitational Acceleration (**g**): U.S. Units = 32.174 ft/s^2
- SI Units = 9.806 m/s^2

Recommended Multiple and Submultiple Units

Prefix	Symbol	Factor
giga	**G**	10^9 or 1,000,000,000
mega	**M**	10^6 or 1,000,000
kilo	**k**	10^3 or 1,000
milli	**m**	10^{-3} or 0.001
micro	**μ**	10^{-6} or 0.000001

INDEX

This page intentionally left blank

ABOUT THE AUTHOR

Ayman S. Mosallam, Ph.D., P.E., M.ASCE, holds professorships in the Departments of Civil and Environmental Engineering and of Materials and Chemical Engineering at the University of California, Irvine. He is also director of the Structural Engineering Testing Hall within the School of Engineering, and is a registered Structural Professional Engineer in the United States with over 30 years of experience in design, fabrication, and

development. While active in a broad area of engineering, he has a specific interest in polymer composites in general and pultruded polymer composites, with a particular emphasis on the importance of joints and connections in engineering practice.

Dr. Mosallam is a member of the Materials Directorate of the Construction Institute of ASCE and a control member of the ASCE Structural Composites and Plastics Committee (SCAP). He has served as chair of both the ASCE/SCAP Subcommittee on Education and the ASCE/SCAP Subcommittee on PFRP Composite Connections. Dr. Mosallam co-developed the "Pre-Standard for Load & Resistance Factor Design (LRFD) of Pultruded Fiber Reinforced Polymer (FRP) Structures," sponsored by ASCE and the Pultrusion Industry Council of the American Composites Manufacturers Association. The Pre-Standard serves as the primary foundation for the in-development ASCE Standard on pultruded composites. His intimate knowledge of the subject has led to his appointment as technical advisor to the ASCE Standards Committee.

Dr. Mosallam is chair of the International Committee on Composite Engineering, a member of the American Concrete Institute ACI 440 Committee, a member of the International Council of Non-Conventional Materials, and a member of the International Council of Multi-Functional Structural Systems, and serves on the Technical Advisory Board of the International Accreditation Service of the International Code Council. Finally, Dr. Mosallam is a leader in green building and sustainable infrastructure and the founder and founding member of several international green building councils.

In the area of pultruded composites in construction, Dr. Mosallam is a true pioneer. Starting in the mid-1980s, Dr. Mosallam completed several novel, frequently cited, and influential studies into the then-uncharted field of PFRP joints and connections. His work raised world-wide awareness regarding the dangers of unsafe "steel-like" pultruded framing connections and triggered an avalanche of research into the proper design and utilization of these critical components. With this background, Dr. Mosallam has served as an international consultant for several government agencies and numerous Fortune 500 companies. He also has acted as an expert witness in dozens of court cases related to damage of pultruded composites in general, and local failure of pultruded joints in particular.

Dr. Mosallam is a major contributor to and co-developer of two widely used acceptance criteria (AC125 and AC178) on the use of FRP composites in strengthening masonry and concrete structures published by the International Code Council. He is on the editorial boards of *Composites Part B: Engineering*, the *Journal of Reinforced Plastics and Composites*, *Materials & Design*, *Smart Structures and Systems*, *Advances in Civil Engineering*, and other journals. He has published over 400 technical papers, chapters, and

reports on structural performance of different building and infrastructural systems, with emphasis on pultruded structures and joints, and is the recipient of numerous prestigious awards, including the Outstanding Research Award from California State University, the Industry Impact Award from *Plastics World* magazine, and the *Modern Plastics* Best Paper Award. He is a two-time recipient of the Best Design Paper Award from the Composite Institute, and was named 2000 Outstanding Engineering Educator of the Year by the Orange County Branch of ASCE and 2007 Outstanding Civil Engineering Faculty Advisor by the Los Angeles Section of ASCE. During his academic career, he has authored, edited, or co-edited five books on composites for infrastructure.